

Dissertation zur Erlangung des Doktorgrades
der Fakultät für Chemie und Pharmazie
der Ludwig-Maximilians-Universität München

**Carbohydrate-Metal Chemistry:
Complexes of Palladium(II) and their Characterization via
NMR Spectroscopy and X-Ray Crystallography**



Thorsten Bastian Allscher

aus

Altötting am Inn

2011

Erklärung

Diese Dissertation wurde im Sinne von § 13 Abs. 3 der Promotionsordnung vom 29. Januar 1998 (in der Fassung der sechsten Änderungssatzung vom 16. August 2010) von Herrn Prof. Dr. Peter Klüfers betreut.

Ehrenwörtliche Versicherung

Diese Dissertation wurde selbständig, ohne unerlaubte Hilfe erarbeitet.

München, den 04. Juli 2011

Thorsten Allscher

Dissertation eingereicht am: 04. Juli 2011

1. Gutachter: Prof. Dr. Peter Klüfers
2. Gutachter: Prof. Dr. Konstantin Karaghiosoff

Mündliche Prüfung am: 02. August 2011

Diese Arbeit wurde in der Zeit von Oktober 2006 bis Juli 2011 am Department für Chemie und Pharmazie der Ludwig-Maximilians-Universität München am Lehrstuhl für Bioanorganische Chemie und Koordinationschemie unter Anleitung von Herrn Prof. Dr. Peter Klüfers durchgeführt.

Meinen Eltern

Contents

1 Introduction	1
1.1 The biological importance of carbohydrates	1
1.2 Industrial applications of carbohydrates	2
1.3 Carbohydrate structure and conformation	8
1.4 NMR spectroscopy and the Karplus equation	14
1.5 Aims of this work	17
2 Results	19
2.1 Palladium(II) fragments: nomenclature and characteristics	19
2.1.1 [Pd(dmen)(OH) ₂] and [Pd(tmen)(OH) ₂]	20
2.1.2 [Pd(tmchxn)(OH) ₂]	21
2.1.3 [Pd(teen)(OH) ₂]	23
2.1.4 [Pd(tn)(OH) ₂]	24
2.1.5 [Pd(bpy)(OH) ₂] and [Pd(phen)(OH) ₂]	24
2.2 Simple diols: ethane-1,2-diol and anhydroerythritol complexes with Pd-phen	26
2.3 The polyols: open-chain carbohydrate complexes of palladium(II)	28
2.3.1 The tetritols: erythritol and D-threitol	30
2.3.2 The pentitols: ribitol and xylitol	33
2.3.3 The hexitols	33
2.4 Palladium(II)–polyol complexes in neutral aqueous solution	47
2.4.1 μ -Triolato-chelation and ligand conformation at pH 8–9	48
2.4.2 Pd ₄ (μ -OH) ₄ -derived <i>threo</i> -tetraolato bridging at pH 7–8	54
2.4.3 Pd ₃ (μ -OH) ₃ -derived triolato bridging at pH 7–8	62
2.5 Dihydroxymalonic acid – complexes of palladium(II) with ketone hydrates	65
2.6 The inositols: from polyols to pyranose rings	66
2.7 Conformational fluctuation in palladium(II)–methyl aldopentopyranoside complexes	74

2.8 Metalation-induced conformational fluctuation of palladium(II)–aldopentose complexes	84
2.8.1 D-Arabinose	85
2.8.2 D-Ribose	91
2.8.3 D-Lyxose	95
2.8.4 D-Xylose	101
2.9 Coordination-induced shift patterns of palladium(II)–methyl hex(ul)oside complexes	105
2.9.1 The methyl hexopyranosides of D-galactose, D-glucose and D-mannose	105
2.9.2 The methyl fructosides	113
2.10 Palladium(II) chelation with Pd-tmen by the common hexoses	118
2.10.1 D-Galactose	119
2.10.2 D-Glucose	121
2.10.3 D-Mannose	123
2.11 The difficult determination of the palladium(II)–hexulose complexes	126
2.11.1 D-Fructose	127
2.11.2 D-Tagatose	130
2.11.3 L-Sorbose	133
2.11.4 D-Psicose	135
2.12 The dialdoses: A first investigation	137
2.12.1 <i>erythro</i> -Tetrodialdose	138
2.12.2 <i>xylo</i> -Pentodialdose	139
2.12.3 <i>galacto</i> -Hexodialdose	142
2.12.4 <i>D-manno</i> -Hexodialdose	145
2.13 The fructose-containing di- and trisaccharides	149
2.13.1 D-Sucrose	150
2.13.2 D-Turanose	152
2.13.3 D-Maltulose	153
2.13.4 D-Lactulose	154
2.13.5 D-Leucrose	155
2.13.6 D-Palatinose	157
2.13.7 D-Melecitose	158

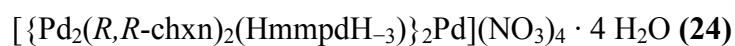
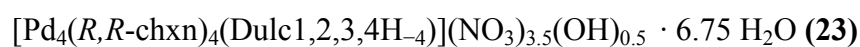
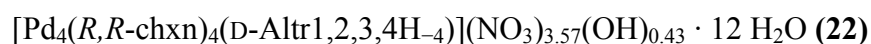
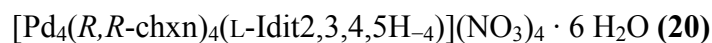
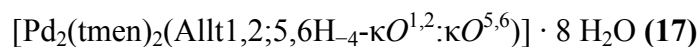
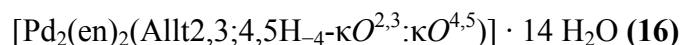
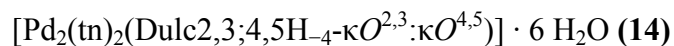
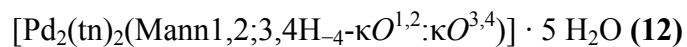
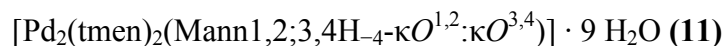
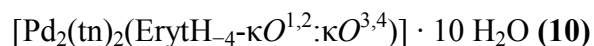
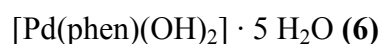
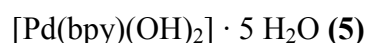
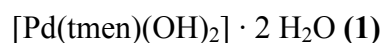
2.13.8 D-Raffinose	159
2.14 From disaccharides to the polysaccharides with β -connected units	161
2.14.1 D-Lactose	161
2.14.2 D-Cellobiose and Cellulose	163
2.15 From disaccharides to the oligosaccharides with α -connected units	166
2.15.1 α,α -D-Trehalose	168
2.15.2 D-Melibiose	169
2.15.3 D-Maltose	171
2.15.4 D-Maltotriose	173
2.15.5 D-Maltoheptaose and amylose	178
2.16 The cyclodextrins	181
3 Discussion	185
3.1 The Pd ^{II} N ₂ fragments: characteristics and differences	185
3.2 The Pd ^{II} N ₂ fragments' influence on the hydrogen-bonding network	186
3.3 Conformational fluctuation in palladium(II)–methyl aldopentopyranoside and aldopentose complexes	188
3.4 Metalation of the methyl hex(ul)osides	190
3.5 Metalation of the hexoses	190
3.6 The hexuloses' chelation preferences	193
3.7. The difficult analysis of the dialdoses	196
3.8 Metalation of di- and oligosaccharides	197
4 Summary	201
5 Experimental Section	207
5.1 Methods and materials	207
5.2 Reagents and solvents	207
5.3 NMR spectroscopy	210
5.4 Crystal structure determination and refinement	211
5.4 Preparation of palladium(II) compounds	212
5.4.1 [Pd(en)Cl ₂]	212
5.4.2 [Pd(en)(OH) ₂] (0.45 M)	212

5.4.3 [Pd(<i>R,R</i> -chxn)Cl ₂]	213
5.4.4 [Pd(<i>R,R</i> -chxn)(OH) ₂] (0.45 M)	213
5.4.5 <i>N,N,N',N'</i> -tetramethyl-(1 <i>R,2R</i>)-cyclohexane-1,2-diamine (tmchxn)	213
5.4.6 [Pd(tmchxn)Cl ₂]	214
5.4.7 [Pd(tmchxn)(OH) ₂] (0.45 M)	214
5.4.8 [Pd(dmen)Cl ₂]	215
5.4.9 [Pd(dmen)(OH) ₂] (0.45 M)	215
5.4.10 [Pd(tmen)Cl ₂]	215
5.4.11 [Pd(tmen)(OH) ₂] (0.45 M)	215
5.4.12 [Pd(teen)Cl ₂]	216
5.4.13 [Pd(teen)(OH) ₂] (0.45 M)	216
5.4.14 [Pd(tn)Cl ₂]	216
5.4.15 [Pd(tn)(OH) ₂] (0.45 M)	217
5.4.16 [Pd(bpy)Cl ₂]	217
5.4.17 [Pd(bpy)(OH) ₂] (0.45 M)	217
5.4.18 [Pd(phen)Cl ₂]	217
5.4.19 [Pd(phen)(OH) ₂] (0.45 M)	218
5.5 Preparation of carbohydrates	218
5.5.1 Methyl α -D-lyxopyranoside	218
5.5.2 Methyl D-fructosides	218
5.5.3 <i>xyl</i> -Pentodialdose	219
5.5.4 <i>galacto</i> -Hexodialdose	219
5.5.5 D- <i>manno</i> -Hexodialdose	220
5.6 Preparation of the crystalline compounds	221
5.6.1 Dihydroxido- <i>N,N,N',N'</i> -tetramethylethane-1,2-diamine-palladium(II) dihydrate	221
5.6.2 η^2 -Carbonato- <i>N,N,N',N'</i> -tetramethyl-(1 <i>R,2R</i>)-cyclohexane-1,2-diamine-palladium(II) hexahydrate	221
5.6.3 <i>N,N,N',N'</i> -tetraethylethane-1,2-diammonium tetrachloridopalladate(II)	221
5.6.4 Dichlorido- <i>N,N,N',N'</i> -tetraethylethane-1,2-diamine-palladium(II) dihydrate	221
5.6.5 2,2'-Bipyridine-dihydroxido-palladium(II) pentahydrate	222

5.6.6 Dihydroxido-1,10-phenanthroline-palladium(II) pentahydrate	222
5.6.7 Ethanediolato- $\kappa O^{1,2}$ -1,10-phenanthroline-palladium(II) heptahydrate	222
5.6.8 Anhydroerythritolato- $\kappa O^{2,3}$ -1,10-phenanthroline-palladium(II) 4.5-hydrate.....	222
5.6.9 Bis(<i>N,N'</i> -dimethylethane-1,2-diamine)(erythritolato- $\kappa O^{1,2}:\kappa O^{3,4}$)dipalladium(II) 14-hydrate.....	222
5.6.10 Dipropane-1,3-diamine(erythritolato- $\kappa O^{1,2}:\kappa O^{3,4}$)dipalladium(II) 10-hydrate	223
5.6.11 Bis(<i>N,N,N',N'</i> -tetramethylethane-1,2-diamine)(mannitolato- $\kappa O^{1,2}:\kappa O^{3,4}$)dipalladium(II) 9-hydrate.....	223
5.6.12 Dipropane-1,3-diamine(mannitolato- $\kappa O^{1,2}:\kappa O^{3,4}$)dipalladium(II) 5-hydrate	223
5.6.13 Bis(<i>N,N'</i> -dimethylethane-1,2-diamine)(dulcitolato- $\kappa O^{2,3}:\kappa O^{4,5}$)dipalladium(II) 8-hydrate	223
5.6.14 Dipropane-1,3-diamine(dulcitolato- $\kappa O^{2,3}:\kappa O^{4,5}$)dipalladium(II) 6-hydrate	224
5.6.15 Bis(<i>N,N,N',N'</i> -tetramethylethane-1,2-diamine)(D-altritolato- $\kappa O^{2,3}:\kappa O^{4,5}$)dipalladium(II) 9-hydrate	224
5.6.16 Diethane-1,2-diamine(allitolato- $\kappa O^{2,3}:\kappa O^{4,5}$)dipalladium(II) 14-hydrate	224
5.6.17 Bis(<i>N,N,N',N'</i> -tetramethylethane-1,2-diamine)(allitolato- $\kappa O^{1,2}:\kappa O^{5,6}$)dipalladium(II) 8-hydrate	224
5.6.18 [(Pd ^{II} N ₂) _n (μ_2 -OH) _n] ⁿ⁺ -derived bridged compounds at pH 7–8.....	225
5.6.19 [Pd ₄ (<i>R,R</i> -chxn) ₄ (C ₃ O ₆)(μ -OH)](NO ₃) ₃ · 8 H ₂ O.....	225
5.6.20 Diethane-1,2-diamine(D- <i>chiro</i> -inositolato- $\kappa O^{1,2}:\kappa O^{5,6}$)dipalladium(II) 8-hydrate	225
5.6.21 Bis(<i>N,N,N',N'</i> -tetramethylethane-1,2-diamine)(<i>neo</i> -inositolato- $\kappa O^{1,6}:\kappa O^{3,4}$)- dipalladium(II) 22-hydrate.....	225
5.6.22 Tris(<i>N,N,N',N'</i> -tetramethylethane-1,2-diamine)(<i>scyllo</i> -inositolato- $\kappa O^{1,2}:\kappa O^{3,4}:\kappa O^{5,6}$)- tripalladium(II) 23-hydrate	226
5.6.23 (1 <i>R</i> ,2 <i>R</i>)-Cyclohexane-1,2-diamine(methyl α -D-lyxopyranos-2,3-O-diato- $\kappa O^{2,3}$)- palladium(II) 2.25-hydrate.....	226
5.6.24 <i>N,N,N',N'</i> -Tetramethylethane-1,2-diamine(methyl β -D-xylopyranos-2,3-O-diato- $\kappa O^{2,3}$)palladium(II)- <i>N,N,N',N'</i> -tetramethylethane-1,2-diamine(methyl β -D-xylopyranos-3,4-O- diato- $\kappa O^{3,4}$)palladium(II) dihydrate	226
5.6.25 Bis(<i>N,N,N',N'</i> -tetramethylethane-1,2-diamine)(β -D-arabinopyranos-1,2;3,4-O-diato- $\kappa O^{1,2}:\kappa O^{3,4}$)dipalladium(II) 10-hydrate	226

5.6.26 Bis(<i>N,N,N',N'</i> -tetramethylethane-1,2-diamine)(β -D-lyxopyranos-1,2;3,4-O-diato- $\kappa O^{1,2}:\kappa O^{3,4}$)dipalladium(II) 10-hydrate	227
5.6.27 <i>N,N,N',N'</i> -Tetramethylethane-1,2-diamine(methyl α -D-galactopyranos-3,4-O-diato- $\kappa O^{3,4}$)palladium(II) 8-hydrate	227
5.6.28 <i>N,N'</i> -Dimethylethane-1,2-diamine(methyl α -D-galactopyranos-3,4-O-diato- $\kappa O^{3,4}$)palladium(II) 9-hydrate.....	227
5.6.29 <i>N,N,N',N'</i> -Tetramethylethane-1,2-diamine(methyl α -D-mannopyranos-2,3-O-diato- $\kappa O^{2,3}$)palladium(II) 3.5-hydrate	227
5.6.30 (1 <i>R</i> ,2 <i>R</i>)-Cyclohexane-1,2-diamine(methyl α -D-fructofuranos-1,3-O-diato- $\kappa O^{1,3}$)palladium(II) 2-hydrate.....	228
5.6.31 Bis(<i>N,N,N',N'</i> -tetramethylethane-1,2-diamine)(α -D-tagatopyranos-1,2;3,4-O-diato- $\kappa O^{1,2}:\kappa O^{3,4}$)dipalladium(II) 8-hydrate	228
5.6.32 Bis(<i>N,N,N',N'</i> -tetramethylethane-1,2-diamine)(<i>erythro</i> -tetrodialdofuranos 1,4;2,3-O-diato- $\kappa O^{1,4}:\kappa O^{2,3}$)dipalladium(II) 8-hydrate	228
5.6.33 [Pd ₃ (teen) ₃ (α -CDH ₋₆)] · 34 H ₂ O	228
5.6.34 [Pd ₃ (tmen) ₃ (α -CDH ₋₆)] · 20.7 H ₂ O · acetone.....	229
5.6.35 [Pd ₄ (teen) ₄ (γ -CDH ₋₈)] · 12 H ₂ O.....	229
5.6.36 [Pd ₄ (tmen) ₄ (γ -CDH ₋₈)] · 65.79 H ₂ O · 0.96 [Pd(tmen)CO ₃]	229
5.7 ¹ H NMR chemical shifts of the methyl pentosides and hex(ul)osides, the pentoses, the hex(ul)oses and the dialdoses.....	230
5.8 Computational methods and results	239
6 Appendix	241
6.1 ¹³ C NMR spectra and chemical shifts of uncoordinated carbohydrates.....	241
6.2 Packing diagrams of the crystal structures.....	282
6.3 Crystallographic tables.....	327
Bibliography.....	343

List of crystal compounds



- [Pd₆(*R,R*-chxn)₆(μ₄-O)(μ-OH)₄](NO₃)₆ · 12.5 H₂O **(25)**
- [Pd₄(*R,R*-chxn)₄(C₃O₆)(μ-OH)](NO₃)₃ · 8 H₂O **(26)**
- [Pd₂(en)₂(*D-chiro*-Ins1,2;5,6H₋₄)] · 8 H₂O **(27)**
- [Pd₂(tmen)₂(*neo*-Ins1,6;3,4H₋₄-κO^{1,6}:κO^{3,4})] · 22 H₂O **(28)**
- [Pd₃(tmen)₃(*scyllo*-InsH₋₆-κO^{1,2}:κO^{3,4}:κO^{5,6})] · 23 H₂O **(29)**
- [Pd(*R,R*-chxn)(Me-α-*D*-Lyxp2,3H₋₂-κO^{2,3})] · 2.25 H₂O **(30)**
- [Pd(tmen)(Me-β-*D*-Xylp2,3H₋₂-κO^{2,3})] [Pd(tmen)(Me-β-*D*-Xylp3,4H₋₂-κO^{3,4})] · 2 H₂O **(31)**
- [Pd₂(tmen)₂(⁴C₁-β-*D*-Arap1,2;3,4H₋₄-κO^{1,2}:κO^{3,4})] · 10 H₂O **(32)**
- [Pd₂(tmen)₂(⁴C₁-β-*D*-Lyxp1,2;3,4H₋₄-κO^{1,2}:κO^{3,4})] · 10 H₂O **(33)**
- [Pd(tmen)(⁴C₁-Me-α-*D*-Galp3,4H₋₂-κO^{3,4})] · 8 H₂O **(34)**
- [Pd(dmen)(⁴C₁-Me-α-*D*-Galp3,4H₋₂-κO^{3,4})] · 9 H₂O **(35)**
- [Pd(tmen)(⁴C₁-Me-α-*D*-Manp2,3H₋₂-κO^{2,3})] · 3.5 H₂O **(36)**
- methyl β-*D*-fructopyranoside **(37)**
- [Pd(*R,R*-chxn)(Me-α-*D*-Fru_f1,3H₋₂-κO^{1,3})] · 2 H₂O **(38)**
- [Pd₂(tmen)₂(α-*D*-Tagp1,2;3,4H₋₄-κO^{1,2}:κO^{3,4})] · 8 H₂O **(39)**
- [Pd₂(tmen)₂(Ery4ald_fH₋₄-κO^{1,4}:κO^{2,3})] · 12 H₂O **(40)**
- 2,3;4,5-di-*O*-isopropylidene-*D*-manno-hexodialdose **(41)**
- [Pd₃(teen)₃(α-CDH₋₆)] · 34 H₂O **(42)**
- [Pd₃(tmen)₃(α-CDH₋₆)] · 20.7 H₂O · acetone **(43)**
- [Pd₄(teen)₄(γ-CDH₋₈)] · 12 H₂O **(44)**
- [Pd₄(tmen)₄(γ-CDH₋₈)] · 65.79 H₂O · 0.96 [Pd(tmen)CO₃] **(45)**

Abbreviations

All abbreviations were chosen according to the guidelines of the IUPAC or were derived from existing abbreviations.

1,6AnGlc	1,6-anhydro- β -D-glucose
an	anhydro
Allt	alltiol
Altr	altritol
AnEryt	anhydroerythritol
Ara	arabinose
Arab	arabitol
bpy	2,2'-bipyridine
CD	cyclodextrin
chxn	(1 <i>R</i> ,2 <i>R</i>)-cyclohexane-1,2-diamine
CIS	Coordination Induced Shift
dmen	<i>N,N'</i> -dimethylethane-1,2-diamine
Dulc	dulcitol
en	ethane-1,2-diamine
Ery4ald	<i>erythro</i> -tetrodialdose
Eryt	erythritol
Ethd	ethane-1,2-diol
<i>f</i>	furanose
Fru	fructose
Gal	galactose
Gal6ald	<i>galacto</i> -hexodialdose
Glc	glucose

Glyc	glycerol
Hmmpd	2-hydroxymethyl-2-methylpropane-1,3-diol
htn	2-hydroxy-propane-1,3-diamine
Idit	iditol
Ins	inositol
Lyx	lyxose
Man	mannose
Man6ald	<i>manno</i> -hexodialdose
Mann	mannitol
ox	oxalate
<i>p</i>	pyranose
Pd-bpy	aqueous solution of [Pd(bpy)(OH) ₂]
Pd-chxn	aqueous solution of [Pd(<i>R,R</i> -chxn)(OH) ₂]
Pd-dmen	aqueous solution of [Pd(dmen)(OH) ₂]
Pd-en	aqueous solution of [Pd(en)(OH) ₂]
Pd-phen	aqueous solution of [Pd(phen)(OH) ₂]
Pd-teen	aqueous solution of [Pd(teen)(OH) ₂]
Pd-tmchxn	aqueous solution of [Pd(tmchxn)(OH) ₂]
Pd-tmen	aqueous solution of [Pd(tmen)(OH) ₂]
Pd-tn	aqueous solution of [Pd(tn)(OH) ₂]
phen	1,10-phenanthroline
Psi	psicose
Rib	ribose
Ribt	ribitol
sc	synclinal
Sor	sorbose
Sorb	sorbitol

Tag	tagatose
teen	<i>N,N,N',N'</i> -tetraethylethane-1,2-diamine
Tetr	tetritol
Thre	threitol
tm-2,1:3,2-tet	1,3-bis(2'-dimethylaminoethyl)hexahydropyrimidine
tmchxn	<i>N,N,N',N'</i> -tetramethyl-(1 <i>R</i> ,2 <i>R</i>)-cyclohexane-1,2-diamine
tmen	<i>N,N,N',N'</i> -tetramethylethane-1,2-diamine
tn	propane-1,3-diamine
Xyl	xylose
Xyl5ald	<i>xyl</i> o-pentodialdose
Xylt	xylitol

1 Introduction

1.1 The biological importance of carbohydrates

Carbohydrates are ubiquitous and belong to the four most important classes of macromolecules in nature, namely nucleic acids, proteins, carbohydrates and lipids. Moreover, only carbohydrates can be found in direct association with all three of the rest. In two important characteristics carbohydrates differ from the other two classes of biological polymers: they can be highly branched molecules, and their monomeric units may be connected to one another by many different linkage types. These characteristic features allow carbohydrates to provide almost unlimited variations in their structures. The terms glycoprotein and glycolipid are used to reflect the fact that the majority of carbohydrates present in cells are attached to proteins or lipids, although carbohydrates can also be present without being attached to other molecules. Furthermore, such a highly branched oligomeric carbohydrate is often referred to as an oligosaccharide.^[1]

In the early days of the functional characterization of biopolymers, it was thought that carbohydrates had two roles, namely structural functions and energy storage. The development of effective methods for characterizing carbohydrate structures and functions during the last decades has revealed that carbohydrates are integrally involved in a multitude of biological systems.^[2] Glycoproteins are fundamental to many important biological processes including fertilization, embryogenesis, immune defense, viral replication, parasitic infection, cell growth, tissue repair, neuronal development, degradation of blood clots and inflammation, among others. Glycoproteins and glycolipids, together with proteoglycans and glycosphosphatidylinositol-linked proteins (GPI anchor) are major components of the outer surface of mammalian cells, with carbohydrates covalently attached through either a nitrogen atom (supplied by the amino acid asparagine) or an oxygen atom (supplied by serine or threonine).^[1, 3] These so-called glycans form an individual layer known as the glycocalyx, ranging from 10 to 100 pm in thickness.^[4]

Structural encoding and storage of biological information is another property of complex oligosaccharides. This information is decoded by non-covalent complexes between carbohydrate ligands and protein receptors. These proteins were called lectins or selectins, specialized to selectively recognize certain sections of oligosaccharides. These carbohydrate–protein interactions are fundamental for many biological processes such as cell–cell adhesion and communication.^[3]

1 Introduction

Oligosaccharide structures change dramatically during development, and it has been shown that specific sets of oligosaccharides are expressed at distinct stages of differentiation. Furthermore, alterations in cell surface oligosaccharides are associated with various pathological conditions including malignant transformation.^[1] Oligosaccharides can modify the intrinsic properties of proteins to which they are attached by altering the stability, protease resistance, or quaternary structure. The large size of oligosaccharides may enable them to cover functionally important areas of proteins, to adjust the interactions of glycoconjugates with other molecules, and to affect the rate of processes which involve conformational changes. Glycosylation is highly sensitive to alterations in cellular function, and abnormal glycosylation is diagnostic of a number of disease states including rheumatoid arthritis and cancer.^[1]

A prominent example for carbohydrate-encoded biological information is the well-known AB0(H) blood group system. It consists of three antigens H, A and B and is the most important in blood transfusions. The H antigen, the precursor for the other two, is the disaccharide α -L-Fucp-(1→2)- β -D-Galp. Addition of *N*-acetyl- α -D-galactosamine in (1→3)-linkage to the β -D-galactopyranose of the H structure gives the A antigen, α -L-Fucp-(1→2)-[α -D-GalpNAc-(1→3)]- β -D-Galp. The B antigen differs from the A antigen in having α -D-galactopyranose instead of *N*-acetyl- α -D-galactosamine. Depending on the presence and/or absence of the A and B antigens, individuals are broadly classified as belonging to one of the four groups: 0, A, B and AB. Individuals in the 0 group express only the H determinant and carry anti-A and anti-B antibodies. Those in the AB group express both the antigens and have antibodies to neither.^[5]

1.2 Industrial applications of carbohydrates

Being polyfunctional in nature, carbohydrates participate in a multitude of chemical and biochemical reactions, making them ideal scaffolds for industrial applications. With the annual worldwide production of about 200 billion tons of carbohydrates by photosynthesis, carbohydrates are the most abundant natural products. About 11% of raw materials used by the German industry are renewable.^[6] Throughout the years 2006–2009, the annual German sugar production fluctuated between 3.5 and 4 million tons and human consumption did not exceed three million tons per year. As a consequence of the European Quota System (Germany's quota 2.9 million tons), significant surpluses exist which cannot be exported to

1 Introduction

the full extent but must be used for industrial conversions. It is estimated that per year, approximately 50,000–60,000 tons of sugar, supplementing molasses, are used for yeast fermentation, 180,000–200,000 tons for the fermentation of fine chemicals, food, feed and pharmaceutical additives and 300,000–400,000 tons for bio ethanol production.^[7]

Since the responsibility for developing appropriate food products with balanced functionality and nutritional value has shifted from domestic kitchens to the development laboratories of food manufacturing companies, polyols and monosaccharides are of considerable interest and value to the commercial food sector. Nutritive sweeteners not only provide nutrition, bulk, sweetness, and moisture control, furthermore, as Maillard reaction products they are important elements in the flavor and color profiles of different foods. In fact, the adulteration of honey using high fructose corn syrup or the application of invert sugar produced by the hydrolysis of the disaccharide sucrose to its component monosaccharides are only two examples of monosaccharide-based sweeteners used in the food industry.^[8]

Another example for the interest of the food industry in monosaccharides is the employment of crystalline fructose to provide sweetness without causing the spike in blood glucose with its resulting elevated insulin level which is important for people with diabetes. D-Fructose is produced commercially by the enzyme-catalyzed epimerization of D-glucose and has been recognized as having a relatively low glycemic index because it is not metabolized as rapidly as glucose is. Also polyols can provide sweetness, texture, and bulk in many sugar-free applications as well and are metabolized more slowly by mammalian systems. They can serve as humectants, cryoprotectants and aids to control freezing point depression. The benefits of polyols in food and confectionery products include reduced caloric content, reduced glycemic response, and reduced cariogenicity, especially with xylitol. Polyols are generally not fermented by oral bacteria, so that acid production is minimized while plaque production is not supported. Xylitol has been reported to actually reduce cariogenesis and, consequently, is in great demand for chewing gum, and sorbitol (glucitol) is used heavily in toothpaste to help maintain its creamy texture. The lack of a free aldehyde or ketone group means that polyols will also not participate in Maillard-type browning reactions.^[8]

The current non-food utilization of carbohydrates as a chemical feedstock—be it for bulk, intermediate or fine chemicals, pharmaceuticals, agrochemicals, or high-value-added speciality chemicals—is modest and only a few examples are presently realized on an industrial scale. The most common example is the bio-based manufacturing of ethanol by

1 Introduction

fermentation of glucose to replace the petrochemically-based process from ethane and its use as a fuel additive. However, the fermentation generates two moles of CO₂ per mole of sugar and therefore, the process does not contribute to the reduction of CO₂ in the environment. Another fermentation-based process starting from glucose-containing materials such as sucrose, whey or starch is the large-scale production of lactic acid. Besides its major use in the food industry, recent non-food applications have made it a large-scale organic commodity chemical, most of which is subsequently polymerized via its cyclic dimer (lactide) to a high molecular weight polyester, polylactic acid. Due to its high strength, it can be fabricated into fibers, films, and rods that are fully biodegradable and compostable, having degraded within two months. Accordingly, polylactic acid and copolymers of lactic and glycolic acid are of particular significance for food packaging and for agricultural or gardening applications. Another development based on lactic acid is its ethyl ester. As a most benign solvent it has the potential to displace various petrochemically based solvents such as acetone, DMF or toluene in industrial processes.^[9]

Sugar-based surfactants, such as sorbitan esters, sucrose esters and alkyl polyglycosides are well established in industrial products due to their advantages with regard to performance, the health of consumers and environmental compatibility compared to some standard products. Considering the amphiphilic structure of a typical surfactant with a hydrophilic head group and a hydrophobic tail, it has always been a challenge to attach a carbohydrate molecule as the perfect hydrophilic group to a fat and oil derivative, such as a fatty acid or a fatty alcohol, due to their numerous hydroxy groups. Although numerous ways of making such linkages with a large number of different carbohydrates used in such reactions are reported in the literature, it is clear from an industrial perspective, since only a few carbohydrates fulfill the criteria of price, quality, and availability, that they are an interesting raw material source. Sorbitan esters are used mainly as emulsifiers for food or as textile auxiliaries at a volume of approx. 20,000 tons per year. With an actual market size of about < 4,000 tons per year, the relatively hydrophobic sucrose esters are applied mainly as emulsifiers for food and cosmetics. Alkyl polyglycosides and fatty acid glucamides represent a perfect amphiphilic structure with excellent surface activity as well as solubility due to highly selective syntheses. A total capacity of approx. 80,000 tons per year of alkyl polyglycosides have been established for industrial processes for use in cosmetics, manual dishwashing and detergent applications.^[10]

1 Introduction

These few examples of industrial sugar-based non-food products represent a modest beginning in the endeavor to replace petrochemicals by carbohydrates as a chemical feedstock. Nevertheless, their potential as an organic raw material for the elaboration of industrially useful chemicals is far from being fully explored.^[9]

In the same way, carbohydrates are a relatively unexploited source of new drugs for the pharmaceutical industry and therefore offer exciting new therapeutic opportunities. Although carbohydrates play an important part in innumerable biological processes, carbohydrates and carbohydrate-derived drugs cover only a limited area of the world of therapeutics. Current advances in the functional understanding of carbohydrate–protein interactions of over eighty carbohydrate-binding proteins have enabled the development of a new class of small-molecule drugs, known as glycomimetics, which form a novel class of therapeutics. These compounds mimic the bioactive function of carbohydrates and evade the disadvantages of carbohydrate lead structures, namely their low activity and insufficient drug-like properties. Pharmacokinetic drawbacks are linked to carbohydrate-based drugs' high polarity – they are unable to cross passively through the enterocyte layer in the small intestine – a prerequisite for oral availability. Prominent examples (Fig. 1.1) are the low-molecular-weight heparins, derived from pigs' small intestine mucosa, and fondaparinux (Arixtra; GlaxoSmithKline), which are used as anticoagulants. In other cases such as the inhibition of α -glycosidases in the brush border of the small intestine for the treatment of diabetes (by voglibose (Basen/Glucostat/Volix; Takeda), miglitol (Glyset; Pfizer) and acarbose (Glucobay/Prandase/Precose; Bayer)) or the inhibition of viral neuraminidases in the pharyngeal mucosa (by zanamivir (Relenza; GlaxoSmithKline)) oral availability is not required. The paradigm of a glycomimetic drug in the classical sense is oseltamivir (Tamilu; Gilead/Roche). Starting from a carbohydrate lead structure 2,3-didehydro-2-deoxy-*N*-acetylneuraminic acid (Neu5Ac2en), an orally available prodrug was designed by systematically eliminating polar groups and metabolic 'soft spots' that were not required for affinity.^[4]

1 Introduction

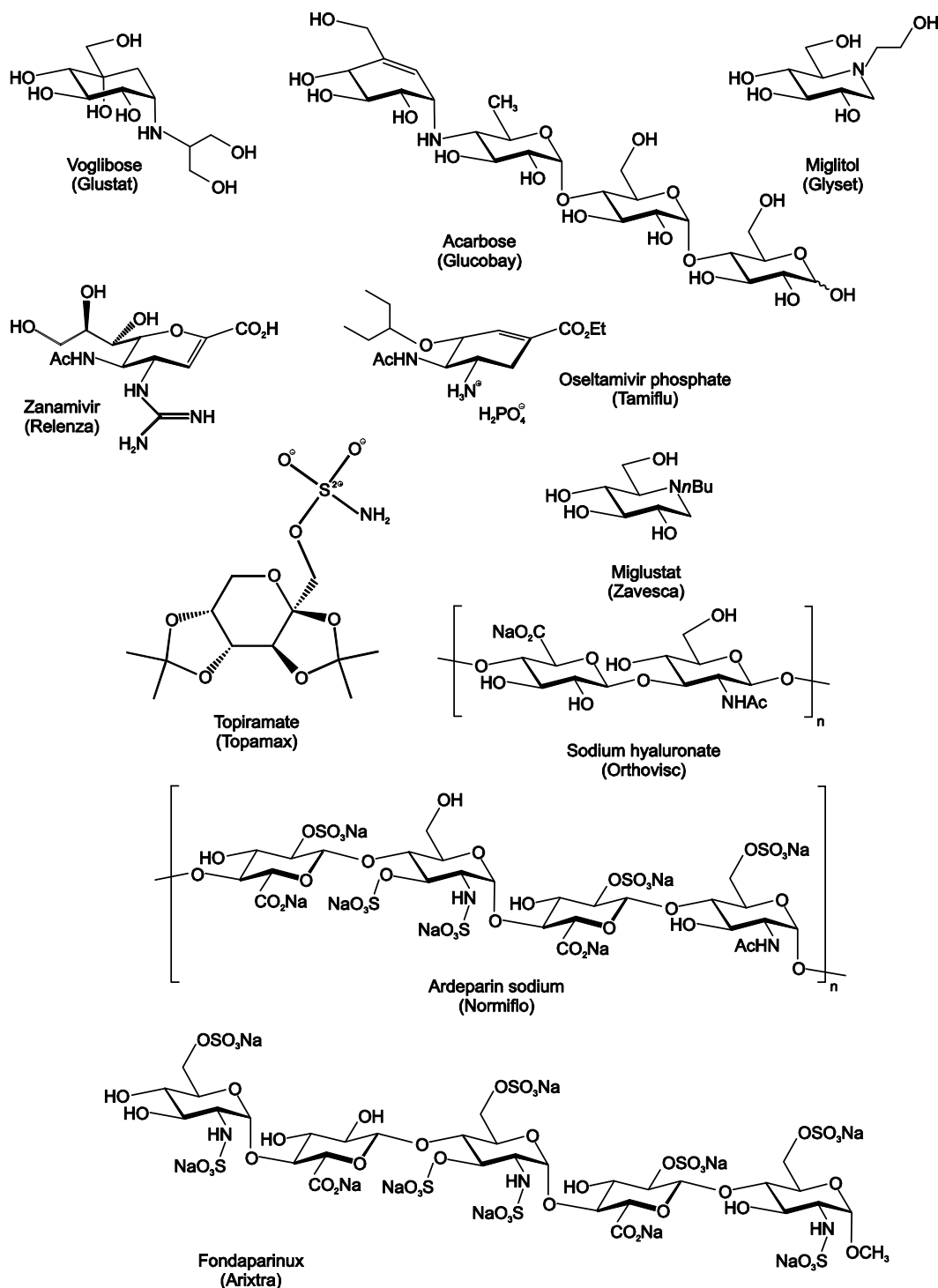


Figure 1.1. Carbohydrate and carbohydrate-derived drugs. Structures of currently approved drugs (trade name in brackets). These include glycosidase inhibitors that prevent the digestion of carbohydrates for the treatment of diabetes (voglibose, acarbose and miglitol) and the prevention of influenza virus infections (zanamivir and osetamivir phosphate). Further carbohydrate-derived drugs are used to treat Gaucher's disease (miglustat), epilepsy (topiramate) and osteoarthritis (sodium hyaluronate). In addition, sulphated glycosaminoglycans, which function as anticoagulants by binding to antithrombin III for the treatment of thrombosis (e.g. ardeparin sodium or fondaparinux).

1 Introduction

Raw starch is used as native, converted into physical-chemical modificates or hydrolyzed to starch sugars. Native starch is derived from wheat, maize or potatoes and the current usage is estimated at 450,000–500,000 tons with a decreasing tendency. Native starch is primarily used in the food industry and in the manufacturing of paper and in corrugating. In all these application areas however, native starch is increasingly being substituted by modified starches as these products comply better with the demand for functionality and streamlined manufacturing processes. Currently, 450,000 tons of modified starches and special starch mixes are used mostly in food and paper manufacturing. 500,000–550,000 tons of extracted raw starch are usually hydrolyzed and converted to maltodextrine, glucose and dextrose syrups.^[7]

Cellulose is the most important plant's structural support molecule; the associated heteropolysaccharides (“hemicelluloses”) serve to provide for moisture sorption, fracture toughness, and storage energy. For industrial use, cellulose is mainly obtained from wood pulp and cotton under removal of lignin and hemicelluloses. It is used not only to produce paperboard and paper; to a smaller extent it is converted into a wide variety of derivative products. The chemical-physical conversion of cellulose in Germany is carried out by only two companies. Both are specialized in ether technology and consequently the total production of cellulose derivatives in the range of 200,000 tons comprizes mostly these products. However, the application of cellulose derivatives outside the traditional sectors of paper and construction is still small and only moderately developing.^[7] Cellulose ethers are applied to cigarette filters, textiles, thermoplasts, explosives, and enamels, while cellulose esters are additives in the detergent industry, the cosmetic industry and the textile industry. Viscose, the oldest industrial-scale manufactured fibre, is produced with regenerated cellulose films and fibres. Nowadays the hundred-years-old CS₂-containing viscose process with cellulose xanthogenate as intermediate has been replaced by the ecological lyocell process which uses *N*-methylmorpholine-*N*-oxide (NMMO) to dissolve cellulose.^[11]

As we see, carbohydrates already play key roles as raw materials in the chemical and pharmaceutical industries. Nevertheless, whereas nature has perfected the use of carbohydrates, the industrial or pharmaceutical application is still in its infancy. In consequence, it is imperative that carbohydrates, as important raw materials, are systematically further investigated.

1.3 Carbohydrate structure and conformation

Carbohydrate molecules have complex personalities.^[12] Reducing sugars exist in solution in various cyclic and acyclic forms.^[13] The common cyclic forms include pyranoses and furanoses, whereas acyclic forms include the carbonyl and hydrate forms, as shown in Figure 1.2 for D-glucose.

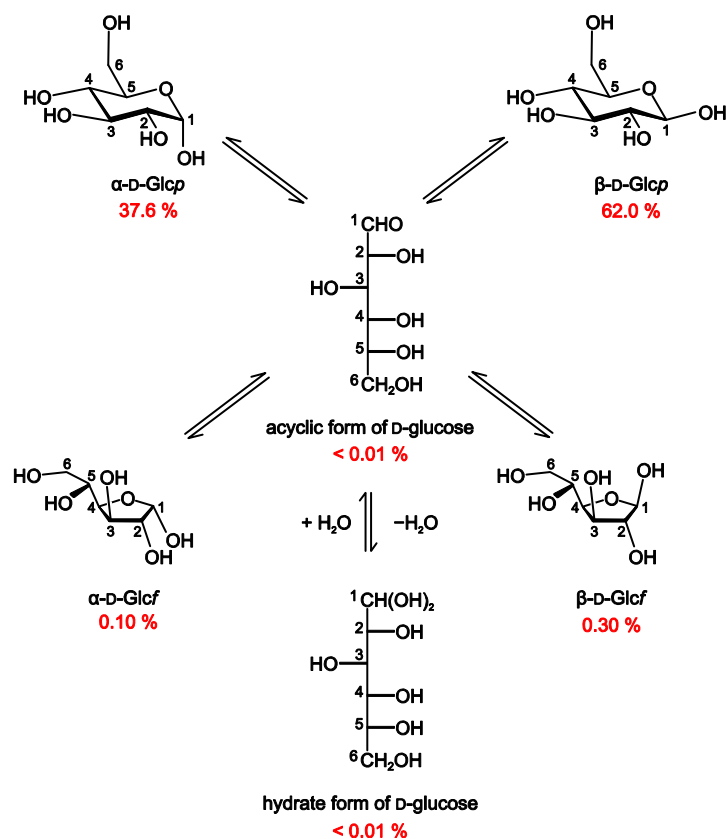


Figure 1.2. The isomerization of D-glucose in aqueous solution. The percentages of cyclic and acyclic forms of D-[1-¹³C]glucose were determined at 30 °C in D₂O.^[14]

The sugars in their pyranose or furanose form can be represented by Haworth projection formulae. These projections are widely used to represent carbohydrates although they suggest mistakenly that the six-membered ring is planar which is not the case. The pyranose ring, in reality, puckers to form different conformations with the approximate shape of a chair.^[5] In general, chair forms are preferred,^[13] although other ring forms such as boat and skew-boat (twist-boat) conformations can also be realized for the pyranose ring. The two chair conformations are mirror images of each other and are designated as ⁴C₁ and ¹C₄. They can be visualized as having two ring atoms puckered above and below the plane formed by the remaining four ring atoms. The atom puckered above the plane is represented as superscript on the left and the atom puckered below as subscript on the right side of the C.

1 Introduction

Altogether, six boat conformations are possible for pyranose rings depending on which pair of atoms are puckered out of the “best plane” and on whether they are above or below. Besides the chair and the boat forms, the pyranose ring can adopt a third puckered form called the twist-boat or skew-boat. In this form, the first and the third atoms are puckered out of the plane formed by the remaining four ring atoms. As with the boat form, six skew-boat forms are possible. It is important to remember that the chair, boat and twist-boat conformations represent distinct families of pyranose ring conformations. Small changes in molecular geometry lead to a number of different conformations which can be categorized under one of these families.

In the chair conformation, the two exocyclic substituents on the ring carbon atoms are not geometrically or chemically equivalent; one of them is oriented parallel to and the other, somewhat perpendicular to the axis of the pyranose ring. They are said to be axial and equatorial, respectively, and are indicated by the corresponding letters “ax” and “eq”. Since 4C_1 and 1C_4 represent two different conformations of the same ring, in principle, it is possible for a sugar molecule to convert from one chair to the other without breaking bonds. Such a conversion brings about a change in orientation of the substituent from axial to equatorial and vice versa. For example, in Fig. 1.2 all the hydroxy groups of β -D-glucopyranose are in equatorial orientations in the 4C_1 conformation, but they are all axial in the 1C_4 conformation. Since β -D-glucopyranose is the mirror image of β -L-glucopyranose, the orientation of the substituents remains the same but the conformation of the pyranose ring changes. Thus, the orientations of the exocyclic substituents for the pento- and hexopyranoses are all the same in 4C_1 (D) and 1C_4 (L) forms.^[5]

For simple monosaccharides, a general rule is that equatorial substituents confer stability to a given chair form, whereas axial substituents are destabilizing. The magnitude of the latter effect is particularly strong for exocyclic hydroxymethyl groups. Thus, for example, the preferred chair form of both anomers of D-glucopyranose is 4C_1 in which no (β -anomer) or only one (O1, α -anomer) substituent is axial. As the number of axial and equatorial substituents within a given chair form become comparable, the difference in the stabilities of both chair forms decreases. In this situation, both chair forms will be present in measurable quantities in solution.

To contribute to a better understanding of the stereochemistry and the resulting conformation of simple sugars, the effect of side groups' various steric arrangements and their effect on the

1 Introduction

stability of the pyranose or furanose ring shapes were investigated in-depth. A first approach was the estimation of the relative free energies of the different pyranose-ring conformations in aqueous solution using empirical additive schemes such as the Hassel and Ottar scheme.^[15] It postulates that the steric arrangement (1,3-diaxial interaction) which places the axially oriented hydroxymethyl and hydroxy groups on the same side of the ring is unstable (also called the Hassel–Ottar effect).

Another approach was the determination of predominant conformations of many methyl glycosides by studying the complexes which some of them form with the cuprammonium reagent by Reeves.^[16-17] According to Reeves, complex formation requires the presence of two hydroxy groups quite close to each other: an equatorial and an axial, or two equatorial. Hydroxy groups on adjacent carbon atoms are suitable, as are two *syn*-axial hydroxy groups. In consequence, the Reeves–Kelly scheme evolved which supplemented the Hassel–Ottar scheme by considering that any axial group other than hydrogen also imparts instability to the pyranose ring. Even though the Reeves–Kelly scheme explained the preferred conformations assigned for aldopyranoses from cuprammonium complexes, it differs from the Hassel–Ottar scheme in many cases. Several important interactions such as *syn*-diaxial hydroxy groups and the anomeric effect were not considered in assigning the relative stabilities of various chair conformations.

Significant progress was made by Angyal^[13] who assigned free energies for all the hexo- and pentopyranoses, taking into account the various interactions which impart instability to the ring and the anomeric effect. In aqueous solutions, the conformations of the aldohexopyranoses are governed mainly by the disposition of the bulkiest substituent, the hydroxymethyl group, which tends to assume an equatorial position. In the absence of a hydroxymethyl group at C5, the conformations of the aldopentopyranoses are governed by the disposition of the hydroxy groups. Thus, the D-arabinopyranoses favor the ¹C₄ form, α-D-lyxopyranose and D-ribopyranose are each conformational mixtures, and the other aldopentoses are predominantly in the ⁴C₁ form.

Besides these interactions, one must take into account the anomeric effect which makes an equatorially attached group on the anomeric carbon atom less stable than an axially attached group. The anomeric effect varies inversely with the dielectric constant of the solvent, and is greatest when the effective charge density on the substituent atom attached directly to C1 is high. Recent MM3 force field calculations^[18-19] back up Angyal's results (see Table 1.1).

1 Introduction

MM3 was used to study ring conformations of the aldopentopyranoses; the obtained energy surfaces exhibit low-energy regions corresponding to the various ring forms.

Table 1.1. Calculated relative interaction energies, according to Angyal^[13], and MM3 relative energies for the MM3 local minima, according to Dowd^[18-19], of the D-pentopyranoses. Energies, originally given in kcal/mol, were converted to kJ/mol.

kJ/mol	Angyal (1969)		Dowd (2002)	
	⁴ C ₁	¹ C ₄	⁴ C ₁	¹ C ₄
α -D-Arap	4.82	0.0	14.28	0.0
β -D-Arap	2.09	0.0	6.09	0.0
α -D-Lyxp	0.0	2.30	0.0	3.87
β -D-Lyxp	0.0	4.40	0.0	10.83
α -D-Ribp	0.0	0.42	7.54	0.0
β -D-Ribp	0.0	2.51	0.0	0.96
α -D-Xylp	0.0	6.91	0.0	7.26
β -D-Xylp	0.0	9.63	0.0	15.95

Currently, intramolecular hydrogen bonding and solvation effects influencing the conformational properties of carbohydrates are being discussed.^[20] These effects consist of a combination of competition between intramolecular and solute–solvent hydrogen bonds, preferential solvation of sterically more accessible hydroxy groups and specific interactions between solute hydroxy groups and tightly bound solvent molecules. These observations have led to the proposal of several models for monosaccharide hydration, among which the axial-equatorial model suggests that equatorial hydroxy groups are more strongly hydrated compared to axial ones because they are sterically more accessible and less likely to be involved in strong intramolecular hydrogen bonds.^[21]

If furanose forms are involved, the assignment of ring conformation is more complicated. This complication arises from the ability of these rings to assume various nonplanar geometries in solution characterized by two generic types, the envelope (*E*) and twist (*T*) forms. The former contains four adjacent coplanar atoms with the remaining atom out-of-plane, whereas the latter contains three adjacent coplanar atoms and two out-of-plane atoms (one above and one below the plane). Twenty idealized nonplanar forms are possible (10 *E* and 10 *T*). These nonplanar forms interconvert readily via pseudorotation or inversion, the latter involving the planar form as an intermediate. Studies have suggested that the energies of nonplanar forms are very similar, and thus it is expected that two or more conformers may be

1 Introduction

present in solution for a given furanose ring. The nature of the conformational equilibrium and dynamics is likely to be very much configuration dependent, so no general rule can be readily applied at the present time to predict preferred geometries. However, several factors influence furanose conformation, namely, the anomeric effect, the preferred quasi-equatorial orientation of side chain, staggered orientation of ring substituents, the gauche effect, and a preference for tetrahedral carbon angles in the ring.

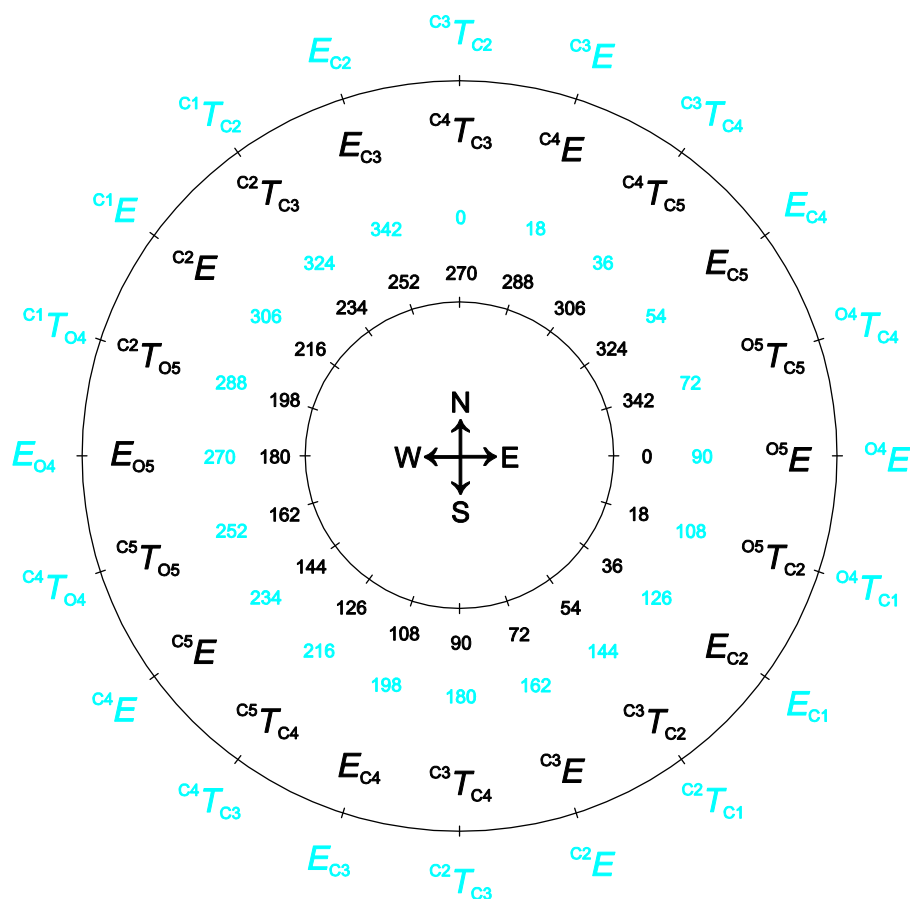


Figure 1.3. Conformational wheel for furanose rings. The inner ring is for the Cremer–Pople^[22] parameters (ϕ_2 , black) and the next ring is for the numeric values of Altona and Sundaralingam^[23] (blue). The next ring gives the letter designators for ketose conformations (black) and the next for aldose conformations (blue). The letter designators are chosen unambiguously, the short form is 3T_2 instead of ${}^{C3}T_{C2}$ or 0E instead of ${}^{O4}E$.

Because each of the twenty characteristic conformers is spaced 18° apart on the conformational wheel, any intermediate can be described in terms of a phase angle. The extent of out-of-plane deviation is called the amplitude. These puckering parameters may be plotted on a plane polar coordinate system, with the amplitude being the radius and the phase

1 Introduction

angle corresponding to the position on the pseudorotational wheel (see Fig. 1.3). Two conventions are used for five-membered rings. One is the Altona–Sundaralingam system,^[23] consisting of a phase angle P , and an amplitude angle, τ_m . The other is the Cremer–Pople system^[22], with a different phase angle, φ , and an amplitude scalar, Q . In the Altona–Sundaralingam system, $P = 0^\circ$ for a T form with the carbon atoms opposite the ring oxygen atom displaced below and above the plane of the other three (e.g. 3T_2 for an aldofuranose). In the C–P description, $\varphi = 0^\circ$ for the 0E form. In both systems, the phase angle increases with clockwise rotation, a reflection of the clockwise numbering of rings when they are viewed in the standard position. The degree of puckering τ_m or the amplitude Q is zero for an all-planar structure that would be depicted at the center of the conformational wheel. Off the center, Q is the mean deviation of the ring atoms from the mean plane. A useful coincidence is that $\tau_m(^{\circ}) = 102.5 Q(\text{\AA})$ and $P = \varphi + 90^\circ$. The Altona–Sundaralingam system is used extensively for nucleotides and nucleosides, while the Cremer–Pople system is favored by some crystallographers because the same system can be applied to rings of other sizes. Given the coordinates of the ring atoms, computer programs can calculate the puckering parameters. Besides the quantitative puckering parameters and the qualitative letter notation, there is an even more informal notation that divides the conformational wheel into four quadrants, labelled north, south, west and east.^[24]

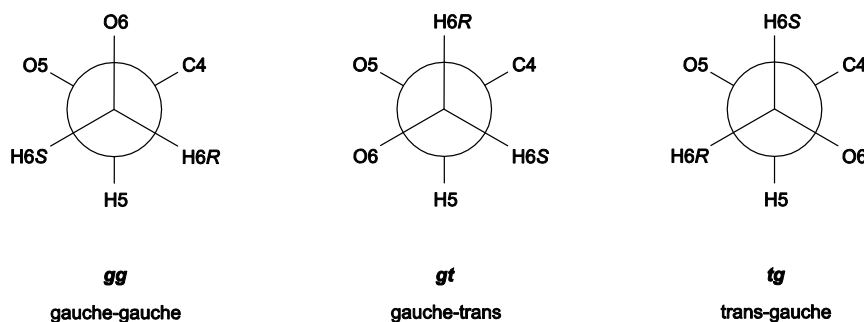


Figure 1.4. The three possible, perfectly staggered rotamers about the exocyclic C5–C6 bond of aldohexopyranoses.

The conformational determination of exocyclic hydroxymethyl groups includes the assessment of the C5–C6 bond’s torsional behavior in aldohexopyranoses (or of the C4–C5 bond in aldopentofuranoses). One can address this problem in several ways. In the first, only three idealized (i.e., perfectly staggered) rotamers (*gg*, *gt*, *tg*, see Fig. 1.4) are considered potential forms in solution. All other rotamers are ignored; in fact, they are implicitly treated

1 Introduction

as transient intermediates in the rapid interconversion of the three staggered forms and thus have very short lifetimes compared to the experimental measurement time. As a consequence of the latter, they do not make a contribution to measured experimental parameters.

In an intermediate approach, the same three rotamers are considered, but may not be perfectly staggered. Finally, in the most complex and less constrained treatment, rotation about the C–C bond is treated as a continuum, that is, all rotamers are considered in the analysis.

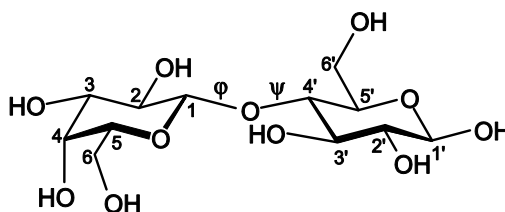


Figure 1.5. Definition of the phi (φ) and psi (ψ) glycosidic torsion angle in a disaccharide (β -lactose).

The conformation about the glycosidic linkage is defined by two or three torsion angles depending on the nature of the linkage. In disaccharides as depicted in Fig. 1.5, only two torsion angles are involved, namely C1–O1 (φ) and O1–C4' (ψ). The φ torsion angle is affected by the exoanomeric effect, whereas both φ and ψ will be influenced by nonbonded interactions and potential interresidue hydrogen bonding. For linkages involving the oxygen of an exocyclic CH₂OH group, a third torsion (ω) is required (e.g., C5–C6) to define geometry.^[12]

1.4 NMR spectroscopy and the Karplus equation

The discovery that the vicinal proton-proton coupling constant ${}^3J_{\text{HH}}$ varies smoothly with the associated H–C–C–H torsion angle φ_{HH} in ethane had a profound impact on the acceptance of NMR as an indispensable tool in stereochemistry and conformational analysis. Initially, VB theory was used by Karplus^[25] to calculate ${}^3J_{\text{HH}}$ in ethane, which could be fitted approximately by the equations:

$$\begin{aligned} {}^3J_{\text{HH}} &= 8.5 \cos^2(\varphi_{\text{HH}}) - 0.28 \quad \text{for } 0^\circ \leq \varphi \leq 90^\circ \text{ and} \\ {}^3J_{\text{HH}} &= 9.5 \cos^2(\varphi_{\text{HH}}) - 0.28 \quad \text{for } 90^\circ \leq \varphi \leq 180^\circ \end{aligned} \quad (1.1)$$

1 Introduction

Later, the equation was restated in a trigonometric form, namely,

$${}^3J_{\text{HH}} = A \cos^2(\varphi_{\text{HH}}) + B \cos(\varphi_{\text{HH}}) + C \quad (1.2)$$

because its quadratic form allows an explicit calculation of φ from the coupling constant, despite a warning from Karplus that “the person who attempts to estimate the dihedral angles to an accuracy of one or two degrees does so at his own peril”.^[25] The general shape of the Karplus curve (Fig. 1.6), large ${}^3J_{\text{HH}}$ at $\varphi = 0^\circ$ (eclipsed) and at or near $\varphi = 180^\circ$ (*trans* or *anti*), and decreasing to a minimum value (${}^3J_{\text{HH}} \approx 0$ Hz) near $\varphi = 90^\circ$, in the course of time was shown to be applicable to many molecular fragments.^[26]

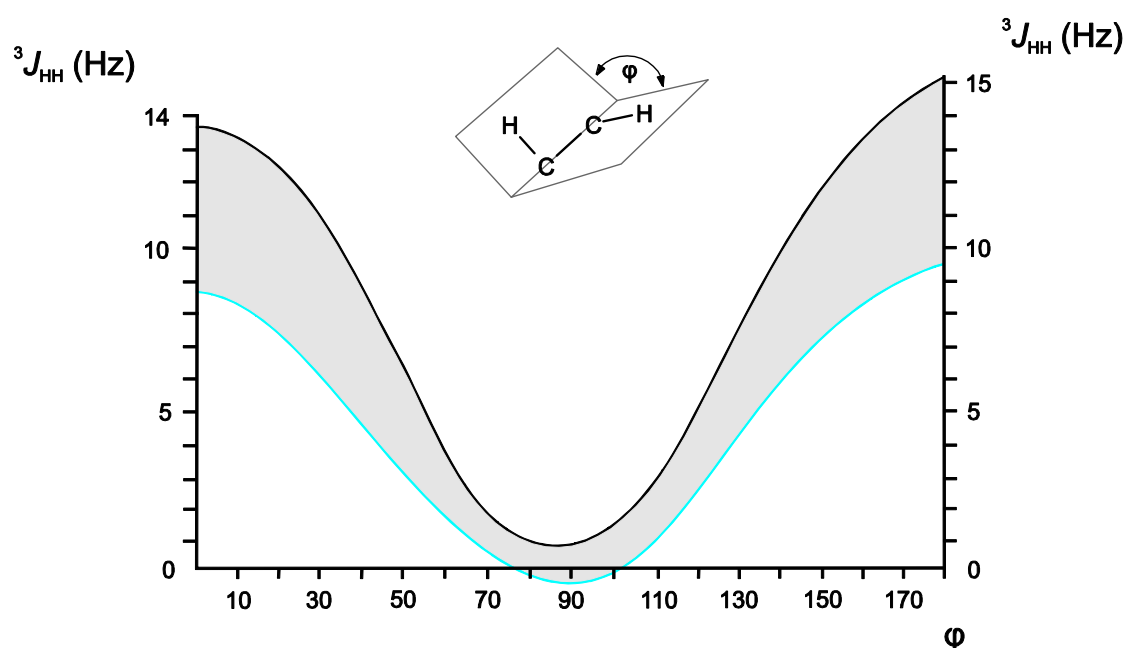


Figure 1.6. Schematic Karplus curve: ${}^3J_{\text{HH}}$ coupling constants' dependence on the H–C–C–H torsion angle φ_{HH} .

Despite the success of ${}^3J_{\text{HH}}$ values as conformational probes, several limitations must be appreciated when applying them in structural studies. The exact form of the Karplus equation depends highly on the structure of the H–C–C–H fragment; the values A, B, and C in the original Karplus equation set to $A = 9.0$, $B = -0.5$ and $C = -0.28$ reflect this dependency.^[27] In particular, the presence of electronegative substituents on or near the H–C–C–H fragment, and their orientation with respect to the coupling pathway, significantly affect the amplitude, and to a lesser extent, the shape of Karplus curves. Since the original report by Karplus, who himself recognized this limitation, several more sophisticated Karplus equations have been proposed that take substitution effects into account. Most notable is that proposed by Altona and co-workers.^[28]

1 Introduction

Thus, ${}^3J_{\text{HH}}$ values cannot be interpreted without access to a Karplus equation appropriate for the coupling pathway under consideration. Furthermore, the interpretation of ${}^3J_{\text{HH}}$ values in a molecule depends on its dynamical properties which are often unknown or assumed in many analyses. The simplest interpretation assumes one and only one conformation in solution. ${}^3J_{\text{HH}}$ values are then assessed to identify this single conformation. However, more often the molecule is not conformationally fixed, that is, it samples two or more conformations in solution with an exchange between these states which is rapid compared to the frequency of observation. Under these circumstances, the observed ${}^3J_{\text{HH}}$ values will be averaged to reflect this heterogeneity. This averaging can be complex depending on the dynamics of the system and the NMR parameter involved.^[12] Nevertheless, systematic investigations into the orientational effects of substituents on ${}^3J_{\text{HH}}$ have resulted in a differentiation of the following three situations:

(a) *Gauche* protons and a substituent in an *anti* orientation: ${}^3J_{\text{HH}}$ decreases strongly with increasing electronegativity of the substituent (Booth's rule);^[29]

(b) *Gauche* protons and a substituent in a *gauche* orientation with respect to its vicinal coupling proton: ${}^3J_{\text{HH}}$ increases with increasing electronegativity of the substituent (Abraham's rule);^[30]

(c) *Anti* or *trans* protons with a substituent necessarily in a *gauche* position: ${}^3J_{\text{HH}}$ decreases with increasing electronegativity of the substituent.

If the substituent is oxygen in conformationally rigid pyranose sugars, a statistical analysis of a large set of couplings clearly illustrates the fact that *gauche* couplings do not obey the simple cosine-square rule. Therefore, for example, Haasnoot et al.^[28] have described a generalized Karplus equation:

$${}^3J_{\text{HH}} = P_1 \cos^2(\varphi_{\text{HH}}) + P_2 \cos(\varphi_{\text{HH}}) + P_3 + \sum_i \Delta_{\chi_i} [P_4 + P_5 \cos^2(\zeta_i(\varphi_{\text{HH}}) + P_6 |\Delta_{\chi_i}|)] \quad (1.3)$$

The parameters P_1 – P_6 were empirically determined with the aid of a test set containing 315 couplings and corresponding φ_{HH} values derived from a variety of pyranosides and related compounds. Each substituent was assigned a Δ_{χ_i} value according to Huggins,^[31] but empirically modified to account for the moderation of the electronegativity of the α substituent by attached atoms or groups (β substituents), other than hydrogen. Finally, ζ_i is a sign factor corresponding to the protons' orientation defined by Haasnoot et al.^[28]

1 Introduction

Although several other Karplus equations exist, the Díez–Donders equation, for example,^[32] the Haasnoot–de Leeuw–Altona equation is favored because of its carbohydrate origin. MESTRE-J,^[33] a graphical tool for the prediction of vicinal $^3J_{\text{HH}}$ coupling constants, allows an easy access to a variety of Karplus equations and was used in this work for the calculation of coupling constants from torsion angles and the other way around.

1.5 Aims of this work

In the middle of the last century, Reeves used copper–ammine-based probes as a tool to unravel the conformation of the glycopyranoses. The method was based on the coordination chemistry of Schweizer’s reagent with carbohydrates.^[16-17] In 1981, Taylor and Waters^[34] published their pioneering work on the first crystal-structure determination of a monosaccharide–metal complex, a dinuclear molybdenum–lyxose complex (Fig. 1.7). For more than a decade, this crystal-structure determination on a heteroleptic oxido-alkoxido complex remained the only one in the field.

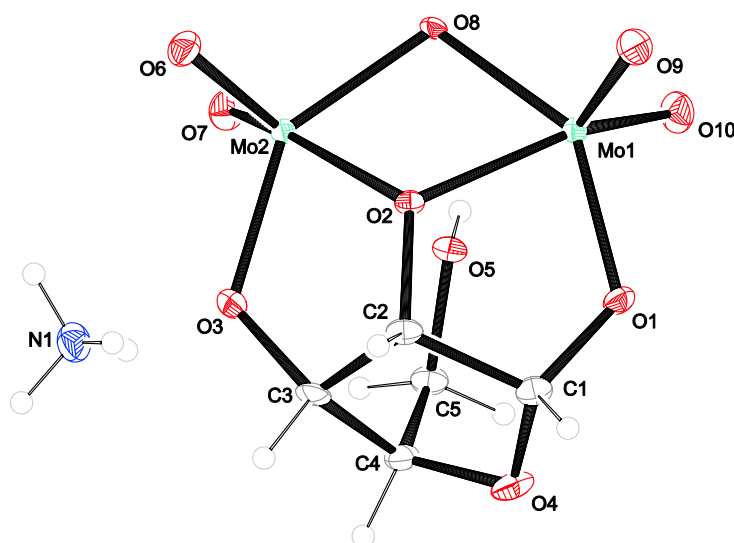


Figure 1.7. $\text{NH}_4[\text{Mo}_2\text{O}_4(\mu\text{-O})(\beta\text{-D-Lyx}/1,2,3\text{H}_{-3}\text{-}\kappa\text{O}^{1,2,3,4})]$, a redetermination of the first monosaccharide–metal complex’s structure.^[35]

Only in the year 2001 was $[\text{Pd}_2(\text{en})_2(\alpha\text{-D-Glcp}1,2;3,4\text{H}_{-4}\text{-}\kappa\text{O}^{1,2};\kappa\text{O}^{3,4})]$ the first published $\text{Pd}^{\text{II}}\text{N}_2$ -complex with D-glucose,^[36] starting a series of publications^[37-39] which expanded the knowledge of carbohydrate-coordination chemistry with $\text{Pd}^{\text{II}}\text{N}_2$ -fragments. Now, the aim of this work is the further investigation of $\text{Pd}^{\text{II}}\text{N}_2$ -complexes with more reactive carbohydrates, such as the ketoses and dialdoses, with di-, tri- and oligosaccharides.

1 Introduction

Also, the coordination chemistry of Pd^{II}N₂-carbohydrate complexes in neutral aqueous solution and the dynamic behavior of methyl pentosides and pentoses should be further investigated. Thus, studies of the effect of the side groups' various steric arrangements and their effect on the stability of the pyranose- or furanose ring shapes contributes greatly to a better understanding of the stereochemistry of simple sugars. Therefore, in a first step, the pool of Pd^{II}N₂-fragments has to be extended with regard to a higher resistance to the reduction to palladium(0) and a better crystallization tendency.

2 Results

2.1 Palladium(II) fragments: nomenclature and characteristics

Metal-containing reagents that had been developed primarily as cellulose solvents have been used as diagnostic tools for basic research on monosaccharides and their derivatives since the early days of carbohydrate chemistry. The first solvent of this kind was ‘Schweizer’s reagent’ (1857), which is a solution of cupric hydroxide in excess aqueous ammonia.^[40] In this work, Schweizer’s reagent (‘cuoxam’, ‘cuprammonium hydroxide’, ‘cupra’) is abbreviated Cu-NH₃, using a nomenclature which was introduced for cellulose solvents. The first palladium-based solvents, Pd-NH₃ and Pd-en, an aqueous solution of [Pd(en)(OH)₂] (en = ethane-1,2-diamine), were introduced about a decade ago.^[41-42] Because the formed complexes are diamagnetic low-spin-d⁸ species in contrast to the copper-containing complexes, they are analytic tools that allow the use of NMR spectroscopy in complexation studies. These palladium solvents are kinetically inert with respect to ligand exchange on the NMR timescale. Therefore, NMR data that are mean values due to the contributions from two or more species (mean chemical shift, mean coupling constants), are indicative of the dynamic behavior of an individual intact complex.

The replacement of the initially applied Pd-en by the related chiral solvent termed Pd-chxn, an aqueous solution of (*R,R*)-cyclohexane-1,2-diamine-dihydroxido-palladium(II), led to a consistent body of data on the metal-binding sites of a glycoside.^[37] A common property of all Pd-based solvents is the magnitude of the so-called ‘coordination-induced shift’ (CIS). Depending on the binding mode of the carbohydrate, these shifts remain almost constant among the solvents. Thus, in the case of five-membered chelate rings, the signals of the carbon atoms experience an approximately 10-ppm downfield shift relative to the free chelator. In the case of six-membered chelate rings, markedly smaller CISs are observed.

Now, as it is the aim of this work to investigate Pd^{II}N₂-complexes with more reactive carbohydrates, in a first step, the pool of Pd^{II}N₂-fragments has to be extended in regard to a higher resistance to reduction to palladium(0) and better crystallization tendency. Therefore, in a first step, suitable C₂-symmetric diamines have to be reacted with PdCl₂ and, in a second step, the chloride ligands have to be substituted by hydroxide ligand. Hereinafter, the most promising of the various tested Pd^{II}N₂ fragments,^[43-45] their properties and their suitability for use will be described.

2 Results

2.1.1 [Pd(dmen)(OH)₂] and [Pd(tmen)(OH)₂]

N,N'-Dimethylethane-1,2-diamine and *N,N,N',N'*-tetramethylethane-1,2-diamine were both commercially available and could be treated with PdCl₂ the same way as ethane-1,2-diamine to obtain the [Pd(dmen)Cl₂] and [Pd(tmen)Cl₂] compounds. Also the treatment with Ag₂O to Pd-dmen and Pd-tmen resulted by the proven method of Pd-en and clear yellow solutions were obtained. In the case of Pd-dmen, this Pd^{II}N₂-fragment was not suitable for NMR investigations because the two methyl groups can form a *syn* and an *anti* isomer which multiply the signals in NMR spectra. Also the resistance to reduction to palladium(0) is comparable to Pd-en which makes Pd-dmen unfavorable for any conversions with reducing carbohydrates such as the ketoses or dialdoses. Nevertheless, with the polyols, a few crystal structures could be determined and are discussed below.

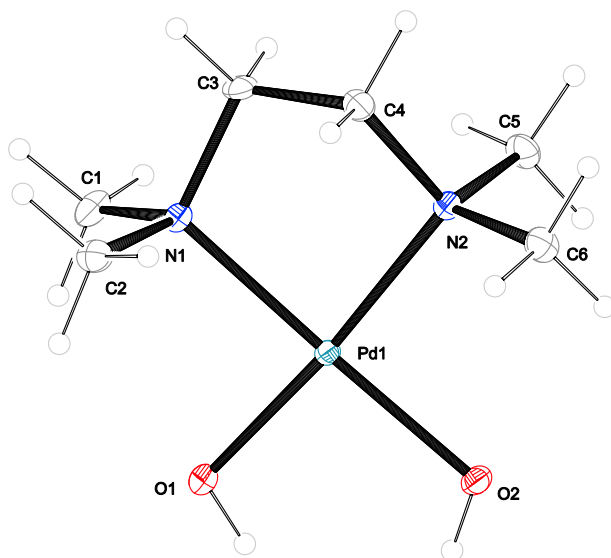


Figure 2.1. The molecular structure of [Pd(tmen)(OH)₂] in crystals of the dihydrate (**1**). ORTEP plot is drawn with 50% probability ellipsoids. Interatomic distances (Å) and angles (°) (standard deviations of the last digit in parentheses): Pd1–O1 1.976(2), Pd1–O2 2.005(2), Pd1–N1 2.067(3), Pd1–N2 2.067(3); O1–Pd1–O2 93.40(9), O1–Pd1–N1 89.69(10), O2–Pd1–N2 91.46(11), N1–Pd1–N2 85.66(12).

In Fig. 2.1, the Pd^{II}N₂-fragment dihydroxido-*N,N,N',N'*-tetramethylethane-1,2-diamine-palladium(II) crystallized from DMF is depicted. The asymmetric unit in the orthorhombic space group *P* 2₁2₁2₁ contained only one [Pd(tmen)(OH)₂] fragment. Compared to the crystal structure of [Pd(en)(OH)₂] {Pd–O 2.017(2) Å, Pd–N 2.028(2) Å, O–Pd–O 93.6(1) °, N–Pd–N 84.0(1) °}, the Pd–O bond distances of [Pd(tmen)(OH)₂] were slightly smaller, while the Pd–N bond distances were extended.^[46] The O–Pd–O and N–Pd–N were almost the same for both compounds. The distances and angles of the hydrogen bonds are listed in Table 2.1.

2 Results

Table 2.1. Distances [Å] and angles [°] of hydrogen bonds in **1**. Standard deviations of the last digit are given in parentheses; values without standard deviation are related to hydrogen atoms at calculated positions. D: donor, A: acceptor.

D	H	A	D–H	H···A	D···A	D–H···A
O1	H1	O2 ⁱ	0.84	2.07	2.903(3)	171.5
O2	H2	O2 ⁱ	0.84	2.65	3.447(2)	159.5
O91	H911	O1	0.84(3)	1.84(3)	2.660(4)	165(3)
O91	H912	O92 ⁱⁱ	0.70(4)	2.37(4)	3.046(5)	165(4)
O92	H921	O2	0.74(4)	2.01(3)	2.747(4)	175(4)
O92	H922	O91 ⁱⁱ	0.75(5)	2.34(5)	3.067(6)	164(5)

Symmetry code: (i) $x+1/2, -y+5/2, -z+2$; (ii) $x-1/2, -y+5/2, -z+2$.

The Pd-tmen solvent's characteristics were determined by the substitution of the N-bonded H atoms of Pd-en by methyl groups. As a result, there was an increased steric demand in the direction of the bonded diolate and hence modified species stabilities and no intramolecular hydrogen bonds could be formed toward adjacent functions of the bonded carbohydrate. The most remarkable property of Pd-tmen is its superior resistance to reduction to palladium(0) in relation to the fragments introduced so far thus making the investigation of dialdoses possible. A common property with other Pd-based solvents was the magnitude of the CIS which enabled the comparison of ¹³C NMR chemical shifts and CIS values of different Pd^{II}N₂-fragments. The only disadvantage of Pd-tmen was the overlap of the tmen's ¹³C NMR signal with the signal of carbohydrates' C6 but this does not necessarily mean a loss of information.

2.1.2 [Pd(tmchxn)(OH)₂]

Due to the various advantages of Pd-tmen, the synthesis of Pd-tmchxn was a corollary. Although not commercially available, *N,N,N',N'*-tetramethyl-(1*R*,2*R*)-cyclohexane-1,2-diamine and its treatment with PdCl₂ is known in the literature and easily accessible.^[47-48] Contrary to all expectations, this fragment did not combine the crystallization tendency of Pd-chxn with the stability of Pd-tmen. Of course, Pd-tmchxn showed an increased crystallization rate. Unfortunately, only η^2 -carbonato-*N,N,N',N'*-tetramethyl-(1*R*,2*R*)-cyclohexane-1,2-diamine-palladium(II) hexahydrate (**2**) was found instead of carbohydrate-containing compounds. Fig. 2.2 shows the compound crystallized in the orthorhombic space group *C* 222₁ with a single carbonate forming a four-membered chelate ring with palladium(II). As a result, with a O–Pd–O angle of 64.86(10)°, the square-planar coordination of palladium(II)

2 Results

was impaired. This motif is also known for Pd-tmen,^[49-50] with bond distances and angles in a comparable range, but without this dominant crystallization tendency.

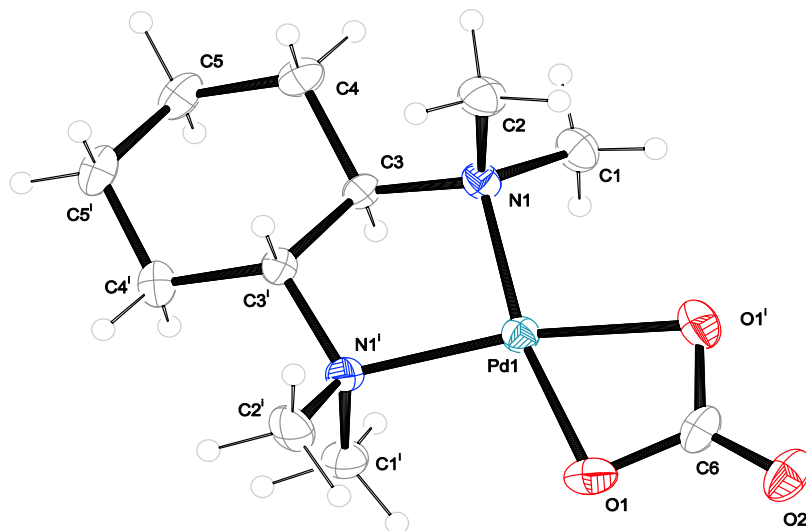


Figure 2.2. The molecular structure of [Pd(tmchxn)(CO₃)] in crystals of the 6-hydrate (**2**). ORTEP plot is drawn with 50% probability ellipsoids. Interatomic distances (Å) and angles (°) (standard deviations of the last digit in parentheses): Pd1–O1 2.047(2), Pd1–N1 2.038(2); O1–Pd1–O1ⁱ 64.86(10), O1–Pd1–N1ⁱ 104.56(10), O1ⁱ–Pd1–N1 104.56(10), N1–Pd1–N1ⁱ 86.03(10); chelate torsion angle: N1–C3–C3ⁱ–N1ⁱ –51.2(3). [Symmetry code: (i) $-x, y, -z + \frac{1}{2}$]

In Table 2.2, the distances and angles of the hydrogen bonds are listed and the hydrogen bonding network has only one single contact with O1 of the molecule.

Table 2.2. Distances [Å] and angles [°] of hydrogen bonds in **2**. Standard deviations of the last digit are given in parentheses; values without standard deviation are related to hydrogen atoms at calculated positions. D: donor, A: acceptor.

D	H	A	D–H	H···A	D···A	D–H···A
O91	H911	O93	0.823(18)	1.97(2)	2.778(5)	166(5)
O92	H921	O93	0.827(18)	2.03(3)	2.785(5)	152(5)
O93	H931	O94	0.823(19)	2.01(3)	2.776(4)	154(7)
O93	H932	O1 ⁱ	0.852(18)	1.95(2)	2.735(3)	154(4)
O94	H941	O92 ⁱⁱ	0.806(19)	2.08(3)	2.854(5)	162(7)
O94	H942	O91 ⁱⁱⁱ	0.813(18)	2.04(2)	2.846(5)	173(6)

Symmetry code: (i) $-x+2, -y+2, z-\frac{1}{2}$; (ii) $x-\frac{1}{2}, y-\frac{1}{2}, z$; (iii) $x+\frac{1}{2}, y-\frac{1}{2}, z$.

NMR experiments with Pd-tmchxn are lacking although the compound would be a chiral and stable Pd^{II}N₂-fragment for the investigation of dialdoses.

2 Results

2.1.3 [Pd(teen)(OH)₂]

To increase the steric demand of the Pd^{II}N₂-fragment, *N,N,N',N'*-tetraethylethane-1,2-diamine was used for the treatment with PdCl₂ instead of tmen. Using the synthesis conditions of [Pd(tmen)Cl₂], yellow crystals could be obtained. Fig. 2.3 (left) shows *N,N,N',N'*-tetraethylethane-1,2-diammonium tetrachloridopalladate(II) crystallized in the monoclinic space group *P* 2₁/*n*. As the crystal-structure analysis showed, the expected product was not obtained. Whereas for en or tmen the chelate effect enforced the splitting off of two equivalents of hydrochloric acid, on teen, the steric demand of the ethyl groups weakened the chelate effect. Only by raising the pH value to 5, could [Pd(teen)Cl₂] be obtained. This method is known for the synthesis of [Pd(*R,R*-chxn)Cl₂] and [Pd(tmchxn)Cl₂] as well.

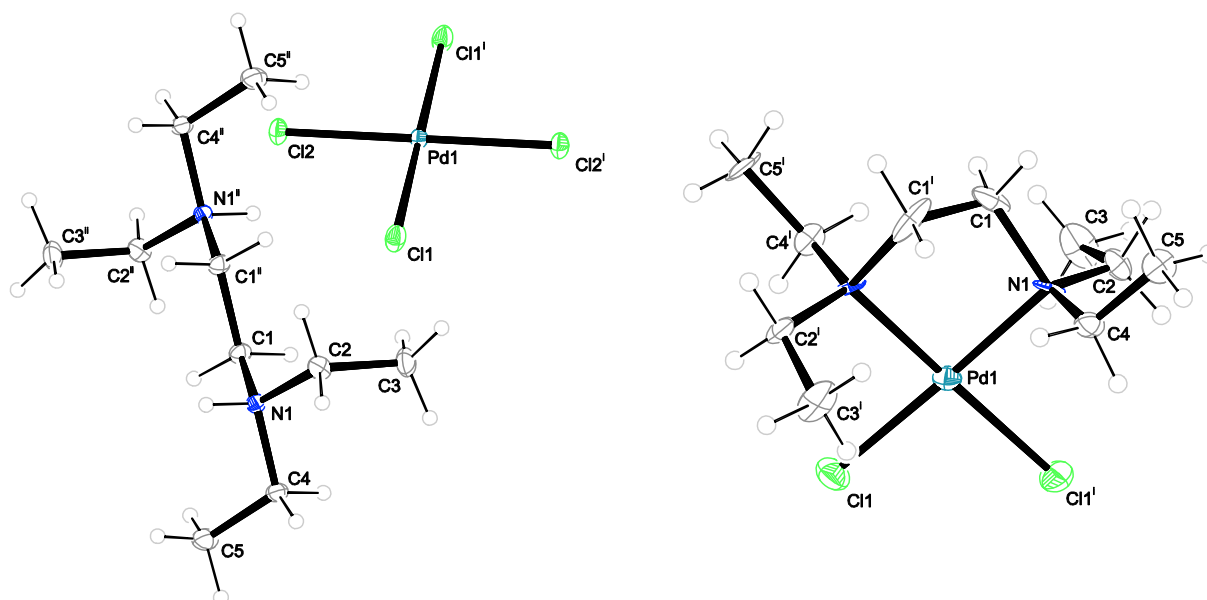


Figure 2.3. The molecular crystal structures of (teenH₂)[PdCl₄] (**3**) (left) and [Pd(teen)Cl₂] (**4**) (right). ORTEP plot is drawn with 50% probability ellipsoids. Interatomic distances (Å) and angles (°) (standard deviations of the last digit in parentheses) of **4**: Pd1–Cl1 2.309(3), Pd1–N1 2.112(8); Cl1–Pd1–Cl1ⁱ 90.72(10), Cl1–Pd1–N1ⁱ 90.6(2), Cl1ⁱ–Pd1–N1 90.6(2), N1–Pd1–N1ⁱ 88.2(3). [Symmetry code: (i) $-x, y, -z + \frac{1}{2}$]

Dichlorido-*N,N,N',N'*-tetraethylethane-1,2-diamine-palladium(II) crystallized in the space group *C* 2/*c* and is depicted in Fig. 2.3 (right). The treatment to Pd-teen with Ag₂O could be performed under identical conditions as for Pd-tmen and a clear yellow solution was obtained which showed an increased resistance to reduction to palladium(0). As for Pd-tmen, the teen's ¹³C NMR signal overlapped with the signal of carbohydrates' C6 but, in comparison to Pd-tmen, with Pd-teen, minor species could be enriched and elucidated. Therefore, the combination of Pd-tmen and Pd-teen promised a maximum of information about the coordination chemistry of carbohydrates with Pd^{II}N₂-fragments.

2 Results

2.1.4 [Pd(tn)(OH)₂]

So far, only five-membered ring Pd^{II}N₂-fragments were applied for the investigation of carbohydrate-metal chemistry, although with [Pd(htn)Cl₂], a six-membered ring Pd^{II}N₂-fragment is known in the literature.^[51-53] Because of the missing C₂-symmetry, 2-hydroxypropane-1,3-diamine was replaced by propane-1,3-diamine to yield [Pd(tn)Cl₂]. After the treatment with Ag₂O to Pd-tn, the ¹³C NMR spectrum revealed the instability of the six-membered ring Pd^{II}N₂-fragment because signals of [Pd(tn)(OH)₂] and free propane-1,3-diamine were detected in equimolar amounts. In consequence, reactions of Pd-tn with polyols yield high amounts of free polyol, whereas the CIS values do not differ from those of five-membered ring Pd^{II}N₂-fragments. Nevertheless, a few crystal structures of Pd-tn with polyols could be obtained and are discussed below.

2.1.5 [Pd(bpy)(OH)₂] and [Pd(phen)(OH)₂]

2,2'-Bipyridine and 1,10-phenanthroline are known as strong chelate ligands, especially for square-planar coordinated metal ions such as palladium(II). Furthermore, the syntheses of [Pd(bpy)(OH)₂] and [Pd(phen)(OH)₂] and their conversion with simple diols such as ethane-1,2-diol are described in the literature.^[54-55]

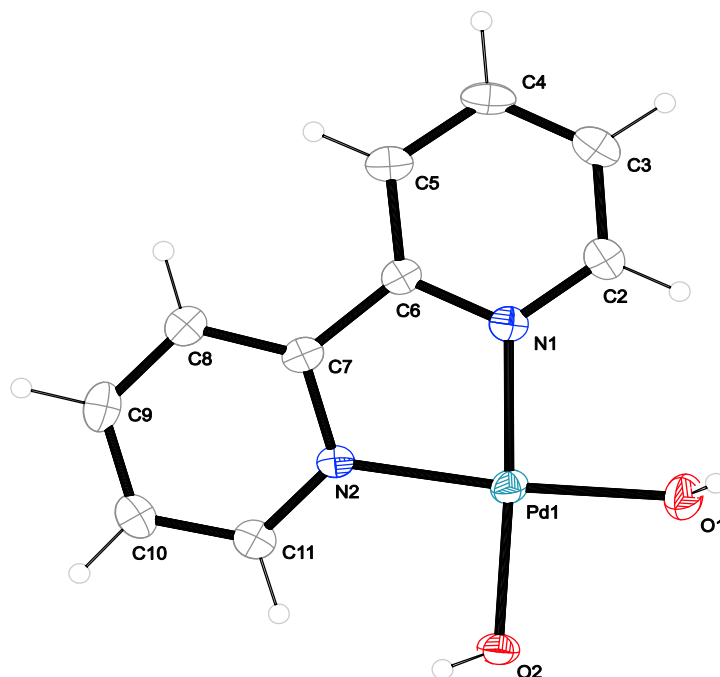


Figure 2.4. The molecular structure of [Pd(bpy)(OH)₂] in crystals of the 5-hydrate (**5**). ORTEP plot is drawn with 50% probability ellipsoids. Interatomic distances (Å) and angles (°) (standard deviations of the last digit in parentheses): Pd1–O1 2.005(5), Pd1–O2 1.988(5), Pd1–N1 1.986(5), Pd1–N2 2.011(5); O1–Pd1–O2 89.9(2), O1–Pd1–N1 93.9(2), O2–Pd1–N2 95.1(2), N1–Pd1–N2 81.0(2).

2 Results

The synthesis of $[\text{Pd}(\text{bpy})\text{Cl}_2]$ and $[\text{Pd}(\text{phen})\text{Cl}_2]$ followed the usual method as far as possible, except for dissolution of bpy and phen acetone was added, the treatment with Ag_2O yielded a clear yellow to orange solution. The aim to reduce the solubility of the $\text{Pd}^{\text{II}}\text{N}_2$ -fragment was definitely overperformed because $[\text{Pd}(\text{bpy})(\text{OH})_2]$ and $[\text{Pd}(\text{phen})(\text{OH})_2]$ rapidly crystallized completely. The crystal structures are shown in Fig. 2.4 and 2.5 where both compounds formed pentahydrates in the asymmetric unit of the monoclinic space group $P 2_1/n$ and the bond distances and angles of palladium(II) are almost identical.

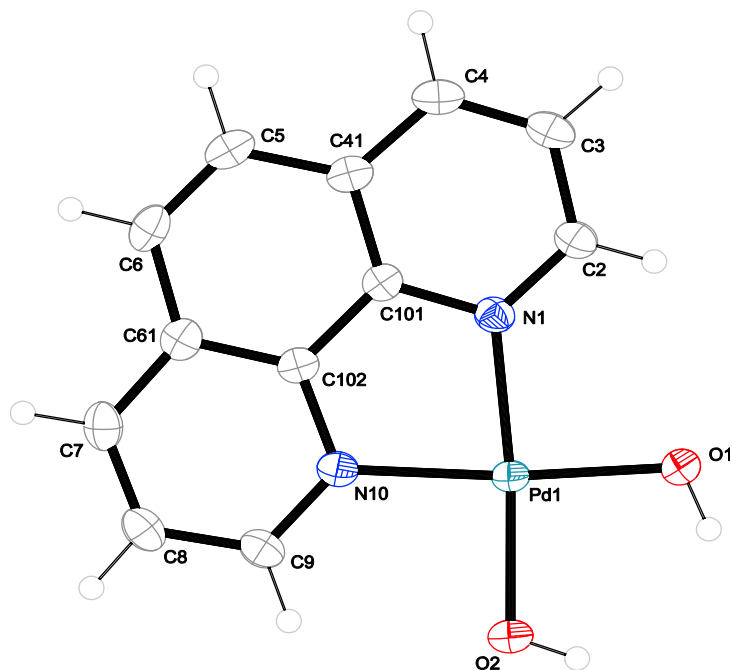


Figure 2.5. The molecular structure of $[\text{Pd}(\text{phen})(\text{OH})_2]$ in crystals of the 5-hydrate (**6**). ORTEP plot is drawn with 50% probability ellipsoids. Interatomic distances (\AA) and angles ($^\circ$) (standard deviations of the last digit in parentheses): Pd1–O1 1.9865(17), Pd1–O2 1.9922(17), Pd1–N1 2.014(2), Pd1–N10 2.016(2); O1–Pd1–O2 93.39(7), O1–Pd1–N1 92.04(7), O2–Pd1–N10 92.43(8), N1–Pd1–N10 82.15(8).

As one can see in Fig. 6.44 and Fig. 6.45 of the Appendix, the $[\text{Pd}(\text{bpy})(\text{OH})_2]$ and $[\text{Pd}(\text{phen})(\text{OH})_2]$ fragments formed close stacks along the crystallographic a axis linked by a hydrogen-bonding network (for **6**, see Table 2.3) which is the reason for the high crystallization tendency. The distance between the individual molecular planes is 3.351 \AA for $[\text{Pd}(\text{bpy})(\text{OH})_2]$ and 3.447 \AA for $[\text{Pd}(\text{phen})(\text{OH})_2]$. This characteristic motif of the planar $[\text{Pd}(\text{bpy})(\text{OH})_2]$ and $[\text{Pd}(\text{phen})(\text{OH})_2]$ fragments was repeated in the crystal structures with the simple diols. Otherwise, due to this stacking, $[\text{Pd}(\text{phen})(\text{OH})_2]$ was almost insoluble in water and only soluble in methanol and, furthermore, crystal structures could only be obtained with planar or almost planar diols whereas non-fitting polyols or carbohydrates formed only amorphous powders or decomposed to oxalate.

2 Results

Table 2.3. Distances [Å] and angles [°] of hydrogen bonds in **6**. Standard deviations of the last digit are given in parentheses; values without standard deviation are related to hydrogen atoms at calculated positions. D: donor, A: acceptor.

D	H	A	D–H	H···A	D···A	D–H···A
O1	H811	O91 ⁱ	0.84	2.17	2.962(3)	156.7
O2	H821	O91 ⁱ	0.84	2.00	2.828(3)	170.0
O91	H911	O92	0.773(13)	1.968(13)	2.741(3)	178(3)
O91	H912	O94	0.779(13)	1.939(13)	2.718(3)	179(3)
O92	H921	O93	0.769(13)	2.064(14)	2.819(3)	167(3)
O92	H922	O1	0.778(13)	2.012(14)	2.785(3)	172(3)
O93	H931	O2 ⁱⁱ	0.781(13)	1.900(14)	2.680(3)	177(3)
O93	H932	O95 ⁱⁱⁱ	0.777(13)	2.055(14)	2.824(4)	171(3)
O94	H941	O93 ^{iv}	0.776(13)	2.043(13)	2.819(3)	177(3)
O94	H942	O1 ^v	0.777(13)	1.981(13)	2.750(3)	171(3)
O95	H951	O2 ^{vi}	0.775(13)	1.957(14)	2.723(3)	170(3)
O95	H952	O95 ⁱⁱⁱ	0.773(14)	2.126(16)	2.889(5)	169(5)

Symmetry code: (i) $x-1/2, -y+1/2, z-1/2$; (ii) $x-1/2, -y+1/2, z+1/2$; (iii) $-x+1, -y, -z+1$; (iv) $x+1/2, -y+1/2, z-1/2$; (v) $x+1, y, z$; (vi) $x+1/2, -y+1/2, z+1/2$.

The crystal structure of [Pd(phen)(oxH₂)] monohydrate is described in the literature.^[56] Compounds with ethane-1,2-diol and anhydroerythritol will be discussed in the next chapter.

2.2 Simple diols: ethane-1,2-diol and anhydroerythritol complexes with Pd-phen

The structures of [Pd(phen)(EthdH₂)] heptahydrate (**7**) and Pd(phen)(AnErytH₂)] 4.5-hydrate (**8**) both crystallized in the monoclinic space group *C* 2/*c* and were stacked along the *c* axis as depicted in Fig. 6.46 and Fig. 6.47 of the Appendix. The nonplanarity of the diols in the case of ethane-1,2-diol resulted in four different positions around the stack of the phenanthroline ligands and did not clearly affect the interplanar distance [3.420 Å for **7**]. For anhydroerythritol, the diols were aligned opposite each other along the stack which also did not remarkably affect the interplanar distance of the phenanthroline ligands [3.510 Å for **8**]. Again, in both cases, the single stacks were held together by a hydrogen-bonding network which is analyzed for **7**. The distances and angles of the hydrogen bonds are listed in Table 2.4. The five-membered oxolane ring of anhydroerythritol was characterized by the puckering parameters^[22] $q = 0.372(3)$ Å and $\varphi = 257.5(5)^\circ$ for the O1–C1–C2–C3–C4 ring. The conformation was approximately *E*₃ indicating an envelope conformation with the C2 atom deviating the most from the respective best-fit plane.

2 Results

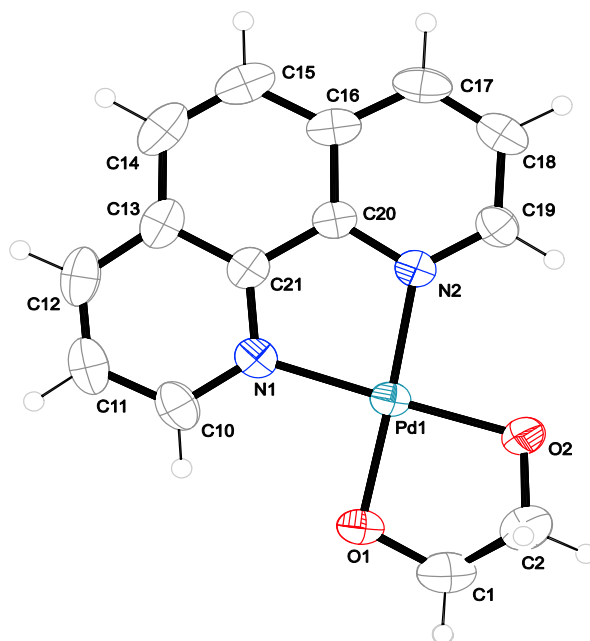


Figure 2.6. The molecular structure of $[\text{Pd}(\text{phen})(\text{EthdH}_{-2})]$ in crystals of the 7-hydrate (**7**). ORTEP plot is drawn with 50% probability ellipsoids. Interatomic distances (\AA) and angles ($^\circ$) (standard deviations of the last digit in parentheses): Pd1–O1 1.987(3), Pd1–O2 1.974(2), Pd1–N1 2.009(3), Pd1–N2 2.013(3); O1–Pd1–O2 85.93(11), O1–Pd1–N1 95.75(11), O2–Pd1–N2 96.25(11), N1–Pd1–N2 82.06(11); chelate torsion angle: O1–C1–C2–O2 $-49.9(5)$.

Table 2.4. Distances [\AA] and angles [$^\circ$] of hydrogen bonds in **7**. Standard deviations of the last digit are given in parentheses; values without standard deviation are related to hydrogen atoms at calculated positions. D: donor, A: acceptor.

D	H	A	D–H	H \cdots A	D \cdots A	D–H \cdots A
O91	H911	O93	0.841(17)	1.90(2)	2.729(4)	169(6)
O91	H912	O91 ⁱ	0.840(18)	2.08(5)	2.785(6)	142(8)
O92	H921	O91	0.837(17)	1.967(18)	2.802(4)	176(5)
O92	H922	O2	0.847(17)	1.854(18)	2.696(4)	173(4)
O93	H931	O92 ⁱⁱ	0.842(17)	1.91(2)	2.731(4)	164(6)
O93	H932	O95 ⁱⁱ	0.836(17)	2.04(2)	2.873(4)	170(6)
O94	H941	O2	0.836(17)	1.88(2)	2.705(4)	167(5)
O94	H942	O94 ⁱⁱⁱ	0.843(18)	1.90(3)	2.712(6)	163(10)
O95	H951	O97	0.839(17)	2.01(3)	2.814(10)	161(5)
O95	H952	O95 ^{iv}	0.838(18)	2.01(3)	2.837(6)	170(11)
O96	H961	O1 ⁱⁱⁱ	0.842(17)	1.84(2)	2.667(4)	166(7)
O96	H962	O91 ^v	0.847(17)	1.96(3)	2.746(5)	154(6)
O97	H971	O96	0.836(17)	1.93(4)	2.629(7)	141(5)
O97	H972	O1 ^v	0.836(17)	1.85(2)	2.664(6)	164(5)

Symmetry code: (i) $-x+2, y, -z+\frac{3}{2}$; (ii) $-x+\frac{3}{2}, -y+\frac{1}{2}, -z+1$; (iii) $-x+\frac{3}{2}, -y+\frac{1}{2}, -z+2$; (iv) $-x+1, y, -z+\frac{3}{2}$; (v) $-x+\frac{3}{2}, y+\frac{1}{2}, -z+\frac{3}{2}$.

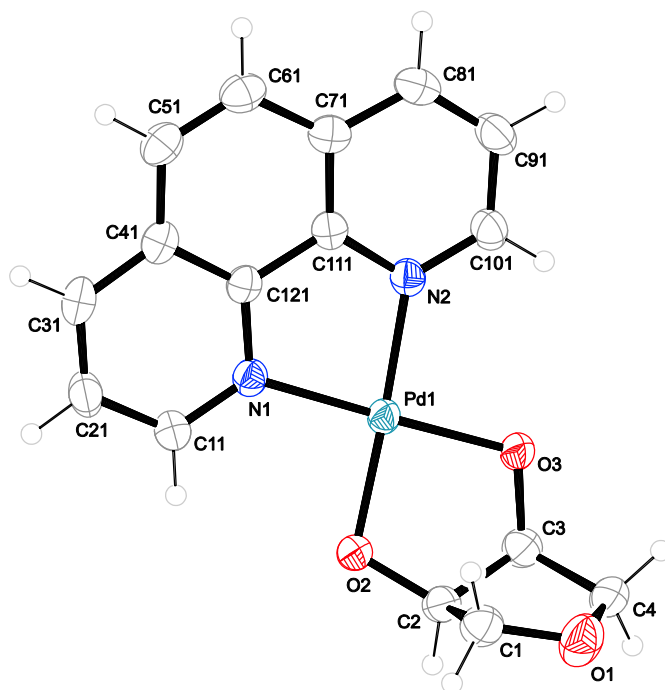


Figure 2.7. The molecular structure of $[\text{Pd}(\text{phen})(\text{AnErytH}_{-2})]$ in crystals of the 4.5-hydrate (**8**). ORTEP plot is drawn with 50% probability ellipsoids. Interatomic distances (\AA) and angles ($^{\circ}$) (standard deviations of the last digit in parentheses): Pd1–O2 1.990(2), Pd1–O3 1.989(2), Pd1–N1 2.024(3), Pd1–N2 2.018(3), O2–Pd1–O3 85.66(9), O2–Pd1–N1 96.00(10), O3–Pd1–N2 96.72(10), N1–Pd1–N2 81.61(10); chelate torsion angles: O1–C1–C2–O2 43.0(3); puckering parameters of the furanose ring O1–C1–C2–C3–C4: $q = 0.372(3) \text{\AA}$, $\varphi = 257.5(5)^{\circ}$.^[22]

The ideal φ value for this conformation is 252° . The observed phase angle indicated a distortion towards a twist conformation 4T_3 , whereas in the known structure of $[\text{Pd}(\text{bpy})(\text{AnErytH}_{-2})]$ 6.5-hydrate,^[57] the oxolane rings showed a 4T_3 twist conformation with a distortion towards an E_3 envelope conformation.

2.3 The polyols: open-chain carbohydrate complexes of palladium(II)

To evaluate the properties of a new $\text{Pd}^{\text{II}}\text{N}_2$ -fragment, the polyols (Fig. 2.8) were an ideal starting point. Well-investigated with Pd-en ^[58] and almost unreactive because of a missing aldehyde function, the polyols promptly indicated the advantages and disadvantages of a $\text{Pd}^{\text{II}}\text{N}_2$ -fragment compared with Pd-en .

Polyols, although open-chain carbohydrate derivatives, are by no means the flexible ligands they are expected to be. Instead, a couple of stereochemical rules determine the ligand properties. Thus, the highest stability is found if (1) the individual chelate ring is formed by a *threo*-configured diol group, (2) two adjacent chelating diol groups are *erythro*-linked, and

2 Results

(3) a δ hydrogen bond, that is, a hydrogen bond whose donor hydroxy and acceptor alkoxido parts are separated by a C_4 chain, can be established. Intramolecular hydrogen bonding seems to be the most competitive variable to metalation of a polyol. If a specific metalation pattern matches all these conditions, such as that of the dimetalated dulcitol, the polyolato ligand is invariably found in this bonding situation. If not, a variety of species of comparable stability is then present in solution.^[58]

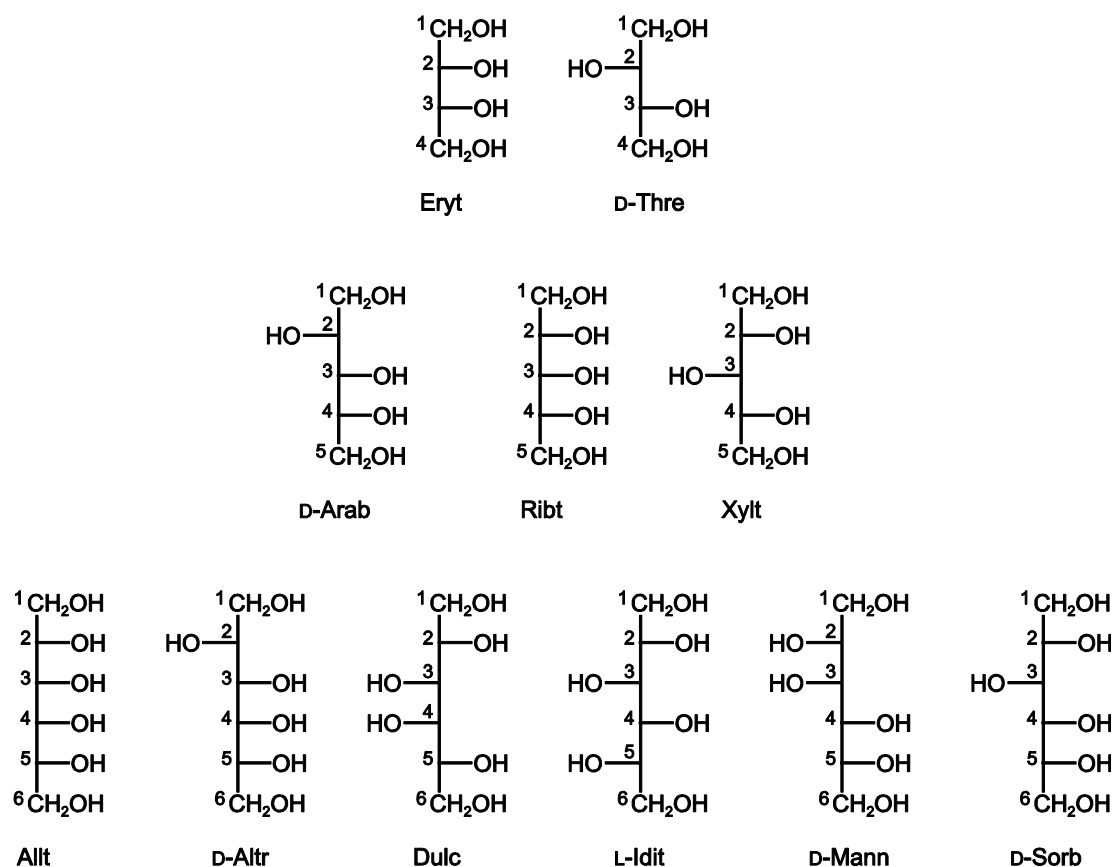


Figure 2.8. Fischer projections and atomic numbering of the C_4 (tetritols, top), C_5 (pentitols, middle) and C_6 (hexitols, bottom) glycitols. From top left to bottom right: erythritol, D-threitol, D-arabitol, ribitol ('adonitol'), xylitol, allitol, D-altritol (= tallitol), dulcitol ('galactitol'), L-iditol, D-mannitol and D-sorbitol ('glucitol', [= gulitol]). Note that, in a Fischer projection, a pair of secondary hydroxy functions at the same side of the carbon backbone is *erythro*-linked, whereas a right-left couple is *threo*-configured. Note that Eryt, Ribt and Allt are *all-erythro*; Thre, Xylt and Idit are *all-threo*. Glycitols lacking the D or L designator are C_1 - or C_5 -symmetric *meso* forms.

Preliminary investigations have eliminated most of the $\text{Pd}^{\text{II}}\text{N}_2$ -fragments introduced so far and have identified the fully alkylated fragments as the most promising ones. In consequence, only ^{13}C NMR spectroscopy results with Pd-tmen, and new results with Pd-en will be presented in the next section. Additionally, crystal structures with all fragments will be discussed.

2 Results

2.3.1 The tetritols: erythritol and D-threitol

With Pd-en, the isomeric tetritols, erythritol and D-threitol, formed the fully metalated $[\text{Pd}_2(\text{en})_2(\text{TetrH}_{-4}\text{-}\kappa\text{O}^{1,2}:\kappa\text{O}^{3,4})]$ species in aqueous solutions of Pd-en/tetritols of a molar ratio of 3:1. With erythritol, the binuclear species was the main species in solution, whereas, as a rough estimate, only half of the D-threitol bound two Pd(en) moieties; the other half acted as a ligand in the mononuclear $[\text{Pd}(\text{en})(\text{D-Thre}_{2,3}\text{H}_{-2}\text{-}\kappa\text{O}^{2,3})]$ species.

This stability of the binuclear $[\text{Pd}_2(\text{en})_2(\text{ErytH}_{-4}\text{-}\kappa\text{O}^{1,2}:\kappa\text{O}^{3,4})]$ and the mononuclear $[\text{Pd}(\text{en})(\text{D-Thre}_{2,3}\text{H}_{-2}\text{-}\kappa\text{O}^{2,3})]$ in the respective solutions dominated the species distribution in 1:1 solutions as well. In the case of erythritol, about one quarter of the tetritol was found as a ligand in the binuclear complex despite the fact that a remarkable amount of erythritol remained uncomplexed in the equimolar solutions. With D-threitol, the $[\text{Pd}(\text{en})(\text{D-Thre}_{2,3}\text{H}_{-2}\text{-}\kappa\text{O}^{2,3})]$ complex was almost the only species in 1:1 solutions. Hence, the analogous complex with the D-Thre_{1,2}H₋₂- $\kappa\text{O}^{1,2}$ ligand was only a minor species in solution.

With Pd-tmen in the 1:1 solutions, the species distribution changed remarkably. With erythritol, the main species was $[\text{Pd}(\text{tmen})(\text{Eryt}_{1,2}\text{H}_{-2}\text{-}\kappa\text{O}^{1,2})]$. Free erythritol and the other species listed in Table 2.5 could be detected only in small amounts. With D-threitol, the dominance of the $[\text{Pd}(\text{tmen})(\text{D-Thre}_{2,3}\text{H}_{-2}\text{-}\kappa\text{O}^{2,3})]$ species was noticeably reduced in favor of $[\text{Pd}(\text{tmen})(\text{D-Thre}_{1,2}\text{H}_{-2}\text{-}\kappa\text{O}^{1,2})]$, $[\text{Pd}_2(\text{tmen})_2(\text{D-ThreH}_{-4}\text{-}\kappa\text{O}^{1,2}:\kappa\text{O}^{3,4})]$ and free

Table 2.5. ¹³C NMR chemical shifts (δ /ppm) and shift differences ($\Delta\delta$) to the free polyol of erythritol and D-threitol ligands in Pd-tmen. Atoms are numbered as in Figure 2.8.

		C1	C2	C3	C4	Chelate
Eryt	δ	63.3	72.7			
Eryt _{1,2} H ₋₂	δ	71.4	81.9	73.2	65.1	
	$\Delta\delta$	8.1	9.2	0.5	1.8	$\kappa\text{O}^{1,2}$
Eryt _{2,3} H ₋₂	δ	62.7	81.5			
	$\Delta\delta$	-0.6	8.8			$\kappa\text{O}^{2,3}$
ErytH ₋₄	δ	75.3	83.6			
	$\Delta\delta$	12.0	10.9			$\kappa\text{O}^{1,2}:\kappa\text{O}^{3,4}$
D-Thre	δ	63.3	72.3			
D-Thre _{1,2} H ₋₂	δ	70.8	80.9	73.8	62.6	
	$\Delta\delta$	7.5	8.6	1.5	-0.7	$\kappa\text{O}^{1,2}$
D-Thre _{2,3} H ₋₂	δ	65.4	80.4			
	$\Delta\delta$	2.1	8.1			$\kappa\text{O}^{2,3}$
D-ThreH ₋₄	δ	72.0	85.2			
	$\Delta\delta$	8.7	12.9			$\kappa\text{O}^{1,2}:\kappa\text{O}^{3,4}$

2 Results

D-threitol occurred only in small amounts. The chemical shifts are listed in Table 2.5. Attempts to crystallize some of the tetritol–palladium complexes were successful for the binuclear erythritolato compound which was obtained in the form of yellow crystals from 3:1 solutions. Crystals of $[\text{Pd}_2(\text{dmen})_2(\text{ErytH}_{-4-\kappa\text{O}^{1,2}}:\kappa\text{O}^{3,4})] \cdot 14 \text{H}_2\text{O}$ (**9**) in the space group $P\bar{1}$ and $[\text{Pd}_2(\text{tn})_2(\text{ErytH}_{-4-\kappa\text{O}^{1,2}}:\kappa\text{O}^{3,4})] \cdot 10 \text{H}_2\text{O}$ (**10**) (Fig. 2.9 and 2.10) in the space group $C2/c$ were composed of almost flat, centrosymmetric molecules whose structures resemble that of the ammine^[59] and the ethane-1,2-diamine^[58] analog. In both cases, the alkoxido O atoms of the fully deprotonated erythritolato ligands acted as hydrogen-bond acceptors in two H bonds each. With the nitrogen-bonded protons of the $\text{Pd}^{\text{II}}\text{N}_2$ -fragment acting as hydrogen-bond donors, both erythritolato compounds were integrated into a hydrogen-bonded network. As one can see in Fig. 6.48, the $[\text{Pd}_2(\text{dmen})_2(\text{ErytH}_{-4-\kappa\text{O}^{1,2}}:\kappa\text{O}^{3,4})]$ molecules formed chains connected via a $\text{N}-\text{H}\cdots\text{O}$ hydrogen bond along the c axis with water molecules linking these chains and forming themselves homodromic six-membered rings around the inversion center; the distances and angles of the hydrogen bonds are listed in Table 2.6. For the crystal structure of $[\text{Pd}_2(\text{tn})_2(\text{ErytH}_{-4-\kappa\text{O}^{1,2}}:\kappa\text{O}^{3,4})]$ a similar motif could be found where chains of molecules were connected by water molecules. The contact between the single molecules was additionally mediated by a water molecule.

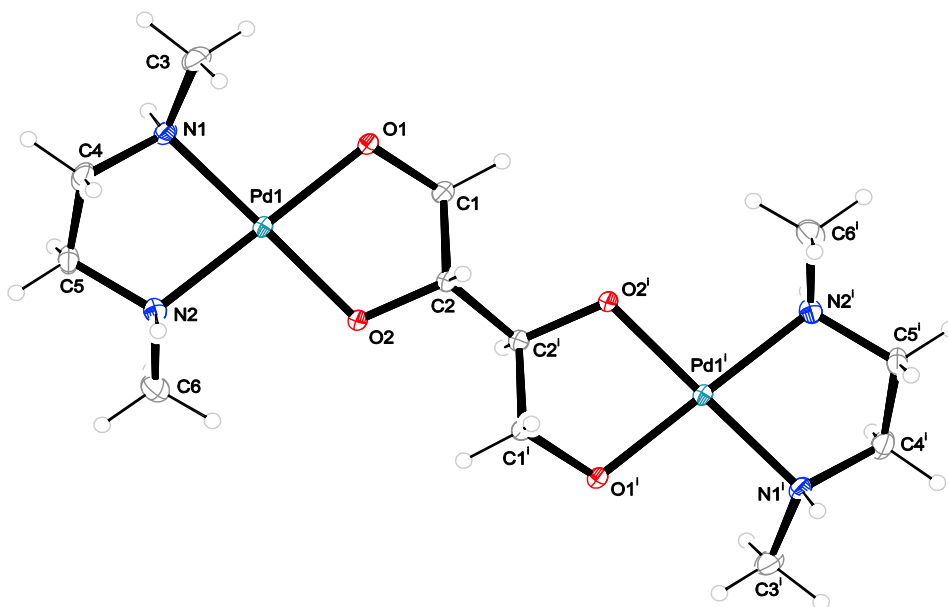


Figure 2.9. The molecular structure of $[\text{Pd}_2(\text{dmen})_2(\text{ErytH}_{-4-\kappa\text{O}^{1,2}}:\kappa\text{O}^{3,4})]$ in crystals of the 14-hydrate (**9**). ORTEP plot is drawn with 50% probability ellipsoids. Interatomic distances (\AA) and angles ($^\circ$) (standard deviations of the last digit in parentheses): Pd1–O1 2.0071(18), Pd1–O2 2.0100(19), Pd1–N1 2.049(2), Pd1–N2 2.040(2), O1–Pd1–O2 85.34(7), O1–Pd1–N1 95.48(9), O2–Pd1–N2 94.91(8), N1–Pd1–N2 84.29(9); chelate torsion angles: N1–C4–C5–N2 56.9(3), O1–C1–C2–O2 52.2(3). [Symmetry code: (i) $-x, -y, -z$]

2 Results

Table 2.6. Distances [Å] and angles [°] of hydrogen bonds in **9**. Standard deviations of the last digit are given in parentheses; values without standard deviation are related to hydrogen atoms at calculated positions. D: donor, A: acceptor.

D	H	A	D–H	H···A	D···A	D–H···A
N1	H711	O1 ⁱ	0.93	1.90	2.817(3)	168.5
N2	H721	O93 ⁱⁱ	0.93	1.99	2.910(4)	171.3
O91	H911	O1	0.731(14)	1.911(15)	2.640(3)	174(4)
O91	H912	O91 ⁱⁱⁱ	0.729(14)	2.045(17)	2.769(4)	172(8)
O92	H921	O2	0.736(13)	2.009(15)	2.743(3)	175(4)
O92	H922	O95	0.726(14)	2.151(18)	2.848(3)	161(4)
O93	H931	O92 ⁱⁱ	0.727(14)	2.16(3)	2.752(4)	139(4)
O93	H932	O94	0.730(14)	2.052(17)	2.752(4)	161(4)
O94	H941	O91	0.729(14)	2.028(14)	2.757(3)	177(4)
O94	H942	O95	0.732(14)	2.096(15)	2.818(4)	169(4)
O95	H951	O96	0.727(14)	2.060(14)	2.784(3)	174(4)
O95	H952	O97	0.721(14)	2.124(14)	2.839(3)	172(4)
O96	H961	O94 ^{iv}	0.726(13)	2.095(15)	2.817(4)	173(4)
O96	H962	O92 ^v	0.730(14)	2.064(16)	2.785(3)	170(4)
O97	H971	O2 ^{vi}	0.730(13)	2.048(14)	2.777(3)	176(4)
O97	H972	O91 ⁱⁱⁱ	0.727(14)	2.080(16)	2.799(3)	170(4)

Symmetry code: (i) $-x+1, -y, -z+1$; (ii) $-x+1, -y, -z+2$; (iii) $-x, -y+1, -z+1$; (iv) $-x, -y+1, -z+2$; (v) $-x, -y+1, -z+2$; (vi) $-x+1, -y+1, -z+1$.

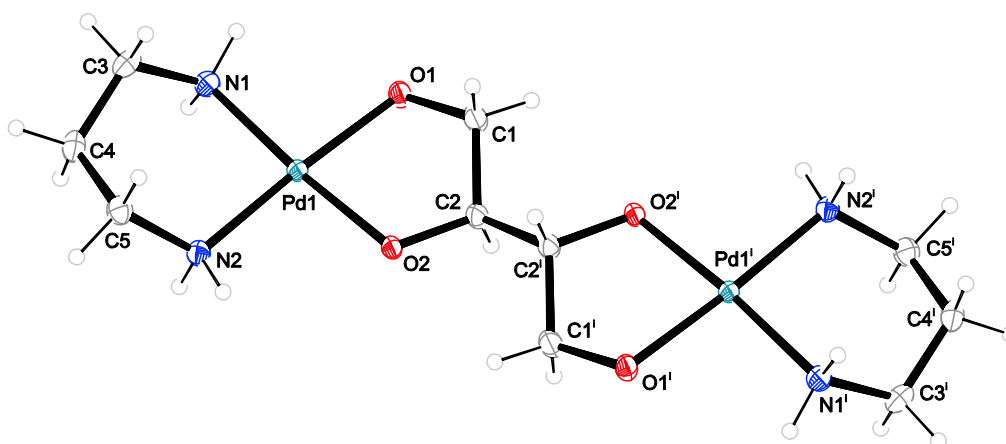


Figure 2.10. The molecular structure of $[\text{Pd}_2(\text{tn})_2(\text{EryH}_{4-\kappa\text{O}^{1,2}}:\kappa\text{O}^{3,4})]$ in crystals of the 10-hydrate (**10**). ORTEP plot is drawn with 50% probability ellipsoids. Interatomic distances (Å) and angles (°) (standard deviations of the last digit in parentheses): Pd1–O1 2.007(3), Pd1–O2 2.011(3), Pd1–N1 2.045(3), Pd1–N2 2.035(3), O1–Pd1–O2 85.39(11), O1–Pd1–N1 91.12(13), O2–Pd1–N2 91.40(12), N1–Pd1–N2 92.12(14); chelate torsion angle: O1–C1–C2–O2 47.3(5). [Symmetry code: (i) $-x, -y, -z$]

2 Results

2.3.2 The pentitols: ribitol and xylitol

Owing to the lack of favorable *threo* chelation and according to the known stereochemical rules, monometalation of ribitol is reliably predictable: the Ribt1,2H₂-κO^{1,2} species is expected to dominate over the Ribt2,3H₂-κO^{2,3} species. With Pd-en at a 1:1 Pd/Ribt ratio, both species and free ribitol could be found in equimolar amounts. Only with Pd-tmen, κO^{1,2}-chelated Ribt1,2H₂ became the main species accompanied by minor amounts of free ribitol, whereas κO^{2,3}-chelated Ribt2,3H₂ was not detected.

At an equimolar Pd/pentitol ratio, xylitol formed the expected chelate ring according to the *threo* rule. As the dimetalated complex was less predominant with xylitol because of a missing *erythro* position which is preferred for dimetalation, with Pd-en the predicted monometalated main species [Pd(en)(Xylt2,3H₂-κO^{2,3})] was observable as well as the terminally chelated [Pd(en)(Xylt1,2H₂-κO^{1,2})] in minor amounts. Both species and free xylitol were also found with Pd-tmen, but now the dominance of Xylt2,3H₂-κO^{2,3} was lessened in favor of Xylt1,2H₂-κO^{1,2}. The chemical shifts for both pentitols are listed in Table 2.7.

Table 2.7. ¹³C NMR chemical shifts (δ/ppm) and shift differences (Δδ) to the free polyol of ribitol and xylitol ligands in Pd-tmen. Atoms are numbered as in Figure 2.8.

		C1	C2	C3	C4	C5	Chelate
Ribt	δ	63.0	72.7	72.9			
Ribt1,2H ₂	δ	71.2	82.5	75.4	72.3	63.0	
	Δδ	8.2	9.8	2.5	-0.4	0.0	κO ^{1,2}
Xylt	δ	63.3	72.6	71.4			
Xylt1,2H ₂	δ	71.0	80.5	72.5	70.7	63.7	
	Δδ	7.7	7.9	1.1	-1.9	0.4	κO ^{1,2}
Xylt2,3H ₂	δ	65.8	79.3	79.6	73.7	62.4	
	Δδ	2.5	6.7	8.2	1.1	-0.9	κO ^{2,3}

2.3.3 The hexitols

Hexitols are composed of three adjacent diol groups, hence a maximum of three Pd^{II}N₂-fragments may be expected to be bonded at high metal/polyol ratios. The two common symmetrical hexitols, D-mannitol and dulcitol, were already investigated with Pd-en, now D-altritol, allitol and D-sorbitol and conversions with both Pd^{II}N₂-fragments, Pd-en and Pd-tmen, have completed the results (chemical shifts are listed in Table 2.8 for Pd-en and in Table 2.9 for Pd-tmen). By using a Pd/hexitol molar ratio of 1:1, the *threo* rule derived above

2 Results

was confirmed. In fact, the *threo*-configured [Pd(en)(Dulc2,3H₂-κO^{2,3})] racemate was the only complex of 1:1 Pd/hexitol stoichiometry. Neither the terminal κO^{1,2}-bonded Dulc1,2H₂ nor the *erythro* κO^{3,4}-bonded Dulc3,4H₂ species was detected by ¹³C NMR spectroscopy. In D-mannitol, the favored *threo* diol occurred only once, but there were two terminal and two *erythro*-configured diol groups. Accordingly, at the 1:1 Pd/Mann ratio, equal amounts of [Pd(en)(D-Mann1,2H₂-κO^{1,2})] and [Pd(en)(D-Mann3,4H₂-κO^{3,4})] were detected; *erythro* coordination did not appear competitive as only weak signals were assigned to [Pd(en)(D-Mann2,3H₂-κO^{2,3})].^[58] With Pd-tmen and dulcitol, the results of the former investigation were confirmed as only κO^{2,3}-bonded Dulc2,3H₂ occurred in solution. The species distribution changed for D-mannitol in Pd-tmen where Mann3,4H₂-κO^{3,4} became the main species and D-Mann1,2H₂-κO^{1,2} is only a minor species in addition to free D-mannitol and traces of higher metalated forms.

Table 2.8. ¹³C NMR chemical shifts (δ/ppm) and shift differences (Δδ) to the free polyol of allitol and D-sorbitol ligands in Pd-en. Atoms are numbered as in Figure 2.8.

		C1	C2	C3	C4	C5	C6	Chelate
Allt	δ	62.3	72.1	72.3				
Allt1,2H ₂	δ	71.3	81.6	73.0	72.5	71.0	62.0	
	Δδ	9.0	9.5	0.7	0.2	-1.1	-0.3	κO ^{1,2}
Allt2,3H ₂	δ	62.7	80.7	82.0	74.4	70.8	61.9	
	Δδ	0.4	8.6	9.7	2.1	-1.3	-0.4	κO ^{2,3}
Allt3,4H ₂	δ	63.7	71.2	82.1				
	Δδ	1.4	-0.9	9.8				κO ^{3,4}
Allt1,2;3,4H ₄	δ	73.0	81.4	82.6	83.0	71.0	64.4	
	Δδ	10.7	9.3	10.3	10.7	-1.1	2.1	κO ^{1,2} :κO ^{3,4}
Allt1,2;4,5H ₄	δ	70.8	81.7	73.0	83.9	81.0	62.1	
	Δδ	8.5	9.6	0.7	11.6	8.9	-0.2	κO ^{1,2} :κO ^{4,5}
Allt1,2;5,6H ₄	δ	69.9	80.5	73.9				
	Δδ	7.6	8.4	1.6				κO ^{1,2} :κO ^{5,6}
Allt2,3;4,5H ₄	δ	62.3	80.8	82.9				
	Δδ	0.0	8.7	10.6				κO ^{2,3} :κO ^{4,5}
D-Sorb	δ	63.1	73.5	70.3	71.7	71.6	63.4	
D-Sorb2,3H ₂	δ	63.2	82.1	80.2	73.1	73.0	64.7	
	Δδ	0.1	8.6	9.9	1.4	1.4	1.3	κO ^{2,3}
D-Sorb3,4H ₂	δ	62.6	74.1	80.3	81.3	73.2	64.6	
	Δδ	-0.5	0.6	10.0	9.6	1.6	1.2	κO ^{3,4}
D-Sorb3,4;5,6H ₄	δ	62.9	74.1	83.5	81.5	83.4	74.0	
	Δδ	-0.2	0.6	13.2	9.8	11.8	10.6	κO ^{3,4} :κO ^{5,6}

2 Results

Table 2.9. ^{13}C NMR chemical shifts (δ/ppm) and shift differences ($\Delta\delta$) to the free polyol of allitol, dulcitol, D-sorbitol and D-mannitol ligands in Pd-tmen. Atoms are numbered as in Figure 2.8.

		C1	C2	C3	C4	C5	C6	Chelate
Allt	δ	62.3	72.1	72.3				
Allt1,2;3,4H ₋₄	δ	72.1	82.3	83.3	83.8	74.2	65.7	
	$\Delta\delta$	9.8	10.2	11.0	11.5	2.1	3.4	$\kappa\text{O}^{1,2}:\kappa\text{O}^{3,4}$
Allt1,2;5,6H ₋₄	δ	72.1	83.0	74.4				
	$\Delta\delta$	9.8	10.9	2.1				$\kappa\text{O}^{1,2}:\kappa\text{O}^{5,6}$
Allt2,3;4,5H ₋₄	δ	62.7	82.0	82.5				
	$\Delta\delta$	0.4	9.9	10.2				$\kappa\text{O}^{2,3}:\kappa\text{O}^{4,5}$
Dulc	δ	63.9	70.8	70.0				
Dulc2,3H ₋₂	δ	66.0	79.8	80.1	71.8	73.7	63.8	
	$\Delta\delta$	2.1	9.0	10.1	1.8	2.9	-0.1	$\kappa\text{O}^{2,3}$
D-Sorb	δ	63.1	73.5	70.3	71.7	71.6	63.4	
D-Sorb3,4H ₋₂	δ	63.1	74.2	79.2	81.6	73.2	65.0	
	$\Delta\delta$	0.0	0.7	8.9	9.9	1.6	1.6	$\kappa\text{O}^{3,4}$
D-Mann	δ	63.8	71.5	69.9				
D-Mann1,2H ₋₂	δ	72.0	80.7	72.1	72.1	72.1	63.8	
	$\Delta\delta$	8.2	9.2	2.2	2.2	0.6	0.0	$\kappa\text{O}^{1,2}$
D-Mann3,4H ₋₂	δ	65.0	73.0	81.7				
	$\Delta\delta$	1.2	1.5	11.8				$\kappa\text{O}^{3,4}$
D-Mann1,2;3,4H ₋₄	δ	73.0	84.4	83.3	84.3	72.7	64.6	
	$\Delta\delta$	9.2	12.9	13.4	14.4	1.2	0.8	$\kappa\text{O}^{1,2}:\kappa\text{O}^{3,4}$
D-Mann1,2;5,6H ₋₄	δ	70.9	82.2	72.7				
	$\Delta\delta$	7.1	10.7	2.8				$\kappa\text{O}^{1,2}:\kappa\text{O}^{5,6}$
D-Mann2,3;4,5H ₋₄	δ	62.6	81.4	81.1				
	$\Delta\delta$	-1.2	9.9	11.2				$\kappa\text{O}^{2,3}:\kappa\text{O}^{4,5}$
D-MannH ₋₆	δ	75.7	84.9	82.6				
	$\Delta\delta$	11.9	13.4	12.7				$\kappa\text{O}^{1,2}:\kappa\text{O}^{3,4}:\kappa\text{O}^{5,6}$

At a higher Pd/hexitol ratio, the dimetalated species became the main solution species for both hexitols. As a reflection of the weakness of *erythro* chelation and the strength of the *erythro* link between two adjacent diol chelators, no symmetrical $[\text{Pd}_2(\text{en})_2(\text{D-Mann2,3;4,5H}_{-4}-\kappa\text{O}^{2,3}:\kappa\text{O}^{4,5})]$ species was detected in the spectra with Pd-en. Instead, the main solution species was $[\text{Pd}_2(\text{en})_2(\text{D-Mann1,2;3,4H}_{-4}-\kappa\text{O}^{1,2}:\kappa\text{O}^{3,4})]$, which comprises pairwise terminal/*threo* chelation with an *erythro* link in between. Accordingly, another dimetalated species, $[\text{Pd}_2(\text{en})_2(\text{D-Mann1,2;5,6H}_{-4}-\kappa\text{O}^{1,2}:\kappa\text{O}^{5,6})]$, was detected as a minor component. Again, with Pd-tmen all species mentioned above occurred in solution, but surprisingly the symmetrical

2 Results

D-Mann2,3;4,5H₋₄-κO^{2,3}:κO^{4,5} species now could be observed in the ¹³C NMR spectra. The crystal structures of [Pd₂(tmen)₂(D-Mann1,2;3,4H₋₄-κO^{1,2}:κO^{3,4})] in Fig. 2.11 and [Pd₂(tn)₂(D-Mann1,2;3,4H₋₄-κO^{1,2}:κO^{3,4})] in Fig. 2.12 both crystallized in the space group *P* 2₁ and highlighted another structural feature which is also known for the Pd-en analogue: the δ hydrogen bond, which is clearly the most stable type of intramolecular hydrogen bond in a polyolato ligand.^[58]

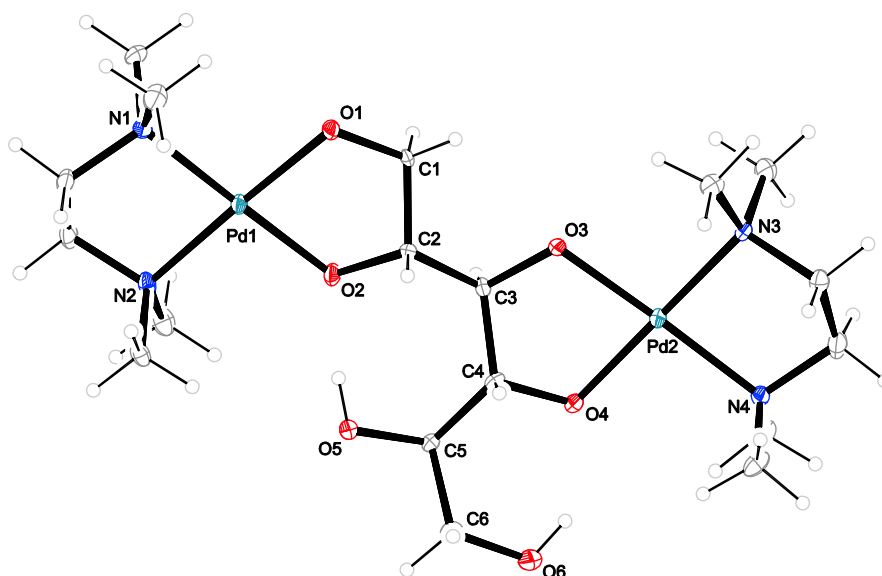


Figure 2.11. The molecular structure of [Pd₂(tmen)₂(Mann1,2;3,4H₋₄-κO^{1,2}:κO^{3,4})] in crystals of the 9-hydrate (**11**). ORTEP plot is drawn with 50% probability ellipsoids. Interatomic distances (Å) and angles (°) (standard deviations of the last digit in parentheses): Pd1–O1 2.002(4), Pd1–O2 2.001(4), Pd1–N1 2.066(5), Pd1–N2 2.046(4), Pd2–O3 1.996(4), Pd2–O4 1.999(3), Pd2–N3 2.057(4), Pd2–N4 2.069(4), O1–Pd1–O2 84.79(16), O1–Pd1–N1 95.42(17), O2–Pd1–N2 94.29(18), N1–Pd1–N2 85.64(19), O3–Pd2–O4 83.90(16), O3–Pd2–N3 95.88(17), O4–Pd2–N4 95.07(16), N3–Pd2–N4 85.08(17); chelate torsion angles: N1–C9–C10–N2 54.9(6), N3–C16–C17–N4 –55.7(6), O1–C1–C2–O2 53.3(6), O3–C3–C4–O4 –50.7(5).

Table 2.10. Distances [Å] and angles [°] of hydrogen bonds in **11**. Standard deviations of the last digit are given in parentheses; values without standard deviation are related to hydrogen atoms at calculated positions. D: donor, A: acceptor.

D	H	A	D–H	H···A	D···A	D–H···A
O5	H851	O2	0.84	1.66	2.495(5)	171.2
O6	H861	O4	0.84	1.89	2.605(5)	142.2
O91	H911	O94 ⁱ	0.812(16)	1.99(2)	2.782(6)	165(7)
O91	H912	O93	0.808(16)	2.10(3)	2.856(6)	155(6)
O92	H921	O98 ⁱⁱ	0.807(16)	1.90(2)	2.680(7)	164(7)
O92	H922	O6 ⁱⁱⁱ	0.810(16)	2.019(18)	2.829(6)	178(5)
O93	H931	O97	0.815(16)	1.95(2)	2.751(6)	166(6)
O93	H932	O1	0.816(16)	1.94(2)	2.737(6)	166(6)

2 Results

Table 2.10. Continued.

D	H	A	D–H	H···A	D···A	D–H···A
O94	H941	O1 ^{iv}	0.815(16)	1.892(18)	2.703(6)	173(5)
O94	H942	O5 ⁱⁱⁱ	0.812(16)	2.045(18)	2.855(6)	175(5)
O95	H951	O92	0.811(16)	2.03(2)	2.817(7)	165(6)
O95	H952	O4 ^v	0.811(16)	2.01(2)	2.804(6)	167(6)
O96	H961	O91 ^{vi}	0.809(16)	1.99(2)	2.780(6)	165(5)
O96	H962	O3	0.808(16)	1.93(2)	2.720(6)	163(6)
O97	H971	O92	0.814(16)	2.04(3)	2.798(7)	155(6)
O97	H972	O5 ^{vi}	0.816(16)	2.05(2)	2.858(6)	170(6)
O98	H981	O99 ^{iv}	0.811(16)	1.94(2)	2.745(7)	170(6)
O98	H982	O96 ⁱ	0.814(16)	1.95(2)	2.747(7)	166(7)
O99	H991	O93	0.809(16)	2.246(18)	3.054(7)	177(6)
O99	H992	O95	0.808(16)	1.898(18)	2.701(7)	172(5)

Symmetry code: (i) $-x+1, y+1/2, -z+1$; (ii) $-x+1, y-1/2, -z$; (iii) $-x+1, y-1/2, -z+1$; (iv) $x+1, y, z$; (v) $x, y, z-1$; (vi) $-x, y-1/2, -z+1$.

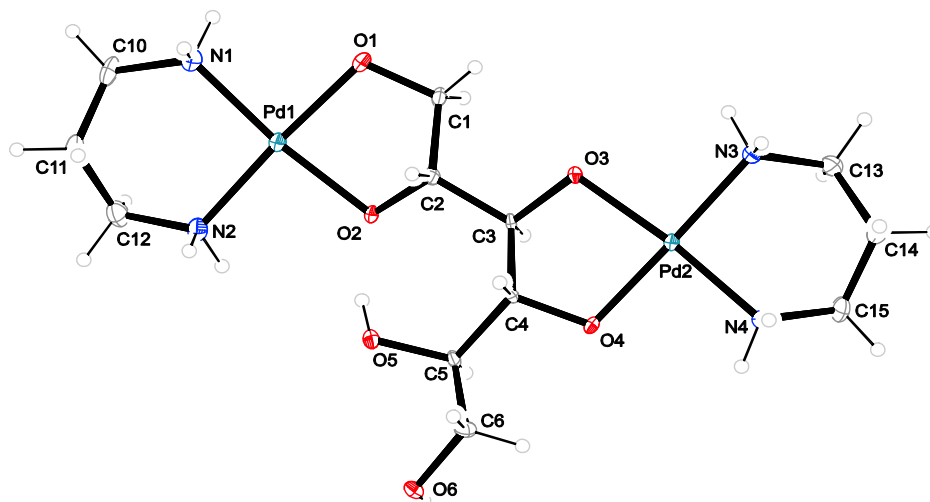


Figure 2.12. The molecular structure of $[\text{Pd}_2(\text{tn})_2(\text{Mann}1,2;3,4\text{H}-4\text{-}\kappa\text{O}^{1,2}:\kappa\text{O}^{3,4})]$ in crystals of the 5-hydrate (**12**). ORTEP plot is drawn with 50% probability ellipsoids. Interatomic distances (Å) and angles (°) (standard deviations of the last digit in parentheses): Pd1–O1 2.000(3), Pd1–O2 2.010(3), Pd1–N1 2.041(5), Pd1–N2 2.046(4), Pd2–O3 2.027(3), Pd2–O4 1.974(3), Pd2–N3 2.054(4), Pd2–N4 2.045(4), O1–Pd1–O2 84.62(13), O1–Pd1–N1 88.63(16), O2–Pd1–N2 91.47(15), N1–Pd1–N2 95.24(18), O3–Pd2–O4 83.99(13), O3–Pd2–N3 94.36(15), O4–Pd2–N4 90.18(16), N3–Pd2–N4 91.48(17); chelate torsion angles: O1–C1–C2–O2 52.3(5), O3–C3–C4–O4 –54.3(5).

2 Results

Table 2.11. Distances [\AA] and angles [$^\circ$] of hydrogen bonds in **12**. Standard deviations of the last digit are given in parentheses; values without standard deviation are related to hydrogen atoms at calculated positions. D: donor, A: acceptor.

D	H	A	D–H	H \cdots A	D \cdots A	D–H \cdots A
O5	H85	O2	0.84	1.73	2.546(5)	163.5
O6	H86	O3 ⁱ	0.84	1.88	2.695(5)	163.9
N1	H711	O6 ⁱⁱ	0.92	1.99	2.886(6)	165.0
N2	H721	O94 ⁱⁱⁱ	0.92	2.14	3.012(7)	157.9
N2	H722	O92 ⁱⁱⁱ	0.92	2.06	2.938(6)	158.6
N3	H731	O6 ^{iv}	0.92	2.29	3.081(6)	143.3
N3	H731	O5 ^{iv}	0.92	2.38	3.153(6)	141.6
N3	H732	O94 ^v	0.92	2.15	3.008(7)	154.1
N4	H742	O93 ^{vi}	0.92	2.28	2.996(6)	134.0
O91	H911	O92	0.828(10)	1.946(18)	2.764(6)	169(6)
O91	H912	O3 ⁱ	0.830(10)	2.03(3)	2.791(6)	153(6)
O92	H921	O4	0.825(10)	1.889(14)	2.710(5)	173(7)
O92	H922	O93 ^{vi}	0.830(10)	1.94(3)	2.709(6)	155(5)
O93	H931	O1 ^{vii}	0.828(10)	1.84(2)	2.634(5)	160(6)
O93	H932	O5	0.824(10)	2.07(3)	2.786(5)	145(5)
O94	H941	O1 ^{viii}	0.830(10)	1.95(3)	2.725(6)	156(8)
O94	H942	O95 ^{vi}	0.828(10)	1.92(2)	2.711(7)	159(7)
O95	H951	O2	0.827(10)	2.017(14)	2.841(6)	174(8)
O95	H952	O91	0.825(10)	2.038(18)	2.845(7)	166(6)

Symmetry code: (i) $-x+1, y+\frac{1}{2}, -z+1$; (ii) $-x+1, y-\frac{1}{2}, -z$; (iii) $x, y, z-1$; (iv) $-x+1, y-\frac{1}{2}, -z+1$; (v) $-x+1, y-\frac{1}{2}, -z+2$; (vi) $x, y, z+1$; (vii) $-x+1, y+\frac{1}{2}, -z$; (viii) $-x, y+\frac{1}{2}, -z+1$.

In **11**, the additional intramolecular γ hydrogen bond O6–H \cdots O4 finally inhibited [Pd₂(tmen)₂(D-Mann1,2;3,4H₋₄- κ O^{1,2}: κ O^{3,4})] from acting as a hydrogen bond donor. Because of the protons' replacement of tmen by methyl groups and the two intramolecular hydrogen bonds of the remaining hydroxy functions, the coordination compound could only accept hydrogen bonds from the nine water molecules in the asymmetric unit. In Table 2.10, the distances and angles of the hydrogen bonds are listed. In contrast, in **12** [Pd₂(tn)₂(D-Mann1,2;3,4H₋₄- κ O^{1,2}: κ O^{3,4})] showed only the δ hydrogen bond again and the terminal hydroxy function connected the single molecules via a O6–H \cdots O3 hydrogen bond. The chains were stabilized by a second hydrogen bonding path via N4–H \cdots O93–H \cdots O1. The remaining N–H functions of the Pd^{II}N₂-fragments and water molecules linked the single chains of the crystal structure, the distances and angles of the hydrogen bonding network are listed in Table 2.11.

2 Results

In the case of dulcitol, all the optimum conditions for dimetalation coincided: each individual palladium atom was incorporated into a *threo* chelate, the two Pd-binding sites were *erythro*-linked, and the terminal hydroxy groups could act as donors in δ hydrogen bonds. When the palladium content of the solution exceeded the Pd/Dulc ratio of 2:1, the result was a simple three-signal ^{13}C NMR spectrum of the expected C_1 -symmetrical Dulc_{2,3;4,5}H₋₄- $\kappa O^{2,3}:\kappa O^{4,5}$ species. Crystallization from 3:1 solutions was successful for $[\text{Pd}_2(\text{dmen})_2(\text{Dulc}_{2,3;4,5}\text{H}_{-4}-\kappa O^{2,3}:\kappa O^{4,5})]$ (Fig. 2.13) and $[\text{Pd}_2(\text{tn})_2(\text{Dulc}_{2,3;4,5}\text{H}_{-4}-\kappa O^{2,3}:\kappa O^{4,5})]$ (Fig. 2.14). Crystallizing in the space group $P\bar{1}$ and, independent of the Pd^{II}N₂-fragment, both compounds presented the S-shaped dulcitol motif fixed by the two intramolecular δ hydrogen bonds. In **13**, the single molecules formed chains along the hydrogen bond N1–H \cdots O21 where the chains were held together by a hydrogen bonding network of eight water molecules. The distances and angles of the hydrogen bonding network are listed in Table 2.12. In **14**, dulcitol appeared with the identical S-shaped motif as in **13**. In contrast, the intermolecular hydrogen-bonding network differed noticeably. No direct hydrogen-bonding contact connected the molecules; all contacts were water-mediated as in N11–H \cdots O93–H \cdots O22 and N12–H \cdots O91–H \cdots O21. Additionally, another water molecule linked the polyols via O11 \cdots H–O94–H \cdots O22 and, acting as a double acceptor, O92 of the corresponding water molecule bridged the tn ligands via N21–H \cdots O92 \cdots H–N22. The remaining distances and angles of the hydrogen bonding network are listed in Table 2.13.

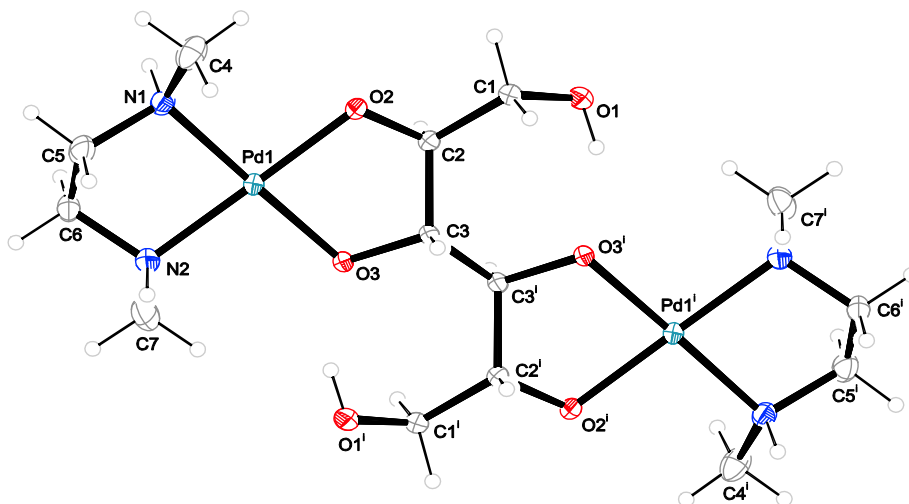


Figure 2.13. The molecular structure of $[\text{Pd}_2(\text{dmen})_2(\text{Dulc}_{2,3;4,5}\text{H}_{-4}-\kappa O^{2,3}:\kappa O^{4,5})]$ in crystals of the 8-hydrate (**13**). ORTEP plot is drawn with 50% probability ellipsoids. Interatomic distances (\AA) and angles ($^\circ$) (standard deviations of the last digit in parentheses): Pd1–O2 1.9968(18), Pd1–O3 2.0032(17), Pd1–N1 2.058(3), Pd1–N2 2.049(3), O2–Pd1–O3 83.63(7), O2–Pd1–N1 95.46(10), O3–Pd1–N2 97.03(9), N1–Pd1–N2 83.88(11); chelate torsion angles: N1–C5–C6–N2 58.9(4), O2–C2–C3–O3 53.7(3). [Symmetry code: (i) $-x, -y, -z$]

2 Results

Table 2.12. Distances [\AA] and angles [$^\circ$] of hydrogen bonds in **13**. Standard deviations of the last digit are given in parentheses; values without standard deviation are related to hydrogen atoms at calculated positions. D: donor, A: acceptor.

D	H	A	D–H	H \cdots A	D \cdots A	D–H \cdots A
O1	H811	O3 ⁱ	0.84	1.80	2.569(3)	151.6
N1	H711	O2 ⁱⁱ	0.93	1.97	2.883(3)	166.4
N2	H712	O91 ⁱⁱⁱ	0.93	1.96	2.845(3)	158.5
O91	H911	O94 ^{iv}	0.943(16)	1.781(17)	2.720(4)	174(4)
O91	H912	O2	0.940(16)	1.761(17)	2.698(3)	174(3)
O92	H921	O1	0.934(16)	1.785(17)	2.716(3)	175(4)
O92	H922	O93 ^v	0.935(16)	1.806(17)	2.729(3)	169(3)
O93	H931	O3	0.932(16)	1.887(17)	2.817(3)	176(4)
O93	H932	O92 ^{vi}	0.930(16)	1.947(17)	2.862(3)	167(3)
O94	H941	O92 ^{vii}	0.948(16)	1.802(17)	2.748(4)	175(4)
O94	H942	O91	0.939(16)	1.93(2)	2.797(4)	152(3)

Symmetry code: (i) $-x+1, -y, -z$; (ii) $-x, -y+1, -z$; (iii) $-x+1, -y+1, -z$; (iv) $-x+1, -y+1, -z-1$; (v) $-x, -y, -z$; (vi) $x, y, z+1$; (vii) $-x+1, -y, -z-1$.

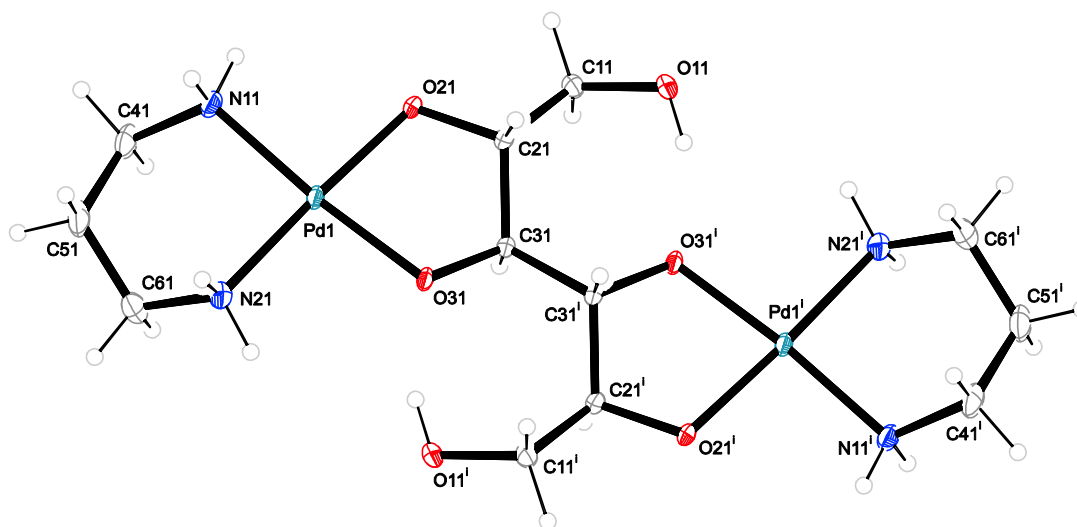


Figure 2.14. The molecular structure of $[\text{Pd}_2(\text{tn})_2(\text{Dulc}_{2,3;4,5}\text{H}_{-4}-\kappa\text{O}^{2,3}:\kappa\text{O}^{4,5})]$ in crystals of the 6-hydrate (**14**). ORTEP plot is drawn with 50% probability ellipsoids. Interatomic distances (\AA) and angles ($^\circ$) (standard deviations of the last digit in parentheses): Pd1–O21 1.989(2), Pd1–O31 1.9925(19), Pd1–N11 2.033(3), Pd1–N21 2.045(3), O21–Pd1–O31 84.11(8), O21–Pd1–N11 91.52(10), O31–Pd1–N21 93.15(10), N11–Pd1–N21 91.24(11); chelate torsion angle: O21–C21–C31–O31 $-50.2(3)$. [Symmetry code: (i) $-x, -y, -z$]

2 Results

Table 2.13. Distances [\AA] and angles [$^\circ$] of hydrogen bonds in **14**. Standard deviations of the last digit are given in parentheses; values without standard deviation are related to hydrogen atoms at calculated positions. D: donor, A: acceptor.

D	H	A	D–H	H \cdots A	D \cdots A	D–H \cdots A
O11	H811	O31 ⁱ	0.84	1.73	2.521(3)	157.0
O12	H812	O32 ⁱⁱ	0.84	1.75	2.538(3)	154.8
N11	H711	O21 ⁱⁱⁱ	0.92	2.20	3.102(3)	166.5
N11	H712	O93	0.92	2.12	2.984(3)	156.7
N12	H721	O91	0.92	2.08	2.946(3)	156.3
N12	H722	O22 ^{iv}	0.92	2.58	3.492(3)	174.4
N21	H713	O94 ^v	0.92	2.56	3.407(3)	152.8
N21	H714	O92 ⁱⁱⁱ	0.92	1.92	2.836(4)	172.3
N22	H723	O94 ^{iv}	0.92	2.05	2.963(3)	170.4
N22	H724	O92 ^{vi}	0.92	2.08	2.927(4)	153.3
O91	H911	O21	0.819(10)	1.940(11)	2.754(3)	173(4)
O91	H912	O94	0.817(10)	2.047(16)	2.789(3)	151(3)
O92	H921	O93	0.867(9)	1.898(8)	2.709(3)	155(2)
O92	H922	O12 ^{vii}	0.848(10)	1.874(8)	2.650(3)	151(2)
O93	H931	O22	0.833(10)	1.995(10)	2.826(3)	175(3)
O93	H932	O951	0.828(10)	1.881(18)	2.699(12)	169(4)
O94	H941	O22	0.832(10)	1.943(10)	2.765(3)	169(3)
O94	H942	O11 ^{viii}	0.824(10)	1.897(10)	2.720(3)	177(3)
O951	H951	O31 ⁱⁱⁱ	0.828(10)	1.941(15)	2.742(8)	163(4)
O951	H952	O96	0.829(10)	1.88(2)	2.654(8)	154(4)
O96	H961	O32 ⁱⁱ	0.829(10)	1.99(2)	2.775(3)	157(6)
O96	H962	O91 ^{viv}	0.829(10)	1.892(12)	2.714(3)	172(5)

Symmetry code: (i) $-x, -y, -z+1$; (ii) $-x+2, -y-1, -z$; (iii) $-x+1, -y-1, -z+1$; (iv) $-x+1, -y, -z$; (v) $-x+1, -y, -z+1$; (vi) $-x+1, -y-1, -z$; (vii) $x-1, y, z$; (viii) $x+1, y, z$; (viv) $x+1, y-1, z$.

With the various contributions to the overall stability of a metal complex of a particular hexitol configuration in mind, complete metalation at high Pd/hexitol ratios appeared possible for mannitol but a challenge in the case of dulcitol. In fact, the three signals of the $[\text{Pd}_3(\text{en})_3(\text{D-MannH}_{-6}\text{-}\kappa\text{O}^{1,2}:\kappa\text{O}^{3,4}:\kappa\text{O}^{5,6})]$ species were detected in solutions of Pd-tmen as for Pd-en, but not even a trace of trimetalated species was observed with dulcitol underlining the high contribution of the δ hydrogen bond to the overall complex stability.

The currently investigated D-Altritol provides one *threo* position at O2/O3 which should be metalated first; the second Pd^{II}N₂-fragment should coordinate at O4/O5 with an *erythro* link between the two adjacent diol chelators. Indeed, the crystal structure of **15** in Fig. 2.15 which

2 Results

was solved in the space group $P 2_1$ confirmed the predictions. Furthermore, $[\text{Pd}_2(\text{tmen})_2(\text{D-Altr}_{2,3;4,5}\text{H}_{-4-\kappa}\text{O}^{2,3};\kappa\text{O}^{4,5})]$ showed a S-shaped motif with two intramolecular δ hydrogen bonds as identified for dulcitol, another proof of the importance of the δ hydrogen bond for the polyols' coordination chemistry.

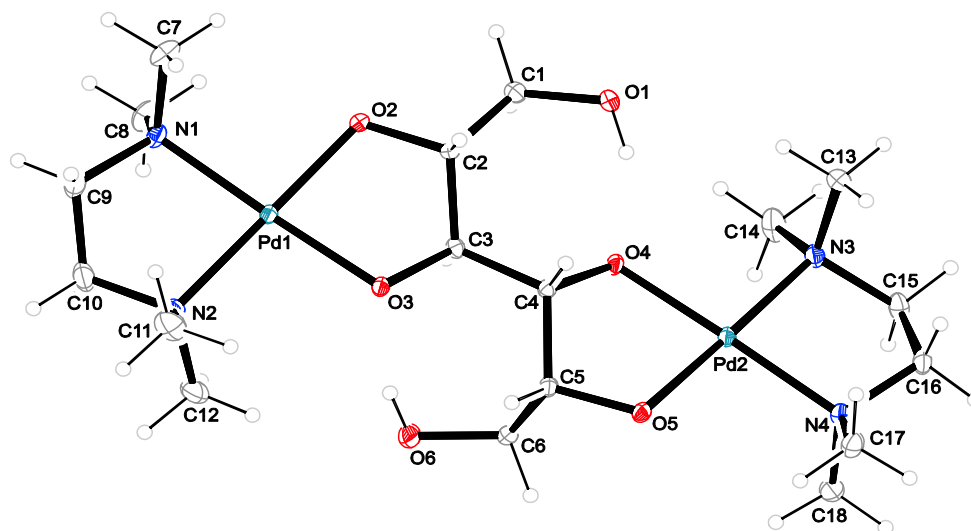


Figure 2.15. The molecular structure of $[\text{Pd}_2(\text{tmen})_2(\text{D-Altr}_{2,3;4,5}\text{H}_{-4-\kappa}\text{O}^{2,3};\kappa\text{O}^{4,5})]$ in crystals of the 9-hydrate (**15**). ORTEP plot is drawn with 50% probability ellipsoids. Interatomic distances (Å) and angles ($^\circ$) (standard deviations of the last digit in parentheses): Pd1–O2 1.998(3), Pd1–O3 2.005(2), Pd1–N1 2.063(3), Pd1–N2 2.062(3), Pd2–O4 2.001(2), Pd2–O5 2.005(2), Pd2–N3 2.068(3), Pd2–N4 2.055(3), O2–Pd1–O3 84.33(9), O2–Pd1–N1 93.91(12), O3–Pd1–N2 96.14(10), N1–Pd1–N2 85.66(12), O4–Pd2–O5 84.33(10), O4–Pd2–N3 95.11(10), O5–Pd2–N4 95.55(13), N3–Pd2–N4 85.11(13); chelate torsion angles: N1–C9–C10–N2 53.3(4), N3–C15–C16–N4 54.5(4), O2–C2–C3–O3 $-53.3(3)$, O4–C4–C5–O5 51.8(3).

Table 2.14. Distances [Å] and angles [$^\circ$] of hydrogen bonds in **15**. Standard deviations of the last digit are given in parentheses; values without standard deviation are related to hydrogen atoms at calculated positions. D: donor, A: acceptor.

D	H	A	D–H	H \cdots A	D \cdots A	D–H \cdots A
O1	H811	O4	0.84	1.78	2.576(3)	157.5
O6	H861	O3	0.84	1.88	2.701(3)	163.9
O91	H911	O2	0.835(10)	2.053(13)	2.871(4)	166(4)
O91	H912	O93 ⁱ	0.834(10)	2.009(11)	2.839(4)	173(4)
O92	H921	O2 ⁱⁱ	0.833(10)	2.025(17)	2.819(4)	159(4)
O92	H922	O95 ⁱⁱ	0.837(10)	1.837(12)	2.667(4)	171(4)
O93	H931	O92	0.831(10)	1.861(12)	2.677(4)	167(3)
O93	H932	O1	0.832(10)	1.999(11)	2.823(4)	170(3)
O94	H941	O4	0.836(10)	1.969(11)	2.804(4)	177(4)
O94	H942	O91	0.833(10)	2.118(11)	2.950(4)	177(5)

2 Results

Table 2.14. Continued.

D	H	A	D–H	H···A	D···A	D–H···A
O95	H951	O98	0.832(10)	1.920(15)	2.737(5)	167(4)
O95	H952	O99	0.831(10)	1.935(15)	2.743(4)	164(4)
O96	H961	O3 ⁱⁱ	0.837(10)	1.955(11)	2.789(4)	175(4)
O96	H962	O93	0.837(10)	2.104(17)	2.914(4)	163(4)
O97	H971	O5 ⁱⁱ	0.840(10)	1.910(11)	2.747(4)	174(5)
O97	H972	O94 ⁱⁱⁱ	0.840(10)	2.137(17)	2.964(4)	168(5)
O98	H981	O96	0.835(10)	1.924(12)	2.752(5)	172(4)
O98	H982	O97	0.836(10)	1.99(3)	2.783(5)	159(7)
O99	H991	O5 ⁱⁱⁱ	0.839(10)	1.880(11)	2.717(3)	175(4)
O99	H992	O94 ^{iv}	0.840(10)	1.961(11)	2.800(4)	180(4)

Symmetry code: (i) $x-1, y, z$; (ii) $-x+1, y-1/2, -z+1$; (iii) $x, y, z-1$; (iv) $-x+1, y+1/2, -z+1$.

As in structure **11** with D-mannitol, $[\text{Pd}_2(\text{tmen})_2(\text{D-Altr}_{2,3;4,5}\text{H}_{-4}\text{-}\kappa\text{O}^{2,3}:\kappa\text{O}^{4,5})]$ could only accept hydrogen bonds from the water-mediated hydrogen-bonding network because of missing hydrogen donors at the $\text{Pd}^{\text{II}}\text{N}_2$ -fragment and the intramolecular hydrogen bonds of the polyol. As depicted in Fig. 6.54 of the Appendix, a prominent hydrogen-bonding pattern of four molecules which was characterized by the ring descriptor $\text{R}_4^2(8)^{[60]}$ and an additional water molecule were involved in the linking of $[\text{Pd}_2(\text{tmen})_2(\text{D-Altr}_{2,3;4,5}\text{H}_{-4}\text{-}\kappa\text{O}^{2,3}:\kappa\text{O}^{4,5})]$ molecules.

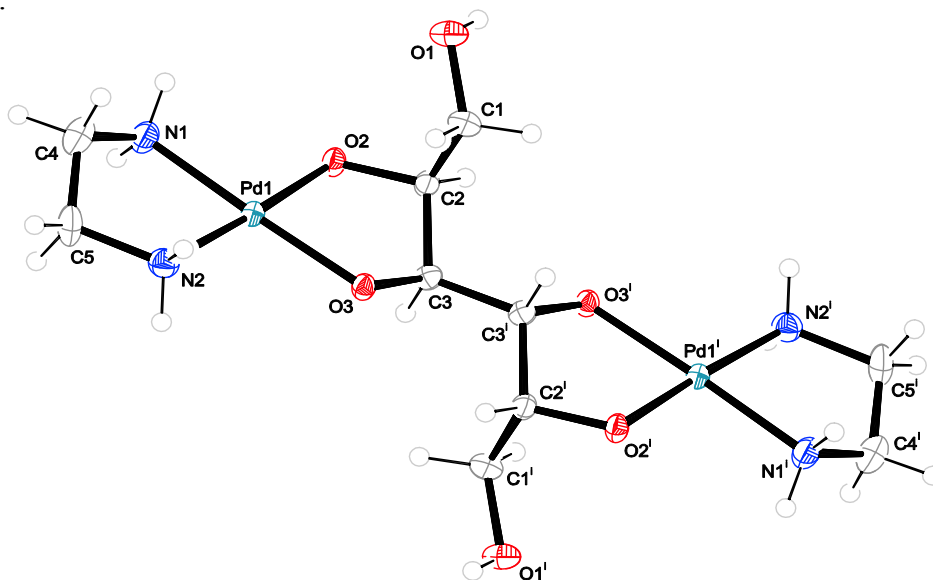


Figure 2.16. The molecular structure of $[\text{Pd}_2(\text{en})_2(\text{Allt}_{2,3;4,5}\text{H}_{-4}\text{-}\kappa\text{O}^{2,3}:\kappa\text{O}^{4,5})]$ in crystals of the 14-hydrate (**16**). ORTEP plot is drawn with 50% probability ellipsoids. Interatomic distances (Å) and angles (°) (standard deviations of the last digit in parentheses): Pd1–O2 1.993(4), Pd1–O3 2.022(4), Pd1–N1 2.034(5), Pd1–N2 2.048(5), O2–Pd1–O3 84.83(14), O2–Pd1–N1 93.09(17), O3–Pd1–N2 98.33(16), N1–Pd1–N2 83.76(18); chelate torsion angles: N1–C4–C5–N2 49.8(6), O2–C2–C3–O3 –54.5(5). [Symmetry code: (i) $-x, -y, -z$]

2 Results

Table 2.15. Distances [\AA] and angles [$^\circ$] of hydrogen bonds in **16**. Standard deviations of the last digit are given in parentheses; values without standard deviation are related to hydrogen atoms at calculated positions. D: donor, A: acceptor.

D	H	A	D–H	H \cdots A	D \cdots A	D–H \cdots A
O1	H1	O91 ⁱ	0.84	1.93	2.748(6)	165.0
N1	H711	O98 ⁱⁱ	0.92	2.60	3.282(7)	131.4
N1	H712	O95	0.92	2.16	3.017(7)	155.4
N2	H721	O94 ⁱⁱⁱ	0.92	2.22	3.013(6)	143.3
N2	H721	O91 ⁱⁱⁱ	0.92	2.58	3.248(7)	130.4
N2	H722	O1 ^{iv}	0.92	2.11	3.013(6)	168.0
O91	H911	O3 ⁱⁱ	0.746(19)	1.89(2)	2.634(5)	173(6)
O91	H912	O92	0.743(19)	2.10(3)	2.827(8)	166(8)
O92	H921	O94	0.738(19)	2.18(4)	2.881(9)	160(8)
O92	H921	O91	0.738(19)	2.48(8)	2.827(8)	111(7)
O92	H922	O96	0.739(19)	2.04(3)	2.764(8)	168(8)
O93	H93	O92	0.739(19)	1.99(2)	2.722(7)	171(8)
O94	H941	O97	0.741(19)	2.34(7)	2.783(5)	120(7)
O94	H942	O2 ⁱ	0.745(19)	1.97(2)	2.703(5)	168(6)
O95	H951	O93 ^v	0.740(19)	2.07(3)	2.776(6)	160(8)
O95	H952	O2 ⁱ	0.739(19)	1.96(2)	2.695(5)	175(7)
O96	H961	O98	0.741(19)	1.98(2)	2.718(7)	175(8)
O96	H962	O95	0.742(19)	2.01(3)	2.733(7)	164(7)
O97	H97	O94 ⁱ	0.736(19)	2.28(6)	2.781(5)	127(7)
O98	H981	O3 ^{vii}	0.741(19)	2.03(2)	2.772(6)	173(8)
O98	H982	O1 ⁱⁱⁱ	0.741(19)	2.21(3)	2.916(6)	158(8)

Symmetry code: (i) $-x, y, -z+1/2$; (ii) $-x+1/2, y-1/2, -z+1/2$; (iii) $-x+1/2, y+1/2, -z+1/2$; (iv) $-x+1/2, -y+1/2, -z+1$; (v) $x-1/2, y+1/2, z$; (vi) $x, -y+1, z-1/2$.

In the ring motif, the water molecules of O97 and O99 as double hydrogen donors, and the alkoxido O5 and the water molecule of O94 as hydrogen bonding acceptors were involved. The water molecule of O94 participated in two hydrogen-bonding paths: O94–H \cdots O4 and O94–H \cdots O91–H \cdots O4. To summarize, the contact of the single molecules of $[\text{Pd}_2(\text{tmen})_2(\text{D-Altr}_{2,3;4,5}\text{H}_{-4-\kappa}\text{O}^{2,3}:\kappa\text{O}^{4,5})]$ was mediated by four water molecules forming a rigid hydrogen-bonding network, without direct hydrogen bonds between the molecules. The distances and angles of the hydrogen bonding network are listed in Table 2.14. The most interesting example of the influence of the Pd^{II}N₂-fragment's ability to form hydrogen bonds was presented by the investigations of Allitol with Pd-en and Pd-tmen. Providing only *erythro*-configured diol groups according to the rules, the terminal chelation sites for metalation should be preferred. At an equimolar Pd/allitol ratio, with Pd-en^[61] all monometalated forms

2 Results

listed in Table 2.8 and free allitol were detected in similar amounts. Small signals could be observed for the dimetalated species in Table 2.8. Increasing the Pd/Allt ratio to 3:1, Allt1,2;3,4H₄-κO^{1,2}:κO^{3,4} became the main species and Allt1,2;4,5H₄-κO^{1,2}:κO^{4,5} a minor species. Weak signals indicated the presence of κO^{1,2}:κO^{5,6}-bonded Allt1,2;5,6H₄ and κO^{2,3}:κO^{4,5}-bonded Allt2,3;4,5H₄ in solution. Nevertheless, attempts to crystallize one of the palladium(II)-allitol complexes were unexpectedly successful for the binuclear compound in Fig. 2.16, [Pd₂(en)₂(Allt2,3;4,5H₄-κO^{2,3}:κO^{4,5})] which crystallized in the space group *C* 2/*c*. Although the terminal diol functions were a suitable distance to form a δ hydrogen bond, for sterical reasons it seemed not to be plausible. The single molecules were linked via two hydrogen bonds: N2-H···O1 and O3···H-O98-H···O1 involving a water molecule. The remaining water molecules in **16** formed a hydrogen-bonding network connecting the chains of coordinated allitol. The distances and angles of the hydrogen bonding network are listed in Table 2.15. The situation changed with Pd-tmen at a 3:1 Pd/Allt ratio. Now, Allt1,2;5,6H₄-κO^{1,2}:κO^{5,6} was obviously the main species and only small signals of Allt1,2;3,4H₄-κO^{1,2}:κO^{3,4} and Allt2,3;4,5H₄-κO^{2,3}:κO^{4,5} could be detected. Structural analysis confirmed the spectroscopic result in Fig. 2.17. where the molecular structure of [Pd₂(tmen)₂(Allt1,2;5,6H₄-κO^{1,2}:κO^{5,6})] is depicted. The crystals of the 8-hydrate **17** were isolated from 3:1 solutions and solved in the space group *P* 2₁/*n*. The first time, the use of two different Pd^{II}N₂-fragments resulted in noticeably different coordination patterns. Analyzing the crystal structure of **17** two facts were especially striking: (1) the use of Pd-tmen inhibited the complex's donor function for hydrogen bonding as it was found for the mannitolato (**11**) and D-altritolato (**15**) compounds and (2) the formation of intramolecular hydrogen bonding was enforced as the two protons of O3 and O3ⁱ form γ hydrogen bonds to O2 and O2ⁱ. These intramolecular hydrogen bonds explained the high formation tendency of κO^{1,2}:κO^{5,6}-chelated Allt1,2;5,6H₄ as opposed to κO^{1,2}:κO^{3,4}-chelated Allt1,2;3,4H₄ which was the main species with Pd-en. As one can see in Fig. 6.56 of the Appendix, the crystal structure could be distinguished from among the hydrophobic part of the tmen fragments, the hydrophilic part of the allitol's hydroxy functions and the hydrogen bonding network of the water molecules. The distances and angles of the hydrogen-bonding network are listed in Table 2.16.

Finally, D-sorbitol is an asymmetric polyol providing two *threo* and one *erythro* position, so in a first metalation step D-Sorb2,3H₂-κO^{2,3} or D-Sorb3,4H₂-κO^{3,4} should be formed. For dimetalation, the main solution species should be the favorable bischelate D-Sorb3,4;5,6H₄-κO^{3,4}:κO^{5,6} which comprised pairwise terminal/*threo* chelation with an *erythro* link in between.

2 Results

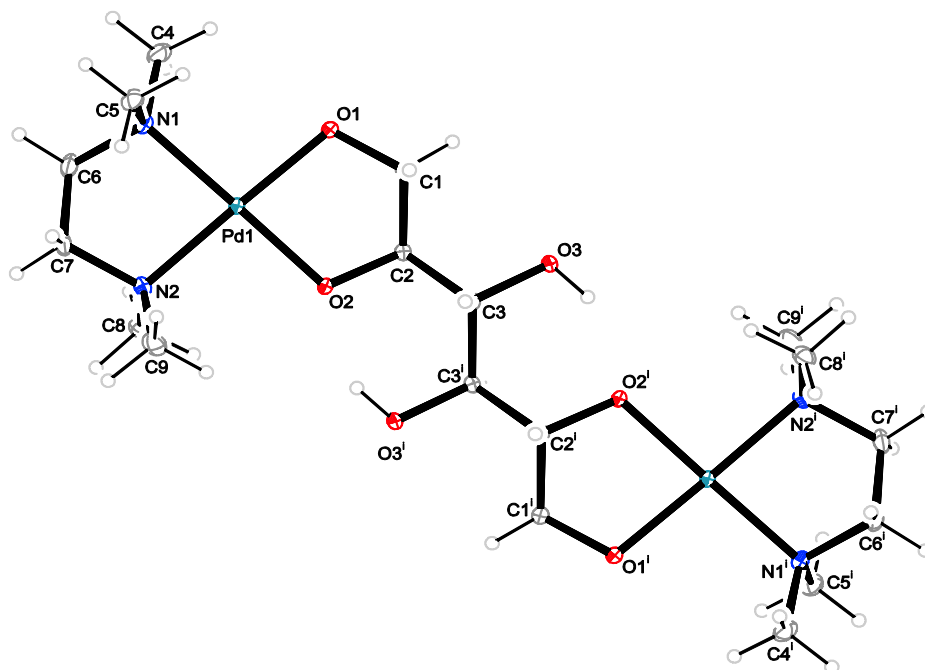


Figure 2.17. The molecular structure of $[\text{Pd}_2(\text{tmen})_2(\text{Allt}_{1,2;5,6}\text{H}_{-4}\text{-}\kappa\text{O}^{1,2}:\kappa\text{O}^{5,6})]$ in crystals of the 8-hydrate (**17**). ORTEP plot is drawn with 50% probability ellipsoids. Interatomic distances (Å) and angles ($^\circ$) (standard deviations of the last digit in parentheses): Pd1–O1 2.0047(12), Pd1–O2 1.9893(12), Pd1–N1 2.0587(16), Pd1–N2 2.0647(15), O1–Pd1–O2 85.15(5), O1–Pd1–N1 95.85(5), O2–Pd1–N2 93.61(6), N1–Pd1–N2 85.54(6); chelate torsion angles: N1–C6–C7–N2 $-54.5(2)$, O1–C1–C2–O2 $-48.05(18)$. [Symmetry code: (i) $-x, -y, -z$]

Table 2.16. Distances [Å] and angles [$^\circ$] of hydrogen bonds in **17**. Standard deviations of the last digit are given in parentheses; values without standard deviation are related to hydrogen atoms at calculated positions. D: donor, A: acceptor.

D	H	A	D–H	H \cdots A	D \cdots A	D–H \cdots A
O3	H831	O2 ⁱ	0.84	1.83	2.5849(17)	149.1
O91	H911	O1 ⁱⁱ	0.795(12)	1.960(12)	2.744(2)	169(2)
O91	H912	O3	0.786(12)	2.084(12)	2.864(2)	172(2)
O92	H921	O1	0.786(11)	1.936(12)	2.7182(19)	174(2)
O92	H922	O94 ⁱⁱⁱ	0.785(11)	2.067(12)	2.851(2)	177(2)
O93	H931	O92	0.787(11)	2.080(12)	2.862(2)	172(2)
O93	H932	O91	0.793(12)	1.960(12)	2.743(2)	169(2)
O94	H941	O92 ⁱⁱ	0.788(12)	2.108(12)	2.892(2)	174(2)
O94	H942	O93	0.791(12)	1.980(12)	2.766(2)	172(2)

Symmetry code: (i) $-x+1, -y+1, -z+1$; (ii) $x+1, y, z$; (iii) $x+1, y, z$.

For both solvents the predictions were valid, $\kappa\text{O}^{3,4}$ -bonded D-Sorb3,4H₂ was the main species for Pd-en and Pd-tmen. Additionally, high amounts of free D-sorbitol were detected for both solvents, in Pd-en, $\kappa\text{O}^{2,3}$ -chelated D-Sorb2,3H₂ formed a minor species. For a Pd/D-sorbitol ratio of 3:1, D-Sorb3,4;5,6H₄- $\kappa\text{O}^{3,4}:\kappa\text{O}^{5,6}$ represented the main species.

2 Results

However, minor species occurred in solution which could not be resolved. ^{13}C NMR shifts of the species identified for Pd-en and Pd-tmen are listed in the Tables 2.8 and 2.9.

2.4 Palladium(II)–polyol complexes in neutral aqueous solution

In previous work,^[58] Pd-en was used without altering its pH value so that the investigation of carbohydrates' solution species was always until now related to a pH value of about 11–12. In Fig. 2.18 we can see a titration curve of the alkaline Pd-en towards the mononuclear diaqua complex. The entire curve was analyzed with HYPERQUAD2008.^[62] With the decreasing pH value of the solution, only the refinement of three intermediate species (see Fig. 2.18 below) besides the known $[\text{Pd}^{\text{II}}\text{N}_2(\text{OH})_2]$ fitted the calculated curve to the measured titration curve.

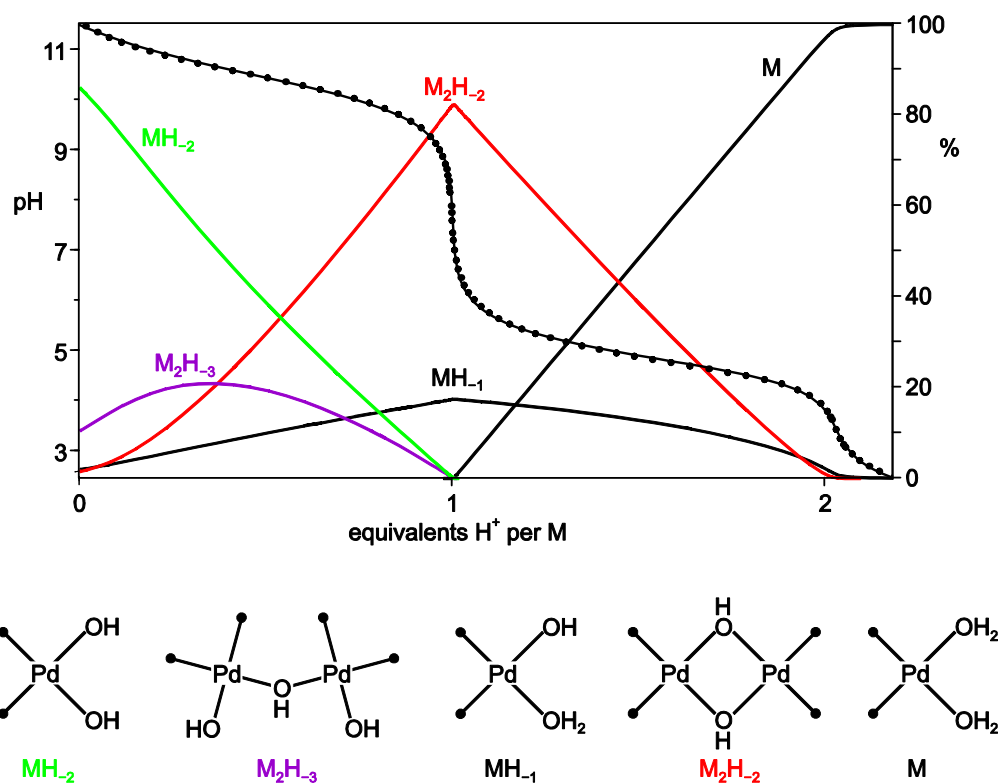


Figure 2.18. Measured and calculated titration curve (dots and line, left ordinate) and species distribution (right ordinate) for the $[\text{Pd}(\text{en})(\text{OH})_2]$ base and its conjugate acids.; $c_0 = 0.1$ M, titration with nitric acid. Curve fitting and species distribution were calculated with HYPERQUAD2008.

In the alkaline regime, $[\text{Pd}^{\text{II}}\text{N}_2(\text{OH})_2]$ was the main solution species and the binuclear hydroxido-bridged species M_2H_{-3} had only a minor share of maximally 15% of the total Pd content at pH 10–11. With the titration's progress, the mentioned species decreased and two new species, the predominant species M_2H_{-2} and the minor species MH_{-1} appeared. It should

2 Results

be noted that due to the method's limitations, slight amounts of species of higher nuclearity may be hidden in this peak. After the addition of one equivalent of acid, both these species reached their maximum at pH 7–8. Further addition of nitric acid enriched only the species M, the mononuclear $[\text{Pd}^{\text{II}}\text{N}_2(\text{OH})_2]$ complex. Most of the refined species in Fig 2.18 correspond with structurally characterized compounds such as $[\text{Pd}(\text{en})(\text{OH})_2]^{[46]}$ or $[\text{Pd}(\text{tmen})(\text{OH})_2]$ (see Fig. 2.1). A mono-hydroxido-bridged dimer with a $\text{Pd}^{\text{II}}\text{N}_3$ core and related to the M_2H_{-3} species has been published recently.^[63] The major binuclear, di-hydroxido-bridged species as well as further species of the common formula $[(\text{Pd}^{\text{II}}\text{N}_2)_n(\mu_2\text{-OH})_n]^{n+}$ with $n = 3$ and 4 and close to the equivalence point are well established both for palladium(II) or platinum(II).^[64-69]

Interpreting the titration's results, a decreasing pH resulted in a decreasing supply of the Lewis-basic hydroxide or alkoxido ligands which are shared by the Lewis-acidic central atoms. This had an effect on the bonding modes: the lower the pH value, the lower the ratio of terminal to bridging hydroxide or alkoxide ligand.

2.4.1 μ -Triolato-chelation and ligand conformation at pH 8–9

As known from previous work,^[58] in a solution of Pd-en with glycerol of a molar ratio of 2:1, the $\kappa\text{O}^{1,2}$ -bonded five-ring chelate $[\text{Pd}(\text{en})(\text{Glyc}1,2\text{H}_2\text{-}\kappa\text{O}^{1,2})]$ is the major species with the isomeric $\kappa\text{O}^{1,3}$ -bonded six-ring chelate and free glycerol occurring in negligible amounts only. After the addition of one equivalent of nitric acid (2:1:1 molar ratio of Pd-en, Glyc, and H^+) in the ^{13}C NMR spectrum (depicted in Fig. 2.19) a new species distribution was detected.

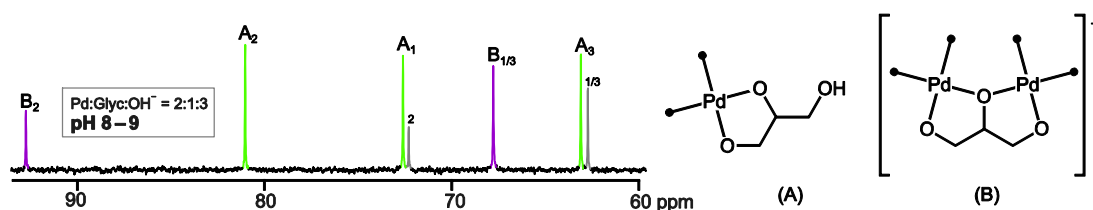


Figure 2.19. Left: ^{13}C NMR spectrum of $[\text{Pd}^{\text{II}}(\text{en})(\text{OD})_2]/\text{D}_2\text{O}$ solution, glycerol, and 2 M nitric acid at a 2:1:1 molar ratio. The signals of the free glycerol are grey-colored; **A** is the $[\text{Pd}(\text{en})(\text{Glyc}1,2\text{H}_2)]$ five-ring chelate, **B** is the binuclear cation $[\text{Pd}_2(\text{en})_2(\text{Glyc}1,2,3\text{H}_3)]^+$. Right: Metalated glycerol species in Pd-en solutions of pH 8–9. The en ligand is encoded by a pair of dots.

Identifying the signals for free glycerol and $[\text{Pd}(\text{en})(\text{Glyc}1,2\text{H}_2\text{-}\kappa\text{O}^{1,2})]$ (**A**), two signals of a new species **B** arose. The 20.5 ppm-CIS of the C2 signal (Table 2.17) could not be interpreted by a single bonding $\text{Pd}^{\text{II}}\text{N}_2$ -fragment, but the chemical shifts of **B** were in agreement with the

2 Results

assignment of a bridging O2 atom, resulting in a CIS such as the value known for the binuclear μ -hydroxido-bridged chelating reagent $[\text{Pd}_2(\text{tm}-2,1:3,2\text{-tet})(\text{OH})_3]$.^[58] Additionally, keeping in mind the postulated species M_2H_{-3} , a structural model, as depicted for **B** in Fig. 2.19, resulted.

This μ -triolato chelation mode could not only be detected for glycerol. Investigations of the polyols depicted in Fig. 2.8 revealed a number of μ -triolato species for the tetritols, pentitols and hexitols which are summarized in Table 2.17.

Table 2.17. ^{13}C NMR chemical shifts (δ/ppm) of μ -triolato-dipalladium complexes (and some tri-palladium derivatives thereof), referenced to 49.5 ppm for the ^{13}C signal of methanol. Atoms are numbered as in Fig. 2.8. $\Delta\delta$ is the difference between the chemical shifts of the free and the palladium-binding polyols taken from the same spectrum in each case. The “%” column shows the amount of bis-chelate relative to total polyol.

	C1	C2	C3	C4	C5	C6	%	Chelate
$\text{C}_s\text{-}[\text{Pd}_2(\text{en})_2(\text{Glyc}1,2,3\text{H}_{-3})]^+$	68.3	93.3	68.3				24	
$\Delta\delta$	5.0	20.5	5.0					$1\kappa\text{O}^1, 1:2\kappa^2\text{O}^2, 2\kappa\text{O}^3$
$[\text{Pd}_2(\text{en})_2(\text{Eryt}1,2,3\text{H}_{-3})]^+$	67.3	93.4	79.1	62.5			26	
$\Delta\delta$	4.0	20.7	6.4	-0.8				$1\kappa\text{O}^1, 1:2\kappa^2\text{O}^2, 2\kappa\text{O}^3$
$[\text{Pd}_2(\text{en})_2(\text{D-Thre}1,2,3\text{H}_{-3})]^+$	70.7	93.0	76.9	63.9			38	
$\Delta\delta$	7.4	20.7	4.6	0.6				$1\kappa\text{O}^1, 1:2\kappa^2\text{O}^2, 2\kappa\text{O}^3$
$[\text{Pd}_2(\text{en})_2(\text{D-Arab}1,2,3\text{H}_{-3})]^+$	71.4	92.8	76.6	73.4	64.6		15	
$\Delta\delta$	7.7	21.9	5.5	1.8	1.0			$1\kappa\text{O}^1, 1:2\kappa^2\text{O}^2, 2\kappa\text{O}^3$
$[\text{Pd}_2(\text{en})_2(\text{Ribt}1,2,3\text{H}_{-3})]^+$	67.5	94.0	78.6	73.3	64.3		25	
$\Delta\delta$	4.5	21.3	5.7	0.6	1.3			$1\kappa\text{O}^1, 1:2\kappa^2\text{O}^2, 2\kappa\text{O}^3$
$[\text{Pd}_3(\text{en})_3(\text{RibtH}_{-5})]^+$	67.7	94.3	80.8	83.2	75.5		21	
$\Delta\delta$	4.7	21.6	7.9	10.5	12.5			$1\kappa\text{O}^1, 1:2\kappa^2\text{O}^2, 2\kappa\text{O}^3, 3\kappa\text{O}^{4,5}$
$[\text{Pd}_2(\text{en})_2(\text{Xylt}1,2,3\text{H}_{-3})]^+$	69.4	93.1	76.8	72.7	64.0		16	
$\Delta\delta$	6.1	20.5	5.4	0.1	0.7			$1\kappa\text{O}^1, 1:2\kappa^2\text{O}^2, 2\kappa\text{O}^3$
$[\text{Pd}_3(\text{en})_3(\text{XyltH}_{-5})]^+$	69.9	93.5	76.6	83.2	73.4		7	
$\Delta\delta$	6.6	20.9	5.2	10.6	10.1			$\kappa\text{O}^{1,2}; \kappa\text{O}^{2,3}; \kappa\text{O}^{4,5}$
$\text{C}_s\text{-}[\text{Pd}_2(\text{en})_2(\text{Xylt}2,3,4\text{H}_{-3})]^+$	63.8	78.4	92.6	78.4	63.8		28	
$\Delta\delta$	0.5	5.8	21.2	5.8	0.5			$1\kappa\text{O}^2, 1:2\kappa^2\text{O}^3, 2\kappa\text{O}^4$
$[\text{Pd}_2(\text{en})_2(\text{Allt}1,2,3\text{H}_{-3})]^+$	67.5	93.8	79.3	74.0	73.1	62.2	28	
$\Delta\delta$	4.5	21.0	6.3	1.0	0.3	-0.8		$1\kappa\text{O}^1, 1:2\kappa^2\text{O}^2, 2\kappa\text{O}^3$
$\text{C}_i\text{-}[\text{Pd}_4(\text{en})_4(\text{AlltH}_{-6})]^+$	67.8	94.0	80.6	80.6	94.0	67.8	11	
$\Delta\delta$	4.8	21.2	7.6	7.6	21.2	4.8		$\kappa\text{O}^{1,2}; \kappa\text{O}^{2,3}; \kappa\text{O}^{4,5}; \kappa\text{O}^{5,6}$
$[\text{Pd}_2(\text{en})_2(\text{Dulc}1,2,3\text{H}_{-3})]^+$	^a	92.7	75.6	^a	^a	63.8	8	
$\Delta\delta$		21.9	5.6			-0.1		$1\kappa\text{O}^1, 1:2\kappa^2\text{O}^2, 2\kappa\text{O}^3$
$[\text{Pd}_3(\text{en})_3(\text{Dulc}1,2,3;4,5\text{H}_{-5})]^+$	72.0	91.3	76.5	85.1	85.7	64.4	34	
$\Delta\delta$	8.1	20.5	6.5	15.1	14.9	0.5		$\kappa\text{O}^{1,2}; \kappa\text{O}^{2,3}; \kappa\text{O}^{4,5}$

^a Assignment ambiguous, $\delta = 72.4, 71.5$ und 71.4 ppm.

2 Results

The 2:1:1 molar Pd-en/polyol/H⁺ ratio used for glycerol was only applicable to the tetrityls, and had to be altered to 3:1:1.5 for the pentitols and to 4:1:2 for the hexitols. For the three pentitols, some rules may be recognized. Hence, if a *threo*-connection was available, it was part of a chelate ring. Thus arabitol formed the $1\kappa O^1, 1:2\kappa^2 O^2, 2\kappa O^3$ chelate by its only terminal/*threo* pair of diol functions and not $1\kappa O^3, 1:2\kappa^2 O^4, 2\kappa O^5$ (an *erythro*/terminal pair of diols) or $1\kappa O^2, 1:2\kappa^2 O^3, 2\kappa O^4$ (a *threo/erythro* pair). Xylitol allowed the exclusion of *erythro*-diol-binding both in its 1,2,3-terminal/*threo* pair (symmetrically equivalent with the 3,4,5-*threo/terminal* site) as well as for the prevailing 2,3,4-*threo/threo* bonding, as Table 2.17 shows. Signals of a higher-metalated species were assigned for ribitol and xylitol. In these species, the new μ -triolato-binding mode was accompanied by the well-known formation of a five-membered chelate ring. The *meso*-hexitols—allitol and dulcitol—exhibited the attempted bonding pattern, too, whereas the C_1 -symmetric D-sorbitol showed spectra that were too signal-rich to be interpreted reliably. Remarkably, mannitol was the only polyol which was not capable of forming the μ -triolato mode. Notably, the all-*erythro meso*-hexitol allitol formed a centrosymmetric species whose three ¹³C-NMR signals were assigned to the only occurrence of a double- μ -triolato pattern.

All attempts to crystallize one of the binuclear μ -triolato species failed, leaving questions of the Pd^{II}N₂-fragment's orientation and the polyol's conformation unanswered. Since a dimetalated triolate function appeared to be sterically burdened, restrictions on its conformation were expected. In terms of torsion angles, $1\kappa O^1:2\kappa^2 O^2, \kappa O^3$ -type palladium chelation required a synclinal (*sc*) conformation about the C-C-bonds. With this boundary condition, the three triolate conformations depicted in Fig. 2.20 remained to be considered. A preliminary DFT study showed that the most overcrowded C_s -symmetric *syn* conformation did not represent a local energy minimum but relaxed into the C_1 -symmetric conformation.^[70] This latter chiral (+*sc*,+*sc*) pattern (and its -*sc*,-*sc* enantiomer) resembled the global minimum. A local minimum, some 10 kJ mol⁻¹ more unstable, was found for the C_s -symmetric *anti* conformation. The computer-chemical result was supplemented by an NMR-spectroscopical investigation on conformationally fixed triol moieties. Suited triols were provided by the methyl aldopentopyranosides. Thus, the C_1 -symmetric, chiral triol conformation was frozen in the arabino- and lyxopyranosides, whereas the *anti* conformation is fixed in the xylopyranosides. Three of the eight methyl D-pentosides were investigated: β -D-arabino-, α -D-lyxo- and β -D-xylopyranoside. Fig. 2.20 depicts these pentosides and highlights the triol moieties.

2 Results

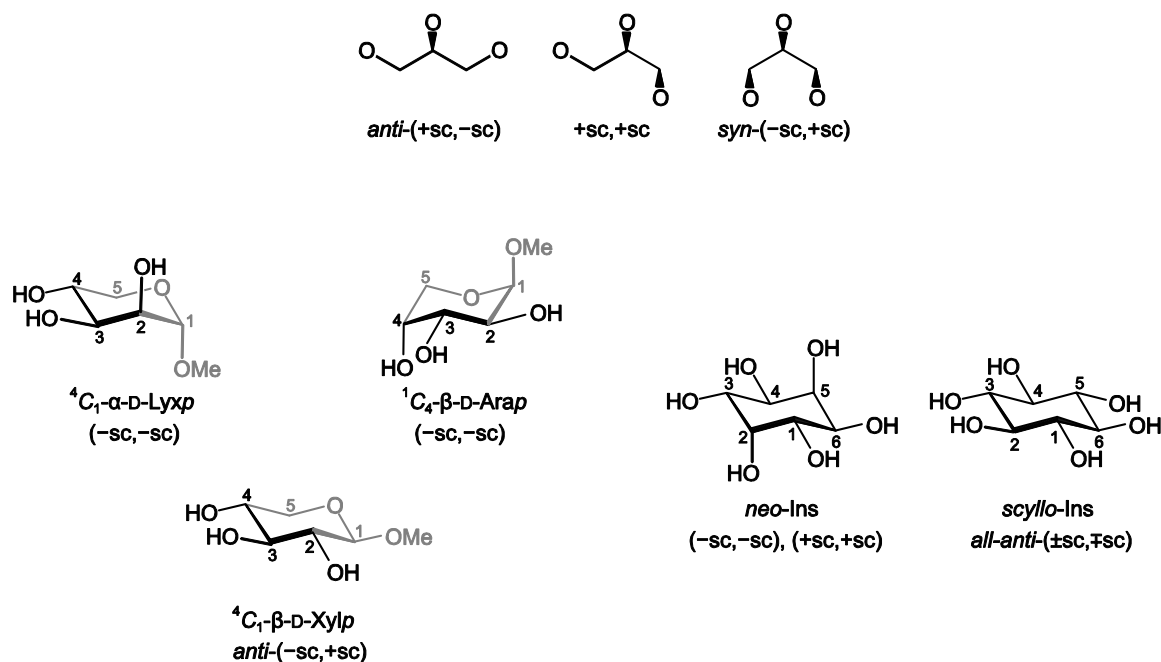


Figure 2.20. The μ -triolato ligand conformation of glycerol, pentopyranosides and inositols. Top: The various combinations of synclinal diol moieties for glycerol. Below: The conformationally fixed triol moieties of the methyl arabino-, lyxo- and xylopyranoside and *neo*- and *scyllo*-inositol. The signs of the specified two torsion angles are given in the order C3-C4 first, C2-C3 second.

The $(-sc,-sc)$ -triol moieties of the methyl D-pyranosides of both β -arabinose and α -lyxose showed the ^{13}C NMR signals of a μ -triolato bis-chelate as a minor species in batches of a molar 2:1:1 ratio of Pd/pyranoside/ H^+ (Table 2.18). The *anti*- $(-sc,+sc)$ -triol group of the β -xylose derivative, however, did not. As a result, a conformationally flexible triol (moiety) was expected to reside preferentially in a bis-synclinal conformation of equal sign ($+sc,+sc$ or $-sc,-sc$) within the binuclear μ -triolato cation. Additional proof of this conclusion was obtained from a preliminary investigation of inositols. The C_{2h} -symmetric *neo*-inositol provides a centrosymmetrically linked enantiomeric pair of triol functions of the $(-sc,-sc)/(+sc,+sc)$ type. In contrast, only *anti* configurations are fixed in the D_{3d} -symmetric *scyllo*-inositol. In this work, the results of experiments that provoke the binucleating μ -triolato bonding mode for the two inositols of higher symmetry (Fig. 2.20) are of special interest. The result of an NMR study confirmed the deductions made above. On the one hand, *scyllo*-inositol is unable to support the attempted structural feature. On the other, *neo*-inositol exhibits this bonding mode. The $[\text{Pd}_2(\text{en})_2(\text{neo-Ins}_{2,3,4}\text{H}_3)]^+$ and its symmetrically equivalent species close to pH 10 were enriched as the major solution species. Though the experimental conditions were unsatisfactorily controlled due to the low solubility of *neo*-inositol, a 2D-NMR analysis succeeded and allowed the assignment of the six signals of the binuclear, $\kappa O^{2,3,4}$ -bonded complex (Table 2.18) as well as the ${}^3J_{\text{H,H}}$ coupling constants.

2 Results

Table 2.18. ^{13}C NMR chemical shifts (δ/ppm) of binuclear μ -triolato bis-chelates complexes (and some tri-palladium derivatives thereof), referenced to 49.5 ppm for the ^{13}C signal of methanol. Atoms are numbered as in Fig. 2.20. $\Delta\delta$ is the difference between the chemical shifts of the free and the palladium-binding polyols taken from the same spectrum in each case. The “%” column shows the amount of bis-chelate relative to total polyol.

	C1	C2	C3	C4	C5	CH ₃ /C6	%	Chelate
$[\text{Pd}_2(\text{en})_2(\text{Me-}\beta\text{-D-Arap2,3,4H-}_3)]^+$	101.8	76.7 ^a	89.2	78.0 ^a	61.7	55.8	20 ^b	
$\Delta\delta$	1.3	7.9	19.8	8.5	-1.4	0.0		$\kappa\text{O}^{2,3};\kappa\text{O}^{3,4}$
$[\text{Pd}_2(\text{en})_2(\text{Me-}\alpha\text{-D-Lyxp2,3,4H-}_3)]^+$	100.9	79.3	92.0	74.4	63.4	55.5	30 ^c	
$\Delta\delta$	-0.9	9.2	20.8	6.9	0.3	-0.4		$\kappa\text{O}^{2,3};\kappa\text{O}^{3,4}$
$[\text{Pd}_2(\text{en})_2(\text{neo-Ins2,3,4H-}_3)]^+$	68.9	77.5	91.2	78.4	71.4	70.6	35 ^d	
$\Delta\delta$	-0.9	5.4	21.4	8.6	-0.7	0.8		$\kappa\text{O}^{2,3};\kappa\text{O}^{3,4}$
$[\text{Pd}_2(\text{R,R-chxn})_2(\text{Glyc1,2,3H-}_3)]^+$	67.1 ^a	93.2	69.2 ^a				30	
$\Delta\delta$	3.9	20.5	6.0					$\kappa\text{O}^{1,2};\kappa\text{O}^{2,3}$
$[\text{Pd}_2(\text{R,R-chxn})_2(\text{Xylt2,3,4H-}_3)]^+$	63.7	77.8	92.6	78.9	63.8		35	
$\Delta\delta$	0.4	5.2	21.2	6.3	0.5			$\kappa\text{O}^{2,3};\kappa\text{O}^{3,4}$

^a Signals may be interchanged. ^b 50% free glycoside, 30% of $[\text{Pd}(\text{en})(\text{Me-}\beta\text{-D-Arap3,4H-}_2)]$, the major species of strongly alkaline solutions. ^c 10% free glycoside, 60% of $[\text{Pd}(\text{en})(\text{Me-}\alpha\text{-D-Lyxp2,3H-}_2)]$, the major species of strongly alkaline solutions. ^d 20% free inositol, 25% of $[\text{Pd}(\text{en})(\text{neo-Ins2,3H-}_2)]$ and 20% of $[\text{Pd}(\text{en})(\text{neo-Ins3,4H-}_2)]$.

In particular the coupling constants within a chelating diol function allowed a final characterization of the open-chain μ -triolato complexes. Reference values were provided by sterically well-defined, rigid chelate rings. Hence, values of 9–11 Hz were expected from Karplus relationships, and were in fact determined for the $^3J_{\text{H,H}}$ constants of *trans*-fixed H-C-C-H units of *neo*-inositol's and xylopyranoside's chelating diol functions. Specifically, the H3-C3-C4-H4 unit of the $[\text{Pd}_2(\text{en})_2(\text{neo-Ins2,3,4H-}_3)]^+$ species which is close to a diaxial arrangement (Fig. 2.20; H3-C3-C4-H4 torsion ca. 170° derived from a typical O3-C3-C4-O4 torsion angle of 50°) led to a $^3J_{\text{H}_3,\text{H}_4}$ constant of 10.1 Hz. More data were contributed by two monometalated xylopyranoside chelates of the general formula $[\text{Pd}(\text{R,R-chxn})(\text{Me-}\beta\text{-D-XylpH-}_2)]$: $^3J_{\text{H}_2,\text{H}_3}$ for the $\kappa\text{O}^{2,3}$ chelate: 9.3 Hz; $^3J_{\text{H}_3,\text{H}_4}$ for the $\kappa\text{O}^{3,4}$ chelate: 9.1 Hz.^[71]

To analyze the bonding situation in an open-chain μ -triolato species, these reference values may be compared with the constants of glycerol and its Pd^{II} complexes. If, for example, the $[\text{Pd}(\text{en})(\text{Glyc1,2H-}_2)]$ species **A** of Fig. 2.19 were a rigid chelate, one of the two H-C1-C2-H angles should be, for the same reasons as above, ca. 170° , and, accordingly, one of the coupling constants should exceed the 9 Hz limit. The $^3J_{\text{H,H}}$ values in Table 2.19, however, are markedly smaller and are rather close to those of free glycerol. The constants thus reflect the

2 Results

non-rigidity of the chelate which dynamically switches between its δ and λ conformation. In terms of the glycerol conformations of Fig. 2.20, this motion connects the *anti*-(+sc,-sc) and the (+sc,+sc) conformation if the dangling hydroxymethyl function is chosen as the left one in both formulae, and the chelate is established with the right one. For the species $[\text{Pd}_2(\text{en})_2(\text{Glyc}1,2,3\text{H}_{-3})]^+$, the coupling constants indicated a very similar situation. Although restricted, flexibility is thus retained in the μ -triolato mode to a large extent. If, despite the results with the inositols and the pyranoside, the spectroscopically determined C_s symmetry would be interpreted in the sense that the binuclear species resides in a rigid *anti*-(+sc,-sc) conformation, the coupling constants would contradict this assumption. In a rigid C_s -symmetric *anti*-(+sc,-sc) complex, again, at least one ${}^3J_{\text{H,H}}$ constant should exceed the 9-Hz limit, but it did not.

Table 2.19. Coupling constants, J/Hz for glycerol and its complexes.

	${}^2J_{\text{H}_1,\text{H}_1'}$	${}^3J_{\text{H}_1,\text{H}_2}$	${}^3J_{\text{H}_1',\text{H}_2}$	${}^3J_{\text{H}_2,\text{H}_3}$	${}^3J_{\text{H}_2,\text{H}_3'}$	${}^2J_{\text{H}_3,\text{H}_3'}$
Glyc	-11.8	4.4	6.5	4.4	6.5	-11.8
$[\text{Pd}(\text{en})(\text{Glyc}1,2\text{H}_{-2})]$	-10.3	3.9	6.8	5.5	7.2	-11.0
$[\text{Pd}_2(\text{en})_2(\text{Glyc}1,2,3\text{H}_{-3})]^+$	-11.0	4.0	5.9	4.0	5.9	-11.0

Combining all the facts so far, a conformationally restricted, but non-rigid $\text{Pd}_2(\mu\text{-triolato})$ unit which exhibits time-averaged C_s symmetry would have explained the results best. The motional restriction was caused by an energetically strongly unfavorable *syn* and a weakly unfavorable *anti* conformation of the triol function (Fig. 2.20). As a result, the complex should prefer to reside in the enantiomeric pair of C_1 -symmetric conformations with the C_s -symmetric *anti* conformation as the intermediate. As expected, the spectroscopic C_s symmetry was lifted if the non-chiral $\text{Pd}(\text{en})$ residue was replaced by a chiral probe. In the $\text{Pd}\text{-chxn}$ solvent, the simple spectrum of Fig. 2.19 thus was altered in a characteristic way. The three signals of species (A) were split since the chiral probe discriminated between the two halves of the *meso* compound glycerol and formed the diastereomeric pair $[\text{Pd}(\text{R,R}\text{-chxn})(\text{Glyc}1,2\text{H}_{-2})]$ and $[\text{Pd}(\text{R,R}\text{-chxn})(\text{Glyc}2,3\text{H}_{-2})]$. The two signals of species (B) split into three since C1 and C3 were no longer equivalent (Table 2.18). In addition to the $[\text{Pd}_2(\text{R,R}\text{-chxn})_2(\text{Glyc}1,2,3\text{H}_{-3})]^+$ cation, a second species of this kind was detected with the $[\text{Pd}_2(\text{R,R}\text{-chxn})_2(\text{Xylt}2,3,4\text{H}_{-3})]^+$ cation (five signals). Again, the symmetry was lifted in the chiral solvent $\text{Pd}\text{-chxn}$ where the three signals of $[\text{Pd}_2(\text{en})_2(\text{Xylt}2,3,4\text{H}_{-3})]^+$ split into five signals (Table 2.17 and Table 2.18).

2 Results

2.4.2 Pd₄(μ-OH)₄-derived *threo*-tetraolato bridging at pH 7–8

The addition of defined amounts of nitric acid to Pd-en/polyol solutions had led to a complexation of a M₂H₋₃ derived Pd₂(μ-triolato) unit with various polyols at a pH value of 8–9. In Fig. 2.21, three ¹³C NMR spectra of threitol-containing solutions at different Pd-en/polyol/H⁺ ratios and pH values should elucidate the effect of Pd-en's further acidification to the species distribution.

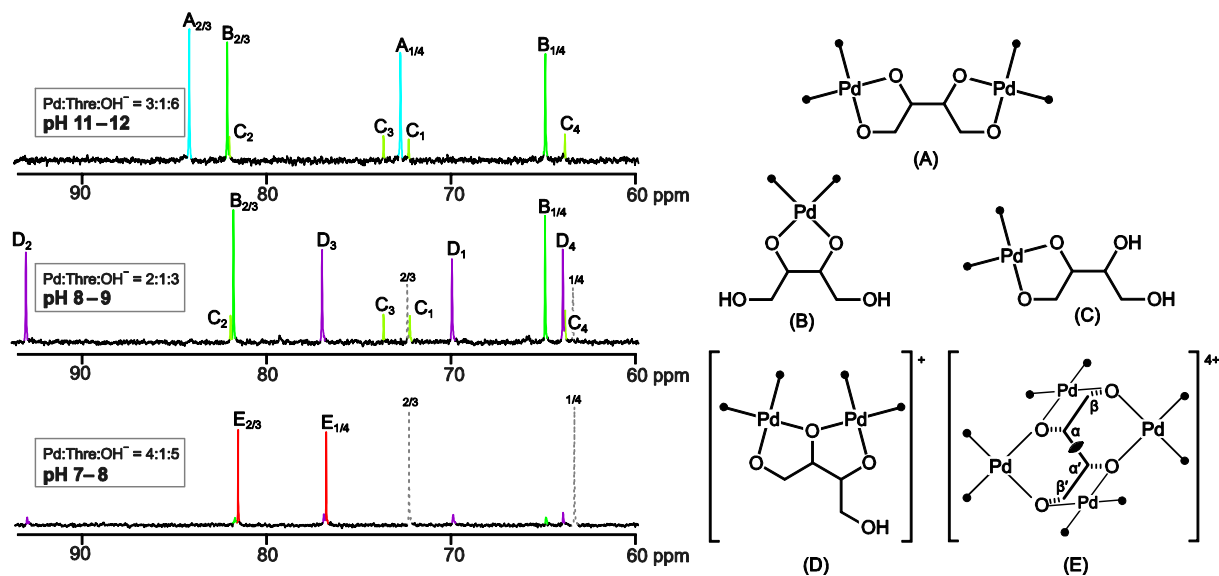


Figure 2.21. Left: ¹³C NMR signals of D-threitol species in Pd-en after pH adjustment with nitric acid. Top: threitol in a threefold molar amount of Pd-en formed dimetalated C₂-symmetric [Pd₂(en)₂(ThreH₋₄)] (A) and monometalated C₂-symmetric [Pd(en)(Thre_{2,3}H₋₂)] (B) as major species, and minor [Pd(en)(Thre_{1,2}H₋₂)] (C). Middle: Threitol in a double molar amount of Pd-en and one equivalent of acid (3 OH⁻ left) formed Pd₂(en)₂(Thre_{1,2,3}H₋₃)⁺ (D) as well as B and C; some free threitol is left (dashed). Bottom: Threitol in a fourfold molar amount of Pd-en with three equivalents of acid added (5 OH⁻ left) formed the dimetalated C₂-symmetric [Pd₄(en)₄(ThreH₋₄)]⁴⁺ complex (E) besides marked amounts of free threitol and minute amounts of B and C. The subscripts refer to the standard atomic numbering along the threitol chain (Fig. 2.23). Right: Metalated tetritol species in Pd-en solutions of various pH values. A–D formed with both threitol and erythritol. E's C₂ axis is highlighted. The α/β notation is used in the text. A–C, the species of the alkaline regime, are known from previous work.^[72] The en ligand is encoded by a pair of dots.

The upper ¹³C NMR spectrum fell back on a published result.^[58] Since only five-membered chelate rings were formed and were characterized by a typical CIS of about 10 ppm, species assignment of A–C was straightforward. As one can see in the middle ¹³C NMR spectrum, the addition of acid made the signals of the dimetalated species vanish, and a signal set of a μ-triolato species D, as presented in the latter section, appeared.

2 Results

Quite by chance, a new species was discovered in polyol-containing solutions at a Pd-en/polyol/ H^+ ratio of 4:1:3 at pH 7–8. First detected for D-mannitol, the ^{13}C NMR spectra of this 4:1:3-composition were dominated by a new species **E** that was accompanied by large amounts of free polyol, as depicted in the last ^{13}C NMR spectrum of the threitol-containing solution in Fig. 2.21. Repeating the experiment with erythritol, this species **E** could not be detected, although the species **A–D** appeared in the corresponding ^{13}C NMR spectra, as it is shown in Fig. 2.22. Obviously, to obtain this new species the polyol must be able to provide a *threo* unit.

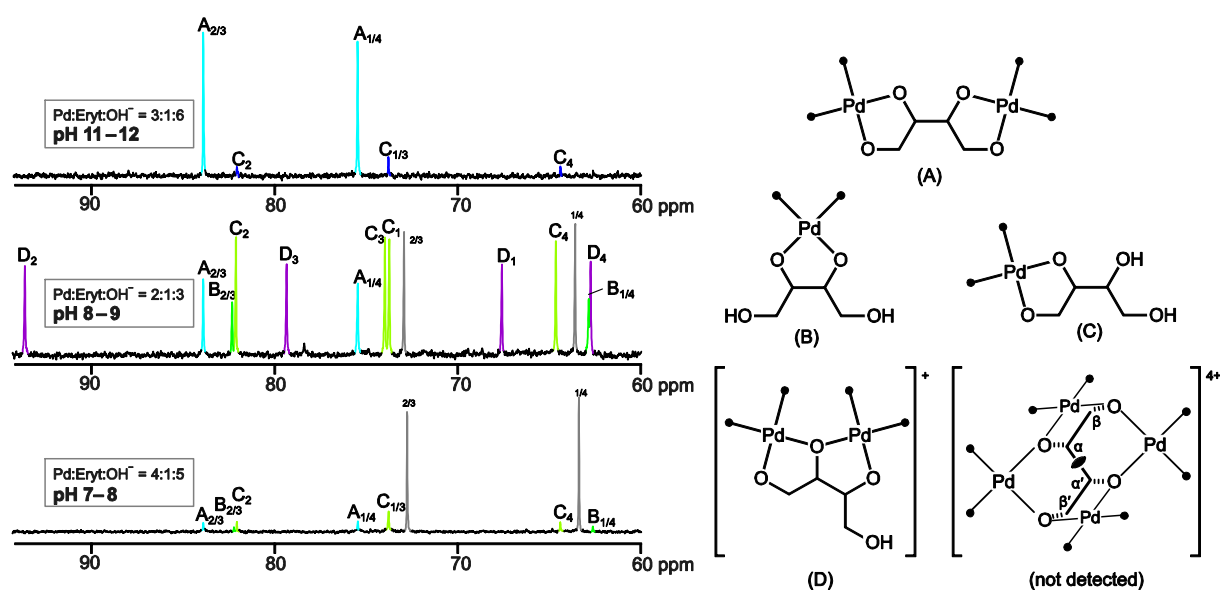


Figure 2.22. Left: ^{13}C NMR signals of erythritol species in Pd-en after pH adjustment with nitric acid. Top: erythritol in a threefold molar amount of Pd-en formed dimetalated C_2 -symmetric $[Pd_2(en)_2(ErytH_{-4})]$ (**A**) and traces of $[Pd(en)(Eryt1,2H_{-2})]$ (**C**). Middle: Erythritol in a double molar amount of Pd-en and one equivalent of acid (3 OH^- left) formed $[Pd_2(en)_2(Eryt1,2,3H_{-3})]^+$ (**D**) as well as $[Pd(en)(Eryt2,3H_{-2})]$ (**B**) and **C**; some free erythritol is left (dashed). Bottom: Erythritol in a fourfold molar amount of Pd-en with three equivalents of acid added (5 OH^- left) formed predominantly free erythritol and minute amounts of **A–C**. The subscripts refer to the standard atomic numbering along the erythritol chain (Fig.2.23). Right: See Fig. 2.21.

The two new signals of **E** in the bottom ^{13}C NMR spectrum in Fig. 2.21 indicated a C_2 -symmetric complex, however, the CIS values differed from those of the C_2 -symmetric $[Pd_2(en)_2(ThreH_{-4}-\kappa O^{1,2}:\kappa O^{3,4})]$. Furthermore, at a 4:1:3 Pd-en/Thre/ H^+ stoichiometry and remembering the μ -alkoxido coordination obtained for a minor Pd-en/Thre/ H^+ ratio of 2:1:1, a higher metalation grade than dimetalation was expected. Compared to the titration's result at a pH value of 7–8, polyol-free solutions were in the regime of $[(Pd^II N_2)_n(\mu_2-OH)_n]^{n+}$ species which are characterized by μ_2 -bridging oxygen ligands. Nevertheless, not until a first crystal

2 Results

structure was determined was **E** identified as the tetranuclear $[\text{Pd}_4(\text{en})_4(\text{ThreH}_{-4})]^{4+}$ tetracation depicted in Fig. 2.21 which contains exclusively bridging alkoxide functions. Subsequently, this new Pd_4 -tetrameric species was found for a number of polyols (see Table 2.20 and Fig. 2.23 for details).

Table 2.20. ^{13}C NMR chemical shifts (ppm) of the tetranuclear complexes, referenced to 49.5 ppm for the ^{13}C NMR signal of methanol. Atoms are numbered as in Fig. 2.23. $\Delta\delta$ is the difference between the chemical shifts of the free and the palladium-binding polyols taken from the same spectrum in each case. The chirality of the chelating tetraol function is given in the second column. C_2 symmetry of a species is noted in the third column; each shift value is tabulated twice in this case. For the *meso*-polyols, the $\kappa\text{O}^{1,2,3,4}$ chelate is the enantiomer of the $\kappa\text{O}^{2,3,4,5}$ (Xylt) or the $\kappa\text{O}^{2,3,4,5}$ chelate (Dulc). The “%” column shows the amount of bis-chelate; the remaining part is free polyol.

	<i>-threo</i>		C1	C2	C3	C4	C5	C6	%	Chelate
$[\text{Pd}_4(\text{en})_4(\text{L-ThreH}_{-4})]^{4+}$	L	C_2	76.8	81.6	81.6	76.8			40	
$\Delta\delta$			13.5	9.3	9.3	13.5				$\kappa\text{O}^{1,2,3,4}$
$[\text{Pd}_4(\text{en})_4(\text{L-Arab1,2,3,4H}_{-4})]^{4+}$	L		76.9	77.1	80.9	84.2	62.9		40	
$\Delta\delta$			13.2	6.2	9.8	12.6	-0.7			$\kappa\text{O}^{1,2,3,4}$
$[\text{Pd}_4(\text{en})_4(\text{Xylt1,2,3,4H}_{-4})]^{4+}$	<i>rac</i>		77.0	83.1	81.5	85.0	64.7		50	
$\Delta\delta$			13.7	10.5	10.1	12.4	1.4			$\kappa\text{O}^{1,2,3,4}$
$[\text{Pd}_4(\text{en})_4(\text{D-Altr1,2,3,4H}_{-4})]^{4+}$	D		77.1	76.4	80.8	82.5	73.6	64.2	40	
$\Delta\delta$			13.4	5.3	9.4	10.3	0.3	1.5		$\kappa\text{O}^{1,2,3,4}$
$[\text{Pd}_4(\text{en})_4(\text{Dulc1,2,3,4H}_{-4})]^{4+}$	<i>rac</i>		76.9	77.3	80.1	84.2	73.9	64.0	30	
$\Delta\delta$			13.0	6.5	10.1	14.2	3.1	0.1		$\kappa\text{O}^{1,2,3,4}$
$[\text{Pd}_4(\text{en})_4(\text{L-Idit2,3,4,5H}_{-4})]^{4+}$	D	C_2	64.7	85.2	83.0	83.0	85.2	64.7	80	
$\Delta\delta$			1.4	12.9	11.3	11.3	12.9	1.4		$\kappa\text{O}^{2,3,4,5}$
$[\text{Pd}_4(\text{en})_4(\text{D-Mann2,3,4,5H}_{-4})]^{4+}$	D	C_2	62.8	84.4	76.4	76.4	84.4	62.8	30	
$\Delta\delta$			-1.0	12.9	6.5	6.5	12.9	-1.0		$\kappa\text{O}^{2,3,4,5}$
$[\text{Pd}_4(\text{en})_4(\text{D-Sorb1,2,3,4H}_{-4})]^{4+}$	L		77.0	83.2	80.2	84.0	71.6 ^a	63.2	25	
$\Delta\delta$			13.9	9.7	9.9	12.3	0.0	-0.2		$\kappa\text{O}^{1,2,3,4}$
$[\text{Pd}_4(\text{en})_4(\text{D-Sorb2,3,4,5H}_{-4})]^{4+}$	D		64.8	85.1	77.2	82.4	84.4	62.9	35	
$\Delta\delta$			1.7	11.6	6.9	10.7	12.8	-0.5		$\kappa\text{O}^{2,3,4,5}$

^a Assignment ambiguous

The formation of a Pd_4 -tetrameric tetracation needs four bridging alkoxide functions which exactly corresponds to the fourfold deprotonated threitol in $[\text{Pd}_4(\text{en})_4(\text{ThreH}_{-4})]^{4+}$. ^{13}C NMR identification without the structural information from X-ray analysis had to fail. Looking exclusively at the CIS values, a clear dividing line between the $\kappa\text{O}^{1,2,3,4}$ and the $\kappa\text{O}^{1,2}:\kappa\text{O}^{3,4}$ bonding mode could not be drawn. Furthermore, for the identification of a μ -alkoxido $\kappa\text{O}^{1,2}:\kappa\text{O}^{2,4}$ bridging atom, a unique CIS, such as the 20-ppm downfield shift of the $\kappa\text{O}^{1,2}:\kappa\text{O}^{2,3}$

2 Results

bonding mode, was missing. Despite these facts, the assignment of the signals succeeded by DEPT and 2D techniques for all investigated polyols.

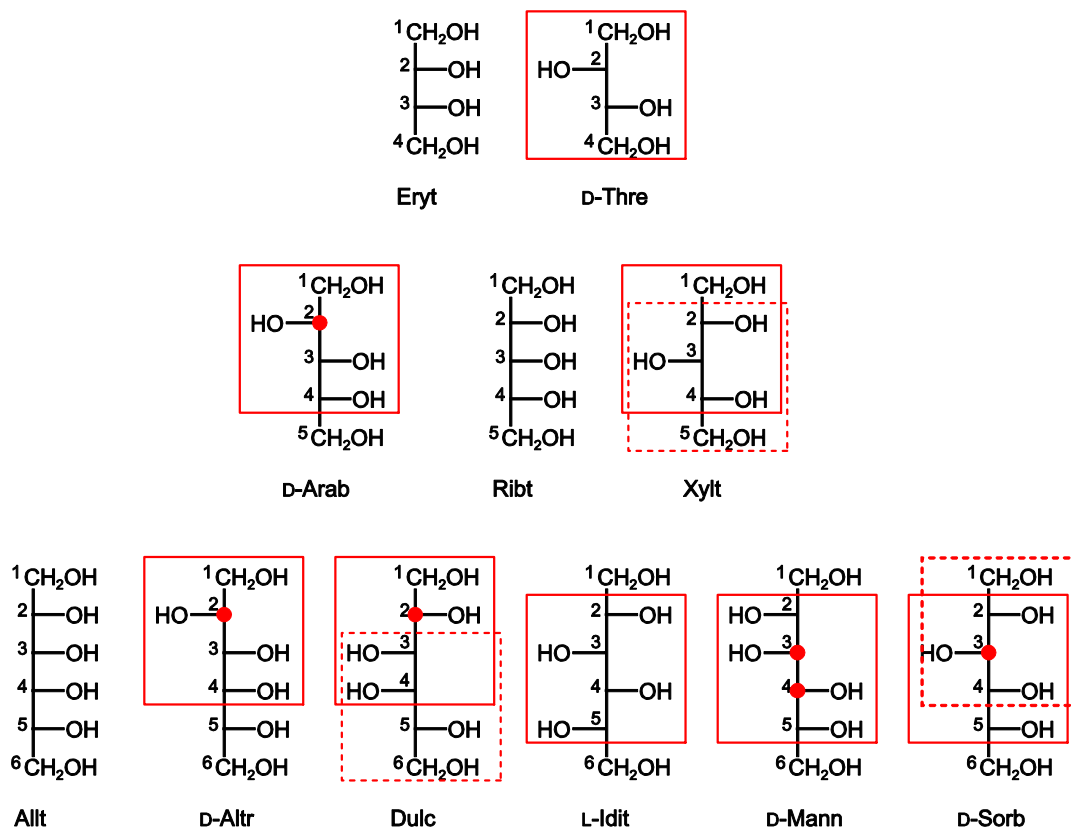


Figure 2.23. Fischer projections and atomic numbering of the C₄ (tetritols, top), C₅ (pentitols, middle) and C₆ (hexitols, bottom) glycitols. From top left to bottom right: erythritol, D-threitol, D-arabitol, ribitol ('adonitol'), xylitol, allitol, D-altritol (= tallitol), dulcitol ('galactitol'), L-iditol, D-mannitol and D-sorbitol ('glucitol', [= gulitol]). Note that in a Fischer projection, a pair of secondary hydroxy functions on the same side of the carbon backbone is *erythro*-linked, whereas a right-left couple is *threo*-configured. Note that Eryt, Ribt and Allt are all-*erythro*; Thre, Xylt and Idit are all-*threo*. Glycitols lacking the D or L designator are C₁- or C₅-symmetric *meso* forms. The boxes enclose the *threo*-configured tetraol units that are capable of forming Pd₄ species in a neutral aqueous solution. For xylitol and dulcitol, the dashed boxes denote symmetrically equivalent O₄ sets. For sorbitol, the dashed box encloses an alternative O₄ set. The circles at some positions mark lower-CIS positions (see text).

As one can see in Fig. 2.23, the pentitols already provide more than a *threo* site for Pd₄-tetrameric coordination. As detected by ¹³C NMR spectroscopy, L-arabitol formed only the Pd₄-tetramer [Pd₄(en)₄(L-Arab1,2,3,4H₋₄)]⁴⁺ in the κO^{1,2,3,4} mode, the κO^{2,3,4,5} mode correspond to an *erythro* site. The *meso*-configured xylitol, on the other hand, provided a pair of suited *threo* sites to coordinate in the κO^{1,2,3,4} or in the κO^{2,3,4,5} mode which were equivalent in Pd-en solutions. The hexitols D-altritol and D-mannitol provide only a single *threo* site and accordingly, they formed the Pd₄-type compound.

2 Results

As shown in Fig. 2.23, D-altritol bonded in a $\kappa O^{1,2,3,4}$ mode and D-mannitol in a C_2 -symmetric $\kappa O^{2,3,4,5}$ mode to the Pd_4 -tetramer as indicated by only three signals in the ^{13}C NMR spectrum. Dulcitol, L-iditol and D-sorbitol provide more than one *threo* site per polyol. The meso-configured dulcitol, like xylitol, provides an enantiomeric pair of suited *threo* sites that were equivalent in Pd-en solutions. The all-*threo* hexitol L-iditol should be able to provide its two more, symmetrically equivalent, $\kappa O^{1,2,3,4}$ and $\kappa O^{3,4,5,6}$ *threo* positions for the construction of a Pd_4 -tetramer, but chose exclusively the depicted $\kappa O^{2,3,4,5}$ -bonding mode. The most complicated case is D-sorbitol. Two unequivalent *threo* sites were provided, and both were used. Hence, both the $[Pd_4(en)_4(D-Sorb1,2,3,4H_-)]^{4+}$ and the $[Pd_4(en)_4(D-Sorb2,3,4,5H_-)]^{4+}$ species were detected in roughly the same quantities.

Despite the initial problems in deriving the metal-binding pattern from the NMR spectra without the support of X-ray work, structural details could be recognized from the shift pattern in retrospect. Thus, the ^{13}C NMR CIS pattern consistently correlated with the configuration of the glycol. Table 2.20 revealed that two CIS patterns occurred for the O_4 -rhomb related signals of four adjacent carbon atoms. The one is $>9 >9 >9 >9$ and the other was similar but one CIS was markedly smaller (two for mannitol). The positions related to the small-CIS signals were marked in Fig. 2.23. Without exception, the small CIS always indicated the same steric environment. By using the β - α - α' - β' designation of the chelating tetraol chain as defined in Fig. 2.21 (right, species E), the small CIS lay on α , if α' - β' was *erythro*-configured (and vice versa on α' if α - β was *erythro*-configured).

The restriction to the *threo* configuration determined whether or not a polyol is suited to support a polyolato complex at a neutral pH. Now, looking at Fig. 2.23, the polyols erythritol, ribitol and allitol weren't able to provide a *threo* unit and could not form Pd_4 -type tetracations. Among the remaining polyols, by using Pd-chxn, crystallization succeeded for L-threitol, xylitol, D-altritol, dulcitol, L-iditol, and D-mannitol, the latter by using the Pd-(*S,S*)-chxn solvent additionally. The isolated crystals were depicted in Fig.2.24–2.29.

The configuration of the tetracations is best presented with L-threitol in Fig. 2.24, all other compounds could be deduced from this structure which crystallized in the space group $P 2_1$. Two $Pd^{II}N_2$ fragments bonded in the C_2 -symmetric $\kappa O^{1,2}:\kappa O^{3,4}$ mode to the two diolato units of L-threitol, additionally two more $Pd^{II}N_2$ fragments bonded in the $\kappa O^{1,3}$ and $\kappa O^{2,4}$ mode to complete the cyclic Pd_4 -tetramer. Linking the $Pd^{II}N_2$ fragments by the polyol's alkoxido functions forced two fragments into an axial position facing each other while two fragments remained in an equatorial position.

2 Results

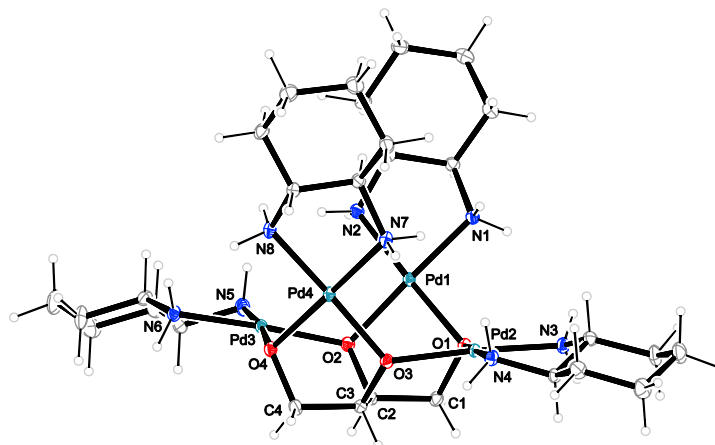


Figure 2.24. The molecular structure of $[\text{Pd}_4(\text{R,R-chxn})_4(\text{L-ThreH}_4)](\text{NO}_3)_4$ in crystals of the 4-hydrate (**18**). ORTEP plot is drawn with 50% probability ellipsoids. Interatomic distances (Å) and angles (°) (standard deviations of the last digit in parentheses): Pd1–O1 2.012(2), Pd1–O2 2.023(2), Pd1–N1 2.025(2), Pd1–N2 2.033(3), Pd2–O1 2.018(2), Pd2–O3 2.035(2), Pd2–N3 2.021(3), Pd2–N4 2.037(3), Pd3–O2 2.016(2), Pd3–O4 2.009(2), Pd3–N5 2.035(3), Pd3–N6 2.022(3), Pd4–O3 2.0314(19), Pd4–O4 2.016(2), Pd4–N7 2.038(3), Pd4–N8 2.022(2), O1–Pd1–O2 84.53(9), N1–Pd1–N2 84.04(10), O1–Pd2–O3 91.44(9), N3–Pd2–N4 83.94(12), O2–Pd3–O4 90.67(9), N5–Pd3–N6 84.26(11), O3–Pd4–O4 84.66(9), N7–Pd4–N8 83.63(11), Pd1–O1–Pd2 108.47(11), Pd1–O2–Pd3 123.95(11), Pd2–O3–Pd4 120.24(11), Pd3–O4–Pd4 110.87(11); chelate torsion angles: O1–C1–C2–O2 54.3(3), O2–C2–C3–O3 –61.1(3), O3–C3–C4–O4 55.3(3).

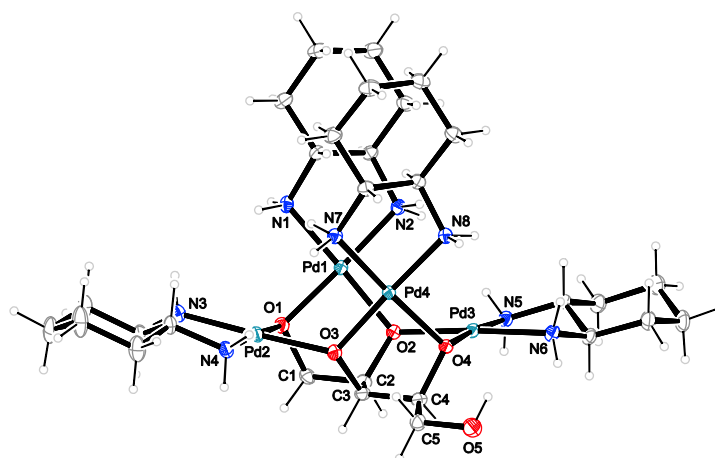


Figure 2.25. The molecular structure of $[\text{Pd}_4(\text{R,R-chxn})_4(\text{Xylt1,2,3,4H}_4)](\text{NO}_3)_4$ in crystals of the 4.7-hydrate (**19**). ORTEP plot is drawn with 50% probability ellipsoids. Interatomic distances (Å) and angles (°) (standard deviations of the last digit in parentheses): Pd1–O1 2.012(3), Pd1–O2 2.019(3), Pd1–N1 2.022(3), Pd1–N2 2.035(3), Pd2–O1 2.015(3), Pd2–O3 2.015(3), Pd2–N3 2.026(4), Pd2–N4 2.022(3), Pd3–O2 2.021(3), Pd3–O4 2.005(3), Pd4–O3 2.026(3), Pd4–O4 2.017(3), Pd4–N7 2.053(3), Pd4–N8 2.016(3), O1–Pd1–O2 84.99(11), N1–Pd1–N2 83.91(13), O1–Pd2–O3 90.42(11), N3–Pd2–N4 83.39(14), O2–Pd3–O4 89.37(11), N5–Pd3–N6 84.06(14), O3–Pd4–O4 84.24(11), N7–Pd4–N8 82.79(15), Pd1–O1–Pd2 111.89(14), Pd1–O2–Pd3 125.59(14), Pd2–O3–Pd4 121.52(13), Pd3–O4–Pd4 113.77(12); chelate torsion angles: O1–C1–C2–O2 –55.4(4), O2–C2–C3–O3 62.7(5), O3–C3–C4–O4 –56.1(4), O4–C4–C5–O5 –59.1(4).

2 Results

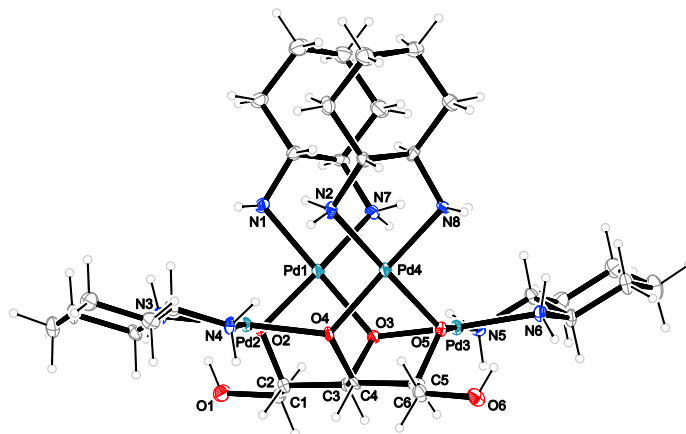


Figure 2.26. The molecular structure of $[\text{Pd}_4(\text{R,R}\text{-chxn})_4(\text{L-Idit2,3,4,5H-4})](\text{NO}_3)_4$ in crystals of the 6-hydrate (**20**). ORTEP plot is drawn with 50% probability ellipsoids. Interatomic distances (Å) and angles (°) (standard deviations of the last digit in parentheses): Pd1–O2 2.019(7), Pd1–O3 2.041(6), Pd1–N1 2.041(8), Pd1–N2 2.055(8), Pd2–O2 2.046(6), Pd2–O4 2.007(6), Pd2–N3 2.045(8), Pd2–N4 2.008(8), Pd3–O3 2.009(7), Pd3–O5 2.041(6), Pd3–N5 2.026(8), Pd3–N6 2.030(9), Pd4–O4 2.025(6), Pd4–O5 2.021(6), Pd4–N7 2.042(8), Pd4–N8 2.040(8), O2–Pd1–O3 84.9(2), N1–Pd1–N2 82.7(3), O2–Pd2–O4 88.2(2), N3–Pd2–N4 83.6(3), O3–Pd3–O5 90.0(2), N5–Pd3–N6 82.9(4), O4–Pd4–O5 83.9(3), N7–Pd4–N8 83.5(3), Pd1–O2–Pd2 112.1(3), Pd1–O3–Pd3 123.5(3), Pd2–O4–Pd4 124.6(3), Pd3–O5–Pd4 113.6(3); chelate torsion angles: O1–C1–C2–O2 $-59.4(10)$, O2–C2–C3–O3 $-56.0(9)$, O3–C3–C4–O4 $62.9(10)$, O4–C4–C5–O5 $-54.1(9)$, O5–C5–C6–O6 $-64.8(11)$.

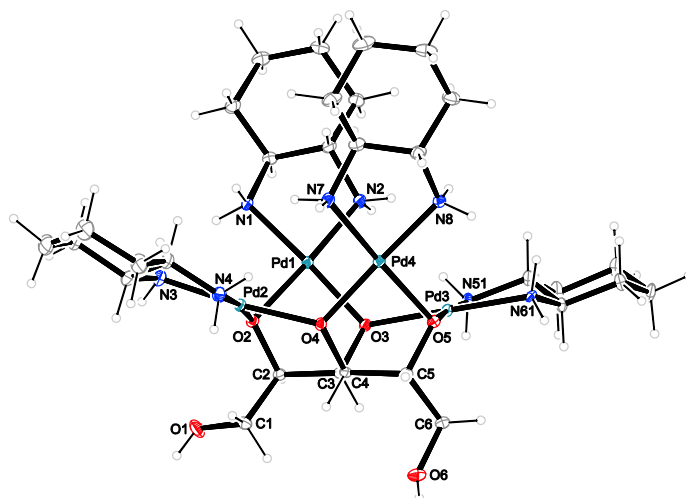


Figure 2.27. The molecular structure of $[\text{Pd}_4(\text{R,R}\text{-chxn})_{1.66}(\text{S,S}\text{-chxn})_{2.34}(\text{D-Mann2,3,4,5H-4})](\text{NO}_3)_4$ in crystals of the 7-hydrate (**21**). ORTEP plot is drawn with 50% probability ellipsoids. Interatomic distances (Å) and angles (°) (standard deviations of the last digit in parentheses): Pd1–O2 2.011(2), Pd1–O3 2.034(3), Pd1–N1 2.020(4), Pd1–N2 2.038(3), Pd2–O2 2.034(3), Pd2–O4 2.015(3), Pd2–N3 2.037(4), Pd2–N4 2.025(4), Pd3–O3 2.008(2), Pd3–O5 2.025(3), Pd3–N51 2.09(4), Pd3–N61 2.04(2), Pd4–O4 2.036(2), Pd4–O5 2.016(2), Pd4–N7 2.030(3), Pd4–N8 2.023(3), O2–Pd1–O3 83.92(10), N1–Pd1–N2 83.23(14), O2–Pd2–O4 92.15(10), N3–Pd2–N4 83.28(15), O3–Pd3–O5 90.64(10), N51–Pd3–N61 85.0(14), O4–Pd4–O5 84.42(10), N7–Pd4–N8 83.88(16), Pd1–O2–Pd2 106.36(11), Pd1–O3–Pd3 122.97(12), Pd2–O4–Pd4 119.76(13), Pd3–O5–Pd4 107.67(11); chelate torsion angles: O1–C1–C2–O2 71.2(4), O2–C2–C3–O3 $-55.5(4)$, O3–C3–C4–O4 59.6(4), O4–C4–C5–O5 $-57.0(4)$, O5–C5–C6–O6 177.0(3).

2 Results

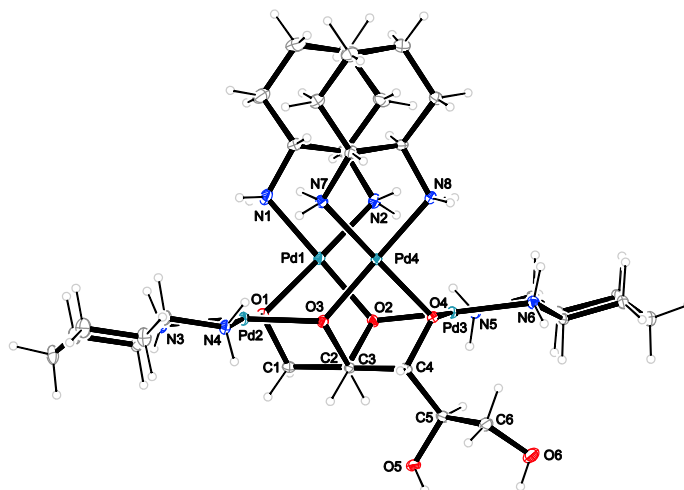


Figure 2.28. The molecular structure of $[\text{Pd}_4(\text{R,R}\text{-chxn})_4(\text{D-Altr1,2,3,4H-4})](\text{NO}_3)_{3.57}(\text{OH})_{0.43}$ in crystals of the 12-hydrate (**22**). ORTEP plot is drawn with 50% probability ellipsoids. Interatomic distances (Å) and angles (°) (standard deviations of the last digit in parentheses): Pd1–O1 2.038(3), Pd1–O2 2.020(3), Pd1–N1 2.017(4), Pd1–N2 2.038(3), Pd2–O1 2.046(3), Pd2–O3 1.993(3), Pd2–N3 2.028(4), Pd2–N4 2.007(4), Pd3–O2 2.006(3), Pd3–O4 2.043(3), Pd3–N5 2.016(4), Pd3–N6 2.026(4), Pd4–O3 2.014(3), Pd4–O4 2.029(3), Pd4–N7 2.035(4), Pd4–N8 2.019(3), O1–Pd1–O2 84.63(12), N1–Pd1–N2 82.41(16), O1–Pd2–O3 88.66(12), N3–Pd2–N4 84.27(15), O2–Pd3–O4 90.00(12), N5–Pd3–N6 83.48(14), O3–Pd4–O4 84.19(12), N7–Pd4–N8 83.13(14), Pd1–O1–Pd2 115.66(14), Pd1–O2–Pd3 124.72(15), Pd2–O3–Pd4 128.77(15), Pd3–O4–Pd4 109.01(13); chelate torsion angles: O1–C1–C2–O2 $-56.3(4)$, O2–C2–C3–O3 $61.3(4)$, O3–C3–C4–O4 $-58.7(4)$, O4–C4–C5–O5 $-157.5(3)$, O5–C5–C6–O6 $73.4(5)$.

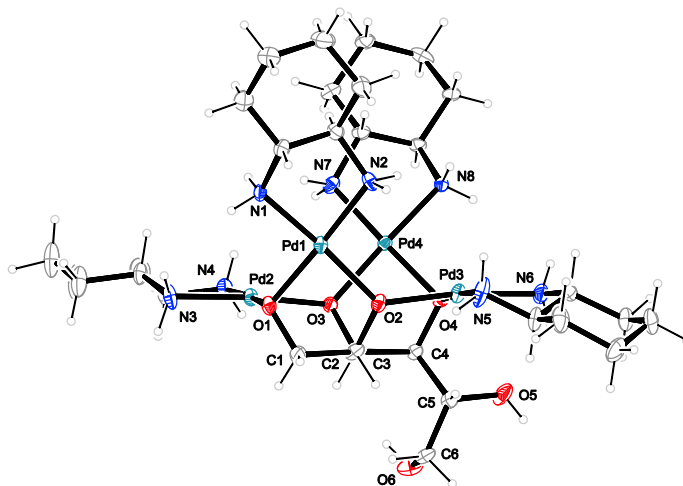


Figure 2.29. The molecular structure of $[\text{Pd}_4(\text{R,R}\text{-chxn})_4(\text{Dulc1,2,3,4H-4})](\text{NO}_3)_{3.5}(\text{OH})_{0.5}$ in crystals of the 6.75-hydrate (**23**). ORTEP plot is drawn with 50% probability ellipsoids. Interatomic distances (Å) and angles (°) (standard deviations of the last digit in parentheses): Pd1–O1 2.011(6), Pd1–O2 2.017(7), Pd1–N1 1.992(8), Pd1–N2 2.044(7), Pd2–O1 1.999(6), Pd2–O3 2.022(6), Pd2–N3 2.005(9), Pd2–N4 2.021(9), Pd3–O2 2.005(6), Pd3–O4 2.026(6), Pd3–N5 2.018(11), Pd3–N6 2.048(9), Pd4–O3 2.015(6), Pd4–O4 2.019(6), Pd4–N7 2.045(8), Pd4–N8 2.019(7), O1–Pd1–O2 84.7(3), N1–Pd1–N2 84.1(3), O1–Pd2–O3 90.8(2), N3–Pd2–N4 84.2(4), O2–Pd3–O4 91.1(2), N5–Pd3–N6 83.6(4), O3–Pd4–O4 84.7(3), N7–Pd4–N8 83.6(3), Pd1–O1–Pd2 107.9(3), Pd1–O2–Pd3 128.8(3), Pd2–O3–Pd4 127.0(3), Pd3–O4–Pd4 109.3(3); chelate torsion angles: O6–C6–C5 113.2(9), O1–C1–C2–O2 55.8(10), O3–C3–C4–O4 55.8(9), O4–C4–C5–O5 $-55.6(10)$, O5–C5–C6–O6 $-70.0(11)$.

2 Results

In crystals of $[\text{Pd}_4(\text{R,R-chxn})_4(\text{Xylt1,2,3,4H-}_4)](\text{NO}_3)_4 \cdot 4.7 \text{ H}_2\text{O}$ of the space group $P 2_1$, the Pd_4 -xylitol moiety, as depicted in Fig. 2.25, formed a zigzag chain extended by the terminal hydroxymethyl function. In Fig. 2.26 and 2.27, the structure analyses revealed C_2 -symmetric Pd_4 complexes for L-iditol and D-mannitol in the space groups $P 1$ and $P 2_12_12_1$, respectively. The two hexitols differed with respect to the environment of the central *threo* function: two more *threo* links for iditol, two *erythro* links for mannitol. The double *threo* link extended the zigzag chain, whereas the *erythro*-linked functions caused a kink in the chain. The same connection of configuration and conformation determined the structure of the alritol and dulcitol isomers. The crystal structures were solved in the space groups $P 2_12_12_1$ for **22** and $P 4_12_12$ for **23**. As shown in Fig. 2.28 and 2.29, the Pd_4 tetramer bonded in a $\kappa\text{O}^{1,2,3,4}$ mode to the zigzag chain of D-alritol and dulcitol. The remaining diolato unit turned away from the cyclohexane-1,2-diamine ligand.

2.4.3 $\text{Pd}_3(\mu\text{-OH})_3$ -derived triolato bridging at pH 7–8

The tetrameric Pd_4 -complexes of the previous section modulated the $\text{Pd}_4(\mu\text{-OH})_4$ core of one of the competing μ -hydroxido species of the common formula $[(\text{Pd}^{\text{II}}\text{N}_2)_n(\mu_2\text{-OH})_n]^{n+}$ (see section 2.4). The concept of stabilizing such a $\text{Pd}_n(\mu\text{-OH})_n$ -core for $n = 3$ (Fig. 2.30, left) by providing a matching polyolato ligand, seemed to work if the demanding sterical requirements typical for this pH region were respected. Thus the more flexible, C_3 -symmetric, non-carbohydrate triol 2-hydroxymethyl-2-methylpropane-1,3-diol, supported the trinuclear pattern.

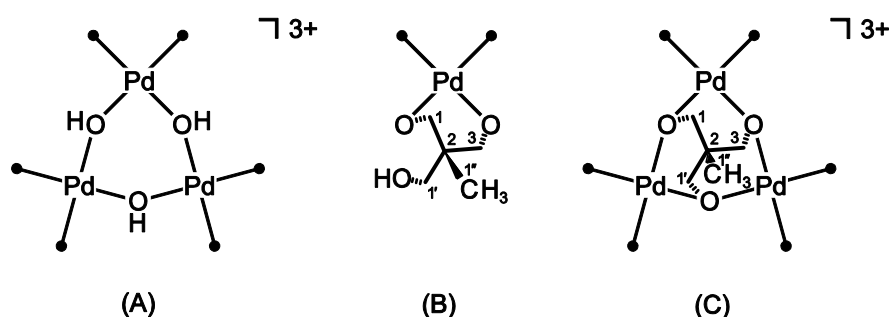


Figure 2.30. (A) The assumed palladium compound; platinum homologues are described with both ammine and (*R,R*)-cyclohexane-1,2-diamine as the nitrogen ligands.^[67, 69] (B) The monometalated species of 2-hydroxy-2-methyl-2-methylpropane-1,3-diol. (C) The trianion of 2-hydroxy-2-methylpropane-1,3-diol as a μ_3 -bridging ligand. The dots represent the N_2 -type ligand(s).

At a molar Pd-en/triol/H^+ ratio of 4:1:3, 70% of the free triol was detected, but about 30% was transformed to the expected C_3 -symmetric, trinuclear complex $[\text{Pd}_3(\text{en})_3(\text{HmmpdH-}_3)]^{3+}$, as

2 Results

indicated by ^{13}C NMR spectroscopy (Table 2.21). For a compound providing exclusively the $\kappa\text{O}^{1,3}$ -diolato functionality, a 11.8 ppm CIS—compare the 4.0 ppm regular CIS for the $\kappa\text{O}^{1,3}$ -diolato coordination of $[\text{Pd}(\text{en})(\text{Hmmpd}1,1'\text{H}_2\text{-}\kappa\text{O}^{1,1'})]$ (Fig. 2.30, middle)]—strongly indicates the coordination of two Pd^{II} fragments per oxygen atom as shown in Fig. 2.30. Attempts to crystallize a triol complex from solutions with an equimolar ratio of palladium(II) and base equivalents failed for the monomer. By elimination of a $[(R,R\text{-chxn})_2\text{Pd}]^{2+}$ cation the compound $[\{\text{Pd}_2(R,R\text{-chxn})_2(\text{HmmpdH}_3)\}_2\text{Pd}](\text{NO}_3)_4 \cdot 4 \text{H}_2\text{O}$ (**24**) crystallized in the space group $P2_1$, as depicted in Fig. 2.31. As predicted by ^{13}C NMR spectroscopy the Hmmpd ligand provided its three bridging alkoxido functions for the formation of a Pd_3 -trimer. The coordination of the alkoxido functions to a first palladium(II) center reduced their Lewis acidity to a level comparable to the N_2 -chelate ligand favoring the elimination of a $R,R\text{-chxn}$ ligand towards dimerization.

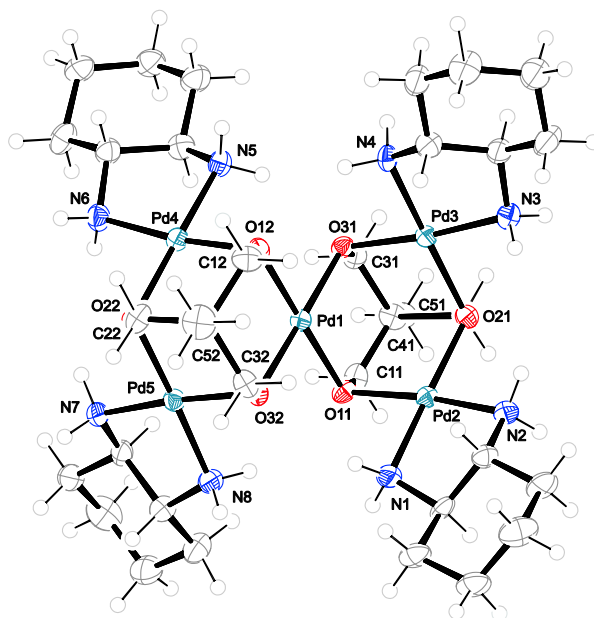


Figure 2.31. The molecular structure of $[\{\text{Pd}_2(R,R\text{-chxn})_2(\text{HmmpdH}_3)\}_2\text{Pd}](\text{NO}_3)_4$ in crystals of the 4-hydrate (**24**). ORTEP plot is drawn with 50% probability ellipsoids. Interatomic distances (\AA) and angles ($^\circ$) (standard deviations of the last digit in parentheses): Pd1–O11 2.020(5), Pd1–O12 2.010(5), Pd1–O31 1.993(5), Pd1–O32 2.028(5), Pd2–O11 2.025(5), Pd2–O21 2.040(5), Pd2–N1 2.019(6), Pd2–N2 2.025(6), Pd3–O21 2.025(5), Pd3–O31 2.016(5), Pd3–N3 2.034(6), Pd3–N4 2.020(6), Pd4–O12 2.018(5), Pd4–O22 2.022(5), Pd4–N5 2.028(6), Pd4–N6 2.028(7), Pd5–O22 2.012(5), Pd5–O32 2.014(5), Pd5–N7 2.024(6), Pd5–N8 2.012(7), O11–Pd1–O31 93.1(2), O11–Pd1–O32 87.2(2), O12–Pd1–O31 86.0(2), O12–Pd1–O32 93.8(2), O11–Pd2–O21 93.0(2), O11–Pd2–N1 89.4(2), O21–Pd2–N2 93.6(2), N1–Pd2–N2 83.9(2), O21–Pd3–O31 92.55(19), O21–Pd3–N3 94.0(2), O31–Pd3–N4 89.4(2), N3–Pd3–N4 84.2(2), O12–Pd4–O22 92.0(2), O12–Pd4–N5 91.0(2), O22–Pd4–N6 92.7(2), N5–Pd4–N6 84.5(3), O22–Pd5–O32 93.89(19), O22–Pd5–N7 92.6(2), O32–Pd5–N8 88.8(2), N7–Pd5–N8 84.8(3), Pd1–O11–Pd2 97.6(2), Pd1–O12–Pd4 99.3(2), Pd2–O21–Pd3 107.7(2), Pd4–O22–Pd5 108.9(2), Pd1–O31–Pd3 97.2(2).

2 Results

Table 2.21. ^{13}C NMR chemical shifts (δ/ppm) of the 2-hydroxymethyl-2-methyl-propane-1,3-diol (Hmmpd) complexes, referenced to 49.5 ppm for the ^{13}C signal of methanol. Atoms are numbered as in Fig. 2.30. $\Delta\delta$ is the difference between the chemical shifts of the free and the palladium-binding polyol taken from the same spectrum in each case. The “%” column shows the amount of chelate; the remaining part is free polyol.

		C1	C1'	C3	C2	C1''	%	Chelate
$[\text{Pd}(\text{en})(\text{Hmmpd}_{1,1'}\text{H}_{-2})]$	C_s	69.0	69.0	66.2	48.5	17.4	55	
$\Delta\delta$		4.0	4.0	1.1	0.0	1.3		$\kappa O^{1,1'}$
$[\text{Pd}_3(\text{en})_3(\text{HmmpdH}_{-3})]^{3+}$	C_3	76.8	76.8	76.8	54.8	17.0	30	
$\Delta\delta$		11.8	11.8	11.8	6.3	0.9		$\kappa O^{1,1',3}$

By the tetrameric and trimeric palladium(II) complexes of the previous sections the concept of stabilizing a $\text{Pd}_n(\mu\text{-OH})_n$ -core by providing a matching polyolato ligand was proved. From Pd-chxn solutions which had a pH value of 7–8 and did not provide a matching polyolato ligand, often an oxido-bridged, hexanuclear derivative of the trinuclear μ -hydroxido species was crystallized (Fig. 2.32).

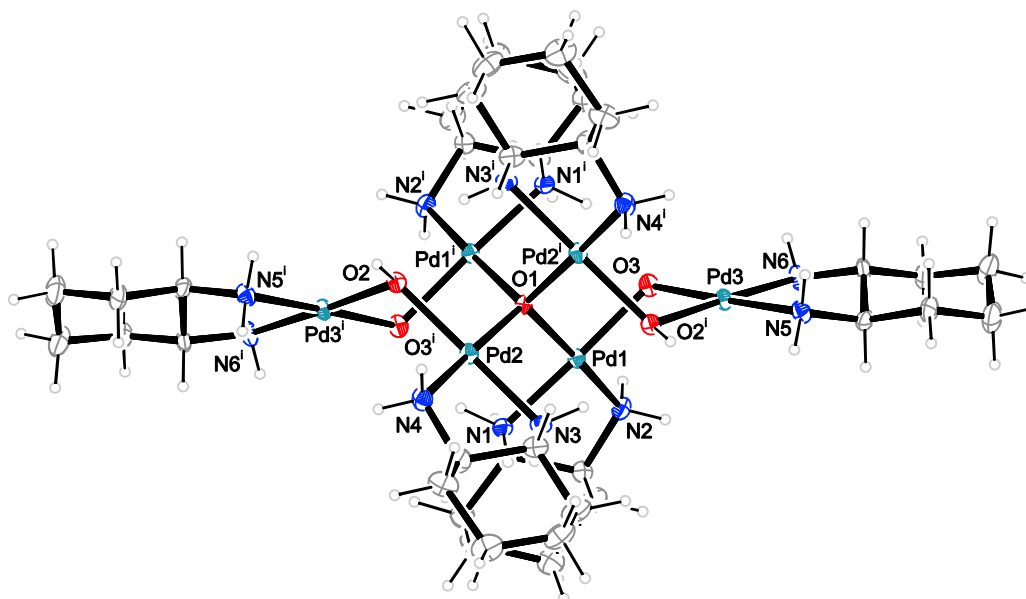


Figure 2.32. The molecular structure of $[\text{Pd}_6(\text{R,R}\text{-chxn})_6(\mu_4\text{-O})(\mu\text{-OH})_4](\text{NO}_3)_6$ in crystals of the 12.5-hydrate (**25**). ORTEP plot is drawn with 50% probability ellipsoids. Interatomic distances (\AA) and angles ($^\circ$) (standard deviations of the last digit in parentheses): Pd1–O1 2.053(4), Pd1–O3 2.029(5), Pd1–N1 2.017(5), Pd1–N2 2.029(6), Pd2–O1 2.047(4), Pd2–O2 2.020(5), Pd2–N3 2.021(6), Pd2–N4 2.040(7), Pd3–O3 2.006(4), Pd3–O2ⁱ 2.016(4), Pd3–N5 2.008(5), Pd3–N6 2.020(5), O1–Pd1–O3 89.12(13), N1–Pd1–N2 84.1(2), O1–Pd2–O2 88.59(12), N3–Pd2–N4 83.6(2), O2ⁱ–Pd3–O3 86.64(18), N5–Pd3–N6 83.6(2), Pd1–O1–Pd2 120.64(2), Pd1–O1–Pd2ⁱ 117.57(2), Pd1ⁱ–O1–Pd2 117.57(2), Pd1ⁱ–O1–Pd2ⁱ 120.64(2), Pd2–O2–Pd3ⁱ 112.7(2), Pd1–O3–Pd3 115.4(2). [Symmetry code: (i) $-x, y, -z + \frac{1}{2}$]

2 Results

Two μ -hydroxido ligands of two trinuclear units condensed and formed a *spiro*-connection of the two cyclic Pd₃ units. The depicted compound, [Pd₆(*R,R*-chxn)₆(μ_4 -O)(μ -OH)₄](NO₃)₆, crystallized in the space group *P* 222₁ and resembled a μ_4 -oxido building unit of palladium(II) oxide which was additionally capped by two Pd(*R,R*-chxn) fragments.^[73] In the literature, μ_4 -oxido bonding was found only once in a tetranuclear species that had formed under less typical conditions.^[74]

2.5 Dihydroxymalonic acid – complexes of palladium(II) with ketone hydrates

Attempts to crystallize a Pd₄-tetraolato species stabilizing the open-chain form of D-threose yielded in a crystal structure with a decomposition product, namely dihydroxymalonic acid. Although the hydrated mesoxalato complex was not the attempted product, [Pd₄(*R,R*-chxn)₄(C₃O₆)(μ -OH)](NO₃)₃ was the first structure of a ketone hydrate acting as a ligand for coordination of Pd^{II}N₂-fragments.

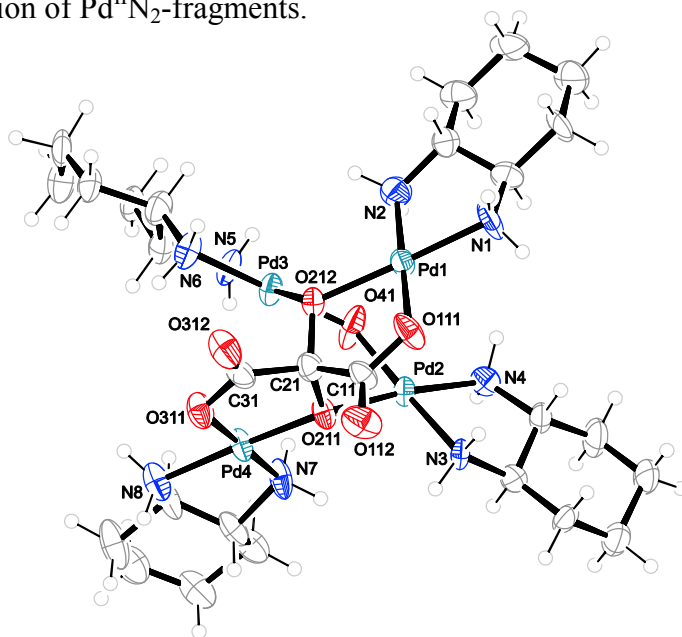


Figure 2.33. The molecular structure of [Pd₄(*R,R*-chxn)₄(C₃O₆)(μ -OH)](NO₃)₃ in crystals of the 8-hydrate (**26**). ORTEP plot is drawn with 50% probability ellipsoids. Interatomic distances (Å) and angles (°) (standard deviations of the last digit in parentheses): Pd1–O111 1.984(11), Pd1–O212 2.012(9), Pd1–N1 2.032(10), Pd1–N2 2.009(11), Pd2–O41 1.997(11), Pd2–O211 2.057(8), Pd2–N3 1.978(10), Pd2–N4 2.026(11), Pd3–O41 2.028(11), Pd3–O212 2.039(9), Pd3–N5 1.986(11), Pd3–N6 2.028(13), Pd4–O211 2.009(9), Pd4–O311 2.022(10), Pd4–N7 1.989(11), Pd4–N8 2.041(12), O111–Pd1–O212 81.7(3), O111–Pd1–N1 95.7(5), O212–Pd1–N2 98.8(4), N1–Pd1–N2 83.8(5), O41–Pd2–O211 90.7(4), O41–Pd2–N4 93.7(4), O211–Pd2–N3 92.4(4), N3–Pd2–N4 83.2(4), O41–Pd3–O212 89.4(4), O41–Pd3–N5 93.7(4), O212–Pd3–N6 93.2(4), N5–Pd3–N6 83.7(5), O211–Pd4–O311 82.4(3), O211–Pd4–N7 98.0(4), O311–Pd4–N8 96.4(5), N7–Pd4–N8 83.2(5), Pd2–O41–Pd3 117.6(4), Pd2–O211–Pd4 119.8(4), Pd1–O212–Pd3 115.7(4); chelate torsion angles: O111–C11–C21–O212 –18.1(15), O212–C21–C31–O312 –72.1(17).

2 Results

The compound **26** crystallized in the triclinic space group $P 1$ with two formula units in the unit cell. The four metal centers in the tetranuclear complex trications were bridged by the geminal alkoxido functions of the entirely deprotonated ketone hydrate (Fig. 2.33) One oxygen atom of each carboxylate group was coordinated to one metal centre, the two oxygen atoms of the hydrated keto group were coordinated to two metal centres. The two palladium atoms that were not part of a chelate ring were bridged by a hydroxido ligand. This coordination mode is an extension of the metal coordination derived for D-erythrulose from spectral data and supports the suggestion that the hydroxy groups of the hydrate are able to coordinate to one metal centre each in a *spiro-bis(chelate)* way.^[72]

2.6 The inositols: from polyols to pyranose rings

The inositols are a link between the open-chain polyols and the pyranose forms of the reducing carbohydrates. Containing one hydroxy group on each of the ring atoms, nine individual inositols are known^[75] and are differentiated by their configuration. The most common isomer is *myo*-inositol. Due to limited commercial availability only three additional isomers were investigated: D-*chiro*-inositol, *neo*-inositol and *scyllo*-inositol.

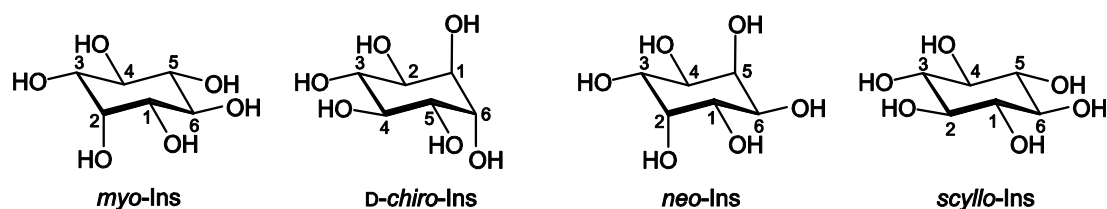


Figure 2.34. Configuration and atomic numbering of the inositols. From left to right: C₃-symmetric *myo*-inositol, C₂-symmetric D-*chiro*-inositol, C_{2h}-symmetric *neo*-inositol and D_{3d}-symmetric *scyllo*-inositol.

As one can see in Fig. 2.34, the inositols are arranged according to their increasing molecular symmetry. This is also reflected in the ¹³C NMR spectra where four signals were detected for the C₃-symmetric *myo*-inositol, three signals for the C₂-symmetric D-*chiro*-inositol, two signals for the C_{2h}-symmetric *neo*-inositol and only one signal was detected for the D_{3d}-symmetric *scyllo*-inositol. This initial molecular symmetry of the inositols prevented an unambiguous assignment of the coordination sites. Instead, with the inositol's increasing molecular symmetry, the number of symmetrically equivalent positions for the coordination of a Pd^{II}N₂ fragment also increased.

2 Results

Myo-inositol, due to its mirror plane across C2 and C5 shows only three independent diolato sites for palladium(II) coordination which are depicted in Fig. 2.35.

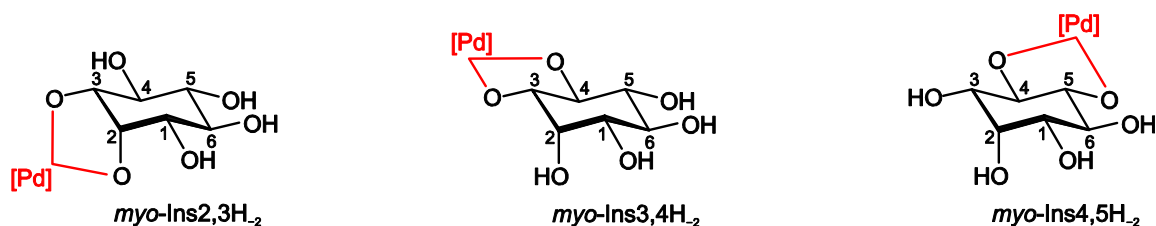


Figure 2.35: Species detected in Pd-en solutions of *myo*-inositol at a 1:1 molar ratio. Due to *myo*-inositol's C_5 -symmetry the depicted species always corresponds to a mirror image which could not be distinguished by ^{13}C NMR spectroscopy. So, *myo*-Ins2,3H₂-κO^{2,3} is identical with *myo*-Ins1,2H₂-κO^{1,2}, *myo*-Ins3,4H₂-κO^{3,4} with *myo*-Ins1,6H₂-κO^{1,6} and *myo*-Ins4,5H₂-κO^{4,5} with *myo*-Ins5,6H₂-κO^{5,6}.

Each coordination site had its equivalent across the mirror plane, so *myo*-Ins2,3H₂-κO^{2,3} was identical with *myo*-Ins1,2H₂-κO^{1,2}, *myo*-Ins3,4H₂-κO^{3,4} with *myo*-Ins1,6H₂-κO^{1,6} and *myo*-Ins4,5H₂-κO^{4,5} with *myo*-Ins5,6H₂-κO^{5,6}. In consequence, the difference between these positions could not be distinguished by ^{13}C NMR spectroscopy as is noted in Table 2.22.

Table 2.22. ^{13}C NMR chemical shifts (δ /ppm) and shift differences ($\Delta\delta$) to the free inositol of *myo*-inositol ligands in Pd-en. Atoms are numbered as in Figure 2.34.

	C1	C2	C3	C4	C5	C6	Chelate
<i>myo</i> -Ins	71.3	72.3	71.3	72.5	74.5	72.5	
[Pd(en)(<i>myo</i> -Ins2,3H ₂)]	70.5	82.2	81.4	76.2	74.5	73.1	
$\Delta\delta$	-0.8	9.9	10.1	3.7	0.0	0.6	κO ^{2,3} ≡ κO ^{1,2}
[Pd(en)(<i>myo</i> -Ins3,4H ₂)]	72.3	71.9	81.6	80.5	74.3	73.3	
$\Delta\delta$	1.0	-0.4	10.3	8.0	-0.2	0.8	κO ^{3,4} ≡ κO ^{1,6}
[Pd(en)(<i>myo</i> -Ins4,5H ₂)]	71.3	73.2	72.9	81.6	83.7	73.1	
$\Delta\delta$	0.0	0.9	1.6	9.1	9.2	0.6	κO ^{4,5} ≡ κO ^{5,6}

All three species were detected in similar amounts in the ^{13}C NMR spectrum, although the κO^{2,3} bonding mode corresponds to a *cis*-vicinal diolato function, whereas the κO^{3,4}- and the κO^{4,5} bonding mode correspond to a *trans*-vicinal diolato function.

D-chiro-inositol had a C_2 -axis to show across the bonds of C3-C4 and C1-C6, so κO^{1,2}-bonded *D-chiro*-Ins1,2H₂ was equivalent to κO^{5,6}-bonded *D-chiro*-Ins5,6H₂. All species detected in Pd-en were depicted in Fig. 2.36, for ^{13}C chemical shifts and CIS value see Table 2.23. At a 1:1 molar ratio (Pd/*D-chiro*-Ins) [Pd(en)(*D-chiro*-Ins1,2H₂-κO^{1,2})] and free inositol were detected in equal amounts and [Pd₂(en)₂(*D-chiro*-Ins1,2;5,6H₄-κO^{1,2}:κO^{5,6})] was found as a

2 Results

minor species. At a 3:1 molar ratio $[\text{Pd}_2(\text{en})_2(\text{D-chiro-Ins}_{1,2;5,6}\text{H}_{-4}\text{-}\kappa\text{O}^{1,2}:\kappa\text{O}^{5,6})]$ and $[\text{Pd}_3(\text{en})_3(\text{D-chiro-InsH}_{-6}\text{-}\kappa\text{O}^{1,2}:\kappa\text{O}^{3,4}:\kappa\text{O}^{5,6})]$ were detected in equal quantities.

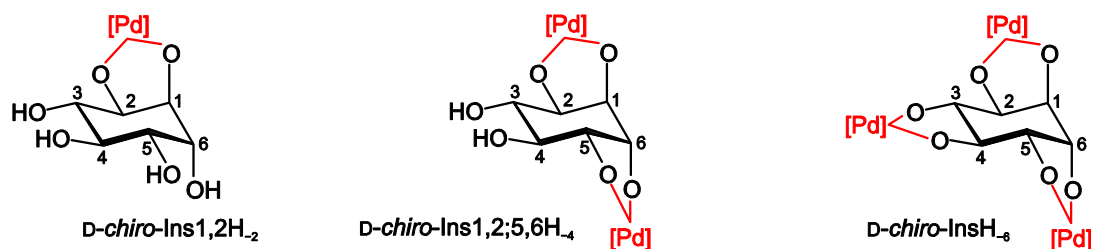


Figure 2.36: Species detected in Pd-en solutions of *D-chiro*-inositol at a 1:1 molar ratio. Due to *D-chiro*-inositol's C_2 -symmetry the depicted species of *D-chiro*- $\text{Ins}_{1,2}\text{H}_{-2}\text{-}\kappa\text{O}^{1,2}$ corresponded to *D-chiro*- $\text{Ins}_{5,6}\text{H}_{-2}\text{-}\kappa\text{O}^{5,6}$.

Additionally, crystals of $[\text{Pd}_2(\text{en})_2(\text{D-chiro-Ins}_{1,2;5,6}\text{H}_{-4})] \cdot 8 \text{H}_2\text{O}$ were obtained. The crystal structure was solved in the space group $P 2_1 2_1 2_1$. The molecular structure in Fig. 2.37 confirmed the NMR spectroscopic result, two Pd(en) fragments were coordinated to the two *cis*-vicinal diolato functions, the *trans*-vicinal diolato function remained uncoordinated.

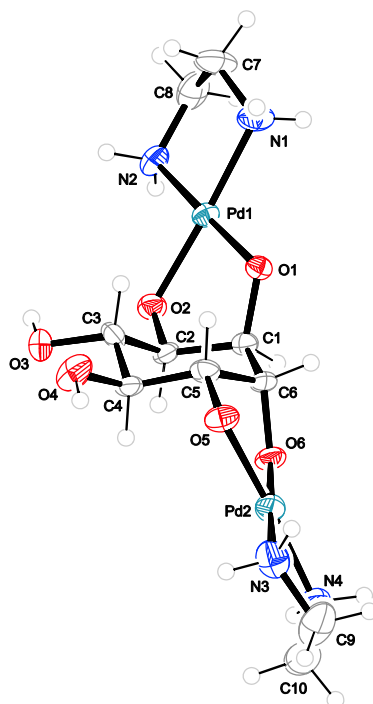


Figure 2.37. The molecular structure of $[\text{Pd}_2(\text{en})_2(\text{D-chiro-Ins}_{1,2;5,6}\text{H}_{-4})]$ in crystals of the 8-hydrate (**27**). ORTEP plot is drawn with 50% probability ellipsoids. Interatomic distances (Å) and angles (°) (standard deviations of the last digit in parentheses): Pd1–O1 2.010(6), Pd1–O2 1.983(6), Pd1–N1 2.042(9), Pd1–N2 2.048(9), Pd2–O5 1.994(7), Pd2–O6 2.008(7), Pd2–N3 2.035(10), Pd2–N4 2.025(10), O1–Pd1–O2 85.7(3), O1–Pd1–N1 95.6(3), O2–Pd1–N2 95.1(3), N1–Pd1–N2 83.6(4), O5–Pd2–O6 85.7(3), O5–Pd2–N3 95.6(4), O6–Pd2–N4 95.8(3), N3–Pd2–N4 83.0(4); chelate torsion angles: O1–C1–C2–O2 50.8(9), O3–C3–C4–O4 –52.5(10), O5–C5–C6–O6 49.3(10); puckering parameters^[22] of the pyranose ring C1–C2–C3–C4–C5–C6: $Q = 0.567(10)$ Å, $\theta = 167.0(10)$.

2 Results

Table 2.23. ^{13}C NMR chemical shifts (δ/ppm) and shift differences ($\Delta\delta$) to the free inositol of D-*chiro*-inositol ligands in Pd-en. Atoms are numbered as in Figure 2.34.

	C1	C2	C3	C4	C5	C6	Chelate
D-<i>chiro</i>-Ins	72.3	71.0	73.3	73.3	71.0	72.3	
[Pd(en)(D- <i>chiro</i> -Ins1,2H ₂)]	83.2	81.0	77.2	73.0	71.8	72.6	
$\Delta\delta$	10.9	10.0	3.9	-0.3	0.8	0.3	$\kappa\text{O}^{1,2} \equiv \kappa\text{O}^{5,6}$
[Pd ₂ (en) ₂ (D- <i>chiro</i> -Ins1,2;5,6H ₄)]	83.5	81.4	76.7	76.7	81.4	83.5	
$\Delta\delta$	11.2	10.4	3.4	3.4	10.4	11.2	$\kappa\text{O}^{1,2};\kappa\text{O}^{5,6}$
[Pd ₃ (en) ₃ (D- <i>chiro</i> -InsH ₆)]	83.5	84.9	86.0	86.0	84.9	83.5	
$\Delta\delta$	11.2	13.9	12.7	12.7	13.9	11.2	$\kappa\text{O}^{1,2};\kappa\text{O}^{3,4};\kappa\text{O}^{5,6}$

neo-Inositol provides two independent chelating sites, a *cis*-vicinal and a *trans*-vicinal diolato function, as depicted in Fig. 2.38. *neo*-Ins2,3H₂- $\kappa\text{O}^{2,3}$, *neo*-Ins1,2H₂- $\kappa\text{O}^{1,2}$, *neo*-Ins4,5H₂- $\kappa\text{O}^{4,5}$ and *neo*-Ins5,6H₂- $\kappa\text{O}^{5,6}$ belong to the *cis*-vicinal diolato function which could not be distinguished by ^{13}C NMR spectroscopy. The *trans*-vicinal diolato function is only represented by two chelating sites, *neo*-Ins3,4H₂- $\kappa\text{O}^{3,4}$ and *neo*-Ins1,6H₂- $\kappa\text{O}^{1,6}$.

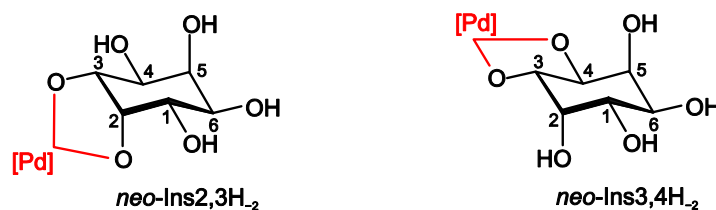


Figure 2.38. Species detected in Pd-en solutions of *neo*-inositol at a 1:1 molar ratio. Due to *neo*-inositol's C_{2h} -symmetry the depicted species of *neo*-Ins2,3H₂- $\kappa\text{O}^{2,3}$ corresponded to *neo*-Ins1,2H₂- $\kappa\text{O}^{1,2}$, *neo*-Ins4,5H₂- $\kappa\text{O}^{4,5}$ and *neo*-Ins5,6H₂- $\kappa\text{O}^{5,6}$. Also, the depicted species of *neo*-Ins3,4H₂- $\kappa\text{O}^{3,4}$ corresponded to *neo*-Ins1,6H₂- $\kappa\text{O}^{1,6}$.

The corresponding chemical shifts and CIS values are summarized in Table 2.24. Higher metalation grades were not investigated by NMR spectroscopy; instead, two crystal structures of a dimetalated *neo*-inositol were available.

Table 2.24. ^{13}C NMR chemical shifts (δ/ppm) and shift differences ($\Delta\delta$) to the free inositol of *neo*-inositol ligands in Pd-en. Atoms are numbered as in Figure 2.34.

	C1	C2	C3	C4	C5	C6	Chelate
<i>neo</i>-Ins	69.8	72.1	69.8	69.8	72.1	69.8	
[Pd(en)(D- <i>neo</i> -Ins2,3H ₂)]	69.4	81.7	80.0	73.6	72.9	70.5	<i>cis</i> -vicinal
$\Delta\delta$	-0.4	9.6	10.2	3.8	0.8	0.7	
[Pd(en)(D- <i>neo</i> -Ins3,4H ₂)]	70.3	71.5	78.5	78.5	71.5	70.3	<i>trans</i> -vicinal
$\Delta\delta$	0.5	-0.6	8.7	8.7	-0.6	0.5	

2 Results

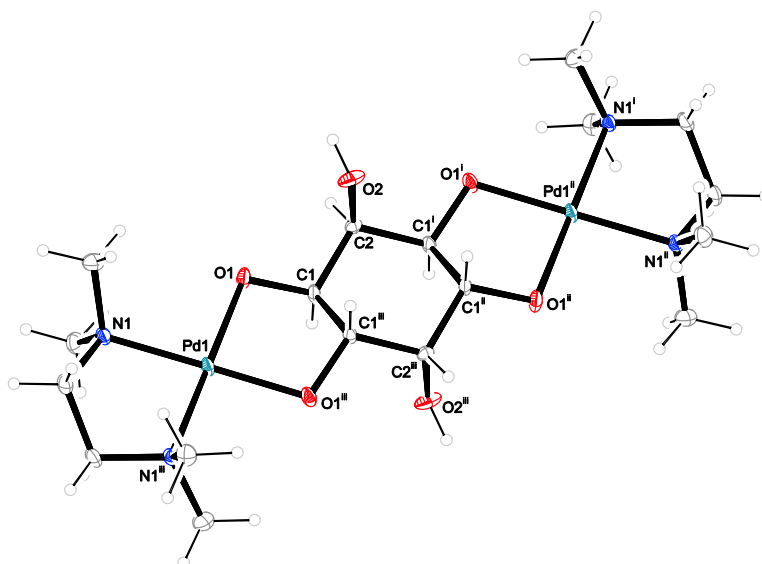


Figure 2.39. The molecular structure of $[\text{Pd}_2(\text{tmen})_2(\text{neo-Ins}1,6;3,4\text{H}_4\text{-}\kappa\text{O}^{1,6};\kappa\text{O}^{3,4})]$ in crystals of the 22-hydrate (**28**). ORTEP plot is drawn with 50% probability ellipsoids. Interatomic distances (Å) and angles ($^\circ$) (standard deviations of the last digit in parentheses): Pd1–O1 1.998(2), Pd1–N1 2.065(2), Pd1–O1ⁱⁱⁱ 1.998(2), Pd1–N1ⁱⁱⁱ 2.065(2), O1–Pd1–N1 94.10(8), O1–Pd1–O1ⁱⁱⁱ 85.95(7), N1–Pd1–N1ⁱⁱⁱ 85.85(8), O1ⁱⁱⁱ–Pd1–N1ⁱⁱⁱ 94.10(8); chelate torsion angles: O1–C1–C2–O2 53.6(3), O1–C1–C1ⁱⁱⁱ–O1ⁱⁱⁱ 57.9(2); puckering parameters^[22] of the pyranose ring C1–C2–C1ⁱ–C1ⁱⁱ–C2ⁱⁱⁱ–C1ⁱⁱⁱ: $Q = 0.587(3)$ Å, $\theta = 180.0(1)^\circ$. [Symmetry code: (i) $-x, y, z$; (ii) $-x, -y, -z$; (iii) $x, -y, -z$]

Table 2.25. Distances [Å] and angles [$^\circ$] of hydrogen bonds in **28**. Standard deviations of the last digit are given in parentheses; values without standard deviation are related to hydrogen atoms at calculated positions. D: donor, A: acceptor.

D	H	A	D–H	H \cdots A	D \cdots A	D–H \cdots A
O2	H82	O92 ⁱ	0.827(10)	1.943(14)	2.759(4)	169(4)
O91	H911	O1 ⁱⁱ	0.819(10)	2.284(16)	3.068(3)	160(4)
O91	H912	O95 ⁱⁱⁱ	0.816(10)	2.052(10)	2.867(3)	177(4)
O92	H92	O91	0.817(9)	2.076(14)	2.840(3)	156(3)
O93	H931	O92	0.833(10)	1.940(11)	2.773(4)	180(5)
O93	H932	O94	0.830(10)	1.930(9)	2.741(3)	165(3)
O94	H941	O1	0.824(10)	1.841(10)	2.663(3)	176(3)
O94	H942	O94 ^{iv}	0.826(10)	1.918(13)	2.742(5)	175(5)
O94	H943	O93	0.825(10)	1.934(12)	2.741(3)	166(4)
O95	H951	O94	0.819(10)	1.912(14)	2.711(3)	165(4)
O95	H952	O91	0.824(10)	1.941(10)	2.763(3)	175(3)
O96	H961	O95	0.825(10)	1.928(10)	2.745(3)	171(3)
O96	H962	O97 ^v	0.811(10)	1.998(10)	2.809(3)	177(4)
O97	H97	O96	0.800(9)	2.031(12)	2.812(3)	165.1(15)

Symmetry code: (i) $-x, y+1/2, -z+1/2$; (ii) $x, y-1, z$; (iii) $x, y-1/2, -z+1/2$; (iv) $x, -y+1, -z$; (v) $-x+1/2, y+1/2, z$.

2 Results

With the first known $[\text{Pd}_2(\text{en})_2(\text{D-}neo\text{-Ins}1,2;4,5\text{H}_{-4}\text{-}\kappa\text{O}^{1,2}:\kappa\text{O}^{4,5})] \cdot 12 \text{H}_2\text{O}$,^[76] the Pd(en) fragments coordinated two opposite *cis*-vicinal diolato functions leaving two equatorial hydroxy functions uncoordinated. With $[\text{Pd}_2(\text{tmen})_2(\text{D-}neo\text{-Ins}1,6;3,4\text{H}_{-4}\text{-}\kappa\text{O}^{1,6}:\kappa\text{O}^{3,4})]$ in crystals of the 22-hydrate, depicted in Fig. 2.39, two Pd(tmen) fragments coordinated two opposite *trans*-vicinal diolato functions leaving two axial hydroxy functions uncoordinated. It is noteworthy that, as in Section 2.3.3, two different coordination compounds could be crystallized with two different Pd^{II}N₂ fragments. Further, with Pd-tmen, the unfavorable *trans*-vicinal diolato-coordinated compound was obtained in the space group *C mce*. Despite the fact that *neo*-inositol showed a perfect undistorted pyranose form of the cyclohexane ring in **28**, the packing diagram of Fig. 6.67 in the Appendix revealed a hydrophobic packing of the tmen ligands and a rigid hydrogen-bonding network in-between the $[\text{Pd}_2(\text{tmen})_2(\text{D-}neo\text{-Ins}1,6;3,4\text{H}_{-4}\text{-}\kappa\text{O}^{1,6}:\kappa\text{O}^{3,4})]$ molecules. The distances and angles of the hydrogen bonding network are listed in Table 2.25. With the Pd(tmen) fragments not participating in the hydrogen-bonding network, each of the coordinating alkoxido functions accepted two hydrogen bonds whereas the axial hydroxy function only acted as a hydrogen-bonding donor underlining the fact that an axially oriented hydroxy function is less suitable for accepting hydrogen bonds than an equatorially oriented hydroxy function.

The highest-symmetric *scyllo*-inositol provides only equatorial *trans*-vicinal diolato functions. At a 3:1 molar ratio Pd-tmen/*scyllo*-Ins, all possible coordination compounds which are shown in Fig. 2.40 could be detected. The dimetalated forms could be found in comparable amounts as the main species, the mono- and the trimetalated forms occurred only as minor species.

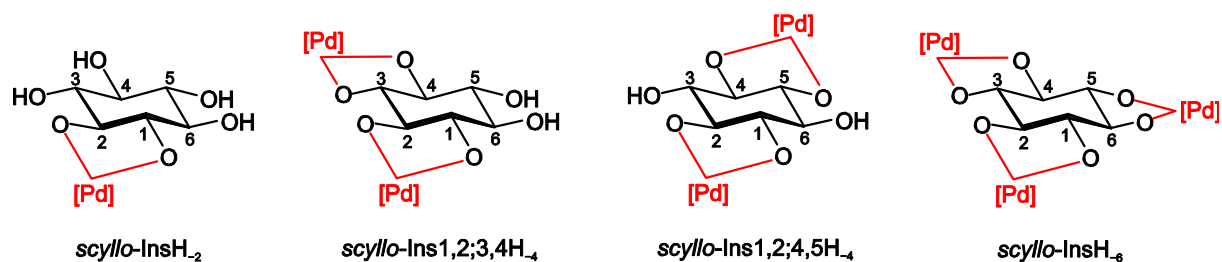


Figure 2.40. Species detected in Pd-en and Pd-tmen solutions of *scyllo*-inositol at various molar ratios. The *scyllo*-inositol's D_{3d} -symmetry decreased by the coordination of Pd^{II}N₂ fragments to a C_2 -symmetry for $\kappa\text{O}^{1,2}$ -chelated *scyllo*-Ins1,2H₂ and $\kappa\text{O}^{1,2}:\kappa\text{O}^{3,4}$ -chelated *scyllo*-Ins1,2;3,4H₄, to a C_{2h} -symmetry for $\kappa\text{O}^{1,2}:\kappa\text{O}^{4,5}$ -chelated *scyllo*-Ins1,2;4,5H₄ and to a D_3 -symmetry for $\kappa\text{O}^{1,2}:\kappa\text{O}^{3,4}:\kappa\text{O}^{5,6}$ -chelated *scyllo*-InsH₆.

Due to *scyllo*-inositol's D_{3d} -symmetry, the depicted species of *scyllo*-Ins1,2H₂- $\kappa\text{O}^{1,2}$ corresponded to *scyllo*-Ins3,4H₂- $\kappa\text{O}^{3,4}$ and *scyllo*-Ins5,6H₂- $\kappa\text{O}^{5,6}$ and couldn't be

2 Results

distinguished from the $\kappa O^{2,3}$ -, the $\kappa O^{4,5}$ - and the $\kappa O^{1,6}$ -coordinated monometalated compounds by ^{13}C NMR spectroscopy. For the same reasons, the numbering of the di- and trimetalated species is reversible because the ^{13}C NMR chemical shifts and shift differences in Table 2.40 only represent the shape of the compound. So, $scyllo\text{-Ins}1,2,3,4\text{H}_{-4}\text{-}\kappa O^{1,2}:\kappa O^{3,4}$ stood for all *scyllo*-inositol species with an uncoordinated diolato function, whereas $\kappa O^{1,2}:\kappa O^{4,5}$ -bonded $scyllo\text{-Ins}1,2;4,5\text{H}_{-4}$ represented all dimetalated species with two separated hydroxy functions. Finally, the ^{13}C signals of $scyllo\text{-InsH}_{-6}\text{-}\kappa O^{1,2}:\kappa O^{3,4}:\kappa O^{5,6}$ also included the enantiomeric mirror image $\kappa O^{2,3}:\kappa O^{4,5}:\kappa O^{1,6}$ -chelated *scyllo*- InsH_{-6} .

Table 2.26. ^{13}C NMR chemical shifts (δ/ppm) and shift differences ($\Delta\delta$) to the free inositol of *scyllo*-inositol ligands in Pd-tmen. Atoms are numbered as in Figure 2.34.

		C1	C2	C3	C4	C5	C6	Chelate
<i>scyllo</i> -Ins	D_{3d}	73.6	73.6	73.6	73.6	73.6	73.6	
[Pd(tmen)(<i>scyllo</i> -Ins1,2H ₋₂)]	C_2	83.8	83.8	75.5	73.9	73.9	75.5	
$\Delta\delta$		10.2	10.2	1.9	0.3	0.3	1.9	$\kappa O^{1,2}$
[Pd ₂ (tmen) ₂ (<i>scyllo</i> -Ins1,2;3,4H ₋₄)]	C_2	84.3	84.6	84.6	84.3	74.6	74.6	
$\Delta\delta$		10.7	11.0	11.0	10.7	1.0	1.0	$\kappa O^{1,2}:\kappa O^{3,4}$
[Pd ₂ (tmen) ₂ (<i>scyllo</i> -Ins1,2;4,5H ₋₄)]	C_{2h}	85.3	85.3	73.0	85.3	85.3	73.0	
$\Delta\delta$		11.7	11.7	-0.6	11.7	11.7	-0.6	$\kappa O^{1,2}:\kappa O^{4,5}$
[Pd ₃ (tmen) ₃ (<i>scyllo</i> -InsH ₋₆)]	D_3	84.7	84.7	84.7	84.7	84.7	84.7	
$\Delta\delta$		11.1	11.1	11.1	11.1	11.1	11.1	$\kappa O^{1,2}:\kappa O^{3,4}:\kappa O^{5,6}$

As for *neo*-inositol, with Pd-en and Pd-tmen two different species were crystallized for *scyllo*-inositol. In previous work,^[76] the crystal structure of the C_{2h} -symmetric dimetalated species [Pd₂(en)₂(*scyllo*-Ins1,2;3,4H₋₄- $\kappa O^{1,2}:\kappa O^{3,4}$)] · 16 H₂O was described. With Pd-tmen, crystals of the minor D_3 -symmetric species [Pd₃(tmen)₃(*scyllo*-InsH₋₆)] · 23 H₂O were obtained (Fig. 2.41) and the structure was solved in the space group $C2/c$. As observed for the previous crystal structures with the Pd(tmen) fragment, two domains could be detected in the structure. By congregation, the Pd(tmen) fragments formed a hydrophobic domain whereas the inositolato fragment together with the high amount of water molecules built the hydrophilic domain of the structure. In Fig. 6.68 (Appendix), together with Table 2.27, one can identify a rigid hydrogen-bonding network. Without a donor hydroxy function, either from the inositol or from the Pd(tmen) fragment, [Pd₃(tmen)₃(*scyllo*-InsH₋₆)] could only accept hydrogen bonds. Therefore, each of the six alkoxido functions accepted two hydrogen bonds from crystal water.

2 Results

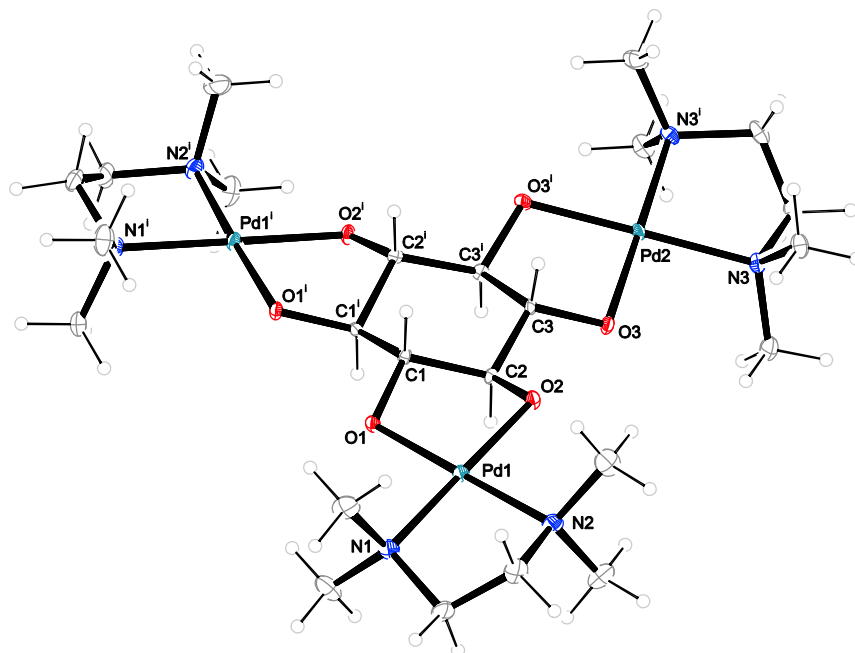


Figure 2.41. The molecular structure of $[\text{Pd}_3(\text{tmen})_3(\text{scyllo-InsH}_6\text{-}\kappa\text{O}^{1,2}:\kappa\text{O}^{3,4}:\kappa\text{O}^{5,6})]$ in crystals of the 23-hydrate (**29**). ORTEP plot is drawn with 50% probability ellipsoids. Interatomic distances (Å) and angles ($^\circ$) (standard deviations of the last digit in parentheses): Pd1–O1 2.037(7), Pd1–O2 2.000(6), Pd1–N1 2.061(9), Pd1–N2 2.061(9), Pd2–O3 2.005(7), Pd2–N3 2.064(9), Pd2–O3ⁱ 2.005(7), Pd2–N3ⁱ 2.064(9), O1–Pd1–O2 84.5(3), O1–Pd1–N1 96.6(3), O2–Pd1–N2 94.0(4), N1–Pd1–N2 85.0(4), O3–Pd2–N3 94.4(3), O3–Pd2–O3ⁱ 85.1(3), N3–Pd2–N3ⁱ 86.2(3), O3ⁱ–Pd2–N3ⁱ 94.4(3); chelate torsion angles: O1–C1–C2–O2 $-55.0(10)$, O3–C3–C3ⁱ–O3ⁱ $-60.8(9)$; puckering parameters^[22] of the pyranose ring C1–C2–C3–C3ⁱ–C2ⁱ–C1ⁱ: $Q = 0.556(11)$ Å, $\theta = 174.2(11)^\circ$. [Symmetry code: (i) $-x, y, -z + \frac{1}{2}$]

Table 2.27. Distances [Å] and angles [$^\circ$] of hydrogen bonds in **29**. Standard deviations of the last digit are given in parentheses; values without standard deviation are related to hydrogen atoms at calculated positions. D: donor, A: acceptor.

D	H	A	D–H	H \cdots A	D \cdots A	D–H \cdots A
O91	H911	O2	0.827(18)	2.14(4)	2.808(6)	138(4)
O91	H912	O3	0.83(2)	1.81(3)	2.625(6)	169(5)
O92	H921	O91	0.82(2)	1.96(2)	2.773(6)	168(4)
O92	H922	O93	0.82(2)	1.97(2)	2.766(6)	166(5)
O93	H931	O94	0.82(2)	1.91(2)	2.759(6)	173(4)
O93	H932	O912	0.82(2)	1.95(2)	2.747(7)	163(4)
O94	H941	O1 ⁱ	0.81(2)	1.93(2)	2.708(6)	161(3)
O94	H942	O910 ⁱⁱ	0.807(19)	2.61(4)	2.773(6)	93(3)
O95	H951	O3 ⁱ	0.82(2)	1.99(2)	2.806(6)	173(4)
O95	H952	O92 ⁱⁱⁱ	0.81(2)	2.08(2)	2.858(6)	159(4)
O96	H961	O97	0.83(2)	2.13(3)	2.780(11)	135(3)
O96	H962	O912 ^{iv}	0.83(2)	2.13(3)	2.820(11)	141(4)

2 Results

Table 2.27. Continued.

D	H	A	D–H	H⋯A	D⋯A	D–H⋯A
O97	H971	O94	0.82(2)	2.00(2)	2.812(6)	172(3)
O97	H972	O95	0.82(2)	1.98(2)	2.789(6)	172(6)
O98	H981	O97	0.82(2)	2.05(3)	2.809(6)	154(5)
O98	H982	O2 ⁱⁱ	0.83(2)	1.99(2)	2.814(6)	171(6)
O99	H99	O98	0.83(2)	2.02(3)	2.832(8)	166(8)
O910	H91	O1	0.83(2)	1.93(2)	2.737(6)	168(4)
O910	H92	O913 ⁱⁱⁱ	0.81(2)	2.17(3)	2.917(7)	153(4)
O911	H191	O910 ⁱ	0.83(2)	1.99(3)	2.792(7)	162(4)
O912	H291	O92 ^v	0.82(2)	2.01(3)	2.795(7)	162(4)
O912	H292	O913 ^{vi}	0.83(2)	2.003(18)	2.819(7)	168(6)
O913	H391	O911	0.82(2)	2.10(3)	2.832(7)	149(4)
O913	H392	O99 ^{vi}	0.82(2)	2.52(5)	3.031(8)	122(5)

Symmetry code: (i) $-x+3/2, -y+1/2, -z+1$; (ii) $x+1/2, -y+1/2, z+1/2$; (iii) $-x+3/2, y-1/2, -z+3/2$; (iv) $-x+3/2, -y+1/2, -z+2$; (v) $x, -y+1, z+1/2$; (vi) $-x+2, -y+1, -z+2$.

2.7 Conformational fluctuation in palladium(II)–methyl aldopentopyranoside complexes

The methyl pentosides provide all the properties needed to get on with the investigation of palladium(II) coordination to reducing carbohydrates. By the methylation of O1 the configuration of the glucose is fixed and the most acidic, anomeric hydroxy group cannot participate in chelate ring formation. Otherwise, in aqueous solutions, some of the methyl pentosides as well as their parent glycoses fluctuate between the two chair conformers.^[5, 17] Methyl α -D-lyxopyranoside and methyl β -D-ribosepyranoside show a dynamic behavior, particularly in the ${}^4C_1 \leftrightarrow {}^1C_4$ chair inversion as it is depicted in Fig. 2.42.

To guarantee full metalation, all reactions were performed under palladium(II) excess conditions at a 2:1 molar Pd/pentoside ratio. The ${}^{13}\text{C}$ NMR chemical shifts of the detected methyl pentopyranosides solution species in Pd-tmen were collected in Table 2.28. The CIS values resulting from coordination did not differ from Pd-chxn^[71] or the formerly used Pd-en,^[39] so the comparability of previous results was guaranteed. Two-dimensional NMR techniques were used to elucidate the ${}^3J_{\text{H,H}}$ coupling constants for determining the conformation of the respective glycosides by means of the Karplus relationship.

2 Results

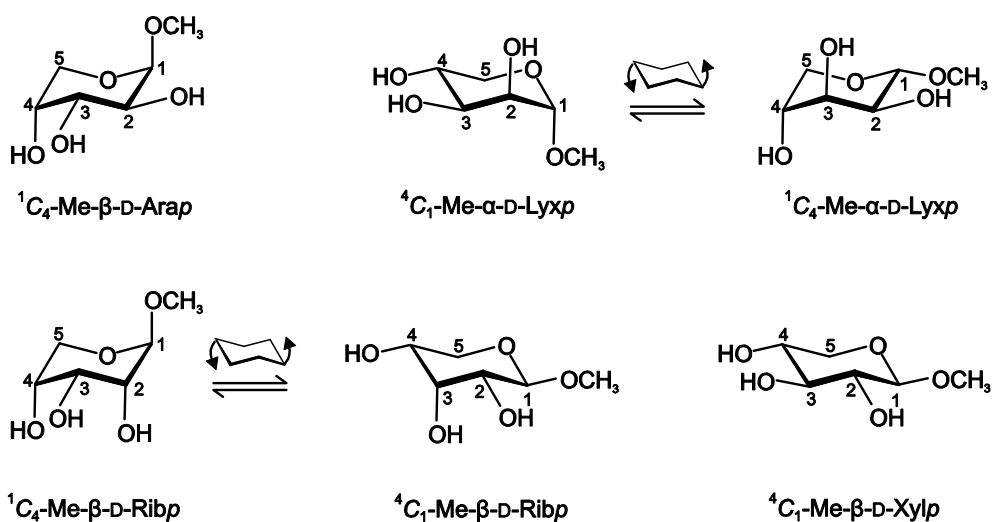


Figure 2.42. Configuration, conformation and atomic numbering of the methyl pentopyranosides. From the top left to the bottom right: 1C_4 -methyl β -D-arabinopyranoside, the fluctuating methyl α -D-lyxopyranoside and β -D-ribopyranoside and 4C_1 -methyl β -D-xylopyranoside.

Table 2.28. ${}^{13}\text{C}$ NMR chemical shifts (δ/ppm) and shift differences ($\Delta\delta$) to the free pentopyranoside of methyl pentopyranosides in Pd-tmen. Atoms are numbered as in Figure 2.42.

		C1	C2	C3	C4	C5	OCH ₃	Chelate
Me- β -D-Arap _{2,3H-2}	δ	102.2	78.1	77.2	72.0	63.2	55.8	
	$\Delta\delta$	1.7	9.3	7.8	2.5	0.1	0.0	$\kappa O^{2,3}$
Me- β -D-Arap _{3,4H-2}	δ	101.1	72.3	78.6	79.1	63.0	55.9	
	$\Delta\delta$	0.6	3.5	9.2	9.6	-0.1	0.1	$\kappa O^{3,4}$
Me- α -D-Lyxp _{2,3H-2}	δ	104.0	79.9	81.1	70.5	63.8	56.4	
	$\Delta\delta$	2.2	9.8	9.9	3.0	0.7	0.5	$\kappa O^{2,3}$
Me- α -D-Lyxp _{3,4H-2}	δ	101.8	72.8	80.9	74.5	64.4	55.4	
	$\Delta\delta$	0.0	2.7	9.7	7.0	1.3	-0.5	$\kappa O^{3,4}$
Me- β -D-Ribp _{2,3H-2}	δ	103.8	81.3	75.7	69.3	64.0	56.4	
	$\Delta\delta$	1.8	10.6	7.4	1.0	0.4	-0.3	$\kappa O^{2,3}$
Me- β -D-Ribp _{3,4H-2}	δ	102.8	70.9	67.0	78.7	65.0	56.5	
	$\Delta\delta$	0.8	0.2	7.7	10.4	1.4	-0.2	$\kappa O^{3,4}$
Me- β -D-Ribp _{2,4H-2}	δ	104.3	69.1	67.6	67.8	65.7	55.3	
	$\Delta\delta$	2.3	-1.6	-0.7	-0.5	2.1	-1.4	$\kappa O^{2,4}$
Me- β -D-Xylp _{2,3H-2}	δ	105.8	82.8	86.4	71.6	66.5	57.4	
	$\Delta\delta$	1.2	9.2	10.1	1.8	0.8	-0.4	$\kappa O^{2,3}$
Me- β -D-Xylp _{3,4H-2}	δ	105.4	75.1	86.2	79.6	65.8	58.0	
	$\Delta\delta$	0.8	1.5	9.9	9.8	0.1	0.2	$\kappa O^{3,4}$
Me- β -D-Xylp _{2,4H-2}	δ	103.1	71.7	68.8	68.5	60.8	55.6	
	$\Delta\delta$	-1.5	-1.9	-7.5	-1.3	-4.9	-2.2	$\kappa O^{2,4}$

2 Results

Methyl β -D-arabinopyranoside is non-fluctuating in its free state but resides in the 1C_4 conformation. The formation of five-membered chelate rings by the attack of a vicinal diol function is the predominant mode of palladium(II)–pyranose binding. Both *cis*- or *trans*-diolate binding is common, the latter requiring a diequatorial conformation. As depicted in Fig. 2.43, *cis* coordination is usually the preferred binding mode of methyl glycopyranosides.

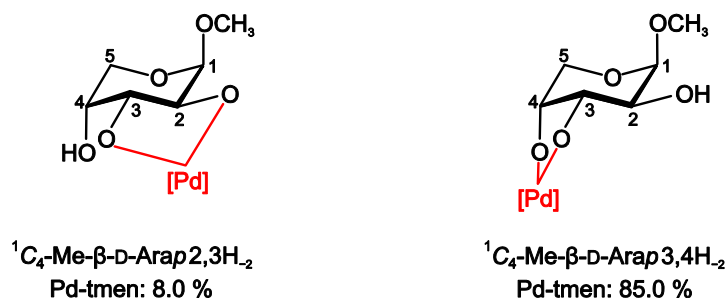


Figure 2.43. Species detected in solutions of methyl β -D-arabinopyranoside in Pd-tmen at a molar 2:1 Pd/pyranoside ratio. Percent values of the species distribution in solution were determined, the remaining pyranoside was found unmetalated.

In the reaction of methyl β -D-arabinopyranoside with Pd-tmen, two kinds of complex species were thus detected in solution: the preferred *cis*-diolato complex of the Me- β -D-Arap3,4H₂- $\kappa O^{3,4}$ as the major, and the *trans*-diolato complex of Me- β -D-Arap2,3H₂- $\kappa O^{2,3}$ as the minor species. The ${}^3J_{H,H}$ coupling constants of Me- β -D-Arap3,4H₂- $\kappa O^{3,4}$ indicated that the 1C_4 conformation of the respective free glycoside was maintained on metalation (Table 2.29).

Table 2.29. Experimental and calculated ${}^3J_{H,H}$ values in Hz for the free glycoside and the major metalated species of methyl β -D-arabinopyranoside in Pd-tmen. Bold: calculated coupling constants which unambiguously represent the specified conformer. For the calculations of constants, the Karplus relationship in Eq. 8 of Ref.^[28] was used in conjunction with the torsion angles of idealized structures (all torsion angles multiples of 60°).

	${}^3J_{H1,H2}$	${}^3J_{H2,H3}$	${}^3J_{H3,H4}$	${}^3J_{H4,H5eq}$	${}^3J_{H4,H5ax}$	Conformation
Free (exp.) ^[77]	2.8	10.0	3.0	2.3	1.0	1C_4 (Ref. ^[77])
D- $\kappa O^{3,4}$	3.5	9.1	4.2	2.2	1.8	1C_4 (<i>cis</i> -vic.)
Idealized	3.2	9.6	3.2	2.5	0.6	1C_4 (Karplus)
Idealized	1.5	4.3	3.5	4.3	10.1	4C_1 (Karplus)

In contrast to methyl β -D-arabinopyranoside, free methyl α -D-lyxopyranoside fluctuates.^[18, 77] The reaction of methyl α -D-lyxopyranoside with Pd-tmen gave the *cis*-chelate $\kappa O^{2,3}$ -bonded Me- α -D-Lyxp2,3H₂ as the major species accompanied by only small amounts of the *trans*-chelate species Me- α -D-Lyxp3,4H₂- $\kappa O^{3,4}$ (Fig. 2.44). In the *trans*-equatorial minor species, fluctuation was frozen because only the 4C_1 conformer was able to act as a ligand.

2 Results

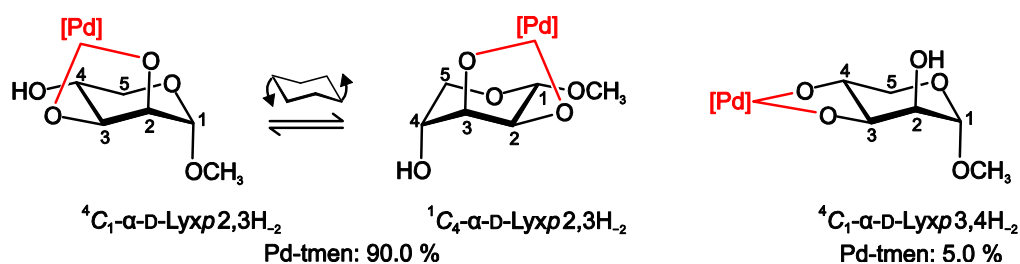


Figure 2.44. Conformational fluctuation of the major $\kappa O^{2,3}$ -binding methyl α -D-lyxopyranoside in Pd-tmen at a molar 2:1 Pd/pyranoside ratio. The minor $\kappa O^{3,4}$ -chelate was found in its only possible conformation. Percent values of the species distribution in solution were determined, the remaining pyranoside was found unmetalated.

For the major species, however, the coupling constants confirmed an equilibrium between the 4C_1 and the 1C_4 conformation of the Me- α -D-Lyxp2,3H₂- $\kappa O^{2,3}$ chelate. Of the two conformers, the 4C_1 chelate predominated (Table 2.30).

Table 2.30. Experimental and calculated ${}^3J_{H,H}$ values in Hz for the free glycoside and the various metalated species of methyl α -D-lyxopyranoside in Pd-tmen. Bold: measured (formation of a *trans*-vicinal chelate) or calculated coupling constants which unambiguously represent the specified conformer. For the calculations of constants, the Karplus relationship in Eq. 8 of Ref.^[28] was used in conjunction with the torsion angles of a X-ray analysis or the angles of idealized structures (all torsion angles multiples of 60°).

	${}^3J_{H1,H2}$	${}^3J_{H2,H3}$	${}^3J_{H3,H4}$	${}^3J_{H4,H5eq}$	${}^3J_{H4,H5ax}$	Conformation
Free (exp.) ^[77]	3.2	3.8	4.0	4.8	9.0	${}^4C_1 \leftrightarrow {}^1C_4$ (Ref. ^[77])
D- $\kappa O^{2,3}$	3.6	4.0	6.7	3.8	7.2	${}^4C_1 \leftrightarrow {}^1C_4$, 7:3 ratio
D- $\kappa O^{3,4}$	1.6	3.2	n.d.	n.d.	n.d.	4C_1 (<i>trans</i> -vic.)
30	1.7	4.5	8.4	4.7	10.1	4C_1 (Karplus)
Idealized	1.8	3.5	9.6	4.3	10.1	4C_1 (Karplus)
Idealized	8.1	3.5	4.3	2.5	0.6	1C_4 (Karplus)

Accordingly, structure analysis of $[Pd(R,R\text{-chxn})(Me\text{-}\alpha\text{-D-Lyxp2,3H}_2\text{-}\kappa O^{2,3})]$ on yellow crystals of the 2.25-hydrate (**30**) revealed the 4C_1 conformation. The crystal structure was solved in the space group $P1$, the asymmetric unit revealed four molecules of the lyxopyranoside complex and nine water molecules. The N–H functions of the Pd($R,R\text{-chxn}$) fragment as well as the remaining hydroxy function of the lyxopyranoside acted as hydrogen-bond donor, each alkoxido function accepted two hydrogen bonds. As one can see in Fig. 6.69 in the Appendix, the hydrogen bonds always connected a pair of $[Pd(R,R\text{-chxn})(Me\text{-}\alpha\text{-D-Lyxp2,3H}_2\text{-}\kappa O^{2,3})]$ molecules forming a two-ply band along the c axis. Two molecules each were arranged alternating the Pd($R,R\text{-chxn}$) fragment with the opposing lyxopyranoside.

2 Results

All the distances and angles of the hydrogen-bonding network are listed in Table 2.31. The *R,R*-chxn ligand together with the lyxopyranoside's methyl group built the hydrophobic edges of the band. Only van der Waals attraction held the bands together in the direction of the *b* axis.

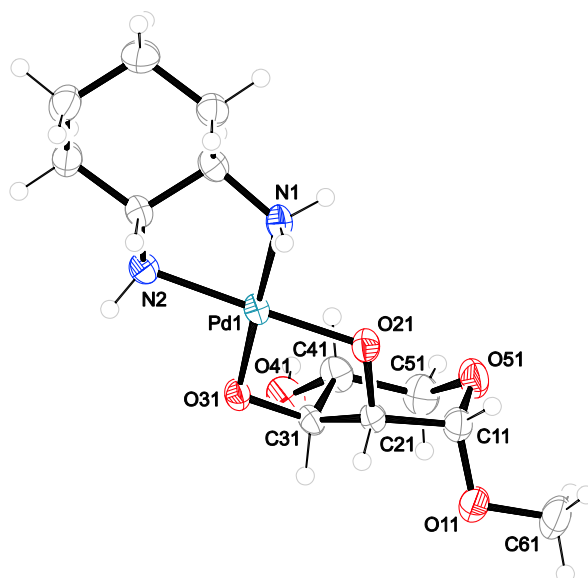


Figure 2.45. The molecular structure of $[\text{Pd}(\text{R,R}\text{-chxn})(\text{Me-}\alpha\text{-D-Lyxp2,3H}_2\text{-}\kappa\text{O}^{2,3})]$ in crystals of the 2.25-hydrate (**30**). ORTEP plot is drawn with 50% probability ellipsoids. Interatomic distances (\AA) and angles ($^\circ$) (standard deviations of the last digit in parentheses): Pd1–O21 1.961(4), Pd1–O31 2.007(3), Pd1–N1 2.045(4), Pd1–N2 2.048(4), Pd2–O22 1.983(3), Pd2–O32 1.993(4), Pd2–N3 2.031(5), Pd2–N4 2.031(4), Pd3–O23 2.003(4), Pd3–O33 2.001(3), Pd3–N6 2.029(5), Pd3–N5 2.046(4), Pd4–O24 1.988(3), Pd4–O34 2.003(3), Pd4–N7 2.037(4), Pd4–N8 2.048(4), O21–Pd1–O31 84.73(13), O21–Pd1–N1 93.93(14), O31–Pd1–N2 97.56(15), N1–Pd1–N2 83.79(16), O22–Pd2–O32 84.82(14), O22–Pd2–N3 95.56(16), O32–Pd2–N4 96.90(17), N3–Pd2–N4 82.70(18), O23–Pd3–O33 85.41(13), O23–Pd3–N5 94.96(14), O33–Pd3–N6 95.80(15), N5–Pd3–N6 83.86(16), O24–Pd4–O34 84.75(13), O24–Pd4–N7 94.01(15), O34–Pd4–N8 97.08(14), N7–Pd4–N8 84.16(16); chelate torsion angles: O21–C21–C31–O31–45.5(5), O22–C22–C32–O32–46.2(5), O23–C23–C33–O33–50.6(5), O24–C24–C34–O34–52.6(5); puckering parameters^[22] of the pyranose ring O51–C11–. . . : $Q = 0.522(5)$ \AA , $\theta = 13.9(7)^\circ$, $\varphi = 310(2)^\circ$; O52–C12–. . . : $Q = 0.552(5)$ \AA , $\theta = 15.2(6)^\circ$, $\varphi = 297(2)^\circ$; O53–C13–. . . : $Q = 0.549(5)$ \AA , $\theta = 5.8(5)^\circ$, $\varphi = 302(6)^\circ$; O54–C14–. . . : $Q = 0.540(5)$ \AA , $\theta = 6.1(5)^\circ$, $\varphi = 269(5)^\circ$.

A detail of the pyranose-puckering analysis was noteworthy. In two of the four molecules in the asymmetric unit, the angle θ was about 14° and 15° , which indicated an unusually large deviation of the chair conformation (the other θ angles in the literature^[71] did not exceed ca. 6°). The phase angle pointed to an admixture of the E_5 conformation to the 4C_1 chair, which resembled a small distortion along the transitional path toward the 1C_4 chair (Fig. 2.45).

2 Results

Table 2.31. Distances [\AA] and angles [$^\circ$] of hydrogen bonds in **30**. Standard deviations of the last digit are given in parentheses; values without standard deviation are related to hydrogen atoms at calculated positions. D: donor, A: acceptor.

D	H	A	D–H	H \cdots A	D \cdots A	D–H \cdots A
O41	H841	O23 ⁱ	0.84	1.99	2.806(5)	162.2
O42	H842	O91	0.84	1.90	2.693(5)	156.3
O43	H843	O96	0.84	1.91	2.734(5)	166.2
O44	H844	O94 ⁱⁱ	0.84	1.90	2.709(5)	160.5
N1	H711	O42	0.92	2.06	2.931(5)	158.0
N1	H712	O54 ⁱⁱⁱ	0.92	2.44	3.169(5)	136.1
N2	H721	O92	0.92	2.63	3.092(5)	111.4
N2	H722	O34	0.92	2.12	3.022(5)	166.0
N3	H731	O95 ^{iv}	0.92	1.99	2.876(6)	160.9
N3	H732	O98	0.92	2.29	3.104(7)	147.0
N4	H741	O96	0.92	2.26	2.964(6)	132.7
N4	H742	O99 ⁱⁱⁱ	0.92	2.37	3.057(6)	131.8
N5	H751	O95 ^v	0.92	1.95	2.850(5)	164.6
N5	H752	O44 ^{iv}	0.92	2.25	3.147(5)	163.5
N6	H761	O91	0.92	2.56	3.113(5)	118.8
N6	H762	O97 ^{vi}	0.92	2.05	2.852(6)	144.5
N7	H771	O43	0.92	2.13	3.033(5)	165.7
N7	H772	O99	0.92	2.22	3.085(6)	157.3
N8	H781	O98 ⁱⁱ	0.92	2.22	3.140(6)	174.2
N8	H782	O31	0.92	1.97	2.843(5)	158.7
O91	H911	O24	0.851(19)	1.84(2)	2.685(4)	173(6)
O91	H912	O33	0.844(19)	1.98(3)	2.759(5)	154(5)
O92	H921	O34	0.837(19)	1.86(2)	2.668(5)	161(5)
O92	H922	O22 ⁱⁱ	0.845(19)	1.87(2)	2.705(5)	172(6)
O93	H931	O24 ⁱⁱⁱ	0.838(19)	1.85(3)	2.626(4)	152(5)
O93	H932	O21	0.838(19)	1.82(2)	2.615(5)	158(5)
O94	H941	O22	0.841(19)	1.91(3)	2.682(5)	152(5)
O94	H942	O23	0.845(19)	1.88(2)	2.698(5)	164(6)
O95	H951	O31	0.836(19)	1.86(2)	2.699(4)	177(7)
O95	H952	O92	0.846(19)	1.85(2)	2.692(5)	172(5)
O96	H961	O21	0.841(19)	1.96(3)	2.779(5)	164(6)
O96	H962	O32	0.838(19)	1.96(2)	2.778(5)	164(6)
O97	H971	O93	0.85(2)	1.90(2)	2.749(6)	175(8)
O97	H972	O32	0.86(2)	1.78(2)	2.636(5)	177(8)
O98	H981	O53	0.86(2)	2.55(7)	3.151(6)	127(7)
O98	H982	O94	0.86(2)	1.93(5)	2.653(6)	141(8)
O99	H991	O33	0.83(2)	1.88(3)	2.688(5)	162.2
O99	H992	O93 ^{vi}	0.83(2)	1.90(4)	2.684(5)	156.3

Symmetry code: (i) $x-1, y, z+1$; (ii) $x, y, z+1$; (iii) $x-1, y, z$; (iv) $x, y, z-1$; (v) $x+1, y, z-1$; (vi) $x+1, y, z$.

2 Results

Aqueous solutions of methyl β -D-ribofuranoside are characterized by the fluctuating glycoside's conformational equidistribution.^[18, 77] The coupling constants thus indicate a 1:1 mixture of the 4C_1 and the 1C_4 conformers of methyl β -D-ribofuranoside. The preferred *cis*-vicinal chelation is possible both for the $\kappa O^{2,3}$ and for the $\kappa O^{3,4}$ attacks on the metal probe. Accordingly, both kinds of species were observed in the respective solutions at about equal quantities (Fig. 2.46).

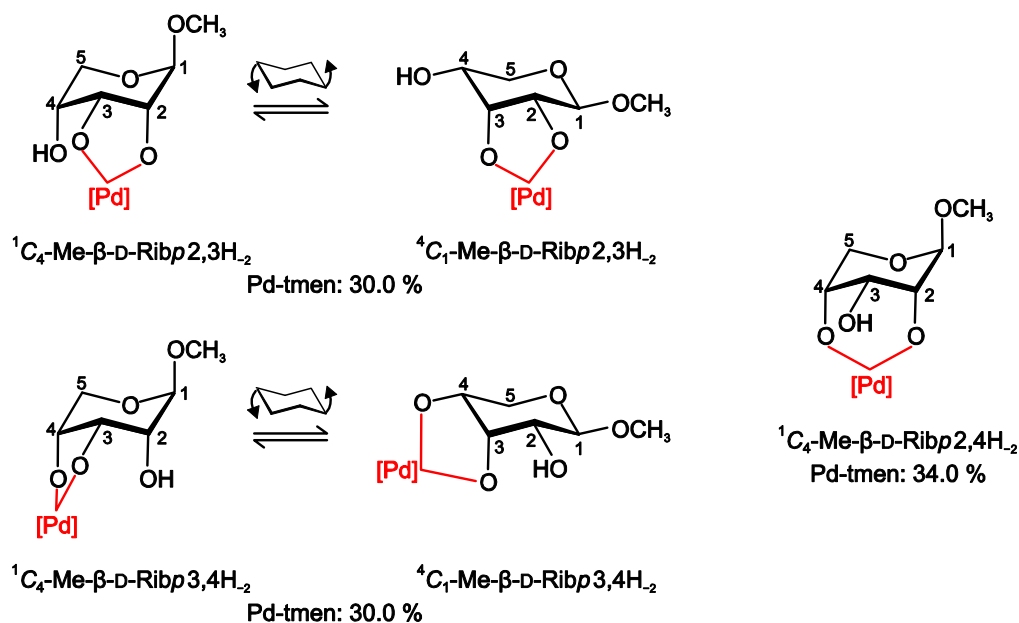


Figure 2.46. Conformational fluctuation of both the $\kappa O^{2,3}$ - and the $\kappa O^{3,4}$ -binding methyl β -D-ribofuranoside ligand in Pd-tmen at a molar 2:1 Pd/pyranoside ratio. The $\kappa O^{2,4}$ -chelate (right) adopted its only possible conformation. Percent values of the species distribution in solution were determined, the remaining pyranoside was found unmetalated.

The ${}^3J_{H,H}$ coupling constants of the complexes closely resembled those of the free ribopyranoside. Also, the [Pd(tmen)Me- β -D-Ribp2,3H₂- $\kappa O^{2,3}$] and the [Pd(tmen)Me- β -D-Ribp3,4H₂- $\kappa O^{3,4}$] chelates fluctuated (Table 2.32). Unlike the arabinopyranoside and the lyxopyranoside, the ribopyranoside provided a special bonding mode to the palladium(II) central metal. For the ribopyranoside, *trans*-vicinal diol bonding was not possible and was replaced by *syn*-diaxial $\kappa O^{2,4}$ bonding.

In the past, the $\kappa O^{1,3}$ -diolato coordination was accepted as a rare coordination mode for palladium(II), appearing only if this binding mode was enforced by sterical restrictions, as in the [Pd(en)(1,6AnGlc2,4H₂)] complex,^[41] by an intramolecular hydrogen bond, as in the [Pd₂(en)₂(β -D-Galf1,3;5,6H₄- $\kappa O^{1,3}$: $\kappa O^{5,6}$)] complex^[39] or by a flexible furanose ring supporting the $\kappa O^{1,3}$ -diolato function as in the [Pd(*R,R*-chxn) α -L-Thrf1,3H₂- $\kappa O^{1,3}$]

2 Results

complex.^[37] With the identification of an all-axial 1C_4 - β -D-Xylp1,3;2,4H₄- $\kappa O^{1,3}$: $\kappa O^{2,4}$ in Pd-en and Pd-chxn^[37] which became the main solution species with the increase of reaction time, the $\kappa O^{1,3}$ -diolato coordination mode was accepted as an equivalent alternative to the $\kappa O^{1,2}$ -diolato binding mode.

Table 2.32. Experimental and calculated ${}^3J_{H,H}$ values in Hz for the free glycoside and the various metalated species of methyl β -D-ribofuranoside in Pd-tmen. Bold: measured (formation of a *syn*-diaxial chelate) or calculated coupling constants which unambiguously represent the specified conformer. For the calculations of constants, the Karplus relationship in Eq. 8 of Ref.^[28] was used in conjunction with the torsion angles of a X-ray analysis or the angles of idealized structures (all torsion angles multiples of 60°).

	${}^3J_{H1,H2}$	${}^3J_{H2,H3}$	${}^3J_{H3,H4}$	${}^3J_{H4,H5eq}$	${}^3J_{H4,H5ax}$	Conformation
Free (exp.) ^[77]	5.1	3.4	3.4	3.5	7.0	${}^4C_1 \leftrightarrow {}^1C_4$ (Ref. ^[77])
D- $\kappa O^{2,3}$	3.5	3.6	3.6	—	—	${}^4C_1 \leftrightarrow {}^1C_4$, 3:7 ratio
D- $\kappa O^{3,4}$	4.5	3.0	3.2	3.0	5.0	${}^4C_1 \leftrightarrow {}^1C_4$, 4:6 ratio
D- $\kappa O^{2,4}$	1.8	3.7	3.7	1.6	2.0	1C_4 (<i>syn</i> -diaxial)
Idealized	1.8	3.5	3.2	2.5	0.6	1C_4 (Karplus)
Idealized	8.1	3.5	3.5	4.3	10.1	4C_1 (Karplus)

[Pd(tmen)(Me- β -D-Ribp2,4H₂- $\kappa O^{2,4}$)] showed a CIS which was substantially different from vicinal $\kappa^{1,2}$ -chelation (Table 2.28). However, the results were in fair agreement with CISs of the [Pd(en)(1,6AnGlc2,4H₂- $\kappa O^{2,4}$)] (1,6AnGlc = 1,6-anhydro- β -D-glucose) complex.^[41] Furthermore, the structure of [Pd(*R,R*-chxn)(Me- β -D-Ribp2,4H₂- $\kappa O^{2,4}$)] in crystals of the trihydrate confirmed the $\kappa O^{2,4}$ -coordination mode.^[78]

Methyl β -D-xylofuranoside is found in the 4C_1 conformation with four equatorial substituents. Conformational fluctuation was also not expected to be induced by metalation because a fluctuating pentoside chelate obviously required a *cis*-vicinal diol function. Instead, two *trans*-vicinal diol sites could attack the metal probes. Due to the similarity of the $\kappa O^{2,3}$ and the $\kappa O^{3,4}$ sites—an analogy to the ribofuranoside which provides two *cis*-vicinal diol functions—equipartition of Me- β -D-Xylp2,3H₂- $\kappa O^{2,3}$ and Me- β -D-Xylp3,4H₂- $\kappa O^{3,4}$ was detected (Fig. 2.47). With the chair-inverted species [Pd(tmen)(Me- β -D-Xylp2,4H₂- $\kappa O^{2,4}$)] found at a quantity of 13%, the unexpected result could be rationalized by the fact that *trans*-vicinal chelation is a second-choice coordination mode. The assignment depended on the coupling-constant analysis (Table 2.33). Because the conformation was different from that of the standard state of the free glycoside, CIS values in this case were meaningless (Table 2.28). This result underlined the stability of the six-ring chelates.

2 Results

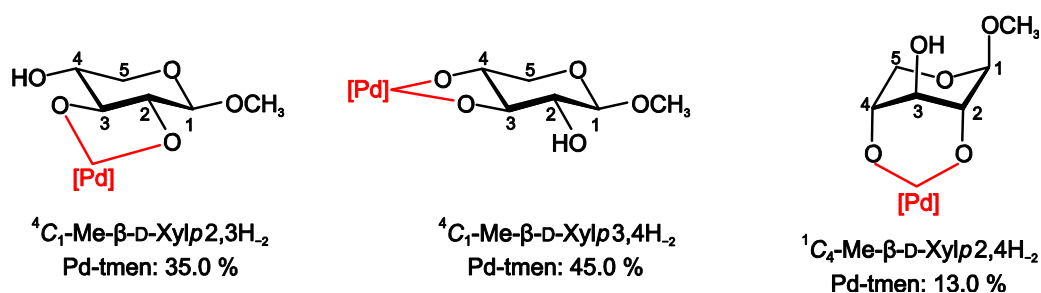


Figure 2.47. Frozen conformations in all monometalated isomers of the methyl β -D-xylopyranoside ligand in Pd-tmen at a molar 2:1 Pd/pyranoside ratio. Percent values of the species distribution in solution were determined, the remaining pyranoside was found unmetalated.

Table 2.33. Experimental and calculated ${}^3J_{H,H}$ values in Hz for the free glycoside and the various metalated species of methyl β -D-xylopyranoside in Pd-tmen. Bold: measured or calculated coupling constants which unambiguously represent the specified conformer. For the calculations of constants, the Karplus relationship in Eq. 8 of Ref.^[28] was used in conjunction with the torsion angles of a X-ray analysis or the angles of idealized structures (all torsion angles multiples of 60°).

	${}^3J_{H1,H2}$	${}^3J_{H2,H3}$	${}^3J_{H3,H4}$	${}^3J_{H4,H5eq}$	${}^3J_{H4,H5ax}$	Conformation
Free (exp.) ^[77]	7.9	9.5	9.5	5.5	11.0	4C_1 (Ref. ^[77])
D- $\kappa O^{2,3}$	7.8	9.5	8.9	5.4	10.0	4C_1 (<i>trans-vic.</i>)
D- $\kappa O^{3,4}$	7.6	9.2	9.3	4.7	10.4	4C_1 (<i>trans-vic.</i>)
31- $\kappa O^{2,3}$	7.9	9.4	9.4	4.1	10.1	4C_1 (Karplus)
31- $\kappa O^{3,4}$	7.8	9.3	9.5	4.4	10.1	4C_1 (Karplus)
Idealized	8.1	9.8	9.6	4.3	10.1	4C_1 (Karplus)
D- $\kappa O^{2,4}$	<2	<2	<2	1.2	1.2	1C_4 (<i>syn-diaxial</i>)
Idealized	1.8	4.3	4.3	2.5	0.6	1C_4 (Karplus)

Despite the fact that all substituents are axial in methyl 1C_4 - β -D-xylopyranoside, sufficient stability was gained by palladium-binding to make the species detectable. The spectroscopic results on the major species were supported by X-ray analysis. From Pd-tmen batches, the two major monometalated isomers, $[\text{Pd}(\text{tmen})(\text{Me-}\beta\text{-D-Xylp}2,3H_2\text{-}\kappa O^{2,3})]$ and its $\kappa O^{3,4}$ -bonded analogue, co-crystallized. Almost undistorted 4C_1 chairs were found in agreement with the spectroscopic result (Fig. 2.48). The crystal structure was solved in the space group $P2_1$. The two xylopyranoside ligands built a hydrogen-bond-bridged dimer forming a homodromic $R_2^2(10)$ ring via the two remaining hydroxy functions. Therefore, the coordinating diolato sites were arranged opposite to each other. These dimeric building units were further linked via two water molecules.

2 Results

As Table 2.34 shows, the water molecule with O91 connected two dimeric units via their alkoxido O42 and O51 atoms, whereas the water with O92 formed a hydrogen bond both to O91 and to the alkoxido O21 of a third dimeric unit.

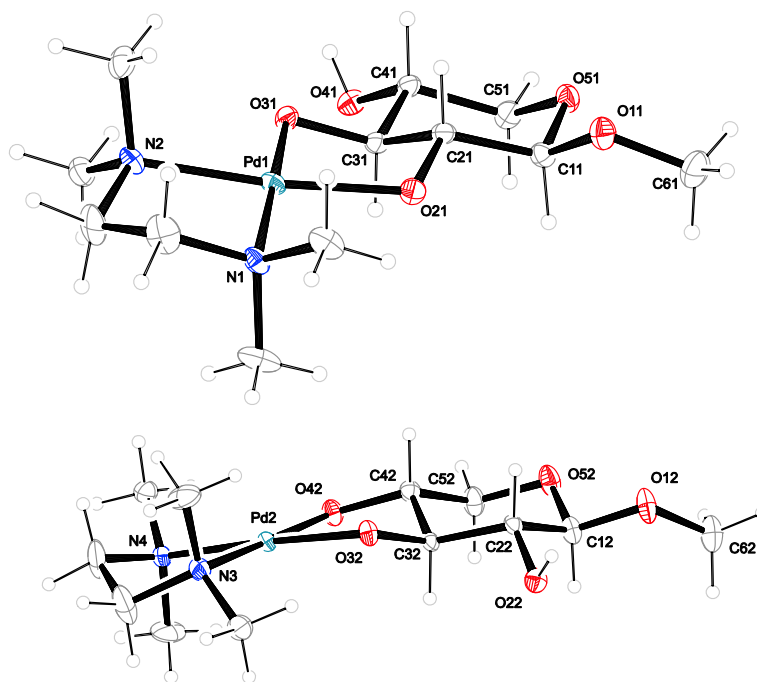


Figure 2.48. The asymmetric unit (water molecules omitted) of [Pd(tmen)(Me-β-D-Xylp_{2,3}H- κ O^{2,3})] [Pd(tmen)(Me-β-D-Xylp_{3,4}H- κ O^{3,4})] in crystals of the dihydrate (**31**). ORTEP plot is drawn with 50% probability ellipsoids. Interatomic distances (Å) and angles (°) (standard deviations of the last digit in parentheses): Pd1–O21 2.004(3), Pd1–O31 2.000(2), Pd1–N1 2.079(3), Pd1–N2 2.055(3), Pd2–O32 1.9945(19), Pd2–O42 2.001(3), Pd2–N3 2.064(3), Pd2–N4 2.067(3); O21–Pd1–O31 85.73(13), N1–Pd1–N2 86.01(17), O32–Pd2–O42 85.86(13), N3–Pd2–N4 85.75(17); chelate torsion angles: O21–C21–C31–O31 57.6(4), O32–C32–C42–O42 –55.4(4), N1–C91–C101–N2 –53.2(5), N3–C92–C102–N4 55.3(5); puckering parameters^[22] of the pyranose ring O51–C11–. . . : $Q = 0.576(4)$ Å, $\theta = 4.4(4)^\circ$; O52–C12–. . . : $Q = 0.564(4)$ Å, $\theta = 3.4(4)^\circ$.

Table 2.34. Distances [Å] and angles [°] of hydrogen bonds in **31**. Standard deviations of the last digit are given in parentheses; values without standard deviation are related to hydrogen atoms at calculated positions. D: donor, A: acceptor.

D	H	A	D–H	H···A	D···A	D–H···A
O41	H41	O32 ⁱ	0.84	1.83	2.661(4)	167.4
O22	H22	O31 ⁱⁱ	0.84	1.87	2.698(4)	171.3
O91	H911	O42	0.825(10)	1.922(13)	2.732(4)	167(4)
O91	H912	O51 ⁱⁱⁱ	0.816(10)	2.049(14)	2.852(3)	168(5)
O92	H921	O21 ^{iv}	0.827(10)	1.93(2)	2.704(4)	156(5)
O92	H922	O91	0.826(10)	2.056(13)	2.878(4)	173(5)

Symmetry code: (i) $x-1, y, z$; (ii) $x+1, y, z$; (iii) $-x, y-1/2, -z$; (iv) $-x, y-1/2, -z$; (v) $-x+1, y-1/2, -z$.

2.8 Metalation-induced conformational fluctuation of palladium(II)–aldopentose complexes

The pentoses not only show one defined configuration in aqueous solutions, instead, anomerization results in the equilibrium of the α - and β -forms of the pyranoses and furanoses. Moreover, contrary to the hexoses, the hydroxymethyl group of C5 is missing which anchors the conformation of the hexopyranoses. Therefore, in some cases the pentopyranoses show a dynamic behavior, particularly in the ${}^4C_1 \Leftrightarrow {}^1C_4$ chair inversion. Fluctuation between the two chair conformations is a common feature of the methyl pentosides as well as the pentoses. In Fig. 2.49, all possible forms of the pentoses are depicted; the bright forms are not detected in aqueous solutions.

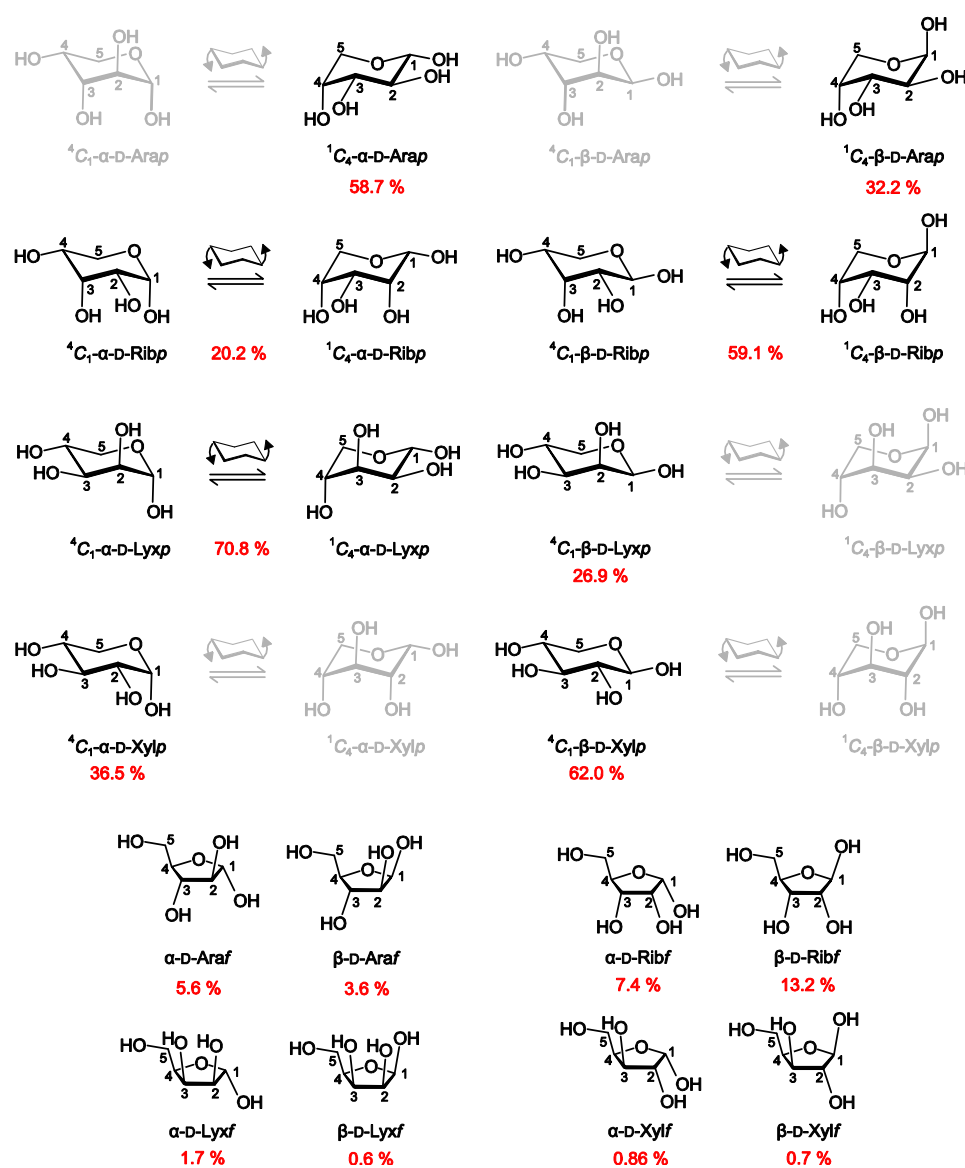


Figure 2.49. All possible configurations and conformations of the four aldopentoses D-arabinose (Ara), D-ribose (Rib), D-lyxose (Lyx) and D-xylose (Xyl). The bright conformers were not detected in aqueous solutions. The percentages of the various cyclic forms of D-[1- ^{13}C]pentoses were determined at 28 °C in D_2O .^[79]

2 Results

As known from previous work,^[37, 46, 78] the formation of five-membered chelate rings by the attack of a vicinal diol function is the predominant binding mode of palladium(II)–pyranose binding, but nevertheless the formation of six-membered chelate rings can be observed, too. Both *cis*- or *trans*-diolato binding is common, the latter requiring a diequatorial conformation. Various Pd^{II} solvents were applied for the investigation of the pentoses to obtain an extensive set of ¹³C NMR shifts and shift differences as well as ³J_{H,H} values representing the carbohydrates' various configurations and conformations.

2.8.1 D-Arabinose

In aqueous solutions, D-arabinose can be found essentially in the pentopyranose form. The D-arabinopyranose anomers are non-fluctuating in their free state but reside in the ¹C₄ conformation.^[5, 18] Fig. 2.50 shows the ¹³C NMR spectra of D-arabinose in Pd-tmen at different Pd/Ara ratios. A high amount of β-D-Araf1,2H₂-κO^{1,2} was noteworthy; enriching the κO^{1,2}-furanose form is a characteristic property of the Pd-tmen and Pd-teen solvents. In Fig. 2.51 the various detected solution species are depicted which were representative for the investigations of D-arabinose with the other Pd^{II} solvents as well. The species could be detected in the Pd^{II} solvents with almost unaltered ¹³C NMR shifts upon comparing the Tables 2.35 and 2.36 and other published data.^[37] On the other hand, the species distribution at different stoichiometries relied on the chosen Pd^{II} solvent as summarized in Table 2.37.

Focusing on the pyranose complex species, at first sight, the crystal structure of [Pd₂(tmen)₂(β-D-Arap1,2;3,4H₄-κO^{1,2}:κO^{3,4})] (Fig. 2.52) attracted attention by showing the ⁴C₁ instead of the initial ¹C₄ conformation. Double metalation obviously resulted in chair inversion of the pyranose ring. The crystal structure was solved in the space group *P* 2₁2₁2₁. The tmen ligands again tended to form hydrophobic areas whereas the carbohydrates were linked via the hydrogen-bonding network. Along the *a* axis an R₄²(8) ring motif^[60] formed by two water molecules (O91 and O92) connected the single carbohydrate molecules via O1 and O4 to a chain. Therefore, the equatorially standing O1 and O4 alkoxido functions accepted four hydrogen bonds and the axially standing O2 and O3 alkoxido functions accepted only one hydrogen bond each (see Table 2.38). Furthermore, two additional crystal structures of a double metalated ⁴C₁-β-D-Arap1,2;3,4H₄ species are known: [Pd₂(en)₂(β-Arap1,2;3,4H₄-κO^{1,2}:κO^{3,4})] in crystals of the heptahydrate^[38] and [Pd₂(*R,R*-chxn)₂(β-D-Arap1,2;3,4H₄-κO^{1,2}:κO^{3,4})] in crystals of the 10-hydrate^[78]. Finally, analysis of the ³J_{H,H} coupling constants confirmed the chair inversion of the solution species ⁴C₁-β-D-Arap1,2;3,4H₄-κO^{1,2}:κO^{3,4} (see Table 2.39).

2 Results

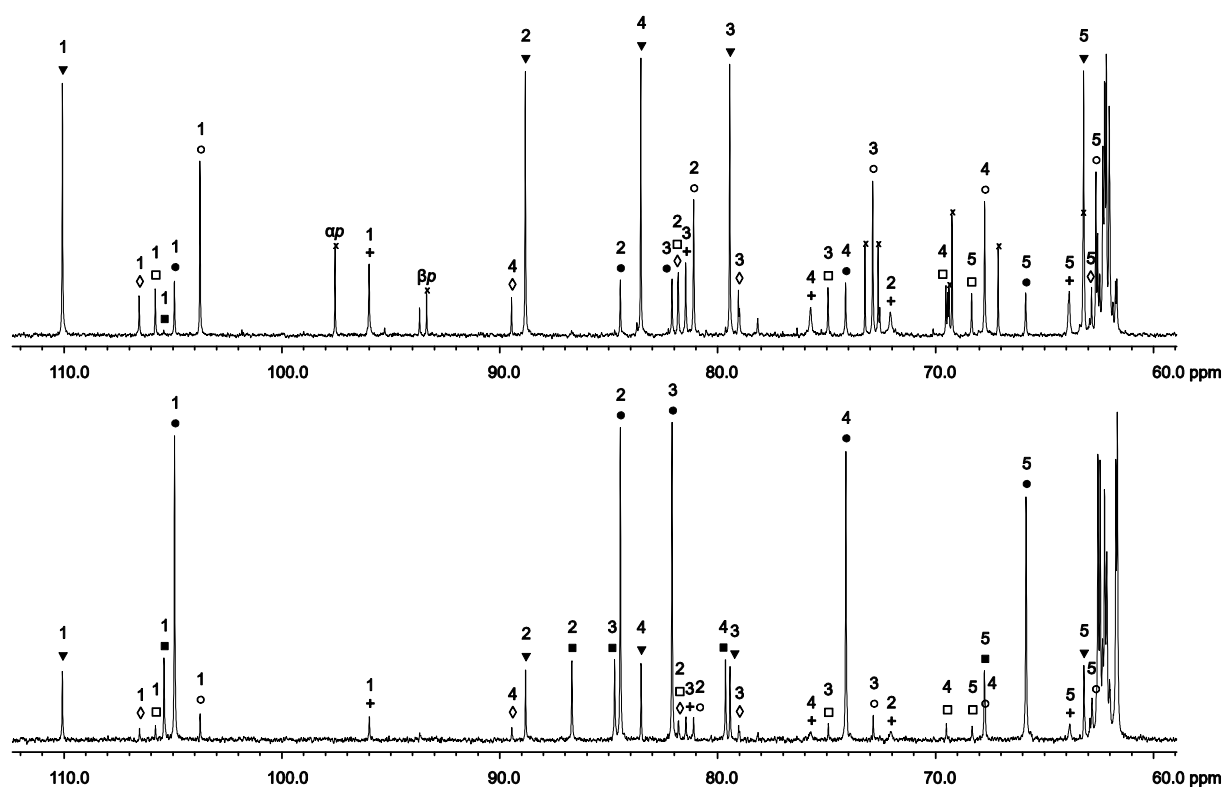


Figure 2.50. ^{13}C NMR spectra of D-arabinose in Pd-tmen at a molar Pd/Ara ratio of 1:1 (top) and 2:1 (bottom). The signals of free D-arabinose are marked with (x); (\square) α -D-Arap1,2H₂- $\kappa\text{O}^{1,2}$, (+) α -D-Arap3,4H₂- $\kappa\text{O}^{3,4}$, (\blacksquare) α -D-Arap1,2;3,4H₄- $\kappa\text{O}^{1,2}:\kappa\text{O}^{3,4}$, (\circ) β -D-Arap1,2H₂- $\kappa\text{O}^{1,2}$, (\bullet) β -D-Arap1,2;3,4H₄- $\kappa\text{O}^{1,2}:\kappa\text{O}^{3,4}$, (\diamond) α -D-Araf1,3H₂- $\kappa\text{O}^{1,3}$ and (\blacktriangledown) β -D-Araf1,2H₂- $\kappa\text{O}^{1,2}$.

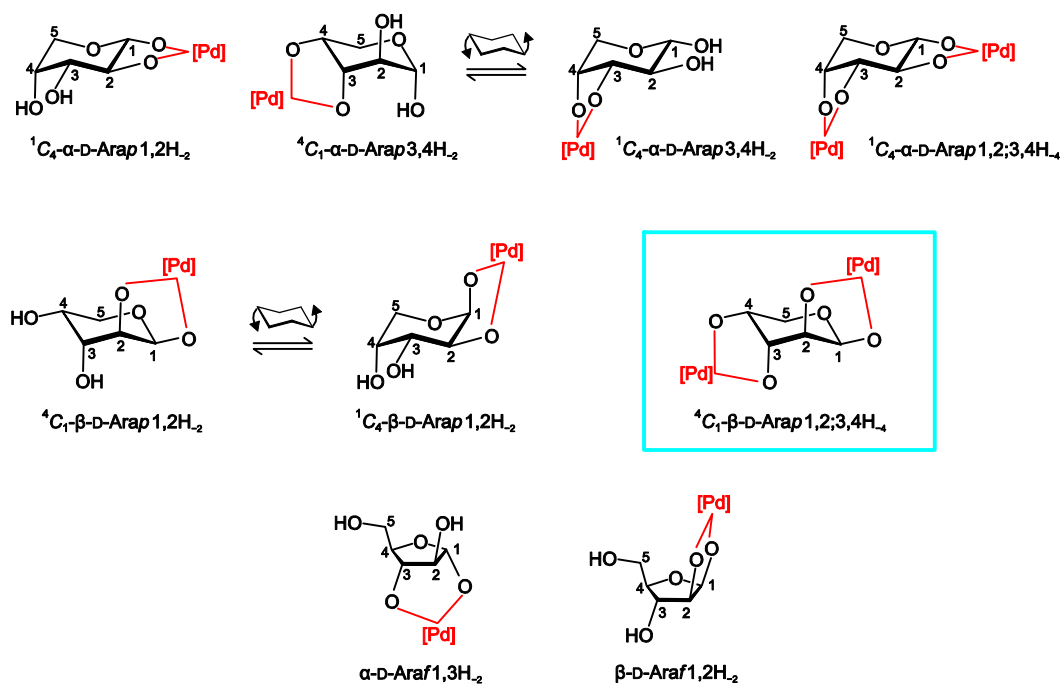


Figure 2.51. Species detected in Pd^{II}-containing solutions of D-arabinose at various molar ratios (for details of molar ratio and percental distribution of species, see Table 2.35). Blue-framed species were confirmed by X-ray analysis (see Fig. 2.52 and Ref.^[39, 78]).

2 Results

Table 2.35. ^{13}C NMR chemical shifts (δ/ppm) and shift differences ($\Delta\delta$) to the free pentose of D-arabinose ligands in Pd-tmen. Atoms are numbered as in Fig. 2.49.

		C1	C2	C3	C4	C5	Chelate
$\alpha\text{-D-Arap1,2H}_{-2}$	δ	105.6	81.6	74.8	69.4	68.2	
	$\Delta\delta$	8.2	9.1	1.7	0.3	1.2	$\kappa\text{O}^{1,2}$
$\beta\text{-D-Arap1,2H}_{-2}$	δ	103.6	80.9	72.7	67.6	62.5	
	$\Delta\delta$	10.4	11.7	3.5	-1.6	-0.6	$\kappa\text{O}^{1,2}$
$\alpha\text{-D-Arap3,4H}_{-2}$	δ	95.8	71.9	81.3	75.6	63.2	
	$\Delta\delta$	-1.6	-0.6	8.2	6.5	-3.8	$\kappa\text{O}^{3,4}$
$\alpha\text{-D-Arap1,2;3,4H}_{-4}$	δ	105.2	86.5	84.6	79.5	67.6	
	$\Delta\delta$	7.8	14.0	11.5	10.4	0.6	$\kappa\text{O}^{1,2};\kappa\text{O}^{3,4}$
$\beta\text{-D-Arap1,2;3,4H}_{-4}$	δ	104.8	84.3	81.9	74.0	65.7	
	$\Delta\delta$	11.6	15.1	12.7	4.8	2.6	$\kappa\text{O}^{1,2};\kappa\text{O}^{3,4}$
$\alpha\text{-D-Araf1,3H}_{-2}$	δ	106.4	81.6	78.9	89.3	62.1	
	$\Delta\delta$	4.7	-0.5	2.7	5.7	0.4	$\kappa\text{O}^{1,3}$
$\beta\text{-D-Araf1,2H}_{-2}$	δ	109.9	88.7	79.3	83.4	63.0	
	$\Delta\delta$	14.3	11.9	4.5	1.4	1.3	$\kappa\text{O}^{1,2}$

Table 2.36. ^{13}C NMR chemical shifts (δ/ppm) and shift differences ($\Delta\delta$) to the free pentose of D-arabinose ligands in Pd-teen. Atoms are numbered as in Fig. 2.49.

		C1	C2	C3	C4	C5	Chelate
$\alpha\text{-D-Arap1,2H}_{-2}$	δ	105.8	82.0	74.6	69.1	67.7	
	$\Delta\delta$	8.4	9.5	1.5	0.09	0.7	$\kappa\text{O}^{1,2}$
$\beta\text{-D-Arap1,2H}_{-2}$	δ	103.4	79.5	72.7	68.5	62.1	
	$\Delta\delta$	10.2	10.3	3.5	-0.7	-1.0	$\kappa\text{O}^{1,2}$
$\alpha\text{-D-Arap3,4H}_{-2}$	δ	95.1	69.9	81.0	73.9	62.4	
	$\Delta\delta$	-2.3	-2.6	7.9	4.8	-4.6	$\kappa\text{O}^{3,4}$
$\alpha\text{-D-Arap1,2;3,4H}_{-4}$	δ	105.6	86.4	85.0	79.6	66.9	
	$\Delta\delta$	8.2	13.9	11.9	10.5	-0.1	$\kappa\text{O}^{1,2};\kappa\text{O}^{3,4}$
$\beta\text{-D-Arap1,2;3,4H}_{-4}$	δ	105.2	84.1	81.7	74.3	65.7	
	$\Delta\delta$	12.0	14.9	12.5	5.1	2.6	$\kappa\text{O}^{1,2};\kappa\text{O}^{3,4}$
$\alpha\text{-D-Araf1,3H}_{-2}$	δ	106.0	81.9	78.7	88.4	64.1	
	$\Delta\delta$	4.3	-0.2	2.5	4.8	2.4	$\kappa\text{O}^{1,3}$
$\beta\text{-D-Araf1,2H}_{-2}$	δ	109.3	88.7	78.7	82.0	62.8	
	$\Delta\delta$	13.7	11.9	3.9	0.0	1.1	$\kappa\text{O}^{1,2}$

2 Results

Table 2.37. Percentage distribution of D-arabinose's metalated species in Pd-chxn, Pd-tmen and Pd-teen of various molar ratios. The values of the pure pentose are taken from Ref.^[79], the values of Pd-chxn from Ref.^[37].

	chelate	0:1	chxn		tmen		teen	
			1:1	3:1	1:1	2:1	1:1	2:1
α -D-Arap		58.7	-	-	9.0	-	10.0	3.0
α -D-Arap1,2H ₋₂	$\kappa O^{1,2}$	-	-	-	5.0	2.0	3.0	12.0
α -D-Arap3,4H ₋₂	$\kappa O^{3,4}$	-	-	-	11.0	4.0	14.0	15.0
α -D-Arap1,2;3,4H ₋₄	$\kappa O^{1,2}:\kappa O^{3,4}$	-	-	10.0	-	16.0	-	10.0
β -D-Arap		32.2	-	-	4.0	-	6.0	-
β -D-Arap1,2H ₋₂	$\kappa O^{1,2}$	-	20.0	-	22.0	5.0	24.0	20.0
β -D-Arap1,2;3,4H ₋₄	$\kappa O^{1,2}:\kappa O^{3,4}$	-	-	90.0	9.0	58.0	6.0	11.0
α -D-Araf		5.6	-	-	-	-	-	-
α -D-Araf1,3H ₋₂	$\kappa O^{1,3}$	-	16	-	5.0	2.0	2.0	3.0
β -D-Araf		3.5	-	-	-	-	-	-
β -D-Araf1,2H ₋₂	$\kappa O^{1,2}$	-	9	-	33.0	13.0	32.0	26.0

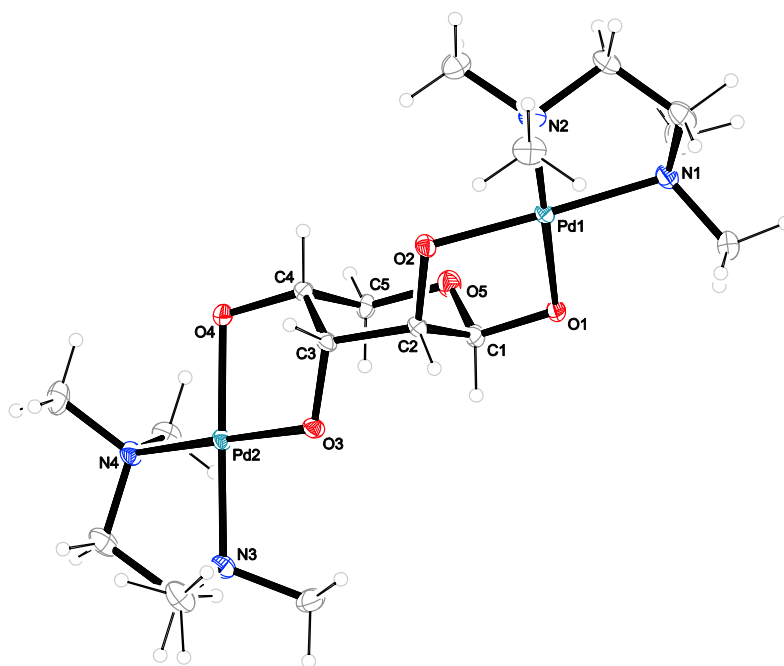


Figure 2.52: The molecular structure of $[\text{Pd}_2(\text{tmen})_2(\beta\text{-D-Arap1,2;3,4H}_{-4}\text{-}\kappa O^{1,2}:\kappa O^{3,4})]$ in crystals of the 10-hydrate (**32**). ORTEP plot is drawn with 50% probability ellipsoids. Interatomic distances (Å) and angles (°) (standard deviations of the last digit in parentheses): Pd1–O1 2.015(2), Pd1–O2 1.979(3), Pd1–N1 2.059(3), Pd1–N2 2.060(3), Pd2–O3 1.985(2), Pd2–O4 2.010(2), Pd2–N3 2.044(3), Pd2–N4 2.049(2), O1–Pd1–O2 85.47(10), N1–Pd1–N2 85.81(13), O3–Pd2–O4 85.79(10), N3–Pd2–N4 86.29(12); chelate torsion angles: O1–C1–C2–O2 51.2(4), O3–C3–C4–O4 50.7(3), N1–C8–C9–N2 53.9(4), N3–C14–C15–N4 54.2(4); puckering parameters^[22] of the pyranose ring O5–C1–C2–C3–C4–C5: $Q = 0.563(4)$ Å, $\theta = 6.1(4)^\circ$.

2 Results

Table 2.38. Distances [Å] and angles [°] of hydrogen bonds in **32**. Standard deviations of the last digit are given in parentheses; values without standard deviation are related to hydrogen atoms at calculated positions. D: donor, A: acceptor.

D	H	A	D–H	H···A	D···A	D–H···A
O91	H911	O4 ⁱ	0.856(14)	1.91(2)	2.728(4)	159(4)
O91	H912	O1 ⁱⁱ	0.853(14)	1.97(2)	2.797(4)	162(5)
O92	H921	O4	0.852(14)	1.890(18)	2.726(4)	166(5)
O92	H922	O1 ⁱⁱⁱ	0.856(14)	1.94(2)	2.756(4)	160(4)
O93	H931	O94 ⁱⁱⁱ	0.860(14)	1.975(17)	2.821(4)	167(4)
O93	H932	O92	0.853(14)	1.955(15)	2.807(4)	178(5)
O94	H941	O3	0.858(14)	1.800(15)	2.652(4)	172(4)
O94	H942	O97	0.865(14)	1.951(15)	2.816(4)	178(5)
O95	H951	O96	0.861(14)	1.994(19)	2.831(4)	164(4)
O95	H952	O2	0.859(14)	1.854(16)	2.701(4)	168(4)
O96	H961	O92	0.857(14)	1.928(15)	2.783(4)	175(4)
O96	H962	O98	0.859(14)	1.961(17)	2.812(4)	171(5)
O97	H971	O95	0.863(14)	1.91(2)	2.723(5)	157(4)
O97	H972	O93 ^{iv}	0.864(14)	1.96(2)	2.758(4)	154(4)
O98	H981	O97 ⁱⁱⁱ	0.861(14)	2.079(17)	2.931(4)	170(4)
O98	H982	O94 ^{iv}	0.853(14)	1.972(16)	2.819(4)	172(4)
O99	H991	O91	0.860(14)	1.856(18)	2.707(6)	170(5)
O99	H992	O910 ^v	0.896(14)	1.92(3)	2.683(8)	142(4)
O910	H913	O5 ⁱ	0.876(14)	2.017(19)	2.862(6)	162(4)
O910	H914	O99 ^{vi}	0.868(14)	1.840(17)	2.704(9)	173(4)

Symmetry code: (i) $x, y+1, z$; (ii) $x-1, y+1, z$; (iii) $x-1, y, z$; (iv) $-x+1, y+1/2, -z+1/2$; (v) $x-1/2, -y+3/2, -z$; (vi) $x+1, y, z$.

With the metalation of the α -D-arabinopyranose's $\kappa O^{1,2}$ -diolato function, the α -D-Arap1,2H₂- $\kappa O^{1,2}$ and the α -D-Arap1,2;3,4H₄- $\kappa O^{1,2};\kappa O^{3,4}$ forms were fixed in the ¹C₄ conformation by the complexation of the diequatorial *trans*-diolato function, whereas the corresponding β -anomer was flexible in conformation. With Pd-chxn, and caused by an incomplete set of coupling constants, the β -D-Arap1,2H₂- $\kappa O^{1,2}$ was postulated to occur exclusively in the ⁴C₁ conformation,^[37] assuming the Pd-chxn fragment would prevent fluctuation of the pyranose ring. Therefore, the ring inversion was interpreted as a consequence of metalation. Now, experiments with Pd-tmen have led to a complete set of coupling constants (Table 2.39) which indicated a fluctuation between the ¹C₄ and ⁴C₁ conformer of β -D-Arap1,2H₂- $\kappa O^{1,2}$, it being the first example of a metalation-induced conformational fluctuation of a pentopyranose. To interpret these results, ³J_{H,H} coupling constants were calculated with the

2 Results

Karplus equation. Comparing the experimentally determined ${}^3J_{\text{H,H}}$ coupling constants of free α - and β -D-arabinopyranose with those calculated by the Karplus equation, in both cases the results obviously confirmed the 1C_4 conformation. Further, the ${}^3J_{\text{H,H}}$ coupling constants of the conformationally fixed forms ${}^1C_4\text{-}\alpha\text{-D-Arap1,2H-}_2\text{-}\kappa\text{O}^{1,2}$ and ${}^1C_4\text{-}\alpha\text{-D-Arap1,2;3,4H-}_4\text{-}\kappa\text{O}^{1,2}:\kappa\text{O}^{3,4}$ and, moreover, the ${}^3J_{\text{H,H}}$ coupling constants of ${}^4C_1\text{-}\beta\text{-D-Arap1,2;3,4H-}_4\text{-}\kappa\text{O}^{1,2}:\kappa\text{O}^{3,4}$ showed good agreement with the calculated coupling constants obtained with the Karplus equation. In contrast, the experimentally determined ${}^3J_{\text{H,H}}$ coupling constants of β -D-Arap1,2H- ${}^2\text{-}\kappa\text{O}^{1,2}$ disagreed with the ${}^3J_{\text{H,H}}$ coupling constants for the various conformations calculated with the Karplus equation. To fit the experimental data, it was necessary to assume a 1:1 conformational equilibrium between the 4C_1 and the 1C_4 conformation. A similar example with comparable ${}^3J_{\text{H,H}}$ coupling constants is known in the literature for 1,2-*O*-alkylidene- β -L-arabinopyranoses.^[80]

Table 2.39. Experimental and calculated ${}^3J_{\text{H,H}}$ values in Hz for the free glucoses and various metalated species of D-arabinopyranose. Bold: calculated or measured (formation of a *trans*-vicinal chelate) constants which unambiguously represent the specified conformer. For the calculation of constants, the Karplus relationship in eq. 8 of Ref. ^[28] was used in conjunction with the torsion angles of the X-ray analyses or the angles of idealized structures (all torsions angles multiples of 60°). To complete the set of coupling constants as thoroughly as possible, the values of compounds with Pd-en and Pd-chxn were used from former work.

	${}^3J_{\text{H1,H2}}$	${}^3J_{\text{H2,H3}}$	${}^3J_{\text{H3,H4}}$	${}^3J_{\text{H4,H5eq}}$	${}^3J_{\text{H4,H5ax}}$	Conformation
free α -D (exp.) ^[77]	7.8	9.8	3.6	1.8	1.3	1C_4 (Ref. ^[5])
α -D (idealised)	3.2	4.3	3.5	4.3	10.1	4C_1 (Karplus)
α -D (idealised)	8.1	9.6	3.2	2.5	0.6	1C_4 (Karplus)
free β -D (exp.) ^[77]	3.6	9.3	3.4	2.5	1.7	1C_4 (Ref. ^[5])
β -D (idealised)	1.3	4.3	3.5	4.3	10.1	4C_1 (Karplus)
β -D (idealised)	3.1	9.6	3.2	2.5	0.6	1C_4 (Karplus)
α -D- $\kappa\text{O}^{1,2}$ (in Pd-tmen)	7.5	10.0	3.2	n.d.	n.d.	1C_4 (trans-vic.)
α -D- $\kappa\text{O}^{3,4}$ (in Pd-tmen)	4.8	5.9	n.d.	n.d.	n.d.	${}^4C_1 \Leftrightarrow {}^1C_4$
β -D- $\kappa\text{O}^{1,2}$ (in Pd-chxn) ^[78]	2.7	5.5	n.d.	n.d.	n.d.	${}^4C_1 \Leftrightarrow {}^1C_4$
β -D- $\kappa\text{O}^{1,2}$ (in Pd-tmen)	2.8	6.4	3.3	3.3	6.7	${}^4C_1 \Leftrightarrow {}^1C_4$
α -D- $\kappa\text{O}^{1,2}:\kappa\text{O}^{3,4}$ (in Pd-chxn) ^[78]	7.6	9.1	4.1	3.4	3.4	1C_4 (trans-vic.)
β -D- $\kappa\text{O}^{1,2}:\kappa\text{O}^{3,4}$ (in Pd-chxn) ^[78]	1.6	3.2	4.5	5.3	10.2	4C_1
β -D- $\kappa\text{O}^{1,2}:\kappa\text{O}^{3,4}$ (in Pd-tmen)	1.9	3.0	3.7	5.4	10.1	4C_1
β -D- $\kappa\text{O}^{1,2}:\kappa\text{O}^{3,4}$ (Pd-en, Ref. ^[39])	2.2	2.0	4.0	4.5	10.1	4C_1 (X-Ray)
β -D- $\kappa\text{O}^{1,2}:\kappa\text{O}^{3,4}$ (Pd-chxn, Ref. ^[78])	2.0	2.4	3.6	3.9	10.1	4C_1 (X-Ray)
β -D- $\kappa\text{O}^{1,2}:\kappa\text{O}^{3,4}$ (32)	1.9	2.8	3.5	4.3	10.1	4C_1 (X-Ray)

2 Results

Searching for additional compounds capable of conformational fluctuation, α -D-Arap3,4H₂- κ O^{3,4} possibly provides a second example for metalation-induced conformational fluctuation. Although the found ³J_{H,H} coupling constants do not allow a final determination of the conformation, the data do not support an exclusive presence of the ⁴C₁ conformation.

2.8.2 D-Ribose

Comparing the four pentoses, aqueous solutions of D-ribose show the highest amount of furanose forms. Furthermore, both D-ribopyranoses fluctuate in conformation. Fig. 2.53 shows the ¹³C NMR spectra of D-ribose in Pd-tmen at different Pd/Rib ratios. Apart from the three detected minor D-ribofuranose species, the reaction of D-ribose with Pd-tmen at a molar ratio of 1:1 gave α -D-Ribp1,2H₂- κ O^{1,2} as the major species, underlining the predominance of diolate chelators derived from a *cis*-vicinal diol function. Unexpectedly, at a molar Pd:Rib ratio of 2:1 α -D-Ribp1,2H₂- κ O^{1,2} stayed the main species accompanied by only minor amounts of the double metalated β -D-Ribp1,2;3,4H₄- κ O^{1,2}: κ O^{3,4} form, indicating a high stability of the α -D-Ribp1,2H₂- κ O^{1,2} species.

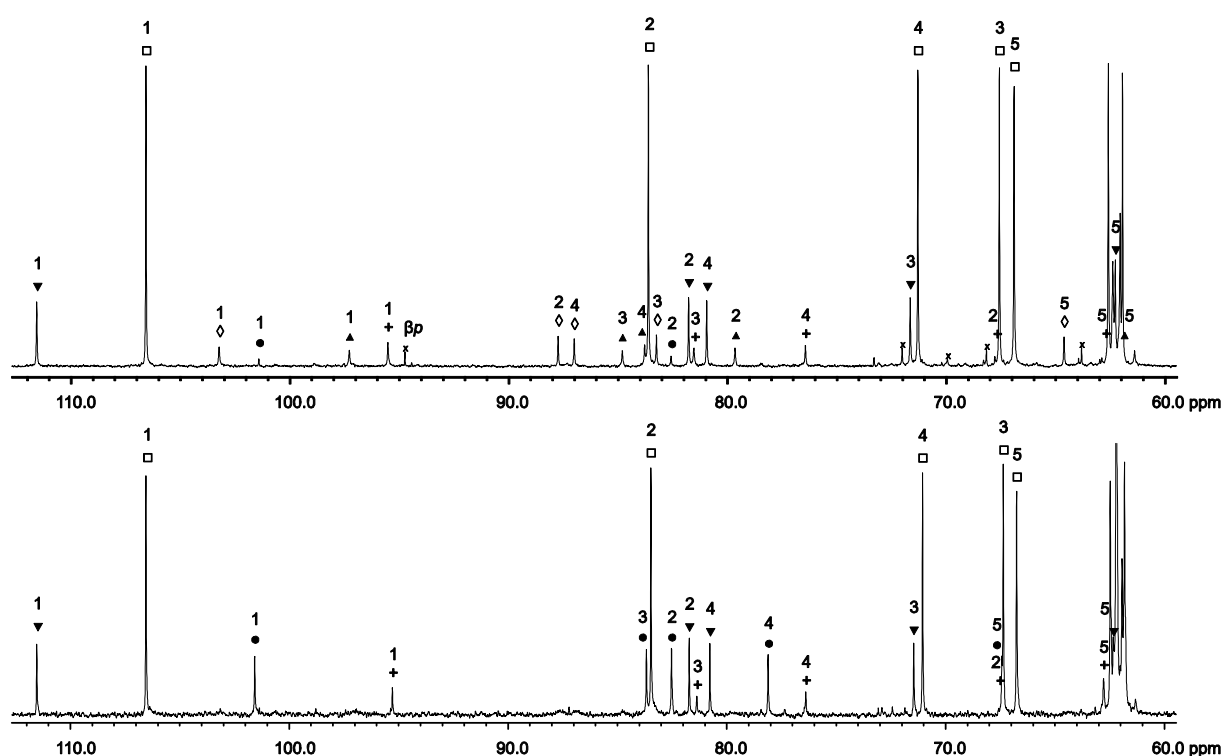


Figure 2.53. ¹³C NMR spectra of D-ribose in Pd-tmen at a molar Pd/Rib ratio of 1:1 (top) and 2:1 (bottom). The signals of free D-ribose are marked with (x); (□) α -D-Ribp1,2H₂- κ O^{1,2}, (+) α -D-Ribp3,4H₂- κ O^{3,4}, (●) β -D-Ribp1,2;3,4H₄- κ O^{1,2}: κ O^{3,4}, (▼) α -D-Ribf1,2H₂- κ O^{1,2}, (▲) α -D-Ribf2,3H₂- κ O^{2,3} and (◇) β -D-Ribf2,3H₂- κ O^{2,3}.

2 Results

All the above-mentioned species were depicted in Fig. 2.54, the species' distribution in various solvents and at different stoichiometries was summarized in Table 2.40.

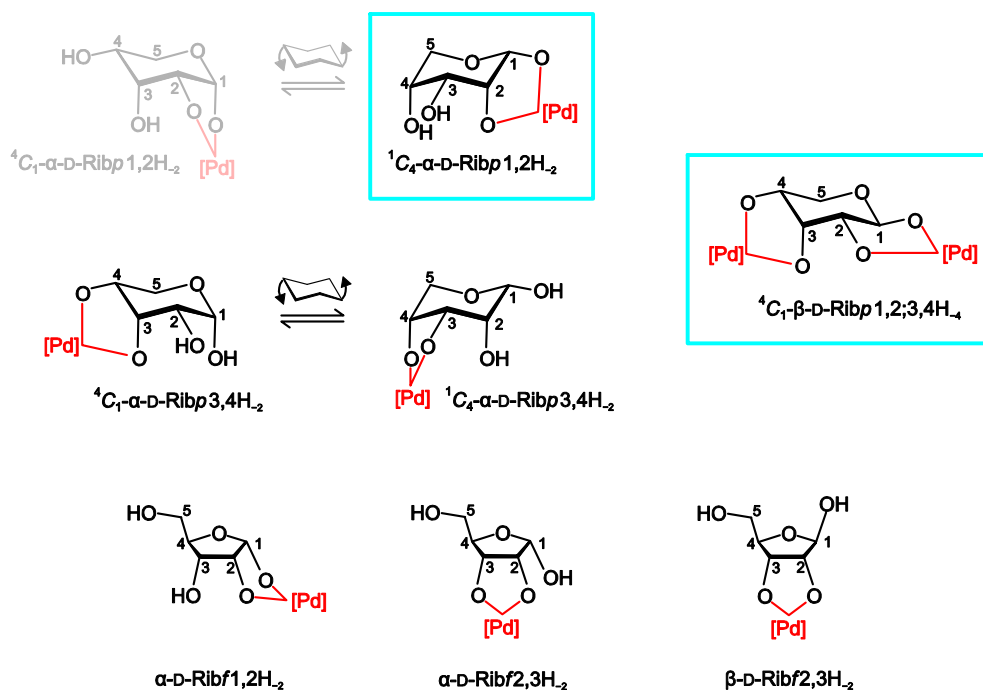


Figure 2.54. Species detected in Pd^{II}-containing solutions of D-ribose at various molar ratios (for details of molar ratio and percental distribution of species, see Table 2.40). Blue-framed species were confirmed by X-ray analysis.^[37, 39]

Table 2.40. Percentage distribution of D-ribose's metalated species in Pd-chxn, Pd-tmen and Pd-teen of various molar ratios. The values of the pure pentose are taken from Ref.^[79], the values of Pd-chxn from Ref.^[37].

chelate		chxn			tmen		teen	
		0:1	1:1	3:1	1:1	2:1	1:1	2:1
α -D-Ribp		20.2	-	-	-	-	-	-
α -D-Ribp1,2H ₋₂	$\kappa O^{1,2}$	-	36.0	15.0	60.0	59.0	49.0	56.0
α -D-Ribp3,4H ₋₂	$\kappa O^{3,4}$	-	-	-	8.0	6.0	6.0	6.0
β -D-Ribp		59.1	-	-	2.0	-	2.0	-
β -D-Ribp1,2;3,4H ₋₄	$\kappa O^{1,2};\kappa O^{3,4}$	-	5.0	70.0	1.0	17.0	-	9.0
α -D-Ribf		7.5	-	-	-	-	-	-
α -D-Ribf1,2H ₋₂	$\kappa O^{1,2}$	-	9.0	5.0	16.0	18.0	20.0	29.0
α -D-Ribf2,3H ₋₂	$\kappa O^{2,3}$	-	-	-	6.0	-	10.0	-
β -D-Ribf		13.2	-	-	-	-	-	-
β -D-Ribf2,3H ₋₂	$\kappa O^{2,3}$	-	-	-	7.0	-	8.0	-

2 Results

In the Tables 2.41 and 2.42 the ^{13}C NMR chemical shifts and shift differences of the detected species with Pd-tmen and Pd-teen are listed; comparing the results revealed only minor differences which confirmed the comparability of the Pd^{II} solvents. Therefore, it should be noted that instead of the double metalated $\alpha\text{-D-Ribp}1,2,3,4\text{H}_{-4}\text{-}\kappa\text{O}^{1,2}:\kappa\text{O}^{3,4}$ species in Ref. [39], the monometalated $\alpha\text{-D-Ribp}1,2\text{H}_{-2}\text{-}\kappa\text{O}^{1,2}$ form was detected, as the authors already suggested.

Table 2.41. ^{13}C NMR chemical shifts (δ/ppm) and shift differences ($\Delta\delta$) to the free pentose of D-ribose ligands in Pd-tmen. Atoms are numbered as in Fig. 2.49.

		C1	C2	C3	C4	C5	Chelate
$\alpha\text{-D-Ribp}1,2\text{H}_{-2}$	δ	106.2	83.3	67.2	71.0	66.6	
	$\Delta\delta$	12.1	12.7	-2.6	3.0	3.0	$\kappa\text{O}^{1,2}$
$\alpha\text{-D-Ribp}3,4\text{H}_{-2}$	δ	95.2	67.4	81.2	76.1	62.2	
	$\Delta\delta$	1.1	-3.2	11.4	8.1	-1.4	$\kappa\text{O}^{3,4}$
$\beta\text{-D-Ribp}1,2,3,4\text{H}_{-4}$	δ	101.3	82.2	83.4	77.8	67.1	
	$\Delta\delta$	6.9	10.6	13.8	10.0	3.5	$\kappa\text{O}^{1,2}:\kappa\text{O}^{3,4}$
$\alpha\text{-D-Ribf}1,2\text{H}_{-2}$	δ	111.2	81.4	71.3	80.6	62.0	
	$\Delta\delta$	14.3	9.9	0.7	-3.0	0.1	$\kappa\text{O}^{1,2}$
$\alpha\text{-D-Ribf}2,3\text{H}_{-2}$	δ	96.9	79.3	84.5	83.4	61.6	
	$\Delta\delta$	0.0	7.8	13.9	-0.2	-0.3	$\kappa\text{O}^{2,3}$
$\beta\text{-D-Ribf}2,3\text{H}_{-2}$	δ	102.9	87.4	82.9	86.7	64.3	
	$\Delta\delta$	1.4	11.6	11.9	3.6	1.2	$\kappa\text{O}^{2,3}$

Table 2.42. ^{13}C NMR chemical shifts (δ/ppm) and shift differences ($\Delta\delta$) to the free pentose of D-ribose ligands in Pd-teen. Atoms are numbered as in Fig. 2.49.

		C1	C2	C3	C4	C5	Chelate
$\alpha\text{-D-Ribp}1,2\text{H}_{-2}$	δ	106.7	83.6	67.6	71.0	66.4	
	$\Delta\delta$	12.6	13.0	-2.2	3.0	2.8	$\kappa\text{O}^{1,2}$
$\alpha\text{-D-Ribp}3,4\text{H}_{-2}$	δ	95.2	66.6	81.9	76.5	61.0	
	$\Delta\delta$	1.1	-4.0	12.1	8.5	-2.6	$\kappa\text{O}^{3,4}$
$\beta\text{-D-Ribp}1,2,3,4\text{H}_{-4}$	δ	102.0	83.0	84.2	78.6	67.2	
	$\Delta\delta$	7.6	11.4	14.6	10.8	3.6	$\kappa\text{O}^{1,2}:\kappa\text{O}^{3,4}$
$\alpha\text{-D-Ribf}1,2\text{H}_{-2}$	δ	112.3	81.2	71.8	80.8	62.2	
	$\Delta\delta$	15.4	9.7	1.2	-2.8	0.3	$\kappa\text{O}^{1,2}$
$\alpha\text{-D-Ribf}2,3\text{H}_{-2}$	δ	96.8	79.4	84.2	83.8	62.3	
	$\Delta\delta$	-0.1	7.9	13.6	0.2	0.4	$\kappa\text{O}^{2,3}$
$\beta\text{-D-Ribf}2,3\text{H}_{-2}$	δ	103.5	87.4	83.3	87.1	64.3	
	$\Delta\delta$	2.0	11.6	12.3	4.0	1.2	$\kappa\text{O}^{2,3}$

2 Results

Comparing the ${}^3J_{\text{H,H}}$ coupling constants listed in Table 2.43, $\alpha\text{-D-Ribp1,2H}_{-2}\text{-}\kappa\text{O}^{1,2}$ had to be frozen in the 1C_4 conformation. Accordingly, structure analysis on crystals of $[\text{Pd}(\text{R,R-chxn})(\alpha\text{-D-Ribp1,2H}_{-2}\text{-}\kappa\text{O}^{1,2})]^{[37]}$ revealed a hydrogen bond $\text{O4-H4}\cdots\text{O2}$ stabilizing this conformation. This hydrogen bond possibly inhibited the double metalation of $\alpha\text{-D-ribopyranose}$, too, since only $\beta\text{-D-Ribp1,2;3,4H}_{-4}\text{-}\kappa\text{O}^{1,2}:\kappa\text{O}^{3,4}$ for higher ratios of Pd^{II} -containing solutions was detected. ${}^1\text{H NMR}$ analysis (Table 2.43) and X-ray analysis on crystals of $[\text{Pd}(\text{en})(\beta\text{-D-Ribp1,2;3,4H}_{-4}\text{-}\kappa\text{O}^{1,2}:\kappa\text{O}^{3,4})]^{[39]}$ both confirmed the 4C_1 conformation, which was obviously forced by *trans*-vicinal coordination of the $\kappa\text{O}^{1,2}$ -diolato unit. For $\alpha\text{-D-Ribp3,4H}_{-2}\text{-}\kappa\text{O}^{3,4}$ the final determination of conformation was unsuccessful because of missing coupling constants, but the similarity with the ${}^3J_{\text{H,H}}$ coupling constants of free $\alpha\text{-D-ribopyranose}$ indicated a conformational fluctuation.

Table 2.43. Experimental and calculated ${}^3J_{\text{H,H}}$ values in Hz for the free glycoses and various metalated species of D-ribopyranose. Bold: calculated or measured (formation of a *trans*-vicinal chelate) constants which unambiguously represent the specified conformer. For the calculation of constants, the Karplus relationship in equation 8 of Ref.^[28] was used in conjunction with the torsion angles of the X-ray analyses or the angles of idealized structures (all torsions angles multiples of 60°). To complete the set of coupling constants as thoroughly as possible, the values of compounds with Pd-en and Pd-chxn were used from former work.

	${}^3J_{\text{H1,H2}}$	${}^3J_{\text{H2,H3}}$	${}^3J_{\text{H3,H4}}$	${}^3J_{\text{H4,H5eq}}$	${}^3J_{\text{H4,H5ax}}$	Conformation
free $\alpha\text{-D}$ (exp.) ^[77]	2.1	3.0	3.0	2.6	5.3	${}^4C_1 \Leftrightarrow {}^1C_4$ (Ref. ^[5])
$\alpha\text{-D}$ (idealised)	3.1	3.5	3.5	4.3	10.1	4C_1 (Karplus)
$\alpha\text{-D}$ (idealised)	1.3	3.5	3.2	2.5	0.6	1C_4 (Karplus)
free $\beta\text{-D}$ (exp.) ^[77]	6.5	3.3	3.2	4.4	8.8	${}^4C_1 \Leftrightarrow {}^1C_4$ (Ref. ^[5])
$\beta\text{-D}$ (idealised)	8.1	3.5	3.5	4.3	10.1	4C_1 (Karplus)
$\beta\text{-D}$ (idealised)	3.2	3.5	3.2	2.5	0.6	1C_4 (Karplus)
$\alpha\text{-D-}\kappa\text{O}^{1,2}$ (in Pd-chxn)	1.3	2.4	n.d.	2.6	0.7	1C_4
$\alpha\text{-D-}\kappa\text{O}^{1,2}$ (Pd-chxn, Ref. ^[37])	1.8–2.1	2.5–2.7	2.3–2.5	2.3–2.8	0.6–0.9	1C_4 (X-Ray)
$\alpha\text{-D-}\kappa\text{O}^{1,2}$ (in Pd-tmen)	1.4	4.6	2.8	2.7	0.8	1C_4
$\alpha\text{-D-}\kappa\text{O}^{1,2}$ (in Pd-teen)	1.3	2.8	2.8	2.9	0.7	1C_4
$\alpha\text{-D-}\kappa\text{O}^{3,4}$ (in Pd-teen)	2.2	2.8	n.d.	n.d.	n.d.	${}^4C_1 \Leftrightarrow {}^1C_4$
$\beta\text{-D-}\kappa\text{O}^{1,2}:\kappa\text{O}^{3,4}$ (in Pd-chxn)	7.9	2.9	3.1	5.6	10.8	4C_1 (<i>trans</i> -vic.)
$\beta\text{-D-}\kappa\text{O}^{1,2}:\kappa\text{O}^{3,4}$ (in Pd-tmen)	8.3	2.8	2.8	n.d.	10.8	4C_1 (<i>trans</i> -vic.)
$\beta\text{-D-}\kappa\text{O}^{1,2}:\kappa\text{O}^{3,4}$ (Pd-en, Ref. ^[39])	7.9–8.3	2.7–2.9	3.6–3.8	2.4–3.3	9.9–10.1	4C_1 (X-Ray)

2.8.3 D-Lyxose

Aqueous solutions of D-lyxose contain only small amounts of α - and β -D-lyxofuranose. The major α -D-lyxopyranose fluctuates between the 4C_1 and the 1C_4 conformation while the minor β -D-lyxopyranose exists only in the 4C_1 conformation. Fig. 2.55 shows the ${}^{13}C$ NMR spectra of D-lyxose in Pd-tmen at different Pd/Lyx ratios. The upper ${}^{13}C$ NMR spectrum was dominated by the α -D-Lyxp2,3H₂- $\kappa O^{2,3}$ and the β -D-Lyxp1,2H₂- $\kappa O^{1,2}$ species, whereas the double metalated 4C_1 - β -D-Lyxp1,2;3,4H₄- $\kappa O^{1,2}:\kappa O^{3,4}$ species dominated the lower ${}^{13}C$ NMR spectrum at a Pd/Lyx ratio of 2:1.

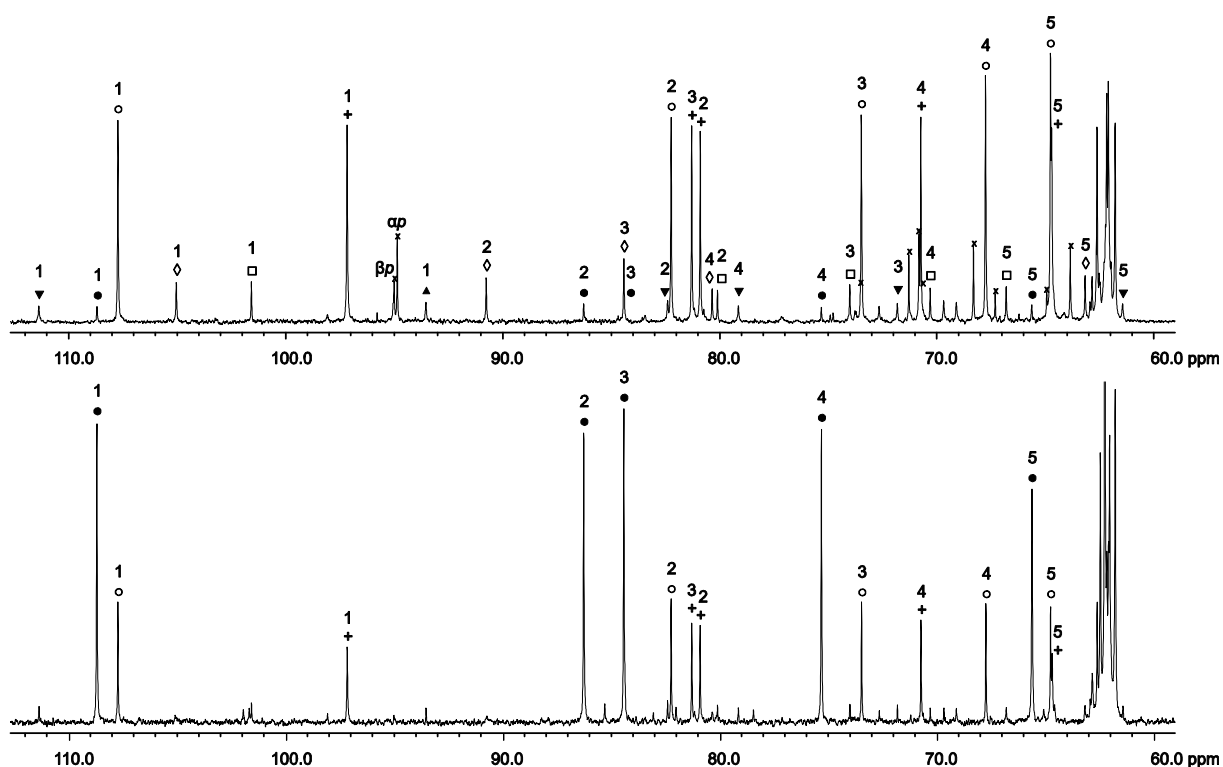


Figure 2.55. ${}^{13}C$ NMR spectra of D-lyxose in Pd-tmen at a molar Pd/Lyx ratio of 1:1 (top) and 2:1 (bottom). The signals of free D-lyxose are marked with (x); (\square) α -D-Lyxp1,2H₂- $\kappa O^{1,2}$, (+) α -D-Lyxp2,3H₂- $\kappa O^{2,3}$, (\circ) β -D-Lyxp1,2H₂- $\kappa O^{1,2}$, (\bullet) β -D-Lyxp1,2;3,4H₄- $\kappa O^{1,2}:\kappa O^{3,4}$, (\diamond) α -D-Lyxf2,3H₂- $\kappa O^{2,3}$, (\blacktriangledown) β -D-Lyxf1,2H₂- $\kappa O^{1,2}$ and (\blacktriangle) β -D-Lyxf1,3H₂- $\kappa O^{1,3}$.

An overview of the solution species detected for the different Pd^{II}-containing solvents is depicted in Fig. 2.56. The preferred *cis*-vicinal chelation was realized both for the α -D-Lyxp2,3H₂- $\kappa O^{2,3}$ and the β -D-Lyxp1,2H₂- $\kappa O^{1,2}$. According to the ${}^3J_{H,H}$ coupling constants in Table 2.49, α -D-Lyxp2,3H₂- $\kappa O^{2,3}$ fluctuated between the 4C_1 and the 1C_4 conformation maintaining the conformational state of the free lyxopyranose. On the other hand, analysis of the ${}^3J_{H,H}$ coupling constants confirmed that β -D-Lyxp1,2H₂- $\kappa O^{1,2}$ only existed in the 4C_1 conformation.

2 Results

Furthermore, both α -D-Lyxp1,2H₂- $\kappa O^{1,2}$ by *trans*-vicinal coordination and β -D-Lyxp1,3H₂- $\kappa O^{1,3}$ by *syn*-diaxial $\kappa O^{1,3}$ -bonding were fixed in the ¹C₄ conformation.

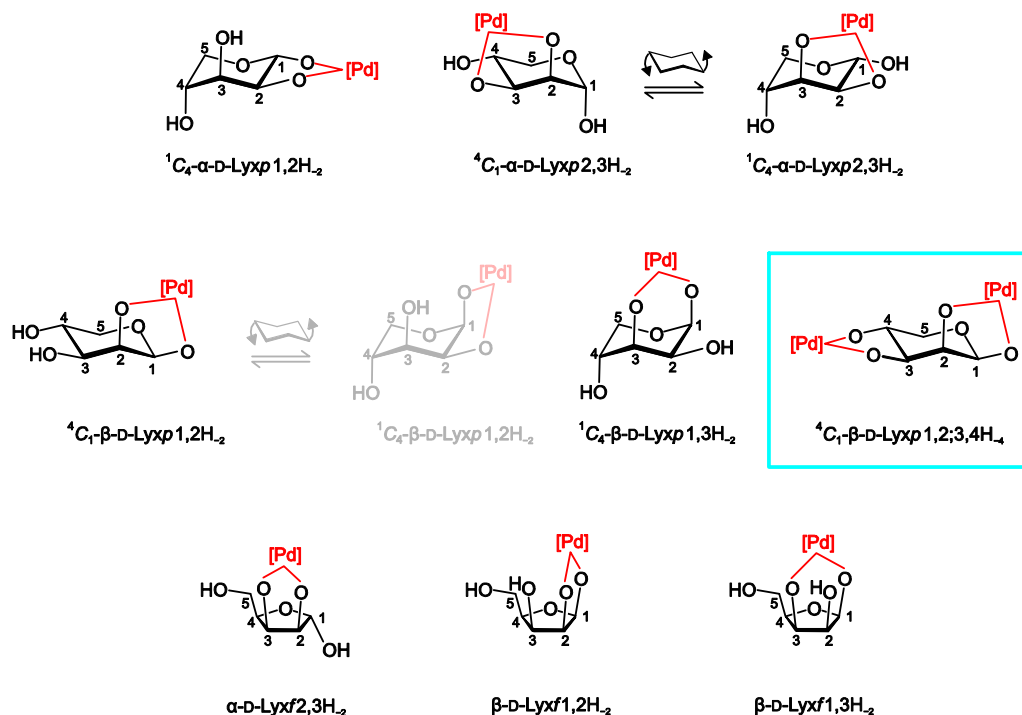


Fig. 2.56. Species detected in Pd^{II}-containing solutions of D-lyxose at various molar ratios (for details of molar ratio and percental distribution of species, see Table 2.44). Blue-framed species were confirmed by X-ray analysis (see Fig. 2.57 and Ref.^[38]).

Table 2.44. Percentage distribution of D-lyxose's metalated species in Pd-chxn, Pd-tmen and Pd-teen of various molar ratios. The values of the pure pentose are taken from Ref.^[79], the values of Pd-chxn from Ref.^[37].

	chelate	en		chxn		tmen		teen		
		0:1	1:1	2:1	1:1	2:1	1:1	2:1	1:1	2:1
α -D-Lyxp		70.8	17.0	-	10.0	-	8.0	-	10.0	4.0
α -D-Lyxp1,2H ₂	$\kappa O^{1,2}$	-	2.0	-	2.0	-	5.0	-	4.0	3.0
α -D-Lyxp2,3H ₂	$\kappa O^{2,3}$	-	29.0	12.0	36.0	35.0	31.0	18.0	31.0	29.0
β -D-Lyxp		26.9	8.0	-	5.0	-	5.0	-	2.0	-
β -D-Lyxp1,2H ₂	$\kappa O^{1,2}$	-	34.0	12.0	33.0	35.0	36.0	20.0	36.0	34.0
β -D-Lyxp1,3H ₂	$\kappa O^{1,3}$	-	10.0	4.0	11.0	11.0	-	-	-	-
β -D-Lyxp1,2;3,4H ₄	$\kappa O^{1,2}:\kappa O^{3,4}$	-	-	72.0	1.0	13.0	2.0	60.0	-	19.0
α -D-Lyxf		1.7	-	-	-	-	-	-	-	-
α -D-Lyxf2,3H ₂	$\kappa O^{2,3}$	-	-	-	-	-	5.0	-	8.0	7.0
β -D-Lyxf		0.6	-	-	-	-	-	-	-	-
β -D-Lyxf1,2H ₂	$\kappa O^{1,2}$	-	-	-	-	-	4.0	-	6.0	4.0
β -D-Lyxf1,3H ₂	$\kappa O^{1,3}$	-	-	-	2.0	6.0	4.0	-	3.0	4.0

2 Results

In Table 2.44, the species distribution for the various palladium reagents and at various stoichiometries is summarized. Because of suspicious CIS values found for the complex species in Pd-en,^[38] a redetermination was carried out. In fact, the postulated $\kappa O^{2,3}$ -chelated β -D-Lyxp2,3H₂ species turned out to be the $\kappa O^{2,3}$ -chelated α -D-Lyxp2,3H₂ species. The correct assignment is given in Table 2.45.

Table 2.45. ¹³C NMR chemical shifts (δ /ppm) and shift differences ($\Delta\delta$) to the free pentose of D-lyxose ligands in Pd-en. Atoms are numbered as in Fig. 2.49.

		C1	C2	C3	C4	C5	Chelate
α -D-Lyxp2,3H ₂	δ	96.7	80.5	81.8	70.7	64.7	
	$\Delta\delta$	2.0	9.9	10.7	2.5	1.0	$\kappa O^{2,3}$
β -D-Lyxp1,2H ₂	δ	107.4	83.0	73.1	67.3	64.9	
	$\Delta\delta$	12.6	12.3	-0.2	0.2	0.1	$\kappa O^{1,2}$
β -D-Lyxp1,3H ₂	δ	91.3	69.2	67.5	71.9	57.2	
	$\Delta\delta$	-3.5	-1.5	-5.8	4.8	-7.6	$\kappa O^{1,3}$
β -D-Lyxp1,2;3,4H ₄	δ	108.9	85.8	84.4	74.9	65.4	
	$\Delta\delta$	14.1	15.1	11.1	7.8	0.6	$\kappa O^{1,2};\kappa O^{3,4}$

Furthermore, in Tables 2.46, 2.47 and 2.48 the chemical shifts and shift differences for the solution species detected in the solvents Pd-chxn, Pd-tmen and Pd-teen are listed. Besides the fact that species distribution varied along the Pd^{II} solvents the chemical shifts almost agreed simplifying the spectrum analysis.

Table 2.46. ¹³C NMR chemical shifts (δ /ppm) and shift differences ($\Delta\delta$) to the free pentose of D-lyxose ligands in Pd-chxn. Atoms are numbered as in Fig. 2.49.

		C1	C2	C3	C4	C5	Chelate
α -D-Lyxp2,3H ₂	δ	96.2	80.1	81.0	70.2	63.8	
	$\Delta\delta$	1.5	9.5	9.9	2.0	0.1	$\kappa O^{2,3}$
β -D-Lyxp1,2H ₂	δ	106.9	82.4	72.6	66.7	64.3	
	$\Delta\delta$	12.1	11.7	-0.7	-0.4	-0.5	$\kappa O^{1,2}$
β -D-Lyxp1,3H ₂	δ	90.8	68.6	67.0	71.4	56.6	
	$\Delta\delta$	-4.0	-2.1	-6.3	4.3	-8.2	$\kappa O^{1,3}$
β -D-Lyxp1,2;3,4H ₄	δ	108.3	85.4	83.7	74.2	64.8	
	$\Delta\delta$	13.5	14.7	10.4	7.1	0.0	$\kappa O^{1,2};\kappa O^{3,4}$
β -D-Lyxf1,3H ₂	δ	96.2	73.4	69.4	80.6	62.8	
	$\Delta\delta$	0.2	0.2	-2.7	-0.2	1.1	$\kappa O^{1,3}$

2 Results

Table 2.47. ^{13}C NMR chemical shifts (δ /ppm) and shift differences ($\Delta\delta$) to the free pentose of D-lyxose ligands in Pd-tmen. Atoms are numbered as in Fig. 2.49.

		C1	C2	C3	C4	C5	Chelate
α -D-Lyxp1,2H ₋₂	δ	101.4	79.9	73.8	70.1	66.6	
	$\Delta\delta$	6.7	9.3	2.7	1.9	2.9	$\kappa\text{O}^{1,2}$
α -D-Lyxp2,3H ₋₂	δ	97.0	80.7	81.1	70.6	64.5	
	$\Delta\delta$	2.3	10.1	10.0	2.4	0.8	$\kappa\text{O}^{2,3}$
β -D-Lyxp1,2H ₋₂	δ	107.5	82.1	73.3	67.6	64.6	
	$\Delta\delta$	12.7	11.4	0.0	0.5	-0.2	$\kappa\text{O}^{1,2}$
β -D-Lyxp1,2;3,4H ₋₄	δ	108.5	86.1	84.2	75.1	65.4	
	$\Delta\delta$	13.7	15.4	10.9	8.0	0.6	$\kappa\text{O}^{1,2};\kappa\text{O}^{3,4}$
α -D-Lyxf2,3H ₋₂	δ	104.9	90.6	84.2	80.2	63.0	
	$\Delta\delta$	3.6	13.0	12.5	-0.3	2.1	$\kappa\text{O}^{2,3}$
β -D-Lyxf1,2H ₋₂	δ	111.2	82.2	71.6	79.0	61.5	
	$\Delta\delta$	15.2	9.0	-0.5	-1.8	-0.2	$\kappa\text{O}^{1,2}$

Table 2.48. ^{13}C NMR chemical shifts (δ /ppm) and shift differences ($\Delta\delta$) to the free pentose of D-lyxose ligands in Pd-teen. Atoms are numbered as in Fig. 2.49.

		C1	C2	C3	C4	C5	Chelate
α -D-Lyxp1,2H ₋₂	δ	101.4	79.4	73.6	69.8	66.3	
	$\Delta\delta$	6.7	8.8	2.5	1.6	2.6	$\kappa\text{O}^{1,2}$
α -D-Lyxp2,3H ₋₂	δ	96.9	80.5	81.3	70.1	64.7	
	$\Delta\delta$	2.2	9.9	10.2	1.9	1.0	$\kappa\text{O}^{2,3}$
β -D-Lyxp1,2H ₋₂	δ	107.1	80.8	73.2	67.8	63.9	
	$\Delta\delta$	12.3	10.1	-0.1	0.7	-0.9	$\kappa\text{O}^{1,2}$
β -D-Lyxp1,2;3,4H ₋₄	δ	108.7	86.2	84.6	75.0	65.6	
	$\Delta\delta$	13.9	15.5	11.3	7.9	0.8	$\kappa\text{O}^{1,2};\kappa\text{O}^{3,4}$
α -D-Lyxf2,3H ₋₂	δ	104.6	91.1	84.0	79.5	62.7	
	$\Delta\delta$	3.3	13.5	12.3	-1.0	1.8	$\kappa\text{O}^{2,3}$
β -D-Lyxf1,2H ₋₂	δ	111.2	83.3	71.2	78.4	61.1	
	$\Delta\delta$	15.2	10.1	-0.9	-2.4	-0.6	$\kappa\text{O}^{1,2}$
β -D-Lyxf1,3H ₋₂	δ	95.6	73.6	69.8	81.2	60.8	
	$\Delta\delta$	-0.4	0.4	-2.3	0.4	-0.9	$\kappa\text{O}^{1,3}$

For all species discussed above, in Table 2.49 the $^3J_{\text{H,H}}$ coupling constants are listed confirming the postulated conformations. Whereas the conformation of *trans*-vicinal chelate species was unambiguous, the high value of $^3J_{\text{H}_3,\text{H}_4}$ indicated the $^4\text{C}_1$ conformation for the β -D-Lyxp1,2H₋₂- $\kappa\text{O}^{1,2}$ species.

2 Results

Table 2.49. Experimental and calculated ${}^3J_{\text{H,H}}$ values in Hz for the free glycoses and various metalated species of D-lyxopyranose. Bold: calculated or measured (formation of a *trans*-vicinal chelate) constants which unambiguously represent the specified conformer. For the calculation of constants, the Karplus relationship in eq. 8 of Ref. [28] was used in conjunction with the torsion angles of the X-ray analyses or the angles of idealized structures (all torsions angles multiples of 60°).

	${}^3J_{\text{H1,H2}}$	${}^3J_{\text{H2,H3}}$	${}^3J_{\text{H3,H4}}$	${}^3J_{\text{H4,H5eq}}$	${}^3J_{\text{H4,H5ax}}$	Conformation
free α -D (exp.) ^[77]	4.9	3.6	7.8	3.8	7.2	${}^4C_1 \leftrightarrow {}^1C_4$ (Ref. ^[5])
α -D (idealised)	3.2	3.5	9.6	4.3	10.1	4C_1 (Karplus)
α -D (idealised)	8.1	3.5	4.3	2.5	0.6	1C_4 (Karplus)
free β -D (exp.) ^[77]	1.1	2.7	8.5	5.1	9.1	4C_1 (Ref. ^[5])
β -D (idealised)	1.3	3.5	9.6	4.3	10.1	4C_1 (Karplus)
β -D (idealised)	3.1	3.5	4.3	2.5	0.6	1C_4 (Karplus)
α -D- $\kappa O^{1,2}$ (in Pd-tmen)	8.0	3.0	n.d.	n.d.	n.d.	1C_4 (trans-vic.)
α -D- $\kappa O^{1,2}$ (in Pd-teen)	7.9	3.1	n.d.	n.d.	n.d.	1C_4 (trans-vic.)
α -D- $\kappa O^{2,3}$ (in Pd-tmen)	5.3	4.0	n.d.	n.d.	n.d.	${}^4C_1 \leftrightarrow {}^1C_4$
α -D- $\kappa O^{2,3}$ (in Pd-teen)	6.0	5.1	4.4	4.3	5.0	${}^4C_1 \leftrightarrow {}^1C_4$
β -D- $\kappa O^{1,2}$ (in Pd-tmen)	1.5	3.5	9.2	5.5	n.d.	4C_1
β -D- $\kappa O^{1,2}$ (in Pd-teen)	1.7	3.5	8.6	4.6	8.9	4C_1
β -D- $\kappa O^{1,2}; \kappa O^{3,4}$ (in Pd-tmen)	1.1	2.8	10.2	5.0	10.5	4C_1 (trans-vic.)
β -D- $\kappa O^{1,2}; \kappa O^{3,4}$ (33)	1.7	2.9	9.7	4.7	10.1	4C_1 (X-Ray)
β -D- $\kappa O^{1,2}; \kappa O^{3,4}$ (Pd-en, Ref. ^[38])	1.9	3.4	9.5	4.6	10.1	4C_1 (X-Ray)

Dimetalation of D-lyxopyranose is possible only for 4C_1 - β -D-Lyxp1,2;3,4H₋₄- $\kappa O^{1,2}; \kappa O^{3,4}$. All other forms are hindered by *trans*-oriented vicinal hydroxy groups. According to the published crystal structure of [Pd₂(en)₂(β -Lyxp1,2;3,4H₋₄- $\kappa O^{1,2}; \kappa O^{3,4}$)],^[38] with Pd-tmen [Pd₂(tmen)₂(β -D-Lyxp1,2;3,4H₋₄- $\kappa O^{1,2}; \kappa O^{3,4}$)] was crystallized (see Fig. 2.57). The crystal structure was solved in the space group *P* 2₁. Structural features were very similar to the double-metalated β -D-arabinopyranose compound **32**. The tmen ligands again tended to form hydrophobic areas whereas the carbohydrate ligands were linked via three water molecules O92, O94 and O95 along the *a* axis. Forming an $R_4^2(8)$ ring motif,^[60] the water molecules O92 and O94 connected the alkoxido O4 to the water molecule O95 which again formed two hydrogen bonds to the alkoxido atoms O2 and O3 of the next carbohydrate ligand. Counting the carbohydrate's accepted hydrogen bonds, the equatorially standing O3 and O4 alkoxido functions accepted four hydrogen bonds, whereas O1 and the axially standing O2 alkoxido functions accepted only one hydrogen bond each (see Table 2.50).

2 Results

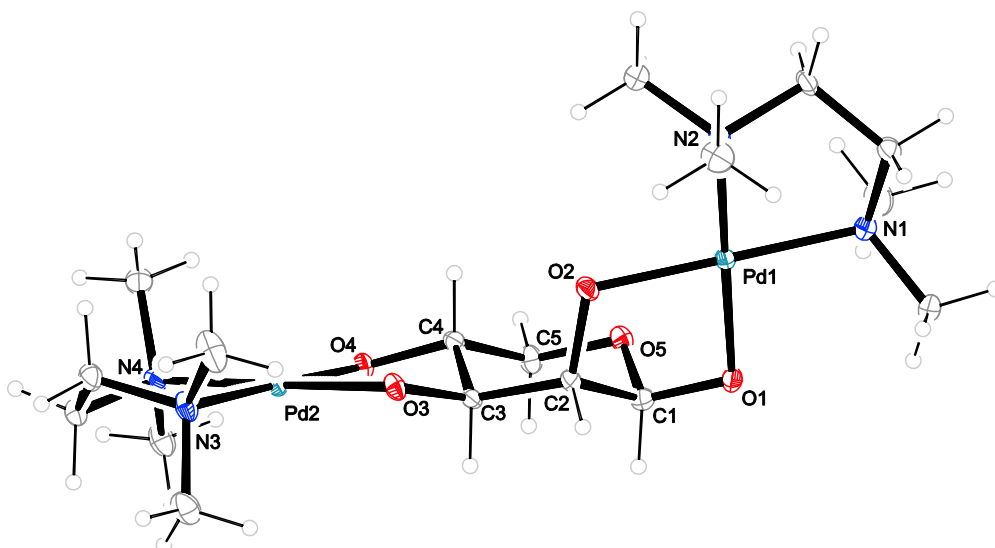


Figure 2.57: The molecular structure of $[\text{Pd}_2(\text{tmen})_2(\beta\text{-D-Lyx}p_{1,2;3,4}\text{H-4-}\kappa\text{O}^{1,2}:\kappa\text{O}^{3,4})]$ in crystals of the 10-hydrate (**33**). ORTEP plot is drawn with 50% probability ellipsoids. Interatomic distances (Å) and angles ($^\circ$) (standard deviations of the last digit in parentheses): Pd1–O1 1.990(3), Pd1–O2 2.006(3), Pd1–N1 2.060(3), Pd1–N2 2.052(3), Pd2–O3 2.015(3), Pd2–O4 2.013(3), Pd2–N3 2.066(3), Pd2–N4 2.063(3), O1–Pd1–O2 85.44(11), N1–Pd1–N2 86.45(13), O3–Pd2–O4 85.96(10), N3–Pd2–N4 85.52(13); chelate torsion angles: O1–C1–C2–O2 50.7(4), O3–C3–C4–O4 $-54.1(4)$, N1–C8–C9–N2 53.2(4), N3–C14–C15–N4 $-54.1(4)$; puckering parameters^[22] of the pyranose ring O5–C1–C2–C3–C4–C5: $Q = 0.584(4)$ Å, $\theta = 2.7(4)^\circ$.

Table 2.50. Distances [Å] and angles [$^\circ$] of hydrogen bonds in **33**. Standard deviations of the last digit are given in parentheses; values without standard deviation are related to hydrogen atoms at calculated positions. D: donor, A: acceptor.

D	H	A	D–H	H \cdots A	D \cdots A	D–H \cdots A
O91	H911	O1	0.800(15)	1.87(2)	2.658(4)	167(5)
O91	H912	O96 ⁱ	0.801(15)	1.96(2)	2.724(5)	161(5)
O92	H921	O4 ⁱ	0.805(15)	2.023(17)	2.826(4)	175(4)
O92	H922	O95	0.800(15)	2.08(2)	2.872(5)	168(5)
O93	H931	O97 ⁱⁱ	0.800(15)	2.060(18)	2.854(5)	171(5)
O93	H932	O99 ⁱⁱ	0.798(15)	1.970(18)	2.762(5)	171(4)
O94	H941	O4 ⁱ	0.801(15)	2.030(18)	2.826(4)	172(5)
O94	H942	O95	0.804(15)	2.024(18)	2.821(5)	171(5)
O95	H951	O3 ⁱⁱⁱ	0.807(15)	1.93(2)	2.696(4)	157(4)
O95	H952	O2 ⁱⁱⁱ	0.807(15)	1.93(3)	2.675(4)	153(5)
O96	H961	O93	0.808(15)	2.00(2)	2.790(5)	164(6)
O96	H962	O94 ^{iv}	0.809(15)	1.96(2)	2.744(5)	164(5)
O97	H971	O98	0.804(15)	1.995(19)	2.788(6)	169(6)
O97	H972	O5	0.805(15)	2.05(2)	2.824(4)	162(4)

2 Results

Table 2.50. Continued.

D	H	A	D–H	H⋯A	D⋯A	D–H⋯A
O98	H981	O91 ^v	0.808(15)	1.882(17)	2.685(5)	172(5)
O98	H982	O92 ^v	0.802(15)	2.16(3)	2.883(5)	151(5)
O99	H991	O910	0.804(15)	2.140(19)	2.935(7)	170(6)
O99	H992	O3 ^{vi}	0.807(15)	1.98(2)	2.773(5)	167(5)
O910	H913	O96	0.805(15)	2.164(17)	2.967(7)	176(6)
O910	H914	O97	0.805(15)	2.10(3)	2.848(7)	155(7)
O911	H915	O97	0.803(16)	2.38(4)	3.154(14)	163(13)
O911	H916	O92	0.804(16)	2.32(10)	3.015(12)	145(15)

Symmetry code: (i) $-x+1, y+\frac{1}{2}, -z+1$; (ii) $x+1, y, z$; (iii) $-x, y+\frac{1}{2}, -z+1$; (iv) $-x+1, y-\frac{1}{2}, -z$; (v) $-x+1, y-\frac{1}{2}, -z+1$; (vi) $x, y, z-1$.

2.8.4 D-Xylose

α - and β -D-Xylopyranose both are found in the 4C_1 conformation. The furanoses appear only in small amounts. Fig. 2.58 shows the ${}^{13}C$ NMR spectra of D-xylose in Pd-tmen at different Pd/Xyl ratios. α -D-Xylp1,2H₂- $\kappa O^{1,2}$ represented the main species in the upper spectrum at a 1:1 molar Pd:Xyl ratio and 4C_1 - β -D-Xylp1,2;3,4H₄- $\kappa O^{1,2};\kappa O^{3,4}$ became the main species at a 3:1 molar Pd:Xyl ratio, as is depicted in the lower spectrum. The amounts of the various solution species for the Pd^{II} solvents can be found in Table 2.51.

Table 2.51. Percentage distribution of D-xylose's metalated species in Pd-chxn, Pd-tmen and Pd-teen of various molar ratios. The values of the pure pentose are taken from Ref.^[79], the values of Pd-chxn from Ref.^[37].

	chelate	chxn			tmen		teen	
		0:1	1:1	3:1	1:1	2:1	1:1	2:1
α -D-Xylp		36.5	6.0	-	3.0	-	3.0	-
α -D-Xylp1,2H ₂	$\kappa O^{1,2}$	-	30.0	2.0	67.0	22.0	70.0	26.0
α -D-Xylp1,2;3,4H ₄	$\kappa O^{1,2};\kappa O^{3,4}$	-	4.0	41.0	-	18.0	-	10.0
β -D-Xylp	$\kappa O^{1,2}$	-	11.0	-	5.0	-	6.0	-
β -D-Xylp1,2H ₂		62.0	15.0	-	9.0	7.0	4.0	9.0
β -D-Xylp1,2;3,4H ₄	$\kappa O^{1,2};\kappa O^{3,4}$	-	-	26.0	-	38.0	-	29.0
β -D-Xylp1,3;2,4H ₄	$\kappa O^{1,3};\kappa O^{2,4}$	-	-	23.0	-	4.0	-	-
α -D-Xylf		0.86	-	-	-	-	-	-
α -D-Xylf1,2H ₂	$\kappa O^{1,2}$	-	6.0	-	13.0	5.0	17.0	16.0
α -D-Xylf1,2;3,5H ₄	$\kappa O^{1,2};\kappa O^{3,5}$	-	-	8.0	-	6.0	-	10.0
β -D-Xylf		0.64	-	-	-	-	-	-
β -D-Xylf1,3H ₂	$\kappa O^{1,3}$	-	13.0	-	-	-	-	-

2 Results

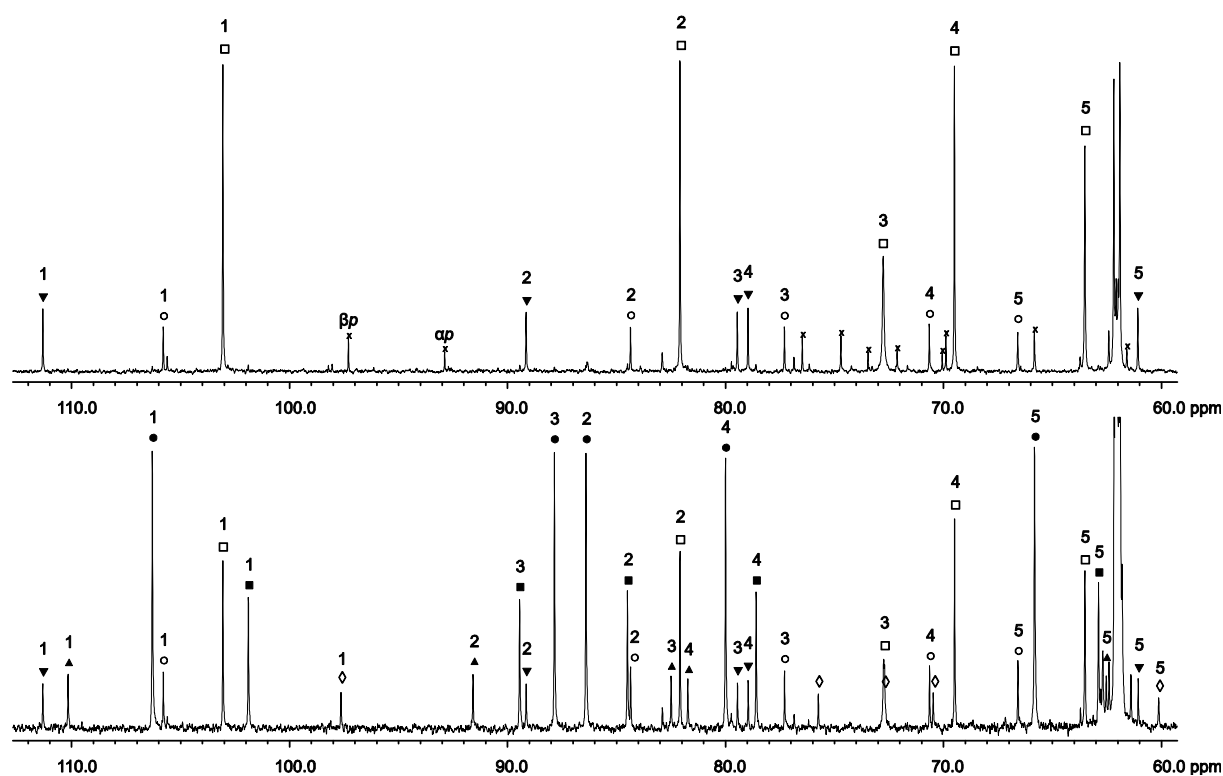


Figure 2.58. ^{13}C NMR spectra of D-xylose in Pd-tmen at a molar Pd/Xyl ratio of 1:1 (top) and 2:1 (bottom). The signals of free D-xylose are marked with (x); (\square) α -D-Xylp1,2H₂-κO^{1,2}, (\blacksquare) α -D-Xylp1,2,3,4H₄-κO^{1,2}:κO^{3,4}, (\circ) β -D-Xylp1,2H₂-κO^{1,2}, (\bullet) β -D-Xylp1,2,3,4H₄-κO^{1,2}:κO^{3,4}, (\blacktriangledown) α -D-Xylf1,2H₂-κO^{1,2}, (\blacktriangle) α -D-Xylf1,2,3,5H₄-κO^{1,2}:κO^{3,5} and (\diamond) β -D-Xylp1,3,2,4H₄-κO^{1,3}:κO^{2,4}.

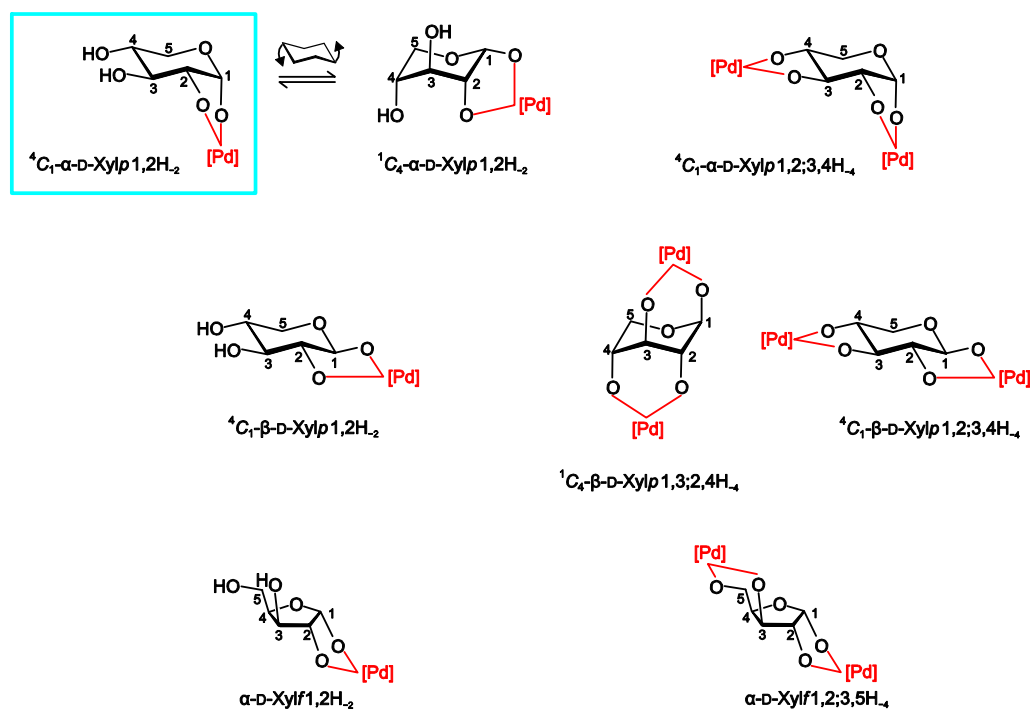


Figure 2.59. Species detected in Pd^{II}-containing solutions of D-xylose at various molar ratios (for details of molar ratio and percental distribution of species, see Table 2.51). Blue-framed species were confirmed by X-ray analysis.^[37]

2 Results

The chemical shifts and shift differences for the solution species detected in the solvents Pd-tmen and Pd-teen are listed in the Tables 2.52 and 2.53. Only two furanose forms were detected. As for the pentoses above, the various Pd^{II} solvents caused an almost identical chemical shift by coordination which made further investigations with new solvents easier.

Table 2.52. ¹³C NMR chemical shifts (δ /ppm) and shift differences ($\Delta\delta$) to the free pentose of D-xylose ligands in Pd-tmen. Atoms are numbered as in Fig. 2.49.

		C1	C2	C3	C4	C5	Chelate
α -D-Xylp1,2H ₋₂	δ	102.9	82.0	72.6	69.4	63.4	
	$\Delta\delta$	10.1	9.9	-0.8	-0.6	1.8	$\kappa O^{1,2}$
β -D-Xylp1,2H ₋₂	δ	105.7	84.2	77.2	70.5	66.5	
	$\Delta\delta$	8.5	9.5	0.8	0.7	0.7	$\kappa O^{1,2}$
α -D-Xylp1,2;3,4H ₋₄	δ	101.8	84.4	89.3	78.5	62.8	
	$\Delta\delta$	9.0	12.3	15.9	8.5	1.2	$\kappa O^{1,2};\kappa O^{3,4}$
β -D-Xylp1,2;3,4H ₋₄	δ	106.2	86.3	87.7	79.9	65.7	
	$\Delta\delta$	9.0	11.6	11.3	10.1	-0.1	$\kappa O^{1,2};\kappa O^{3,4}$
α -D-Xylf1,2H ₋₂	δ	111.2	89.0	79.3	78.8	61.0	
	$\Delta\delta$	15.1	12.3	3.8	-0.1	0.0	$\kappa O^{1,2}$
α -D-Xylf1,2;3,5H ₋₄	δ	110.0	91.5	82.4	81.6	62.6	
	$\Delta\delta$	13.9	14.8	6.9	2.7	1.6	$\kappa O^{1,2};\kappa O^{3,5}$

Table 2.53. ¹³C NMR chemical shifts (δ /ppm) and shift differences ($\Delta\delta$) to the free pentose of D-xylose ligands in Pd-teen. Atoms are numbered as in Fig. 2.49.

		C1	C2	C3	C4	C5	Chelate
α -D-Xylp1,2H ₋₂	δ	103.2	82.1	73.4	69.6	62.8	
	$\Delta\delta$	10.4	10.0	0.0	-0.4	1.2	$\kappa O^{1,2}$
β -D-Xylp1,2H ₋₂	δ	106.2	85.1	77.2	70.6	66.3	
	$\Delta\delta$	9.0	10.4	0.8	0.8	0.5	$\kappa O^{1,2}$
α -D-Xylp1,2;3,4H ₋₄	δ	102.4	84.6	88.6	78.9	63.0	
	$\Delta\delta$	9.6	12.5	15.2	8.9	1.4	$\kappa O^{1,2};\kappa O^{3,4}$
β -D-Xylp1,2;3,4H ₋₄	δ	106.7	86.7	88.0	80.3	65.8	
	$\Delta\delta$	9.5	12.0	11.6	10.5	0.0	$\kappa O^{1,2};\kappa O^{3,4}$
α -D-Xylf1,2H ₋₂	δ	111.8	89.1	79.6	78.9	61.0	
	$\Delta\delta$	15.7	12.4	4.1	0.0	0.0	$\kappa O^{1,2}$
α -D-Xylf1,2;3,5H ₋₄	δ	108.3	90.9	82.9	82.4	63.4	
	$\Delta\delta$	12.2	14.2	7.4	3.5	2.4	$\kappa O^{1,2};\kappa O^{3,5}$

2 Results

The various metalated species of D-xylose are depicted in Fig. 2.59. With four equatorial substituents and *trans*-vicinal chelation for 4C_1 - β -D-Xylp1,2H₂- $\kappa O^{1,2}$ and 4C_1 - β -D-Xylp1,2;3,4H₄- $\kappa O^{1,2}:\kappa O^{3,4}$ conformational fluctuation was not expected. Therefore, the detection of a *syn*-diaxial $\kappa O^{1,3}:\kappa O^{2,4}$ bonded 1C_4 - β -D-Xylp1,2;3,4H₄- $\kappa O^{1,3}:\kappa O^{2,4}$ was remarkable.^[37] This result was confirmed by 1C_4 -Me- β -D-Xylp2,4H₂- $\kappa O^{2,4}$ ^[71] and proved the D-xylopyranose's ability for metalation-induced conformational conversion. Thus, the assumption of a metalation-induced conformational fluctuation for α -D-Xylp1,2H₂- $\kappa O^{1,2}$, indicated by the comparison of the ${}^3J_{H,H}$ coupling constants in Table 2.54, is reasonable.

Table 2.54. Experimental and calculated ${}^3J_{H,H}$ values in Hz for the free glycoses and various metalated species of D-xylopyranose. Bold: calculated or measured (formation of a *trans*-vicinal chelate) constants which unambiguously represent the specified conformer. For the calculation of constants, the Karplus relationship in eq. 8 of Ref.^[28] was used in conjunction with the torsion angles of the X-ray analyses or the angles of idealized structures (all torsions angles multiples of 60°). To complete the set of coupling constants as thoroughly as possible, the values of compounds with Pd-en and Pd-chxn were used from former work.

	${}^3J_{H1,H2}$	${}^3J_{H2,H3}$	${}^3J_{H3,H4}$	${}^3J_{H4,H5eq}$	${}^3J_{H4,H5ax}$	Conformation
free α -D (exp.) ^[77]	3.7	9.8	9.1	5.1	10.2	4C_1 (Ref. ^[5])
α -D (idealised)	3.1	9.8	9.6	4.3	10.1	4C_1 (Karplus)
α -D (idealised)	1.3	4.3	4.3	2.5	0.6	1C_4 (Karplus)
free β -D (exp.) ^[77]	7.8	9.2	9.0	5.6	10.5	4C_1 (Ref. ^[5])
β -D (idealised)	8.1	9.8	9.6	4.3	10.1	4C_1 (Karplus)
β -D (idealised)	3.2	4.3	4.3	2.5	0.6	1C_4 (Karplus)
α -D- $\kappa O^{1,2}$ (in Pd-chxn)	2.9	6.9	7.1	3.5	10.7	4C_1
α -D- $\kappa O^{1,2}$ (Pd-chxn, Ref. ^[37])	4.7	8.0	9.0	4.0	10.1	4C_1 (X-Ray)
α -D- $\kappa O^{1,2}$ (in Pd-tmen)	2.2	5.1	5.7	2.6	5.5	${}^4C_1 \leftrightarrow {}^1C_4$
α -D- $\kappa O^{1,2}$ (in Pd-teen)	2.6	6.4	6.4	n.d.	n.d.	${}^4C_1 \leftrightarrow {}^1C_4$
β -D- $\kappa O^{1,2}$ (in Pd-chxn)	7.6	9.4	8.9	5.5	n.d.	4C_1 (trans-vic.)
β -D- $\kappa O^{1,2}$ (in Pd-tmen)	7.5	9.3	8.8	n.d.	n.d.	4C_1 (trans-vic.)
β -D- $\kappa O^{1,2}$ (in Pd-teen)	7.3	9.4	8.9	5.6	9.3	4C_1 (trans-vic.)
α -D- $\kappa O^{1,2}:\kappa O^{3,4}$ (in Pd-chxn)	3.7	8.9	9.2	4.8	7.4	4C_1
β -D- $\kappa O^{1,2}:\kappa O^{3,4}$ (in Pd-chxn)	7.2	9.2	9.1	n.d.	n.d.	4C_1 (trans-vic.)
β -D- $\kappa O^{1,2}:\kappa O^{3,4}$ (in Pd-tmen)	7.2	9.2	9.1	n.d.	n.d.	4C_1 (trans-vic.)
β -D- $\kappa O^{1,2}:\kappa O^{3,4}$ (in Pd-teen)	7.3	8.7	8.7	4.5	n.d.	4C_1 (trans-vic.)
β -D- $\kappa O^{1,3}:\kappa O^{2,4}$ (in Pd-chxn)	≈ 1	n.d.	n.d.	1.4	≈ 1	1C_4

Although X-ray analysis^[37] confirmed the 4C_1 -form of α -D-Xylp1,2H₂- $\kappa O^{1,2}$, the calculated ${}^3J_{H,H}$ coupling constants could not be explained by the exclusive presence of the 4C_1 -form.

2 Results

Finally, comparing α -D-Xylp1,2H₂- κ O^{1,2} with α -D-Ribp1,2H₂- κ O^{1,2}, a hydrogen bond O4–H4...O2 stabilizing the ¹C₄ conformation of α -D-Ribp1,2H₂- κ O^{1,2} also should be able to stabilize the ¹C₄ conformation of α -D-Xylp1,2H₂- κ O^{1,2} inducing the conformational fluctuation. Double metalation of α -D-xylopyranose could only be realized in the ⁴C₁ conformation. Thus, it is noteworthy that the ratio of α -D-Xylp1,2;3,4H₄- κ O^{1,2}: κ O^{3,4} and β -D-Xylp1,2;3,4H₄- κ O^{1,2}: κ O^{3,4} depended on the palladium-containing solvent. In Pd-chxn α -D-Xylp1,2;3,4H₄- κ O^{1,2}: κ O^{3,4} dominated the solution's species distribution, in Pd-tmen and Pd-teen β -D-Xylp1,2;3,4H₄- κ O^{1,2}: κ O^{3,4} was preferred.

2.9 Coordination-induced shift patterns of palladium(II)–methyl hex(ul)oside complexes

Despite the progress in analytical methods, the ¹³C NMR investigation of oligosaccharides and polysaccharides is still difficult. Just a glance at a ¹³C NMR spectrum of a disaccharide with a minimum of twelve signals reveals the problems of analysis which will be caused by the formation of various reaction products and the resulting crowded ¹³C NMR spectra. Realizing the high similarity of a disaccharide's ¹³C NMR spectrum to the ¹³C NMR spectra of its monomeric building units, the reaction of coordinating agents as Pd-chxn or Pd-tmen with the methyl hex(ul)osides should provide characteristic shift patterns which allow the identification of the corresponding signals in a di- or oligosaccharide ¹³C NMR spectrum.

2.9.1 The methyl hexopyranosides of D-galactose, D-glucose and D-mannose

With the methyl D-galactopyranosides, the *cis* coordination is usually the preferred binding mode in the solution which was realized by the Me-D-Galp3,4H₂- κ O^{3,4} species, while the *trans*-diequatorial diolato coordination mode was represented by the minor Me-D-Galp2,3H₂- κ O^{2,3} species (see Fig. 2.60). The detected chemical shifts and ³J_{H,H} coupling constants are denoted in the Tables 2.55 and 2.56. Probably the axially oriented hydroxy group of C4 prevented a κ O^{1,3}-diolato coordination of O4 and O6 which was detected for the methyl glucopyranosides. The Me-D-Galp3,4H₂- κ O^{3,4} species could be crystallized with the solvents Pd-tmen and Pd-dmen; [Pd(tmen)(⁴C₁-Me- α -D-Galp3,4H₂- κ O^{3,4})] · 8 H₂O (**34**) and [Pd(dmen)(⁴C₁-Me- α -D-Galp3,4H₂- κ O^{3,4})] · 9 H₂O (**35**) both were solved in the space group *P* 1 and were very similar to each other.

2 Results

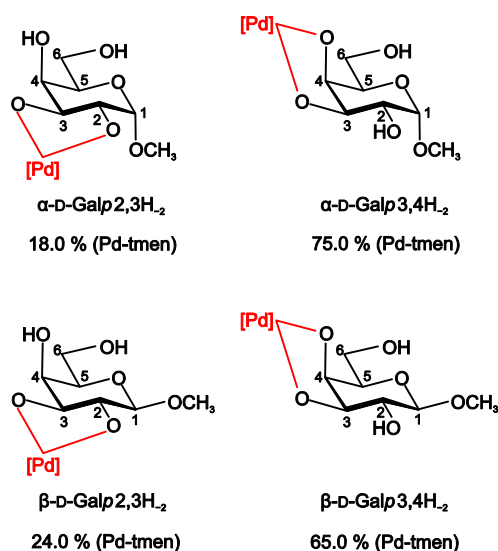


Figure 2.60. Species detected in Pd^{II}-containing solutions of methyl α - and methyl β -D-galactopyranoside. The difference between the given percentages and 100 % always represents free methyl pyranoside. The Me- α -D-Galp3,4H₂- κ O^{3,4} species was confirmed by X-ray analysis (see Fig. 2.61 and 2.62).

Table 2.55. ¹³C NMR chemical shifts (δ /ppm) and shift differences ($\Delta\delta$) to the free methyl glycoside of D-galactopyranoside ligands in Pd-tmen at a molar Pd/Me-Galp ratio of 2:1. Atoms are numbered as in Fig. 2.60.

		C1	C2	C3	C4	C5	C6	CH ₃	Chelate
Me- α -D-Galp2,3H ₂	δ	101.2	77.3	79.1	72.1	71.7	61.9	55.6	
	$\Delta\delta$	1.2	8.5	9.0	2.3	0.4	0.0	0.0	κ O ^{2,3}
Me- α -D-Galp3,4H ₂	δ	100.7	72.8	79.7	80.6	69.8	63.3	55.6	
	$\Delta\delta$	0.7	4.0	9.6	10.8	-1.5	1.4	0.0	κ O ^{3,4}
Me- β -D-Galp2,3H ₂	δ	105.7	79.2	84.2	71.8	76.7	61.7	57.5	
	$\Delta\delta$	1.3	7.8	10.8	2.5	1.0	0.1	-0.3	κ O ^{2,3}
Me- β -D-Galp3,4H ₂	δ	104.5	74.3	83.8	80.2	75.6	63.1	57.6	
	$\Delta\delta$	0.1	2.9	10.4	10.9	-0.1	1.5	-0.2	κ O ^{3,4}

Table 2.56. Experimental ³J_{H,H} values in Hz for the methyl D-galactopyranosides and various metalated species.

	³ J _{H1,H2}	³ J _{H2,H3}	³ J _{H3,H4}	³ J _{H4,H5}	³ J _{H5,H6}	³ J _{H5,H6'}	Conformation
free α -D (exp.) ^[77]	3.0	9.8	2.3	1.0	8.2	4.6	⁴ C ₁
free β -D (exp.) ^[77]	8.0	10.0	3.8	0.8	7.6	4.4	⁴ C ₁
α -D- κ O ^{2,3} (in Pd-tmen)	3.0	10.5	2.9	–	–	–	⁴ C ₁
α -D- κ O ^{3,4} (in Pd-tmen)	3.9	9.6	4.1	–	–	–	⁴ C ₁
β -D- κ O ^{2,3} (in Pd-tmen)	7.6	–	–	1.1	7.6	4.7	⁴ C ₁
β -D- κ O ^{3,4} (in Pd-tmen)	8.1	9.1	4.1	1.5	7.0	3.6	⁴ C ₁

2 Results

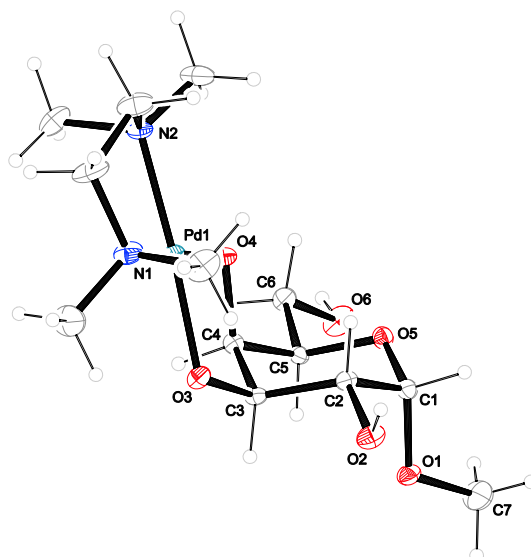


Figure 2.61. The molecular structure of $[\text{Pd}(\text{tmen})(^4\text{C}_1\text{-Me-}\alpha\text{-D-Galp3,4H}_2\text{-}\kappa\text{O}^{3,4})]$ in crystals of the 8-hydrate (**34**). ORTEP plot drawn with 50% probability ellipsoids. Interatomic distances (Å) and angles (°) (with standard deviations of the last digit in parentheses): Pd1–O3 2.001(4), Pd1–O4 2.008(4), Pd1–N1 2.070(5), Pd1–N2 2.070(4), O3–Pd1–O4 85.24(15), O3–Pd1–N1 94.05(17), O3–Pd1–N2 176.54(16), O4–Pd1–N1 176.56(19), O4–Pd1–N2 96.36(16), N1–Pd1–N2 84.53(18); chelate torsion angles: O3–C3–C4–O4 49.4(4), N1–C10–C11–N2 52.1(7); puckering parameters of the pyranose ring C1–C2–C3–C4–C5–O5: $Q = 0.543(4)$ Å, $\theta = 2.0(3)^\circ$.

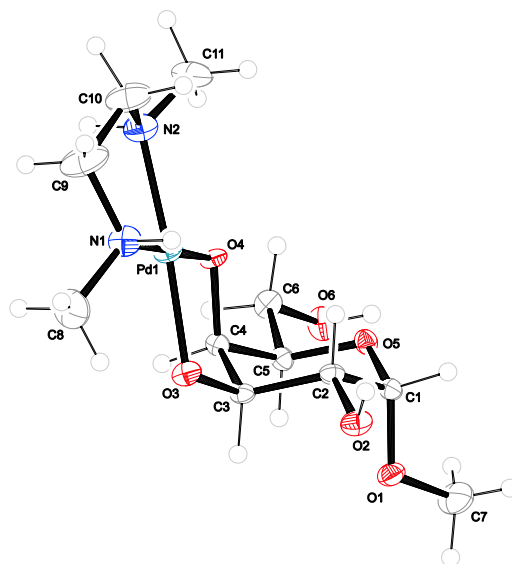


Figure 2.62. The molecular structure of $[\text{Pd}(\text{dmen})(^4\text{C}_1\text{-Me-}\alpha\text{-D-Galp3,4H}_2\text{-}\kappa\text{O}^{3,4})]$ in crystals of the 9-hydrate (**35**). ORTEP plot drawn with 50% probability ellipsoids. Interatomic distances (Å) and angles (°) (with standard deviations of the last digit in parentheses): Pd1–O3 2.001(3), Pd1–O4 2.010(3), Pd1–N1 2.059(3), Pd1–N2 2.047(4), O3–Pd1–O4 85.27(10), O3–Pd1–N1 95.61(12), O4–Pd1–N2 95.31(13), N1–Pd1–N2 83.94(15); chelate torsion angles: O3–C3–C4–O4 53.3(3), N1–C9–C10–N2 50.1(5); puckering parameters of the pyranose ring C1–C2–C3–C4–C5–O5: $Q = 0.554(3)$ Å, $\theta = 3.1(3)^\circ$.

2 Results

Table 2.57. Distances [Å] and angles [°] of hydrogen bonds in **35**. Standard deviations of the last digit are given in parentheses; values without standard deviation are related to hydrogen atoms at calculated positions. D: donor, A: acceptor.

D	H	A	D–H	H···A	D···A	D–H···A
O2	H821	O95	0.84	1.89	2.711(3)	163.8
O6	H861	O97 ⁱ	0.84	1.96	2.765(3)	159.8
N1	H711	O94	0.93	2.16	3.077(4)	170.7
N2	H721	O94 ⁱⁱ	0.93	2.34	3.252(5)	166.5
O91	H911	O99	0.827(13)	1.983(15)	2.803(4)	171(6)
O91	H912	O2	0.819(13)	2.19(4)	2.858(3)	139(6)
O91	H912	O1	0.819(13)	2.45(3)	3.169(4)	147(5)
O92	H921	O93	0.824(12)	1.958(13)	2.782(4)	178(5)
O92	H922	O91 ⁱⁱⁱ	0.822(12)	1.95(2)	2.723(4)	155(5)
O93	H931	O96	0.811(12)	2.050(15)	2.823(3)	159(3)
O93	H932	O4	0.811(12)	2.072(15)	2.866(3)	166(4)
O94	H941	O95	0.820(12)	1.899(13)	2.719(3)	178(4)
O94	H942	O96 ^{iv}	0.817(12)	2.016(17)	2.808(3)	163(3)
O95	H951	O4 ^v	0.820(12)	1.830(13)	2.643(3)	170(3)
O95	H952	O92	0.824(12)	1.889(13)	2.709(4)	173(3)
O96	H961	O98	0.813(12)	2.037(16)	2.827(3)	164(3)
O96	H962	O97 ⁱ	0.813(12)	1.992(14)	2.796(3)	170(4)
O97	H971	O99	0.812(12)	2.163(16)	2.933(3)	159(3)
O97	H972	O3	0.817(12)	2.027(18)	2.781(3)	153(3)
O97	H972	O2	0.817(12)	2.53(3)	3.107(3)	129(3)
O98	H981	O3 ^{vi}	0.820(12)	1.851(13)	2.671(3)	178(3)
O98	H982	O6 ^v	0.817(12)	1.986(14)	2.790(3)	168(3)
O99	H991	O94 ^{vii}	0.836(12)	2.20(3)	2.884(3)	139(4)
O99	H992	O98 ^{iv}	0.828(12)	1.963(14)	2.785(3)	171(5)

Symmetry code: (i) $x, y, z+1$; (ii) $x+1, y, z$; (iii) $x, y+1, z$; (iv) $x, y, z-1$; (v) $x-1, y, z$; (vi) $x-1, y, z+1$, (vii) $x, y-1, z$.

In both structures, the methyl α -D-galactopyranoside showed an almost undistorted 4C_1 pyranose ring. Furthermore, along the c axis, chains of molecules were linked by the same ring motif of hydrogen bonds. In **34**, an $R_4^3(8)$ motif^[60] connected two methyl galactopyranosides by two water molecules (O91 and O94) with O3 acting as a double hydrogen-bond acceptor and O6–H as a hydrogen-bond donor. In **35**, the same motif could be identified (O97 and O98). Further hydrogen bonds linked the chains, as one can see in Fig. 6.73 and 6.74 in the Appendix. The methyl group of the galactopyranoside was oriented towards the methyl groups of the Pd^{II}N₂ fragment. For structure **34**, the distances and angles

2 Results

of the hydrogen bonds are listed in Table 2.57. The hydrogen-bonding network of structure **35** was not resolved properly, therefore a table was not prepared.

The methyl glucopyranosides provide only *trans*-vicinal diolato units, nevertheless the $\kappa O^{2,3}$ -diolato coordination was preferred to the $\kappa O^{3,4}$ -diolato coordination. Fig. 2.63 shows all the metalated species. The α - and β -anomers of methyl glucopyranoside resulted in the same compounds with almost an identical share of solution equilibrium, and contrary to the methyl galactopyranosides, $\kappa O^{4,6}$ -diolato coordination was detected for the glucopyranosides.

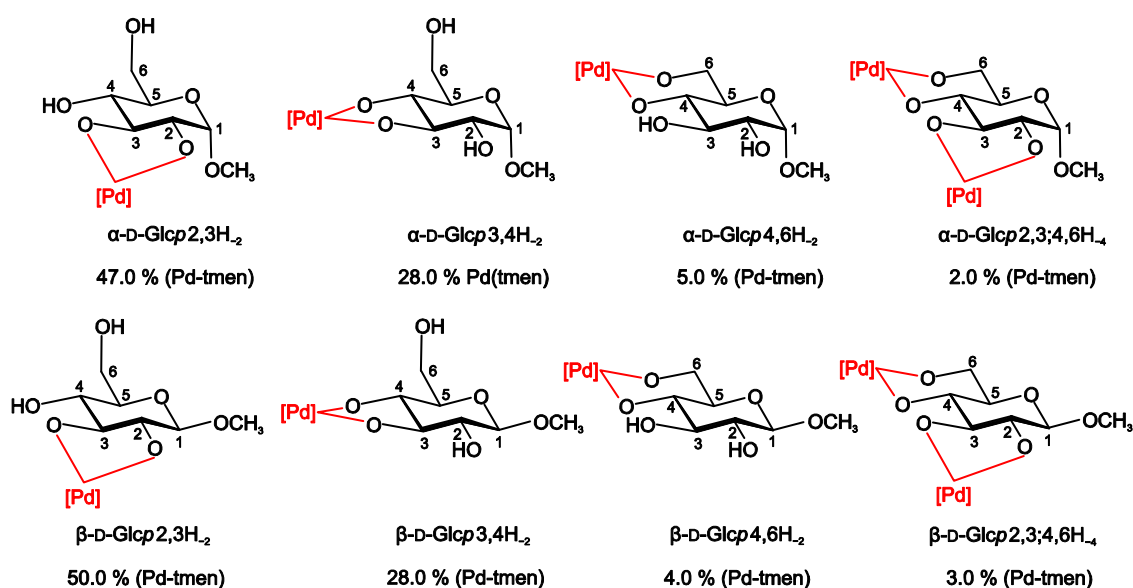


Figure 2.63. Species detected in Pd^{II}-containing solutions of methyl α - and methyl β -D-glucopyranoside. The difference between the given percentages and 100 % always represents free methyl pyranoside. The $\kappa O^{3,4}$ -Me- β -D-Glcp3,4H₂ species was confirmed by X-ray analysis.^[78]

Small amounts of Me-D-Glcp4,6H₂- $\kappa O^{4,6}$ and Me-D-Glcp2,3;4,6H₄- $\kappa O^{2,3}:\kappa O^{4,6}$ were found for both anomers at a molar Pd/Me-Glcp ratio of 2:1 underlining the weak formation tendency of a $\kappa O^{1,3}$ -diolato coordination with a hydroxymethyl group, especially in competition with a $\kappa O^{1,2}$ -diolato coordination. The detected chemical shifts and $^3J_{H,H}$ coupling constants were listed in the Tables 2.58 and 2.59. The coupling constants clearly indicated a 4C_1 conformation of the pyranose ring with the hydroxymethyl group anchoring the conformation for all investigated compounds. It is noteworthy that the $\kappa O^{4,6}$ -diolato coordination was indicated by 7.0–9.7 ppm CIS values. Formerly detected $\kappa O^{1,3}$ -diolato coordinated species showed only a minor or at least non-specific CIS, whereas significant CIS values were detected for the $\kappa O^{1,3}$ -diolato coordination of the methyl glucosides.

2 Results

Table 2.58. ^{13}C NMR chemical shifts (δ/ppm) and shift differences ($\Delta\delta$) to the free methyl glycoside of D-glucopyranoside ligands in Pd-tmen at a molar Pd/Me-Glcp ratio of 2:1. Atoms are numbered as in Fig. 2.63.

	C1	C2	C3	C4	C5	C6	CH ₃	Chelate
Me- α -D-Glcp2,3H ₋₂	100.9	81.8	82.0	72.2	72.6	61.1	55.5	
$\Delta\delta$	1.0	10.0	8.3	2.0	0.4	-0.1	-0.1	$\kappa\text{O}^{2,3}$
Me- α -D-Glcp3,4H ₋₂	100.1	74.1	83.0	79.9	74.1	61.5	55.5	
$\Delta\delta$	0.2	2.3	9.3	9.7	1.9	0.3	-0.1	$\kappa\text{O}^{3,4}$
Me- α -D-Glcp4,6H ₋₂	100.0	72.1	74.0	79.6	73.4	68.8	55.6	
$\Delta\delta$	0.1	0.3	0.3	9.4	1.2	7.6	0.0	$\kappa\text{O}^{4,6}$
Me- α -D-Glcp2,3;4,6H ₋₄	101.2	82.1	82.4	79.9	73.3	68.9	55.6	
$\Delta\delta$	1.3	10.3	8.7	9.7	1.1	7.7	0.0	$\kappa\text{O}^{2,3};\kappa\text{O}^{4,6}$
Me- β -D-Glcp2,3H ₋₂	104.7	83.0	86.2	72.1	77.5	61.5	57.4	
$\Delta\delta$	0.9	9.3	9.8	1.8	1.0	0.1	-0.4	$\kappa\text{O}^{2,3}$
Me- β -D-Glcp3,4H ₋₂	105.0	75.4	86.5	80.3	76.9	61.8	56.0	
$\Delta\delta$	1.2	1.7	10.1	10.0	0.4	0.4	-1.8	$\kappa\text{O}^{3,4}$
Me- β -D-Glcp4,6H ₋₂	104.0	74.0	76.4	79.6	76.8	68.4	57.8	
$\Delta\delta$	0.2	0.3	0.0	9.3	0.3	7.0	0.0	$\kappa\text{O}^{4,6}$
Me- β -D-Glcp2,3;4,6H ₋₄	104.9	83.6	86.5	81.3	78.1	68.6	57.3	
$\Delta\delta$	1.1	9.9	10.1	11.0	1.6	7.2	-0.5	$\kappa\text{O}^{2,3};\kappa\text{O}^{4,6}$

Table 2.59. Experimental $^3J_{\text{H,H}}$ values in Hz for the methyl D-glucopyranosides and various metalated species.

	$^3J_{\text{H1,H2}}$	$^3J_{\text{H2,H3}}$	$^3J_{\text{H3,H4}}$	$^3J_{\text{H4,H5}}$	$^3J_{\text{H5,H6}}$	$^3J_{\text{H5,H6}'}$	Conformation
free α -D (exp.) ^[77]	4.0	10.0	10.0	10.0	2.8	5.8	$^4\text{C}_1$
free β -D (exp.) ^[77]	8.2	9.6	9.6	9.6	2.4	6.4	$^4\text{C}_1$
α -D- $\kappa\text{O}^{2,3}$ (in Pd-tmen)	3.6	9.8	8.9	10.0	2.2	5.9	$^4\text{C}_1$
α -D- $\kappa\text{O}^{3,4}$ (in Pd-tmen)	3.9	9.8	8.9	10.2	2.3	5.8	$^4\text{C}_1$
β -D- $\kappa\text{O}^{2,3}$ (in Pd-tmen)	7.9	9.4	9.4	9.4	1.9	6.3	$^4\text{C}_1$
β -D- $\kappa\text{O}^{3,4}$ (in Pd-tmen)	7.7	9.3	9.3	9.4	2.4	7.2	$^4\text{C}_1$

Methyl α -D-mannopyranoside, as the methyl galactopyranosides, provides a *cis*- and a *trans*-vicinal diolato unit for coordination. With Me- α -D-Manp2,3H₋₂- $\kappa\text{O}^{2,3}$, again the *cis*-vicinal diolato coordination was preferred, and the *trans*-vicinal coordinated Me- α -D-Manp3,4H₋₂- $\kappa\text{O}^{3,4}$ species was found only in very small amounts (see Fig. 2.64). Unexpectedly, the Me- α -D-Manp4,6H₋₂- $\kappa\text{O}^{4,6}$ species was not detected, although it had been described for Pd-chxn.^[78] The detected chemical shifts and $^3J_{\text{H,H}}$ coupling constants are denoted in the Tables 2.61 and 2.62, the latter confirming the $^4\text{C}_1$ conformation of [Pd(tmen)(Me- α -D-Manp2,3H₋₂- $\kappa\text{O}^{2,3}$)].

2 Results

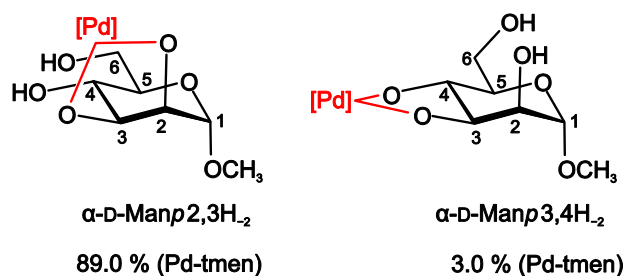


Figure 2.64. Species detected in Pd^{II}-containing solutions of methyl α -D-mannopyranoside. The difference between the given percentages and 100 % always represents free methyl pyranoside. The Me- α -D-Manp2,3H₂- $\kappa O^{2,3}$ species was confirmed by X-ray analysis (see Fig. 2.65).

This species was also crystallized and solved in the space group $P 2_1$. Crystals of the 3.5-hydrate contained two molecules in the asymmetric unit which were held together by two water molecules (O91 and O94) forming hydrogen bonds to the alkoxido atoms O2 and O3. These dimeric units were linked by hydrogen bonds of the hydroxymethyl groups and two additional water molecules (O92 and O93). The distances and angles of the hydrogen bonds are listed in Table 2.60.

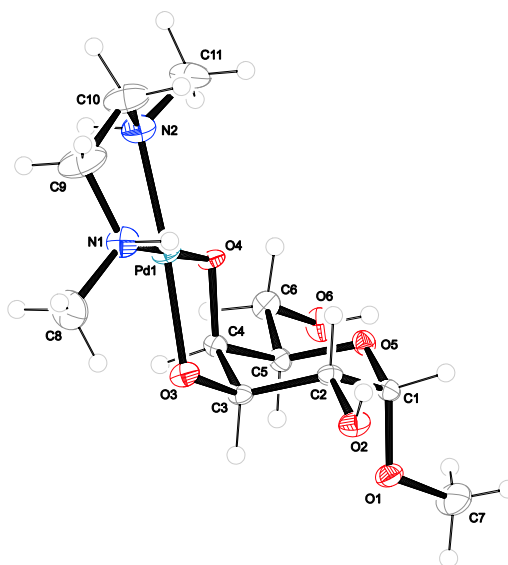


Figure 2.65. The molecular structure of $[\text{Pd}(\text{tmen})(^4\text{C}_1\text{-Me-}\alpha\text{-D-Manp2,3H}_2\text{-}\kappa\text{O}^{2,3})]$ in crystals of the 3.5-hydrate (**36**). ORTEP plot drawn with 50% probability ellipsoids. Interatomic distances (Å) and angles (°) (with standard deviations of the last digit in parentheses): Pd1–O21 2.018(2), Pd1–O31 1.990(2), Pd1–N1 2.067(3), Pd1–N2 2.052(3), Pd2–O22 2.011(2), Pd2–O32 1.988(2), Pd2–N3 2.067(3), Pd2–N4 2.061(3), O21–Pd1–O31 85.22(9), O21–Pd1–N1 97.64(11), O31–Pd1–N2 92.30(10), N1–Pd1–N2 84.93(12), O22–Pd2–O32 86.23(9), O22–Pd2–N3 95.66(10), O32–Pd2–N4 92.23(11), N3–Pd2–N4 85.90(12); chelate torsion angles: O21–C21–C31–O31 $-48.9(3)$, O22–C22–C32–O32 $-52.8(3)$, N1–C101–C111–N2 $-49.9(5)$, N3–C102–C112–N4 $53.3(4)$; puckering parameters of the pyranose ring O51–C11–C21–C31–C41–C51: $Q = 0.540(3)$ Å, $\theta = 8.8(4)^\circ$; O52–C12–. . . : $Q = 0.552(3)$ Å, $\theta = 4.9(4)^\circ$.

2 Results

Table 2.60. Distances [\AA] and angles [$^\circ$] of hydrogen bonds in **36**. Standard deviations of the last digit are given in parentheses; values without standard deviation are related to hydrogen atoms at calculated positions. D: donor, A: acceptor.

D	H	A	D–H	H \cdots A	D \cdots A	D–H \cdots A
O41	H841	O62 ⁱ	0.84	2.03	2.859(3)	2.859(3)
O42	H842	O98	0.84	2.06	2.692(11)	2.692(11)
O61	H861	O93 ⁱⁱ	0.84	1.91	2.736(4)	2.736(4)
O62	H862	O91 ^{vi}	0.84	1.95	2.731(4)	2.731(4)
O91	H911	O31	0.822(10)	1.854(19)	2.643(3)	2.643(3)
O91	H912	O32	0.828(10)	1.923(12)	2.747(3)	2.747(3)
O92	H921	O91	0.825(10)	2.013(13)	2.832(4)	2.832(4)
O92	H922	O22 ⁱ	0.828(10)	1.96(2)	2.762(4)	2.762(4)
O93	H931	O95 ⁱⁱⁱ	0.830(10)	2.025(13)	2.841(4)	2.841(4)
O93	H932	O94	0.831(10)	1.968(15)	2.787(4)	2.787(4)
O94	H941	O21 ⁱ	0.829(10)	1.927(18)	2.728(4)	2.728(4)
O94	H942	O22 ⁱ	0.829(10)	2.006(16)	2.819(4)	2.819(4)
O95	H951	O41 ^{iv}	0.831(10)	2.011(11)	2.840(4)	2.840(4)
O95	H952	O96 ^v	0.833(10)	1.980(15)	2.784(4)	2.784(4)
O96	H961	O21 ^{iv}	0.836(10)	1.947(11)	2.782(3)	2.782(3)
O96	H962	O61 ^{iv}	0.830(10)	2.214(12)	3.041(4)	3.041(4)

Symmetry code: (i) $-x+1, y-1/2, -z+1$; (ii) $x-1, y, z+1$; (iii) $x+1, y, z$; (iv) $x, y, z-1$; (v) $-x, y-1/2, -z$; (vi) $-x+1, y+1/2, -z+1$.

Table 2.61. ^{13}C NMR chemical shifts (δ/ppm) and shift differences ($\Delta\delta$) to the free methyl glycoside of D-mannopyranoside ligands in Pd-tmen at a Pd/Me-Man p ratio of 2:1. Atoms are numbered as in Fig. 2.65.

	C1	C2	C3	C4	C5	C6	CH ₃	Chelate
Me- α -D-Man p 2,3H ₋₂	101.7	80.7	80.8	70.9	72.8	61.6	55.3	
$\Delta\delta$	0.3	10.2	9.6	3.5	-0.3	0.0	0.0	$\kappa\text{O}^{2,3}$
Me- α -D-Man p 3,4H ₋₂	102.0	73.2	81.5	75.7	75.1	61.6	55.3	
$\Delta\delta$	0.6	2.7	10.3	8.3	2.0	0.0	0.0	$\kappa\text{O}^{3,4}$

Table 2.62. Experimental $^3J_{\text{H,H}}$ values in Hz for the methyl α -D-mannopyranoside and the metalated species.

	$^3J_{\text{H1,H2}}$	$^3J_{\text{H2,H3}}$	$^3J_{\text{H3,H4}}$	$^3J_{\text{H4,H5}}$	$^3J_{\text{H5,H6}}$	$^3J_{\text{H5,H6}'}$	Conformation
free α -D (exp.) ^[77]	1.6	3.5	10.0	10.0	1.9	5.8	$^4\text{C}_1$
α -D- $\kappa\text{O}^{2,3}$ (in Pd-tmen)	1.3	4.1	8.9	10.3	2.3	5.8	$^4\text{C}_1$

2 Results

2.9.2 The methyl fructosides

To identify the characteristic shift pattern of disaccharide's monomeric building units, the methyl hex(ul)osides had to be investigated, too. According to the literature,^[81] methyl β -D-fructopyranoside and both methyl D-fructofuranosides could be obtained easily. The former crystallized (Fig. 2.66), and the crystal structure was solved in the space group $C 2$.

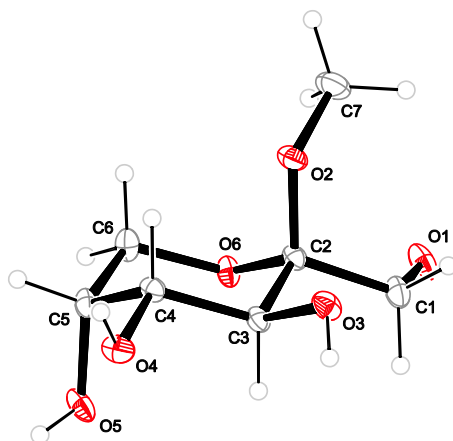


Figure 2.66. The molecular structure of methyl β -D-fructopyranoside (**37**). ORTEP plot drawn with 50% probability ellipsoids. Puckering parameters of the pyranose ring O5–C1–C2–C3–C4–C5: $Q = 0.581(2)$ Å, $\theta = 177.13(19)^\circ$. For further details, see ^[82].

Methyl β -D-fructopyranoside was treated with Pd-chxn and Pd-tmen to utilize the various characteristics of both solvents. Fig. 2.67 presents the results of the investigation.

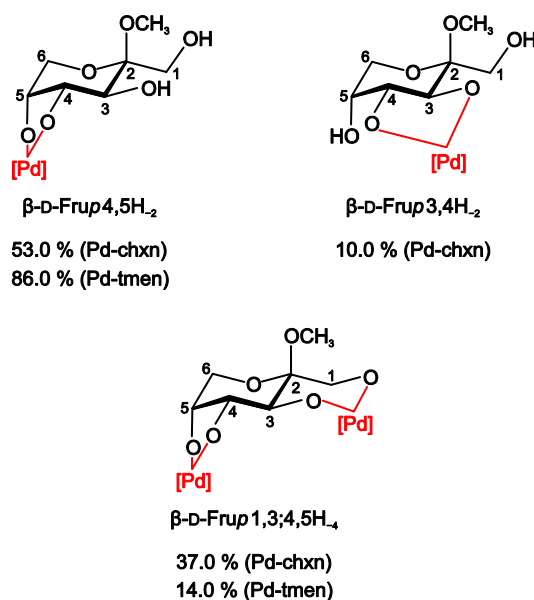


Figure 2.67. Species detected in Pd^{II}-containing solutions of methyl β -D-fructopyranoside. The difference between the given percentage and 100 % always represents free methyl pyranoside.

2 Results

As expected, the *cis*-vicinal Me- β -D-Frup4,5H₂- κ O^{4,5} species was the major species in both solvents, the *trans*-vicinal Me- β -D-Frup3,4H₂- κ O^{3,4} species was detected only with Pd-chxn. Additionally, in both solvents, the dimetalated Me- β -D-Frup1,3;4,5H₄- κ O^{1,3}: κ O^{4,5} was found. The detected chemical shifts and ³J_{H,H} coupling constants are listed in Tables 2.63, 2.64 and 2.65, the latter confirming the ²C₅ conformation of the pyranose ring. It should be noted that the C1 atom showed a low CIS as was expected for the κ O^{1,3}-diolato coordination whereas the C3 atom showed a regular CIS as would be obtained for a κ O^{1,2}-diolato coordination, too. Furthermore, a comparison of the chemical shifts of both solvents revealed that Pd-tmen caused a higher CIS.

Table 2.63. ¹³C NMR chemical shifts (δ /ppm) and shift differences ($\Delta\delta$) to the free methyl hexuloside of methyl β -D-fructopyranoside ligands in Pd-chxn. Atoms are numbered as in Fig. 2.67.

	C1	C2	C3	C4	C5	C6	CH ₃	Chelate
Me- β -D-Frup3,4H ₂	61.9	102.5	77.7	79.3	72.3	65.3	49.2	
$\Delta\delta$	0.4	1.5	8.7	9.1	2.6	0.9	0.1	κ O ^{3,4}
Me- β -D-Frup4,5H ₂	61.9	101.1	72.6	79.3	79.7	63.8	49.0	
$\Delta\delta$	0.4	0.1	3.6	9.1	10.0	-0.6	-0.1	κ O ^{4,5}
Me- β -D-Frup1,3;4,5H ₄	64.6	104.1	77.7	79.9	80.3	61.9	48.4	
$\Delta\delta$	3.1	3.1	8.7	9.7	10.6	-2.5	-0.7	κ O ^{1,3} : κ O ^{4,5}

Table 2.64. ¹³C NMR chemical shifts (δ /ppm) and shift differences ($\Delta\delta$) to the free methyl hexuloside of methyl β -D-fructopyranoside ligands in Pd-tmen. Atoms are numbered as in Fig. 2.67.

	C1	C2	C3	C4	C5	C6	CH ₃	Chelate
Me- β -D-Frup4,5H ₂	61.5	101.3	72.0	79.1	79.7	63.8	49.1	
$\Delta\delta$	0.0	0.3	3.0	8.9	10.0	-0.6	0.0	κ O ^{4,5}
Me- β -D-Frup1,3;4,5H ₄	66.6	104.3	79.4	81.2	79.9	62.2	48.5	
$\Delta\delta$	5.1	3.3	10.4	11.0	10.2	-2.2	-0.6	κ O ^{1,3} : κ O ^{4,5}

Table 2.65. Experimental ³J_{H,H} values in Hz for various metallated species of methyl β -D-fructopyranoside.

	³ J _{H3,H4}	³ J _{H4,H5}	³ J _{H5,H6}	³ J _{H5,H6'}	Conformation
β -D- κ O ^{4,5} (in Pd-chxn)	9.2	4.4	1.4	1.5	² C ₅
β -D- κ O ^{1,3} : κ O ^{4,5} (in Pd-chxn)	8.9	4.3	1.5	1.9	² C ₅
β -D- κ O ^{4,5} (in Pd-tmen)	9.4	4.2	3.4	3.5	² C ₅

2 Results

Fixed in the furanose form, the methyl D-fructofuranosides provided only $\kappa O^{1,3}$ -diolato units. As with methyl β -D-fructopyranoside, the methyl fructofuranosides were treated with Pd-chxn and Pd-tmen to utilize the various characteristics of both solvents. Fig. 2.68 presents the results of the investigation.

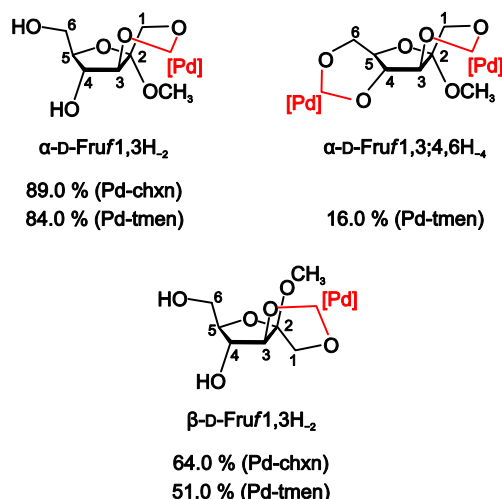


Figure 2.68. Species detected in Pd^{II}-containing solutions of methyl α - and β -D-fructofuranoside. The difference between the given percentages and 100 % always represents free methyl furanoside. The Me- α -D-Fruf1,3H₂- $\kappa O^{1,3}$ species was confirmed by X-ray analysis (see Fig. 2.69).

$\kappa O^{1,3}$ -diolato coordination was favored for the α - instead of the β -anomer of methyl D-fructofuranoside, the latter being more restricted in the conformational fluctuation of the furanose ring. Furthermore, according to the $^3J_{H,H}$ coupling constants in Table 2.66, monometalation of methyl β -D-fructofuranoside resulted in a ${}^C2T_{C3}-E_{C3}$ conformation of the ring. This inhibited a second Pd^{II}N₂ fragment from coordinating to the atoms O4 and O6 because, for this furanose-ring conformation, the distance of the atoms is too great for metalation. Otherwise, monometalation of methyl α -D-fructofuranoside fixed the furanose ring in a $E_{C5}-O^5T_{C5}$ conformation which was perfect for the coordination of a second Pd^{II}N₂ fragment. Therefore, with Pd-tmen, the Me- α -D-Fruf1,3;4,6H₄ species was found at a quantity of 16%. In the Tables 2.67 and 2.68 the ^{13}C NMR chemical shifts and shift differences for the various species detected in solution are listed.

Table 2.66. Experimental $^3J_{H,H}$ values in Hz for various metalated species of methyl D-fructofuranosides.

	$^3J_{H3,H4}$	$^3J_{H4,H5}$	$^3J_{H5,H6}$	$^3J_{H5,H6'}$	Conformation
α -D- $\kappa O^{1,3}$ (in Pd-tmen)	6.5	9.1	2.3	5.2	$E_{C5}-O^5T_{C5}$
β -D- $\kappa O^{1,3}$ (in Pd-chxn)	8.3	6.9	3.1	7.6	${}^C2T_{C3}-E_{C3}$
β -D- $\kappa O^{1,3}$ (in Pd-tmen)	8.6	—	—	—	${}^C2T_{C3}-E_{C3}$

2 Results

Table 2.67. ^{13}C NMR chemical shifts (δ/ppm) and shift differences ($\Delta\delta$) to the free methyl hexuloside of methyl D-fructofuranoside ligands in Pd-chxn. Atoms are numbered as in Fig. 2.68.

	C1	C2	C3	C4	C5	C6	CH ₃	Chelate
Me- α -D-Fruf1,3H ₋₂	61.3	110.7	85.1	79.1	79.6	60.8	48.5	
$\Delta\delta$	3.0	1.8	4.4	1.1	-4.3	-1.1	-0.3	$\kappa\text{O}^{1,3}$
Me- β -D-Fruf1,3H ₋₂	62.6	109.2	83.6	75.2	83.2	64.0	48.4	
$\Delta\delta$	2.3	4.8	6.2	-0.4	1.4	0.8	-1.1	$\kappa\text{O}^{1,3}$

Table 2.68. ^{13}C NMR chemical shifts (δ/ppm) and shift differences ($\Delta\delta$) to the free methyl hexuloside of methyl D-fructofuranoside ligands in Pd-tmen. Atoms are numbered as in Fig. 2.68.

	C1	C2	C3	C4	C5	C6	CH ₃	Chelate
Me- α -D-Fruf1,3H ₋₂	63.0	112.1	86.3	79.0	80.3	61.6	49.7	
$\Delta\delta$	4.7	3.2	5.6	1.0	-3.6	-0.4	0.9	$\kappa\text{O}^{1,3}$
Me- α -D-Fruf1,3;4,6H ₋₄	63.0	113.7	86.9	81.0	80.3	67.2	48.8	
$\Delta\delta$	4.7	4.8	6.2	3.0	3.6	5.3	0.0	$\kappa\text{O}^{1,3};\kappa\text{O}^{4,6}$
Me- β -D-Fruf1,3H ₋₂	64.7	108.6	85.9	75.2	83.4	64.2	48.6	
$\Delta\delta$	4.4	4.2	8.5	-0.4	1.6	1.0	-0.9	$\kappa\text{O}^{1,3}$

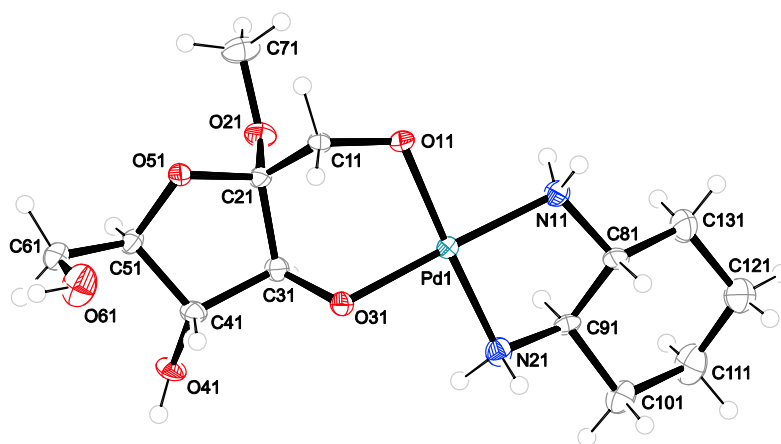


Figure 2.69. The molecular structure of $[\text{Pd}(\text{R,R}\text{-chxn})(\text{Me-}\alpha\text{-D-Fruf1,3H}_2\text{-}\kappa\text{O}^{1,3})]$ in crystals of the dihydrate (**38**). ORTEP plot drawn with 50% probability ellipsoids. Interatomic distances (\AA) and angles ($^\circ$) (with standard deviations of the last digit in parentheses): Pd1–O11 2.005(4), Pd1–O31 2.004(5), Pd1–N11 2.052(6), Pd1–N21 2.052(6), Pd2–O12 2.005(5), Pd2–O32 2.001(5), Pd2–N12 2.048(6), Pd2–N22 2.049(7), O11–Pd1–O31 89.47(18), O11–Pd1–N11 92.5(2), O31–Pd1–N21 93.8(2), N11–Pd1–N21 84.2(2), O12–Pd2–O32 90.37(18), O12–Pd2–N12 92.4(2), O32–Pd2–N22 92.9(2), N12–Pd2–N22 84.5(3); chelate torsion angles: N11–C81–C91–N21 $-53.4(7)$, N12–C82–C92–N22 $-55.5(8)$; puckering parameters of the furanose ring O51–C21–C31–C41–C51–O51: $Q_2 = 0.341(6)$ \AA , $\varphi_2 = 334.5(12)^\circ$, O52–C12–. . . : $Q_2 = 0.341(6)$ \AA , $\varphi_2 = 333.0(11)^\circ$; puckering parameters of the pyranose ring Pd1–O11–C11–C21–C31–O31: $Q = 0.888(6)$ \AA , $\theta = 82.3(4)^\circ$, $\varphi = 310.7(4)^\circ$, Pd2–O11–. . . : $Q = 0.836(6)$ \AA , $\theta = 81.6(4)^\circ$, $\varphi = 309.9(4)^\circ$.

2 Results

The monometalated Me- α -D-Fruf1,3H₂ species was crystallized with Pd-chxn with the molecular structure depicted in Fig. 2.69. According to the Cremer–Pople puckering parameters, the furanose ring's conformation could be determined exactly between the E_{C_5} and ${}^{O5}T_{C_5}$ conformation. The structure was solved in the space group $P 1$ with two molecules in the asymmetric unit arranged alternating the Pd(R,R -chxn) fragment with the opposing methyl α -D-fructofuranoside. Each two [Pd(R,R -chxn)(Me- α -D-Fruf1,3H₂- $\kappa O^{1,3}$)] molecules were connected by one water molecule (O94) along the a axis, accepting two hydrogen bonds from the N–H functions N11 and N12 of two Pd(chxn) fragments and building two hydrogen bonds to the alkoxido functions O31 and O32. These double-layered bands themselves were linked by the remaining three water molecules also forming homodromic chains $C_3^3(6)^{[60]}$ along the a axis. The distances and angles of all hydrogen bonds are listed in Table 2.69.

Table 2.69. Distances [\AA] and angles [$^\circ$] of hydrogen bonds in **38**. Standard deviations of the last digit are given in parentheses; values without standard deviation are related to hydrogen atoms at calculated positions. D: donor, A: acceptor.

D	H	A	D–H	H \cdots A	D \cdots A	D–H \cdots A
O41	H841	O11 ⁱ	0.84	1.68	2.519(6)	177.7
O42	H842	O12 ⁱ	0.84	1.69	2.532(6)	179.0
O61	H861	O52 ⁱⁱ	0.84	2.03	2.861(7)	171.0
O62	H862	O51 ⁱⁱⁱ	0.84	2.00	2.821(7)	165.6
N11	H711	O93 ^{iv}	0.92	2.35	3.254(8)	166.6
N11	H712	O94 ^{iv}	0.92	2.02	2.936(8)	175.1
N12	H721	O91 ^v	0.92	2.06	2.967(7)	169.1
N12	H722	O94 ^{iv}	0.92	2.00	2.917(8)	172.7
N21	H713	O32	0.92	2.23	3.092(7)	155.1
N21	H714	O92	0.92	2.45	3.199(8)	138.5
N22	H723	O31	0.92	2.33	3.190(8)	155.7
N22	H724	O93 ^v	0.92	2.59	3.260(9)	129.8
O91	H911	O93 ^{iv}	0.833(10)	2.002(14)	2.833(7)	176(8)
O91	H912	O42 ^{vi}	0.830(10)	1.90(2)	2.703(6)	163(8)
O92	H921	O91	0.830(10)	2.06(4)	2.845(8)	158(10)
O92	H922	O22 ^{vii}	0.829(10)	2.12(2)	2.932(7)	166(8)
O93	H931	O92	0.830(10)	2.02(4)	2.816(8)	159(10)
O93	H932	O41	0.832(10)	1.93(3)	2.744(6)	166(10)
O94	H941	O31	0.830(10)	1.87(3)	2.680(8)	164(7)
O94	H942	O32	0.828(10)	1.899(14)	2.725(7)	176(9)

Symmetry code: (i) $x+1, y, z$; (ii) $x+1, y, z+1$; (iii) $x, y, z-1$; (iv) $x-1, y, z$; (v) $x, y+1, z$; (vi) $x-1, y-1, z$; (vii) $x, y-1, z$.

2 Results

2.10 Palladium(II) chelation with Pd-tmen by the common hexoses

The common hexoses D-galactose, D-glucose and D-mannose can be found essentially in the hexopyranose form in aqueous solutions. The various configurations and their percentage in solution are depicted in Fig. 2.70. Contrary to the pentopyranoses, the conformational fluctuation of the hexopyranoses with respect to ring inversion between 4C_1 and 1C_4 is frozen to the conformer that bears the terminal hydroxymethyl function in the equatorial position. For Pd-en and Pd-chxn, palladium(II) chelation by the hexoses has been well investigated and several facts are known.^[36-37, 39] There is a preference for the participation of the most acidic, anomeric hydroxy group to the chelate rings. With the exception of mannose, chelates that leave O1 unbonded are minor species. Further, *cis*-vicinal chelation is always preferred to *trans*-vicinal chelation. Finally, the hexoses not only provide the pyranose form for metalation, but both *cis*- $\kappa O^{1,2}$ - and *cis*- $\kappa O^{1,3}$ -furanose chelation are also observed. Most of the metalated species have been characterized, so the assignment of ${}^{13}C$ signals is supported by the former results.^[37]

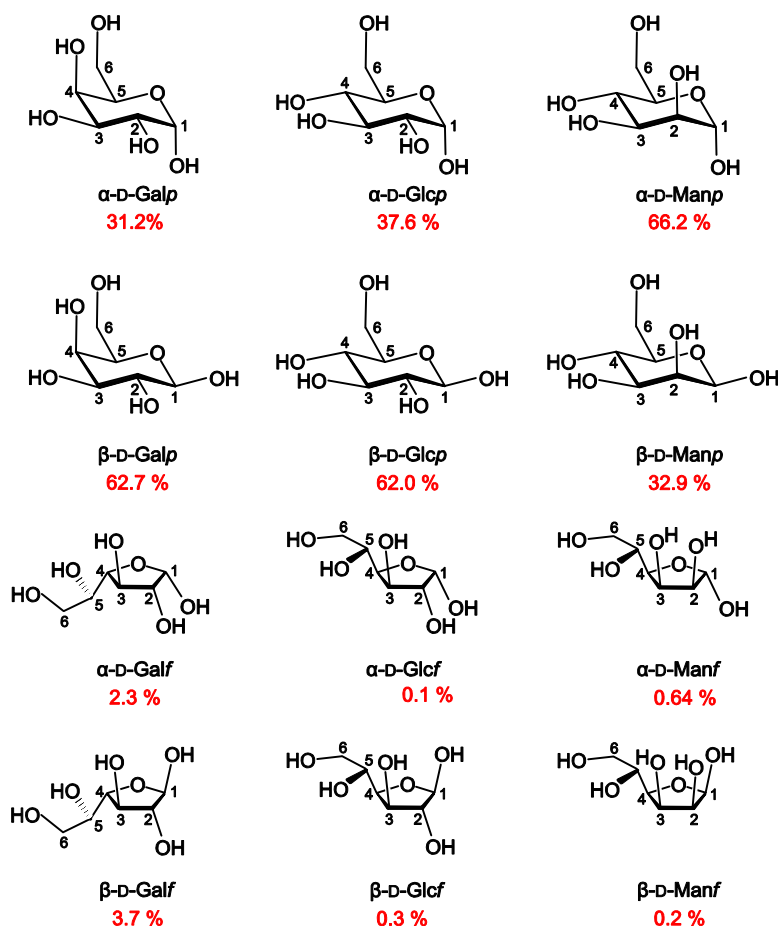


Figure 2.70. All possible configurations of the three investigated aldohexoses D-galactose (Gal), D-glucose (Glc) and D-mannose (Man). The percentages of the various cyclic forms of D-[${}^{13}C$]aldohexoses were determined at 30 °C in D_2O .^[14]

2 Results

2.10.1 D-Galactose

According to Fig. 2.70 the β -D-galactopyranose configuration is the main species in aqueous solutions of D-galactose. It is noteworthy that both furanose forms of D-galactose can be detected in the ^{13}C NMR spectra without enriching the ^{13}C isotopes. So it was interesting to identify metalated furanose forms as the main species at various Pd-tmen/D-Gal ratios. The ^{13}C NMR spectra of equimolar and 3:1 molar ratio of Pd-tmen/D-Gal are depicted in Fig. 2.71.

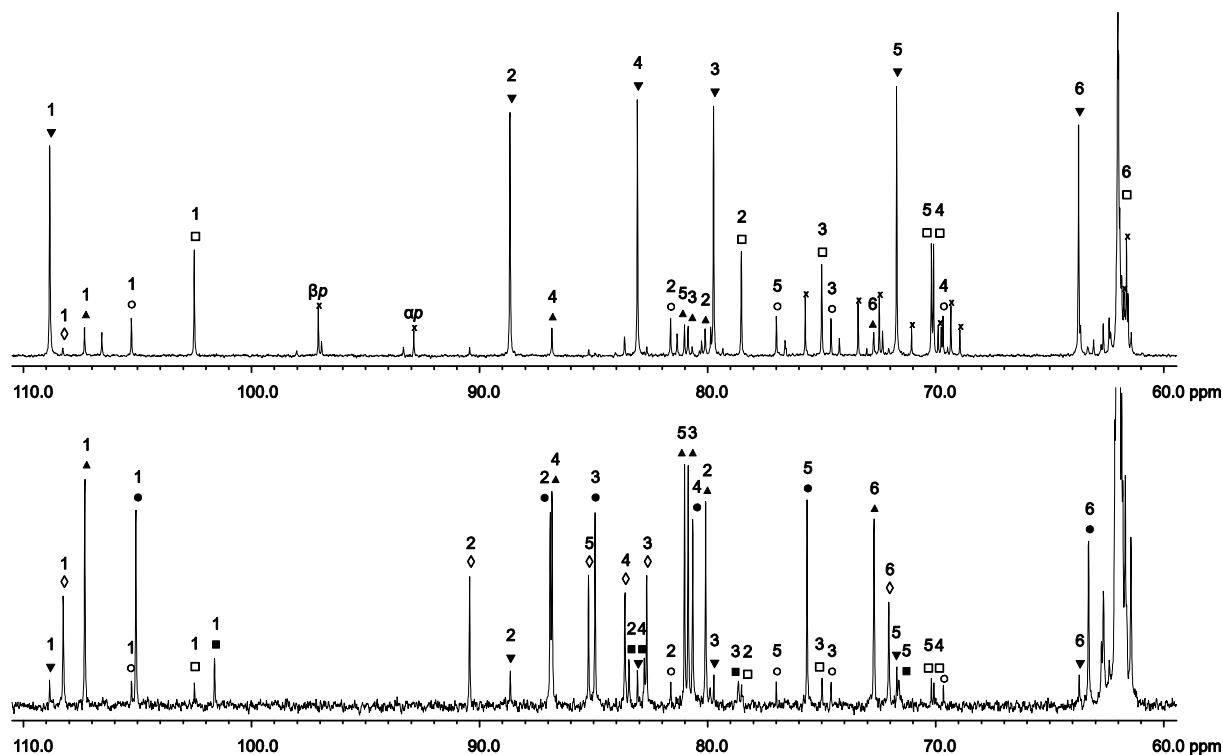


Figure 2.71. ^{13}C NMR spectra of D-galactose in Pd-tmen at a molar Pd/Gal ratio of 1:1 (top) and 3:1 (bottom). The signals of free D-galactose are marked with (x); (□) α -D-Galp1,2H₂-κO^{1,2}, (■) α -D-Galp1,2,3,4H₄-κO^{1,2}:κO^{3,4}, (○) β -D-Galp1,2H₂-κO^{1,2}, (●) β -D-Galp1,2,3,4H₄-κO^{1,2}:κO^{3,4}, (▼) α -D-Galf1,2H₂-κO^{1,2}, (◇) α -D-Galf1,2,5,6H₄-κO^{1,2}:κO^{5,6} and (▲) β -D-Galf1,3,5,6H₄-κO^{1,3}:κO^{5,6}.

Even at an equimolar Pd-tmen/D-Gal ratio, the α -D-Galf1,2H₂-κO^{1,2} species was the main product in solution, whereas the former main β -D-galactopyranose species was only metalated for 7% due to *trans*-vicinal chelation. Instead, the *cis*-vicinal coordinated β -D-Galp1,2H₂-κO^{1,2} was found at higher amounts. At higher Pd-tmen/D-Gal ratios, β -D-Galf1,3,5,6H₄-κO^{1,3}:κO^{5,6} became the main species. The structure of [Pd₂(en)₂(β -D-Galf1,3,5,6H₄-κO^{1,3}:κO^{5,6})]^[39] revealed a hydrogen bond O2–H \cdots O5 stabilizing this bonding mode and explaining the high formation tendency against α -D-Galf1,2,5,6H₄-κO^{1,2}:κO^{5,6}. All detected species are pictured together in Fig. 2.72.

2 Results

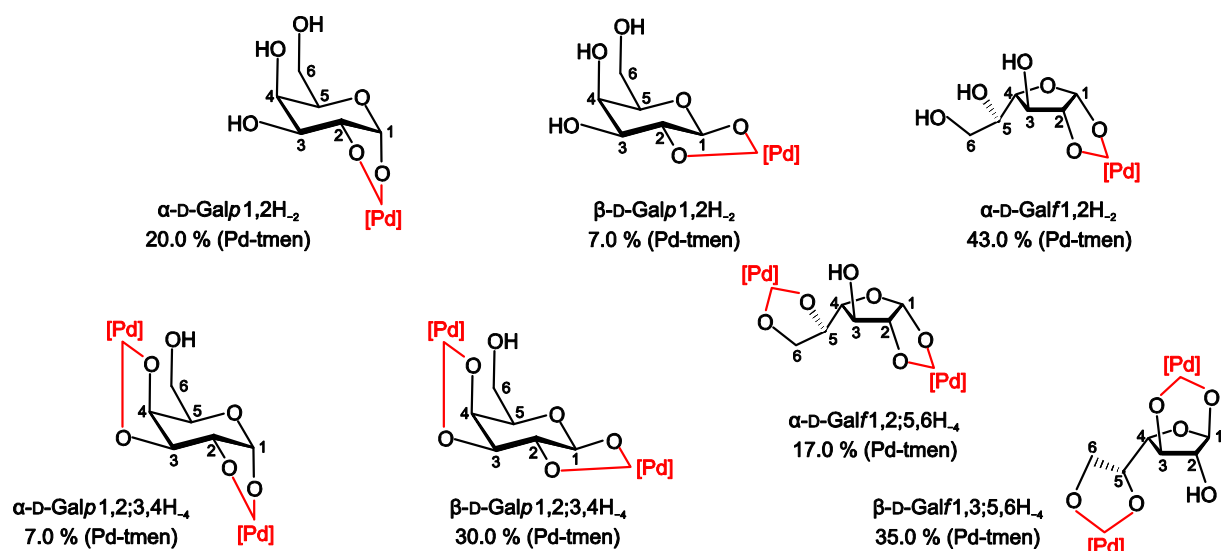


Figure 2.72. Species detected in solutions of Pd-tmen and D-galactose at different molar ratios (proportional distribution of species refer to a molar Pd/Gal ratio of 1:1 for monometalated and to 3:1 for dimetalated species, see ¹³C NMR spectra in Fig. 2.71).

The corresponding ¹³C NMR chemical shifts and shift differences are listed in Table 2.70. It should be noted that C3 showed a high CIS even without coordination of a Pd(tmen) fragment, especially for α -D-Galf1,2;5,6H₄-κO^{1,2}:κO^{5,6}. The detected ³J_{H,H} coupling constants are summed up in Table 2.71.

Table 2.70. ¹³C NMR chemical shifts (δ/ppm) and shift differences (Δδ) to the free hexose of D-galactose ligands in Pd-tmen. Atoms are numbered as in Fig. 2.72.

		C1	C2	C3	C4	C5	C6	Chelate
α -D-Galp1,2H ₂	δ	102.5	78.5	75.0	70.1	70.2	61.8	κO ^{1,2}
	Δδ	9.6	9.5	5.2	0.2	-0.9	0.0	
β -D-Galp1,2H ₂	δ	105.3	81.6	74.6	69.7	77.0	61.6	κO ^{1,2}
	Δδ	8.2	9.1	1.2	0.3	1.2	0.0	
α -D-Galp1,2;3,4H ₄	δ	101.8	83.7	83.0	78.9	71.9	62.6	κO ^{1,2} :κO ^{3,4}
	Δδ	8.9	14.7	13.2	9.0	0.8	0.8	
β -D-Galp1,2;3,4H ₄	δ	105.3	87.1	85.1	80.9	75.8	63.5	κO ^{1,2} :κO ^{3,4}
	Δδ	8.2	14.6	11.7	11.5	0.0	1.9	
α -D-Galf1,2H ₂	δ	108.9	88.7	79.7	83.1	71.7	63.7	κO ^{1,2}
	Δδ	13.3	11.8	4.9	1.8	-0.7	0.6	
α -D-Galf1,2;5,6H ₄	δ	108.5	90.6	82.9	83.8	85.4	72.3	κO ^{1,2} :κO ^{5,6}
	Δδ	12.9	13.7	8.1	2.5	13.0	9.2	
β -D-Galf1,3;5,6H ₄	δ	107.5	80.3	81.1	87.0	81.2	72.9	κO ^{1,3} :κO ^{5,6}
	Δδ	5.9	-1.6	4.8	4.5	9.9	9.6	

2 Results

Table 2.71. Experimental $^3J_{\text{H,H}}$ values in Hz for the metalated species of D-galactose in Pd-tmen.

	$^3J_{\text{H1,H2}}$	$^3J_{\text{H2,H3}}$	$^3J_{\text{H3,H4}}$	$^3J_{\text{H4,H5}}$	$^3J_{\text{H5,H6}}$	$^3J_{\text{H5,H6}}$	Conformation
α -D-Galp1,2H ₋₂	3.9	9.1	3.3	1.7	6.3	6.3	4C_1
β -D-Galp1,2H ₋₂	7.6	9.9	–	–	–	–	4C_1
α -D-Galp1,2;3,4H ₋₄	3.4	–	–	–	–	–	4C_1
β -D-Galp1,2;3,4H ₋₄	7.6	9.0	4.4	1.2	–	–	4C_1
α -D-Galf1,2H ₋₂	3.3	4.4	4.4	2.4	6.4	6.5	–
α -D-Galf1,2;5,6H ₋₄	3.9	5–6	5–6	–	6.3	–	–
β -D-Galf1,3;5,6H ₋₄	>1	1.5–2	1.5–2	1.5–2	3.7	10.0	E_{C2}

The 4C_1 conformation of the various metalated pyranose compounds was confirmed by the approximately 9 Hz of the $^3J_{\text{H2,H3}}$ coupling constants. The furanoses' conformation couldn't be determined unambiguously. Remembering the dynamic puckering of the furanose ring, it is generally hard to fix a single conformation. β -D-Galf1,3;5,6H₋₄- $\kappa O^{1,3}:\kappa O^{5,6}$ was an exception because $\kappa O^{1,3}$ -chelation of the furanose ring enforced the E_{C2} conformation. Without further stabilizing factors such as $\kappa O^{1,3}$ -chelation or intramolecular hydrogen bonds, the coupling constants of the remaining α -D-galactofuranose species were disputable. In consequence, no conformation could be determined for the α -D-galactofuranoses' furanose ring.

2.10.2 D-Glucose

In aqueous solutions of D-glucose only the pyranose forms could be detected, with the β -glucopyranose dominating the α -anomer (see Fig. 2.70). In equimolar solutions of D-glucose in Pd-tmen, the *cis*-vicinal coordinated α -D-Glcp1,2H₋₂- $\kappa O^{1,2}$ was the main species and the *trans*-vicinal coordinated β -D-Glcp1,2H₋₂- $\kappa O^{1,2}$ only the minor species (Fig. 2.73). In comparison with D-galactose, the α -D-Glcf1,2H₋₂- $\kappa O^{1,2}$ species was formed only at 6%. Conversely, at higher Pd-tmen/D-Glc ratios the dimetallated species of α -D-Glcf1,2;5,6H₋₄- $\kappa O^{1,2}:\kappa O^{5,6}$ and β -D-Glcp1,2;3,4H₋₄- $\kappa O^{1,2}:\kappa O^{3,4}$ were found at equal portions, α -D-Glcp1,2;3,4H₋₄- $\kappa O^{1,2}:\kappa O^{3,4}$ built a minor species. The various species and their proportional distribution are shown in Fig. 2.74. It is conspicuous that no $\kappa O^{1,3}$ -coordinated furanose form was detected. This fact underlined the importance of intramolecular hydrogen bonds. The corresponding ^{13}C NMR chemical shifts and shift differences are listed in Table 2.72. For the calculation of the D-glucofuranose compounds' shift differences, only C1 NMR shift values are available.^[14] Therefore, the C2–C6 NMR shift values of the methyl D-glucofuranoses were used for proximity.^[83]

2 Results

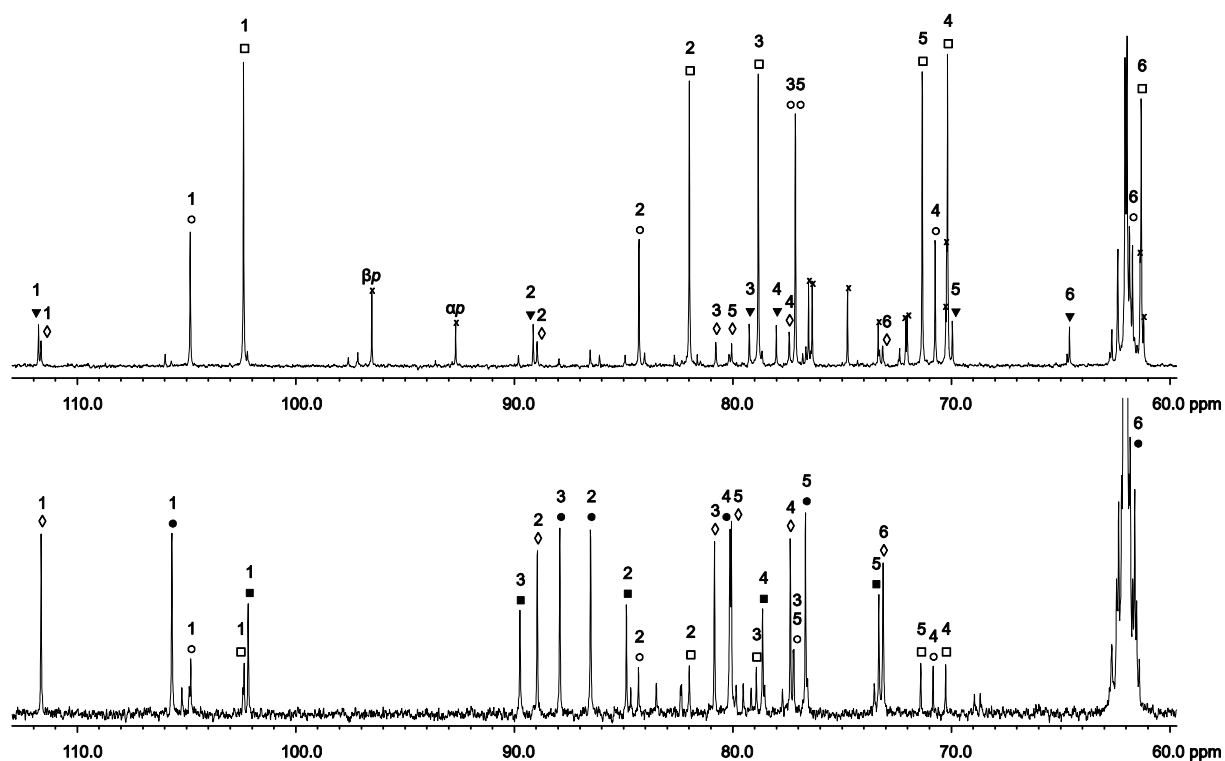


Figure 2.73. ^{13}C NMR spectra of D-glucose in Pd-tmen at a molar Pd/Glc ratio of 1:1 (top) and 3:1 (bottom). The signals of free D-glucose are marked with (x); (\square) α -D-Glcp1,2H₂-κO^{1,2}, (\blacksquare) α -D-Glcp1,2,3,4H₄-κO^{1,2}:κO^{3,4}, (\circ) β -D-Glcp1,2H₂-κO^{1,2}, (\bullet) β -D-Glcp1,2,3,4H₄-κO^{1,2}:κO^{3,4}, (\blacktriangledown) α -D-Glcf1,2H₂-κO^{1,2} and (\diamond) α -D-Glcf1,2,5,6H₄-κO^{1,2}:κO^{5,6}.

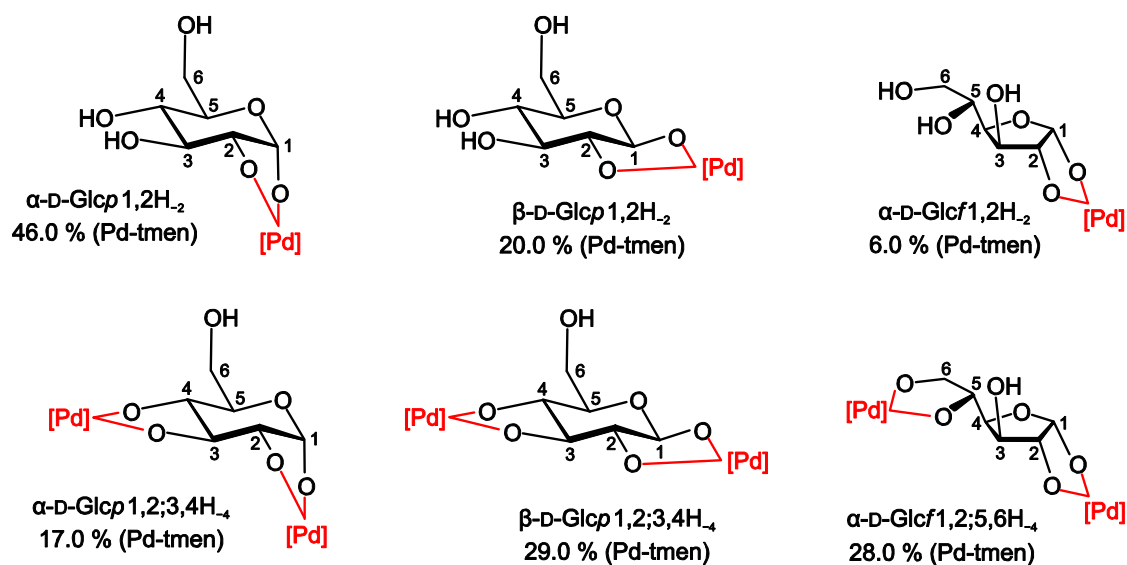


Figure 2.74. Species detected in solutions of Pd-tmen and D-glucose at different molar ratios (proportional distribution of species refer to a molar Pd/Glc ratio of 1:1 for monometalated and to 3:1 for dimetalated species, see ^{13}C NMR spectra in Fig. 2.73).

2 Results

Table 2.72. ^{13}C NMR chemical shifts (δ /ppm) and shift differences ($\Delta\delta$) to the free hexose of D-glucose ligands in Pd-tmen. Atoms are numbered as in Fig. 2.74.

		C1	C2	C3	C4	C5	C6	Chelate
α -D-Glcp1,2H ₋₂	δ	102.4	82.0	78.8	70.2	71.3	61.3	
	$\Delta\delta$	9.7	9.9	5.4	0.0	-0.7	0.1	$\kappa\text{O}^{1,2}$
β -D-Glcp1,2H ₋₂	δ	104.8	84.3	77.1	70.7	77.1	61.8	
	$\Delta\delta$	8.2	9.6	0.7	0.4	0.5	0.4	$\kappa\text{O}^{1,2}$
α -D-Glcp1,2;3,4H ₋₄	δ	102.2	84.9	89.7	78.6	73.3	–	
	$\Delta\delta$	9.5	12.8	16.3	8.4	1.3	–	$\kappa\text{O}^{1,2};\kappa\text{O}^{3,4}$
β -D-Glcp1,2;3,4H ₋₄	δ	105.7	86.5	87.9	80.1	76.7	–	
	$\Delta\delta$	9.1	11.8	11.5	9.8	0.1	–	$\kappa\text{O}^{1,2};\kappa\text{O}^{3,4}$
α -D-Glcf1,2H ₋₂	δ	111.8	89.1	79.3	78.0	70.0	64.6	
	$\Delta\delta$	(14.4)	(10.9)	(2.2)	(-1.3)	(-1.2)	(-0.1)	$\kappa\text{O}^{1,2}$
α -D-Glcf1,2;5,6H ₋₄	δ	111.7	89.0	80.8	77.4	80.1	73.1	
	$\Delta\delta$	(14.3)	(10.8)	(3.7)	(-1.9)	(8.9)	(8.4)	$\kappa\text{O}^{1,2};\kappa\text{O}^{5,6}$

The $^3J_{\text{H,H}}$ coupling constants in Table 2.73 confirmed the postulated $^4\text{C}_1$ conformation for all pyranose compounds. The coupling constants of the *trans*-vicinal protons β -H1, H2, H3 and H4 were all in a range of 8–10 Hz which was expected for the $^4\text{C}_1$ conformation. As mentioned for the metalated D-galactofuranoses, the dynamic puckering of the furanose ring complicated the determination of a conformation. Nevertheless, 1.6 Hz was a very low value detected for the $^3J_{\text{H}_2,\text{H}_3}$ constant of two *trans*-vicinal protons. Therefore, the angle of the two protons should be close to 90° and, in consequence, the conformation could be limited to a range between $^{\text{C}^3}\text{T}_{\text{C}4}$ and $E_{\text{C}4}$.

Table 2.73. Experimental $^3J_{\text{H,H}}$ values in Hz for the metalated species of D-glucose in Pd-tmen.

	$^3J_{\text{H}_1,\text{H}_2}$	$^3J_{\text{H}_2,\text{H}_3}$	$^3J_{\text{H}_3,\text{H}_4}$	$^3J_{\text{H}_4,\text{H}_5}$	$^3J_{\text{H}_5,\text{H}_6}$	$^3J_{\text{H}_5,\text{H}_6'}$	Conformation
α -D-Glcp1,2H ₋₂	3.9	8.7	9.0	9.7	2.5	5.2	$^4\text{C}_1$
β -D-Glcp1,2H ₋₂	7.5	9.5	8.8	9.8	2.2	5.7	$^4\text{C}_1$
α -D-Glcp1,2;3,4H ₋₄	4.1	8.8	9.1	9.7	2.6	5.5	$^4\text{C}_1$
β -D-Glcp1,2;3,4H ₋₄	7.3	9.1	9.1	9.5	2.5	6.8	$^4\text{C}_1$
α -D-Glcf1,2;5,6H ₋₄	3.1	1.6	3.4	6.8	4.0	5.9	$^{\text{C}^3}\text{T}_{\text{C}4}-E_{\text{C}4}$

2.10.3 D-Mannose

In contrast to D-galactose and D-glucose, the α -pyranose is the main species in aqueous solutions of D-mannose. Furthermore, in equimolar solutions of Pd-tmen/D-Man the main species α -D-Manp2,3H₋₂- $\kappa\text{O}^{2,3}$ is the only hexopyranose species leaving the O1 unbonded.

2 Results

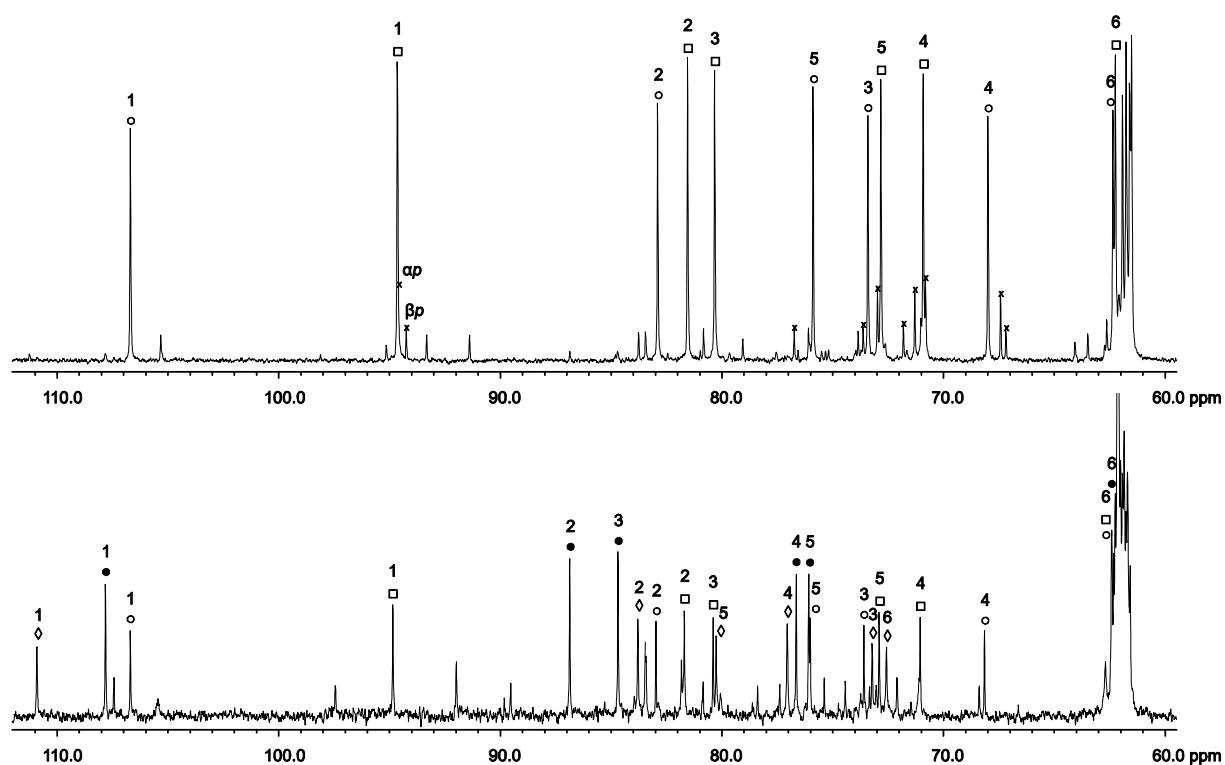


Figure 2.75. ^{13}C NMR spectra of D-mannose in Pd-tmen at a molar Pd/Man ratio of 1:1 (top) and 3:1 (bottom). The signals of free D-mannose are marked with (x); (\square) α -D-Man $p2,3\text{H}_2$ - $\kappa\text{O}^{2,3}$, (\circ) β -D-Man $p1,2\text{H}_2$ - $\kappa\text{O}^{1,2}$, (\bullet) β -D-Man $p1,2;3,4\text{H}_4$ - $\kappa\text{O}^{1,2}:\kappa\text{O}^{3,4}$ and (\diamond) β -D-Man $f1,2;5,6\text{H}_4$ - $\kappa\text{O}^{1,2}:\kappa\text{O}^{5,6}$.

Only the β -D-Man $p1,2\text{H}_2$ was able to bond a Pd(tmen) fragment by $\kappa\text{O}^{1,2}$ -chelation. Comparing the ^{13}C NMR spectra in Fig. 2.75, one could see high amounts of monometalated species even at a molar Pd-tmen/D-Man ratio of 3:1. Additionally, two dimetalated species were detected, β -D-Man $p1,2;3,4\text{H}_4$ - $\kappa\text{O}^{1,2}:\kappa\text{O}^{3,4}$ and β -D-Man $f1,2;5,6\text{H}_4$ - $\kappa\text{O}^{1,2}:\kappa\text{O}^{5,6}$. The *trans*-positioned hydroxy groups of C1 and C2 prevented not only the monometalated α -D-Man $p1,2\text{H}_2$ - $\kappa\text{O}^{1,2}$ but also the dimetalated α -D-Man $p1,2;3,4\text{H}_4$ - $\kappa\text{O}^{1,2}:\kappa\text{O}^{3,4}$ species.

Table 2.74. ^{13}C NMR chemical shifts (δ /ppm) and shift differences ($\Delta\delta$) to the free hexose of D-mannose ligands in Pd-tmen. Atoms are numbered as in Fig. 2.76.

		C1	C2	C3	C4	C5	C6	Chelate
α -D-Man $p2,3\text{H}_2$	δ	94.7	81.6	80.4	71.0	72.9	62.3	
	$\Delta\delta$	0.0	10.3	9.6	3.5	-0.1	0.7	$\kappa\text{O}^{2,3}$
β -D-Man $p1,2\text{H}_2$	δ	106.7	83.0	73.5	68.0	75.9	62.4	
	$\Delta\delta$	12.4	11.2	-0.2	0.8	-0.9	0.8	$\kappa\text{O}^{1,2}$
β -D-Man $p1,2;3,4\text{H}_4$	δ	107.9	86.9	84.7	76.1	76.6	62.3	
	$\Delta\delta$	13.6	15.1	11.0	8.9	-0.2	0.7	$\kappa\text{O}^{1,2}:\kappa\text{O}^{3,4}$
β -D-Man $f1,2;5,6\text{H}_4$	δ	110.9	83.8	73.1	77.0	80.4	72.6	
	$\Delta\delta$	(14.7)	(10.2)	(1.4)	(-4.2)	(8.9)	(7.7)	$\kappa\text{O}^{1,2}:\kappa\text{O}^{5,6}$

2 Results

The ^{13}C NMR chemical shifts and shift differences of the various metalated compounds are summarized in Table 2.74. For the calculation of the $\beta\text{-D-Manp}1,2;5,6\text{H}_{-4}\text{-}\kappa\text{O}^{1,2}:\kappa\text{O}^{5,6}$ species' shift differences, only the C1 NMR shift value was available.^[14] Therefore, the C2–C6 NMR shift values of the methyl $\beta\text{-D-mannofuranose}$ were used for proximity.^[83] The given proportional distribution of species in Fig. 2.76 referred to a molar Pd-tmen/D-Man ratio of 1:1 for monometalated and to 3:1 ratio for dimetalated species. Whereas the remaining 15% of the equimolar conversion was assigned to free D-mannopyranose, there was still 25% of $\alpha\text{-D-Manp}2,3\text{H}_{-2}\text{-}\kappa\text{O}^{2,3}$ and 20% of $\beta\text{-D-Manp}1,2\text{H}_{-2}\text{-}\kappa\text{O}^{1,2}$ at the 3:1 conversion (see Fig. 2.75).

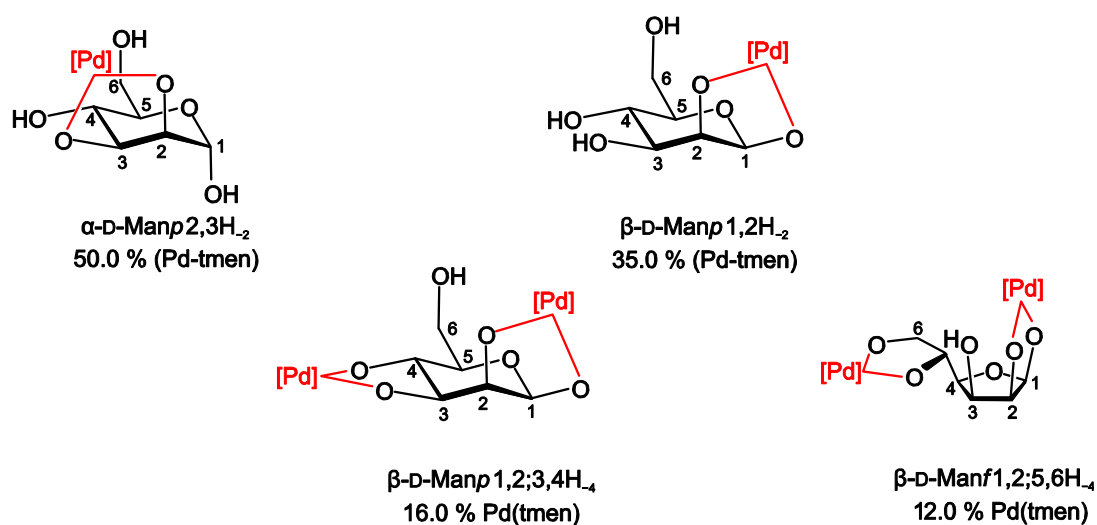


Figure 2.76. Species detected in solutions of Pd-tmen and D-mannose at different molar ratios (proportional distribution of species refer to a molar Pd/Man ratio of 1:1 for monometalated and to 3:1 for dimetalated species, see ^{13}C NMR spectra in Fig. 2.75).

Table 2.75. Experimental $^3J_{\text{H,H}}$ values in Hz for the metalated species of D-mannose in Pd-tmen.

	$^3J_{\text{H1,H2}}$	$^3J_{\text{H2,H3}}$	$^3J_{\text{H3,H4}}$	$^3J_{\text{H4,H5}}$	$^3J_{\text{H5,H6}}$	$^3J_{\text{H5,H6}'}$	Conformation
$\alpha\text{-D-Manp}2,3\text{H}_{-2}$	1.6	4.1	8.8	9.8	—	—	$^4\text{C}_1$
$\beta\text{-D-Manp}1,2\text{H}_{-2}$	1.4	3.6	9.7	9.7	2.5	6.0	$^4\text{C}_1$
$\beta\text{-D-Manp}1,2;3,4\text{H}_{-4}$	1.3	2.9	10.2	9.2	2.8	6.3	$^4\text{C}_1$

As for the other two hexoses, the $^3J_{\text{H,H}}$ coupling constants in Table 2.75 confirmed the postulated $^4\text{C}_1$ conformation for all pyranose compounds. The coupling constants of the *trans*-vicinal protons H3, H4 and H5 were all in a range of 8–10 Hz which was expected for the $^4\text{C}_1$ conformation.

2.11 The difficult determination of the palladium(II)–hexulose complexes

The equilibrium compositions of the four ketoses D-fructose, D-psicose, L-sorbose and D-tagatose differ substantially from that of the aldoses. Whereas the aldoses essentially form the α - and β -pyranoses, the ketoses show a different behavior in aqueous solution. L-sorbose almost exclusively provides the α -pyranose form, D-fructose, above all, exists in the β -pyranose form with a minor share of the β -furanose form. For D-tagatose and D-psicose both the pyranose and the furanose forms can be detected in solution, the α -pyranose dominating the ^{13}C spectrum of D-tagatose. Finally, D-psicose shows almost equidistribution of species with a tendency towards α -D-psicofuranose. Fig. 2.77 gives an overall view on the hexuloses' species and their proportional distribution in aqueous solution.

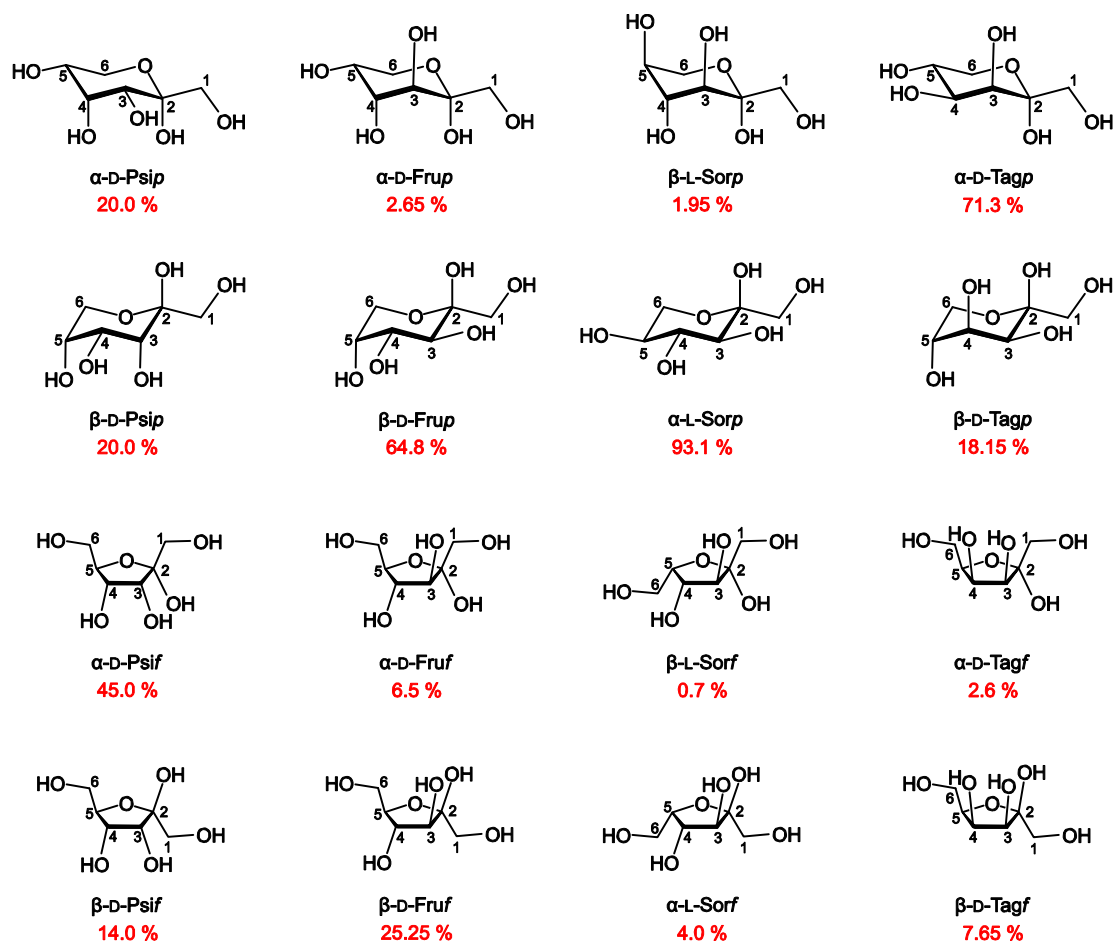


Figure 2.77. All possible configurations of the four ketoses D-psicose (Psi), D-fructose (Fru), L-sorbose (Sor) and D-tagatose (Tag). The proportional distribution of the various cyclic forms of the hexuloses were determined in D_2O at 31 °C (temperature for D-psicose not known).^[84-85]

In fact, the presence of two substituents on the carbon atom C2 alters the interactions in comparison to those found in the aldoses. Summarizing the facts, equatorially oriented hydroxy groups are preferred to axially oriented ones. Furthermore, the hydroxymethyl group

2 Results

is always oriented equatorially. In consequence, with the ketoses, the hydroxy group at C2 is constantly oriented axially. Now, looking at α -L-sorbopyranose which is the most favorable ketoses' pyranose form, all substituents are oriented equatorially except the hydroxy group at C2. In comparison, the axially oriented hydroxy group at C3 of the α -D-tagatopyranose decreases the share of this form in equilibrium because the *gauche* interaction between O3 and the rotating hydroxymethyl group increases. Also, for the ketofuranoses, the more stable form is the one in which O2 and O3 are *cis*-vicinal avoiding the greater interaction between O3 and the hydroxymethyl group. For the same reason, *trans*-orientation of the hydroxy function at C4 and the hydroxymethyl group at C5 is favored. In α -D-psicofuranose, these conditions are fulfilled resulting in the high amount of this form in solution.^[86]

Another difference from the aldoses is the missing proton at C2 which makes it difficult to assign the ^{13}C signals to the correct species and to determine the configuration of the anomers. Therefore, the differences of signal intensity for the various species become important for the assignment of matching signals. So, with the various $\text{Pd}^{\text{II}}\text{N}_2$ solvents, the composition of the solution equilibrium can be altered and several species are enriched.

2.11.1 D-Fructose

The treatment of the most common ketose D-fructose with Pd-tmen resulted in the spectra depicted in Fig. 2.78. Starting from β -D-fructopyranose in aqueous solutions, at an equimolar ratio of D-fructose in Pd-tmen, $\kappa\text{O}^{2,3}$ -chelated β -D-Fruf2,3H₂ dominated the spectrum. Increasing the ratio of Pd-tmen:Fru showed a still high amount of $\kappa\text{O}^{2,3}$ -chelated β -D-Fruf2,3H₂, whereas the two dimetalated species β -D-Frup1,2;4,5H₄- $\kappa\text{O}^{1,2}$: $\kappa\text{O}^{4,5}$ and β -D-Frup2,3;4,5H₄- $\kappa\text{O}^{2,3}$: $\kappa\text{O}^{4,5}$ were found at a minor share. As discussed in the literature,^[87] two intramolecular hydrogen bonds O6-H \cdots O3 and O1-H \cdots O4 would explain the high stability of the β -D-Fruf2,3H₂- $\kappa\text{O}^{2,3}$ species. In Pd-teen and at an equimolar ratio, two more monometalated D-fructopyranose species, which were detected in small amounts for Pd-tmen, too, could be enriched (see Fig. 2.79). Especially the $\kappa\text{O}^{4,5}$ -bonded α -D-Frup4,5H₂ form is noteworthy because in aqueous solutions the α -D-fructopyranose cannot be found. Furthermore, the $\kappa\text{O}^{2,3}$ -bonded β -D-Frup2,3H₂ form is expected to be preferred to the α -D-Frup4,5H₂- $\kappa\text{O}^{4,5}$ species. On the other hand, an intramolecular hydrogen bond O2-H \cdots O4 would explain the formation of this species. The ^{13}C NMR chemical shifts and shift differences of the detected species in Pd-tmen and Pd-teen are listed in the Tables 2.76 and 2.77.

2 Results

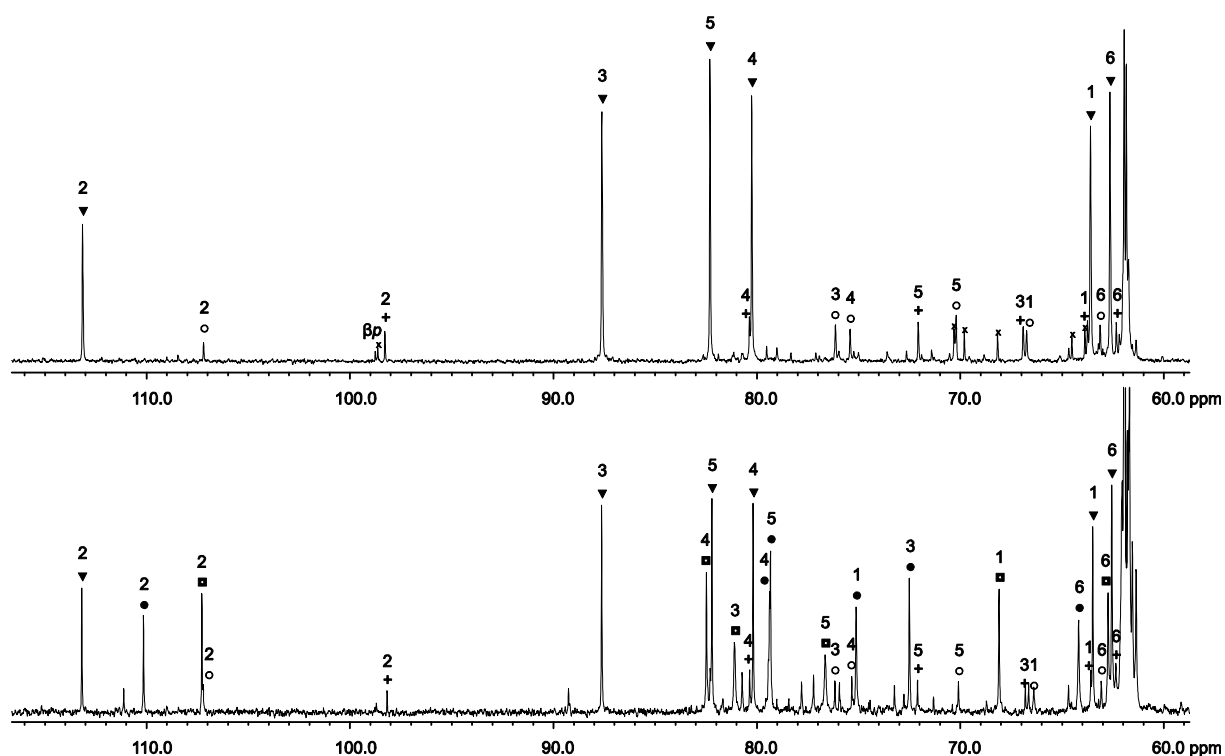


Figure 2.78. ^{13}C NMR spectra of D-fructose in Pd-tmen at a molar Pd/Fru ratio of 1:1 (top) and 2:1 (bottom). The signals of free D-fructose are marked with (x); (▼) $\beta\text{-D-Frup}2,3\text{H}_2\text{-}\kappa\text{O}^{2,3}$, (○) $\beta\text{-D-Frup}2,3\text{H}_2\text{-}\kappa\text{O}^{2,3}$, (+) $\alpha\text{-D-Frup}4,5\text{H}_2\text{-}\kappa\text{O}^{4,5}$, (●) $\beta\text{-D-Frup}1,2;4,5\text{H}_4\text{-}\kappa\text{O}^{1,2};\kappa\text{O}^{4,5}$ and (■) $\beta\text{-D-Frup}2,3;4,5\text{H}_4\text{-}\kappa\text{O}^{2,3};\kappa\text{O}^{4,5}$.

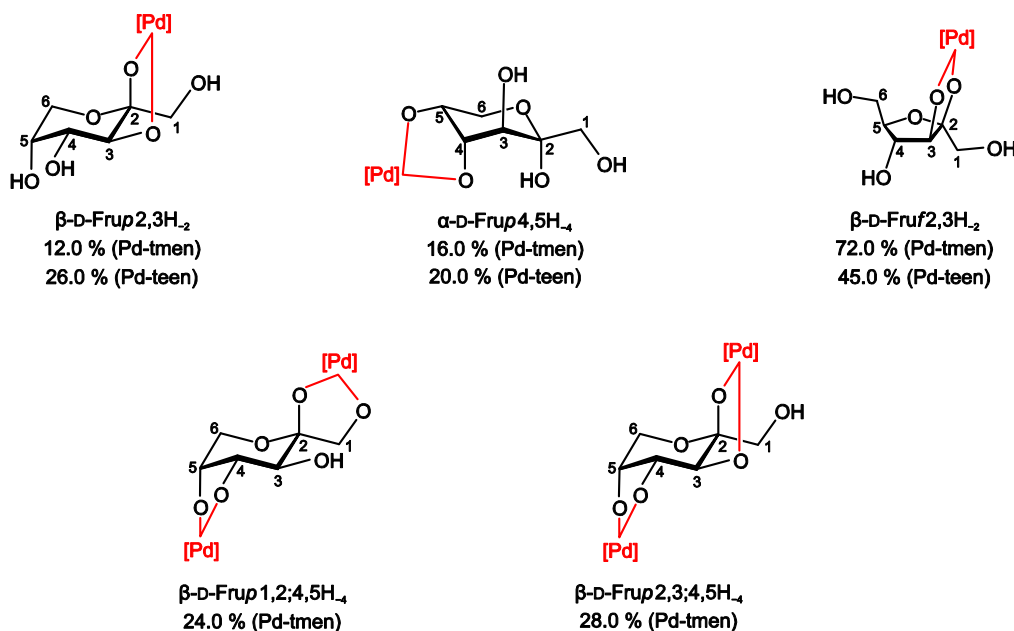


Figure 2.79. Species detected in solutions of Pd-tmen and D-fructose at various molar ratios (proportional distribution of species refer to a molar Pd/Fru ratio of 1:1 for monometalated and to 2:1 for dimetalated species, see ^{13}C NMR spectra in Fig. 2.78).

2 Results

Table 2.76. ^{13}C NMR chemical shifts (δ/ppm) and shift differences ($\Delta\delta$) to the free hexulose of D-fructose ligands in Pd-tmen. Atoms are numbered as in Fig. 2.79.

		C1	C2	C3	C4	C5	C6	Chelate
$\alpha\text{-D-Frup4,5H}_{-2}$	δ	63.8	98.3	66.7	80.4	72.1	62.3	
	$\Delta\delta$	-2.0	-0.3	-4.0	9.3	10.3	0.6	$\kappa\text{O}^{4,5}$
$\beta\text{-D-Frup2,3H}_{-2}$	δ	66.7	107.2	76.1	75.4	70.2	63.1	
	$\Delta\delta$	2.2	8.5	7.9	5.1	0.4	-0.9	$\kappa\text{O}^{2,3}$
$\beta\text{-D-Frup1,2;4,5H}_{-4}$	δ	75.3	110.3	72.7	79.5	79.5	64.4	
	$\Delta\delta$	10.8	11.6	4.5	9.2	9.7	0.4	$\kappa\text{O}^{1,2};\kappa\text{O}^{4,5}$
$\beta\text{-D-Frup2,3;4,5H}_{-4}$	δ	68.3	107.4	81.3	82.6	76.8	62.9	
	$\Delta\delta$	3.8	8.7	13.1	12.3	7.0	-1.1	$\kappa\text{O}^{2,3};\kappa\text{O}^{4,5}$
$\beta\text{-D-Fruf2,3H}_{-2}$	δ	63.6	113.1	87.6	80.3	82.3	62.6	
	$\Delta\delta$	0.3	11.0	11.6	5.2	1.0	-0.4	$\kappa\text{O}^{2,3}$

Table 2.77. ^{13}C NMR chemical shifts (δ/ppm) and shift differences ($\Delta\delta$) to the free hexulose of D-fructose ligands in Pd-teen. Atoms are numbered as in Fig. 2.79.

		C1	C2	C3	C4	C5	C6	Chelate
$\alpha\text{-D-Frup4,5H}_{-2}$	δ	63.7	98.3	66.8	81.1	72.3	62.4	
	$\Delta\delta$	-2.1	-0.3	-3.9	10.0	10.5	0.7	$\kappa\text{O}^{4,5}$
$\beta\text{-D-Frup2,3H}_{-2}$	δ	66.8	107.8	76.1	75.2	70.3	63.2	
	$\Delta\delta$	2.3	9.1	7.9	4.9	0.5	-0.8	$\kappa\text{O}^{2,3}$
$\beta\text{-D-Fruf2,3H}_{-2}$	δ	63.6	113.3	87.3	79.8	82.2	62.9	
	$\Delta\delta$	0.3	11.2	11.3	4.7	0.9	-0.1	$\kappa\text{O}^{2,3}$

Table 2.78. Experimental $^3J_{\text{H,H}}$ values in Hz for the metalated species of D-fructose in Pd-tmen.

	$^2J_{\text{H1,H1}'}$	$^3J_{\text{H3,H4}}$	$^3J_{\text{H4,H5}}$	$^3J_{\text{H5,H6}}$	$^3J_{\text{H5,H6}'}$	$^2J_{\text{H6,H6}'}$	Conformation
$\beta\text{-D-Fruf2,3H}_{-2}$	12.1	6.5	6.5	–	–	–	–
$\beta\text{-D-Frup1,2;4,5H}_{-4}$	10.2	8.7	4.2	–	–	–	$^2\text{C}_5$
$\beta\text{-D-Frup2,3;4,5H}_{-4}$	11.2	5.8	4.3	–	–	–	$^2\text{C}_5 \Leftrightarrow ^5\text{C}_2$

Table 2.79. Experimental $^3J_{\text{H,H}}$ values in Hz for the metalated species of D-fructose in Pd-teen.

	$^2J_{\text{H1,H1}'}$	$^3J_{\text{H3,H4}}$	$^3J_{\text{H4,H5}}$	$^3J_{\text{H5,H6}}$	$^3J_{\text{H5,H6}'}$	$^2J_{\text{H6,H6}'}$	Conformation
$\alpha\text{-D-Frup4,5H}_{-2}$	11.6	3.7	3.7	6.1	10.2	–	$^5\text{C}_2$
$\beta\text{-D-Frup2,3H}_{-2}$	11.2	8.9	3.5	1.2	2.1	12.4	$^2\text{C}_5$
$\beta\text{-D-Fruf2,3H}_{-2}$	12.0	6.8	6.7	2.7	3.8	11.9	–

2 Results

The $^3J_{\text{H,H}}$ coupling constants for the species in Pd-tmen and Pd-teen are summarized in the Tables 2.78 and 2.79. For the $\beta\text{-D-Fru}\alpha\text{2,3H}_{-2}$ species no conformation was determined, however, the two minor values of $^3J_{\text{H}_5,\text{H}_6}$ and $^3J_{\text{H}_5,\text{H}_6'}$ indicated the orientation of the hydroxymethyl group which is necessary for the formation of a $\text{O}_6\text{-H}\cdots\text{O}_3$ hydrogen bond. Except for the $\beta\text{-D-Fru}\alpha\text{2,3;4,5H}_{-4}$ species, the $^3J_{\text{H,H}}$ coupling constants confirmed the species in Fig. 2.79 and their conformation. A DFT calculation (for details see Section 5.8) found the $^5\text{C}_2$ conformation energetically favorable to the $^2\text{C}_5$ conformation by 9.15 kJ/mol.

2.11.2 D-Tagatose

Solving D-tagatose in Pd-tmen at an equimolar ratio, the $\alpha\text{-D-Tag}\alpha\text{1,2H}_{-2}\text{-}\kappa\text{O}^{1,2}$ species was formed almost exclusively. As discussed above, the stability of $\alpha\text{-D-tagatopyranose}$ is decreased only by the *gauche* interaction between O_3 and the rotating hydroxymethyl group. Conversely, the stability of the $\alpha\text{-D-Tag}\alpha\text{1,2H}_{-2}\text{-}\kappa\text{O}^{1,2}$ species was increased when $\kappa\text{O}^{1,2}$ -chelation fixed the hydroxymethyl group in a position opposite to O_3 . At a 2:1 ratio of Pd-tmen:Tag three dimetalated forms appeared in the ^{13}C NMR spectrum (see Fig. 2.80).

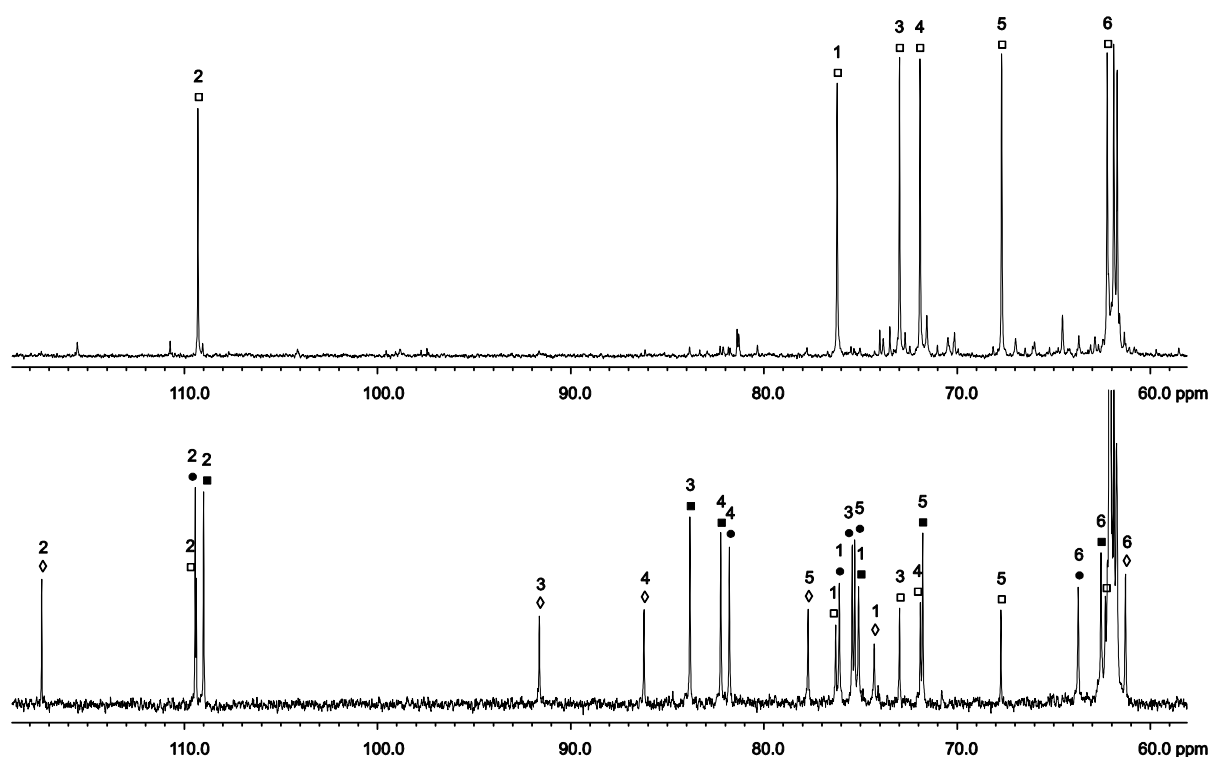


Figure 2.80. ^{13}C NMR spectra of D-tagatose in Pd-tmen at a molar Pd/Tag ratio of 1:1 (top) and 2:1 (bottom). The signals of free D-tagatose are marked with (x); (\square) $\alpha\text{-D-Tag}\alpha\text{1,2H}_{-2}\text{-}\kappa\text{O}^{1,2}$, (\bullet) $\alpha\text{-D-Tag}\alpha\text{1,2;4,5H}_{-4}\text{-}\kappa\text{O}^{1,2}\text{:}\kappa\text{O}^{4,5}$, (\blacksquare) $\alpha\text{-D-Tag}\alpha\text{1,2;3,4H}_{-4}\text{-}\kappa\text{O}^{1,2}\text{:}\kappa\text{O}^{3,4}$ and (\diamond) $\alpha\text{-D-Tag}\alpha\text{1,2;3,4H}_{-4}\text{-}\kappa\text{O}^{1,2}\text{:}\kappa\text{O}^{3,4}$.

2 Results

As one can see in Fig. 2.81, the species α -D-Tagp1,2;4,5H₄-κO^{1,2}:κO^{4,5} and α -D-Tagp1,2;3,4H₄-κO^{1,2}:κO^{3,4} were just the dimetalated forms of the monometalated κO^{1,2}-chelated α -D-Tagp1,2H₂ species. Unexpectedly, there was no favoring of *cis*- to *trans*-vicinal chelation. With the α -D-Tagf1,2;3,4H₄-κO^{1,2}:κO^{3,4} species a furanose form was also detected, and the anomer was determined in agreement with literature.^[88] Whereas the uncoordinated ketoses prefer the *cis*-vicinal orientation of O2 and O3, a *trans*-vicinal diolato unit preferably linked the two metalation sites of the depicted species.

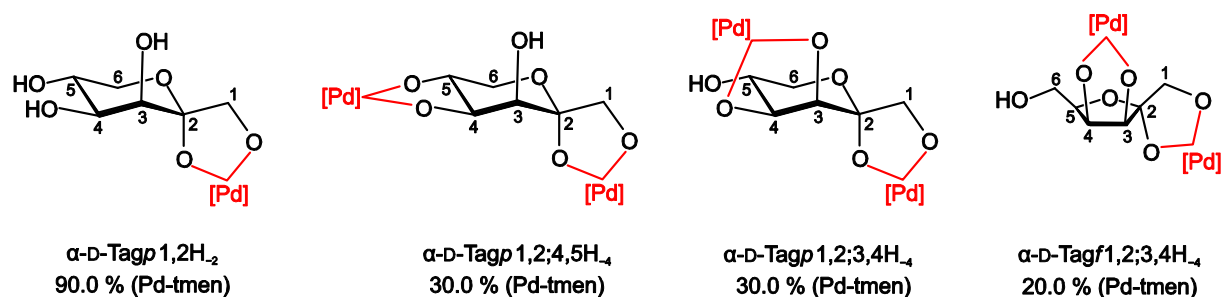


Figure 2.81. Species detected in solutions of Pd-tmen and D-tagatose at various molar ratios (proportional distribution of species refer to a molar Pd/Tag ratio of 1:1 for monometalated and to 2:1 for dimetalated species, see ¹³C NMR spectra in Fig. 2.80).

The ¹³C NMR chemical shifts and shift differences of the detected species are given in Table 2.80, the ³J_{H,H} coupling constants in Table 2.81.

Table 2.80. ¹³C NMR chemical shifts (δ/ppm) and shift differences (Δδ) to the free hexulose of D-tagatose ligands in Pd-tmen. Atoms are numbered as in Fig. 2.81.

		C1	C2	C3	C4	C5	C6	Chelate
α -D-Tagp1,2H ₂	δ	76.2	109.3	73.0	71.9	67.7	62.2	
	Δδ	11.7	10.5	2.6	0.4	0.7	-0.6	κO ^{1,2}
α -D-Tagp1,2;3,4H ₄	δ	75.1	109.0	83.8	82.2	71.8	62.6	
	Δδ	10.6	10.2	13.4	10.7	4.8	-0.2	κO ^{1,2} :κO ^{3,4}
α -D-Tagp1,2;4,5H ₄	δ	76.1	109.4	75.4	81.8	75.3	63.7	
	Δδ	11.6	10.6	5.0	10.3	8.3	0.9	κO ^{1,2} :κO ^{4,5}
α -D-Tagf1,2;3,4H ₄	δ	74.3	117.4	91.6	86.2	77.7	61.3	
	Δδ	11.3	11.8	14.3	14.4	-2.1	0.6	κO ^{1,2} :κO ^{3,4}

The ³J_{H4,H5} coupling constants of the D-tagatopyranose species obviously confirmed the ⁵C₂ conformation of the various chelation species. The α -D-Tagf1,2;3,4H₄-κO^{1,2}:κO^{3,4} species only provide *cis*-vicinal oriented protons, so the coupling constants could hardly be used to determine the conformation due to the fluctuation of the furanose ring.

2 Results

Table 2.81. Experimental $^3J_{\text{H,H}}$ values in Hz for the metalated species of D-tagatose in Pd-tmen.

	$^2J_{\text{H1,H1}'}$	$^3J_{\text{H3,H4}}$	$^3J_{\text{H4,H5}}$	$^3J_{\text{H5,H6}}$	$^3J_{\text{H5,H6}'}$	$^2J_{\text{H6,H6}'}$	Conformation
α -D-Tagp1,2H ₋₂	10.3	3.3	9.4	–	–	11.3	5C_2
α -D-Tagp1,2;3,4H ₋₄	10.2	4.0	8.7	5.7	10.7	–	5C_2
α -D-Tagp1,2;4,5H ₋₄	10.2	3.0	9.9	–	–	–	5C_2
α -D-Tagf1,2;3,4H ₋₄	10.2	4.8	5.0	2.7	3.5	12.0	–

With $[\text{Pd}_2(\text{tmen})_2(\alpha\text{-D-Tagp1,2;3,4H}_{-4}\text{-}\kappa\text{O}^{1,2}:\kappa\text{O}^{3,4})] \cdot 8 \text{H}_2\text{O}$, a metalated ketopyranose was crystallized for the first time. Solved in the space group $P 2_12_12_1$, the resulting structure is depicted in Fig. 2.82. The α -D-tagatopyranose formed an almost undistorted pyranose ring in 5C_2 conformation. The hydrogen-bond network couldn't be resolved completely but the complex molecules were ordered uniformly and linked via all four alkoxido atoms. The alkoxido atoms O1, O3 and O4 are connected each via two water molecules to their counterparts generated by symmetry; the remaining atoms possibly accepted a hydrogen bond from O5–H.

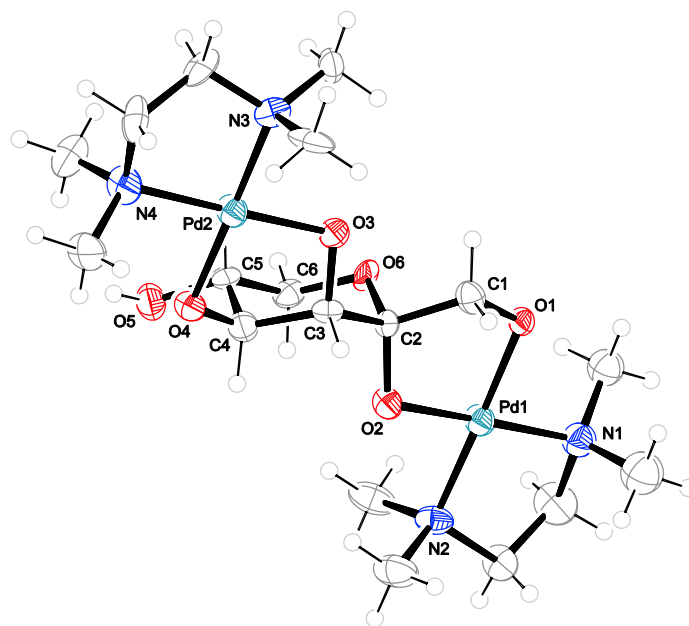


Figure 2.82: The molecular structure of $[\text{Pd}_2(\text{tmen})_2(\alpha\text{-D-Tagp1,2;3,4H}_{-4}\text{-}\kappa\text{O}^{1,2}:\kappa\text{O}^{3,4})]$ in crystals of the 8-hydrate (**39**). ORTEP plot is drawn with 50% probability ellipsoids. Interatomic distances (Å) and angles (°) (standard deviations of the last digit in parentheses): Pd1–O1 1.991(7), Pd1–O2 1.996(8), Pd1–N1 2.053(10), Pd1–N2 2.049(11), Pd2–O3 2.018(8), Pd2–O4 1.998(7), Pd2–N3 2.087(8), Pd2–N4 2.056(10), O1–Pd1–O2 84.6(3), O1–Pd1–N1 94.9(4), O2–Pd1–N2 94.2(4), N1–Pd1–N2 86.3(4), O3–Pd2–O4 85.3(3), O3–Pd2–N3 97.0(3), O4–Pd2–N4 93.0(4), N3–Pd2–N4 84.8(4); chelate torsion angles: O1–C1–C2–O2 50.1(12), O3–C3–C4–O4 –51.5(13), N1–C9–C10–N2 53.0(18), N3–C15–C16–N4 –51.3(14); puckering parameters^[22] of the pyranose ring C2–C3–C4–C5–C6–O6: $Q = 0.571(13)$ Å, $\theta = 1.2(12)^\circ$.

2 Results

2.11.3 L-Sorbose

In contrast to the three other hexuloses, only the L-enantiomer of sorbose is commercially available. At a molar 1:1 Pd-tmen: Sor ratio, three monometalated species could be detected (see Fig. 2.83). Remembering the α -L-sorbopyranose as being the most favored ketopyranose form, it was interesting to also find an high amount of the $\kappa O^{2,3}$ -chelated α -L-Sorf2,3H₂ species. Whereas $\kappa O^{1,2}$ -bonded α -D-Tagp1,2H₂ was exclusively formed supported by an axially oriented hydroxy group (O3), the α -L-Sorp1,2H₂- $\kappa O^{1,2}$ species was impaired by an equatorially oriented hydroxy group (O3). Instead, the α -L-Sorf2,3H₂- $\kappa O^{2,3}$ form became the most favored coordination species. Comparing the α -L-Sorf2,3H₂- $\kappa O^{2,3}$ species with the β -D-Fruf2,3H₂- $\kappa O^{2,3}$ a hydrogen bond O1-H...O4 possibly stabilized the furanose species.

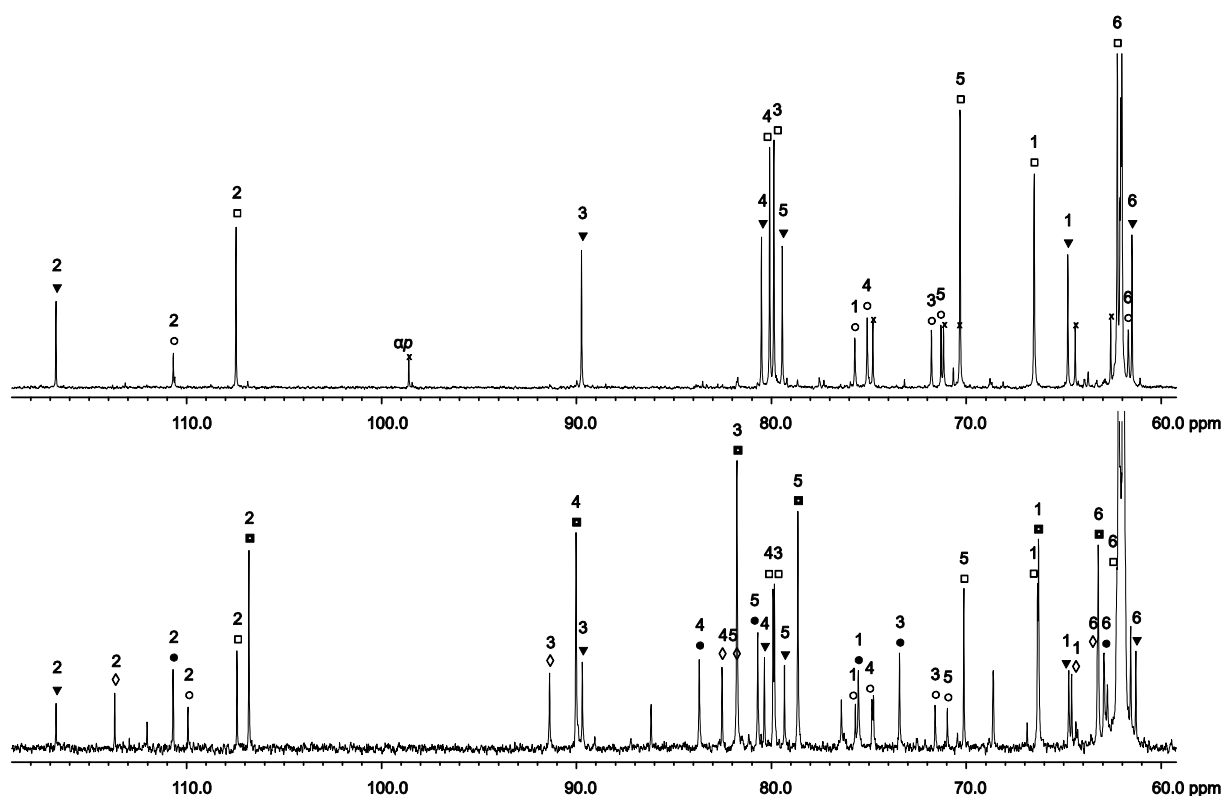


Figure 2.83. ^{13}C NMR spectra of L-sorbose in Pd-tmen at a molar Pd/Sor ratio of 1:1 (top) and 2:1 (bottom). The signals of free L-sorbose are marked with (x); (○) α -L-Sorp1,2H₂- $\kappa O^{1,2}$, (□) α -L-Sorf2,3H₂- $\kappa O^{2,3}$, (▼) α -L-Sorf2,3H₂- $\kappa O^{2,3}$, (●) α -L-Sorp1,2;4,5H₄- $\kappa O^{1,2}$: $\kappa O^{4,5}$, (■) α -L-Sorf2,3;4,5H₄- $\kappa O^{2,3}$: $\kappa O^{4,5}$ and (◇) α -L-Sorf2,3;4,6H₄- $\kappa O^{2,3}$: $\kappa O^{4,6}$.

Adding another equivalent of Pd-tmen, both α -L-sorbopyranose forms were attacked additionally at the *trans*-vicinal $\kappa O^{4,5}$ -diolato unit. With the α -L-Sorf2,3;4,6H₄- $\kappa O^{2,3}$: $\kappa O^{4,6}$ species, a rare $\kappa O^{4,6}$ -chelation was detected. All discussed species are depicted in Fig. 2.84, the ^{13}C NMR chemical shifts and shift differences are listed in Table 2.82.

2 Results

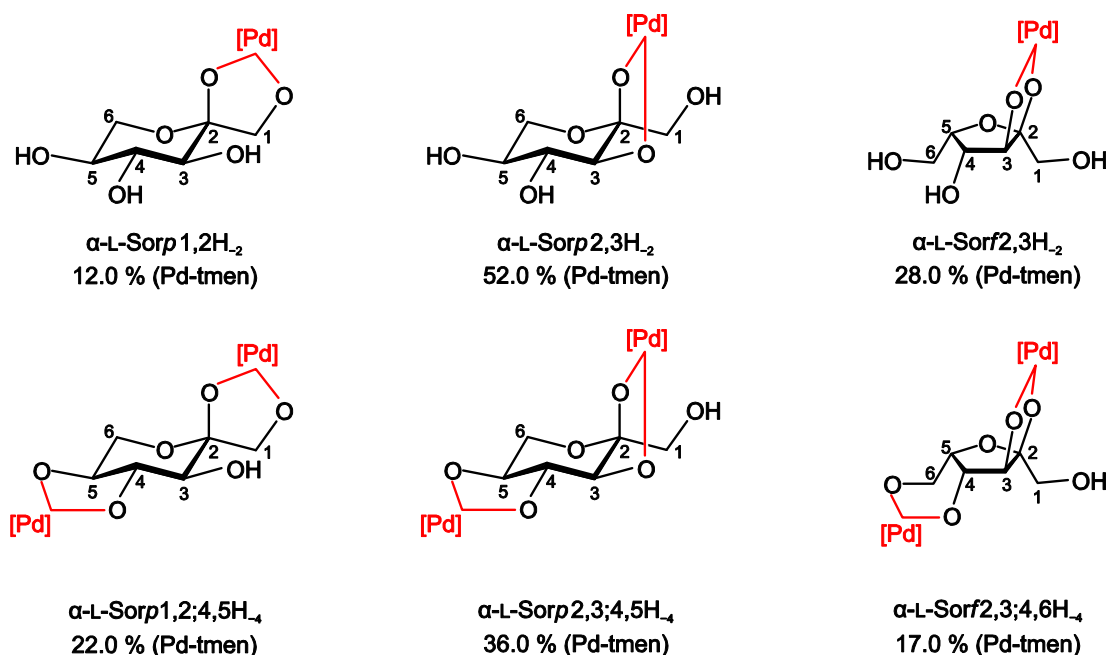


Figure 2.84. Species detected in solutions of Pd-tmen and L-sorbose at various molar ratios (proportional distribution of species refer to a molar Pd/Sor ratio of 1:1 for monometalated and to 2:1 for dimetalated species, see ¹³C NMR spectra in Fig. 2.83).

Table 2.82. ¹³C NMR chemical shifts (δ /ppm) and shift differences ($\Delta\delta$) to the free hexulose of L-sorbose ligands in Pd-tmen. Atoms are numbered as in Fig. 2.84.

		C1	C2	C3	C4	C5	C6	Chelate
α -L-Sorp1,2H ₋₂	δ	75.5	110.4	71.5	74.8	71.0	61.4	
	$\Delta\delta$	11.4	12.1	0.5	0.3	1.0	-1.0	$\kappa O^{1,2}$
α -L-Sorp2,3H ₋₂	δ	66.3	107.2	79.6	79.8	70.1	62.0	
	$\Delta\delta$	2.2	8.9	8.6	5.3	0.1	-0.4	$\kappa O^{2,3}$
α -L-Sorp1,2;4,5H ₋₄	δ	75.6	110.7	73.6	83.8	80.7	63.0	
	$\Delta\delta$	11.5	12.4	2.6	9.3	10.7	0.6	$\kappa O^{1,2};\kappa O^{4,5}$
α -L-Sorp2,3;4,5H ₋₄	δ	66.4	106.9	81.8	90.1	78.7	63.3	
	$\Delta\delta$	2.3	8.6	10.8	15.6	8.7	0.9	$\kappa O^{2,3};\kappa O^{4,5}$
α -L-Sorf2,3H ₋₂	δ	64.5	116.4	89.5	80.3	79.2	61.3	
	$\Delta\delta$	0.8	14.0	12.9	4.4	0.9	0.0	$\kappa O^{2,3}$
α -L-Sorf2,3;4,6H ₋₄	δ	65.0	113.8	91.4	82.5	81.8	63.4	
	$\Delta\delta$	1.3	11.4	14.8	6.6	3.5	2.1	$\kappa O^{2,3};\kappa O^{4,6}$

The ³J_{H,H} coupling constants given in Table 2.83 confirmed the ²C₅ conformation of all L-sorbopyranose species by the high values of ³J_{H3,H4} and ³J_{H4,H5}. Comparing the coupling constants of the α -L-Sorf2,3H₋₂ species with the constants of the α -L-Sorf2,3;4,6H₋₄ species, significant changes were obvious. Although a final determination of the furanoses'

2 Results

conformation was not possible, the low ${}^3J_{H3,H4}$ value of a *trans*-vicinal pair of protons indicated that the conformations of $E_{C3}-E_{C5}$ were of less importance for the furanose ring puckering of the α -L-Sor p 2,3H $_{-2}$ form. On the other hand, the high ${}^3J_{H4,H5}$ value of the α -L-Sor f 2,3;4,6H $_{-4}$ species pointed out the $\kappa O^{4,6}$ -chelation fixing the protons in a small torsion angle.

Table 2.83. Experimental ${}^3J_{H,H}$ values in Hz for the metalated species of L-sorbose in Pd-tmen.

	${}^2J_{H1,H1'}$	${}^3J_{H3,H4}$	${}^3J_{H4,H5}$	${}^3J_{H5,H6}$	${}^3J_{H5,H6'}$	${}^2J_{H6,H6'}$	Conformation
α -L-Sor p 1,2H $_{-2}$	10.3	9.4	–	–	–	–	2C_5
α -L-Sor p 2,3H $_{-2}$	11.4	8.4	9.2	5.2	10.5	–	2C_5
α -L-Sor p 1,2;4,5H $_{-4}$	10.3	9.6	9.6	4.9	10.5	–	2C_5
α -L-Sor p 2,3;4,5H $_{-4}$	11.3	8.3	9.5	4.7	10.4	10.5	2C_5
α -L-Sor f 2,3H $_{-2}$	11.5	2.5	4.4	4.5	6.7	–	–
α -L-Sor f 2,3;4,6H $_{-4}$	11.5	4.8	7.3	2.9	5.8	–	–

2.11.4 D-Psicose

In aqueous solutions, D-psicose shows almost equidistribution of species with a tendency towards α -D-psicofuranose. Three monometalated species were detected in Pd-tmen at an equimolar ratio, one α -D-psicopyranose and two α -D-psicofuranose forms. The detection of the $\kappa O^{2,3}$ -chelated α -D-Psi f 2,3H $_{-2}$ and $\kappa O^{3,4}$ -chelated α -D-Psi f 3,4H $_{-2}$ species was consistent with α -D-psicofuranose, being the favored D-psicose form. On the other hand, the α -D-Psi p 4,5H $_{-2}$ - $\kappa O^{4,5}$ species corresponded to the α -D-Frup4,5H $_{-2}$ - $\kappa O^{4,5}$ form and was possibly also stabilized by an intramolecular hydrogen bond O2–H \cdots O4. The $\kappa O^{1,2}$ -chelation of α -D-psicopyranose was impaired by an equatorially oriented hydroxy group (O3). At a 2:1 molar ratio of Pd-tmen/Psi two dimetalated complexes were additionally found. Whereas the $\kappa O^{4,5}$ -bonded α -D-Psi p 4,5H $_{-2}$ form was found for monometalation, the equatorial oriented hydroxy function of C3 hindered $\kappa O^{1,2}$ -chelation. Therefore the D-psicopyranose switched into the β -form to result in the β -D-Psi p 1,2;4,5H $_{-4}$ - $\kappa O^{1,2}$: $\kappa O^{4,5}$ species. This latter species corresponded to the α -D-Tag f 1,2;3,4H $_{-4}$ - $\kappa O^{1,2}$: $\kappa O^{3,4}$ form and also this anomer was determined in agreement with literature.^[89] The above discussed ${}^{13}C$ NMR spectra and all detected species are depicted in Fig. 2.85 and 2.86 and the ${}^{13}C$ NMR chemical shifts and shift differences of the detected species in Pd-tmen are listed in Table 2.84. The ${}^3J_{H,H}$ coupling constants are summed up in Table 2.85 and both described pyranose forms are confirmed by the coupling constants.

2 Results

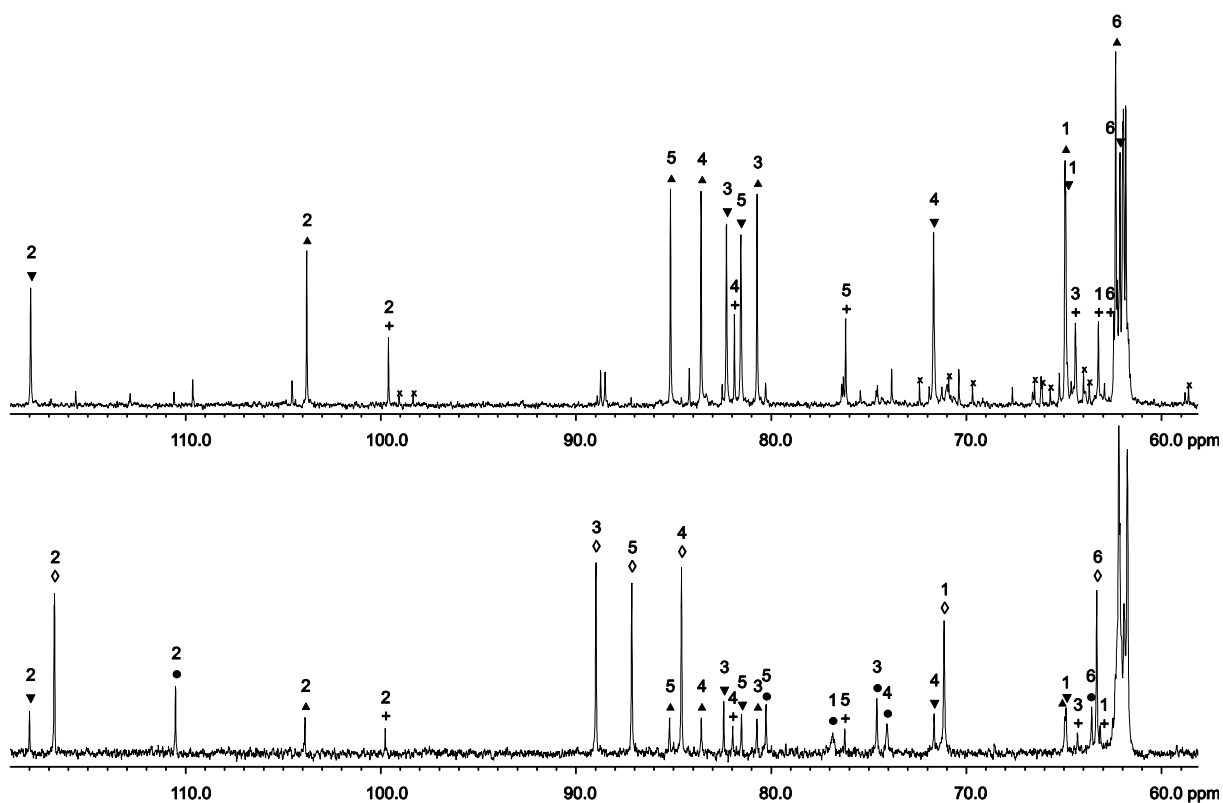


Figure 2.85. ^{13}C NMR spectra of D-psicose in Pd-tmen at a molar Pd/Psi ratio of 1:1 (top) and 2:1 (bottom). The signals of free D-psicose are marked with (x); (∇) α -D-Psif 2,3H₂- κ O^{2,3}, (\blacktriangle) α -D-Psif 3,4H₂- κ O^{3,4}, (+) α -D-Psip 4,5H₂- κ O^{4,5}, (\diamond) β -D-Psif 1,2;3,4H₄- κ O^{1,2}: κ O^{3,4} and (\bullet) β -D-Psip 1,2;4,5H₄- κ O^{1,2}: κ O^{4,5}.

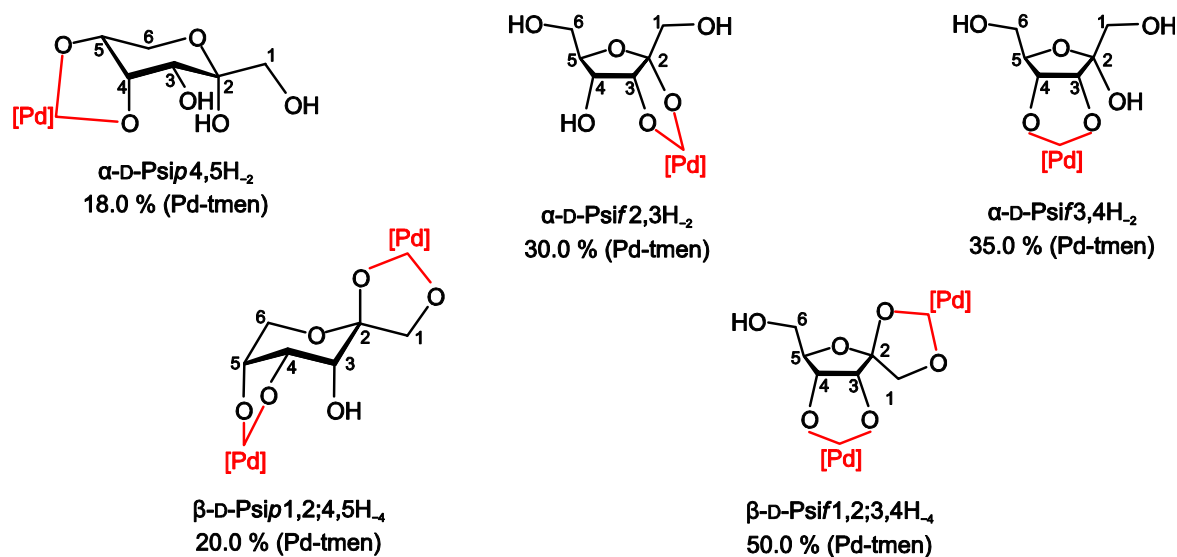


Figure 2.86. Species detected in solutions of Pd-tmen and D-psicose at various molar ratios (proportional distribution of species refer to a molar Pd/Psi ratio of 1:1 for monometalated and to 2:1 for dimetalated species, see ^{13}C NMR spectra in Fig. 2.85).

2 Results

Table 2.84. ^{13}C NMR chemical shifts (δ/ppm) and shift differences ($\Delta\delta$) to the free hexulose of D-psicose ligands in Pd-tmen. Atoms are numbered as in Fig. 2.86.

		C1	C2	C3	C4	C5	C6	Chelate
$\alpha\text{-D-Psip}4,5\text{H}_{-2}$	δ	63.2	99.6	64.4	81.9	76.2	61.8	
	$\Delta\delta$	-0.5	1.3	-1.7	9.6	9.7	3.2	$\kappa\text{O}^{4,5}$
$\beta\text{-D-Psip}1,2;4,5\text{H}_{-4}$	δ	76.9	110.5	74.6	74.1	80.3	63.6	
	$\Delta\delta$	12.3	11.5	3.8	8.4	10.7	-1.2	$\kappa\text{O}^{1,2};\kappa\text{O}^{4,5}$
$\alpha\text{-D-Psif}2,3\text{H}_{-2}$	δ	64.9	117.9	82.3	71.6	81.5	62.1	
	$\Delta\delta$	1.0	14.0	11.3	0.6	-1.8	0.2	$\kappa\text{O}^{2,3}$
$\alpha\text{-D-Psif}3,4\text{H}_{-2}$	δ	64.9	103.8	80.7	83.6	85.1	62.3	
	$\Delta\delta$	1.0	-0.1	9.7	12.6	1.8	0.4	$\kappa\text{O}^{3,4}$
$\beta\text{-D-Psif}1,2;3,4\text{H}_{-4}$	δ	71.2	116.7	89.0	84.6	87.1	63.3	
	$\Delta\delta$	8.2	10.5	13.7	13.0	3.8	-0.1	$\kappa\text{O}^{1,2};\kappa\text{O}^{3,4}$

Both $\alpha\text{-D-psicofuranose}$ species showed very similar coupling constants, however the $^3J_{\text{H}_4,\text{H}_5}$ values of the *trans*-vicinal protons indicated that the $^{\text{C}^3}\text{E}-\text{E}_{\text{C}^4}$ conformations were of less importance for furanose ring puckering of the $\alpha\text{-D-Psif}2,3\text{H}_{-2}$ and $\alpha\text{-D-Psif}3,4\text{H}_{-2}$ forms.

Table 2.85. Experimental $^3J_{\text{H},\text{H}}$ values in Hz for the metalated species of D-psicose in Pd-tmen.

	$^2J_{\text{H}_1,\text{H}_1'}$	$^3J_{\text{H}_3,\text{H}_4}$	$^3J_{\text{H}_4,\text{H}_5}$	$^3J_{\text{H}_5,\text{H}_6}$	$^3J_{\text{H}_5,\text{H}_6'}$	$^2J_{\text{H}_6,\text{H}_6'}$	Conformation
$\alpha\text{-D-Psip}4,5\text{H}_{-2}$	11.7	2.4	3.4	6.5	10.4	–	$^5\text{C}_2$
$\beta\text{-D-Psip}1,2;4,5\text{H}_{-4}$	10.3	4.7	5.7	2.1	3.6	11.8	$^2\text{C}_5$
$\alpha\text{-D-Psif}2,3\text{H}_{-2}$	11.7	6.4	8.3	2.9	5.2	12.4	–
$\alpha\text{-D-Psif}3,4\text{H}_{-2}$	11.7	5.2	8.6	2.3	5.8	12.4	–

2.12 The dialdoses: A first investigation

Besides the common aldoses by the conversion of the terminal hydroxymethyl group to a second aldehyde group, a new class of compounds comes up, namely the dialdoses. In this section, three dialdoses (see Fig. 2.87) were investigated and additionally, a crystal structure obtained incidentally from a side product is shown.

The introduction of this second reactive group abolishes the boundary between the D- and the L-series of *xylo*- and *galacto*-dialdose, whereas D-*manno*-dialdose remains in the D-series. There is little known in the literature about the dialdoses, only a few synthetic routes were developed and the structures and the behavior in solution were described even less. So, not only the treatment of the dialdoses with $\text{Pd}^{\text{II}}\text{N}_2$ solvents is of interest, but also the aqueous

2 Results

solution species have to be determined. Usually, the aldehyde group which is not involved in the formation of a pyranose or furanose ring forms a dihydrate in aqueous solution.

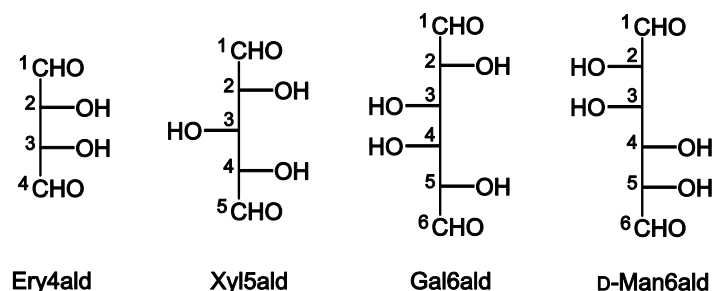


Figure 2.87. Fischer projections and atomic numbering of the four investigated dialdoses. From left to right: *erythro*-tetrodialdose (Ery4ald), *xylo*-pentodialdose (Xyl5ald), *galacto*-hexodialdose (Gal6ald) and *D-manno*-hexodialdose (D-Man6ald).

Comparing the ^{13}C NMR spectra of the dialdoses to those of their parent aldoses, the spectra of the hexodialdoses and aldoses differ only in the position of the C6 signal, whereas the spectra of *xylo*-pentodialdose and xylose appear to be completely different.

2.12.1 *erythro*-Tetrodialdose

Unexpectedly, the crystal structure of $[\text{Pd}_2(\text{tmen})_2(\text{Ery4ald})\text{H}_{-4}-\kappa\text{O}^{1,4}:\kappa\text{O}^{2,3}]$ was obtained from a solution of Pd-tmen and *D-manno*-hexodialdose (Pd/Man6ald ratio of 2:1) which was saturated with acetone. The impurity of *D-manno*-hexodialdose could be explained by the synthesis's pathway. Losing an isopropylidene group, 1,2;5,6-di-*O*-isopropylidene-*D-chiro*-inositol or 1,2;5,6-di-*O*-isopropylidene-*D-manno*-dialdose could react twice with the sodium periodate in a glycol-splitting reaction.

The structure, depicted in Fig. 2.88, was solved in the space group $P 2_1$ although the molecule was not chiral. In an attempt with $P 2_1/c$, the inversion center moved into the molecule impairing a solution of the crystal structure and, additionally, several reflexes which should be systematically absent were detected. Furthermore, the structure was refined only isotropically because anisotropic refinement would reveal a disordered second molecule which would be generated by rotating the molecule along a C_2 axis through the C1–C2 and C3–C4 bonds. According to the Cremer–Pople puckering parameters, the furanose ring's conformation could be determined to the ${}^{\text{O}5}E$ conformation which was fixed by the $\kappa\text{O}^{1,4}$ -chelation of the Pd(tmen) fragment. Along the a axis an $R_4^2(8)$ ring motif^[60] formed by two water molecules (O92 and O94) connected the single carbohydrate molecules via O2 and O4 to a chain.

2 Results

Therefore, the O2 and O4 alkoxido functions accepted four hydrogen bonds. Additional water molecules capped the remaining alkoxido O1 and O3 functions and the acceptor functions of O92 and O94 to form a strong hydrogen-bonding network between the single molecules.

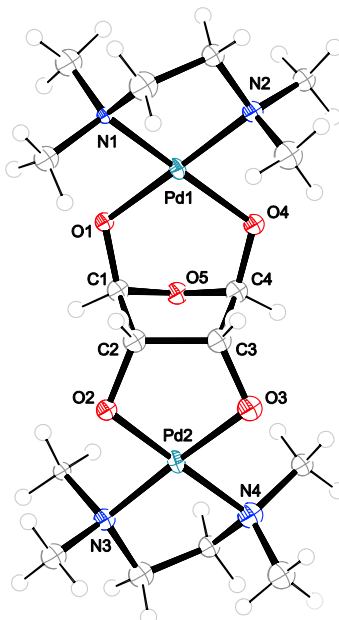


Figure 2.88. The molecular structure of $[\text{Pd}_2(\text{tmen})_2(\text{Ery4ald}/\text{H}_{-4}\text{-}\kappa\text{O}^{1,4};\kappa\text{O}^{2,3})]$ in crystals of the 12-hydrate (**40**). ORTEP plot is drawn with 50% probability ellipsoids. Interatomic distances (Å) and angles ($^\circ$) (standard deviations of the last digit in parentheses): Pd1–O1 2.008(9), Pd1–O4 2.068(8), Pd1–N1 2.031(12), Pd1–N2 2.066(11), Pd2–O2 1.961(8), Pd2–O3 2.006(10), Pd2–N3 2.027(11), Pd2–N4 2.065(13), O1–Pd1–O4 88.1(4), O1–Pd1–N1 94.5(4), O4–Pd1–N2 91.2(4), N1–Pd1–N2 86.3(4), O2–Pd2–O3 86.3(4), O2–Pd2–N3 95.5(4), O3–Pd2–N4 93.3(5), N3–Pd2–N4 85.0(5); chelate torsion angles: O2–C2–C3–O3 2.0(11), N1–C7–C8–N2 $-56.2(16)$, N3–C13–C14–N4 50.7(16); puckering parameters^[22] of the furanose ring C1–C2–C3–C4–O5: $Q = 0.399(9)$ Å, $\varphi = 1.9(16)^\circ$.

2.12.2 xylo-Pentodialdose

The xylo-pentodialdose was obtained from 1,2-*O*-isopropylidene- α -D-glucofuranose by a glycol-splitting reaction and subsequent removal of the isopropylidene group. Comparing the ^{13}C NMR spectra of D-xylose with that of xylo-pentodialdose, no similarity could be detected. In Fig. 2.89 all species which could be formed are shown and identical forms which could not distinguished in the ^{13}C NMR spectra are arranged together. As one can see, xylo-pento-dialdose cannot be classified in the usual D- and the L-forms of pyranoses and furanoses. Nevertheless, only two pyranose species were detected in the ^{13}C NMR spectra of aqueous solution, $1_{\text{ax}},5_{\text{eq}}\text{-Xyl5aldp}$ at 52 % and $[1,5]_{\text{eq}}\text{-Xyl5aldp}$ at 38 %, small signals indicated the presence of the furanose forms, too.

2 Results

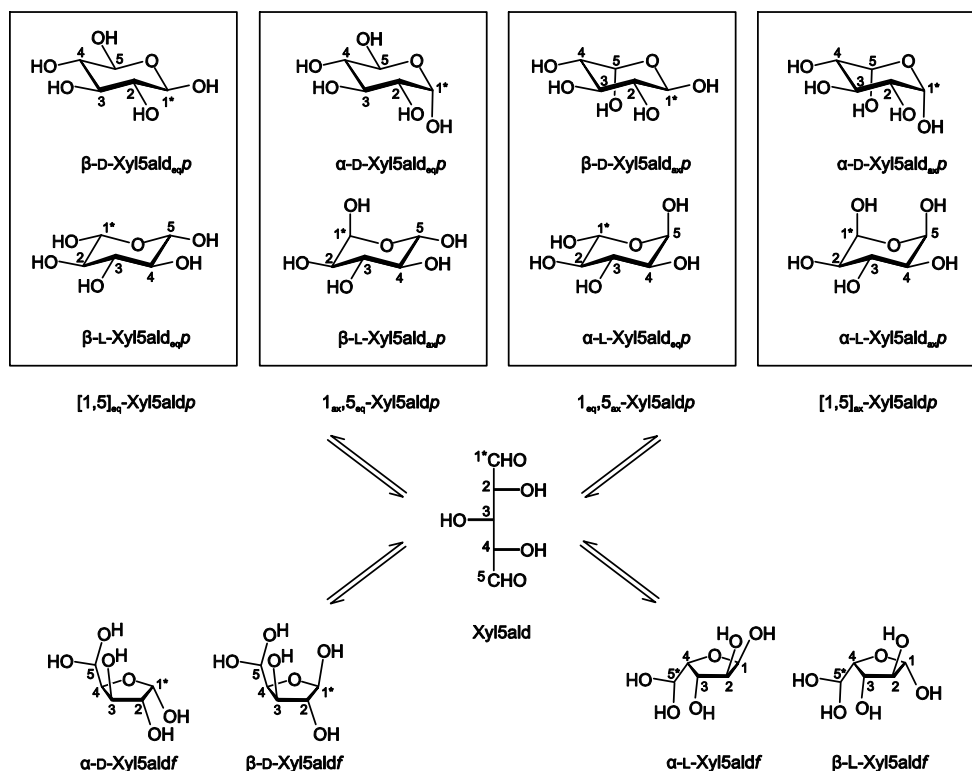


Figure 2.89. All possible configurations of *xylo*-pentodialdopose in aqueous solutions. The configurations in each box are identical, no distinction is possible between the D- and the L-forms of $[1,5]_{\text{eq}}\text{-Xyl5aldp}$ and $[1,5]_{\text{ax}}\text{-Xyl5aldp}$. Only $1_{\text{ax}},5_{\text{eq}}\text{-Xyl5aldp}$ and $1_{\text{eq}},5_{\text{ax}}\text{-Xyl5aldp}$ represent the D- and L-form of *xylo*-pentodialdopose, nevertheless both forms cannot be distinguished in the ^{13}C NMR spectra.

The ^{13}C NMR chemical shifts and the $^3J_{\text{H,H}}$ coupling constants are summed up in Tables 2.86 and 2.87, the $^4\text{C}_1$ conformation of both described pyranose forms was confirmed by the coupling constants.

Table 2.86. ^{13}C NMR chemical shifts (δ/ppm) and proportional distribution of *xylo*-pentodialdopose species at 25 °C in D_2O . Atoms are numbered as in Fig. 2.89.

		C1	C2	C3	C4	C5	%
$1_{\text{ax}},5_{\text{eq}}\text{-Xyl5aldp}$	δ	92.3	71.9	71.9	75.1	91.7	52
$[1,5]_{\text{eq}}\text{-Xyl5aldp}$	δ	93.5	74.8	74.2	74.8	93.5	38

Table 2.87. Experimental $^3J_{\text{H,H}}$ values in Hz of *xylo*-pentodialdopose species in D_2O . Atoms are numbered as in Fig. 2.89.

	$^3J_{\text{H}_1,\text{H}_2}$	$^3J_{\text{H}_2,\text{H}_3}$	$^3J_{\text{H}_3,\text{H}_4}$	$^3J_{\text{H}_4,\text{H}_5\text{eq}}$	Conformation
$1_{\text{ax}},5_{\text{eq}}\text{-Xyl5aldp}$	3.6	9.6	9.6	8.0	$^4\text{C}_1$
$[1,5]_{\text{eq}}\text{-Xyl5aldp}$	8.0	9.3	9.3	8.0	$^4\text{C}_1$

2 Results

The dissolution of *xyl*o-pentodialdose in Pd-tmen resulted in the identified species (see Fig. 2.90) according to the stoichiometry of the solution. At an equimolar ratio, uncoordinated *xyl*o-pentodialdose was detected at 18 %, the species $1_{ax,5eq}\text{-Xyl5ald}p1,2H_{-2}$ at 21 % and $\alpha\text{-Xyl5ald}f1,2H_{-2}$ at 23 %. The double-metalated species $1_{ax,5eq}\text{-Xyl5ald}p1,2;3,5H_{-4}$ was already detected at 17 % indicating the high stability of this species which is probably caused by the intramolecular hydrogen bond $O4\text{-H}\cdots O2$.

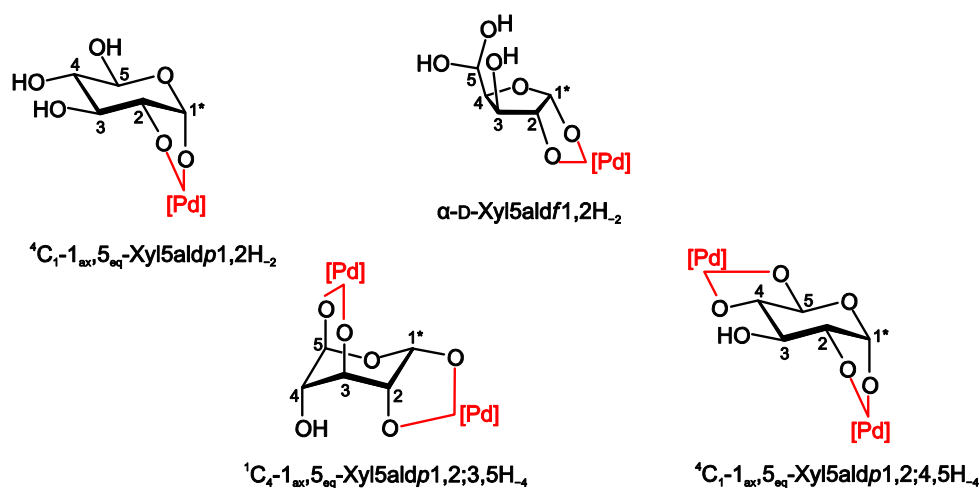


Figure 2.90. Species detected in solutions of Pd-tmen and *xyl*o-pentodialdose at different molar ratios (species refer to a molar Pd/*xyl*o-pentodialdose ratio of 1:1 for monometalated and to 2:1 for dimetalated forms).

At a molar Pd/*xyl*o-pentodialdose ratio of 2:1 the monometalated species disappeared, only $1_{ax,5eq}\text{-Xyl5ald}p1,2;3,5H_{-4}$ at 55 % and $1_{ax,5eq}\text{-Xyl5ald}p1,2;4,5H_{-4}$ at 16 % were identified. The species in Fig. 2.90 were assigned according to the ^{13}C NMR chemical shifts and shift differences in Table 2.88 and confirmed by the coupling constants in Table 2.89.

Table 2.88. ^{13}C NMR chemical shifts (δ/ppm) and shift differences ($\Delta\delta$) to the free pentodialdose of *xyl*o-pentodialdose ligands in Pd-tmen. Atoms are numbered as in Fig. 2.90.

	C1	C2	C3	C4	C5	Chelate
$1_{ax,5eq}\text{-Xyl5ald}p1,2H_{-2}$	101.9	81.8	76.4	74.3	91.8	
$\Delta\delta$	9.6	9.9	4.5	-0.8	0.1	$\kappa O^{1,2}$
$\alpha\text{-Xyl5ald}f1,2H_{-2}$	112.2	88.8	79.2	81.0	89.7	
$\Delta\delta$	16.1 ^a	12.1 ^a	5.6 ^b	-1.8 ^b	1.6 ^b	$\kappa O^{1,2}$
$1_{ax,5eq}\text{-Xyl5ald}p1,2;3,5H_{-4}$ ^c	98.4	84.0	70.5	73.7	99.2	
$\Delta\delta$	6.1	12.1	-1.4	-1.4	7.5	$\kappa O^{1,2};\kappa O^{3,5}$
$1_{ax,5eq}\text{-Xyl5ald}p1,2;4,5H_{-4}$	102.9	82.6	78.5	84.3	98.9	
$\Delta\delta$	10.6	10.7	6.6	9.2	7.2	$\kappa O^{1,2};\kappa O^{4,5}$

^a shift differences ($\Delta\delta$) to $\alpha\text{-D-xylofuranose}$; ^b shift differences ($\Delta\delta$) to 1,2-*O*-isopropylidene-*xyl*o-pentodialdofuranose. ^c Calc. ^{13}C NMR chemical shift values confirmed the assignment (for details see Section 5.8).

2 Results

Table 2.89. Experimental $^3J_{H,H}$ values in Hz for the metalated species of *xyl*-pentodialdose in Pd-tmen.

	$^3J_{H1,H2}$	$^3J_{H2,H3}$	$^3J_{H3,H4}$	$^3J_{H4,H5eq}$	Conformation
$1_{ax,5_{eq}}\text{-Xyl5aldp}1,2H_{-2}$	3.7	8.2	8.9	7.6	4C_1
$1_{ax,5_{eq}}\text{-Xyl5aldp}1,2;3,5H_{-4}$	1.8	3.3	3.4	2.0	1C_4
$1_{ax,5_{eq}}\text{-Xyl5aldp}1,2;4,5H_{-4}$	3.9	9.0	9.4	7.8	4C_1

2.12.3 galacto-Hexodialdose

Enzymatic oxidation of D-galactose by D-galactose oxidase produced *galacto*-hexodialdose according to literature.^[90-93] In the ^{13}C NMR spectra of aqueous solutions, two species were detected which are discussed in the above-mentioned literature. Therein, Kieboom and coworkers formulated bicyclic hemiacetalic forms whereas Rabiller and coworkers identified the monomeric hydrate forms. By interpretation of the measured two-dimensional spectra including the $^3J_{H,H}$ coupling constants and by comparison of the ^{13}C NMR spectra to the spectra of D-galactose, the presence of a bicyclic hemiacetalic form could not be corroborated. Therefore, all possible configurations of *galacto*-hexodialdose are shown in Fig. 2.91. As one can see, caused by the *meso*-open-chain form of the dialdose, *galacto*-hexodialdose can form the D- and the L-configurations of pyranoses and furanoses. Nevertheless, in the ^{13}C NMR spectra of an aqueous solution, only the α - and β -pyranoses could be detected, whereas no distinction was possible for the D- and the L-configurations. The ^{13}C NMR chemical shifts and the coupling constants are listed in the Tables 2.90 and 2.91 and were almost identical to the values of D-galactose except the C6 chemical shift.

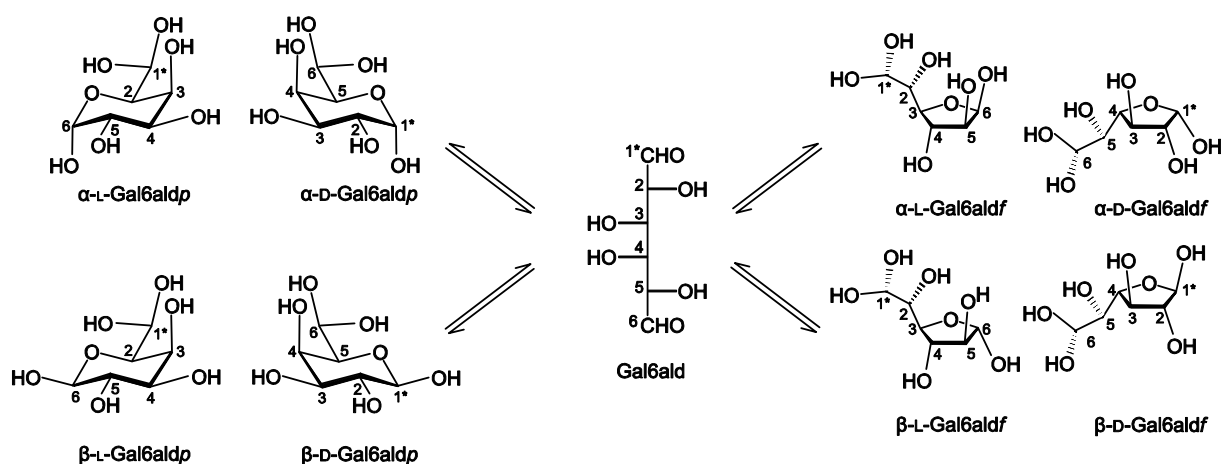


Figure 2.91. All possible configurations of *galacto*-hexodialdose in aqueous solutions. No distinction is possible between the D- and the L-forms of *galacto*-hexodialdose in the ^{13}C NMR spectra. The asterisk labels the original D-C1.

2 Results

Table 2.90. ^{13}C NMR chemical shifts (δ/ppm) and proportional distribution of *galacto*-hexodialdose species in D_2O . Atoms are numbered as in Fig. 2.91.

		C1	C2	C3	C4	C5	C6	%
α -Gal6aldp	δ	92.9	68.9	69.8	69.4	72.8	89.1	36
β -Gal6aldp	δ	97.2	72.3	73.3	68.9	77.5	88.8	64

Table 2.91. Experimental $^3J_{\text{H,H}}$ values in Hz of *galacto*-hexodialdose species in D_2O . Atoms are numbered as in Fig. 2.91.

	$^3J_{\text{H}_1,\text{H}_2}$	$^3J_{\text{H}_2,\text{H}_3}$	$^3J_{\text{H}_3,\text{H}_4}$	$^3J_{\text{H}_4,\text{H}_5}$	$^3J_{\text{H}_5,\text{H}_6}$	Conformation
α -Gal6aldp	3.6	—	3.0	>1	7.4	$^4\text{C}_1$
β -Gal6aldp	8.0	9.9	3.3	>1	7.4	$^4\text{C}_1$

Solutions of *galacto*-hexodialdose with Pd-en and Pd-chxn were highly reactive and revealed the formation of palladium(0) after a few minutes whereas with Pd-tmen the solutions were stable for the period of the NMR measurement. In Fig. 2.92 the ^{13}C NMR spectra of *galacto*-dialdose in Pd-tmen at a molar Pd/Gal6ald ratio of 1:1 (top) and 2:1 (bottom) are depicted.

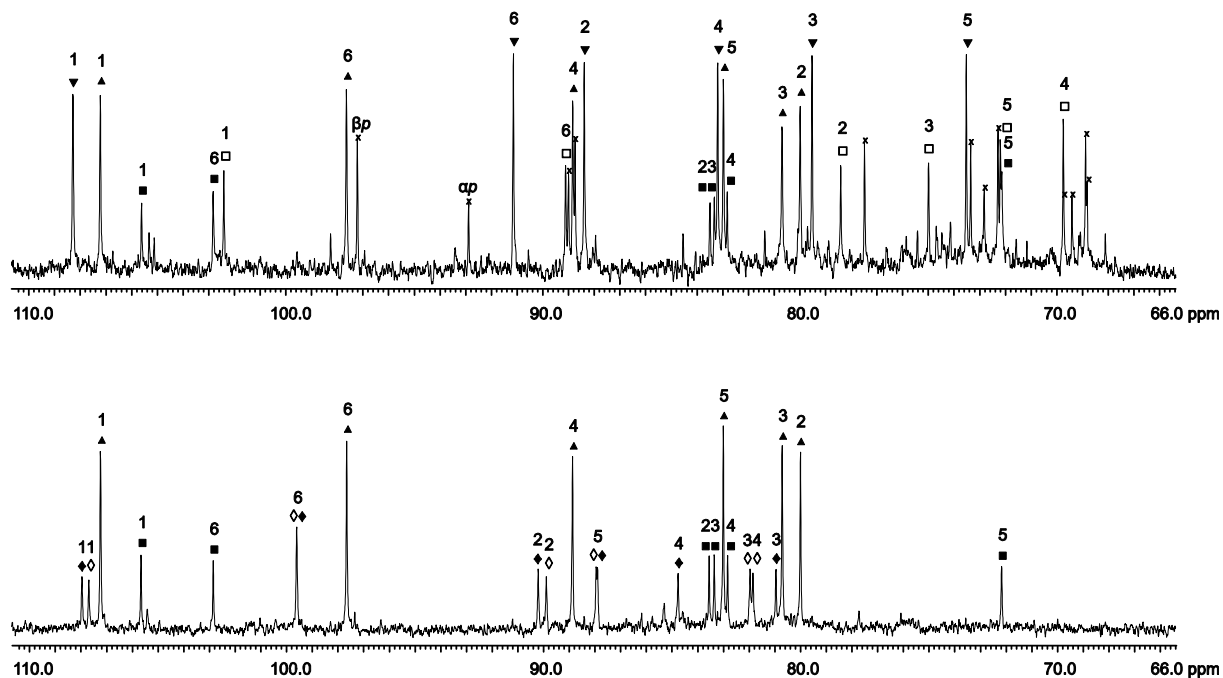


Figure 2.92. ^{13}C NMR spectra of *galacto*-dialdose in Pd-tmen at a molar Pd/Gal6ald ratio of 1:1 (top) and 2:1 (bottom). The signals of free *galacto*-dialdose are marked with (x); (\square) α -Gal6aldp1,2H₂-κO^{1,2}, (\blacksquare) 3,6-anhydro- α -Gal6aldp1,2H₂-κO^{1,2}, (\blacktriangledown) α -Gal6aldf1,2H₂-κO^{1,2}, (\diamond) (6R)- α -Gal6aldf1,2;5,6H₄-κO^{1,2}:κO^{5,6}, (\blacklozenge) (6S)- α -Gal6aldf1,2;5,6H₄-κO^{1,2}:κO^{5,6} and (\blacktriangle) β -Gal6aldf1,3;5,6H₄-κO^{1,3}:κO^{5,6}.

2 Results

As for the unmetalated *galacto*-hexodialdose, the ^{13}C NMR chemical shifts and shift differences of the various metalated species were almost identical to the ^{13}C NMR chemical shifts and shift differences of the corresponding metalated species of D-galactose in section 2.10.1 except for the C6 signal which was shifted downfield by the additional oxygen atom. Therefore, the species' identification and the assignment of the signals were successful for almost every species which is depicted in Fig. 2.93.

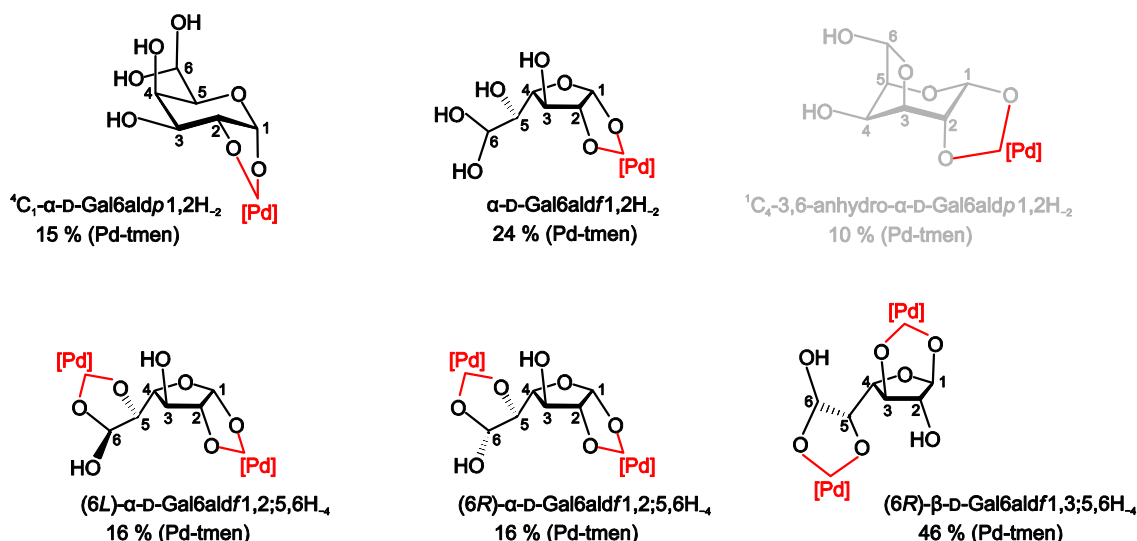


Figure 2.93. Species detected in solutions of Pd-tmen and *galacto*-hexodialdose at different molar ratios (proportional distribution of species refer to a molar Pd/*galacto*-hexodialdose ratio of 1:1 for monometalated and to 2:1 for dimetalated forms). The species are depicted in the D-configuration, although the ^{13}C NMR signals also correspond to the L-configuration of the compounds. The grey colored species is of equivocal evidence.

Corresponding to the ^{13}C NMR spectra in Fig. 2.92, at a molar Pd/Gal6ald ratio of 1:1 28 % of uncoordinated *galacto*-hexodialdose, 15 % of the species α -Gal6aldp1,2H₂- $\kappa\text{O}^{1,2}$, 24 % of α -Gal6aldf1,2H₂- $\kappa\text{O}^{1,2}$, 10 % of 3,6-anhydro- α -Gal6aldp1,2H₂- $\kappa\text{O}^{1,2}$ and 23 % of β -Gal6aldf1,3;5,6H₄- $\kappa\text{O}^{1,3}$: $\kappa\text{O}^{5,6}$ were detected. Elevating the Pd/Gal6ald ratio to 2:1 β -Gal6aldf1,3;5,6H₄- $\kappa\text{O}^{1,3}$: $\kappa\text{O}^{5,6}$ became the main species at 46 %, $\kappa\text{O}^{1,2}$: $\kappa\text{O}^{5,6}$ -chelated (6R)- α -Gal6aldf1,2;5,6H₄ and (6S)- α -Gal6aldf1,2;5,6H₄ each were detected at 16 % and 3,6-anhydro- α -Gal6aldp1,2H₂- $\kappa\text{O}^{1,2}$ at 22 %. The ^{13}C NMR chemical shifts and shift differences are listed in Table 2.92, the $^3J_{\text{H,H}}$ coupling constants in Table 2.93. As mentioned above, the species' identification and the assignment of ^{13}C NMR signals were successful for almost every species by comparison of the ^{13}C NMR signals and the $^3J_{\text{H,H}}$ coupling constants. Especially the dimetalated forms were identified by the interpretation of the coupling constants. On the other hand, the correct determination of the 3,6-anhydro- α -Gal6aldp1,2H₂- $\kappa\text{O}^{1,2}$ could not be guaranteed.

2 Results

Table 2.92. ^{13}C NMR chemical shifts (δ/ppm) and shift differences ($\Delta\delta$) to the free hexodialdose of *galacto*-hexodialdose ligands in Pd-tmen. Atoms are numbered as in Fig. 2.93.

	C1	C2	C3	C4	C5	C6	Chelate
α -Gal6aldp1,2H ₋₂	102.4	78.4	75.0	69.7	72.2	89.1	
$\Delta\delta$	9.5	9.5	5.2	0.3	-0.6	0.0	$\kappa\text{O}^{1,2}$
$^1\text{C}_4$ -3,6-an- α -Gal6aldp1,2H ₋₂ ^a	105.6	83.5	83.3	83.0	72.2	102.8	$\kappa\text{O}^{1,2}$
α -Gal6aldf1,2H ₋₂	108.3	88.4	79.5	83.2	73.5	91.1	$\kappa\text{O}^{1,2}$
(6 <i>R</i>)- α -Gal6aldf1,2;5,6H ₋₄	107.7	89.9	82.0	81.8	87.9	99.6	$\kappa\text{O}^{1,2};\kappa\text{O}^{5,6}$
(6 <i>S</i>)- α -Gal6aldf1,2;5,6H ₋₄	107.9	90.2	80.9	84.8	87.9	99.6	$\kappa\text{O}^{1,2};\kappa\text{O}^{5,6}$
β -Gal6aldf1,3;5,6H ₋₄ ^a	107.2	80.0	80.7	88.9	83.0	97.6	$\kappa\text{O}^{1,3};\kappa\text{O}^{5,6}$

^a Calculated ^{13}C NMR chemical shift values confirmed the assignment (for details see Section 5.8).

Table 2.93. Experimental $^3J_{\text{H,H}}$ values in Hz for the metalated species of *galacto*-hexodialdose in Pd-tmen.

	$^3J_{\text{H1,H2}}$	$^3J_{\text{H2,H3}}$	$^3J_{\text{H3,H4}}$	$^3J_{\text{H4,H5}}$	$^3J_{\text{H5,H6}}$	Conformation
$^1\text{C}_4$ -3,6-an- α -Gal6aldp1,2H ₋₂	2.5	5.4	<1	<1	<1	$^1\text{C}_4$
(6 <i>R</i>)- α -Gal6aldf1,2;5,6H ₋₄	3.6	5.4	6.1	9.0	<1	–
(6 <i>S</i>)- α -Gal6aldf1,2;5,6H ₋₄	3.9	5.8	6.1	8.0	4.2	–
β -Gal6aldf1,3;5,6H ₋₄	<1	<1	<1	<1	7.5	$E_{\text{C}2}$

The large ^{13}C NMR chemical shifts would have indicated a dimetalated species, however, the low $^3J_{\text{H,H}}$ coupling constants impaired the assumption of a pyranose and indicated a furanose form. Indeed, all possible dimetalated furanose forms were already identified. 3,6-anhydro- α -Gal6aldp1,2H₋₂- $\kappa\text{O}^{1,2}$ would have explained the high ^{13}C NMR chemical shifts and the low coupling constants and corresponded also with the monometalated 3,6-anhydro-form of *D-manno*-hexodialdose, nevertheless, for unequivocal evidence reliable reference values of an unmetalated species were missing.

2.12.4 *D-manno*-Hexodialdose

According to literature,^[94-96] the synthesis of *D-manno*-hexodialdose started from *D-chiro*-inositol which was converted into 1,2;5,6-di-*O*-isopropylidene-*D-chiro*-inositol. The two remaining hydroxy groups underwent a glycol-splitting reaction resulting in 2,3;4,5-di-*O*-isopropylidene-*D-manno*-hexodialdose which was crystallized. The structure, depicted in Fig. 2.94, was solved in the space group $P 2_1$. By removal of the isopropylidene groups *D-manno*-hexodialdose was obtained.

2 Results

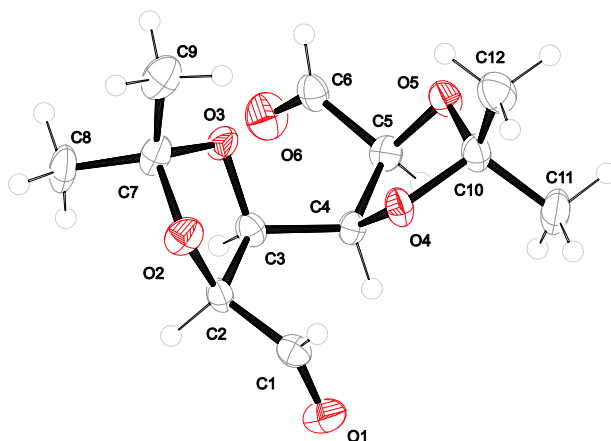


Figure 2.94: The molecular structure of 2,3;4,5-di-*O*-isopropylidene-*D*-manno-hexodialdose (**41**). ORTEP plot is drawn with 50% probability ellipsoids.

In the ^{13}C NMR spectra of an aqueous solution four species could be detected. Comparing the ^{13}C NMR spectra of *D*-mannose to *D*-manno-hexodialdose, the two pyranose species could be identified with only the C6 signal shifted downfield. The remaining two species were assigned to the 3,6-anhydro-forms of *D*-manno-hexodialdofuranose as depicted in Fig. 2.95.

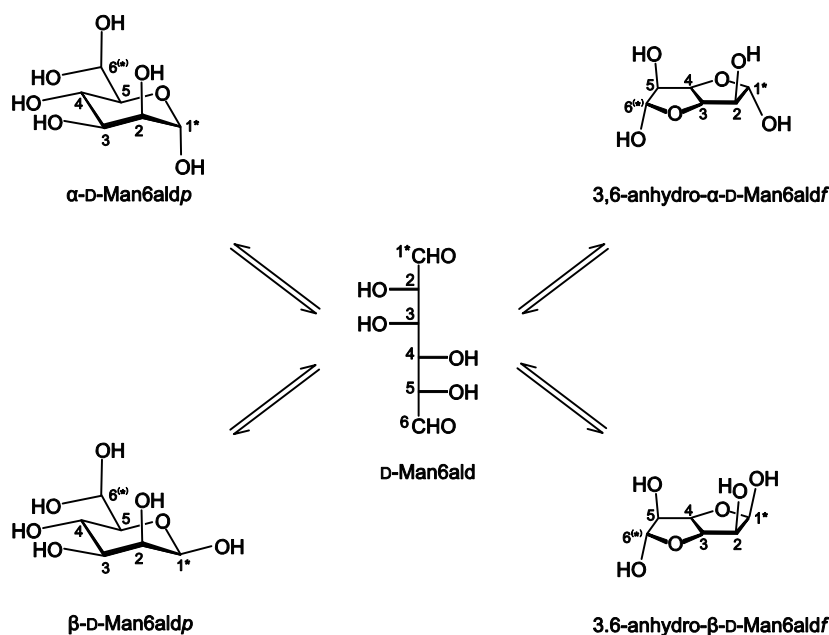


Figure 2.95. All detected configurations of *D*-manno-hexodialdose in aqueous solutions. *Manno*-hexodialdose exists only in the *D*-configuration, although the C1 also could be found at the C6 position and *vice versa*.

Only the symmetrical 3,6-anhydro- α -*D*-Man6aldf species, instead of a regular furanose form, would correspond to three ^{13}C NMR signals which were detected in the spectrum. Furthermore, an anhydro-form for the dimethyl *D*-manno-hexodialdoside is also discussed.^[97] The ^{13}C NMR chemical shifts and the $^3J_{\text{H,H}}$ coupling constants are summed up in Tables 2.94 and 2.95.

2 Results

Table 2.94. ^{13}C NMR chemical shifts (δ/ppm) and proportional distribution of *manno*-hexodialdose species in D_2O . Atoms are numbered as in Fig. 2.95.

		C1	C2	C3	C4	C5	C6	%
$\alpha\text{-D-Man6aldp}$	δ	94.7	71.2	70.7	67.9	73.7	88.9	50
$\beta\text{-D-Man6aldp}$	δ	94.6	71.8	73.5	67.6	77.3	88.7	20
3,6-anhydro- $\alpha\text{-D-Man6aldf}$	δ	102.6	76.8	79.5	79.5	76.8	102.6	15
3,6-anhydro- $\beta\text{-D-Man6aldf}$	δ	96.6	72.6	79.3	80.0	77.1	102.2	15

Table 2.95. Experimental $^3J_{\text{H,H}}$ values in Hz of *manno*-hexodialdose species in D_2O . Atoms are numbered as in Fig. 2.95.

	$^3J_{\text{H1,H2}}$	$^3J_{\text{H2,H3}}$	$^3J_{\text{H3,H4}}$	$^3J_{\text{H4,H5}}$	$^3J_{\text{H5,H6}}$	Conformation
$\alpha\text{-D-Man6aldp}$	1.8	–	–	–	1.3	$^4\text{C}_1$
$\beta\text{-D-Man6aldp}$	1.1	–	–	9.4	2.2	$^4\text{C}_1$
3,6-anhydro- $\alpha\text{-D-Man6aldf}$	6.6	–	3.6	–	6.6	–
3,6-anhydro- $\beta\text{-D-Man6aldf}$	5.1	5.2	4.7	5.2	5.3	–

The treatment of Pd-tmen with *D-manno*-hexodialdose at the molar Pd/*manno*-hexodialdose ratios 1:1 and 2:1 resulted in very similar spectra. At an equimolar ratio, already 70 % of the dimetalated $\beta\text{-D-Man6aldf1,2;5,6H}_{-4}\text{-}\kappa\text{O}^{1,2}:\kappa\text{O}^{5,6}$ species which became the only detected species at a 2:1 ratio and only 30 % of the monometalated 3,6-an- $\beta\text{-D-Man6aldf1,2H}_{-2}\text{-}\kappa\text{O}^{1,2}$ were detected. The species are depicted in Fig. 2.96.

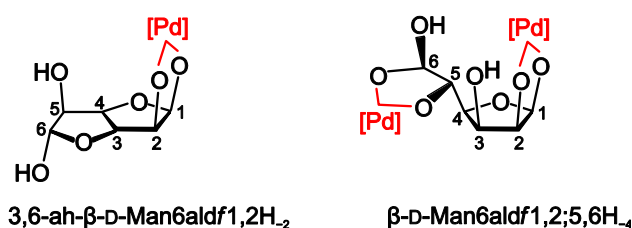


Figure 2.96. Species detected in solutions of Pd-tmen and *manno*-hexodialdose at various molar ratios.

The high amount of the dimetalated species at a seemingly equimolar ratio could possibly be explained by impurities of the *manno*-hexodialdose which altered the ratio in favor of Pd-tmen. The ^{13}C NMR chemical shifts and the coupling constants are listed in the Tables 2.96 and 2.97. Whereas the monometalated species could be compared to the unmetalated 3,6-anhydro- $\beta\text{-D-Man6aldf}$ form, no ^{13}C NMR chemical shifts are available for the regular furanose form of *D-manno*-hexodialdose for comparison to the dimetalated species. Nevertheless, the six ^{13}C NMR signals as well as the $^3J_{\text{H,H}}$ coupling constants indicated an

2 Results

asymmetric furanose form which impaired a dimetalated $\kappa O^{1,2};\kappa O^{5,6}$ -anhydro-hexodialdo-furanose species.

Table 2.96. ^{13}C NMR chemical shifts (δ/ppm) and shift differences ($\Delta\delta$) to the free hexodialdose of *manno*-hexodialdose ligands in Pd-tmen. Atoms are numbered as in Fig. 2.96.

	C1	C2	C3	C4	C5	C6	Chelate
3,6-an- β -D-Man6aldf1,2H ₋₂	109.6	85.3	81.9	80.9	73.5	99.0	
	13.0	12.7	2.6	0.9	-3.6	-3.2	$\kappa O^{1,2}$
β -D-Man6aldf1,2;5,6H ₋₄ ^a	109.9	83.7	80.7	81.6	75.4	105.0	$\kappa O^{1,2};\kappa O^{5,6}$

^a Calculated ^{13}C NMR chemical shift values confirmed the assignment (for details see Section 5.8).

Table 2.97. Experimental $^3J_{\text{H,H}}$ values in Hz for the metalated species of *manno*-hexodialdose in Pd-tmen. Atoms are numbered as in Fig. 2.96.

	$^3J_{\text{H1,H2}}$	$^3J_{\text{H2,H3}}$	$^3J_{\text{H3,H4}}$	$^3J_{\text{H4,H5}}$	$^3J_{\text{H5,H6}}$	Conformation
3,6-an- β -D-Man6aldf1,2H ₋₂	4.3	5.0	4.8	5.3	4.8	–
β -D-Man6aldf1,2;5,6H ₋₄	3.6	6.3	6.3	6.1	1.3	–

2.13 The fructose-containing di- and trisaccharides

Fig. 2.97 overviews the investigated di- and trisaccharides of D-fructose. For the reducing disaccharides the percentages of the various configurations, determined at 20 °C in D₂O, are given.

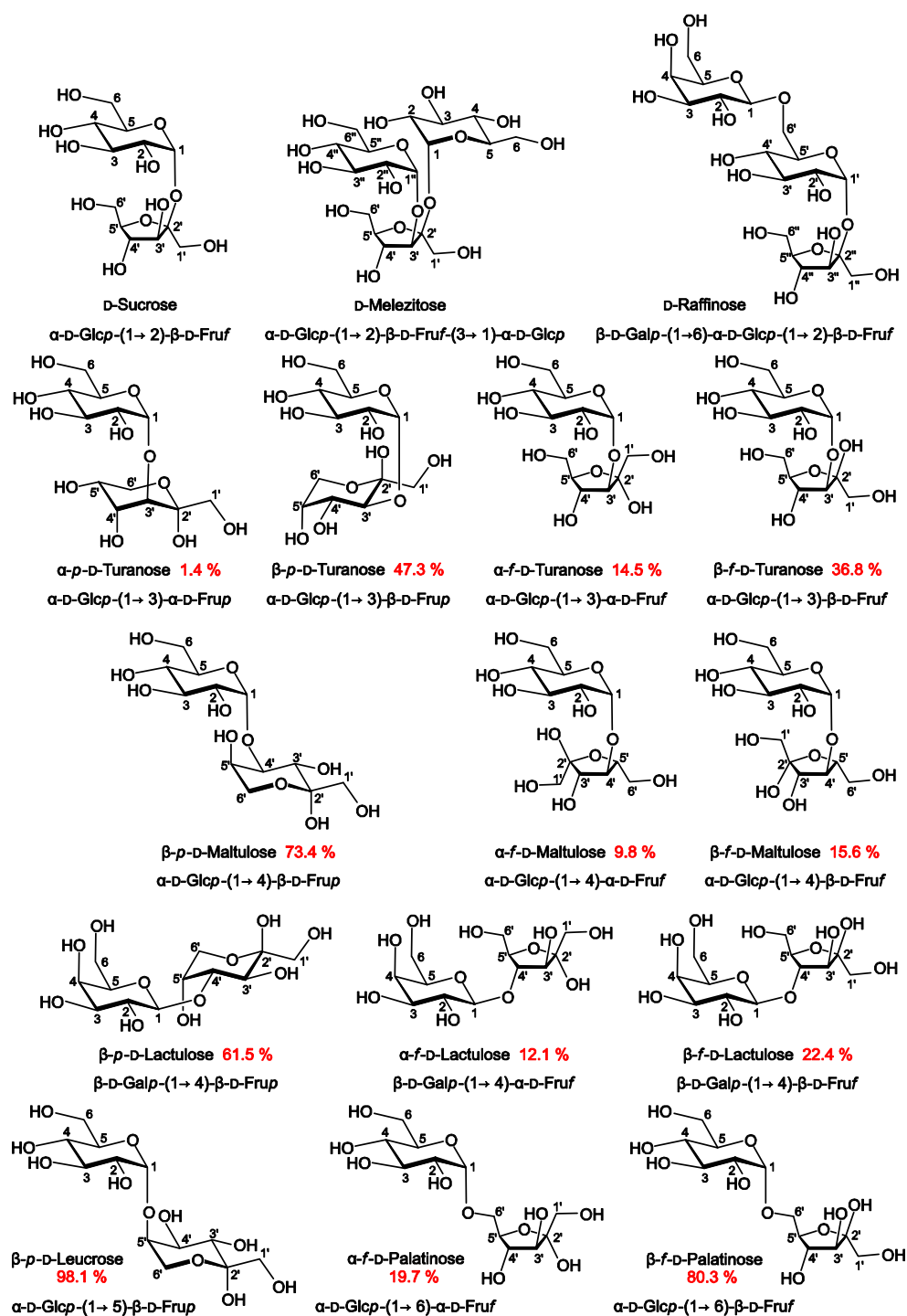


Figure 2.97. All configurations detected in the ¹³C NMR spectra of the investigated fructose-containing di- and trisaccharides in D₂O (see Appendix 6.1). The percentages of the various configurations were determined at 20 °C in D₂O.^[87, 98]

2 Results

From D-sucrose to D-palatinose the glycosidic oxygen atom varies from O2 to O6, affecting the equilibrium composition of the fructose unit. Whereas with the non-reducing D-sucrose and its derivatives the fructose unit is fixed in the β -D-fructofuranose form, with the remaining reducing disaccharides the fructose unit exists in various solution equilibria. The glycosidic bond to O5 of D-leucrose inhibits the formation of furanose forms. On the other hand, the glycosidic bond to O6 of D-palatinose inhibits the formation of pyranose forms. For the remaining three disaccharides, the D-lactulose's proportional distribution of fructose species is closest to that of D-fructose. In the Fig. 6.25–6.32 the ^{13}C NMR spectra of the mentioned di- and trisaccharides are compared to the ^{13}C NMR spectra of the single components. Realizing the high similarity of a di- or trisaccharide's spectrum to the spectra of its monomeric building units, the reaction of coordinating agents as Pd-tmen with the methyl hex(ul)osides and hexoses should provide characteristic shift patterns which allow the identification of the corresponding signals in a di- or oligosaccharide ^{13}C NMR spectrum. In fact, the detected shift differences of the monomeric units and the di- and trisaccharides are almost identical, so that the assignment of signals and species in Pd-tmen become possible even for complex ^{13}C NMR spectra.

2.13.1 D-Sucrose

D-sucrose is the most common disaccharide because of its use as table sugar and is well investigated. In the crystal structure of D-sucrose^[99] two intramolecular hydrogen bonds $\text{O1}'\text{-H}\cdots\text{O2}$ and $\text{O6}'\text{-H}\cdots\text{O5}$ were found, whereas, suggesting a flexible conformation, the presence and nature of such hydrogen bonds in solution has remained controversial.^[5] Predicting the chelation sites, the glucopyranoside unit will act first as chelate ligand, the fructofuranoside unit will provide only a less-favored $\kappa\text{O}^{1,3}$ -diolato unit for chelation as shown for the methyl β -D-fructofuranoside. Indeed, in equimolar solutions two monometalated forms were identified, 64 % of $\kappa\text{O}^{2,3}$ -chelated $\alpha\text{-D-Glcp}2,3\text{H}_{-2}\text{-(1}\rightarrow\text{2)-}\beta\text{-D-Fruf}$ and 13 % of $\kappa\text{O}^{3,4}$ -chelated $\alpha\text{-D-Glcp}3,4\text{H}_{-2}\text{-(1}\rightarrow\text{2)-}\beta\text{-D-Fruf}$ (see Fig. 2.98). At a Pd/sucrose ratio of 2:1 the former species remained the main species at 52 %, the latter species was found at 10 %. Additionally, two dimetalated forms were detected, $\alpha\text{-D-Glcp}2,3;4,6\text{H}_{-4}\text{-(1}\rightarrow\text{2)-}\beta\text{-D-Fruf}$ with 21 % and $\alpha\text{-D-Glcp}3,4\text{H}_{-2}\text{-(1}\rightarrow\text{2)-}\beta\text{-D-Fruf}1,3\text{H}_{-2}$ at 8 %. Higher Pd/sucrose ratios slightly changed the species' equilibrium in favor of $\alpha\text{-D-Glcp}2,3;4,6\text{H}_{-4}\text{-(1}\rightarrow\text{2)-}\beta\text{-D-Fruf}$. The ^{13}C NMR chemical shifts and shift differences of the various species are summed up in Table 2.98.

2 Results

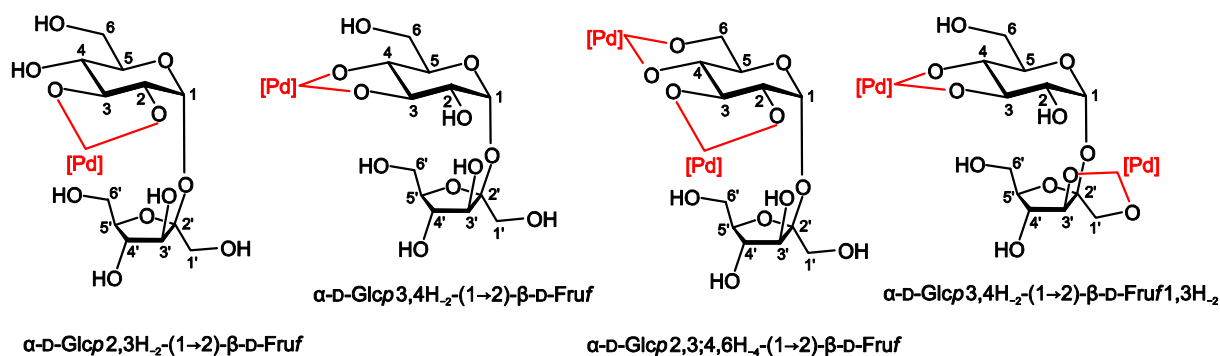


Figure 2.98. Species detected in solutions of Pd-tmen and D-sucrose at different molar ratios (species refer to a molar Pd/sucrose ratio of 1:1 for monometalated and to 2:1 for dimetalated forms).

Table 2.98. ^{13}C NMR chemical shifts (δ/ppm) and shift differences ($\Delta\delta$) to the free disaccharide of D-sucrose ($\alpha\text{-D-Glcp-(1}\rightarrow\text{2)-}\beta\text{-D-Fruf}$) ligands in Pd-tmen. Atoms are numbered as in Fig. 2.98.

		C1	C2	C3	C4	C5	C6	Chelate
$\alpha\text{-D-Glcp}2,3\text{H}_2\text{ (C)}$	δ	93.2	81.4	81.7	71.8	73.7	60.6	
	$\Delta\delta$	0.5	9.8	8.6	2.0	0.7	-0.1	$\kappa\text{O}^{2,3}$
$\beta\text{-D-Fruf (C')}$	δ	63.3	103.6	79.8	75.3	82.0	63.0	
	$\Delta\delta$	1.4	-0.6	2.8	0.7	0.1	0.1	-
$\alpha\text{-D-Glcp}3,4\text{H}_2\text{ (C)}$	δ	92.9	73.9	82.4	79.6	74.9	61.0	
	$\Delta\delta$	0.2	2.3	9.3	9.8	1.9	0.3	$\kappa\text{O}^{3,4}$
$\beta\text{-D-Fruf (C')}$	δ	61.9	104.1	77.2	74.5	81.8	62.8	
	$\Delta\delta$	0.0	-0.1	0.2	-0.1	-0.1	-0.1	-
$\alpha\text{-D-Glcp}2,3;4,6\text{H}_4\text{ (C)}$	δ	93.5	82.1	83.1	81.8	74.7	69.0	
	$\Delta\delta$	0.8	10.5	10.0	12.0	1.7	8.3	$\kappa\text{O}^{2,3};\kappa\text{O}^{4,6}$
$\beta\text{-D-Fruf (C')}$	δ	63.3	103.6	79.6	75.4	82.1	63.1	
	$\Delta\delta$	1.4	-0.6	2.6	0.8	0.2	0.2	-
$\alpha\text{-D-Glcp}3,4\text{H}_2\text{ (C)}$	δ	93.1	74.1	82.9	78.2	75.2	60.9	
	$\Delta\delta$	0.4	2.5	9.8	8.4	2.2	0.2	$\kappa\text{O}^{3,4}$
$\beta\text{-D-Fruf}1,3\text{H}_2\text{ (C')}$	δ	66.8	107.6	85.6	74.9	84.0	63.7	
	$\Delta\delta$	4.9	3.4	8.6	0.3	2.1	0.8	$\kappa\text{O}^{1,3}$

The minor $\alpha\text{-D-Glcp}3,4\text{H}_2\text{-(1}\rightarrow\text{2)-}\beta\text{-D-Fruf}1,3\text{H}_2$ species was crystallized with two Pd(en) fragments revealing an intramolecular hydrogen bond $\text{O}2\text{-H}\cdots\text{O}1'$ to the fructoside's alkoxido atom.^[41] As indicated by the investigation of methyl $\beta\text{-D-fructofuranoside}$ and methyl $\alpha\text{-D-glucopyranoside}$, the glucopyranose unit's $\kappa\text{O}^{2,3}$ -chelation site is favored. Furthermore, the glucopyranose unit's $\kappa\text{O}^{4,6}$ -chelation site is preferred to the fructofuranoside's $\kappa\text{O}^{1,3}$ -diolato site. Although the presence of intramolecular hydrogen bonds in solution was not investigated, the known intramolecular hydrogen bonds $\text{O}1'\text{-H}\cdots\text{O}2$ and $\text{O}6'\text{-H}\cdots\text{O}5$ were not

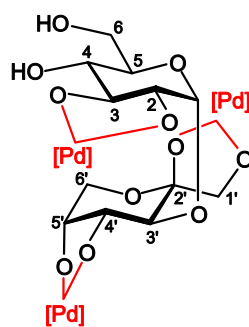
2 Results

impaired. For the species with a $\kappa O^{2,3}$ -chelator the importance of the former hydrogen bond should even increase by the alkoxido O2 acceptor. Instead, a new intramolecular hydrogen bond O2–H···O1' became possible for α -D-Glcp3,4H₂-(1→2)- β -D-Fruf1,3H₂.^[41] The minor presence of this species in solution, however, didn't indicate a stabilizing effect of this hydrogen bond.

2.13.2 D-Turanose

D-Turanose is a (1→3)-linked reducing disaccharide with α -D-Glcp-(1→3)-D-Frup as the major species in aqueous solutions. This pyranose form is also known from a crystal structure,^[100] the gluco- and fructopyranose rings were found in the ⁴C₁ and ²C₅ conformations, respectively, and a hydrogen bond O4'–H···O2 was detected.

The (1→3)-linkage impaired the formation of the important $\kappa O^{2,3}$ -chelated β -D-Fruf or β -D-Frup species resulting in uninterpretable ¹³C NMR spectra at equimolar Pd/turanose ratios. Not until a Pd/turanose ratio of 4:1 was a main species was detected, namely, the trimetallated α -D-Glcp2,3H₂-(1→3)- β -D-Frup1,2;4,5H₄ species which is depicted in Fig. 2.99. The corresponding ¹³C NMR chemical shifts and shift differences are listed in Table 2.99.



α -D-Glcp2,3H₂-(1→3)- β -D-Frup1,2;4,5H₄

Figure 2.99. Species detected in Pd-tmen at a molar Pd/tagatose ratio of 4:1.

Table 2.99. ¹³C NMR chemical shifts (δ /ppm) and shift differences ($\Delta\delta$) to the free disaccharide of D-turanose (α -D-Glcp-(1→3)-D-Fru) ligands in Pd-tmen. Atoms are numbered as in Fig. 2.99.

		C1	C2	C3	C4	C5	C6	Chelate
α -D-Glcp2,3H ₂ (C)	δ	98.2	82.1	81.4	72.1	73.9	61.0	
	$\Delta\delta$	-3.3	9.4	8.0	2.2	0.6	-0.1	$\kappa O^{2,3}$
β -D-Frup1,2;4,5H ₄ (C')	δ	76.3	110.2	73.0	81.1	81.5	62.6	
	$\Delta\delta$	11.6	11.9	-4.3	10.2	11.8	-1.4	$\kappa O^{1,2};\kappa O^{4,5}$

2 Results

The metalation of D-turanose agreed with the results obtained for D-fructose and methyl α -D-glucopyranoside. The (1 \rightarrow 3)-linkage impairing the $\kappa O^{2,3}$ -chelation site enforced the metalation mode of β -D-Fruf1,2;4,5H $_4$: $\kappa O^{1,2}$: $\kappa O^{4,5}$ and the preference of α -D-Glcp2,3H $_2$: $\kappa O^{2,3}$ was already proven for the methyl glucoside. Contrary to D-sucrose, the fructose unit was dimetalated first because of the preference of $\kappa O^{1,2}$ -diolato to $\kappa O^{1,3}$ -diolato chelation.

2.13.3 D-Maltulose

D-Maltulose is a (1 \rightarrow 4)-linked reducing disaccharide with α -D-Glcp-(1 \rightarrow 4)-D-Fruf as major species in aqueous solutions. In contrast to D-sucrose and D-turanose, now the $\kappa O^{2,3}$ -chelation site was provided. In agreement with the D-fructose's investigation results, at an equimolar ratio of Pd/maltulose the main species was α -D-Glcp-(1 \rightarrow 4)- β -D-Fruf2,3H $_2$ at 74 %. A minor α -D-Glcp-(1 \rightarrow 4)- β -D-Fruf2,3H $_2$ species was detected at 19 %. At a Pd/maltulose ratio of 2:1 the monometalated species could be still detected in minor amounts. The new main species was α -D-Glcp2,3H $_2$ -(1 \rightarrow 4)- β -D-Fruf2,3H $_2$ at 37 %, α -D-Glcp2,3H $_2$ -(1 \rightarrow 4)- β -D-Fruf2,3H $_2$ was detected at 10 %. The four mentioned species are depicted in Fig. 2.100 and additional signals close to the C1 and C2' signals of the monometalated species also indicated the glucopyranose unit's $\kappa O^{3,4}$ -metalation of these species.

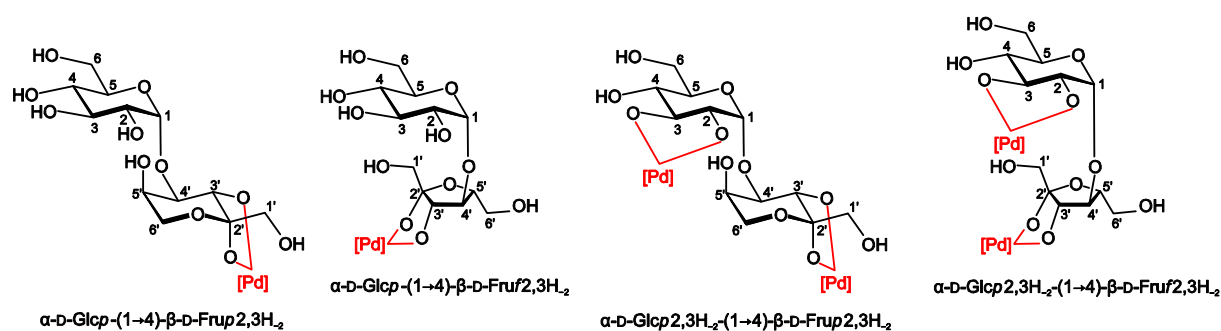


Figure 2.100. Species detected in solutions of Pd-tmen and D-maltulose at different molar ratios (species refer to a molar Pd/maltulose ratio of 1:1 for monometalated and to 2:1 for dimetalated forms).

The ^{13}C NMR chemical shifts and shift differences of the four identified species are listed in Table 2.100. The (1 \rightarrow 4)-linkage impaired the fructose unit's double metalation and the unfavorable $\kappa O^{1,2}$ -chelation was also not detected. In contrast to D-turanose, only the high formation tendency of the $\kappa O^{2,3}$ -chelated fructose unit made the assignment of the ^{13}C NMR spectra possible. Furthermore, the exclusive metalation of the reducing unit at equimolar ratios was in agreement with previous results.

2 Results

On the other hand, the subsequent metalation of the α -D-glucopyranose unit corresponds with the behavior of the methyl glucoside.

Table 2.100. ^{13}C NMR chemical shifts (δ/ppm) and shift differences ($\Delta\delta$) to the free disaccharide of D-maltulose (α -D-Glcp-(1 \rightarrow 4)-D-Fru) ligands in Pd-tmen. Atoms are numbered as in Fig. 2.100.

		C1	C2	C3	C4	C5	C6	Chelate
α -D-Glcp (C)	δ	100.4	72.2	73.5	70.1	73.0	61.0	
	$\Delta\delta$	1.5	0.4	0.2	0.1	0.0	0.0	–
β -D-Fruf _{2,3H₂} (C')	δ	62.7	112.4	88.9	86.7	81.3	62.9	
	$\Delta\delta$	–0.6	9.8	13.1	4.9	0.7	–0.1	$\kappa\text{O}^{2,3}$
α -D-Glcp (C)	δ	101.7	72.8	73.9	70.3	72.9	61.2	
	$\Delta\delta$	0.6	0.4	0.4	0.1	0.0	0.0	–
β -D-Frup _{2,3H₂} (C')	δ	67.0	107.4	74.9	84.7	70.2	63.3	
	$\Delta\delta$	2.6	8.5	7.4	6.0	0.4	–0.7	$\kappa\text{O}^{2,3}$
α -D-Glcp _{2,3H₂} (C)	δ	102.0	82.1	81.5	72.1	73.5	61.0	
	$\Delta\delta$	3.1	10.3	8.2	2.1	0.5	0.0	$\kappa\text{O}^{2,3}$
β -D-Fruf _{2,3H₂} (C')	δ	62.4	112.2	89.1	86.6	81.4	62.8	
	$\Delta\delta$	–0.6	9.6	13.3	4.8	0.8	–0.2	$\kappa\text{O}^{2,3}$
α -D-Glcp _{2,3H₂} (C)	δ	101.9	80.1	83.3	72.2	73.1	61.2	
	$\Delta\delta$	0.8	7.7	9.8	2.0	0.2	0.0	$\kappa\text{O}^{2,3}$
β -D-Frup _{2,3H₂} (C')	δ	67.0	107.2	74.8	84.4	70.3	63.2	
	$\Delta\delta$	2.6	8.3	7.3	5.7	0.5	–0.8	$\kappa\text{O}^{2,3}$

2.13.4 D-Lactulose

D-Lactulose is an isomerization product of D-lactose at high temperatures and is used as an indicator for the heat treatment of milk. The crystal structure of β -D-Galp-(1 \rightarrow 4)- β -D-Fruf revealed a bifurcated hydrogen bond from O3' to O5 and O6.^[101] In aqueous solutions, D-lactulose shows an almost identical species distribution of the various fructose forms as D-fructose itself. The ^{13}C NMR signals in Fig. 6.28 were assigned according to literature.^[102]

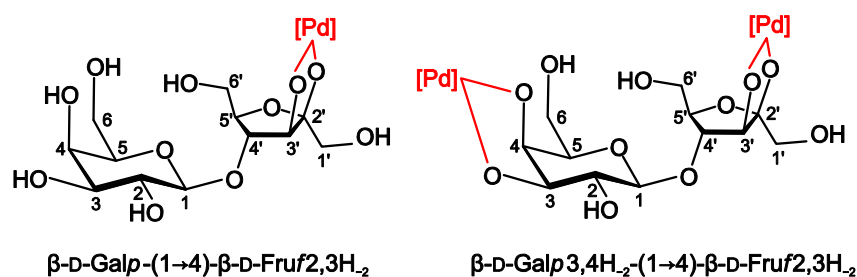


Figure 2.101. Species detected in solutions of Pd-tmen and D-lactulose at different molar ratios (species refer to a molar Pd/lactulose ratio of 1:1 for monometalated and to 2:1 for dimetalated forms).

2 Results

Just like D-maltulose, the β -D-Galp-(1 \rightarrow 4)-D-Fru-linked disaccharide provides the fructose's preferred $\kappa O^{2,3}$ -chelation site. Therefore, as shown in Fig. 2.101, the expected and detected main species at an equimolar Pd/lactulose ratio was β -D-Galp-(1 \rightarrow 4)- β -D-Fruf2,3H₂ at 75 %. Due to the preference of *cis*-vicinal chelation, the main species at a Pd/lactulose ratio of 2:1 was β -D-Galp3,4H₂-(1 \rightarrow 4)- β -D-Fruf2,3H₂ at 60 %. The ¹³C NMR chemical shifts and shift differences of the two identified species are listed in Table 2.101.

Table 2.101. ¹³C NMR chemical shifts (δ /ppm) and shift differences ($\Delta\delta$) to the free disaccharide of D-lactulose (β -D-Galp-(1 \rightarrow 4)-D-Fru) ligands in Pd-tmen. Atoms are numbered as in Fig. 2.101.

		C1	C2	C3	C4	C5	C6	Chelate
β -D-Galp (C)	δ	102.6	71.1	73.2	69.2	75.9	61.6	
	$\Delta\delta$	-0.9	-0.2	0.0	0.1	0.0	-0.1	-
β -D-Fruf2,3H ₂ (C')	δ	63.6	113.5	86.6	86.6	82.0	63.2	
	$\Delta\delta$	-0.5	10.5	11.3	1.8	1.3	-0.1	$\kappa O^{2,3}$
β -D-Galp3,4H ₂ (C)	δ	102.5	74.0	83.4	80.2	75.9	61.5	
	$\Delta\delta$	-1.0	2.7	10.2	11.1	0.0	-0.2	$\kappa O^{3,4}$
β -D-Fruf2,3H ₂ (C')	δ	63.5	113.4	86.6	86.8	82.4	63.9	
	$\Delta\delta$	0.4	10.4	11.3	2.0	1.7	0.6	$\kappa O^{2,3}$

Besides these two characterized species, the remaining signals were too small to perform a full assignment of species. Nevertheless, according to the shift differences and the previous results, monometalated β -D-Galp-(1 \rightarrow 4)- β -D-Fruf2,3H₂ and various dimetalated forms with a $\kappa O^{3,4}$ -chelated and $\kappa O^{2,3}$ -chelated galactopyranose unit could also be assumed in small amounts. It is noteworthy that the (β 1 \rightarrow 4)-linkage repressed the $\kappa O^{2,3}$ -chelated β -D-fructopyranose unit, whereas with the D-maltulose's (α 1 \rightarrow 4)-linkage the β -D-Fruf2,3H₂- $\kappa O^{2,3}$ form was detected at almost 20 %.

2.13.5 D-Leucrose

D-Leucrose is a (1 \rightarrow 5)-linked reducing disaccharide with α -D-Glcp-(1 \rightarrow 5)- β -D-Frup as unique detectable species in aqueous solutions. Due to the (1 \rightarrow 5)-linkage, the furanose forms are impaired, whereas the α -anomer of fructopyranose has, in comparison to D-fructose, no importance in equilibrium. In the crystal structure,^[103] the gluco- and fructopyranose rings were found in the ⁴C₁ and ²C₅ conformations. However, no intramolecular hydrogen bond was detected. At a Pd/leucrose ratio of 1:1, the main species α -D-Glcp-(1 \rightarrow 5)- β -D-Frup2,3H₂ was found at 56 %, a minor signal at 110.7 ppm indicated the formation of α -D-Glcp-(1 \rightarrow 5)-

2 Results

β -D-Frup1,2H₂, although this $\kappa O^{1,2}$ -coordination mode so far was detected only for the dimetalated β -D-Frup1,2;4,5H₄ species. At a higher Pd/leucrose ratio of 2:1, the main species was α -D-Glcp2,3H₂-(1→5)- β -D-Frup2,3H₂ at 40 %. The two assigned species are depicted in Fig. 2.102 and the corresponding ¹³C NMR chemical shifts and shift differences are listed in Table 2.102.

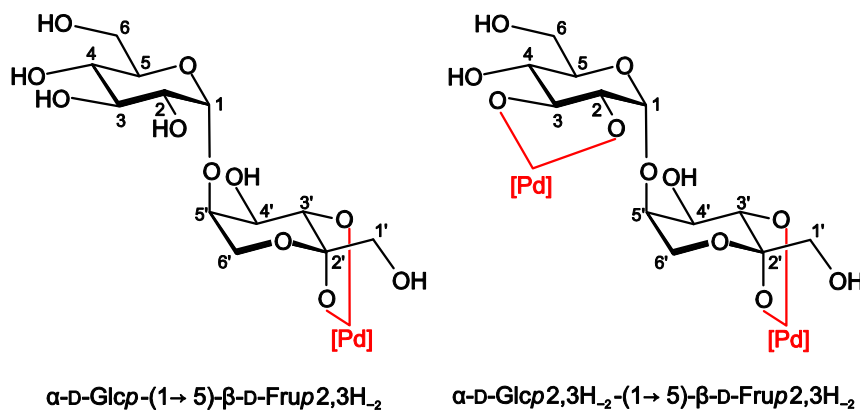


Figure 2.102. Species detected in solutions of Pd-tmen and D-leucrose at different molar ratios (species refer to a molar Pd/leucrose ratio of 1:1 for monometalated and to 2:1 for dimetalated forms).

Table 2.102. ¹³C NMR chemical shifts (δ /ppm) and shift differences ($\Delta\delta$) to the free disaccharide of D-leucrose (α -D-Glcp-(1→5)-D-Frup) ligands in Pd-tmen. Atoms are numbered as in Fig. 2.102.

		C1	C2	C3	C4	C5	C6	Chelate
α -D-Glcp (C)	δ	100.8	73.5	75.5	70.5	72.6	61.4	
	$\Delta\delta$	-0.2	0.9	2.0	0.2	0.0	0.1	–
β -D-Frup2,3H ₂ (C')	δ	66.8	107.3	76.7	72.4	80.1	62.1	
	$\Delta\delta$	2.4	8.6	8.2	1.8	0.4	-0.6	$\kappa O^{2,3}$
α -D-Glcp2,3H ₂ (C)	δ	101.4	82.7	81.4	72.7	75.6	61.4	
	$\Delta\delta$	0.4	10.1	7.9	2.4	3.0	0.1	$\kappa O^{2,3}$
β -D-Frup2,3H ₂ (C')	δ	66.9	107.4	77.0	72.5	79.7	62.3	
	$\Delta\delta$	2.5	8.7	8.5	1.9	0.0	-0.4	$\kappa O^{2,3}$

Additionally, smaller signals were detected which could not be reliably assigned to metalated species. However, in comparison to the previous results, one can assume $\kappa O^{1,2}$ -chelation with the fructopyranose unit as well as $\kappa O^{3,4}$ -chelation with the glucopyranose unit.

2 Results

2.13.6 D-Palatinose

D-Palatinose or D-isomaltulose is a α -D-Glcp-(1 \rightarrow 6)-D-Fruf disaccharide which is fixed in the furanose form by the (1 \rightarrow 6)-linkage of the monomeric units. A crystal structure was known in the literature which revealed an intramolecular hydrogen bond O2–H \cdots O2'.^[104]

As was expected, at an equimolar Pd/palatinose ratio α -D-Glcp-(1 \rightarrow 6)- β -D-Fruf_{2,3H₂} was the only detected species at 90 %. At a molar ratio of 2:1, this species was still detected at 18 % and two additional dimetalated forms were identified. The $\kappa O^{2,3}$ -chelated dimetalated species α -D-Glcp_{2,3H₂}-(1 \rightarrow 6)- β -D-Fruf_{2,3H₂} was found at 56 % and the $\kappa O^{3,4}$ -chelated α -D-Glcp_{3,4H₂}-(1 \rightarrow 6)- β -D-Fruf_{2,3H₂} species at 26 %. The three assigned species are depicted in Fig. 2.103 and the corresponding ¹³C NMR chemical shifts and shift differences are listed in Table 2.103.

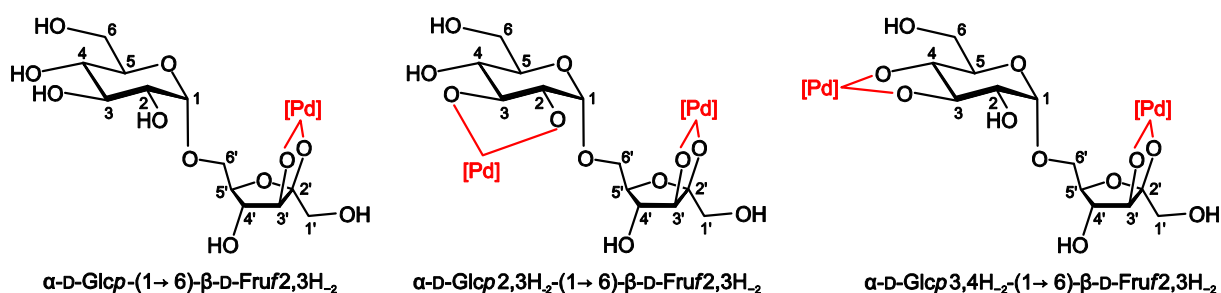


Figure 2.103. Species detected in solutions of Pd-tmen and D-palatinose at different molar ratios (species refer to a molar Pd/palatinose ratio of 1:1 for monometalated and to 2:1 for dimetalated forms).

Table 2.103. ¹³C NMR chemical shifts (δ /ppm) and shift differences ($\Delta\delta$) to the free disaccharide of D-palatinose (α -D-Glcp-(1 \rightarrow 6)-D-Fruf) ligands in Pd-tmen. Atoms are numbered as in Fig. 2.103.

		C1	C2	C3	C4	C5	C6	Chelate
α -D-Glcp (C)	δ	97.9	71.2	72.9	69.4	71.6	60.4	
	$\Delta\delta$	-1.0	-0.8	-0.8	-0.8	-0.9	-0.8	–
β -D-Fruf _{2,3H₂} (C')	δ	63.8	113.2	86.8	77.9	79.9	68.8	
	$\Delta\delta$	0.5	10.8	10.9	2.7	0.3	0.4	$\kappa O^{2,3}$
α -D-Glcp _{2,3H₂} (C)	δ	99.6	82.0	82.2	72.4	73.1	61.3	
	$\Delta\delta$	0.7	10.0	8.5	2.2	0.6	0.1	$\kappa O^{2,3}$
β -D-Fruf _{2,3H₂} (C')	δ	64.8	114.1	87.9	78.3	81.0	69.0	
	$\Delta\delta$	1.5	11.7	12.0	3.1	1.4	0.6	$\kappa O^{2,3}$
α -D-Glcp _{3,4H₂} (C)	δ	99.0	74.3	83.3	80.1	74.5	61.6	
	$\Delta\delta$	0.1	2.3	9.6	9.9	2.0	0.4	$\kappa O^{3,4}$
β -D-Fruf _{2,3H₂} (C')	δ	64.7	114.0	87.7	78.8	80.8	69.5	
	$\Delta\delta$	1.4	11.6	11.8	3.6	1.2	1.1	$\kappa O^{2,3}$

2 Results

The detected ratio of the two dimetalated forms was similar to the ratio of $\kappa O^{2,3}$ - and $\kappa O^{3,4}$ -chelated methyl α -D-glucopyranoside which underlines again the close relation between the methylated glycosides to the monomeric units of a disaccharide. The intramolecular hydrogen bond found in the crystal structure could possibly be formed in the monometalated and in the α -D-Glcp_{3,4H₂}-(1→6)- β -D-Fruf_{2,3H₂} complex but not in the $\kappa O^{2,3}$ -chelated dimetalated species.

2.13.7 D-Melecitose

D-Melecitose is a trisaccharide which is made up of D-sucrose and an α -D-Glcp unit at the O3' atom. In the crystal structure,^[105] an intramolecular hydrogen bond O6'-H...O5, as in sucrose, was found. 60 % D-melecitose was detected in equimolar solutions of Pd/melecitose together with 40 % of the α -D-Glcp_{2,3H₂}-(1→2)- β -D-Fruf_{2,3H₂}-(3→1)- α -D-Glcp species, whereas no signals of a $\kappa O^{2,3}$ -chelated glucopyranose unit linked to O3' could be identified. This is noteworthy because the glucopyranose units were assumed to be equally available for metalation. Elevating the Pd/melecitose ratio to 4:1, the dimetalated species α -D-Glcp_{2,3H₂}-(1→2)- β -D-Fruf_{2,3H₂}-(3→1)- α -D-Glcp_{2,3H₂} was detected at 70 % and both metalated species did not influence the formation tendency of the above-mentioned intramolecular hydrogen bond. The identified species are depicted in Fig. 2.104.

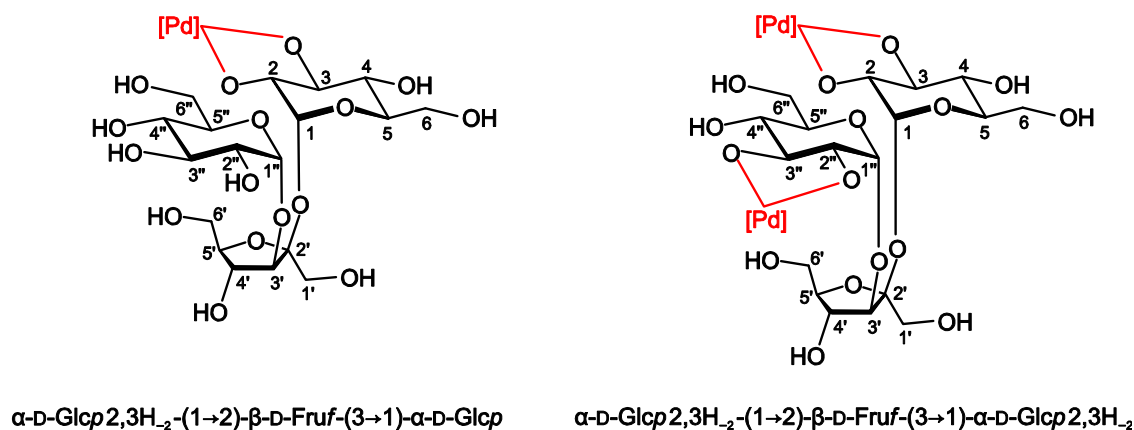


Figure 2.104. Species detected in solutions of Pd-tmen and D-melecitose at different molar ratios (species refer to a molar Pd/melecitose ratio of 1:1 for monometalated and to 2:1 for dimetalated forms).

The ¹³C NMR chemical shifts and shift differences of the two species are listed in Table 2.103. Nevertheless, several small ¹³C NMR signals indicated the presence of further unidentified species.

2 Results

Table 2.104. ^{13}C NMR chemical shifts (δ/ppm) and shift differences ($\Delta\delta$) to the free trisaccharide of D-melecitose ($\alpha\text{-D-Glcp-(1}\rightarrow\text{2)-}\beta\text{-D-Fruf-(3}\rightarrow\text{1)-}\alpha\text{-D-Glcp}$) ligands in Pd-tmen. Atoms are numbered as in Fig. 2.104.

		C1	C2	C3	C4	C5	C6	Chelate
$\alpha\text{-D-Glcp2,3H}_2$ (C)	δ	92.8	81.4	82.6	72.0	73.7	60.8	
	$\Delta\delta$	0.4	9.8	8.9	1.8	0.8	-0.1	$\kappa\text{O}^{2,3}$
$\beta\text{-D-Fruf}$ (C')	δ	64.8	104.3	86.1	74.7	82.6	62.6	
	$\Delta\delta$	2.2	0.0	2.2	0.8	0.8	-0.2	–
$\alpha\text{-D-Glcp}$ (C'')	δ	100.5	72.3	73.7	69.8	72.7	61.3	
	$\Delta\delta$	-0.4	0.2	0.3	-0.4	-0.2	0.1	–
$\alpha\text{-D-Glcp2,3H}_2$ (C)	δ	92.8	81.5	82.2	72.1	73.8	60.8	
	$\Delta\delta$	0.4	9.9	8.5	1.9	0.9	-0.1	$\kappa\text{O}^{2,3}$
$\beta\text{-D-Fruf}$ (C')	δ	64.9	104.3	86.0	74.2	81.8	62.8	
	$\Delta\delta$	2.3	0.0	2.1	0.4	0.0	0.0	–
$\alpha\text{-D-Glcp2,3H}_2$ (C'')	δ	101.3	82.6	82.1	71.7	73.2	61.2	
	$\Delta\delta$	0.4	10.5	8.7	1.5	0.3	0.0	$\kappa\text{O}^{2,3}$

2.13.8 D-Raffinose

D-Raffinose is a trisaccharide which could be obtained by adding a $\beta\text{-D-Galp}$ unit at the O6 atom of D-sucrose. The (1 \rightarrow 6)-linkage does not impair the intramolecular hydrogen bond O6'-H \cdots O5 which is found in sucrose. The ^{13}C NMR spectroscopic investigation of D-raffinose in Pd-tmen revealed 50 % of unmetalated trisaccharide and various dimetalated forms which were not identified until a molar Pd/raffinose ratio of 2:1. At this molar Pd/raffinose ratio, two dimetalated forms could be identified which are depicted in Fig. 2.105.

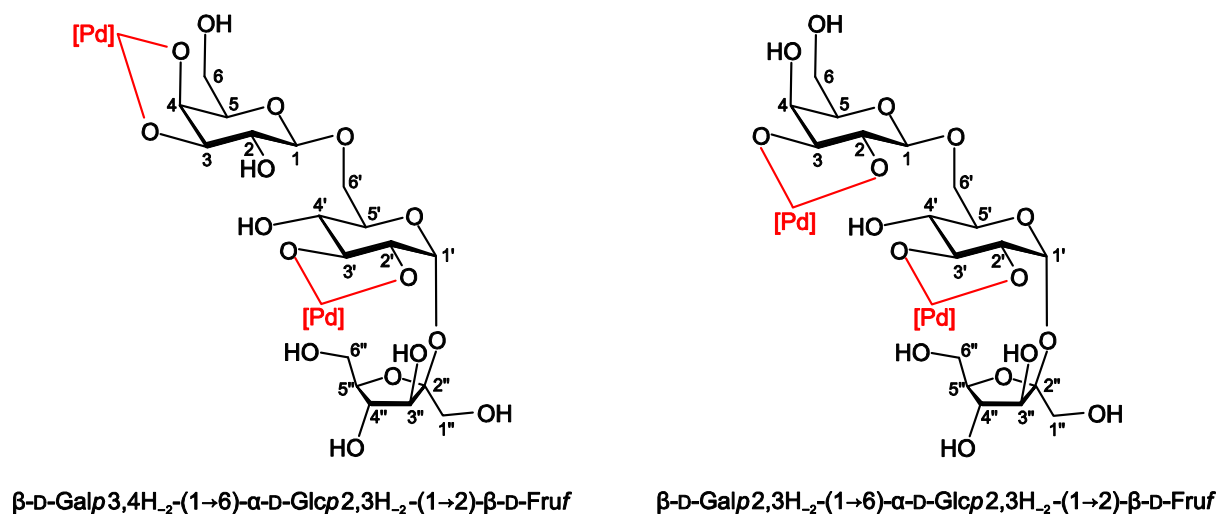


Figure 2.105. Species detected in solutions of Pd-tmen and D-raffinose at a molar Pd/raffinose ratio of 2:1.

2 Results

The dimetalated species β -D-Galp3,4H₂-(1→6)- α -D-Glcp2,3H₂-(1→2)- β -D-Fruf was detected at 60 % of the species distribution, β -D-Galp2,3H₂-(1→6)- α -D-Glcp2,3H₂-(1→2)- β -D-Fruf at 30 %. Elevating the molar Pd/raffinose ratio to 4:1, the previously mentioned compounds' share of species distribution decreased to 55 % and 20 %, whereas a trimetalated species β -D-Galp3,4H₂-(1→6)- α -D-Glcp2,3H₂-(1→2)- β -D-Fruf1,3H₂ was detected at 10 %. However, this last species was identified only by its C2 signal of the fructose unit, the ¹³C NMR chemical shifts and shift differences of the two dimetalated species are summarized in Table 2.105.

Table 2.105. ¹³C NMR chemical shifts (δ /ppm) and shift differences ($\Delta\delta$) to the free trisaccharide of D-raffinose (β -D-Galp-(1→6)- α -D-Glcp-(1→2)- β -D-Fruf) ligands in Pd-tmen. Atoms are numbered as in Fig. 2.105.

		C1	C2	C3	C4	C5	C6	Chelate
β -D-Galp3,4H ₂ (C)	δ	99.7	73.2	79.8	80.6	70.0	63.2	
	$\Delta\delta$	0.6	4.1	9.7	10.8	-1.6	1.5	$\kappa O^{3,4}$
α -D-Glcp2,3H ₂ (C')	δ	93.1	81.4	81.8	72.0	72.8	66.5	
	$\Delta\delta$	0.4	9.8	8.5	2.0	0.8	0.0	$\kappa O^{2,3}$
β -D-Fruf (C'')	δ	63.6	103.6	79.7	75.2	82.0	63.6	
	$\Delta\delta$	1.6	-0.8	2.7	0.6	0.0	0.2	-
β -D-Galp2,3H ₂ (C)	δ	99.7	77.8	78.7	72.0	71.5	61.8	
	$\Delta\delta$	0.6	8.7	8.6	2.2	-0.1	0.1	$\kappa O^{2,3}$
α -D-Glcp2,3H ₂ (C')	δ	93.2	81.6	81.9	72.0	72.6	65.1	
	$\Delta\delta$	0.5	10.0	8.6	2.0	0.6	-1.4	$\kappa O^{2,3}$
β -D-Fruf (C'')	δ	63.5	103.7	79.2	75.2	82.0	63.1	
	$\Delta\delta$	1.5	-0.7	2.7	0.6	0.0	0.0	-

Again, the detected metalated species corresponded to the preferred metalation sites of the methyl glycosides which simplified the interpretation of the ¹³C NMR spectra. The intramolecular hydrogen bond O2-H...O1' detected for the dimetalated sucrose species α -D-Glcp3,4H₂-(1→2)- β -D-Fruf1,3H₂ would also be possible for the trimetalated D-raffinose species.

2.14 From disaccharides to the polysaccharides with β -connected units

D-Lactose, D-cellobiose and cellulose (see Fig. 2.106) have the β -(1 \rightarrow 4)-glycosidic bond in common which is decisive for the conformation of the carbohydrate. As a result, the $\kappa O^{2,3}$ -diolato units of the monomers are oriented opposite to each other and an intramolecular hydrogen bond O3–H'...O5 stabilizes this conformation. The crystal structures of D-lactose^[106] and D-cellobiose^[107] confirmed this hydrogen bond, whereas in aqueous solution it seems to be insignificant.^[5, 108] Cellulose, the most common polysaccharide in nature, is a linear homopolymer of β -(1 \rightarrow 4)-linked cellobiose unit which is insoluble in water because of strong intra- and intermolecular hydrogen bonds stabilizing cellulose fibers. The most prominent cellulose solvent is cuprammonium hydroxide from which the palladium solvents are derived.

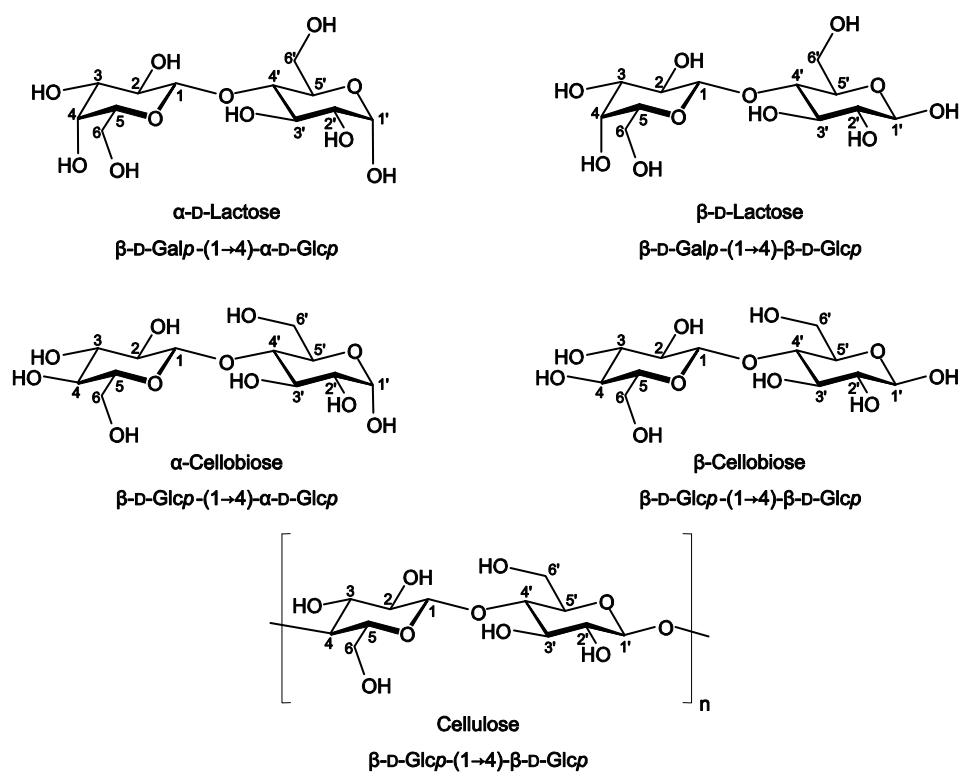


Figure 2.106. All configurations detected in the ^{13}C NMR spectra of the investigated β -connected disaccharides in D_2O and the configuration of the monomeric building unit of cellulose. The proportional distribution of the various forms can be estimated from the corresponding spectra depicted in the Appendix.

2.14.1 D-Lactose

D-Lactose is a β -D-Galp-(1 \rightarrow 4)- α -D-Glcp disaccharide which is found in the milk of mammals. As described above, a possible intramolecular hydrogen bond O3–H'...O5 stabilizes the syndiotactic conformation depicted in Fig. 2.106. Predicting the preferred

2 Results

metalation sites, a first Pd(tmen) fragment will coordinate to the $\kappa O^{1,2}$ -diolato unit of the reducing β -D-Glcp monomer thereby not affecting the possible intramolecular hydrogen bond. A second Pd(tmen) fragment will coordinate predominantly to the $\kappa O^{3,4}$ -diolato unit of the non-reducing β -D-Galp monomer. Analysis of the various ^{13}C NMR spectra confirmed these assumptions. At an equimolar Pd/lactose ratio apart from 20 % of the educt, two monometalated species were detected, 36 % β -D-Galp-(1 \rightarrow 4)- α -D-Glcp1,2H $_2$ and 21 % β -D-Galp-(1 \rightarrow 4)- β -D-Glcp1,2H $_2$. Small signals close to the C1' signals also indicated the formation of the α - and β -anomer of the monometalated Galp3,4H $_2$ -(1 \rightarrow 4)-D-Glcp species. Elevating the Pd/lactose ratio to 2:1, 42 % of the predicted dimetalated β -D-Galp3,4H $_2$ -(1 \rightarrow 4)- α -D-Glcp1,2H $_2$ species and 32 % of the β -D-Galp3,4H $_2$ -(1 \rightarrow 4)- β -D-Glcp1,2H $_2$ species were found. The species are depicted in Fig. 2.107 and the ^{13}C NMR chemical shifts and shift differences are summarized in Table 2.106.

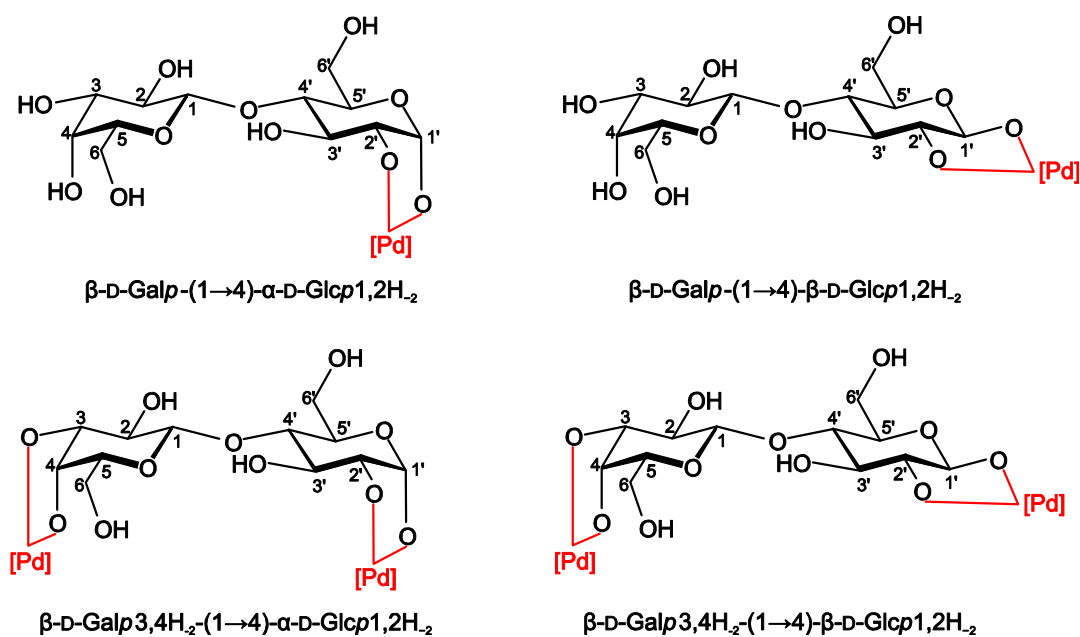


Figure 2.107. Species detected in solutions of Pd-tmen and D-lactose at different molar ratios (species refer to a molar Pd/lactose ratio of 1:1 for monometalated and to 2:1 for dimetalated forms).

Additionally, two minor dimetalated species were detected each at 13 %. Although a complete assignment of signals was impossible, the species could be identified as β -D-Galp2,3H $_2$ -(1 \rightarrow 4)- α -D-Glcp1,2H $_2$ (C1 104.8 ppm, C1' 102.3 ppm) and β -D-Galp2,3H $_2$ -(1 \rightarrow 4)- β -D-Glcp1,2H $_2$ (C1, C1' 105.0 ppm) according to the C1 signals. The coordination of a Pd(tmen) fragment to the $\kappa O^{2,3}$ -diolato unit of the reducing β -D-Glcp monomer could be precluded by the absence of corresponding signals at approximately 100 ppm.

2 Results

Table 2.106. ^{13}C NMR chemical shifts (δ/ppm) and shift differences ($\Delta\delta$) to the free disaccharide of D-lactose ($\beta\text{-D-Galp-(1}\rightarrow\text{4)-D-Glc}$) ligands in Pd-tmen. Atoms are numbered as in Fig. 2.107.

		C1	C2	C3	C4	C5	C6	Chelate
$\beta\text{-D-Galp (C)}$	δ	103.5	71.8	73.3	69.3	76.0	61.8	
	$\Delta\delta$	0.0	0.2	0.1	0.1	0.0	0.1	–
$\alpha\text{-D-Glcp1,2H}_2\text{ (C')}$	δ	102.2	81.9	77.4	79.0	70.1	60.7	
	$\Delta\delta$	9.8	10.1	5.4	–0.1	–0.6	0.1	$\kappa\text{O}^{1,2}$
$\beta\text{-D-Galp (C)}$	δ	103.7	71.6	73.2	69.2	76.1	61.7	
	$\Delta\delta$	0.2	0.0	0.0	0.0	0.1	0.0	–
$\beta\text{-D-Glcp1,2H}_2\text{ (C')}$	δ	104.7	84.0	79.9	80.2	75.6	60.7	
	$\Delta\delta$	8.3	9.6	4.9	1.3	0.2	0.0	$\kappa\text{O}^{1,2}$
$\beta\text{-D-Galp3,4H}_2\text{ (C)}$	δ	103.5	74.4	83.5	80.1	75.7	61.9	
	$\Delta\delta$	0.0	2.8	10.3	10.9	–0.3	0.2	$\kappa\text{O}^{3,4}$
$\alpha\text{-D-Glcp1,2H}_2\text{ (C')}$	δ	102.2	81.9	76.3	77.7	70.2	61.4	
	$\Delta\delta$	9.8	10.1	4.3	–1.4	–0.5	0.2	$\kappa\text{O}^{1,2}$
$\beta\text{-D-Galp3,4H}_2\text{ (C)}$	δ	103.8	74.3	83.5	79.9	75.7	61.9	
	$\Delta\delta$	0.3	2.7	10.3	10.7	–0.3	0.2	$\kappa\text{O}^{3,4}$
$\beta\text{-D-Glcp1,2H}_2\text{ (C')}$	δ	104.7	84.1	77.3	78.9	76.0	61.4	
	$\Delta\delta$	8.3	9.7	2.3	0.0	0.6	0.7	$\kappa\text{O}^{1,2}$

2.14.2 D-Cellobiose and Cellulose

D-Cellobiose, the monomeric building unit of cellulose, and cellulose itself are built of (1 \rightarrow 4)-linked $\beta\text{-D-Glcp}$ units. Again, the above described hydrogen bond O3–H' \cdots O5 stabilizes the conformation depicted in Fig. 2.106. According to the former results, the D-cellobiose's $\kappa\text{O}^{1,2}$ -diolato unit of the reducing monomer and the $\kappa\text{O}^{2,3}$ -diolato unit of the non-reducing monomer should be metalated in this order. Interpreting the ^{13}C NMR spectra depicted in Fig. 2.108 at an equimolar Pd/cellobiose ratio apart from 26 % of the educt, two monometalated species were detected, 37 % $\beta\text{-D-Glcp-(1}\rightarrow\text{4)-}\alpha\text{-D-Glcp1,2H}_2$ and 20 % $\beta\text{-D-Glcp-(1}\rightarrow\text{4)-}\beta\text{-D-Glcp1,2H}_2$. Elevating the Pd/cellobiose ratio to 2:1, the two previous monometalated species were still detected at 15 % and 9 %, the dimetalated species labeled in Fig. 2.108 were found at 38 % for $\beta\text{-D-Glcp2,3H}_2\text{-(1}\rightarrow\text{4)-}\alpha\text{-D-Glcp1,2H}_2$ and 24 % for $\beta\text{-D-Glcp2,3H}_2\text{-(1}\rightarrow\text{4)-}\beta\text{-D-Glcp1,2H}_2$. As one can see, small unassigned signals remained at the bottom ^{13}C NMR spectrum in Fig. 2.108 which should correspond to the α - and β -anomer of $\beta\text{-D-Glcp3,4H}_2\text{-(1}\rightarrow\text{4)-D-Glcp1,2H}_2$. The completely assigned species are depicted in Fig. 2.109 and the ^{13}C NMR chemical shifts and shift differences are summarized in Table 2.107.

2 Results

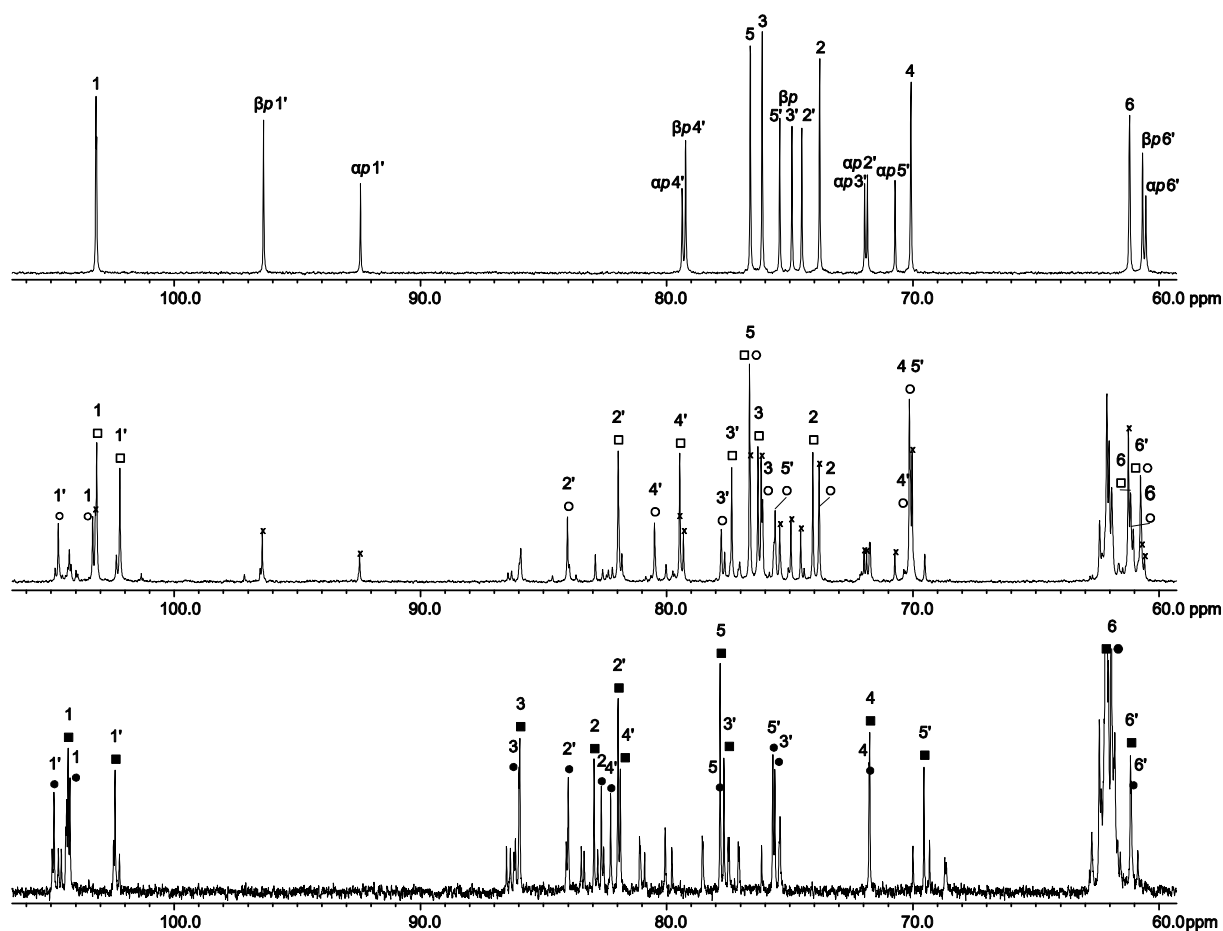


Figure 2.108. ^{13}C NMR spectra of D-cellobiose in Pd-tmen at a molar Pd/cellobiose ratio of 0:1 (top), 1:1 (middle) and 2:1 (bottom). The signals of free D-cellobiose are marked with (x); (\square) $\beta\text{-D-Glcp-(1}\rightarrow\text{4)-}\alpha\text{-D-Glcp1,2H}_2$, (\blacksquare) $\beta\text{-D-Glcp2,3H}_2\text{-(1}\rightarrow\text{4)-}\alpha\text{-D-Glcp1,2H}_2$, (\circ) $\beta\text{-D-Glcp-(1}\rightarrow\text{4)-}\beta\text{-D-Glcp1,2H}_2$ and (\bullet) $\beta\text{-D-Glcp2,3H}_2\text{-(1}\rightarrow\text{4)-}\beta\text{-D-Glcp1,2H}_2$.

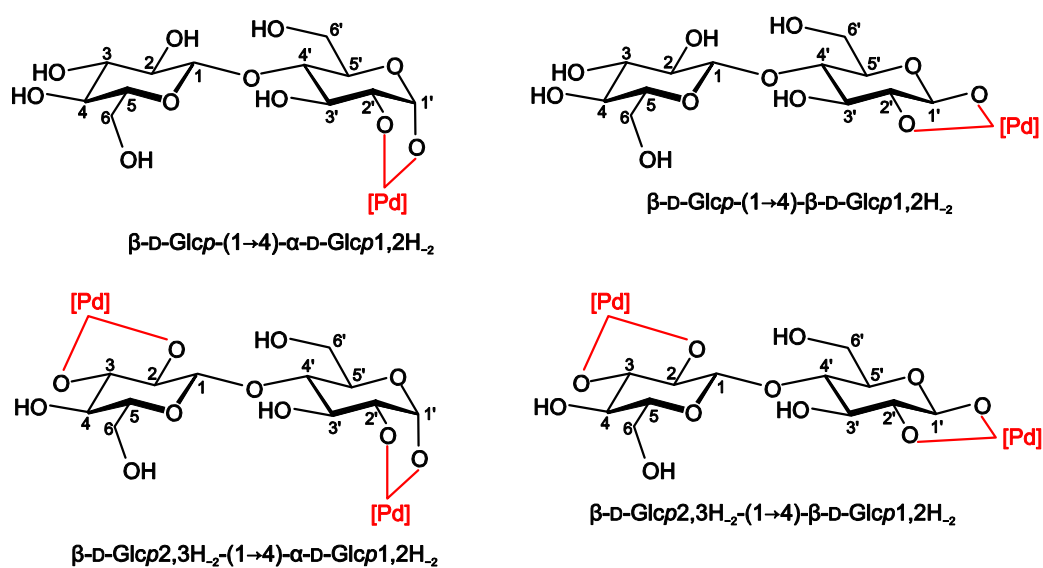


Figure 2.109. Species detected in solutions of Pd-tmen and D-cellobiose at different molar ratios (species refer to a molar Pd/cellobiose ratio of 1:1 for monometalated and to 2:1 for dimetalated forms).

2 Results

Table 2.107. ^{13}C NMR chemical shifts (δ/ppm) and shift differences ($\Delta\delta$) to the free disaccharide of D-cellobiose ($\beta\text{-D-Glcp-(1}\rightarrow\text{4)-D-Glc}$) ligands in Pd-tmen. Atoms are numbered as in Fig. 2.109.

		C1	C2	C3	C4	C5	C6	Chelate
$\beta\text{-D-Glcp (C)}$	δ	103.1	74.1	76.3	70.0	76.6	61.2	
	$\Delta\delta$	-0.1	0.3	0.2	-0.1	0.0	0.0	-
$\alpha\text{-D-Glcp1,2H}_2\text{ (C')}$	δ	102.2	82.0	77.4	79.5	70.0	60.8	
	$\Delta\delta$	9.8	10.2	5.4	0.1	-0.7	0.3	$\kappa\text{O}^{1,2}$
$\beta\text{-D-Glcp (C)}$	δ	103.3	73.8	76.1	70.1	76.6	61.1	
	$\Delta\delta$	0.1	0.0	0.0	0.0	0.0	-0.1	-
$\beta\text{-D-Glcp1,2H}_2\text{ (C')}$	δ	104.7	84.0	77.8	80.5	75.6	60.8	
	$\Delta\delta$	8.3	9.5	2.9	1.3	0.2	0.1	$\kappa\text{O}^{1,2}$
$\beta\text{-D-Glcp2,3H}_2\text{ (C)}$	δ	104.3	82.9	85.9	71.7	77.8	61.9	
	$\Delta\delta$	1.1	9.1	9.8	1.6	1.2	0.7	$\kappa\text{O}^{2,3}$
$\alpha\text{-D-Glcp1,2H}_2\text{ (C')}$	δ	102.4	81.9	77.6	81.8	69.5	61.1	
	$\Delta\delta$	10.0	10.1	5.6	2.4	-1.2	0.6	$\kappa\text{O}^{1,2}$
$\beta\text{-D-Glcp2,3H}_2\text{ (C)}$	δ	104.2	82.6	85.9	71.7	77.8	61.9	
	$\Delta\delta$	1.0	8.8	9.8	1.6	1.2	0.7	$\kappa\text{O}^{2,3}$
$\beta\text{-D-Glcp1,2H}_2\text{ (C')}$	δ	104.8	84.0	75.6	82.2	75.6	61.1	
	$\Delta\delta$	8.4	9.5	0.7	3.0	0.2	0.4	$\kappa\text{O}^{1,2}$

It is known that Pd-en as Schweizer's reagent is able to dissolve cellulose.^[41] To complete the investigation of β -connected oligosaccharides, hydrocellulose ($M_w = 23250$) was treated with Pd-tmen. After two days under stirring at 5 °C the treatment of Pd-tmen and hydrocellulose—two equivalents of Pd-tmen per $\kappa\text{O}^{2,3}$ -diolato unit—resulted in a clear yellow viscous solution. The ^{13}C NMR spectrum is depicted in Fig. 2.110, the chemical shifts of cellulose in Pd-tmen are listed in Table 2.108. As one can see, essentially one set of signals was detected which corresponded to the assumed $\kappa\text{O}^{2,3}$ -chelated fully metalated cellulose polysaccharide.

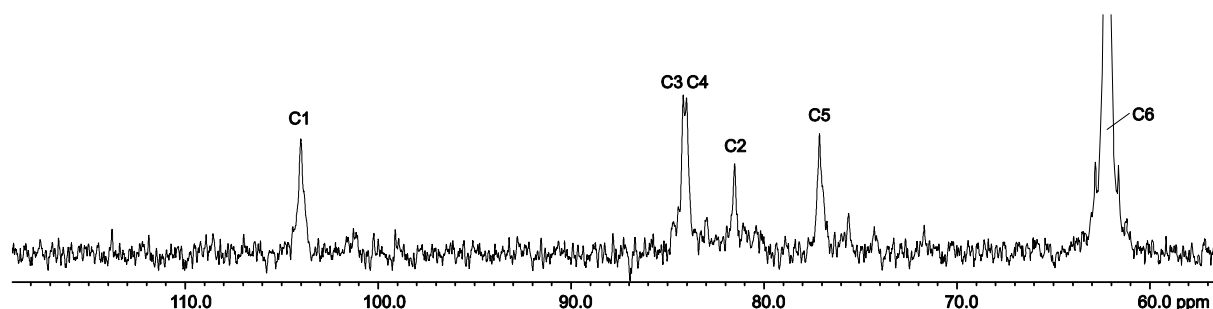


Figure 2.110. ^{13}C NMR spectrum of hydrocellulose ($M_w = 23250$) in Pd-tmen. The stoichiometry of Pd-tmen and D-cellobiose 2:1 was set to enforce full metalation.

2 Results

Table 2.108. ^{13}C NMR chemical shifts (δ/ppm) of cellulose in Pd-tmen.

		C1	C2	C3	C4	C5	C6	Chelate
$[\beta\text{-D-Glcp2,3H}_2\text{-}]_n$	δ	104.0	81.5	84.1	84.1	77.1	62.3	$\kappa\text{O}^{2,3}$

No reference ^{13}C NMR signals are available for the calculation of CIS values of the metalated cellulose because of the cellulose's insolubility in water. Nevertheless, comparing the signals of D-cellobiose to those of cellulose, the $\kappa\text{O}^{2,3}$ -chelation was confirmed. The discussed cellulose species is shown in Fig. 2.111.

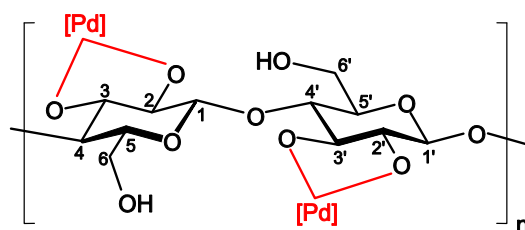


Figure 2.111. Species detected in solutions of Pd-tmen and cellulose.

An intramolecular hydrogen bond $\text{O6}'\text{-H}\cdots\text{O2}$ from the hydroxymethyl group to the alkoxido O2 atom to stiffen the metalated cellulose in Pd-en is described in the literature.^[41] With Pd-tmen promoting intramolecular hydrogen bonding, this effect could possibly be intensified.

2.15 From disaccharides to the oligosaccharides with α -connected units

Di- and oligosaccharides with α -connected units, depicted in Fig. 2.112, are integrated into this section. The non-reducing α,α -D-trehalose is a symmetric (1 \rightarrow 1)-linked glucopyranoside dimer whereas D-melibiose consists of an α -D-galactopyranoside which is (1 \rightarrow 6)-linked to a glucopyranoside unit. The focus is set on D-maltose and maltose-derived oligosaccharides which all consist of (1 \rightarrow 4)-linked glucopyranoside units. Contrary to D-cellobiose and cellulose, the $\kappa\text{O}^{2,3}$ -diolato units of the glucopyranoside monomers were oriented on the same site which makes the formation of an intramolecular hydrogen bond $\text{O3}'\text{-H}\cdots\text{O2}$, or the other way round, possible. This hydrogen bond was confirmed in the crystal structures of α - and β -D-maltose^[109-110] and could be assumed for the maltose-derived oligomers, too. Also in aqueous solution, the (1 \rightarrow 4)-linked glucopyranoside oligomers were found in an isotatic conformation referred to the $\kappa\text{O}^{2,3}$ -chelation sites.^[111] The polymeric (1 \rightarrow 4)-linked glucopyranoside called amylose is the minor component of starch, the major component is amylopectin. Amylose is soluble in water and supposed to form a random coil

2 Results

that has a somewhat helical character.^[112] The results of the treatment of Pd-tmen with the introduced compounds are presented herein.

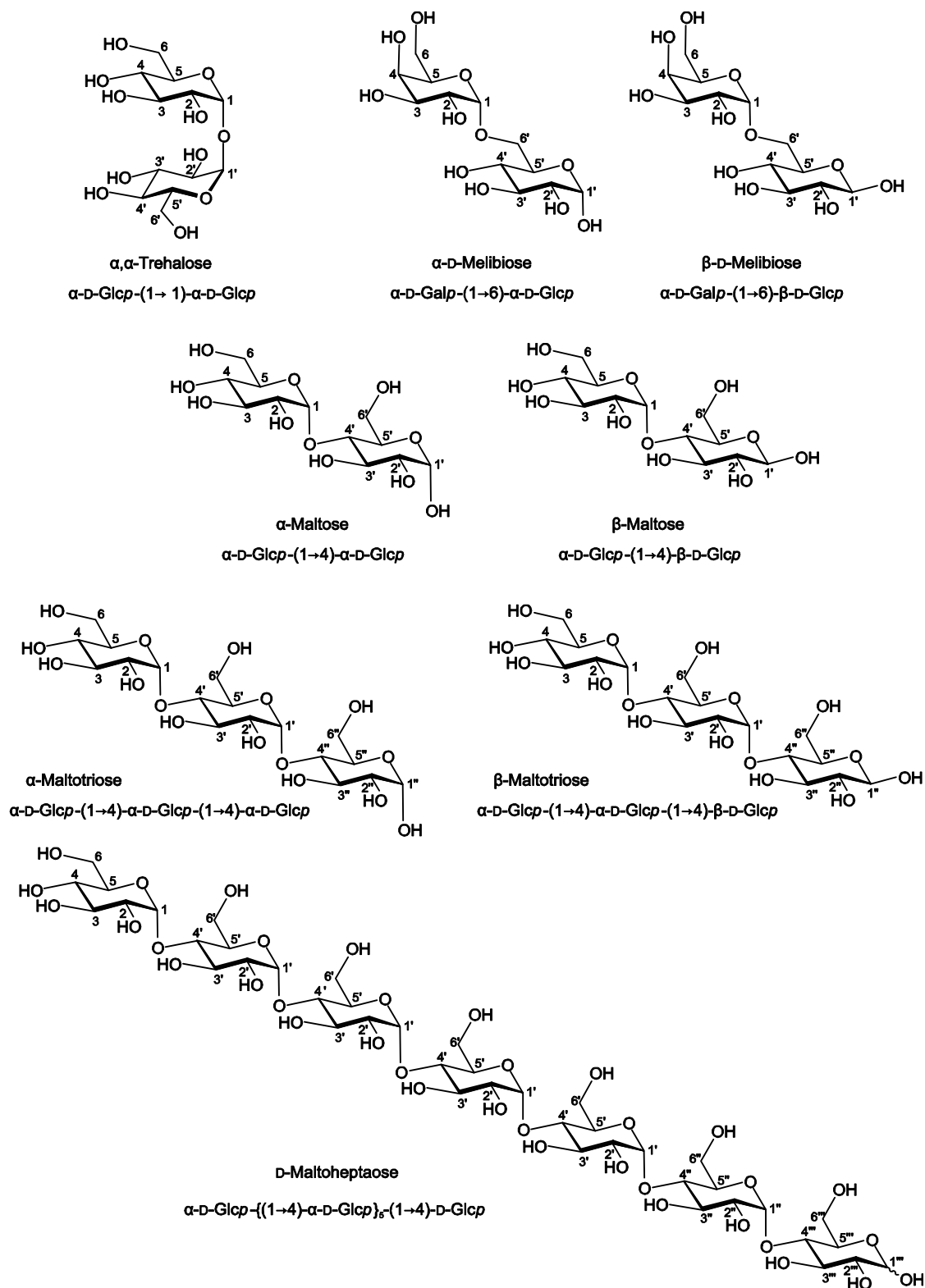


Figure 2.112. All configurations detected in the ^{13}C NMR spectra of the investigated α -connected di- and oligosaccharides in D_2O . The proportional distribution of the various forms can be estimated from the corresponding spectra depicted in the Appendix.

2 Results

2.15.1 α,α -D-Trehalose

The C_2 -symmetric α,α -D-trehalose shows only six instead of twelve signals in the ^{13}C NMR spectrum but with double the intensity. Whereas the ^{13}C NMR spectra of higher metalation ratios could not be assigned due to the comparable signals' intensity, at an equimolar ratio of Pd/ α,α -trehalose two monometalated species could be assigned. Both species are depicted in Fig. 2.113, the corresponding ^{13}C NMR chemical shifts and shift differences are summed up in Table 2.109.

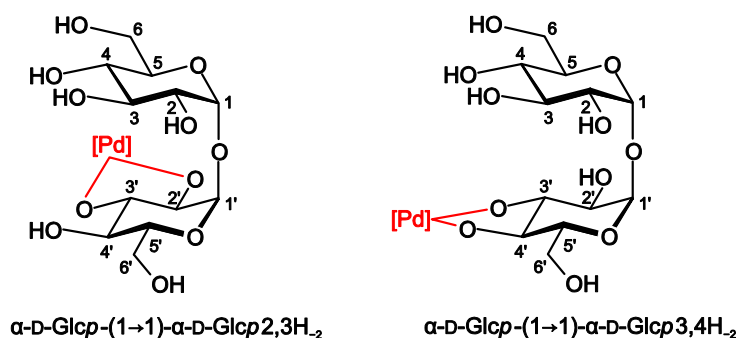


Figure 2.113. Species detected in solutions of Pd-tmen and α,α -D-trehalose at a molar Pd/trehalose ratio of 1:1.

Besides 38 % unmetalated α,α -D-trehalose, with 29 % $\alpha\text{-D-Glcp-(1}\rightarrow\text{1)-}\alpha\text{-D-Glcp2,3H}_2$ and 25 % $\alpha\text{-D-Glcp-(1}\rightarrow\text{1)-}\alpha\text{-D-Glcp3,4H}_2$, an almost equidistribution of solution's species was found.

Table 2.109. ^{13}C NMR chemical shifts (δ /ppm) and shift differences ($\Delta\delta$) to the free disaccharide of α,α -D-trehalose ($\alpha\text{-D-Glcp-(1}\rightarrow\text{1)-}\alpha\text{-D-Glcp}$) ligands in Pd-tmen. Atoms are numbered as in Fig. 2.113.

		C1	C2	C3	C4	C5	C6	Chelate
$\alpha\text{-D-Glcp (C)}$	δ	93.6	71.9	73.2	70.5	72.5	61.1	
	$\Delta\delta$	-0.2	0.3	0.1	0.2	-0.2	0.0	–
$\alpha\text{-D-Glcp2,3H}_2 (C')$	δ	94.4	81.3	81.8	72.2	73.0	61.6	
	$\Delta\delta$	0.6	9.7	8.7	1.9	0.3	0.5	$\kappa\text{O}^{2,3}$
$\alpha\text{-D-Glcp (C)}$	δ	93.8	71.8	73.1	70.3	72.6	61.1	
	$\Delta\delta$	0.0	0.2	0.0	0.0	-0.1	0.0	–
$\alpha\text{-D-Glcp3,4H}_2 (C')$	δ	94.0	73.9	82.4	79.9	74.8	61.9	
	$\Delta\delta$	0.2	2.3	9.3	9.6	2.1	0.8	$\kappa\text{O}^{3,4}$

With Pd-chxn, two dimetalated compounds were enriched and already assigned.^[78] Keeping the original C_2 -symmetry, the main species was identified to be $\alpha\text{-D-Glcp3,4-(1}\rightarrow\text{1)-}\alpha\text{-D-Glcp3,4H}_2$, the minor species was found to be $\alpha\text{-D-Glcp2,3-(1}\rightarrow\text{1)-}\alpha\text{-D-Glcp3,4H}_2$. These compounds were also identified in solutions of Pd-tmen by their C1 signals.

2 Results

The C1 of α -D-Glcp3,4-(1 \rightarrow 1)- α -D-Glcp3,4H₂ was found at 94.0 ppm with double intensity and the C1 and C1' of the minor α -D-Glcp2,3-(1 \rightarrow 1)- α -D-Glcp3,4H₂ species were found at 94.2 and 93.6 ppm, respectively.

2.15.2 D-Melibiose

D-Melibiose is a α -D-Galp-(1 \rightarrow 6)- α -D-Glcp disaccharide which can be formed by invertase-mediated hydrolysis of raffinose. Caused by the (1 \rightarrow 6)-linkage of the two monomeric building units, D-melibiose is the only investigated disaccharide which provides three $\kappa O^{1,2}$ -diolato units for metalation. Therefore, the investigation of D-melibiose revealed a three-step metalation which confirmed all the rules of Pd^{II}N₂ metalation formulated so far. First, the reducing $\kappa O^{1,2}$ -diolato unit was metalated, second the *cis*-vicinal $\kappa O^{3,4}$ -diolato unit of the α -D-Galp unit and last the *trans*-vicinal $\kappa O^{3,4}$ -diolato unit of the glucopyranose unit. All assigned species are shown in Fig. 2.114.

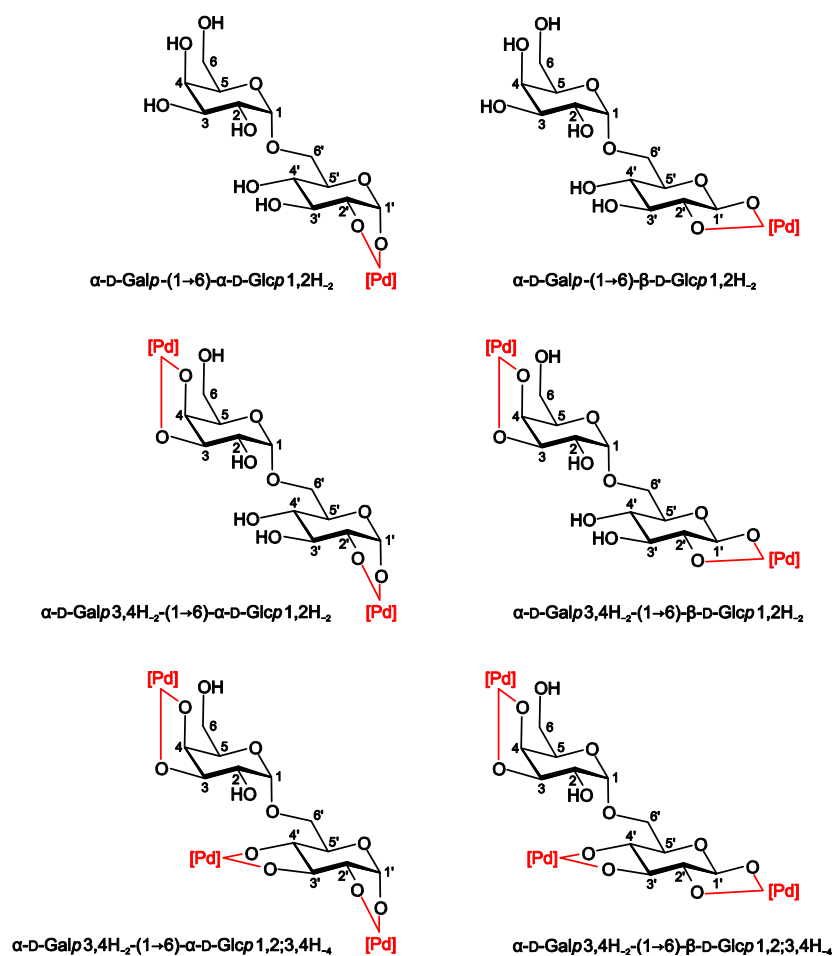


Figure 2.114. Species detected in solutions of Pd-tmen and D-melibiose at different molar ratios (species refer to a molar Pd/melibiose ratio of 1:1 for monometalated, to 2:1 for dimetalated and to 4:1 for higher metalated forms).

2 Results

At an equimolar Pd/melibiose ratio, α -D-Galp-(1 \rightarrow 6)- α -D-Glcp1,2H₂ was found to be the main species with 41 % of the percentual distribution of solution's species. Minor species were the unmetalated D-melibiose at 33 % and α -D-Galp-(1 \rightarrow 6)- β -D-Glcp1,2H₂ at 9 %. Additionally, a C1 signal at 112.3 ppm indicated the presence of 5 % of the α -D-Galp-(1 \rightarrow 6)- α -D-Glcf1,2H₂ species. At a molar Pd/melibiose ratio of 2:1 the monometalated forms α -D-Galp-(1 \rightarrow 6)- α -D-Glcp1,2H₂ and α -D-Galp-(1 \rightarrow 6)- β -D-Glcp1,2H₂ were still detected at 20 % and 7 % of the percentual distribution of solution's species. At 35 %, the main species was α -D-Galp3,4H₂-(1 \rightarrow 6)- α -D-Glcp1,2H₂, accompanied by 20 % of α -D-Galp2,3H₂-(1 \rightarrow 6)- α -D-Glcp1,2H₂. Elevating the Pd/melibiose ratio to 4:1, the β -anomer of the reducing D-Glcp unit was the dominating trimetalated form in the ¹³C NMR spectrum. Therefore, 32 % of α -D-Galp3,4H₂-(1 \rightarrow 6)- β -D-Glcp1,2;3,4H₄ and 15 % of α -D-Galp3,4H₂-(1 \rightarrow 6)- α -D-Glcp1,2;3,4H₄ were identified in the spectrum. Besides those, 14 % of α -D-Galp3,4H₂-(1 \rightarrow 6)- α -D-Glcp1,2H₂ and 9 % of α -D-Galp2,3H₂-(1 \rightarrow 6)- α -D-Glcp1,2H₂ were still found. The ¹³C NMR chemical shifts and shift differences of the assigned species are listed in Table 2.110.

Table 2.110. ¹³C NMR chemical shifts (δ /ppm) and shift differences ($\Delta\delta$) to the free disaccharide of D-melibiose (α -D-Galp-(1 \rightarrow 6)-D-Glc) ligands in Pd-tmen. Atoms are numbered as in Fig. 2.114.

		C1	C2	C3	C4	C5	C6	Chelate
α -D-Galp (C)	δ	98.8	69.2	70.1	69.8	71.5	61.7	
	$\Delta\delta$	0.0	0.1	0.0	0.0	-0.1	0.0	-
α -D-Glcp1,2H ₂ (C')	δ	102.6	82.0	79.1	70.2	70.0	66.7	
	$\Delta\delta$	9.8	10.0	5.5	0.0	-0.7	0.2	$\kappa O^{1,2}$
α -D-Galp (C)	δ	98.8	69.2	70.1	69.8	71.5	61.7	
	$\Delta\delta$	0.0	0.1	0.0	0.0	-0.1	0.0	-
β -D-Glcp1,2H ₂ (C')	δ	104.9	84.3	77.2	70.9	75.5	66.2	
	$\Delta\delta$	8.2	9.6	0.7	0.9	0.5	-0.2	$\kappa O^{1,2}$
α -D-Galp2,3H ₂ (C)	δ	99.4	77.9	78.8	71.9	71.76	61.6	
	$\Delta\delta$	0.6	8.8	8.7	2.1	0.1	-0.1	$\kappa O^{2,3}$
α -D-Glcp1,2H ₂ (C')	δ	102.7	82.1	79.3	70.0	70.0	66.4	
	$\Delta\delta$	9.9	10.1	5.7	-0.2	-0.7	-0.1	$\kappa O^{1,2}$
α -D-Galp3,4H ₂ (C)	δ	99.4	69.8	79.9	80.6	73.2	61.4	
	$\Delta\delta$	0.6	0.7	9.8	10.8	1.6	-0.3	$\kappa O^{3,4}$
α -D-Glcp1,2H ₂ (C')	δ	102.6	82.0	79.2	70.0	70.0	63.2	
	$\Delta\delta$	9.8	10.0	5.6	-0.2	-0.7	-3.3	$\kappa O^{1,2}$

2 Results

Table 2.110. Continued.

		C1	C2	C3	C4	C5	C6	Chelate
α -D-Galp3,4H ₂ (C)	δ	99.7	69.9	79.9	80.6	73.0	61.6	
	$\Delta\delta$	0.9	0.8	9.8	10.8	1.4	-0.1	$\kappa O^{3,4}$
α -D-Glcp1,2;3,4H ₄ (C')	δ	102.3	84.8	89.8	79.0	72.3	67.2	
	$\Delta\delta$	9.5	12.8	16.2	8.8	1.7	0.7	$\kappa O^{1,2};\kappa O^{3,4}$
α -D-Galp3,4H ₂ (C)	δ	98.9	69.7	79.9	80.7	73.1	61.5	
	$\Delta\delta$	0.1	0.6	9.8	10.9	1.5	-0.2	$\kappa O^{3,4}$
β -D-Glcp1,2;3,4H ₄ (C')	δ	105.7	86.6	88.1	80.4	75.0	63.3	
	$\Delta\delta$	9.0	11.9	11.6	10.4	0.0	-3.1	$\kappa O^{1,2};\kappa O^{3,4}$

2.15.3 D-Maltose

D-Maltose is an α -D-Glcp-(1 \rightarrow 4)-D-Glcp disaccharide which is a degradation product of starch and therefore the smallest building unit of amylose. Conversions of Pd-tmen with D-maltose resulted in the ¹³C NMR spectra shown in Fig. 2.115.

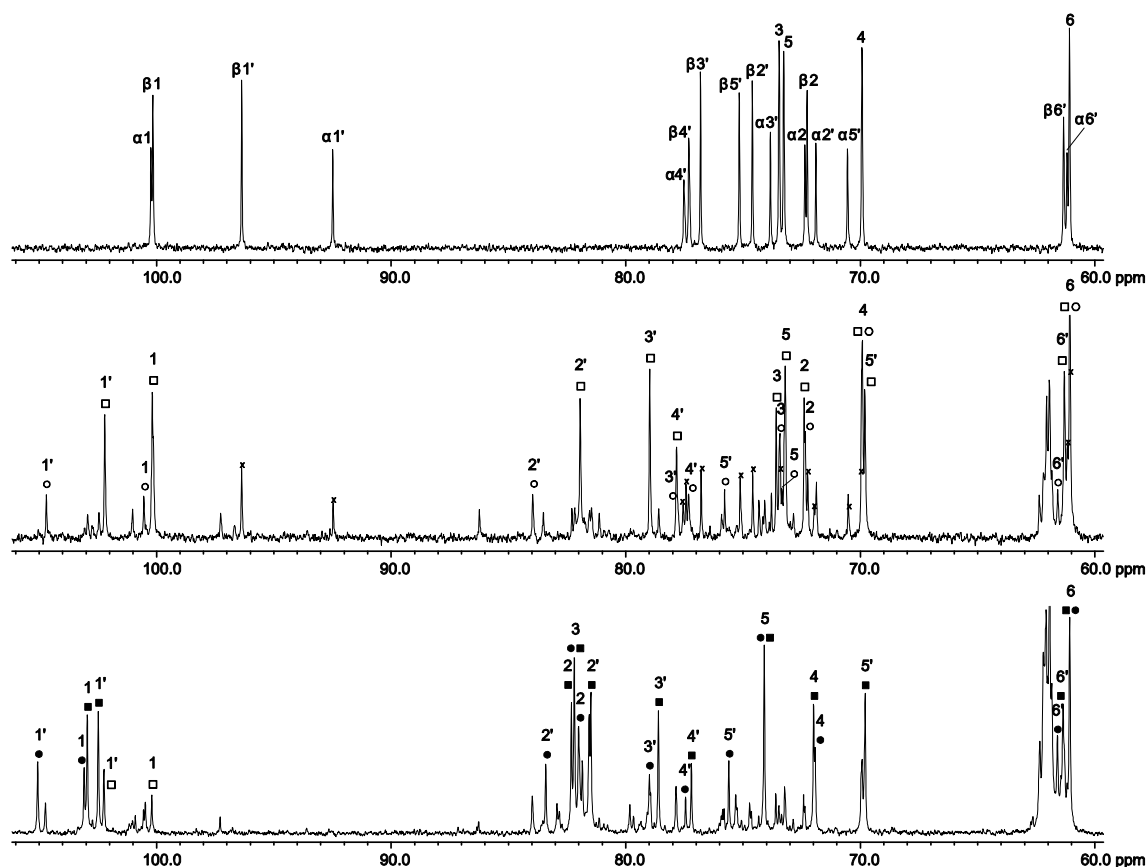


Figure 2.115. ¹³C NMR spectra of D-maltose in Pd-tmen at a molar Pd:maltose ratio of 0/1 (top), 1:1 (middle) and 2:1 (bottom). The signals of free D-maltose are marked with (x); (□) α -D-Glcp-(1 \rightarrow 4)- α -D-Glcp1,2H₂, (■) α -D-Glcp2,3H₂-(1 \rightarrow 4)- α -D-Glcp1,2H₂, (○) α -D-Glcp-(1 \rightarrow 4)- β -D-Glcp1,2H₂, (●) α -D-Glcp2,3H₂-(1 \rightarrow 4)- β -D-Glcp1,2H₂.

2 Results

As one can see in the middle ^{13}C NMR spectrum, at an equimolar Pd/maltose ratio, 32 % of D-maltose remained unmetalated. The main species was made up by the $\alpha\text{-D-Glcp-(1}\rightarrow\text{4)-}\alpha\text{-D-Glcp1,2H}_2$ species at 37 %, and the minor species by $\alpha\text{-D-Glcp-(1}\rightarrow\text{4)-}\beta\text{-D-Glcp1,2H}_2$ at 14 %. In the bottom ^{13}C NMR spectrum the Pd/maltose ratio amounted to 2:1. The two monometalated $\alpha\text{-D-Glcp-(1}\rightarrow\text{4)-}\alpha\text{-D-Glcp1,2H}_2$ and $\alpha\text{-D-Glcp-(1}\rightarrow\text{4)-}\beta\text{-D-Glcp1,2H}_2$ forms were still found at 12 % and 10 %, respectively. The new dimetalated main species is assigned as $\alpha\text{-D-Glcp2,3H}_2\text{-(1}\rightarrow\text{4)-}\alpha\text{-D-Glcp1,2H}_2$ at 37 % which was accompanied by a minor $\alpha\text{-D-Glcp2,3H}_2\text{-(1}\rightarrow\text{4)-}\beta\text{-D-Glcp1,2H}_2$ species at 22 %. The discussed species are depicted in Fig. 2.116.

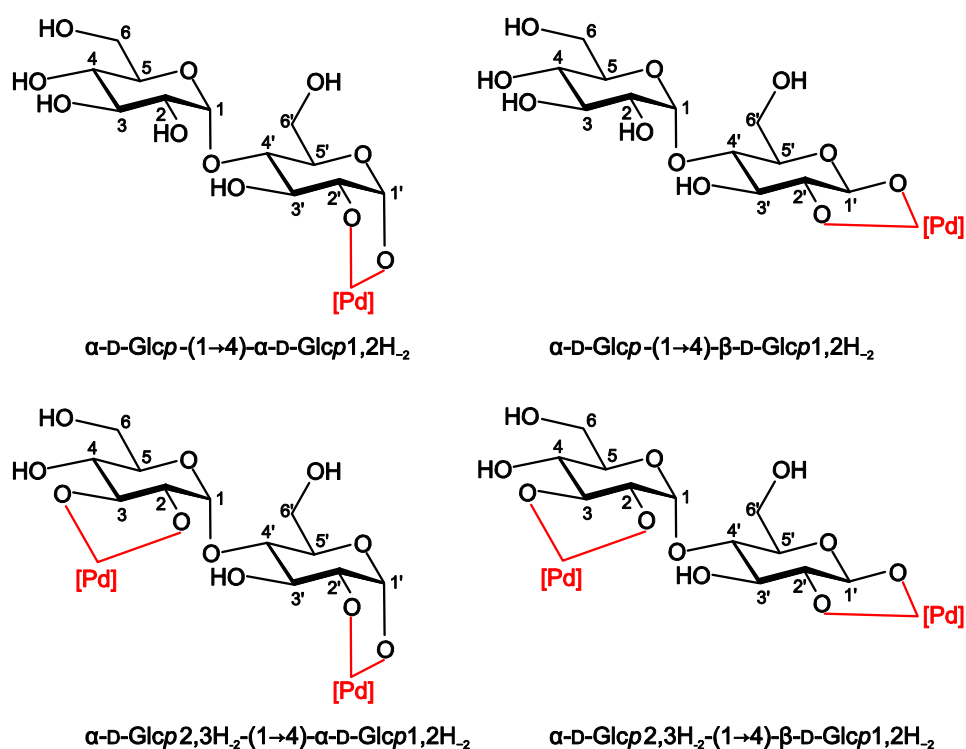


Figure 2.116. Species detected in solutions of Pd-tmen and D-maltose at different molar ratios (species refer to a molar Pd/maltose ratio of 1:1 for monometalated and to 2:1 for dimetalated forms).

The corresponding ^{13}C NMR chemical shifts and shift differences of the depicted complexes are listed in Table 2.111. Small ^{13}C NMR signals in the spectra of Fig. 2.115 indicated the presence of further minor species but the signals could not be assigned reliably. Again, in a first step, the reducing $\kappa\text{O}^{1,2}$ -diolato unit was metalated and only then, in a second step, the nonreducing $\alpha\text{-D-glucopyranoside}$'s $\kappa\text{O}^{2,3}$ -diolato unit was metalated in agreement with the results found for the metalation of methyl $\alpha\text{-D-glucopyranoside}$.

2 Results

Table 2.111. ^{13}C NMR chemical shifts (δ/ppm) and shift differences ($\Delta\delta$) to the free disaccharide of D-maltose ($\alpha\text{-D-Glcp-(1}\rightarrow\text{4)-D-Glc}$) ligands in Pd-tmen. Atoms are numbered as in Fig. 2.116.

		C1	C2	C3	C4	C5	C6	Chelate
$\alpha\text{-D-Glcp}$ (C)	δ	100.2	72.4	73.6	70.0	73.2	61.1	
	$\Delta\delta$	0.0	0.0	0.1	0.1	-0.1	0.0	-
$\alpha\text{-D-Glcp1,2H}_2$ (C')	δ	102.2	82.0	79.9	77.9	69.8	61.3	
	$\Delta\delta$	9.7	10.1	5.2	0.4	-0.8	0.1	$\kappa\text{O}^{1,2}$
$\alpha\text{-D-Glcp}$ (C)	δ	100.6	72.4	73.5	69.9	73.4	61.1	
	$\Delta\delta$	0.4	0.1	0.0	0.0	0.1	0.0	-
$\beta\text{-D-Glcp1,2H}_2$ (C')	δ	104.7	84.0	77.9	77.4	75.8	61.6	
	$\Delta\delta$	8.3	9.4	1.1	0.1	0.6	0.3	$\kappa\text{O}^{1,2}$
$\alpha\text{-D-Glcp2,3H}_2$ (C)	δ	103.0	82.4	82.2	72.0	74.1	61.1	
	$\Delta\delta$	2.8	10.0	8.7	2.1	0.8	0.0	$\kappa\text{O}^{2,3}$
$\alpha\text{-D-Glcp1,2H}_2$ (C')	δ	102.5	81.6	78.6	77.2	74.1	61.4	
	$\Delta\delta$	10.0	9.7	4.8	-0.3	3.5	0.2	$\kappa\text{O}^{1,2}$
$\alpha\text{-D-Glcp2,3H}_2$ (C)	δ	103.1	82.1	82.2	72.0	74.1	61.1	
	$\Delta\delta$	2.9	9.8	8.7	2.1	0.8	0.0	$\kappa\text{O}^{2,3}$
$\beta\text{-D-Glcp1,2H}_2$ (C')	δ	105.1	83.4	79.1	77.5	75.6	61.6	
	$\Delta\delta$	8.7	8.8	2.3	0.2	0.4	0.3	$\kappa\text{O}^{1,2}$

2.15.4 D-Maltotriose

Adding an $\alpha\text{-D-glucopyranoside}$ unit by (1 \rightarrow 4)-linkage to D-maltose produces D-maltotriose. The interpretation of the ^{13}C NMR spectra becomes even more difficult because of by six additional signals as can be seen in Fig. 2.117. For comparison, the top ^{13}C NMR spectrum shows the treatment of D-maltotriose with Pd-tmen at a molar Pd/maltotriose ratio of 2:1 and the bottom spectrum D-maltotriose in D_2O . At this ratio, two dimetalated species could be identified, $\alpha\text{-D-Glcp-(1}\rightarrow\text{4)-}\alpha\text{-D-Glcp2,3H}_2\text{-(1}\rightarrow\text{4)-}\alpha\text{-D-Glcp1,2H}_2$ and $\alpha\text{-D-Glcp-(1}\rightarrow\text{4)-}\alpha\text{-D-Glcp2,3H}_2\text{-(1}\rightarrow\text{4)-}\beta\text{-D-Glcp1,2H}_2$ at a distribution of 6:4 among each other. The ^{13}C NMR chemical shifts and shift differences of the two species are listed in Table 2.112.

It is noteworthy that two dimetalated species could be unambiguously identified at a molar ratio of 2:1 which remained unmetalated at the $\kappa\text{O}^{2,3}$ -chelation site of the terminal non-reducing $\alpha\text{-D-glucopyranoside}$ unit. A statistical metalation of both the $\kappa\text{O}^{2,3}$ -chelation sites of the middle and terminal $\alpha\text{-D-glucopyranoside}$ unit would have been possible as well. Indeed, there was an evident preference for the $\kappa\text{O}^{2,3}$ -diolato unit of the middle $\alpha\text{-D-glucopyranoside}$ unit.

2 Results

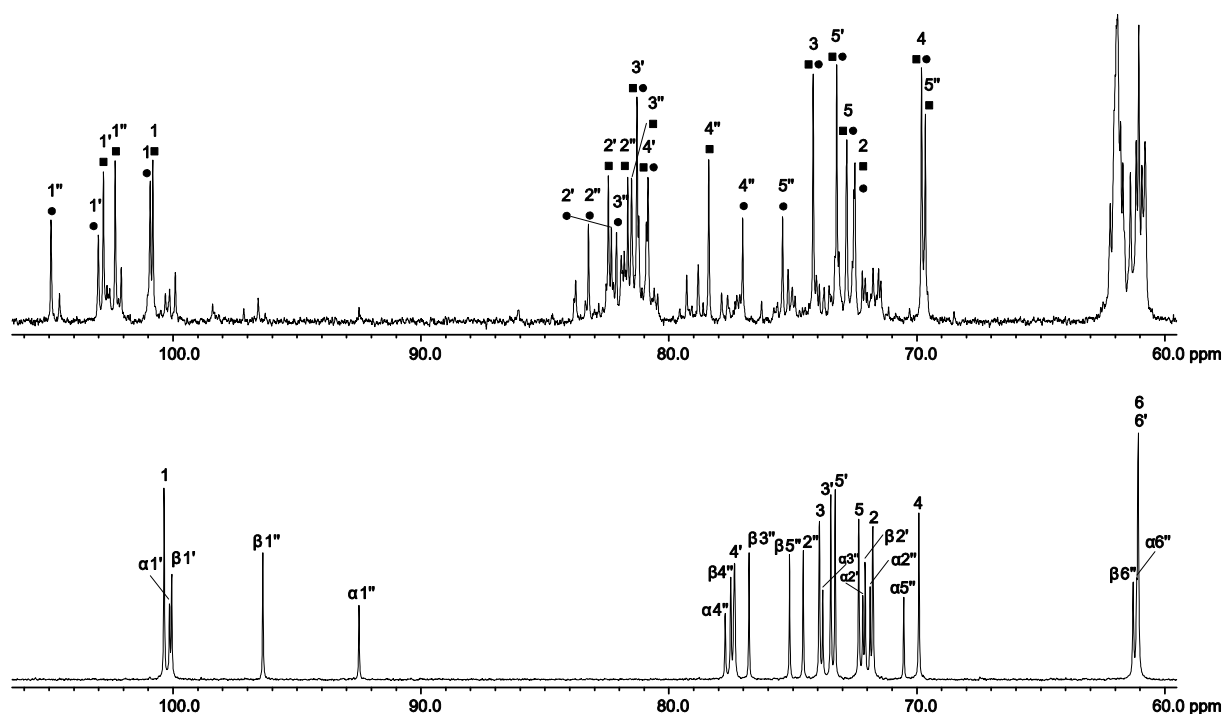


Figure 2.117. ^{13}C NMR spectra of D-maltotriose in Pd-tmen at a molar ratio of 2:1 (top) and in D_2O (bottom). (■) $\alpha\text{-D-Glcp-(1}\rightarrow\text{4)-}\alpha\text{-D-Glcp2,3H}_2\text{-(1}\rightarrow\text{4)-}\alpha\text{-D-Glcp1,2H}_2$, (●) $\alpha\text{-D-Glcp-(1}\rightarrow\text{4)-}\alpha\text{-D-Glcp2,3H}_2\text{-(1}\rightarrow\text{4)-}\beta\text{-D-Glcp1,2H}_2$.

Although the ^{13}C NMR spectra of conversions at a molar Pd/maltotriose ratio of 1:1 and 4:1 could not be assigned completely, the occurring species could be identified. Looking at the enlarged regions of the ^{13}C NMR spectra in Fig. 2.118, at the molar ratios of 2:1 and 4:1 the blue-colored ^{13}C NMR signals represent the terminal non-reducing $\alpha\text{-D-glucopyranoside}$ unit. As one can see, elevating the molar ratio from 2:1 to 4:1 resulted in a clear downfield shift of the C3 and C4 NMR signals indicating an attack of the Pd(tmen) fragment on the $\kappa\text{O}^{3,4}$ -diolato unit. This is remarkable because a $\kappa\text{O}^{2,3}$ -chelation would have been expected, as derived from the previous results. This result is clear evidence for the presence of two intramolecular hydrogen bonds $\text{O2-H}\cdots\text{O3}'$ and $\text{O3}''\text{-H}\cdots\text{O2}'$ which stabilize the identified metalation pattern as depicted in Fig. 2.119. Looking at the dimetalated species, metalation of the $\kappa\text{O}^{1,2}$ -diolato unit of the reducing D-glucopyranoside and the $\kappa\text{O}^{2,3}$ -diolato unit of the middle $\alpha\text{-D-glucopyranoside}$ increased the formation tendency of a hydrogen bond $\text{O3}''\text{-H}\cdots\text{O2}'$ by an alkoxido acceptor. With the third Pd(tmen) fragment attacking the $\kappa\text{O}^{3,4}$ -diolato unit of the terminal $\alpha\text{-D-glucopyranoside}$ a second hydrogen bond $\text{O2-H}\cdots\text{O3}'$ to an alkoxido acceptor additionally supported the metalation pattern. On the other hand, an attack of the third Pd(tmen) fragment on the $\kappa\text{O}^{2,3}$ -diolato unit of the terminal $\alpha\text{-D-glucopyranoside}$ would impair this stabilizing hydrogen bond.

2 Results

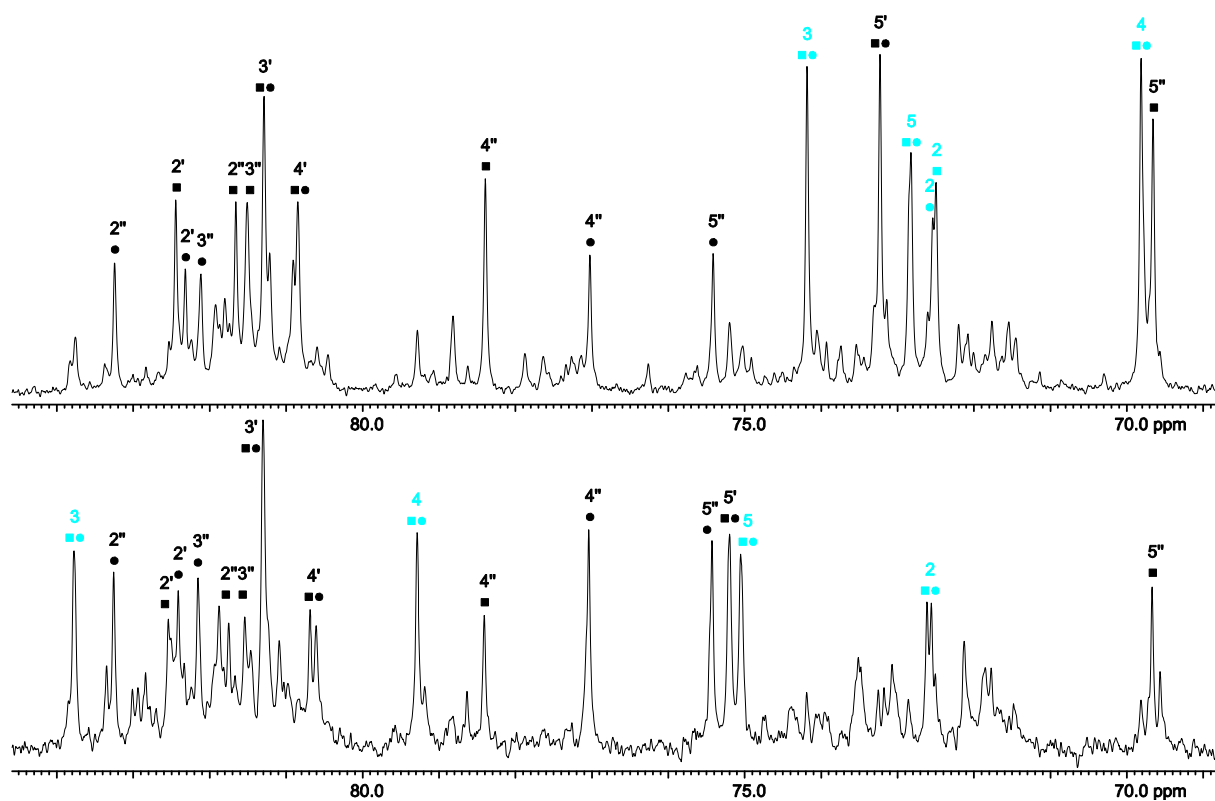


Figure 2.118. Enlarged region of the ^{13}C NMR spectra of D-maltotriose in Pd-tmen at a molar Pd/maltotriose ratio of 2:1 (top) and 4:1 (bottom). The downfield shift of the blue signals indicated $\kappa\text{O}^{2,3}$ -metalation at the remaining $\alpha\text{-D-Glcp}$ unit (C) at a ratio of 4:1.

Table 2.112. ^{13}C NMR chemical shifts (δ/ppm) and shift differences ($\Delta\delta$) to the free trisaccharide of D-maltotriose ($\alpha\text{-D-Glcp-(1}\rightarrow\text{4)-}\alpha\text{-D-Glcp-(1}\rightarrow\text{4)-}\alpha\text{-D-Glc}$) ligands in Pd-tmen at a molar Pd/maltotriose ratio of 2:1. Atoms are numbered as in Fig. 2.119.

		C1	C2	C3	C4	C5	C6	Chelate
$\alpha\text{-D-Glcp}$ (C)	δ	100.9	72.6	74.3	69.9	72.9	61.2	
	$\Delta\delta$	0.5	0.8	0.4	0.0	0.6	0.1	–
$\alpha\text{-D-Glcp}_{2,3\text{H}_2}$ (C')	δ	102.9	82.6	81.4	81.0	73.4	60.9	
	$\Delta\delta$	2.7	10.4	7.9	3.6	0.1	–0.2	$\kappa\text{O}^{2,3}$
$\alpha\text{-D-Glcp}_{1,2\text{H}_2}$ (C'')	δ	102.5	81.8	81.6	78.4	69.8	61.3	
	$\Delta\delta$	10.0	9.9	7.8	0.7	–0.7	0.2	$\kappa\text{O}^{1,2}$
$\alpha\text{-D-Glcp}$ (C)	δ	101.0	72.7	74.3	69.9	72.9	61.2	
	$\Delta\delta$	0.6	0.9	0.4	0.0	0.6	0.1	–
$\alpha\text{-D-Glcp}_{2,3\text{H}_2}$ (C')	δ	103.1	82.4	81.3	81.0	73.4	61.0	
	$\Delta\delta$	3.0	10.3	7.8	3.6	0.1	–0.1	$\kappa\text{O}^{2,3}$
$\beta\text{-D-Glcp}_{1,2\text{H}_2}$ (C'')	δ	105.0	83.4	82.2	77.1	75.5	61.5	
	$\Delta\delta$	8.6	8.8	5.4	–0.4	0.4	0.2	$\kappa\text{O}^{1,2}$

2 Results

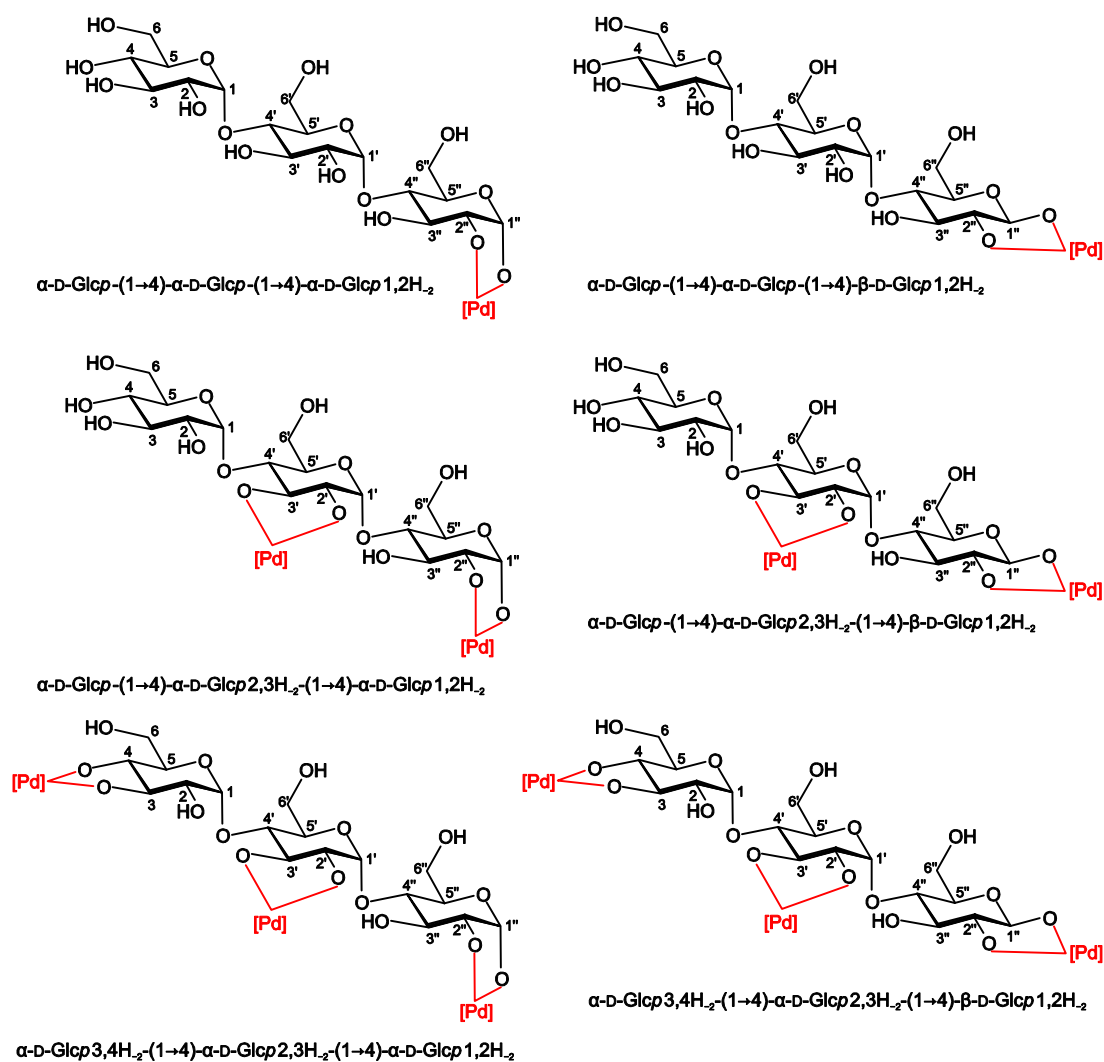


Figure 2.119. Species detected in solutions of Pd-tmen and D-maltotriose at different molar ratios (species refer to a molar Pd/maltotriose ratio of 1:1 for monometalated, to 2:1 for dimetalated and to 4:1 for higher metalated forms).

The C1-regions of D-maltotriose and D-maltose in Pd-tmen can be compared to each other in Fig. 2.120. Comparing the top ¹³C NMR spectrum to the remaining spectra, all species of D-maltotriose in Pd-tmen at an equimolar Pd/maltotriose ratio could be identified. Besides unmetalated D-maltotriose and the two known dimetalated species, six further monometalated forms were assigned. The two major monometalated species are the $\kappa O^{1,2}$ -chelated forms α -D-Glcp-(1→4)- α -D-Glcp-(1→4)- α -D-Glcp 1,2H₂ and α -D-Glcp-(1→4)- α -D-Glcp-(1→4)- β -D-Glcp 1,2H₂, accompanied by two minor species, α -D-Glcp-(1→4)- α -D-Glcp 2,3H₂-(1→4)- α -D-Glcp and α -D-Glcp-(1→4)- α -D-Glcp 2,3H₂-(1→4)- β -D-Glcp. The favored formation of the two latter species could be explained again by the two intramolecular hydrogen bonds O2–H···O3' and O3''–H···O2' which stabilize the monometalated forms. Small signals also indicated the remarkable presence of two further monometalated species, α -D-Glcp-(1→4)- α -

2 Results

D-Glcp-(1→4)- α -D-Glcp2,3H₂ and α -D-Glcp-(1→4)- α -D-Glcp-(1→4)- β -D-Glcp2,3H₂. This unusual $\kappa O^{2,3}$ -chelation mode at the reducing D-glucopyranose unit could only be explained by a stabilization by an intramolecular hydrogen bond O2'-H \cdots O3''.

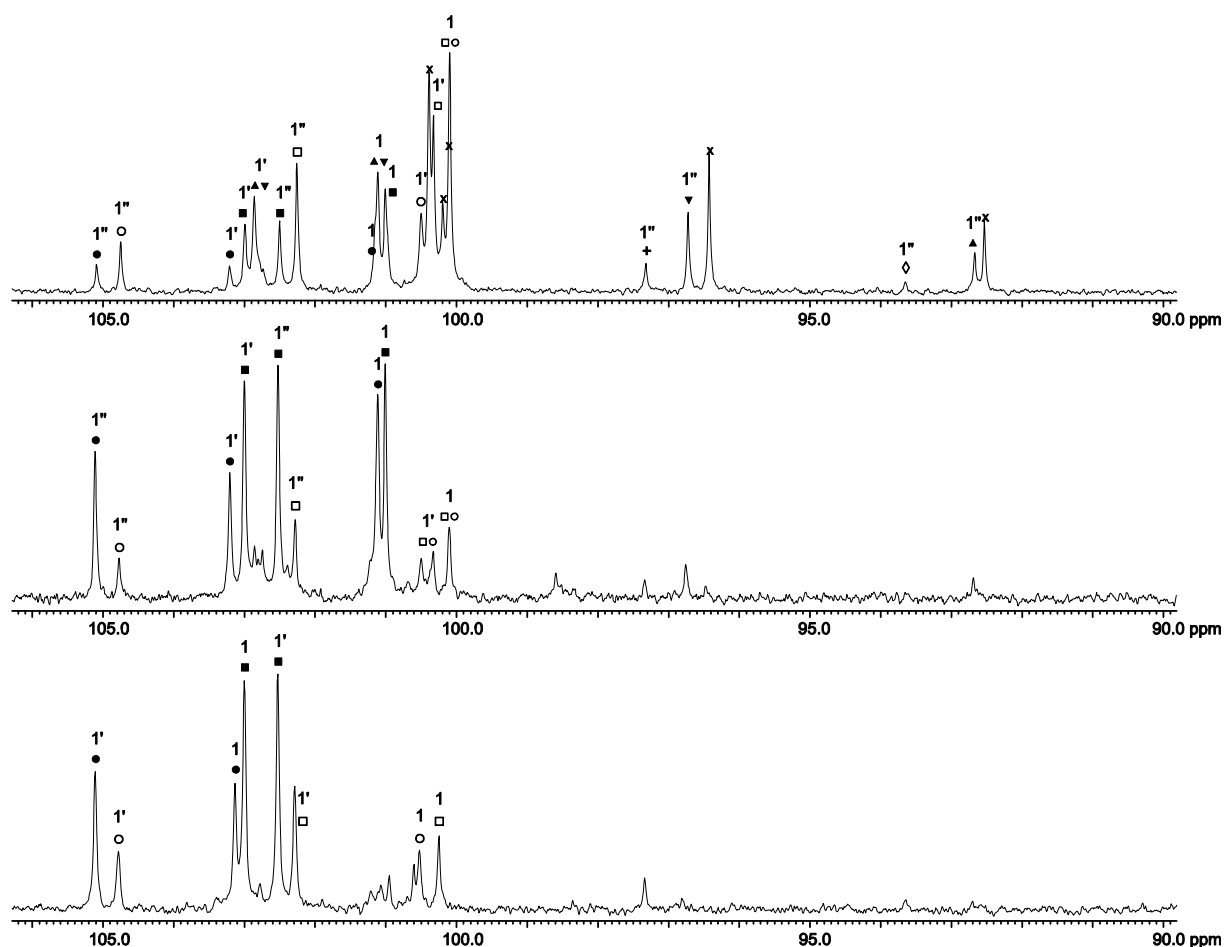


Figure 2.120. Enlarged regions of the ¹³C NMR spectra of D-maltotriose and D-maltose in Pd-tmen; Pd/maltotriose ratio of 1:1 (top), 2:1 (middle) and Pd:maltose ratio of 2:1 (bottom). The signals (top and middle ¹³C NMR spectrum) of free D-maltotriose are marked with (x); (□) α -D-Glcp-(1→4)- α -D-Glcp-(1→4)- α -D-Glcp1,2H₂, (■) α -D-Glcp-(1→4)- α -D-Glcp2,3H₂-(1→4)- α -D-Glcp1,2H₂, (○) α -D-Glcp-(1→4)- α -D-Glcp-(1→4)- β -D-Glcp1,2H₂, (●) α -D-Glcp-(1→4)- α -D-Glcp2,3H₂-(1→4)- β -D-Glcp1,2H₂, (▲) α -D-Glcp-(1→4)- α -D-Glcp2,3H₂-(1→4)- α -D-Glcp, (▼) α -D-Glcp-(1→4)- α -D-Glcp2,3H₂-(1→4)- β -D-Glcp, (◇) α -D-Glcp-(1→4)- α -D-Glcp-(1→4)- α -D-Glcp2,3H₂, (+) α -D-Glcp-(1→4)- α -D-Glcp-(1→4)- β -D-Glcp2,3H₂.

To sum up the results of the D-maltotriose's investigation, a very distinct hydrogen bonding pattern determined the metalation of the trisaccharide. The strong intramolecular hydrogen bonds not only enforced a rigid metalation pattern which would not be found in the absence of the hydrogen bonds but also stabilized metalated species such as the α -D-Glcp-(1→4)- α -D-Glcp-(1→4)- α -D-Glcp2,3H₂ form which were only present because of the hydrogen bond's stabilization.

2.15.5 D-Maltoheptaose and amylose

Further elongation of D-maltotriose resulted in D-maltoheptaose which consists of seven α -(1 \rightarrow 4)-connected D-glucopyranose units. Investigating D-maltoheptaose should further reveal the influence of the above-mentioned intramolecular hydrogen bonds from an unmetalated $\kappa O^{2,3}$ -diolato unit to the adjacent metalated diolato units. Assuming full metalation, two metalation patterns which are depicted in Fig. 2.121 were taken into consideration. Starting with $\kappa O^{1,2}$ -chelation of the reducing D-glucopyranose unit and taking into account the mentioned hydrogen bonds, one would obtain a fivefold metalated MaltoheptH₋₁₀ whereas, starting with $\kappa O^{2,3}$ -chelation of the terminal α -D-glucopyranoside unit, a fourfold metalated D-MaltoheptH₋₈ would be obtained.

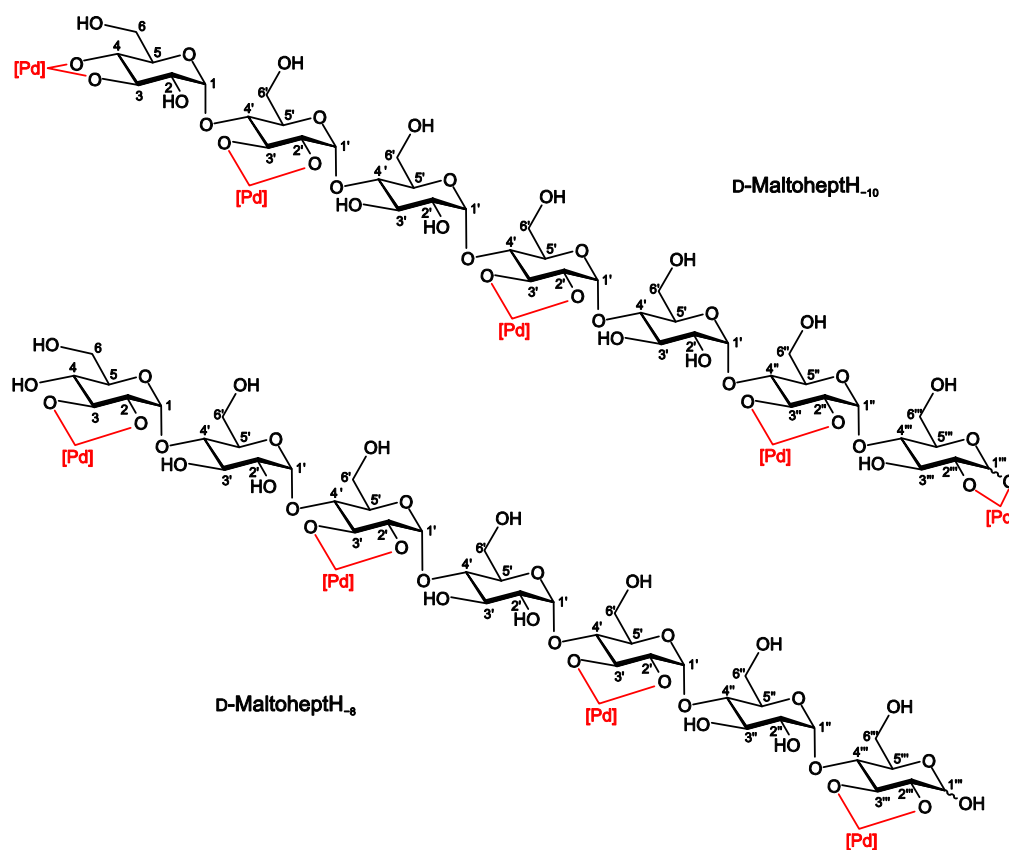


Figure 2.121. The two possible full-metalated species in solutions of Pd-tmen and D-maltoheptaose at a molar Pd/maltoheptaose ratio of 7:1.

Three ^{13}C NMR spectra are depicted in Fig. 2.122. The bottom spectrum shows the signals of D-maltoheptaose in aqueous solution. As one can see, the four inner α -D-glucopyranoside units cannot be distinguished in the ^{13}C NMR spectrum. Now, comparing the ^{13}C NMR spectrum of D-maltoheptaose at a molar Pd/maltoheptaose ratio of 7:1 to the spectrum of

2 Results

D-maltotriose at a molar Pd/maltotriose ratio of 4:1, it is obvious that in the first spectrum the composition of solution species was less defined than in the latter spectrum.

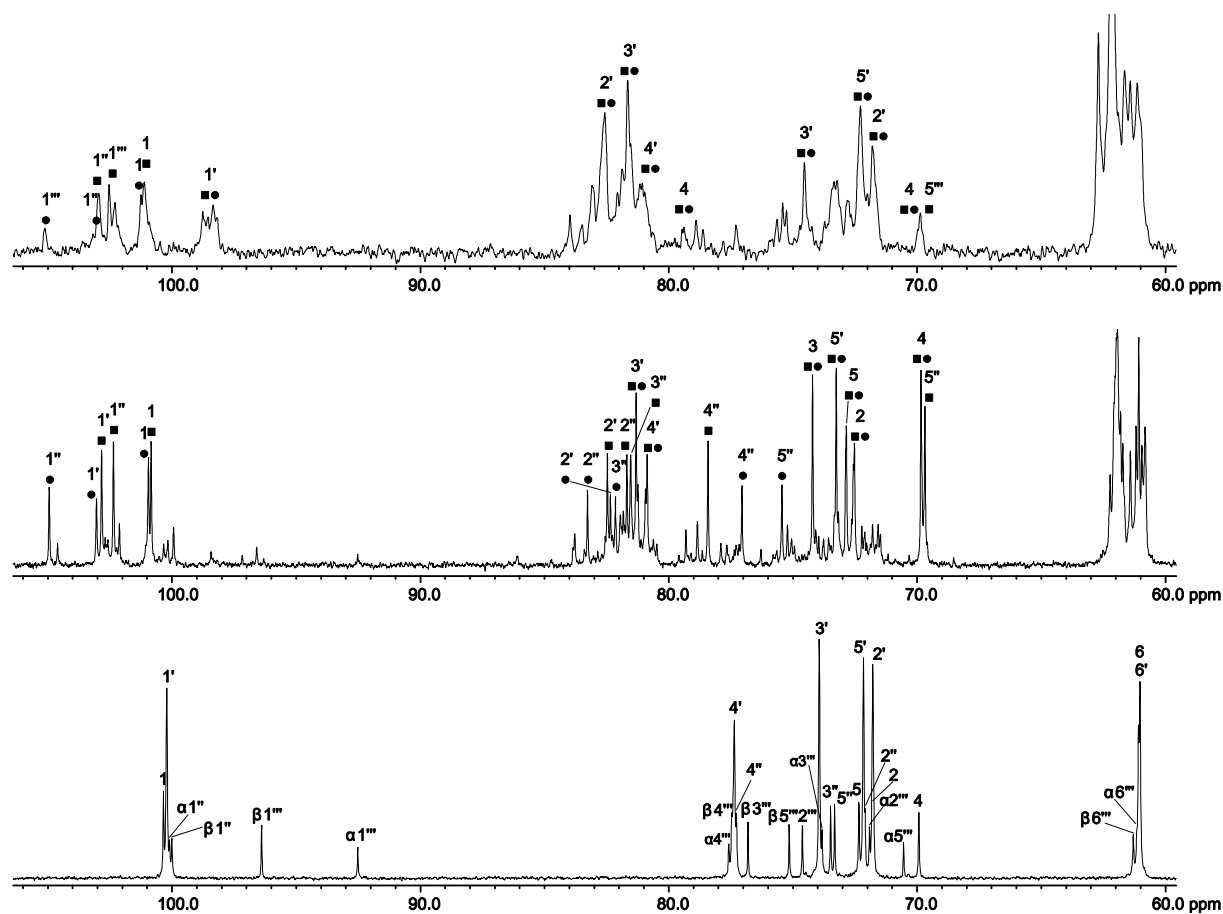


Figure 2.122. ^{13}C NMR spectra of D-maltoheptaose (7:1, top) and D-maltotriose (2:1, middle) in Pd-tmen; ^{13}C NMR spectrum of D-maltoheptaose in D_2O (bottom). Top ^{13}C NMR spectrum: α -anomer (■) and β -anomer (●) of metalated D-maltoheptaose; middle ^{13}C NMR spectrum: (■) α -D-Glcp-(1 \rightarrow 4)- α -D-Glcp2,3H $_2$ -(1 \rightarrow 4)- α -D-Glcp1,2H $_2$ and (●) α -D-Glcp-(1 \rightarrow 4)- α -D-Glcp2,3H $_2$ -(1 \rightarrow 4)- β -D-Glcp1,2H $_2$.

The poor resolution of the top ^{13}C NMR spectrum prevented an exact assignment of the signals, nevertheless several signals could be identified. The spectrum's poor resolution gave evidence that, contrary to the treatment of Pd-tmen and D-maltotriose, the metalation of D-maltoheptaose was less regular. Comparing the shift pattern of the C1 signal, $\kappa\text{O}^{1,2}$ -chelation of the α - and β -anomer of the reducing D-glucopyranose unit was detected for D-maltoheptaose. On the other hand, no signal indicated the $\kappa\text{O}^{2,3}$ -chelation of the reducing D-glucopyranose unit. Looking at the positions of the C2' and C3' signals for metalated and unmetalated diolato units, signals could be found at both positions indicating that at least half of the $\kappa\text{O}^{2,3}$ -diolato units were metalated. However, looking at the C4 signal of the terminal D-glucopyranoside unit, two signals could be found, one at the position of an unmetalated

2 Results

$\kappa O^{3,4}$ -diolato site and one at the position of a metalated $\kappa O^{3,4}$ -diolato site. To sum up the results the $\kappa O^{1,2}$ -diolato site of the reducing D-glucopyranose unit was completely and exclusively metalated whereas $\kappa O^{3,4}$ -diolato site of the terminal D-glucopyranoside unit was not. Taking also into account the spectrum's poor resolution, this indicated a weakening of the hydrogen bonds' controlling function for the metalation which was found for D-maltotriose.

Finally, amylose as a polymer of α -linked D-glucopyranoside units was investigated to test the structure-determining features of intramolecular hydrogen bonding. Comparing the ^{13}C NMR spectra of amylose in aqueous solution and in Pd-tmen, the shift pattern in Fig. 2.123 indicated that only half of the available $\kappa O^{2,3}$ -diolato units were metalated although Pd-tmen was used in excess. Also the ^{13}C NMR chemical shifts and shift differences in Table 2.113 confirmed this assumption. Therefore, the intramolecular hydrogen bonds determine the metalation pattern also in the polysaccharide. Furthermore, not even the alkaline conditions of Pd-tmen got the remaining hydroxy functions deprotonated.

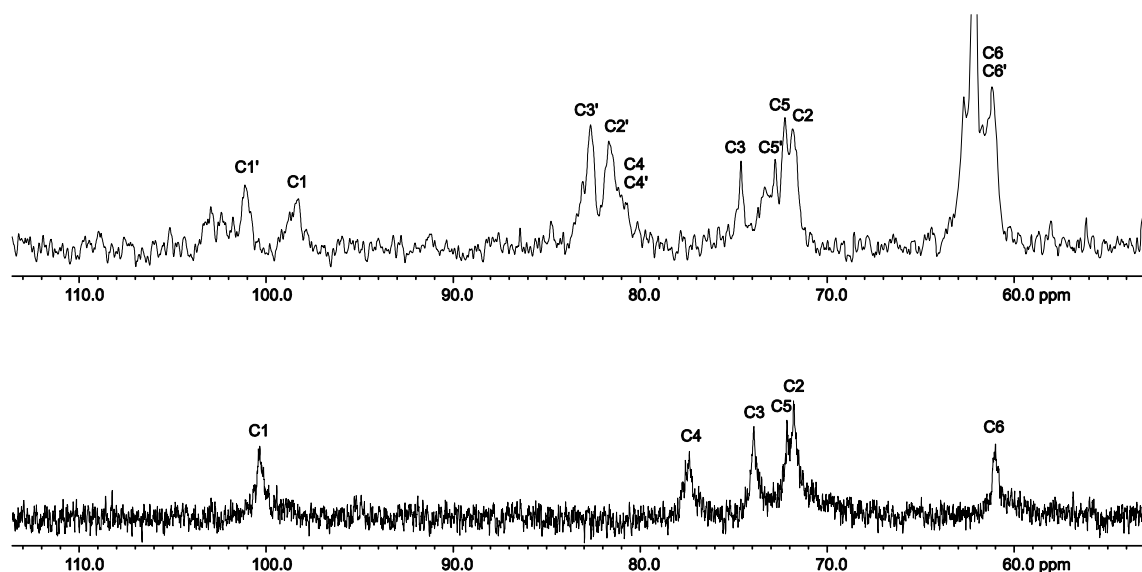


Figure 2.123. ^{13}C NMR spectra of amylose in Pd-tmen (surplus; top) and in D_2O (MeOH = 49.5 ppm; bottom).

Table 2.113. ^{13}C NMR chemical shifts (δ/ppm) and shift differences ($\Delta\delta$) to the free polysaccharide of amylose ligand in Pd-tmen at Pd/tmen surplus.

		C1	C2	C3	C4	C5	C6	Chelate
amylose	δ	100.4	71.8	73.9	77.4	72.3	61.0	
$\alpha\text{-D-Glcp}$ (C)	δ	98.3	71.8	74.6	80.7	72.2	61.2	
	$\Delta\delta$	-2.1	0.0	0.7	3.3	-0.1	0.2	-
$\alpha\text{-D-Glcp}2,3\text{H}_2$ (C')	δ	101.1	81.6	82.7	80.7	72.8	61.2	
	$\Delta\delta$	0.7	9.8	8.8	3.3	0.5	0.2	$\kappa O^{2,3}$

2.16 The cyclodextrins

The cyclodextrins are cyclic oligosaccharides composed of six or more α -(1 \rightarrow 4)-linked D-glucopyranoside units. The so-called α -cyclodextrin, β -cyclodextrin and γ -cyclodextrin comprise six, seven and eight glucopyranoside units, respectively. With the polar hydroxy groups of the glucopyranoside units pointing outwardly, all the cyclodextrins have cavities which have interiors that are more lipophilic than their more hydrophilic exteriors. Such a cavity has a diameter of 4.7–5.3 Å for α -cyclodextrin and 7.5–8.3 Å for γ -cyclodextrin. The hosting of a large variety of lipophilic substrates is the most interesting industrial feature of the cyclodextrins. A strong hydrogen-bonding network between the 2'-hydroxy and 3-hydroxy group of an adjacent glucopyranoside unit exists both in solid state and in solution.^[113]

The four crystal structures $[\text{Pd}_3(\text{teen})_3(\alpha\text{-CDH}_6)] \cdot 34 \text{ H}_2\text{O}$ (**42**), $[\text{Pd}_3(\text{tmen})_3(\alpha\text{-CDH}_6)] \cdot 20.7 \text{ H}_2\text{O} \cdot \text{acetone}$ (**43**), $[\text{Pd}_4(\text{teen})_4(\gamma\text{-CDH}_8)] \cdot 12 \text{ H}_2\text{O}$ (**44**) and $[\text{Pd}_4(\text{tmen})_4(\gamma\text{-CDH}_8)] \cdot 65.79 \text{ H}_2\text{O} \cdot 0.96 [\text{Pd}(\text{tmen})\text{CO}_3]$ (**45**) were obtained from conversions of the cyclodextrins with Pd-tmen and Pd-teen. Independent of the stoichiometry, only half the cyclodextrins' $\kappa\text{O}^{2,3}$ -diolato sites were alternately metalated in all experiments. Again, the strong intramolecular hydrogen bonds between an unmetalated $\kappa\text{O}^{2,3}$ -diolato site to the adjacent glucopyranoside unit's metalated $\kappa\text{O}^{2,3}$ -diolato sites impaired complete deprotonation. Therefore, no crystal structure was obtained for β -cyclodextrin because the odd-even number of glucopyranoside units disturbed the hydrogen-bond-mediated alternating metalation pattern. $[\text{Pd}_3(\text{teen})_3(\alpha\text{-CDH}_6)] \cdot 34 \text{ H}_2\text{O}$ (**42**) was solved in the space group $P 6_3$ with only a third of the molecule in the asymmetric unit. Despite a cell volume of only 5839.3 Å³ anisotropic refinement was successful and no disorder had to be resolved. $[\text{Pd}_3(\text{tmen})_3(\alpha\text{-CDH}_6)] \cdot 20.7 \text{ H}_2\text{O} \cdot \text{acetone}$ (**43**) was solved in the space group $P 2_1$ with a cell volume of 4740.2 Å³. A complete metalated cyclodextrin with one acetone molecule in the hydrophobic cavity was found in the asymmetric unit. Again, anisotropic refinement was possible, although some of the hydroxymethyl groups were disordered. Crystal packing of the cyclodextrins is described either as a channel- or a cage-type structure.^[113] In channel-type structures, cyclodextrin molecules stack in such a way as to align their cavities linearly to form channels through the crystal. On the other hand, cage-type structures form isolated cavities which are blocked off on both sites by neighboring cyclodextrin molecules. In **42**, layers of cyclodextrin rings were packed staggered along the c axis. Nevertheless channels were formed along c as depicted in Fig. 6.81 of the Appendix.

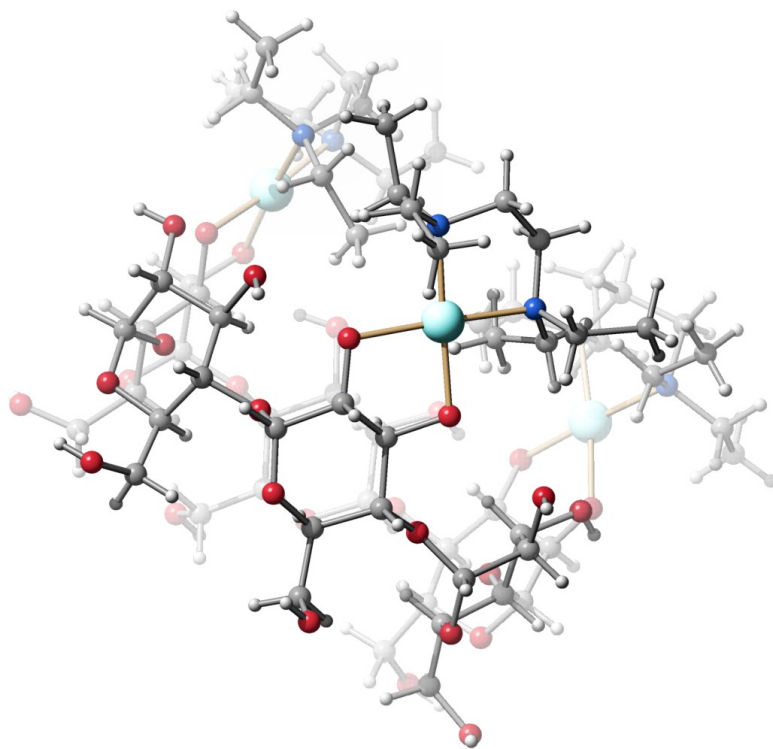


Figure 2.124. SCHAKAL plot of the molecular structure of $[\text{Pd}_3(\text{teen})_3(\alpha\text{-CDH-}_6)] \cdot 34 \text{ H}_2\text{O}$ (**42**).

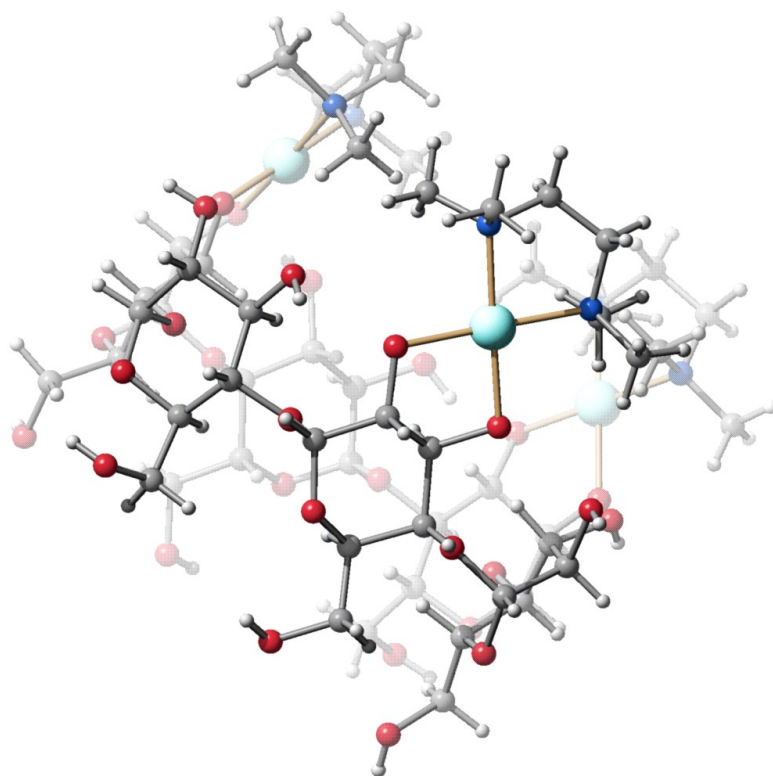


Figure 2.125. SCHAKAL plot of the molecular structure of $[\text{Pd}_3(\text{tmen})_3(\alpha\text{-CDH-}_6)] \cdot 20.7 \text{ H}_2\text{O} \cdot \text{acetone}$ (**43**).

2 Results

In **43**, channels were formed along the a axis as one can see in Fig. 6.82 of the Appendix. $[\text{Pd}_4(\text{teen})_4(\gamma\text{-CDH-8})] \cdot 12 \text{H}_2\text{O}$ (**44**) was solved in the space group $P 2_1 2_1 2_1$ with a cell volume of 13424.4 \AA^3 . Because of the cell volume's extent and the increasing disorder of the movable parts of the complex as the N,N,N',N' -tetraethylethane-1,2-diamine ligands or the hydroxymethyl side chains, an anisotropic refinement was abandoned. Nevertheless, besides the hydrogen-bond mediated fourfold metalation, one can recognize a slight deformation of the γ -cyclodextrin ring in Fig. 2.126. Channels were formed by the crystal packing in the direction of the a axis as depicted in Fig. 6.83 of the Appendix.

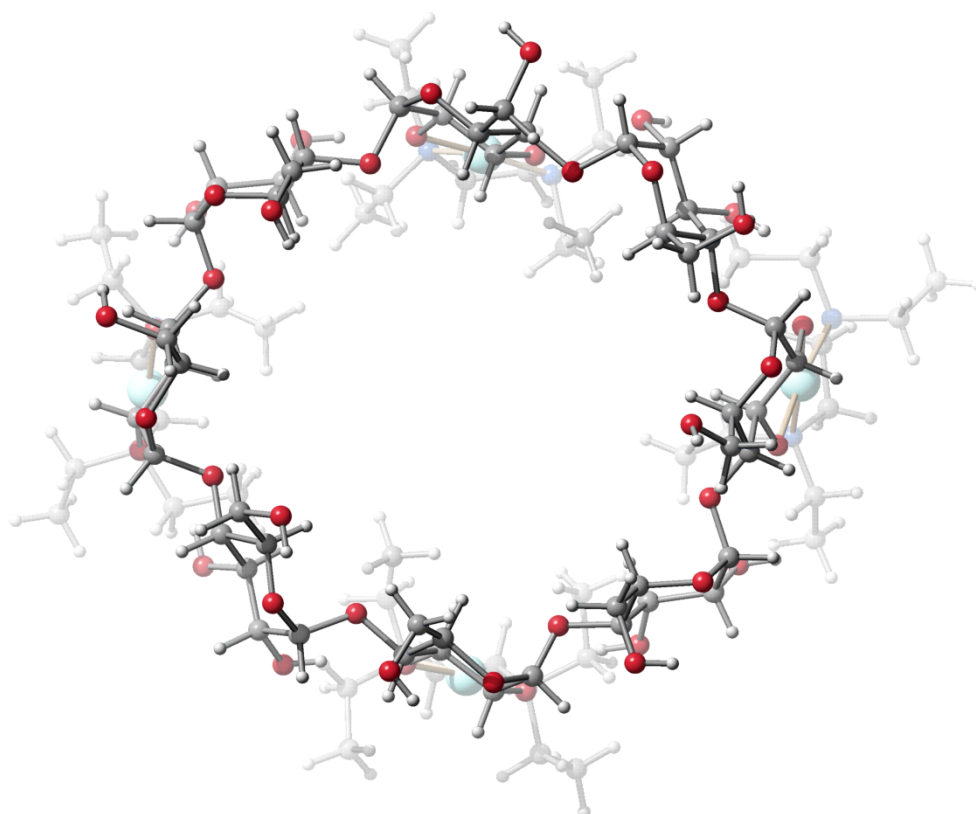


Figure 2.126. SCHAKAL plot of the molecular structure of $[\text{Pd}_4(\text{teen})_4(\gamma\text{-CDH-8})] \cdot 12 \text{H}_2\text{O}$ (**44**).

$[\text{Pd}_4(\text{tmen})_4(\gamma\text{-CDH-8})] \cdot 65.79 \text{H}_2\text{O} \cdot 0.96 [\text{Pd}(\text{tmen})\text{CO}_3]$ (**45**) was solved in the space group $P 2_1$ with a cell volume of 13766.8 \AA^3 . With two complete metalated molecules in the asymmetric unit and because of serious disorder, structure solution was complicated and anisotropic refinement was abandoned. As a feature, in 96 % of the cavities which formed channels along the a axis a $[\text{Pd}(\text{tmen})\text{CO}_3]$ molecule was included. It is noteworthy that contrary to the planar structure of $[\text{Pd}(\text{tmen})\text{CO}_3]$ which is known from literature,^[49] the $[\text{Pd}(\text{tmen})\text{CO}_3]$ structure in the cavity showed an angle of almost 120° . This result was

2 Results

dubious but due to the highly disordered structure, a final determination of the embedded complex was not possible. An alternative solution would be an embedded $[\text{Pd}(\text{tmen})(\text{OH})_2]$ complex and additional disordered water molecules. Comparing the structure of **44** to the structure of **45** (see Fig. 2.127) the storage of $[\text{Pd}(\text{tmen})\text{CO}_3]$ prevented the deformation of the cyclodextrin ring.

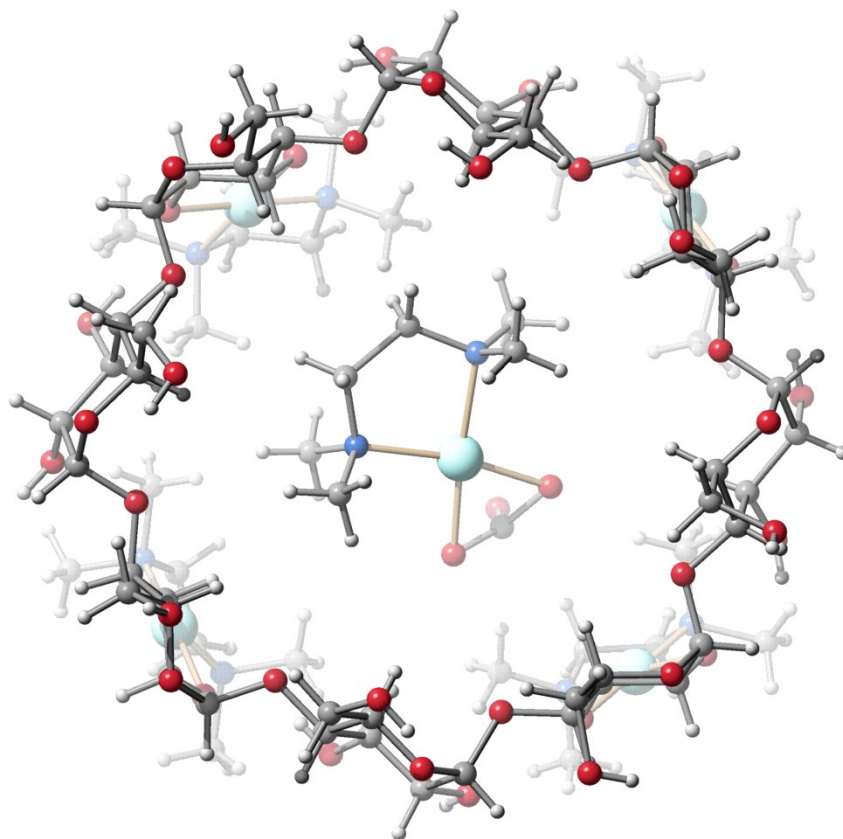


Figure 2.127. SCHAKAL plot of the molecular structure of $[\text{Pd}_4(\text{tmen})_4(\gamma\text{-CDH}_8)] \cdot 0.96 [\text{Pd}(\text{tmen})\text{CO}_3]$ in crystals of the 65.79-hydrate (**45**).

3 Discussion

3.1 The Pd^{II}N₂ fragments: characteristics and differences

In this work, in addition to the well established Pd^{II}N₂ reagents [Pd(en)(OH)₂] and [Pd(*R,R*-chxn)(OH)₂], seven new Pd^{II}N₂ fragments were introduced. A common property of all Pd-based solvents is the magnitude of the so-called ‘coordination-induced shift’ (CIS), in fact, the CIS of the various fragments is almost identical with only minor deviations. A first difference was the fragments’ resistance to reduction to palladium(0). Whereas Pd-en and Pd-chxn were rapidly reduced to palladium(0), Pd-tmen, Pd-teen and Pd-tmchxn showed a higher resistance to reduction. Contrary, Pd-dmen and Pd-tn were reduced as rapidly as Pd-en. Therefore, only the complete alkylation of the chelate ligands’ amino functions retarded the reduction of palladium(II). Furthermore, it should be noted that the $\kappa N^{1,3}$ chelation of Pd-tn was not so stable as the $\kappa N^{1,2}$ chelation of the other ligands. The stability of [Pd(bpy)(OH)₂] and [Pd(phen)(OH)₂] could not be assessed because of the poor solubility of these fragments in water which was caused by the stacked packing in the crystal structures.

To avoid signal overlap it is important that none of the Pd^{II}N₂ fragments has ¹³C NMR signals in the region between 120–60 ppm. Most of the fragments met this condition, although the C6 signal of the carbohydrates coincided with the signals of Pd-tmen. The most important feature of Pd-tmen and Pd-teen is their ability to stabilize species which were not detected with Pd-en and Pd-chxn or were only there in minor amounts. With Pd-tmen, for example, the furanose forms of reducing carbohydrates became major species. On the other hand, palladium(II)–polyol complexes in neutral aqueous solution were possible only for Pd-en and Pd-chxn whereas with Pd-tmen no μ -hydroxido-bridged species was detected.

Another aim of the investigation was an increase in crystallization tendency. A first condition therefore was the stability of the complex which should be crystallized. Pd-tmen met this condition and, in fact, a series of crystal structures was obtained. Nevertheless, each Pd^{II}N₂ fragment had its characteristic features and therefore, the alteration of Pd-en, Pd-chxn and Pd-tmen resulted in a series of structures which differed in the coordination mode.

Also, as mentioned above, the Pd-tmen fragment enriched the furanose forms of some reducing carbohydrates. For comparison, the average distances and angles of the various [Pd^{II}N₂(OH)₂] complexes are listed in Table 3.1.

3 Discussion

Table 3.1. The average distances [Å] and angles [°] of the various [Pd^{II}N₂(OH)₂] compounds.

[Pd ^{II} N ₂ (OH) ₂]	<i>d</i> _{Pd-O}	<i>d</i> _{Pd-N}	N-Pd-N	O-Pd-O
en ^[46]	2.017	2.028	83.98	93.59
tmen	1.991	2.067	85.66	93.40
bpy	1.997	1.999	81.0	89.9
phen	1.989	2.015	82.15	93.39

As one can see, the distances and angles did not differ from each other so much as to explain the different behavior of Pd-en and Pd-tmen. On the other hand, the fourfold methylation of en increased the hydrophobic character of the fragment which resulted in a separation of hydrophobic and hydrophilic regions in the crystal structures of the Pd(tmen) fragment with carbohydrates. Therefore, Pd-tmen is a less polar solvent than Pd-en or Pd-chxn and, additionally, the steric demand increased because of the methylation which is possibly a further reason for the different coordination behavior of Pd-tmen to Pd-en. The application of Pd-teen did not increase the advantages of Pd-tmen because the coordination tendency of the carbohydrates decreased and only syrup-like substances could be obtained from attempts to crystallize a Pd(teen) complex. Finally, the synthesis of Pd-tmchxn should have combined the positive properties of Pd-chxn and Pd-tmen. However, the carbonate [Pd(tmchxn)CO₃] (**2**) showed a higher formation and crystallization tendency than a corresponding carbohydrate complex, therefore further investigations were omitted. Nevertheless, it should be mentioned that a ¹³C NMR investigation of Pd-tmchxn with the various carbohydrates is unfinished.

3.2 The Pd^{II}N₂ fragments' influence on the hydrogen-bonding network

The Pd(tmen) fragment showed a different behavior compared to that of the Pd(en) and Pd(*R,R*-chxn) fragment. Various crystal structures revealed a marked difference in the formation of the hydrogen-bonding network. Comparing the crystal structures of the Pd^{II} complexes of allitol (**16**, **17**) and mannitol (**11**, **12**, ^[58]) and the various Pd^{II}N₂ fragments to each other, in the structures of the Pd(tmen) fragment, the polyols' remaining hydroxy groups formed exclusively intramolecular hydrogen bonds whereas in the structures with other Pd^{II}N₂ fragments the hydroxy groups formed hydrogen bonds to adjacent water molecules. In the case of allitol, an alternating bonding mode resulted from this effect. Probably, the hydrophobic tmen ligands expelled water molecules from the polyol's closest vicinity and enforced the intramolecular hydrogen bonds in this way, whereas non-alkylated

3 Discussion

chelate ligands such as en or chxn can act as hydrogen-bond donors to arrange water molecules close to the complex. On the other hand, an $R_4^2(8)$ ring motif^[60] formed by two water molecules and the alkoxido atoms of a polyolato complex with Pd(tmen) connecting the single molecules was repeatedly detected. With the crystal structures of the Pd^{II} complexes of dulcitol (**13**, **14**,^[58]), the S-shaped motif of dulcitol is independent of the Pd^{II}N₂ fragments underlining the importance of the δ hydrogen bond.

Upon addition of acid to the polyols' solutions with Pd-en or Pd-chxn, the hydrogen-bonding network lost its influence and the bonding mode was exclusively mediated by the μ -hydroxido-bridged Pd^{II}N₂ fragments. As described in Section 2.4, the acid-dependent formation of bridged palladium species and their interaction with a suitable polyol is well understood. This chemistry was impossible with the Pd(tmen) fragment because all attempts resulted in the formation of a μ -hydroxido-bridged Pd(tmen) dimer.^[114] On the other hand, the structure of the hexanuclear cation **25** pointed to the possibility of consecutive reactions that eliminate the available palladium species from the equilibria that determine the titration curve.

Within the inositols, *neo*- and *scyllo*-inositol formed different crystal structures with Pd-en^[76] and Pd-tmen (**28**, **29**). With $[\text{Pd}_2(\text{en})_2(\text{D-}neo\text{-Ins}1,2;4,5\text{H-}_4\text{-}\kappa\text{O}^{1,2};\kappa\text{O}^{4,5})] \cdot 12 \text{H}_2\text{O}$,^[76] the Pd(en) fragments coordinated two opposite *cis*-vicinal diolato functions leaving two equatorial hydroxy functions uncoordinated. With $[\text{Pd}_2(\text{tmen})_2(\text{D-}neo\text{-Ins}1,6;3,4\text{H-}_4\text{-}\kappa\text{O}^{1,6};\kappa\text{O}^{3,4})] \cdot 22 \text{H}_2\text{O}$, two Pd(tmen) fragments coordinated two opposite *trans*-vicinal diolato functions leaving two axial hydroxy functions uncoordinated. Thus, the unfavorable *trans*-vicinal diolato-coordinated compound was obtained with the Pd(tmen) fragments not participating in the hydrogen-bonding network. Keeping in mind the fact that an axial hydroxy function is less suitable for accepting hydrogen bonds than an equatorial hydroxy function, and the realization that the Pd(tmen) fragment expelled water molecules from the inositol's closest vicinity, the formation of **28** seemed to be the logical consequence. Each of the coordinating alkoxido functions accepted two hydrogen bonds whereas the axial hydroxy function acted only as a hydrogen-bonding donor underlining the fact that an axially oriented hydroxy function is less suitable for accepting hydrogen bonds than an equatorially oriented hydroxy function. With this in mind the formation of $[\text{Pd}_3(\text{tmen})_3(\text{scyllo-InsH-}_6)] \cdot 23 \text{H}_2\text{O}$ should be favored for the identical reasons. The dimetalated form would provide two equatorial hydroxy functions whereas the trimetalated compound accepted twelve hydrogen bonds.

3.3 Conformational fluctuation in palladium(II)–methyl aldopentopyranoside and aldopentose complexes

Conformational fluctuation of a *cis*-vicinal chelated pyranose was investigated in a couple of aldopentopyranosides. As a result, for *cis*-vicinal diol functions, anellation of a chelate and a pyranose ring does not freeze the interconversion of the two chair conformers in terms of NMR spectroscopy. Instead, intermediate coupling constants can serve as a measure of the conformational equilibrium's position. In agreement with the number of *cis*-vicinal diol functions, the investigated methyl pyranosides of lyxose, ribose and xylose exhibited one, two and zero fluctuating palladium(II) chelates, respectively. Furthermore, *syn*-diaxial pyranose chelation which was detected previously with a dimetallated 1C_4 -all-axial conformer of β -D-xylopyranose was confirmed.^[37] This chelation mode was found for the complexes of two pentosides: $[Pd(tmen)(Me-\beta\text{-D-Rib}p2,4H_2)]$ and $[Pd(tmen)(Me-\beta\text{-D-Xyl}p2,4H_2)]$. The formation of six-membered chelate rings results in the absence of pronounced coordination-induced shifts. Therefore, a caveat on CIS values should be noted. On the one hand, levoglucosan, a conformationally fixed bicyclic molecule, did not alter its shape markedly on coordination.^[41] Methyl β -D-ribopyranoside, on the other hand, is fluctuating in its non-bonded standard state, but is fixed in the $\kappa O^{2,4}$ -bonded chelate. Consequently, the CIS values were not affected solely by the coordination of palladium(II) (as is implied in the term coordination-induced shift), but were biased by a component caused by freezing out one conformer. However, the ${}^{13}C$ NMR values of the free pyranoside, which were used for calculation of the CIS values, are flawed by the equilibrium of conformations. In consequence, the CIS values not only represented the coordination of palladium(II) but also the change of conformation, which can be read off from the ${}^{13}C$ NMR shifts that appear to all carbon atoms. Moreover, the expected small shifts were biased by a conformational change. Thus, both pentosides were fixed in their 1C_4 conformer, which resembled a freezing of the ribopyranoside fluctuation and the inversion of the xylopyranoside chair. Hence, in both cases, the standard state of the CIS calculation was different from the chelating conformation, an effect that was more pronounced for the xylopyranoside and less so in the case of the ribopyranoside.

The metalation of pentoses in Pd^{II} -containing solvents influences the conformation of pyranoses in various cases. Four cases could be detected: (1) metalation didn't affect the pyranose's initial conformation, (2) metalation caused an inversion of pyranose's initial conformation, (3) metalation froze a fluctuating pyranose in one conformation and

3 Discussion

(4) metalation induced conformational fluctuation of a pyranose. Different effects were responsible for these results: the kind of metalation, electrostatic interactions and hydrogen bonding. The effects of *trans*-vicinal and *syn*-diaxial bonded palladium fragments forcing the pyranose to assume one defined conformation are easy to interpret. *Cis*-vicinal metalation affecting the pyranose's conformation was controlled by intra- and intermolecular hydrogen bonds. So, for 1C_4 -[Pd(*R,R*-chxn)(α -D-Ribp1,2H₂- $\kappa O^{1,2}$)],^[37] an intramolecular hydrogen bond could be identified by X-ray analysis explaining the conformational fluctuation's freezing and the impossibility of double metalation of α -D-Ribp. Transferring this argument to the other pentopyranoses, an intramolecular hydrogen bond O4–H4...O2 also explained the induced conformational fluctuation for a $\kappa O^{1,2}$ -bonded α -D-Xylp1,2H₂. Also the missing hydrogen bond is responsible for the stable 4C_1 conformation of a $\kappa O^{1,2}$ -bonded β -D-Lyxp1,2H₂.

However, none of these arguments can explain the double-metalation caused inversion of D-arabinopyranose's conformation. Here, electrostatic interactions were responsible for the conformational inversion of β -D-Arap1,2;3,4H₄- $\kappa O^{1,2}:\kappa O^{3,4}$ allowing the two negatively charged substituents of C2 and C3 to occupy an axial position in the 4C_1 instead of the initial 1C_4 conformation; the conformational fluctuation of α -D-Arap1,2H₂- $\kappa O^{1,2}$ and α -D-Arap3,4H₂- $\kappa O^{3,4}$ was induced by the same electrostatic repulsion. This could be considered to be a more general case of the anomeric effect which is usually linked with the C1 position. Recent results indicate that the hyperconjugation from the lone pairs on the ring heteroatom to the antibonding orbital between the anomeric carbon and its linking substituent are not responsible for the anomeric effect and that it is better interpreted in terms of electrostatic interactions.^[115] Further, the 4C_1 conformation allows better access for water molecules to build hydrogen bonds to the deprotonated oxygen atoms. This accessibility of oxygen atoms for hydrogen bonding would also explain the different behavior of D-xylopyranose in Pd-chxn and Pd-tmen/Pd-teen. In Pd-chxn the cyclohexane-1,2-diamine itself acts as a fourfold hydrogen bond donor suppressing the need of a $\kappa O^{1,2}:\kappa O^{3,4}$ -bonded α -D-Xylp1,2;3,4H₄ to accept hydrogen bonds. Otherwise, *N,N,N',N'*-tetraethylethane-1,2-diamine didn't provide hydrogen bonds forcing the $\kappa O^{1,2}:\kappa O^{3,4}$ -bonded β -D-Xylp1,2;3,4H₄ species which enabled the formation of hydrogen bonds to the diolato units.

Testing all the detected species for the appearance of the anomeric effect at C1, electrostatic repulsion of all substituents of the pyranose ring and hydrogen bonding clearly dominated the conformational behavior of metallated pentopyranoses.

3.4 Metalation of the methyl hex(ul)osides

Comparing the detected metalated methyl hex(ul)oside species in the various Pd^{II}-containing solvents and their proportional distribution referred to a molar Pd/methyl hex(ul)oside ratio of 2:1 in Fig. 3.1 and the known rules^[78] of palladium(II) chelation were confirmed. The $\kappa O^{1,2}$ -diolato coordination mode is preferred to the $\kappa O^{1,3}$ -diolato coordination mode. Within the $\kappa O^{1,2}$ -diolato coordination mode *cis*-vicinal chelation is preferred to *trans*-diequatorial chelation. The orientation of the anomeric hydroxy group had only minor effects on the chelation modes. Therefore, it was not surprising to find the *cis*-vicinal $\kappa O^{3,4}$ -diolato coordination mode favored over the $\kappa O^{2,3}$ -chelation with the methyl galactopyranosides, the *cis*-vicinal $\kappa O^{2,3}$ -diolato coordination mode favored over the $\kappa O^{3,4}$ -diolato chelation with methyl α -D-mannopyranoside and the *cis*-vicinal $\kappa O^{4,5}$ -diolato coordination mode favored over the $\kappa O^{3,4}$ -diolato chelation with methyl β -D-fructopyranoside. With the methyl D-glucopyranosides only *trans*-diequatorial chelation was possible. It is remarkable that Pd-tmen and Pd-chxn favored different chelation sites. With Pd-tmen the $\kappa O^{2,3}$ -bonded Me-D-Glcp2,3H₂ species represented the major form, whereas with Pd-chxn the $\kappa O^{3,4}$ -bonded Me-D-Glcp3,4H₂ form was found as the major species. Furthermore, $\kappa O^{1,3}$ -diolato chelation was detected for all the methyl hex(ul)osides except the methyl galactopyranosides. Obviously, an axially oriented hydroxy group together with the hydroxymethyl group impaired the $\kappa O^{1,3}$ -diolato chelation. Comparing the α - and β -form of the methyl D-fructofuranosides, $\kappa O^{1,3}$ -diolato chelation was detected for both anomers, nevertheless a *cis*-vicinal orientation of the hydroxymethyl group and the hydroxy group at C3 made chelation easier.

3.5 Metalation of the hexoses

With the hexoses, a first obvious difference between Pd-tmen and Pd-chxn is Pd-tmen's preference to stabilize the furanose forms by $\kappa O^{1,2}$ -diolato chelation whereas the Pd-chxn's tendency to attack by $\kappa O^{1,3}$ -diolato chelation is underlined by the presence of 29.7 % of the β -D-Galf1,3H₃ species in equimolar solutions.^[37] Otherwise, the various D-galactose species were detected at almost the same percentual share in equimolar solutions. With Pd-tmen the monometalated α -D-Glcp1,2H₂- $\kappa O^{1,2}$ and α -D-Manp2,3H₂- $\kappa O^{2,3}$ species became the main species with an almost 50 % share of the percentual distribution in solution whereas with Pd-chxn, the α -configured species did not dominate the species distribution.

3 Discussion

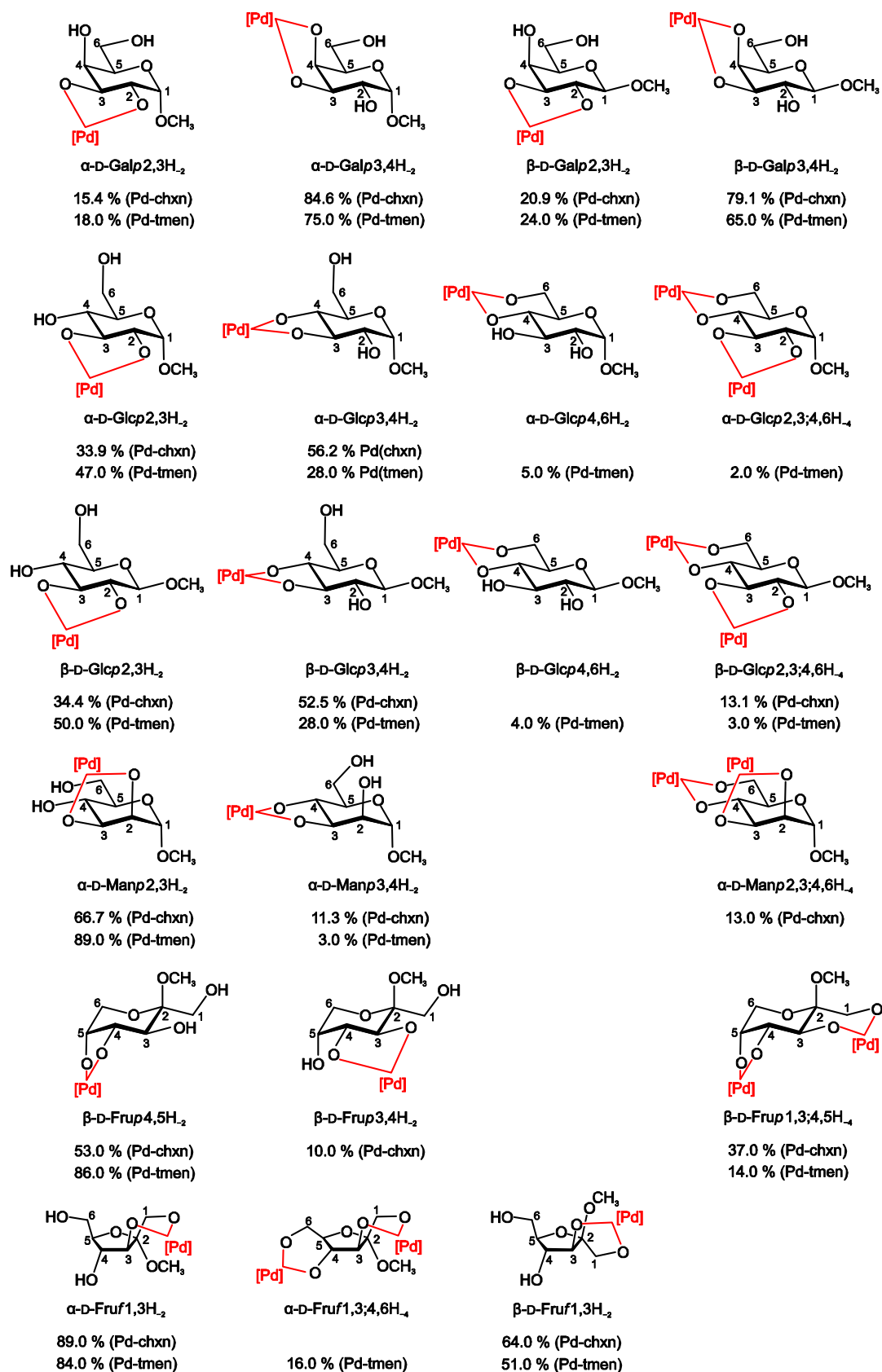


Figure 3.1. Overview of the detected metalated methyl hex(ul)oside species in the various Pd^{II}-containing solvents. The proportional distribution of species refer to a molar Pd/methyl hex(ul)oside ratio of 2:1.

3 Discussion

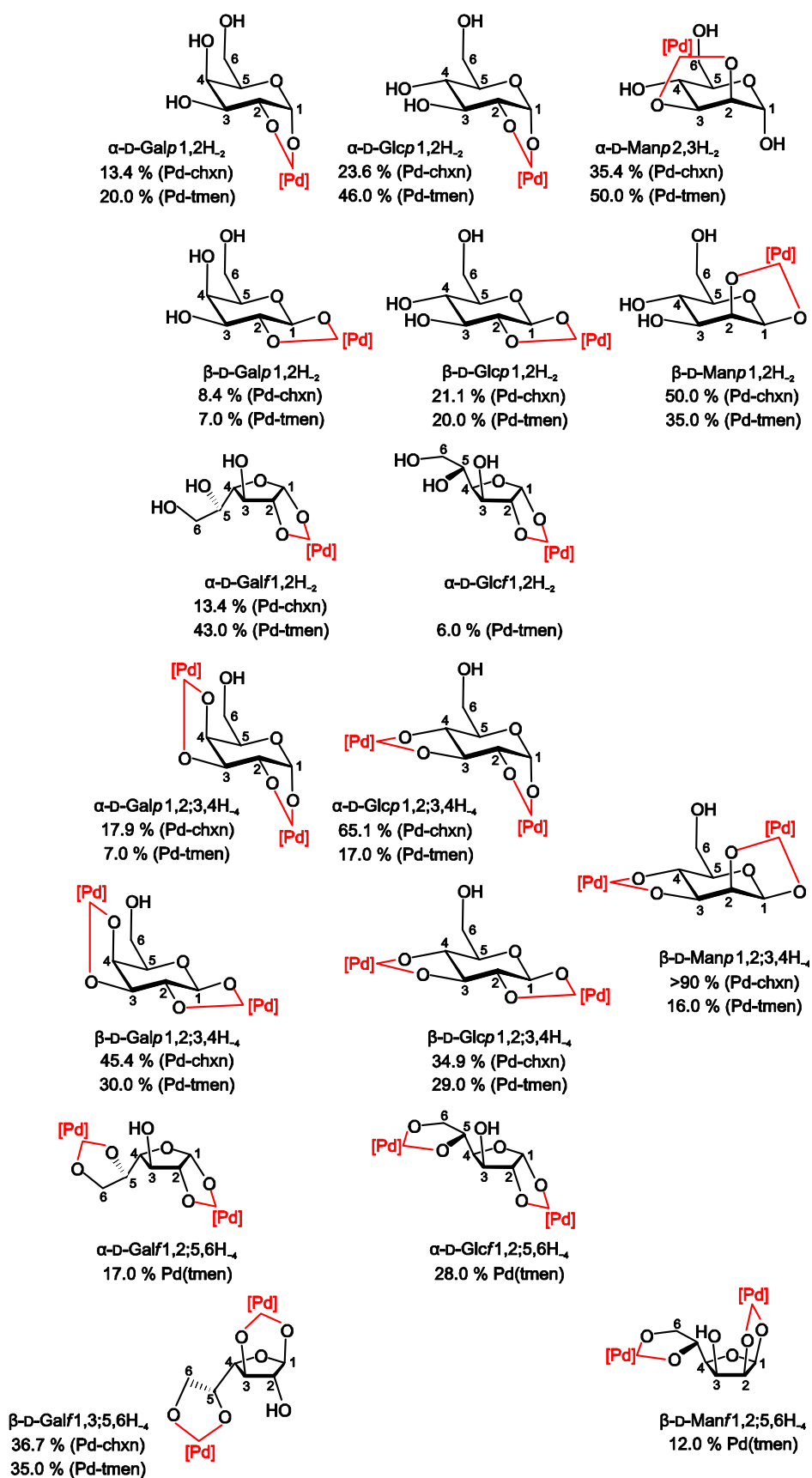


Figure 3.2. Overview of the detected metalated aldohexose species in the various Pd^{II}-containing solvents. The proportional distribution of species refer to a molar Pd/aldohexose ratio of 1:1 for monometalated and to 3:1 for dimetalated species.

3 Discussion

Moreover, with Pd-chxn, the β -D-Manp1,2H₂- $\kappa O^{1,2}$ species was the main species in solution. As for the pentoses, the more hydrophobic vicinity of a Pd(tmen) complex could possibly not compensate the anomeric effect as well as a more hydrophilic Pd(R,R-chxn) complex.

At a molar Pd/hexose ratio of 3:1, all three hexoses formed a $\kappa O^{1,2}:\kappa O^{5,6}$ -dimetalated furanose complex with Pd-tmen whereas with Pd-chxn, only the α -D-Galp1,2;5,6H₄- $\kappa O^{1,2}:\kappa O^{5,6}$ form which is stabilized by an intramolecular hydrogen bond was detected. Furthermore, with Pd-chxn the $\kappa O^{1,2}:\kappa O^{3,4}$ -dimetalated β -forms of D-glucose and D-mannose were found as dominating species whereas with Pd-tmen various species were detected concurrently. In conclusion, the former proposed rules for the chelation of reducing carbohydrates with Pd^{II}N₂ fragments were confirmed. Additionally, Pd-tmen's preference for the stabilization of furanose forms had to be added.

3.6 The hexuloses' chelation preferences

Comparing the species detected in aqueous and in Pd^{II}-containing solutions, predominantly the former major species were metalated. The Figures 3.3 and 3.4 give an overview of the distribution of mono- and dimetalated species. As one can see, $\kappa O^{1,2}$ - and $\kappa O^{2,3}$ -chelation was the preferred mode for monometalation involving the most acidic hydroxy function O2. Now, comparing the $\kappa O^{1,2}$ -chelated α -D-Tagp1,2H₂ species to the α -L-Sorp1,2H₂ species, the hydroxy group at C3 in the axial position was clearly favored because of minor interactions with the $\kappa O^{1,2}$ -chelated hydroxymethyl group. Whereas the $\kappa O^{1,2}$ -chelated α -D-Tagp1,2H₂ species was the dominant species in solution, the α -L-Sorp1,2H₂- $\kappa O^{1,2}$ species was suppressed in favor of α -L-Sorp2,3H₂- $\kappa O^{2,3}$ and α -L-Sorf2,3H₂- $\kappa O^{2,3}$ both of which avoided the unfavored interaction of a hydroxy group with the Pd(tmen) fragment. Additionally, the $\kappa O^{2,3}$ -bonded α -L-Sorf2,3H₂ could be stabilized by an intramolecular hydrogen bond O1-H...O4. As discussed in the literature,^[87] two intramolecular hydrogen bonds O6-H...O3 and O1-H...O4 would explain the high stability of the β -D-Fruf2,3H₂- $\kappa O^{2,3}$ species. Nevertheless, two additional species, the $\kappa O^{2,3}$ -chelated β -D-Fruf2,3H₂ species and the $\kappa O^{4,5}$ -chelated α -D-Frup4,5H₂ species, were detected. The former species corresponded to α -L-Sorp2,3H₂- $\kappa O^{2,3}$ and was favored for the same reasons, the latter species could be stabilized by two intramolecular hydrogen bonds, the known hydrogen bond O2-H...O4 and an additional hydrogen bond O3-H...O1. The α -D-Psip4,5H₂- $\kappa O^{4,5}$ species could be stabilized by the same intramolecular hydrogen bonds.

3 Discussion

Furthermore, the most favored furanose form, α -D-psicofuranose, yielded two metalated species, the $\kappa O^{2,3}$ -bonded α -D-Psif $2,3H_{-2}$ and the $\kappa O^{3,4}$ -bonded α -D-Psif $3,4H_{-2}$ species which were favored for the same reasons as the unmetalated furanose.

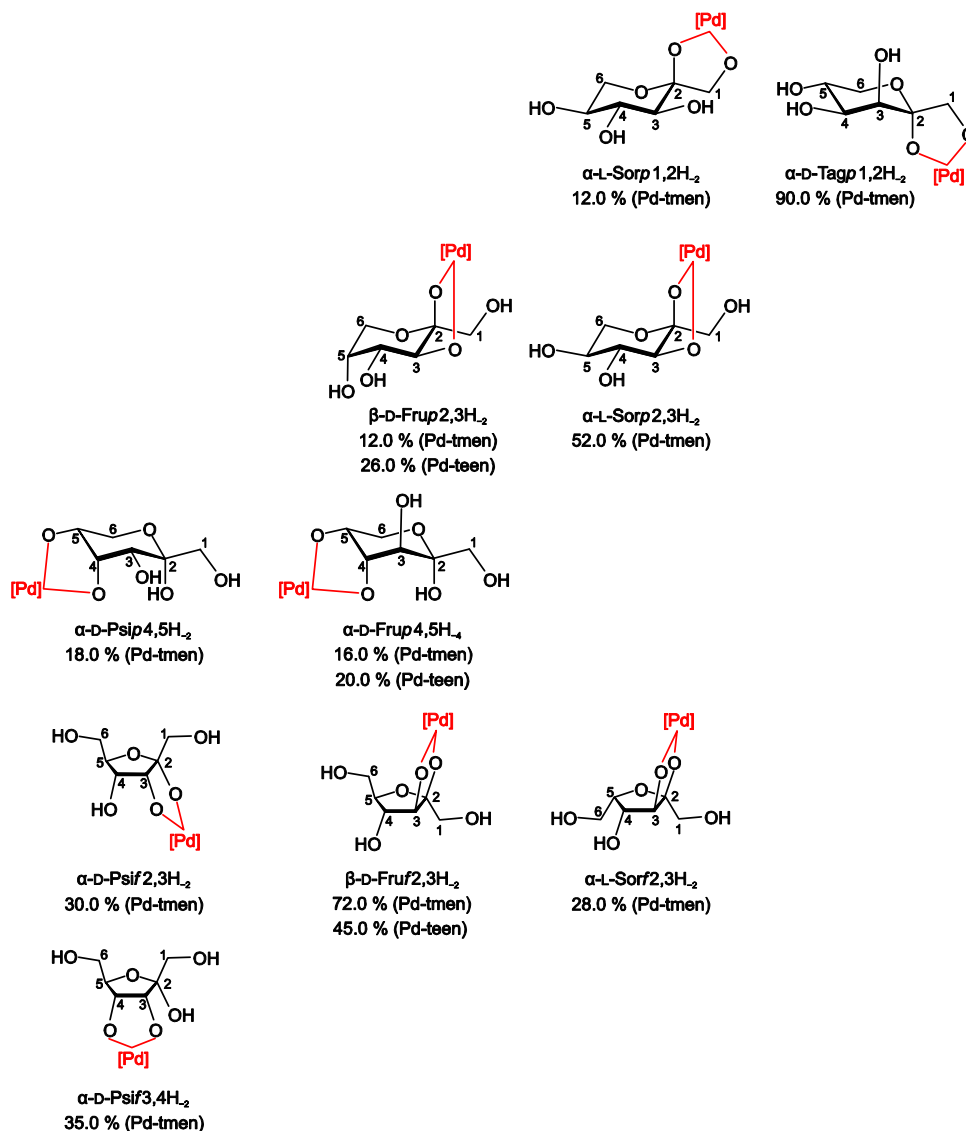


Figure 3.3. Overview of the detected monometalated hexulose species in the various Pd^{II}-containing solvents. The proportional distribution of species refer to a molar Pd:hexulose ratio of 1:1.

With double metalation of the hexuloses, first and foremost the suitable monometalated forms were metalated a second time whereas unsuitable monometalated forms were expelled or transformed. The unfavored equatorially standing hydroxy group at C3 was metalated only by $\kappa O^{2,3}$ -chelation and never by $\kappa O^{3,4}$ -chelation. Therefore, neither a $\kappa O^{1,2}:\kappa O^{3,4}$ -chelated β -D-Frup $1,2;3,4H_{-4}$ nor a $\kappa O^{1,2}:\kappa O^{3,4}$ -chelated α -L-Sorp $1,2;3,4H_{-4}$ species were detected.

3 Discussion

For the same reason, the $\kappa O^{1,2}:\kappa O^{3,4}$ -dimetalated furanose species of D-tagatose and D-psicose were identified in the α - and β -form respectively. Finally, also for this reason, the $\kappa O^{2,3}:\kappa O^{4,5}$ -bonded α -L-Sorp2,3;4,5H₄ species was preferred to the α -L-Sorp1,2;4,5H₄- $\kappa O^{1,2}:\kappa O^{4,5}$ species. The above-mentioned intramolecular hydrogen bond O2–H···O4 and electrostatic repulsion of two 1,3-diaxially oriented alkoxido atoms impaired further metalation of the α -D-Frup4,5H₂- $\kappa O^{4,5}$ and α -D-Psip4,5H₂- $\kappa O^{4,5}$ species to the $\kappa O^{1,2}:\kappa O^{4,5}$ -dimetalated α -forms. Therefore, the less favored β -D-Frup1,2;4,5H₄- $\kappa O^{1,2}:\kappa O^{4,5}$ species was detected.

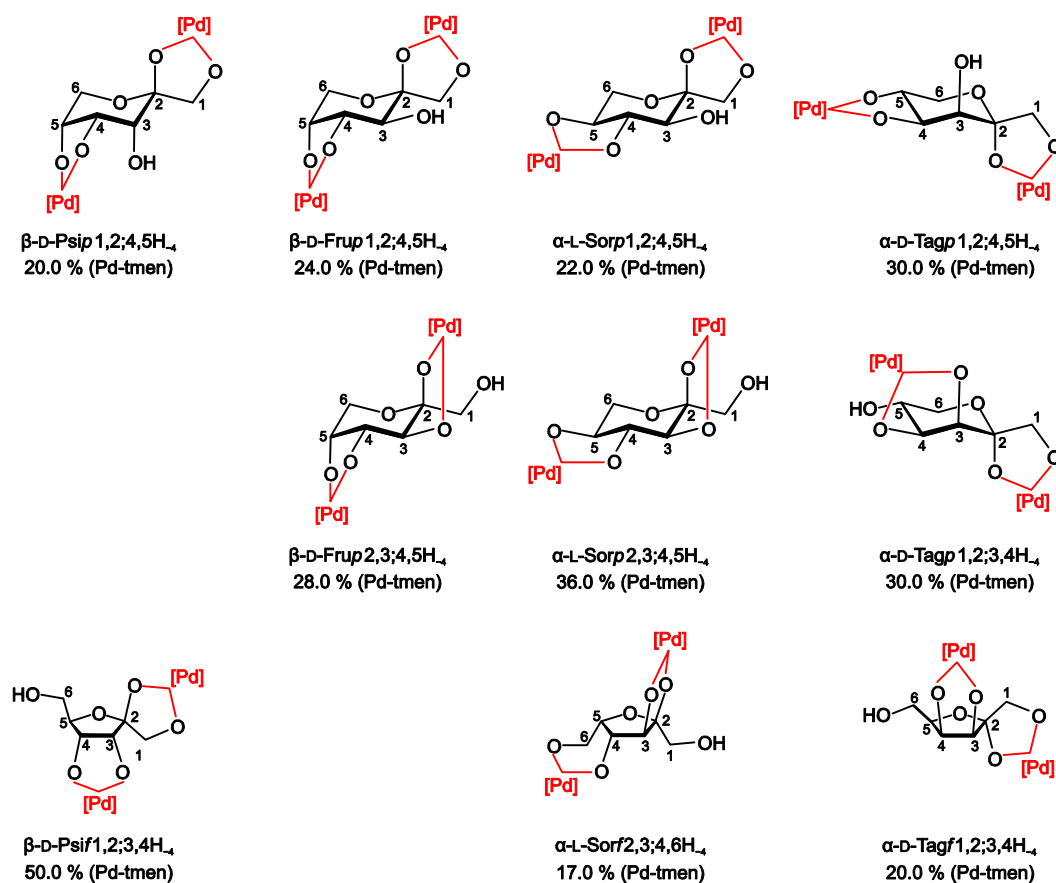


Figure 3.4. Overview of the detected dimetalated hexulose species in the various Pd^{II}-containing solvents. The proportional distribution of species refer to a molar Pd:hexulose ratio of 2:1.

The analysis of $^3J_{H,H}$ coupling constants indicated a fluctuation of the $\kappa O^{2,3}:\kappa O^{4,5}$ -chelated β -D-Frup2,3;4,5H₄ species between the between the 5C_2 and the 2C_5 conformation. A possible intramolecular hydrogen bond O1–H···O4 could stabilize the $\kappa O^{2,3}:\kappa O^{4,5}$ -chelated β -D-Frup2,3;4,5H₄ species in the 5C_2 conformation which was also found energetically favorable to the 2C_5 conformation. Unfortunately, α -L-Sorp2,3;4,5H₄- $\kappa O^{2,3}:\kappa O^{4,5}$ provided a *trans*-diequatorial $\kappa O^{4,5}$ -chelation site which impaired conformational fluctuation as well as a further analysis.

3.7. The difficult analysis of the dialdoses

In the literature, little is known about the class of dialdoses. Comparing the ^{13}C NMR spectra of D-galactose and D-mannose to the spectra of *galacto*- and D-*manno*-dialdose, the similarity of the spectra, except for the C6 signal, was evident. Assuming the regular pyranose forms containing an aldehyde hydrate at the C6 atom, the signals could be assigned. Two further species in the ^{13}C NMR spectrum of D-*manno*-dialdose were found as the two 3,6-anhydro-D-*manno*-dialdofuranose forms whereas no furanose forms were detected for *galacto*-dialdose in aqueous solution. The ^{13}C NMR spectrum of *xylo*-dialdose in water did not resemble the ^{13}C NMR spectrum of D-xylose. Nevertheless, two species were unambiguously assigned. With the pentodialdoses, the aldehyde hydrate is part of the pyranose ring and therefore, the influence on the chemical shifts is higher than with the hexodialdoses. Additionally, the symmetric *meso*-dialdoses' ability to alternate between the D- and L-form complicated the final determination of species in solution.

In equimolar solutions of Pd-tmen and *xylo*- or *galacto*-dialdose the same species were found as for the corresponding aldoses. However, in contrast to the mono-metalated $\alpha\text{-D-Xylp1,2H}_2\text{-}\kappa\text{O}^{1,2}$ species of D-xylose, the additional hydroxy group at C5 impaired the conformational fluctuation which is detected for $\kappa\text{O}^{1,2}$ -bonded $\alpha\text{-D-Xylp1,2H}_2$. Also with *galacto*-hexodialdose, two species were found which corresponded to the D-galactose species. Additionally, a third species was identified and is still not certainly assigned. Excluding the known species, only $\kappa\text{O}^{1,2}$ -3,6-anhydro- $\alpha\text{-Gal6aldp1,2H}_2$ was eligible. It is noteworthy that no ^{13}C NMR chemical shift values were available for such an unmetalated conformation, so a definite determination of CIS values was not possible.

With D-mannose the main species was the $\kappa\text{O}^{2,3}$ -chelated $\alpha\text{-D-Manp2,3H}_2$ for mono-metalation. Transferring this chelation mode to D-*manno*-hexodialdose, both the most acidic hydroxy groups remained unmetalated and an obviously unfavored species would be formed. Therefore, it was not surprising to detect high amounts of the dimetalated $\beta\text{-D-Man6aldf1,2;5,6H}_4\text{-}\kappa\text{O}^{1,2}:\kappa\text{O}^{5,6}$ species which was the only species with both the most acidic hydroxy groups metalated.

At a molar Pd-tmen/*galacto*-dialdose ratio of 2:1, three dimetalated furanose species were detected with both acidic, anomeric hydroxy groups participating to the chelate rings. For this reason, no dimetalated pyranose form was found because the participation of the two specific hydroxy functions could be realized only by an unfavored $\kappa\text{O}^{1,3}$ -chelation.

3 Discussion

With the dimetalated $1_{ax},5_{eq}$ -Xyl5aldp1,2;3,5H₋₄ species both aldehyde hydrate functions were metalated and, additionally, an intramolecular hydrogen bond O4–H···O2 stabilized the 1C_4 -conformation to result in a perfectly matching complex. The minor species $1_{ax},5_{eq}$ -Xyl5aldp1,2;4,5H₋₄ missed out the stabilizing intramolecular hydrogen bond whereas $[1,5]_{eq}$ -Xyl5aldp1,2;4,5H₋₄ was not formed because of unfavorable electrostatic repulsions between all-equatorially standing alkoxido functions.

To sum up the results, the second aldehyde function of a dialdose in aqueous solution always formed an aldehyde hydrate either with a water molecule or by intramolecular ring formation as with *xylo*- and *D-manno*-dialdose. The general rules of palladium(II) metalation were confirmed by the investigation of the three available dialdoses. Additionally, the participation of both of the most acidic, anomeric hydroxy groups to the chelate rings seems to be a prerequisite for dimetalation. In fact, this was confirmed by the crystal structure of $[Pd_2(tmen)_2(Ery4ald/H_{-4}-\kappa O^{1,4};\kappa O^{2,3})]$ (**40**).

3.8 Metalation of di- and oligosaccharides

In discussing the metalation of di- and oligosaccharides, the building units of the investigated carbohydrate has to be taken into account. A fructose-containing di- or trisaccharide should not be compared to a di- or trisaccharide that only contains glucopyranose units and vice versa. The conservative shift patterns of similar coordination modes and moreover, identical CIS values for similar palladium(II)–glycose complexes enabled the identification of metalated species and the assignment of corresponding ${}^{13}C$ NMR values. Combining the previous results of hex(ul)osides and hex(ul)oses the metalation sites and the order of metalation can be reliably predicted.

Starting with the fructose-containing di- and trisaccharides, one had to distinguish whether the fructose's O2/O3 diolato unit is blocked by the glycosidic linkage or not. In the case of *D*-maltulose, *D*-lactulose, *D*-leucrose and *D*-palatinose the glycosidic linkage was formed by fructose's O4, O5 or O6 remaining the O2/O3 diolato unit ready for metalation. At equimolar Pd-tmen/disaccharide solutions this diolato unit was metalated exclusively in accordance with the $\kappa O^{2,3}$ - β -D-Fruf2,3H₋₂ species which was found to be the most stable monometalated fructose species. With *D*-leucrose which cannot provide the fructofuranose form, the pyranose form was $\kappa O^{2,3}$ -chelated. In the case of *D*-sucrose and *D*-turanose this preferred $\kappa O^{2,3}$ -diolato unit was not available for metalation and the variety of species

3 Discussion

increased. The two investigated trisaccharides do not provide the fructose's favored $\kappa O^{2,3}$ -chelation site, therefore the gluco- and galactopyranoside units were stepwise metalated according to the results of the corresponding methyl glycopyranosides.

The investigation of the selected β -(1 \rightarrow 4)-glycosidic-linked disaccharides confirmed the previous results. In a first step, the most acidic, anomeric hydroxy groups of the reducing glucopyranose unit participated in $\kappa O^{1,2}$ -chelation by Pd-tmen. The α/β anomeric ratio corresponded to the ratio of monometalated D-glucose. The (1 \rightarrow 4)-glycosidic linkage impaired further metalation of the reducing glucopyranose unit. Therefore, in a second step, the non-reducing α -D-glucopyranoside/ β -D-galactopyranoside units were metalated according to the results of the corresponding methyl glycopyranoside. No further restrictions for the metalation were detected a fact which is confirmed by the full metalation of cellulose.

Transferring the results to general rules so far, (1) a preference for the participation of the most acidic, anomeric hydroxy group to the chelate rings is realized. (2) $\kappa O^{1,2}$ -diolato chelation is preferred to $\kappa O^{1,3}$ -diolato chelation and *cis*-vicinal diolato chelation is preferred to *trans*-diequatorial diolato chelation. (3) The reducing units of the disaccharides react in the same way as the corresponding hex(ul)oses, the non-reducing units of the di- and trisaccharides react in the same way as the corresponding methyl hex(ul)osides. (4) Therefore, the shift patterns and CIS values of the monomeric model compounds can be used for the assignment of the oligomeric metalated species.

Within the investigated α -(1 \rightarrow 4)-glycosidic linked di- and oligosaccharides the formulated rules did not completely explain the detected metalation pattern. D-Melibiose is the only disaccharide which could be dimetalated at the reducing glucopyranose unit. With monometalation, as expected, α -D-Galp-(1 \rightarrow 6)- α -D-Glcp1,2H₂ was found to be the main species accompanied by small amounts of α -D-Galp-(1 \rightarrow 6)- β -D-Glcp1,2H₂ and α -D-Galp-(1 \rightarrow 6)- α -D-Glcf1,2H₂. Adding a second Pd-tmen fragment, the galactopyranoside unit of α -D-Galp-(1 \rightarrow 6)- β -D-Glcp1,2H₂ was metalated. Only with a third Pd(tmen) fragment dimetalation of the reducing glucopyranose unit was achieved with the α -D-Galp3,4H₂-(1 \rightarrow 6)- β -D-Glcp1,2;3,4H₄ species which provided the β -configuration for dimetalation. In agreement with the D-turanose's results, another rule can be postulated. (5) Starting with $\kappa O^{1,2}$ -diolato chelation of the most acidic, anomeric hydroxy group, each unit of a disaccharide had to be metalated first before dimetalation occurs.

3 Discussion

Finally, investigations of the maltose-derived oligosaccharides and the cyclodextrins revealed the wide influence of intramolecular hydrogen bonds to the metalation. Whereas the mono- and dimetalation of D-maltose could be explained by the above-listed rules, with D-maltotriose the metalation of the terminal α -D-glucopyranoside unit deviated from the expected $\kappa O^{2,3}$ -diolato chelation. Instead, the Pd(tmen) fragment coordinated at the $\kappa O^{3,4}$ -diolato unit of the terminal α -D-glucopyranoside which has so far been uncommon within the investigations. An intramolecular hydrogen bond $O2-H\cdots O3'$ caused the displacement of the expected $\kappa O^{2,3}$ -diolato chelation. In general, a strong hydrogen-bonding network passed along the hydroxy groups $O2-H$ and $O3-H$ of an α -(1 \rightarrow 4)-linked glucopyranose chain. In the cyclodextrins' crystal structures **42–45**, for example, every other $\kappa O^{2,3}$ -diolato site was metalated because the uncoordinated hydroxy groups $O2-H$ and $O3-H$ formed hydrogen bonds to the adjacent alkoxido functions. For this reason, a complete metalation of the cyclodextrins was never achieved. Returning to D-maltotriose, these intramolecular hydrogen bonds stabilized a metalation pattern which deviated from the expected one. With monometalation, the species α -D-Glcp-(1 \rightarrow 4)- α -D-Glcp-(1 \rightarrow 4)- α -D-Glcp_{2,3H₂} and α -D-Glcp-(1 \rightarrow 4)- α -D-Glcp-(1 \rightarrow 4)- β -D-Glcp_{2,3H₂} were detected. This unusual $\kappa O^{2,3}$ -chelation mode at the reducing D-glucopyranose unit could only be explained by a stabilization by an intramolecular hydrogen bond $O2'-H\cdots O3''$.

The investigation of D-maltoheptaose revealed the limits of a controlling hydrogen-bonding network which was found for D-maltotriose and the cyclodextrins. With such a controlling hydrogen-bonding network a resulting well-defined complex should have provided a well-defined ¹³C NMR spectrum as well. The broad signals gave evidence that, contrary to the treatment of Pd-tmen and D-maltotriose, the metalation of D-maltoheptaose was less regular. This indicated a weakening of the hydrogen bonds' controlling function for the metalation which is found for D-maltotriose. Furthermore, looking at solutions of amylose in Pd-tmen and in spite of the weakened controlling function of the hydrogen bonds, only half of the available $\kappa O^{2,3}$ -diolato sites were metalated. It is presumed that the hydrogen-bonding network did not control the complete polysaccharide. Nevertheless, in restricted domains along the polysaccharide, the hydrogen bonds determine the metalation of only every other $\kappa O^{2,3}$ -diolato site, although it could not be clarified if this is a statistical effect or caused by two competing patterns.

4 Summary

This thesis deals with carbohydrate complexes of palladium(II) and their characterization via NMR spectroscopy and X-ray analysis. The aim of this work was the further investigation of Pd^{II}N₂-complexes with more reactive carbohydrates such as the ketoses and dialdoses and with di-, tri- and oligosaccharides. Also, the coordination chemistry of Pd^{II}N₂-carbohydrate complexes in neutral aqueous solution and the dynamic behavior of methyl pentosides and pentoses was further investigated. Therefore, in a first step, the pool of Pd^{II}N₂-fragments was extended with regard to a higher resistance to the reduction to palladium(0) and a better crystallization tendency. The first part of this work deals with a series of seven new Pd^{II}N₂ fragments (see Section 2.1). Pd-dmen, Pd-tmen, Pd-tmchxn, Pd-teen, Pd-tn, Pd-bpy and Pd-phen were successfully synthesized and five crystal structures were obtained, [Pd(tmen)(OH)₂] · 2 H₂O (**1**), [Pd(tmchxn)(CO₃)] · 6 H₂O (**2**), [Pd(teen)Cl₂] (**4**), [Pd(bpy)(OH)₂] · 5 H₂O (**5**) and [Pd(phen)(OH)₂] · 5 H₂O (**6**). Pd-tmen is a less polar solvent than Pd-en or Pd-chxn and, additionally, the steric demand increased because of the methylation which is possibly a further reason for the differing coordination behavior of Pd-tmen to Pd-en. The application of Pd-teen did not increase the advantages of Pd-tmen because the coordination tendency to the carbohydrates decreased and only syrupy substances could be obtained from attempts to crystallize a Pd(teen) complex. Finally, the synthesis of Pd-tmchxn combined the positive properties of Pd-chxn and Pd-tmen. However, **2** showed a higher formation and crystallization tendency than a corresponding carbohydrate complex, therefore further investigations were omitted. Nevertheless, it should be mentioned that a ¹³C NMR investigation of Pd-tmchxn with the various carbohydrates is lacking. The structures **5–8** revealed a repeating stacked packing of the Pd(bpy) and Pd(phen) fragments. Two structures were obtained for ethane-1,2-diol (**7**) and anhydroerythritol (**8**) both of which provide only one diolato unit. Attempts to treat Pd-bpy and Pd-phen with a carbohydrate providing more than one diolate unit resulted in insoluble precipitates. Obviously, molecules which do not support this stacked packing cannot be crystallized.

It was possible to crystallize various polyol complexes with the mentioned Pd^{II}N₂ fragments (see Section 2.3). The crystal structures **9–17** revealed a marked difference in the formation of the hydrogen-bonding network depending on the used Pd^{II}N₂ fragment. Comparing the crystal structures of the Pd^{II} derivatives of the polyols allitol (**16**, **17**) and mannitol (**11**, **12**, ^[58]), in

4 Summary

the structures of the Pd(tmen) fragment the polyols' remaining hydroxy groups formed exclusively intramolecular hydrogen bonds whereas in the structures with other Pd^{II}N₂ fragments the hydroxy groups formed hydrogen bonds to adjacent water molecules. In the case of allitol, an alternating bonding mode resulted from this effect. Probably, the hydrophobic tmen ligands expelled water molecules from the polyol's closest vicinity and enforced the intramolecular hydrogen bonds in this way, whereas non-alkylated chelate ligands such as en or chxn acted as hydrogen-bond donors to arrange water molecules close to the complex. With the crystal structures of dulcitol (**13**, **14**, ^[58]) the S-shaped motif of dulcitol is independent of the Pd^{II}N₂ fragments underlining the importance of the δ hydrogen bond.

The acid-dependent formation of bridged palladium species and their interaction with suitable polyols was described in Section 2.4. Along the titration curve, the addition of defined amounts of nitric acid to Pd-en/polyol solutions led to the formation of a binuclear hydroxido-bridged species Pd₂H₋₃ and further species of the common formula [(Pd^{II}N₂)_n(μ_2 -OH)_n]^{m+} with $n = 3$ and 4 close to neutral pH. A series of Pd₄(μ -OH)₄-derived *threo*-tetraolato tetracations **18–23** was crystallized with various polyols which provide a *threo*-configured tetraol unit. Additionally, a Pd₃(μ -OH)₃-derived triolato trication **24** was crystallized in the form of a dimer by the elimination of a [(*R,R*-chxn)₂Pd]²⁺ cation. Furthermore, the structure of the hexanuclear cation **25** pointed to the possibility of consecutive reactions that eliminate the available palladium species from the equilibria that determine the titration curve.

Attempts to crystallize a Pd₄-tetraolato species stabilizing the open-chain form of D-threose yielded a crystal structure with a decomposition product, namely dihydroxy-malonic acid. Although the hydrated mesoxalato complex was not the attempted product, **26** was the first structure of a ketone hydrate acting as a ligand for coordination of Pd^{II}N₂-fragments.

In Section 2.6, within the inositols *neo*- and *scyllo*-inositol formed different crystal structures with Pd-en^[76] and Pd-tmen (**28**, **29**), whereas with D-*chiro*-inositol a crystal structure was only obtained with the Pd(en) fragment (**27**).

Evidence was collected for the maintenance of a pyranose's conformational fluctuation in the case of a cis-vicinal chelator in the Sections 2.7 and 2.8. Conformational fluctuation of this type was investigated in a couple of aldopentopyranosides, namely methyl β -D-arabino-pyranoside, methyl α -D-lyxopyranoside, β -D-ribosepyranoside and methyl β -D-xylopyranoside as the basis for a discussion of the possible dynamic behavior of similar chelates formed by the parent glycoses. As a result, for cis-vicinal diol functions, anellation of a chelate and a

4 Summary

pyranose ring did not freeze the interconversion of the two chair conformers in terms of NMR spectroscopy. Instead, intermediate coupling constants could serve as a measure of the conformational equilibrium's position. In agreement with the number of *cis*-vicinal diol functions, the investigated methyl pyranosides of lyxose, ribose and xylose exhibit one, two and zero fluctuating palladium(II) chelates, respectively. The two crystal structures of the monometalated species of methyl α -D-lyxopyranoside (**30**) and methyl β -D-xylopyranoside (**31**) completed the methyl pentopyranosides' investigation.

The metalation of pentoses in Pd^{II}-containing solvents influenced the conformation of pyranoses in various cases. Four cases could be detected: (1) metalation did not affect the pyranose's initial conformation, (2) metalation caused an inversion of pyranose's initial conformation, (3) metalation froze a fluctuating pyranose in one conformation and (4) metalation induced conformational fluctuation of a pyranose. Different effects were responsible for these results – the kind of metalation, electrostatic interactions and hydrogen bonding. The effects of *trans*-vicinal and *syn*-diaxial bonded palladium fragments forcing the pyranose to assume one defined conformation were easy to interpret. *Cis*-vicinal metalation affecting the pyranose's conformation was controlled by intra- and intermolecular hydrogen bonds. Testing all the detected species for the appearance of the anomeric effect at C1, electrostatic repulsion of all substituents of the pyranose ring and hydrogen bonding clearly dominated the conformational behavior of metallated pentopyranoses. The dimetalated species of D-arabinose (**32**) and D-lyxose (**33**) could be crystallized with Pd-tmen.

Investigating the reaction of coordinating agents such as Pd-chxn or Pd-tmen with the methyl hex(ul)osides provided characteristic shift patterns which allowed the identification of the corresponding signals in a di- or oligosaccharide's ¹³C NMR spectrum (see Section 2.9). Furthermore, the preferred coordination modes, besides the most acidic O1 atom, were examined. The $\kappa O^{1,2}$ -diolato coordination mode was preferred to the $\kappa O^{1,3}$ -diolato coordination mode, within the $\kappa O^{1,2}$ -diolato coordination mode *cis*-vicinal chelation was preferred to *trans*-diequatorial chelation. The orientation of the anomeric hydroxy group has only minor effects on the chelation modes. Therefore, it was not surprising to find the *cis*-vicinal diolato coordination in the structures **34** and **35** of methyl α -D-galactopyranoside and in structure **36** of methyl α -D-mannopyranoside. Comparing the α - and β -form of the methyl D-fructo-furanosides $\kappa O^{1,3}$ -diolato chelation was detected for both anomers and confirmed in **38**. Nevertheless a *cis*-vicinal orientation of the hydroxymethyl group and the hydroxy group at C3 made the chelation easier.

4 Summary

Section 2.11 deals with the Pd^{II}N₂ complexes of the hexuloses which were characterized for the first time. With [Pd₂(tmen)₂(α-D-Tagp1,2;3,4H₋₄-κO^{1,2}:κO^{3,4})] · 8 H₂O (**39**), the first Pd^{II}N₂-complex of a ketopyranose was obtained. The complete investigation of the hexuloses revealed the reasons for the favored and unfavored coordination modes and extended the knowledge of carbohydrates' metalation with Pd^{II}N₂-fragments.

In the literature, less is known about the class of dialdoses. Therefore, *xylo*-, *galacto*- and *D-manno*-dialdose were prepared and investigated and, additionally, a crystal structure of [Pd₂(tmen)₂(Ery4ald/H₋₄-κO^{1,4}:κO^{2,3})] · 12 H₂O (**40**) was obtained. To sum up the results of Section 2.12, the second aldehyde function of a dialdose in aqueous solution always formed an aldehyde hydrate either with a water molecule or by intramolecular ring formation as with *xylo*- and *D-manno*-dialdose. The general rules of palladium(II) metalation were confirmed by the investigation of the three available dialdoses, additionally the participation of both of the most acidic, anomeric hydroxy groups to the chelate rings seemed to be a prerequisite for dimetalation.

The last part of this work deals with the investigation of fructose-containing di- and trisaccharides, β-(1→4)-glycosidic- and α-(1→4)-glycosidic-linked disaccharides in Pd-tmen. Transferring the results to general rules, (1) a preference for the participation of the most acidic, anomeric hydroxy group to the chelate rings was realized. (2) κO^{1,2}-diolato chelation was preferred to κO^{1,3}-diolato chelation and *cis*-vicinal diolato chelation was preferred to *trans*-diequatorial diolato chelation. (3) The reducing units of the disaccharides reacted in the same way as the corresponding hex(ul)oses, the non-reducing units of the di- and trisaccharides reacted in the same way as the corresponding methyl hex(ul)osides. (4) Therefore, the shift patterns and CIS values of the monomeric model compounds were used for the assignment of the oligomeric metalated species. Within the investigated α-(1→4)-glycosidic linked di- and oligosaccharides the formulated rules did not completely explain the detected metalation pattern. In agreement with the *D*-turanose's and *D*-melibiose's results another rule can be postulated: (5) starting with κO^{1,2}-diolato chelation of the most acidic, anomeric hydroxy group, each unit of a disaccharides had to be metalated first before dimetalation occurred.

Finally, investigations of the maltose-derived oligosaccharides and the cyclodextrins revealed the wide influence of intramolecular hydrogen bonds to the metalation. Four crystal structures **42–45** were obtained from conversions of the cyclodextrins with Pd-tmen and Pd-teen.

4 Summary

Independent of the stoichiometry, only half the cyclodextrins' $\kappa O^{2,3}$ -diolato sites were alternatingly metalated in all experiments. Again, the strong intramolecular hydrogen bonds between an unmetalated $\kappa O^{2,3}$ -diolato site to the adjacent glucopyranoside unit's metalated $\kappa O^{2,3}$ -diolato sites impaired complete deprotonation.

The conclusion is that, despite the numerous hydroxy functions which are provided by the carbohydrates, rules control the coordination of metal probes as the $Pd^{II}N_2$ fragments to the various carbohydrates. The introduction of new palladium(II) fragments allowed the investigation of highly-reactive compounds as the dialdoses and revealed the influence of the hydrogen bonds to the metalation. The investigation of di- and trisaccharides in metalating agents was intensified and regularities were elucidated.

5 Experimental Section

5.1 Methods and materials

Reagent grade chemicals were purchased from Aldrich, Fluka, Merck, Omicron or TCI and were used as supplied. The synthesis of $[\text{Pd}^{\text{II}}\text{N}_2(\text{OH})_2]$ and $[\text{Pd}^{\text{II}}\text{N}_2(\text{OD})_2]$ was carried out under an atmosphere of nitrogen using standard Schlenk techniques. All $\text{Pd}^{\text{II}}\text{N}_2/\text{carbohydrate}$ complexes were prepared under air atmosphere and ice-bath cooling. For NMR investigation, the carbohydrates were dissolved in stoichiometric proportions, e.g. 2:1 (Pd-tmen: carbohydrate) or 4:1:3 (Pd-en:polyol: HNO_3) in 1 mL of the palladium-containing solvent and were stirred minimum 2 hours up to 24 hours at 4 °C. To obtain the yellow crystals in a good quality, crystallization was interrupted typically at a yield of 25%. The elemental analyses were collected on an Elementar Vario EL Apparatur.

5.2 Reagents and solvents

(1 <i>R</i> ,2 <i>R</i>)-cyclohexane-1,2-diamine	≥ 98.0% (Fluka)
1,10-phenanthroline monohydrate	≥ 99.0% (Fluka)
1,2- <i>O</i> -isopropylidene- α -D-glucofuranose	≥ 98.5% (Fluka)
2,2'-bipyridine	≥ 98% (Fluka)
2,2-dimethoxypropane	≥ 99.0% (Acros)
α -cyclodextrin	98% (Wacker)
γ -cyclodextrin	98% (Wacker)
acetic acid conc.	99.8% (Riedel-de Haën)
acetone	≥ 99.5% (Fluka)
allitol	– (Omicron Biochemicals)
amylose	– (Merck)
anhydroerythritol	97% (Aldrich)
catalase (Bovine)	2950 u/mg solid (Sigma RBI)
cellulose	synthesis
chloroform	p.a. ≥ 99.8% (Fluka)
D-altritol	– (TCI Europe)
D-arabinose	> 99.0% (Fluka)
D-arabitol	≥ 99% (Fluka)

5 Experimental Section

D-cellobiose	> 99.0% (Fluka)
D- <i>chiro</i> -inositol	98% (New Zealand Pharmaceuticals)
D-erythrose	synthesis
deuterium oxide (D ₂ O)	99.90% (Eurisotop)
D-fructose	> 99.0% (Fluka)
D-galactose	≥ 99.0% (Fluka)
D-glucose monohydrate	≥ 99.5% (Fluka)
dichlormethane	p.a. (Fluka)
diethyl ether	≥ 99.8% (Fluka)
D-lactose	reinst (Grüssing)
D-lactulose	> 98.0% (Fluka)
D-leucrose	≥ 98.0% (Fluka)
D-lyxose	99% (ABCR)
D-maltoheptaose	95.0% (Fluka)
D-maltose	≥ 99.0% (Fluka)
D-maltotriose	– (Senn Chemicals)
D-maltulose	≥ 98.0% (Sigma Aldrich)
D-mannitol	≥ 99.5% (Fluka)
D-mannose	≥ 99% (Fluka)
D-melecitose	> 99.0% (Fluka)
D-melibiose	> 98.0% (Merck)
DMF	p.a. (Fluka)
Dowex 1x2 16-100	– (Supelco)
D-palatinose	– (Südzucker)
D-psicose	> 98.0% (TCI Europe)
D-raffinose	> 99.0% (Fluka)
D-ribose	99% (Acros)
D-sorbitol	≥ 99.5% (Fluka)
D-sucrose	≥ 99.5% (Fluka)
D-tagatose	96% (ABCR)
D-threitol	≥ 98.0% (Fluka)
D-threose	– (Omicron)
α,α-D-trehalose	> 99.0% (Fluka)
D-turanose	≥ 98.0% (Sigma Aldrich)

5 Experimental Section

dulcitol	≥ 99% (Fluka)
D-xylose	> 98.0% (Fluka)
erythritol	≥ 99% (Fluka)
ethane-1,2-diamine	99% (Grüssing)
ethanol	≥ 99.8% (Fluka)
ethyl acetate	p.a. (Fluka)
ethyleneglycol	≥ 99.5% (Fluka)
formaldehyde	37% (Acros)
formic acid aq.	p.a. (Fluka)
galactose oxidase (<i>Dactylium dendroides</i>)	6,710 u /g solid (Sigma)
glycerine anhydrous	≥ 99.5% (Fluka)
hydrochloric acid conc.	37% (Biesterfeld Graën)
Ion Exchange Resin III (OH ⁻)	– (Merck)
Levogulosan = 1,6-Anhydro-β-D-glucopyranose	> 99% (Glycon)
L-gulose	> 99.0% (TCI Europe)
L-iditol	– (Senn Chemicals)
L-sorbose	≥ 98% (Fluka)
L-threitol	≥ 98.5% (Fluka)
methanol	≥ 99.9% (Biesterfeld Graën)
methyl α-D-fructofuranoside	synthesis
methyl α-D-galactopyranoside	≥ 98% (Fluka)
methyl α-D-glucopyranoside	≥ 99% (Fluka)
methyl α-D-lyxopyranoside	synthesis
methyl α-D-mannopyranoside	≥ 98% (Fluka)
methyl β-D-arabinopyranoside	synthesis
methyl β-D-fructofuranoside	synthesis
methyl β-D-fructopyranoside	synthesis
methyl β-D-galactopyranoside	≥ 98% (Fluka)
methyl β-D-glucopyranoside	≥ 99% (Fluka)
methyl β-D-ribofuranoside	synthesis
methyl β-D-ribopyranoside	> 99% (Glycon)
methyl β-D-xylopyranoside	≥ 99% (TCI Europe)
<i>myo</i> -inositol	≥ 98% (Fluka)
<i>N,N'</i> -dimethylethane-1,2-diamine	≥ 98.0% (Fluka)

5 Experimental Section

<i>N,N,N',N'</i> -tetraethylethane-1,2-diamine	≥ 99.0% (Acros)
<i>N,N,N',N'</i> -tetramethylethane-1,2-diamine	≥ 99.5% (Sigma Aldrich)
<i>neo</i> -inositol	synthesis
nitric acid	p.a. (Fluka)
palladium(II)chloride , purum	60% Pd (Fluka, AppliChem)
petrolether	p.a. (Fluka)
potassium chloride	p.a. (Fluka)
potassium hydroxide	p.a. (Merck)
propane-1,3-diamine	99.0% (Aldrich)
p-toluenesulfonic acid	p.a. (Fluka)
ribitol	> 99.0% (Fluka)
<i>scyllo</i> -inositol	synthesis
silver(I)oxide	> 99.0% (Merck)
sodium hydrogen carbonate	p.a. (Fluka)
sodium hydroxide	≥ 98% (Fluka)
sodium periodate	99.0% (Acros)
sodium thiosulfate	p.a. (Fluka)
sulphuric acid	p.a. (Fluka)
toluene	p.a. (Fluka)
triethylamine	99% (Riedel-de Haën)
trifluoroacetic acid	p.a. (Fluka)
water deionized	house installation with ion exchange resin
xylitol	≥ 99% (Fluka)

5.3 NMR spectroscopy

NMR spectra were recorded at room temperature on a Jeol Eclipse 400 spectrometer (^1H : 400 MHz, $^{13}\text{C}\{^1\text{H}\}$: 101 MHz) or a Jeol Eclipse spectrometer 500 (^1H : 500.16 MHz, $^{13}\text{C}\{^1\text{H}\}$: 125.77 MHz). The signals of the deuterated solvent ($^{13}\text{C}\{^1\text{H}\}$) and the residual protons therein (^1H) were used as an internal secondary reference for the chemical shift.

When D_2O was used as a solvent, one drop of methanol was added to the sample tube (5 mm) in order to obtain a reference signal ($\delta = 49.5$ ppm) in the $^{13}\text{C}\{^1\text{H}\}$ NMR spectra.

When necessary, the ^1H and $^{13}\text{C}\{^1\text{H}\}$ NMR signals were assigned by means of ^1H - ^1H -COSY or ^1H - ^1H -DFQ-COSY, DEPT135, ^1H - ^{13}C -HMQC and ^1H - ^{13}C -HMBC experiments in

5 Experimental Section

solutions of $[\text{Pd}^{\text{II}}\text{N}_2(\text{OD})_2]$ (0.45 M) in D_2O . DQF-COSY differs from simple COSY in that the former suppresses the detection of singlets (these often intense signals obscure nearby signals and do not supply useful coupling information) and provides better resolution of crosspeaks near the diagonal, and is thus usually preferred over COSY. Shift differences are given as $\delta(\text{C}_{\text{complex}}) - \delta(\text{C}_{\text{free polyol}})$. The values for the free sugars are determined for the respective sugar in its neutral aqueous solution, and were referenced to 49.5 ppm for the ^{13}C NMR signal of methanol.

5.4 Crystal structure determination and refinement

Crystals suitable for X-ray crystallography were selected with the aid of a polarization microscope (Leica MZ6 with polarization filters), covered with liquid paraffin, mounted on the tip of a glass fiber and investigated at 200 K on a Nonius Kappa CCD diffractometer or a Oxford XCalibur 3 diffractometer with graphite-monochromated $\text{Mo K}\alpha$ radiation ($\lambda = 0.71073 \text{ \AA}$). The structures were solved by direct methods (SHELXS-97^[116] or SIR97^[117]) and refined by full-matrix, least-squares calculations on F^2 (SHELXL-97^[116]). Anisotropic displacement parameters were refined for all non-hydrogen atoms. The refined structures were analyzed with PLATON^[118] and visualized with ORTEP-3^[119] and SCHAKAL^[120]. Further details on the structures are listed in the Appendix, Tables 6.41–6.55. The values given there are defined as follows:

$$R(F) = \frac{\sum ||F_o| - |F_c||}{\sum |F_o|} \quad (5.1)$$

$$R_{\text{int}} = \frac{\sum |F_o^2 - \langle F_o \rangle^2|}{\sum F_o^2} \quad (5.2)$$

$$R_w(F^2) = \sqrt{\frac{\sum w(F_o^2 - F_c^2)^2}{\sum w(F_o^2)^2}} \quad (5.3)$$

$$S = \sqrt{\frac{\sum w(F_o^2 - F_c^2)^2}{N_{\text{hkl}} - N_{\text{parameter}}}} \quad (5.4)$$

The weighting factors w and P are defined as follows:

$$w = \frac{1}{\sigma^2(F_o^2) + (xP)^2 + yP} \quad \text{with} \quad P = \frac{\max(F_o^2, 0) + 2F_c^2}{3} \quad (5.5)$$

5 Experimental Section

In analogy to SHELXL-97, the values of the parameters x and y were adopted minimize the variance of $w(F_c^2/F_o^2)$ for several (intensity-ordered) groups of reflexes.

The coefficient U_{eq} is defined as:

$$U_{\text{eq}} = \frac{1}{3} \sum_{i=1}^3 \sum_{j=1}^3 U_{ij} a_i a_j a_i^* a_j^* \quad (5.6)$$

5.4 Preparation of palladium(II) compounds

5.4.1 [Pd(en)Cl₂]

To a suspension of PdCl₂ (5.00 g, 28.2 mmol) in water (25 mL) was added HCl (5.00 mL, 37%), and the mixture was stirred for 10 min until a brown solution was formed. Under stirring, a pink precipitate of [Pd(en)₂][PdCl₄] formed on the dropwise addition of ethane-1,2-diamine (6.04 g, 100.50 mmol) in water (15 mL). After heating to 45 °C, the addition of ethane-1,2-diamine solution was continued until the precipitate redissolved to give a pale yellow solution. The solution was filtered and acidified with HCl (semi-conc.) to precipitate [Pd(en)Cl₂]. After the suspension was cooled to about 4 °C for a few hours, the yellow complex was filtered through a G4 filter, washed with cold water (5 × 20 mL) and dried in vacuo. Further product was collected by concentrating the filtrate. The yield was 6.54 g (96%). Anal. Calcd for C₂H₈Cl₂N₂Pd: C, 10.12; H, 3.40; N, 11.80; Cl, 29.86. Found: C, 10.16; H, 3.36; N, 11.77; Cl, 29.83.

5.4.2 [Pd(en)(OH)₂] (0.45 M)

[Pd(en)Cl₂] (2.67 g, 11.25 mmol), Ag₂O (2.80 g, 12.08 mmol) and water (25 mL) were stirred under nitrogen with exclusion of light at 40 °C. After 15 min AgCl was removed by filtration through a G4 filter under nitrogen atmosphere, leaving a yellow solution. For the preparation of [Pd(en)(OD)₂], D₂O was used. The alkaline [Pd(en)(OH)₂] solution (pH 12 for 0.45 M) was kept under a nitrogen atmosphere at 4 °C to prevent absorption of carbon dioxide. The exact concentration of the solution was determined by ICP with a Varian-Vista simultaneous spectrometer. ¹³C {¹H} NMR (100.63 MHz, D₂O): δ 46.4 (2C, CH₂).

5 Experimental Section

5.4.3 [Pd(*R,R*-chxn)Cl₂]

To a suspension of PdCl₂ (5.00 g, 28.2 mmol) in water (50 mL) at 45 °C potassium chloride (4.20 g, 56.3 mmol) was added, and the mixture was stirred for 10 min until a brown solution of K₂[PdCl₄] was formed. (1*R*,2*R*)-cyclohexane-1,2-diamine (3.22 g, 28.2 mmol) dissolved in water (95 mL) and HCl (5 mL, 37%) was slowly added. After the reaction mixture was stirred for 1 h at 45 °C, the pH was raised by a solution of NaOH (2 M) to 7.0, and the yellow complex precipitated from the solution. The reaction mixture was stirred for other 3 h at 45 °C, (during the first hour, the pH value was repeatedly adjusted). After the suspension was cooled to room temperature, the yellow complex was filtered through a G4 filter, washed with cold water (5 × 20 mL) and dried in vacuo. The yield was 7.7 g (93%). Anal. Calcd for C₆H₁₄Cl₂N₂Pd: C, 24.72; H, 4.84; N, 9.61; Cl, 24.32. Found: C, 24.70; H, 4.73; N, 9.58; Cl, 24.35. ¹³C{¹H} NMR (100.63 MHz, DMSO-d₆): δ 23.7 (2C, γ-CH₂), 32.2 (2C, β-CH₂), 61.0 (2C, α-CH₂).

5.4.4 [Pd(*R,R*-chxn)(OH)₂] (0.45 M)

[Pd(*R,R*-chxn)Cl₂] (3.28 g, 11.25 mmol), Ag₂O (2.80 g, 12.08 mmol) and water (25 mL) were stirred under nitrogen with exclusion of light at 40 °C. After 2 h AgCl was removed by filtration through a G4 filter under nitrogen atmosphere, leaving a yellow solution. Solutions of higher or lower concentration were prepared by varying the amount of water. The alkaline [Pd(*R,R*-chxn)(OH)₂] solution (pH 12 for 0.45 M) was kept under a nitrogen atmosphere at 4 °C to prevent absorption of carbon dioxide. The exact concentration of the solution was determined by ICP with a Varian-Vista simultaneous spectrometer. ¹³C{¹H} NMR (100.63 MHz, D₂O): δ 24.3 (2C, γ-CH₂), 33.7 (2C, β-CH₂), 60.9 (2C, α-CH₂).

5.4.5 *N,N,N',N'*-tetramethyl-(1*R*,2*R*)-cyclohexane-1,2-diamine (tmchxn)

According to literature,^[47] *N,N,N',N'*-tetramethyl-(1*R*,2*R*)-cyclohexane-1,2-diamine (tmchxn) was prepared from (1*R*,2*R*)-cyclohexane-1,2-diamine with use of the Eschweiler-Clark methylation of amines as follows: (1*R*,2*R*)-cyclohexane-1,2-diamine (8.00 g, 0.07 mol) was cooled to 0 °C. Following the dropwise addition of 50 mL of 88% aqueous formic acid, 75 mL of 37% aqueous formaldehyde were added. Gradual heating to 60 °C initiates rapid gas evolution. The reaction was allowed to proceed without further heating until gas evolution subsided and was then heated to 80 °C for 24 h. The reaction mixture was cooled, acidified

5 Experimental Section

with 20% aqueous HCl, and extracted three times with 100-mL portions of ether. The aqueous layer was stirred in an ice bath and brought to pH 12 by the dropwise addition of 40% aqueous NaOH without allowing the internal temperature to exceed 25 °C. Following the separation of the resulting amine/ aqueous layers, the aqueous layer was further extracted three times with 100-mL portions of ether. These combined organic layers were dried over KOH pellets by stirring. Distillation in vacuo provided tmchxn, the yield was 5.72 g (48%). ^1H NMR (400 MHz, CDCl_3): δ 1.11 (m, 4H, CH_2), 1.74 (m, 2H, CH_2), 1.84 (m, 2H, CH_2), 2.27 (s, 12H, CH_3), 2.38 (m, 2H, CH). $^{13}\text{C}\{^1\text{H}\}$ NMR (100 MHz, CDCl_3): δ 21.7, 24.5, 38.9 (broadened signal), 62.7.

5.4.6 [$\text{Pd}(\text{tmchxn})\text{Cl}_2$]

KCl (4.20 g, 56.3 mmol) was added to a suspension of PdCl_2 (5.00 g, 28.2 mmol) in water (50 mL) at room temperature, and the mixture was stirred for 10 min until a brown solution of $\text{K}_2[\text{PdCl}_4]$ was formed. *N,N,N',N'*-tetramethyl-(1*R*,2*R*)-cyclohexane-1,2-diamine (4.80 g, 28.2 mmol) dissolved in water (95 mL) and HCl (5 mL, 37%) was slowly added. After the reaction mixture was stirred for 15 minutes, the pH was raised by a solution of NaOH (1 M) to 6.5, and the dark green complex precipitated from the solution. The reaction mixture was stirred for other 1.5 h at room temperature, (during the first hour, the pH value was repeatedly adjusted). After the suspension was cooled to room temperature the green complex was filtered through a G4 filter, washed with cold water (5×20 mL) and dried in vacuo. The yield was 7.45 g (76%). Anal. Calcd for $\text{C}_{10}\text{H}_{22}\text{Cl}_2\text{N}_2\text{Pd}$: C, 34.55; H, 6.38; N, 8.06; Cl, 20.40. Found: C, 33.63; H, 5.79; N, 7.87.

5.4.7 [$\text{Pd}(\text{tmchxn})(\text{OH})_2$] (0.45 M)

$[\text{Pd}(\text{tmchxn})\text{Cl}_2]$ (3.91 g, 11.25 mmol), Ag_2O (2.90 g, 12.51 mmol) and water (25 mL) were stirred under nitrogen with exclusion of light at 40 °C. After 1 h AgCl was removed by filtration through a G4 filter under nitrogen atmosphere, leaving a yellow solution. The alkaline $[\text{Pd}(\text{tmchxn})(\text{OH})_2]$ solution (pH 12 for 0.45 M) was kept under a nitrogen atmosphere at 4 °C to prevent absorption of carbon dioxide. $^{13}\text{C}\{^1\text{H}\}$ NMR (100.63 MHz, D_2O): δ 23.8 (2C, $\gamma\text{-CH}_2$), 24.6 (2C, $\beta\text{-CH}_2$), 42.9 (2C, CH_3), 48.7 (2C, CH_3), 71.5 (2C, $\alpha\text{-CH}_2$).

5 Experimental Section

5.4.8 [Pd(dmen)Cl₂]

To a suspension of PdCl₂ (5.00 g, 28.2 mmol) in water (170 mL), HCl (5.00 mL, 37%) was added, and the mixture was stirred for 10 min until a brown solution was formed. Under stirring, *N,N'*-dimethylethane-1,2-diamine (6.0 g, 67.96 mmol) in water (180 mL) was added dropwise to give a pale yellow solution. The solution was filtered and acidified with HCl (semi-conc.) to precipitate [Pd(dmen)Cl₂]. After stirring for 30 min, the yellow complex was filtered through a G4 filter, washed with cold water and dried in vacuo. The yield was 4.68 g (63%). Anal. Calcd for C₄H₁₂Cl₂N₂Pd: C, 18.10; H, 4.56; N, 10.55; Cl, 26.71. Found: C, 17.93; H, 4.40; N, 10.47; Cl, 26.09.

5.4.9 [Pd(dmen)(OH)₂] (0.45 M)

[Pd(dmen)Cl₂] (1.79 g, 6.74 mmol), Ag₂O (1.56 g, 6.73 mmol) and water (15 mL) were stirred under nitrogen with exclusion of light at 40 °C. After 30 min AgCl was removed by filtration through a G4 filter under nitrogen atmosphere, leaving a yellow solution. The alkaline [Pd(dmen)(OH)₂] solution was kept under a nitrogen atmosphere at 4 °C to prevent absorption of carbon dioxide. ¹³C{¹H} NMR (100.63 MHz, D₂O): δ 38.4 (syn), 38.8 (anti) (2C, CH₃), 53.5 (syn), 54.4 (anti) (2C, CH₂).

5.4.10 [Pd(tmen)Cl₂]

HCl (5.00 mL, 37%) was added to a suspension of PdCl₂ (5.00 g, 28.2 mmol) in water (85 mL), and the mixture was stirred for 10 min until a brown solution was formed. Under stirring, on the dropwise addition of *N,N,N',N'*-tetramethylethane-1,2-diamine (6.04 g, 52.00 mmol) in water (15 mL) a yellow precipitate formed. After stirring for 30 min, the yellow complex was filtered through a G4 filter, washed with cold water and dried in vacuo. The yield was 7.68 g (93%). Anal. Calcd for C₆H₁₆Cl₂N₂Pd: C, 24.55; H, 5.49; N, 9.54; Cl, 24.16. Found: C, 24.37; H, 5.36; N, 9.50; Cl, 24.12.

5.4.11 [Pd(tmen)(OH)₂] (0.45 M)

[Pd(tmen)Cl₂] (3.30 g, 11.24 mmol), Ag₂O (2.80 g, 12.08 mmol) and water (25 mL) were stirred under nitrogen with exclusion of light at 40 °C. After 30 min AgCl was removed by filtration through a G4 filter under nitrogen atmosphere, leaving a yellow solution. For the preparation of [Pd(tmen)(OD)₂] D₂O was used. The alkaline [Pd(tmen)(OH)₂] solution was

5 Experimental Section

kept under a nitrogen atmosphere at 4 °C to prevent absorption of carbon dioxide. $^{13}\text{C}\{^1\text{H}\}$ NMR (100.63 MHz, D_2O): δ 50.2 (4C, CH_3), 62.1 (2C, CH_2).

5.4.12 [Pd(teen)Cl₂]

HCl (5.00 mL, 37%) was added to a suspension of PdCl₂ (5.00 g, 28.2 mmol) in water (85 mL), and the mixture was stirred for 10 min until a brown solution was formed. Under stirring, on the dropwise addition of *N,N,N',N'*-tetraethylethane-1,2-diamine (9.6 g, 55.71 mmol) in water (90 mL) a yellow precipitate formed. After stirring for 15 min, the pH value of the solution was set to 6.5 with NaOH (2M). After another 15 min the yellow complex was filtered through a G4 filter, washed with cold water and dried in vacuo. The yield was 9.62 g (97%). Anal. Calcd for C₁₀H₂₄Cl₂N₂Pd: C, 34.35; H, 6.92; N, 8.01; Cl, 20.28. Found: C, 34.19; H, 6.84; N, 7.95; Cl, 20.37.

5.4.13 [Pd(teen)(OH)₂] (0.45 M)

[Pd(teen)Cl₂] (2.67 g, 11.25 mmol), Ag₂O (2.80 g, 12.08 mmol) and water (25 mL) were stirred under nitrogen with exclusion of light at 40 °C. After 15 min AgCl was removed by filtration through a G4 filter under nitrogen atmosphere, leaving a yellow solution. For the preparation of [Pd(teen)(OD)₂] D₂O was used. The alkaline [Pd(teen)(OH)₂] solution was kept under a nitrogen atmosphere at 4 °C to prevent absorption of carbon dioxide. $^{13}\text{C}\{^1\text{H}\}$ NMR (100.63 MHz, D_2O): δ 11.0 (4C, CH_3), 52.6 (2C, $\text{NCH}_2\text{CH}_2\text{N}$), 53.6 (4C, CH_2CH_3).

5.4.14 [Pd(tn)Cl₂]

HCl (5.00 mL, 37%) was added to a suspension of PdCl₂ (5.00 g, 28.2 mmol) in water (85 mL), and the mixture was stirred for 10 min until a brown solution was formed. Under stirring, on the dropwise addition of propane-1,3-diamine (4.19 g, 56.50 mmol) in water (90 mL) a yellow precipitate formed. After 15 min the yellow complex was filtered through a G4 filter, washed with cold water and dried in vacuo. The yield was 3.32 g (47%). Anal. Calcd for C₃H₁₀Cl₂N₂Pd: C, 14.33; H, 4.01; N, 11.14; Cl, 28.20. Found: C, 14.15; H, 4.04; N, 11.03; Cl, 28.01.

5 Experimental Section

5.4.15 [Pd(tn)(OH)₂] (0.45 M)

[Pd(tn)Cl₂] (0.57 g, 2.25 mmol), Ag₂O (0.54 g, 2.33 mmol) and water (5 mL) were stirred under nitrogen with exclusion of light at room temperature. After 60 min AgCl was removed by filtration through a G4 filter under nitrogen atmosphere, leaving a yellow solution. The alkaline [Pd(tn)(OH)₂] solution was kept under a nitrogen atmosphere at 4 °C to prevent absorption of carbon dioxide. ¹³C{¹H} NMR (100.63 MHz, D₂O): δ 28.3 (1C, CH₂CH₂CH₂), 41.5 (2C, CH₂NH₂).

5.4.16 [Pd(bpy)Cl₂]

HCl (2.50 mL, 37%) was added to a suspension of PdCl₂ (2.50 g, 14.1 mmol) in water (85 mL), and the mixture was stirred for 10 min until a brown solution was formed. Under stirring, on the dropwise addition of 2,2'-bipyridine (2.19 g, 14.02 mmol) in water (190 mL) and acetone (60 mL) a pale yellow precipitate formed. After stirring for 15 min, the pH value of the solution was set to 6.5 with NaOH (2M). After 15 min the yellow complex was filtered through a G4 filter, washed with cold water and dried in vacuo. The yield was 4.29 g (92%). Anal. Calcd for C₁₀H₈Cl₂N₂Pd: C, 36.01; H, 2.42; N, 8.40; Cl, 21.26. Found: C, 35.93; H, 2.49; N, 8.45; Cl, 19.21.

5.4.17 [Pd(bpy)(OH)₂] (0.45 M)

[Pd(bpy)Cl₂] (2.27 g, 6.81 mmol), Ag₂O (1.56 g, 6.73 mmol) and water (15 mL) were stirred under nitrogen with exclusion of light at 40 °C. After 20 min AgCl was removed by filtration through a syringe filter, leaving a yellow solution. The alkaline [Pd(bpy)(OH)₂] solution was kept under a nitrogen atmosphere at 4 °C to prevent absorption of carbon dioxide. ¹³C{¹H} NMR (100.63 MHz, D₂O): δ 123.0 (2C, C4/C4'), 127.3 (2C, C6/C6'), 140.8 (2C, C5/C5'), 148.0 (2C, C3/C3'), 154.2 (2C, C1/C1').

5.4.18 [Pd(phen)Cl₂]

HCl (2.50 mL, 37%) was added to a suspension of PdCl₂ (2.50 g, 14.1 mmol) in water (85 mL), and the mixture was stirred for 10 min until a brown solution was formed. Under stirring, on the dropwise addition of 1,10-phenanthroline (2.78 g, 14.02 mmol) in water (190 mL) and acetone (50 mL) a yellow precipitate formed. After stirring for 15 min, the pH value of the solution was set to 6.5 with NaOH (2M). After 15 min the yellow complex was

5 Experimental Section

filtered through a G4 filter, washed with cold water and dried in vacuo. The yield was 4.88 g (98%). Anal. Calcd. for $C_{12}H_8Cl_2N_2Pd$: C, 40.31; H, 2.26; N, 7.84; Cl, 19.83. Found: C, 40.51; H, 2.25; N, 7.87; Cl, 19.62.

5.4.19 [Pd(phen)(OH)₂] (0.45 M)

[Pd(phen)Cl₂] (2.43 g, 6.81 mmol), Ag₂O (1.56 g, 6.73 mmol) and water (15 mL) were stirred under nitrogen with exclusion of light at 40 °C. After 20 min AgCl was removed by filtration through a syringe filter, leaving a yellow solution. The alkaline [Pd(phen)(OH)₂] solution was kept under a nitrogen atmosphere at 4 °C to prevent absorption of carbon dioxide. ¹³C{¹H} NMR (100.63 MHz, D₂O): δ 125.5 (2C, C3/C8), 126.4 (2C, C5/C6), 128.0 (2C, C41/C61), 138.3 (2C, C4/C7), 142.6 (2C, C101/C102), 147.9 (2C, C2/C3).

5.5 Preparation of carbohydrates

5.5.1 Methyl α-D-lyxopyranoside

Following literature,^[121] methyl α-D-lyxopyranoside was synthesized from D-lyxose by Fischer glycosylation. To a solution of D-lyxose (1.50 g, 10.0 mmol) in methanol (25 mL) H₂SO₄ (0.15 mL, conc.) was added. The mixture was stirred for one week; the addition of ion exchange resin III (2.5 g, OH⁻ form) terminated the reaction. The solution was filtered and then evaporated to dryness in a rotary evaporator. The solid was recrystallized from ethyl acetate to obtain methyl α-D-lyxopyranoside. The yield was 1.46 g (89%). For ¹³C NMR shifts, see Table 6.3 in the Appendix.

5.5.2 Methyl D-fructosides

According to literature,^[81] a mixture of methyl β-D-fructopyranoside, methyl α-D-fructofuranoside and methyl β-D-fructofuranoside was synthesized from D-fructose by Fischer anomerization and separated by ion exchange resin chromatography. To a solution of D-fructose (10.00 g, 58.3 mmol) in methanol (250 mL) was added H₂SO₄ (0.9 mL, conc.). The mixture was stirred for two days; the addition of ion exchange resin III (20 g, OH⁻ form) terminated the reaction. The solution was filtered and then evaporated to dryness in a rotary evaporator. To remove remaining D-fructose, the resulting syrup was dissolved in water (100 mL) and NaBH₄ (0.50 g, 13.2 mmol) was added to the stirring solution. After 6–8 h,

5 Experimental Section

acetic acid (6 mL, 2 M) was added and the solution was evaporated to dryness in a rotary evaporator. The product was then dissolved repeatedly in methanol and evaporated to dryness.

The obtained mixture of methyl D-fructopyranosides was separated by ion exchange resin chromatography with Dowex 1x2 16-100 mesh, for details see ^[81]. The various fractions were analyzed by the amount of rotation. Fractions with no rotation didn't contain a methyl D-fructopyranoside. The compounds appear in the following order: first β -D-fructopyranoside (yield 3.85 g, 34%), then methyl β -D-fructofuranoside (yield 3.06 g, 27%) and finally, methyl α -D-fructofuranoside (yield 1.58 g, 14%). For ¹³C NMR shifts, see Tables 6.12–6.14 in the Appendix.

5.5.3 *xylo*-Pentodialdose

According to literature,^[122] 1,2-*O*-isopropylidene- α -D-glucofuranose (4.40 g, 20.0 mmol) and sodium hydrogen carbonate (1.00 g) were dissolved in water (30 mL), after which sodium periodate (4.72 g) was added portionwise. After 20 min, sodium thiosulfate (0.1 g) was added until the solution was no longer oxidative (starch–iodide test). The solution was then filtered and extracted five times with chloroform (5 x 30 mL). The combined organic layers were dried over anhydrous sodium sulfate and evaporated to dryness at 50 °C in a rotary evaporator to yield 1,2-*O*-isopropylidene- α -D-*xylo*-dialdo-furanose. ¹³C{¹H} NMR (100.63 MHz, D₂O): δ 25.2 (1C, CH₃), 25.7 (1C, CH₃), 73.6 (1C, C3), 82.8 (1C, C4), 84.6 (1C, C2), 88.1 (1C, C5_{hydrate}), 104.7 (1C, C1), 112.8 (1C, C_q).

Trifluoroacetic acid solution (100 mL, 20% v/v) was added, and the solution was heated at 80 °C and stirred for 1 h and then evaporated to dryness in a rotary evaporator at 50 °C. Water (25 mL) was added, and subsequently evaporated to dryness at 50 °C. The dry residue was rinsed with 95% ethanol. Another 25 mL of water were added, and the solution was again evaporated to dryness at 50 °C in a rotary evaporator. The yield was 0.91 g (31%). For ¹³C NMR shifts, see Table 2.86.

5.5.4 *galacto*-Hexodialdose

According to literature,^[92] D-galactose (0.9 g, 5.00 mmol) was dissolved in phosphate buffer (0.01 M, pH 7.3) in a 1 L-round-bottom flask. Under stirring, galactose oxidase (150 mg, 6.710 U/g solid) and catalase (62 mg, 2950 U/mg solid) were added and the flask was sealed with a septum. Oxygen was applied for 5 min and this was repeated 24h later. The mixture

5 Experimental Section

was stirred for 5 days at room temperature; afterwards the enzymes were filtered off with a 0.45 μ membrane filter. The solution was evaporated to dryness with a freeze dryer. The yield was 0.39 g (44%). For ^{13}C NMR shifts, see Table 2.90.

5.5.5 D-manno-Hexodialdose

According to literature,^[94-95] to a solution of D-*chiro*-inositol (20g, 111.1 mmol) in DMF (110 mL), acetone (120 mL, 1.67 mol) and 2,2-dimethoxypropane (100 mL, 0.78 mol) *p*-toluenesulfonic acid (2.00 g) was added. The mixture was stirred overnight at 60 °C, then neutralized with triethylamine and concentrated. The resulting syrup was dissolved in CH_2Cl_2 , washed with water several times and dried over MgSO_4 . The solution was evaporated to dryness in a rotary evaporator and crystallized from petrolether to yield 1,2;3,4;5,6-tri-*O*-isopropylidene-D-*chiro*-inositol (5.2 g, 16%). $^{13}\text{C}\{^1\text{H}\}$ NMR (100.63 MHz, CDCl_3): δ 24.6 (2C, CH_3), 27.1 (2C, CH_3), 27.3 (2C, CH_3), 76.5 (2C, inositol), 78.2 (2C, inositol), 79.5 (2C, inositol), 110.8 (2C, C_q), 113.6 (2C, C_q).

1,2;3,4;5,6-tri-*O*-isopropylidene-D-*chiro*-inositol (10.0 g, 33.3 mmol) was dissolved in acetic acid (100 mL, conc.) and stirred for 20 h at 70–80 °C. The solution was evaporated to dryness in a rotary evaporator, toluene (50 mL) was added twice and evaporated to dryness and finally, CH_2Cl_2 was added. After filtration, the solution was evaporated to dryness in a rotary evaporator and the residue was recrystallized from toluene to yield 1,2;5,6-di-*O*-isopropylidene-D-*chiro*-inositol (2.6 g, 30%). $^{13}\text{C}\{^1\text{H}\}$ NMR (100.63 MHz, CDCl_3): δ 25.2 (2C, CH_3), 27.7 (2C, CH_3), 72.5 (2C, inositol), 76.4 (2C, inositol), 78.8 (2C, inositol), 109.8 (2C, C_q).

According to literature,^[96] aqueous sodium periodate (2.6 g in 10 mL water) was heated to 75 °C and stirred over a period of 20 min. Silica (10 g) was added to the stirred solution. The mixture was then cooled and shaken vigorously for 20 min to give a coarse powder. CH_2Cl_2 (55 mL) was added and to this stirred mixture a solution of 1,2;5,6-di-*O*-isopropylidene-D-*chiro*-inositol (2.0 g) in CH_2Cl_2 (55 mL) was added. The reaction mixture was stirred at room temperature for 80 min, then filtered and washed with CH_2Cl_2 . The combined supernatant was concentrated in vacuo. The solid was crystallized from ethyl acetate to give 2,3;4,5-di-*O*-isopropylidene-D-*manno*-hexodialdose (1.1 g, 43%). The crystal structure is depicted in Fig.2.94. $^{13}\text{C}\{^1\text{H}\}$ NMR (100.63 MHz, CDCl_3): δ 25.1 (2C, CH_3), 26.6 (2C, CH_3), 76.8 (2C, C3/C4), 80.5 (2C, C2/C5), 111.6 (2C, C_q), 201.9 (2C, C1/C6).

5 Experimental Section

2,3;4,5-di-*O*-isopropylidene-*D*-manno-hexodialdose was dissolved in trifluoroacetic acid solution (50 mL, 20% v/v) which was heated at 80 °C and stirred for 1 h and then evaporated to dryness in a rotary evaporator at 50 °C. Water (25 mL) was added, and subsequently evaporated to dryness at 50 °C. The dry residue was rinsed with 95% ethanol. Another 25 mL of water were added, and the solution was again evaporated to dryness at 50 °C in a rotary evaporator to yield *D*-manno-hexodialdose (0.43 g, 57%). For ¹³C NMR shifts, see Table 2.94.

5.6 Preparation of the crystalline compounds

5.6.1 Dihydroxido-*N,N,N',N'*-tetramethylethane-1,2-diamine-palladium(II) dihydrate

Pd-tmen (0.45 M) was prepared according to preparation 5.4.11. 5 ml of DMF were added to 5 ml of the Pd-tmen solution, then the volume was reduced in vacuo to 6 ml and filtered. Yellow crystals were obtained within 1 week at 5 °C. To obtain crystals of good quality, crystallization was interrupted at a typical yield of 30%.

5.6.2 η^2 -Carbonato-*N,N,N',N'*-tetramethyl-(1*R*,2*R*)-cyclohexane-1,2-diamine-palladium(II) hexahydrate

Pd-tmchxn (0.45 M) was prepared according to preparation 5.4.7. Solutions of Pd-tmchxn tended to absorb CO₂ from air. Crystals of the compound grew within a few days at 5 °C. To obtain crystals of good quality, crystallization was interrupted at a typical yield of 30%.

5.6.3 *N,N,N',N'*-tetraethylethane-1,2-diammonium tetrachloridopalladate(II)

2.50 g (14.10 mmol) palladium(II) chloride were dissolved in 85 ml water and 2.5 ml hydrochloric acid (37%). Under stirring, a solution of 4.80 g (27.86 mmol) *N,N,N',N'*-tetraethylethane-1,2-diamine, 190 ml water and 50 ml acetone was added dropwise. The yellow precipitate was filtered off, hydrochloric acid (37%) was added to the remaining brown solution up to pH 1. Brown crystals were obtained within 1 hour at room temperature at a yield of 87%.

5.6.4 Dichlorido-*N,N,N',N'*-tetraethylethane-1,2-diamine-palladium(II) dihydrate

2.50 g (14.10 mmol) palladium(II) chloride were dissolved in 85 ml water and 2.5 ml hydrochloric acid (37%). Under stirring, a solution of 4.80 g (27.86 mmol) *N,N,N',N'*-

5 Experimental Section

tetraethylethane-1,2-diamine, 190 ml water and 50 ml acetone was added dropwise. The yellow precipitate was filtered off, 2 M NaOH was added to the remaining brown solution up to pH 6.5. The solution was stored at 5 °C. Yellow crystals were obtained within one day at 5 °C at a yield of 97%.

5.6.5 2,2'-Bipyridine-dihydroxido-palladium(II) pentahydrate

Pd-bpy (0.45 M) was prepared according to preparation 5.4.17. Yellow crystals were obtained within two weeks at 5 °C, crystallization was interrupted at a typical yield of 30%.

5.6.6 Dihydroxido-1,10-phenanthroline-palladium(II) pentahydrate

Pd-phen (0.45 M) was prepared according to preparation 5.4.19. Yellow crystals were obtained within one day at 5 °C at a yield of 95%.

5.6.7 Ethanediolato- $\kappa O^{1,2}$ -1,10-phenanthroline-palladium(II) heptahydrate

According to literature,^[54] crystals of (6) (0.22 g) were dissolved in 50 mL water containing 0.1 g NaOH and adding drop wise ethane-1,2-diol (0.2 g). Crystals (84% yield) formed in a few minutes and were collected and washed carefully with ice-cold distilled water.

5.6.8 Anhydroerythritolato- $\kappa O^{2,3}$ -1,10-phenanthroline-palladium(II) 4.5-hydrate

According to literature,^[54] crystals of (6) (0.22 g) were dissolved in 50 mL water containing 0.1 g NaOH and adding drop wise anhydroerythritol (0.2 g). Crystals (79% yield) formed in a few minutes and were collected and washed carefully with ice-cold distilled water.

5.6.9 Bis(*N,N'*-dimethylethane-1,2-diamine)(erythritolato- $\kappa O^{1,2}:\kappa O^{3,4}$)dipalladium(II) 14-hydrate

Erythritol (0.027 g, 0.22 mmol) was dissolved in Pd-dmen (1 ml, 0.45 M, 0.45 mmol), and stirred for 2 h at 4 °C. The solution was saturated with acetone; subsequently, acetone vapors were allowed to diffuse into the solution. Pale yellow crystals were formed within one week at 5 °C. To obtain crystals of good quality, crystallization was interrupted at a typical yield of 30%.

5.6.10 Dipropane-1,3-diamine(erythritolato- $\kappa O^{1,2}:\kappa O^{3,4}$)dipalladium(II) 10-hydrate

Erythritol (0.018 g, 0.15 mmol) was dissolved in Pd-tn (1 ml, 0.3 M, 0.30 mmol), and stirred for 2 h at 4 °C. The solution was saturated with acetone; subsequently, acetone vapors were allowed to diffuse into the solution. Pale yellow crystals were formed within two weeks at 5 °C. To obtain crystals of good quality, crystallization was interrupted at a typical yield of 30%.

5.6.11 Bis(*N,N,N',N'*-tetramethylethane-1,2-diamine)(mannitolato- $\kappa O^{1,2}:\kappa O^{3,4}$)-dipalladium(II) 9-hydrate

D-Mannitol (0.041 g, 0.225 mmol) was dissolved in Pd-tmen (1 ml, 0.45 M, 0.45 mmol), and stirred for 2 h at 4 °C. The solution was saturated with acetone; subsequently, acetone vapors were allowed to diffuse into the solution. Pale yellow crystals were formed within one week at 5 °C. To obtain crystals of good quality, crystallization was interrupted at a typical yield of 30%.

5.6.12 Dipropane-1,3-diamine(mannitolato- $\kappa O^{1,2}:\kappa O^{3,4}$)dipalladium(II) 5-hydrate

D-Mannitol (0.027 g, 0.15 mmol) was dissolved in Pd-tn (1 ml, 0.3 M, 0.30 mmol), and stirred for 2 h at 4 °C. The solution was saturated with acetone; subsequently, acetone vapors were allowed to diffuse into the solution. Pale yellow crystals were formed within two weeks at 5 °C. To obtain crystals of good quality, crystallization was interrupted at a typical yield of 30%.

5.6.13 Bis(*N,N'*-dimethylethane-1,2-diamine)(dulcitolato- $\kappa O^{2,3}:\kappa O^{4,5}$)dipalladium(II) 8-hydrate

Dulcitol (0.041 g, 0.225 mmol) was dissolved in Pd-dmen (1 ml, 0.45 M, 0.45 mmol), and stirred for 2 h at 4 °C. The solution was saturated with acetone; subsequently, acetone vapors were allowed to diffuse into the solution. Pale yellow crystals were formed within one week at 5 °C. To obtain crystals of good quality, crystallization was interrupted at a typical yield of 30%.

5 Experimental Section

5.6.14 Dipropane-1,3-diamine(dulcitolato- $\kappa O^{2,3}:\kappa O^{4,5}$)dipalladium(II) 6-hydrate

Dulcitol (0.027 g, 0.15 mmol) was dissolved in Pd-tn (1 ml, 0.3 M, 0.30 mmol), and stirred for 2 h at 4 °C. The solution was saturated with acetone; subsequently, acetone vapors were allowed to diffuse into the solution. Pale yellow crystals were formed within two weeks at 5 °C. To obtain crystals of good quality, crystallization was interrupted at a typical yield of 30%.

5.6.15 Bis(*N,N,N',N'*-tetramethylethane-1,2-diamine)(D-altritolato- $\kappa O^{2,3}:\kappa O^{4,5}$)-dipalladium(II) 9-hydrate

D-Altritol (0.02 g, 0.113 mmol) was dissolved in Pd-tmen (1 ml, 0.45 M, 0.45 mmol), and stirred for 2 h at 4 °C. The solution was saturated with acetone; subsequently, acetone vapors were allowed to diffuse into the solution. Pale yellow crystals were formed within one day at 5 °C. To obtain crystals of good quality, crystallization was interrupted at a typical yield of 30%.

5.6.16 Diethane-1,2-diamine(allitolato- $\kappa O^{2,3}:\kappa O^{4,5}$)dipalladium(II) 14-hydrate

Allitol (0.0284 g, 0.156 mmol) was dissolved in Pd-en (1 ml, 0.467 M, 0.467 mmol), and stirred for 2 h at 4 °C. The solution was saturated with acetone; subsequently, acetone vapors were allowed to diffuse into the solution. Pale yellow crystals were formed within one week at 5 °C. To obtain crystals of good quality, crystallization was interrupted at a typical yield of 30%.

5.6.17 Bis(*N,N,N',N'*-tetramethylethane-1,2-diamine)(allitolato- $\kappa O^{1,2}:\kappa O^{5,6}$)-dipalladium(II) 8-hydrate

Allitol (0.041 g, 0.225 mmol) was dissolved in Pd-tmen (1 ml, 0.45 M, 0.45 mmol), and stirred for 2 h at 4 °C. The solution was saturated with acetone; subsequently, acetone vapors were allowed to diffuse into the solution. Pale yellow crystals were formed within one week at 5 °C. To obtain crystals of good quality, crystallization was interrupted at a typical yield of 30%.

5.6.18 $[(\text{Pd}^{\text{II}}\text{N}_2)_n(\mu_2\text{-OH})_n]^{n+}$ -derived bridged compounds at pH 7–8

The respective polyol was dissolved in a aqueous solution of $[\text{Pd}(\text{R,R-chxn})(\text{OH})_2]$ (1 ml, 0.5 M, 0.5 mmol; exact concentration was determined by ICP) and HNO_3 (2 M) in stoichiometric proportions. After stirring for 2 h at 4 °C, the solution was stored at 4 °C. Yellow crystals were formed within one week up to six month. To obtain crystals of good quality, crystallization was interrupted at a typical yield of 30%.

Compounds **18–24** were obtained with the stoichiometry 4:1:3 (Pd-chxn:polyol: HNO_3) with the respective polyol, the same as compound **25**, which was found as a side product, for example with *scyllo*-inositol.

5.6.19 $[\text{Pd}_4(\text{R,R-chxn})_4(\text{C}_3\text{O}_6)(\mu\text{-OH})](\text{NO}_3)_3 \cdot 8 \text{H}_2\text{O}$

To 1 mL of a solution of D-threose (0.28 M) in water, a solution of $[(\text{R,R-chxn})\text{Pd}(\text{OD})_2]$ (4 mL, 0.285 M) and HNO_3 (0.42 mL, 2 M) were added under cooling and stirred for 2 h. The yellow solution was stored at 4 °C and eventually precipitating palladium metal was filtered off. Few brown crystals of **26** were obtained within four weeks.

5.6.20 Diethane-1,2-diamine(D-*chiro*-inositolato- $\kappa\text{O}^{1,2}:\kappa\text{O}^{5,6}$)dipalladium(II) 8-hydrate

D-*chiro*-Inositol (0.0405 g, 0.225 mmol) was dissolved in Pd-en (1 ml, 0.45 M, 0.45 mmol), and stirred for 2 h at 4 °C. The solution was saturated with acetone; subsequently, acetone vapors were allowed to diffuse into the solution. Pale yellow crystals were formed within one week at 5 °C. To obtain crystals of good quality, crystallization was interrupted at a typical yield of 30%.

5.6.21 Bis(N,N,N',N'-tetramethylethane-1,2-diamine)(*neo*-inositolato- $\kappa\text{O}^{1,6}:\kappa\text{O}^{3,4}$)dipalladium(II) 22-hydrate

neo-Inositol (0.0405 g, 0.225 mmol) was dissolved in Pd-tmen (1 ml, 0.45 M, 0.45 mmol), and stirred for 2 h at 4 °C. The solution was saturated with acetone; subsequently, acetone vapors were allowed to diffuse into the solution. Pale yellow crystals were formed within one week at 5 °C. To obtain crystals of good quality, crystallization was interrupted at a typical yield of 30%.

5.6.22 Tris(*N,N,N',N'*-tetramethylethane-1,2-diamine)(*scyllo*-inositolato- $\kappa O^{1,2}:\kappa O^{3,4}:\kappa O^{5,6}$)tripalladium(II) 23-hydrate

scyllo-Inositol (0.0270 g, 0.15 mmol) was dissolved in Pd-tmen (1 ml, 0.45 M, 0.45 mmol), and stirred for 2 h at 4 °C. The solution was saturated with acetone; subsequently, acetone vapors were allowed to diffuse into the solution. Pale yellow crystals were formed within one week at 5 °C. To obtain crystals of good quality, crystallization was interrupted at a typical yield of 30%.

5.6.23 (1*R*,2*R*)-Cyclohexane-1,2-diamine(methyl α -D-lyxopyranos-2,3-O-diato- $\kappa O^{2,3}$)-palladium(II) 2.25-hydrate

Me- α -D-Lyxopyranoside (213.0 mg, 0.13 mmol) was dissolved in [Pd(*R,R*-chxn)(OH)₂] (1 ml, 0.26 M, 0.26 mmol), and stirred for 2 h at 4 °C. The solution was saturated with acetone; subsequently, acetone vapors were allowed to diffuse into the solution. Pale yellow crystals were formed within 1 day at 5 °C. To obtain crystals of good quality, crystallization was interrupted at a typical yield of 30%.

5.6.24 *N,N,N',N'*-Tetramethylethane-1,2-diamine(methyl β -D-xylopyranos-2,3-O-diato- $\kappa O^{2,3}$)palladium(II)-*N,N,N',N'*-tetramethylethane-1,2-diamine(methyl β -D-xylopyranos-3,4-O-diato- $\kappa O^{3,4}$)palladium(II) dihydrate

Me- β -D-Xylopyranoside (44.0 mg, 0.225 mmol) was dissolved in [Pd(tmen)(OH)₂] (1 ml, 0.45 M, 0.45 mmol), and stirred for 2 h at 4 °C. The solution was saturated with acetone; subsequently, acetone vapors were allowed to diffuse into the solution. Pale yellow crystals were formed within 4 month at 5 °C.

5.6.25 Bis(*N,N,N',N'*-tetramethylethane-1,2-diamine)(β -D-arabinopyranos-1,2;3,4-O-diato- $\kappa O^{1,2}:\kappa O^{3,4}$)dipalladium(II) 10-hydrate

D-Arabinose (34.0 mg, 0.225 mmol) was dissolved in [Pd(tmen)(OH)₂] (1 ml, 0.45 M, 0.45 mol), and stirred for 2 h at 4 °C. The solution was saturated with acetone; subsequently, acetone vapours were allowed to diffuse into the solution. Pale yellow crystals were formed within 2 weeks at 5 °C. To obtain crystals of good quality, crystallization was interrupted at a typical yield of 30%.

5.6.26 Bis(*N,N,N',N'*-tetramethylethane-1,2-diamine)(β -D-lyxopyranos-1,2;3,4-O-diato- $\kappa O^{1,2}:\kappa O^{3,4}$)palladium(II) 10-hydrate

D-Lyxose (34.0 mg, 0.225 mmol) was dissolved in [Pd(tmen)(OH)₂] (1 ml, 0.45 M, 0.45 mmol), and stirred for 2 h at 4 °C. The solution was saturated with acetone; subsequently, acetone vapours were allowed to diffuse into the solution. Pale yellow crystals were formed within 2 weeks at 5 °C. To obtain crystals of good quality, crystallization was interrupted at a typical yield of 30%.

5.6.27 *N,N,N',N'*-Tetramethylethane-1,2-diamine(methyl α -D-galactopyranos-3,4-O-diato- $\kappa O^{3,4}$)palladium(II) 8-hydrate

Me- α -D-Galactopyranoside (44.0 mg, 0.225 mmol) was dissolved in [Pd(tmen)(OH)₂] (1 ml, 0.45 M, 0.45 mmol), and stirred for 2 h at 4 °C. The solution was saturated with acetone; subsequently, acetone vapours were allowed to diffuse into the solution. Pale yellow crystals were formed within 2 weeks at 5 °C. To obtain crystals of good quality, crystallization was interrupted at a typical yield of 30%.

5.6.28 *N,N'*-Dimethylethane-1,2-diamine(methyl α -D-galactopyranos-3,4-O-diato- $\kappa O^{3,4}$)palladium(II) 9-hydrate

Me- α -D-Galactopyranoside (44.0 mg, 0.225 mmol) was dissolved in [Pd(dmen)(OH)₂] (1 ml, 0.45 M, 0.45 mmol), and stirred for 2 h at 4 °C. The solution was saturated with acetone; subsequently, acetone vapours were allowed to diffuse into the solution. Pale yellow crystals were formed within 2 weeks at 5 °C. To obtain crystals of good quality, crystallization was interrupted at a typical yield of 30%.

5.6.29 *N,N,N',N'*-Tetramethylethane-1,2-diamine(methyl α -D-mannopyranos-2,3-O-diato- $\kappa O^{2,3}$)palladium(II) 3.5-hydrate

Me- α -D-Galactopyranoside (44.0 mg, 0.225 mmol) was dissolved in [Pd(tmen)(OH)₂] (1 ml, 0.45 M, 0.45 mmol), and stirred for 2 h at 4 °C. The solution was saturated with acetone; subsequently, acetone vapours were allowed to diffuse into the solution. Pale yellow crystals were formed within 2 weeks at 5 °C. To obtain crystals of good quality, crystallization was interrupted at a typical yield of 30%.

5.6.30 (1*R*,2*R*)-Cyclohexane-1,2-diamine(methyl α -D-fructofuranos-1,3-O-diato- $\kappa O^{1,3}$) palladium(II) 2-hydrate

Me- α -D-Fructofuranoside (44.0 mg, 0.225 mmol) was dissolved in [Pd(*R,R*-chxn)(OH)₂] (1 ml, 0.45 M, 0.45 mmol), and stirred for 2 h at 4 °C. The solution was saturated with acetone; subsequently, acetone vapours were allowed to diffuse into the solution. Pale colorless crystals were formed within 2 week at 5 °C. To obtain crystals of good quality, crystallization was interrupted at a typical yield of 30%.

5.6.31 Bis(*N,N,N',N'*-tetramethylethane-1,2-diamine)(α -D-tagatopyranos-1,2;3,4-O-diato- $\kappa O^{1,2}:\kappa O^{3,4}$)dipalladium(II) 8-hydrate

D-Tagatose (40.5 mg, 0.225 mmol) was dissolved in [Pd(tmen)(OH)₂] (1 ml, 0.45 M, 0.45 mmol), and stirred for 2 h at 4 °C. The solution was saturated with acetone; subsequently, acetone vapours were allowed to diffuse into the solution. Few yellow crystals were formed within 2 days at 5 °C.

5.6.32 Bis(*N,N,N',N'*-tetramethylethane-1,2-diamine)(*erythro*-tetrodialdofuranos1,4;2,3-O-diato- $\kappa O^{1,4}:\kappa O^{2,3}$)dipalladium(II) 8-hydrate

D-*manno*-hexodialdose (44.1 mg, 0.225 mmol) which was obviously impured with *erythro*-tetrodialdose was dissolved in [Pd(tmen)(OH)₂] (1 ml, 0.45 M, 0.45 mmol), and stirred for 2 h at 4 °C. The solution was saturated with acetone; subsequently, acetone vapours were allowed to diffuse into the solution. Few yellow crystals were formed within 2 days at 5 °C.

5.6.33 [Pd₃(teen)₃(α -CDH₋₆)] · 34 H₂O

α -Cyclodextrin (146.0 mg, 0.15 mmol) was dissolved in [Pd(teen)(OH)₂] (1 ml, 0.45 M, 0.45 mmol), and stirred for 2 h at 4 °C. The solution was saturated with acetone; subsequently, acetone vapours were allowed to diffuse into the solution. Yellow crystals were formed within 2 days at 5 °C. To obtain crystals of good quality, crystallization was interrupted at a typical yield of 30%.

5 Experimental Section

5.6.34 [Pd₃(tmen)₃(α -CDH-6)] · 20.7 H₂O · acetone

α -Cyclodextrin (146.0 mg, 0.15 mmol) was dissolved in [Pd(tmen)(OH)₂] (1 ml, 0.45 M, 0.45 mmol), and stirred for 2 h at 4 °C. The solution was saturated with acetone; subsequently, acetone vapours were allowed to diffuse into the solution. Yellow crystals were formed within 2 days at 5 °C. To obtain crystals of good quality, crystallization was interrupted at a typical yield of 30%.

5.6.35 [Pd₄(teen)₄(γ -CDH-8)] · 12 H₂O

γ -Cyclodextrin (73.0 mg, 0.056 mmol) was dissolved in [Pd(teen)(OH)₂] (1 ml, 0.45 M, 0.45 mmol), and stirred for 2 h at 4 °C. The solution was saturated with acetone; subsequently, acetone vapours were allowed to diffuse into the solution. Yellow crystals were formed within 1 week at 5 °C. To obtain crystals of good quality, crystallization was interrupted at a typical yield of 30%.

5.6.36 [Pd₄(tmen)₄(γ -CDH-8)] · 65.79 H₂O · 0.96 [Pd(tmen)CO₃]

γ -Cyclodextrin (73.0 mg, 0.056 mmol) was dissolved in [Pd(tmen)(OH)₂] (1 ml, 0.45 M, 0.45 mmol), and stirred for 2 h at 4 °C. The solution was saturated with acetone; subsequently, acetone vapours were allowed to diffuse into the solution. Yellow crystals were formed within 1 week at 5 °C. To obtain crystals of good quality, crystallization was interrupted at a typical yield of 30%.

5 Experimental Section

5.7 ^1H NMR chemical shifts of the methyl pentosides and hex(ul)osides, the pentoses, the hex(ul)oses and the dialdosés

Table 5.1. ^1H NMR chemical shifts of methyl pentopyranoside ligands with Pd-tmen.

	H-1	H-2	H-3	H-4	H-5	H-5'	CH_3
Me- β -D-Arap3,4H ₂	4.77 (d)	4.39 (dd)	2.99 (dd)	3.72 (m)	3.66 (m)	3.49 (m)	3.32 (s)
Me- α -D-Lyxp2,3H ₂	4.73 (d)	3.16 (m)	3.06 (m)	3.93-4.00 (m)	3.68 (dd)	3.31 (dd)	3.29 (s)
Me- α -D-Lyxp3,4H ₂	4.32 (d)	3.72 (dd)	- -	- -	- -	- -	- -
Me- β -D-Ribp2,3H ₂	4.97 (d)	3.34 (m)	3.26 (m)	- -	- -	- -	3.42 (s)
Me- β -D-Ribp3,4H ₂	4.70 (d)	3.45 (m)	3.45 (m)	3.53 (m)	4.16 (dd)	3.79 (dd)	3.42 (s)
Me- β -D-Ribp2,4H ₂	4.76 (d)	2.75 (m)	3.77 (m)	2.79 (ddd)	3.83 (dd)	3.68 (dd)	3.40 (s)
Me- β -D-Xylp2,3H ₂	4.05 (d)	2.89 (dd)	3.14 (dd)	3.37 (ddd)	3.62 (dd)	2.92 (dd)	3.34 (s)
Me- β -D-Xylp3,4H ₂	3.97 (d)	3.02 (dd)	3.16 (m)	3.25 (ddd)	3.63 (dd)	3.07 (m)	3.38 (s)
Me- β -D-Xylp2,4H ₂	4.53 (d)	3.13 -	2.46 (m)	2.44 (m)	3.94 (dd)	- -	3.29 (s)

Table 5.2. ^1H NMR chemical shifts of D-arabinose ligands with Pd-tmen.

	H-1	H-2	H-3	H-4	H-5	H-5'
α -D-Arap1,2H ₂	4.12 (d)	3.18 (dd)	3.44 (dd)	3.58 (m)	- -	- -
β -D-Arap1,2H ₂	4.70 (d)	3.28 (dd)	4.30 (dd)	3.99 (m)	3.82 (m)	3.46 (dd)
α -D-Arap3,4H ₂	4.60 (d)	3.94 (m)	3.35 (m)	3.51 (m)	- -	- -
β -D-Arap1,2;3,4H ₄	4.24 (d)	3.28 (dd)	3.44 (m)	3.15 (m)	4.18 (m)	3.56 (m)
α -D-Araf1,3H ₂	4.51 (d)	3.46 (m)	3.07 (m)	4.56 (m)	- -	- -
β -D-Araf1,2H ₂	4.94 (d)	3.50 (m)	4.37 (m)	3.86-3.80 (m)	3.86-3.80 (m)	3.86-3.80 (m)

5 Experimental Section

Table 5.3. ^1H NMR chemical shifts of D-ribose ligands with Pd-tmen.

	H-1	H-2	H-3	H-4	H-5	H-5'
α -D-Ribp1,2H ₋₂	4.18 (d)	3.80 (m)	3.56 (m)	3.66 (m)	3.90 (dd)	3.42 (dd)
β -D-Ribp1,2;3,4H ₋₄	4.72 (d)	- -	3.87 (m)	- -	4.54 (m)	- -
α -D-Ribf1,2H ₋₂	4.93 (d)	3.54 (dd)	3.68 (m)	4.77 (m)	3.87 (dd)	3.67 (dd)
α -D-Ribf2,3H ₋₂	5.13 (d)	- -	- -	- -	- -	- -
β -D-Ribf2,3H ₋₂	5.16 (d)	- -	- -	- -	- -	- -

Table 5.4. ^1H NMR chemical shifts of D-ribose ligands with Pd-teen.

	H-1	H-2	H-3	H-4	H-5	H-5'
α -D-Ribp1,2H ₋₂	4.11 (d)	3.79 (m)	3.55 (m)	3.63 (m)	3.86 (dd)	3.38 (dd)
α -D-Ribp3,4H ₋₂	4.83 (d)	3.44 (m)	3.95 (m)	3.13 (m)	- -	- -
α -D-Ribf1,2H ₋₂	4.88 (d)	3.51 (dd)	3.63 (m)	4.75 (ddd)	3.84 (dd)	3.63 (dd)
α -D-Ribf2,3H ₋₂	5.10 (d)	3.67 (m)	3.24 (dd)	4.80 (m)	3.83 (m)	3.57 (m)
β -D-Ribf2,3H ₋₂	5.19 (d)	- -	- -	- -	- -	- -

5 Experimental Section

Table 5.5. ¹H NMR chemical shifts of D-lyxose ligands with Pd-tmen.

	H-1	H-2	H-3	H-4	H-5	H-5'
α -D-Lyxp1,2H ₋₂	4.45 (d)	3.19 (dd)	- -	- -	- -	- -
α -D-Lyxp2,3H ₋₂	5.31 (d)	3.09 (m)	3.34 (m)	3.83–3.76 (m)	- -	- -
β -D-Lyxp1,2H ₋₂	4.19 (d)	3.75 (dd)	3.33 (m)	3.87 (m)	- -	- -
β -D-Lyxp1,2;3,4H ₋₄	3.98 (d)	3.85 (dd)	3.13 (dd)	3.81–3.73 (m)	3.68 (dd)	2.90 (m)
α -D-Lyxf2,3H ₋₂	5.76 (d)	3.46 (m)	3.98 (m)	- -	- -	- -
β -D-Lyxf1,2H ₋₂	4.75 (d)	- -	- -	- -	- -	- -

Table 5.6. ¹H NMR chemical shifts of D-lyxose ligands with Pd-teen.

	H-1	H-2	H-3	H-4	H-5	H-5'
α -D-Lyxp1,2H ₋₂	4.53 (d)	3.24 (d)	3.89 (m)	3.44 (m)	- -	- -
α -D-Lyxp2,3H ₋₂	5.42	2.97 (m)	3.49 (m)	3.87–3.83 (m)	3.87–3.83 (m)	3.54 (dd)
β -D-Lyxp1,2H ₋₂	4.27 (d)	3.72 (dd)	3.37 (dd)	3.83–3.78 (m)	3.83–3.78 (m)	3.02 (dd)
α -D-Lyxf2,3H ₋₂	6.01 (d)	3.39 (m)	4.00 (m)	- -	- -	- -
β -D-Lyxf1,2H ₋₂	4.71 (d)	3.64–3.58 (m)	3.99–3.96 (m)	3.70–3.68 (m)	- -	- -

Table 5.7. ¹H NMR chemical shifts of D-xylose ligands with Pd-tmen.

	H-1	H-2	H-3	H-4	H-5	H-5'
α -D-Xy1p1,2H ₋₂	4.60 (d)	3.20 (dd)	4.14 (m)	3.45 (m)	3.75 (dd)	3.66 (dd)
β -D-Xy1p1,2H ₋₂	4.29 (d)	3.00 (dd)	3.24 (m)	3.42–3.35 (m)	3.13 (m)	- -
α -D-Xy1f1,2H ₋₂	4.96 (d)	3.56 (m)	4.10 (m)	5.16 (ddd)	3.79 (dd)	3.66 (dd)

5 Experimental Section

Table 5.8. ^1H NMR chemical shifts of D-xylose ligands with Pd-teen.

	H-1	H-2	H-3	H-4	H-5	H-5'
α -D-Xylp1,2H ₋₂	4.74 (d)	3.12–3.08 (m)	4.25 (m)	3.50–3.46 (m)	3.84 (dd)	3.73 (dd)
β -D-Xylp1,2H ₋₂	4.34 (d)	3.15 (dd)	3.27 (d)	3.43 (ddd)	-	-
α -D-Xylp1,2;3,4H ₋₄	4.84 (d)	-	-	-	-	-
β -D-Xylp1,2;3,4H ₋₄	4.15 (d)	3.06 (dd)	3.20 (dd)	3.20–3.13 (m)	3.55 (dd)	3.10 (dd)
α -D-Xylf1,2H ₋₂	4.98 (d)	3.57 (dd)	4.13 (m)	5.26 (ddd)	3.89 (dd)	3.76 (dd)
α -D-Xylf1,2;3,5H ₋₄	4.94 (d)	3.42 (dd)	4.88 (dd)	4.62 (ddd)	-	-

Table 5.9. ^1H NMR chemical shifts of methyl hexopyranoside ligands with Pd-tmen.

	H-1	H-2	H-3	H-4	H-5	H-6	H-6'	CH ₃
Me- α -D-Galp2,3H ₋₂	4.64 (d)	3.57 (dd)	3.51 (dd)	3.80 (d)	(m)	3.69–3.59 (m)	(m)	-
Me- α -D-Galp3,4H ₋₂	4.80 -	4.64 (dd)	2.93 (dd)	3.80 (d)	(m)	3.69–3.59 (m)	(m)	3.30 (s)
Me- β -D-Galp2,3H ₋₂	4.10 (d)	3.29–3.28 (m)	3.74 (m)	3.41 (ddd)	-	3.75–3.62 (m)	-	3.50 (s)
Me- β -D-Galp3,4H ₋₂	4.13 (d)	4.44 (dd)	2.83 (dd)	3.74 (m)	3.50 (ddd)	3.71 (dd)	3.64 (dd)	3.51 (s)
Me- α -D-Glcp2,3H ₋₂	4.59 (d)	3.23 (dd)	3.49 (dd)	3.22 (dd)	3.31 (ddd)	3.77 (dd)	3.60 (dd)	3.28 (s)
Me- α -D-Glcp3,4H ₋₂	4.51 (d)	3.37 (dd)	3.44 (dd)	2.95 (dd)	3.51 (ddd)	3.75 (dd)	3.68 (dd)	3.29 (s)
Me- β -D-Glcp2,3H ₋₂	4.15 (d)	2.98 (dd)	3.28 (dd)	3.16–3.14 (m)	(m)	3.82 (dd)	3.58 (dd)	3.42 (s)
Me- β -D-Glcp3,4H ₋₂	4.09 (d)	3.08 (dd)	3.36 (dd)	3.03 (dd)	3.30 (ddd)	3.79 (dd)	3.51 (dd)	3.46 (s)
Me- α -D-Manp2,3H ₋₂	4.45 (d)	3.62 (dd)	2.80 (dd)	4.28 (dd)	3.42 (ddd)	3.84 (dd)	3.76 (dd)	3.26 (s)

5 Experimental Section

Table 5.10. ^1H NMR chemical shifts of methyl hexulopyranoside ligands with Pd-chxn.

	H-1	H-1'	H-3	H-4	H-5	H-6	H-6'	CH_3
Me- β -D-Frup4,5H ₂	3.75 (m)	3.75 (m)	4.36 (d)	3.05 (dd)	3.75 (m)	3.64 (dd)	3.43 (dd)	3.17 (s)
Me- β -D-Frup1,3;4,5H ₄	3.09 (d)	3.05 (d)	3.78 (d)	2.81 (dd)	3.67 (m)	3.53 (dd)	3.26 (dd)	3.17 (s)
Me- β -D-Fruf1,3H ₂	3.56 –	2.83 (d)	3.55 (d)	3.78 (dd)	3.80 (m)	3.69 (dd)	3.55 (dd)	– –

Table 5.11. ^1H NMR chemical shifts of methyl hexulopyranoside ligands with Pd-tmen.

	H-1	H-1'	H-3	H-4	H-5	H-6	H-6'	CH_3
Me- β -D-Frup4,5H ₂	3.74 –	3.74 –	4.52 (d)	2.94 (dd)	3.77 –	3.59 (d)	3.45 (d)	3.17 (s)
Me- α -D-Fruf1,3H ₂	2.97 (d)	2.91 (d)	3.66 (d)	4.20 (dd)	3.80 (ddd)	3.85 (dd)	3.68 (dd)	3.29 (s)
Me- β -D-Fruf1,3H ₂	3.26 (d)	2.98 (d)	3.89 (d)	3.82–3.75 (m)	3.82–3.75 (m)	3.67 (d)	3.55 (s)	3.29 (s)

Table 5.12. ^1H NMR chemical shifts of D-galactose ligands with Pd-tmen.

	H-1	H-2	H-3	H-4	H-5	H-6	H-6'
α -D-Galp1,2H ₂	5.09 (d)	2.93 (dd)	4.85 (dd)	3.94 (m)	4.07 (m)	– –	– –
β -D-Galp1,2H ₂	4.22 (d)	3.19 (dd)	3.42 (dd)	– –	– –	– –	– –
α -D-Galp1,2;3,4H ₄	5.03 (d)	– –	– –	– –	– –	– –	– –
β -D-Galp1,2;3,4H ₄	4.07 (d)	4.22 (dd)	– –	3.54 (dd)	– –	– –	– –
α -D-Galf1,2H ₂	4.96 (d)	3.46 (dd)	4.53 (m)	3.87 (dd)	3.82 (ddd)	– –	– –
α -D-Galf1,2;5,6H ₄	4.85 (d)	3.36 (m)	4.53 (m)	3.73 (m)	3.87 (m)	3.39 (dd)	3.26 (dd)
β -D-Galf1,3;5,6H ₄	4.43 (s)	3.20 (s)	3.19 (s)	4.29 (s)	– –	3.36 (dd)	2.98 (dd)

5 Experimental Section

Table 5.13. ^1H NMR chemical shifts of D-glucose ligands with Pd-tmen.

	H-1	H-2	H-3	H-4	H-5	H-6	H-6'
$\alpha\text{-D-Glcp1,2H}_{-2}$	5.07 (d)	2.73 (dd)	4.74 (m)	3.28 (m)	3.81 (ddd)	–	–
$\beta\text{-D-Glcp1,2H}_{-2}$	4.36 (d)	3.01 (dd)	3.29 (dd)	3.16 (dd)	3.28 (m)	3.76 (dd)	3.61 (dd)
$\alpha\text{-D-Glcp1,2;3,4H}_{-4}$	4.84 (d)	–	4.80 (m)	2.83 (m)	3.82 (ddd)	–	–
$\beta\text{-D-Glcp1,2;3,4H}_{-4}$	4.18 (d)	2.99 (dd)	3.30 (m)	2.90 (m)	3.24 (ddd)	3.70 (dd)	3.50 (dd)
$\alpha\text{-D-Glcf1,2;5,6H}_{-4}$	4.95 (d)	3.61 (dd)	4.27 (dd)	5.19 (dd)	3.53 (m)	3.39 (dd)	3.32 (dd)

Table 5.14. ^1H NMR chemical shifts of D-mannose ligands with Pd-tmen.

	H-1	H-2	H-3	H-4	H-5	H-6	H-6'
$\alpha\text{-D-Manp2,3H}_{-2}$	4.91 (d)	3.65 (dd)	2.93 (dd)	4.31 (dd)	3.63 (m)	–	–
$\beta\text{-D-Manp1,2H}_{-2}$	4.22 (d)	3.89 (dd)	3.44 (dd)	3.61 (dd)	3.15 (m)	–	–
$\beta\text{-D-Manp1,2;3,4H}_{-4}$	4.04 (d)	3.92 (dd)	3.28 (dd)	3.54 (dd)	3.06 (m)	–	–

Table 5.15. ^1H NMR chemical shifts of D-fructose ligands with Pd-tmen.

	H-1	H-1'	H-3	H-4	H-5	H-6	H-6'
$\beta\text{-D-Frup2,3H}_{-2}$	3.71 (d)	3.25 (d)	3.38 (d)	4.76 (m)	(m)	3.75–3.63 (m)	(m)
$\beta\text{-D-Frup1,2;4,5H}_{-4}$	3.73 (dd)	3.03 (d)	4.02 (d)	3.02 (dd)	3.62 (m)	3.92 (m)	–
$\beta\text{-D-Frup2,3;4,5H}_{-4}$	4.10 (d)	3.36 (d)	3.46 (d)	3.59 (dd)	3.62 (m)	–	–

5 Experimental Section

Table 5.16. ^1H NMR chemical shifts of D-fructose ligands with Pd-teen.

	H-1	H-1'	H-3	H-4	H-5	H-6	H-6'
α -D-Frup4,5H ₋₂	–	–	3.66	3.95	3.20	–	–
	–	–	(d)	(m)	(ddd)	–	–
β -D-Frup2,3H ₋₂	–	3.27	2.90	4.61	3.90	3.98	3.46
	–	(d)	(m)	(dd)	(m)	(dd)	(dd)
β -D-Fruf2,3H ₋₂	3.86	3.31	3.38	4.74	3.76	3.71	3.66
	(d)	(d)	(d)	(m)	(m)	(dd)	(dd)

Table 5.17. ^1H NMR chemical shifts of D-tagatose ligands with Pd-tmen.

	H-1	H-1'	H-3	H-4	H-5	H-6	H-6'
α -D-Tagp1,2H ₋₂	3.40	3.08	3.89	3.78	–	–	–
	(d)	(d)	(d)	(dd)	–	–	–
α -D-Tagp1,2;3,4H ₋₄	3.32	2.98	4.07	2.97	4.53	–	–
	(d)	(d)	(d)	(dd)	(ddd)	–	–
α -D-Tagp1,2;4,5H ₋₄	3.37	3.06	3.90	3.50	3.44	–	–
	(d)	(d)	(d)	(m)	(m)	–	–
α -D-Tagf1,2;3,4H ₋₄	3.92	3.78	3.78	4.12	3.97	4.11	3.84
	(d)	(dd)	(d)	(m)	(ddd)	(dd)	(dd)

Table 5.18. ^1H NMR chemical shifts of L-sorbose ligands with Pd-tmen.

	H-1	H-1'	H-3	H-4	H-5	H-6	H-6'
α -L-Sorp1,2H ₋₂	3.60	2.67	2.92	–	–	–	–
	(d)	(d)	(d)	–	–	–	–
α -L-Sorp2,3H ₋₂	3.92	3.08	2.59	4.37	3.28	–	–
	(d)	(d)	(d)	(dd)	(ddd)	–	–
α -L-Sorp1,2;4,5H ₋₄	3.70	–	2.94	3.33	3.13	–	–
	(d)	–	(d)	(m)	(ddd)	–	–
α -L-Sorp2,3;4,5H ₋₄	4.08	3.25	–	4.36	3.03	3.55	3.32
	(d)	(d)	–	(dd)	(m)	(m)	(dd)
α -L-Sorf2,3H ₋₂	3.45	3.19	3.40	4.15	5.19	3.67	3.57
	(d)	(d)	(d)	(dd)	(ddd)	(dd)	(dd)
α -L-Sorf2,3;4,6H ₋₄	3.78	3.37	3.86	4.86	4.62	–	–
	(d)	(d)	(d)	(dd)	(ddd)	–	–

5 Experimental Section

Table 5.19. ^1H NMR chemical shifts of D-psicose ligands with Pd-tmen.

	H-1	H-1'	H-3	H-4	H-5	H-6	H-6'
α -D-Psif4,5H ₋₂	3.64 (d)	3.34 (d)	3.52 (dd)	4.07 (dd)	3.19 (ddd)	–	–
β -D-Psif1,2;4,5H ₋₄	3.46 (d)	3.23 (d)	4.10 (d)	3.74 (m)	4.51 (m)	3.64 (dd)	3.53 (dd)
α -D-Psif2,3H ₋₂	–	–	2.55 (d)	3.68 (dd)	5.07 (ddd)	3.93 (dd)	3.75 (dd)
α -D-Psif3,4H ₋₂	–	–	3.57 (d)	3.31 (dd)	4.97 (ddd)	3.86 (dd)	3.62 (dd)

Table 5.20. ^1H NMR chemical shifts of D-xylor-pentodialdose in D₂O.

	H-1	H-2	H-3	H-4	H-5
1 _{ax} ,5 _{eq} -Xyl5aldp	5.13 (d)	3.51 (dd)	3.63 (m)	3.19 (dd)	4.94 (d)
[1,5] _{eq} -Xyl5aldp	4.62 (d)	3.20 (dd)	3.37 (m)	3.20 (dd)	4.62 (d)

Table 5.21. ^1H NMR chemical shifts of D-xylor-pentodialdose ligands with Pd-tmen.

	H-1	H-2	H-3	H-4	H-5
1 _{ax} ,5 _{eq} -Xyl5aldp1,2H ₋₂	–	2.86 (dd)	4.60 (m)	3.16 (dd)	–
1 _{ax} ,5 _{eq} -Xyl5aldp1,2;3,5H ₋₄	4.39 –	3.03 –	2.79 –	3.58 –	7.49 –
1 _{ax} ,5 _{eq} -Xyl5aldp1,2;4,5H ₋₄	4.92 (d)	– –	4.56 (m)	– –	4.87 (d)

Table 5.22. ^1H NMR chemical shifts of D-galacto-hexodialdose in D₂O.

	H-1	H-2	H-3	H-4	H-5	H-6
α -Gal6aldp	5.25 (d)	3.81 (dd)	– –	4.11 (dd)	3.78 (m)	5.08 (d)
β -Gal6aldp	4.56 (d)	3.48 (dd)	3.62 (dd)	4.06 (dd)	3.40 (m)	5.11 (d)

5 Experimental Section

Table 5.23. ^1H NMR chemical shifts of D-*galacto*-hexodialdose ligands with Pd-tmen.

	H-1	H-2	H-3	H-4	H-5	H-6
$^1\text{C}_4$ -3,6-an- α -Gal6aldp1,2H ₋₂	4.38 (d)	3.59 (dd)	3.86 (m)	3.49 –	3.75 (m)	– –
(6 <i>R</i>)- α -Gal6aldf1,2;5,6H ₋₄	4.60 (d)	3.18 (m)	4.47 (m)	3.33 (dd)	3.72 (m)	4.42 (m)
(6 <i>S</i>)- α -Gal6aldf1,2;5,6H ₋₄	4.67 (d)	3.23 (m)	4.47 (m)	3.64 (dd)	3.23 (m)	4.42 (m)
β -Gal6aldf1,3;5,6H ₋₄	4.25 –	3.02 –	2.94 –	4.10 –	2.94 (d)	4.63 (d)

Table 5.24. ^1H NMR chemical shifts of D-*manno*-hexodialdose in D₂O.

	H-1	H-2	H-3	H-4	H-5	H-6
α -D-Man6aldp	5.15 (d)	3.86 (m)	3.78 (m)	3.69–3.67 (m)	– (m)	5.20 (d)
β -D-Man6aldp	4.84 (d)	3.87 (m)	–	3.59 (dd)	3.25 (dd)	5.17 (d)
3,6-anhydro- α -D-Man6aldf	5.15 (d)	3.95 (m)	4.70 (m)	4.70 (m)	3.95 (m)	5.15 (d)
3,6-anhydro- β -D-Man6aldf	5.32 (d)	4.12 (m)	4.66 (m)	4.54 (m)	3.92 (m)	5.35 (d)

Table 5.25. ^1H NMR chemical shifts of D-*manno*-hexodialdose ligands with Pd-tmen.

	H-1	H-2	H-3	H-4	H-5	H-6
3,6-an- β -D-Man6aldf1,2H ₋₂	5.00 (d)	3.43 (m)	4.16 (m)	4.21 (m)	3.99 (m)	5.15 (d)
β -D-Man6aldf1,2;5,6H ₋₄	4.89 (d)	3.33 (dd)	4.37 (m)	4.64 (m)	3.81 (dd)	5.64 –

5 Experimental Section

5.8 Computational methods and results

To estimate the correctness of ^{13}C NMR and species assignment, energies, ^{13}C NMR shift values and $^3J_{\text{H,H}}$ coupling constants of selected palladium(II)–glycose complexes were calculated in a simple procedure. Within the Gaussian 03 program package^[123] the BLYP DFT method was used. The 6-31+G(2d,p) basis set was applied for the geometry optimization of all atoms except palladium. A CEP-4G^[124] effective core potential with the corresponding valence basis set was used for palladium. GIAO NMR chemical shifts were calculated by the PBE1PBE method with the same basis sets used in the geometry optimization and refer to $\delta = 0$ for tetramethylsilane, calculated by the same procedure. To take solvent effects into account, the PCM method was used during NMR calculations. The use of a linear correlation was abandoned since only selected complexes were calculated instead of a series of similar compounds. The starting geometries were determined from known crystal structures or estimated in accordance with measured $^3J_{\text{H,H}}$ coupling constants. Remaining hydroxy groups were forced to build intramolecular hydrogen bonds.

Table 5.26. Observed and calculated ^{13}C NMR chemical shifts (δ/ppm) and shift differences ($\Delta\delta$) of $[\text{Pd}(\text{tmen})(^1\text{C}_4\text{-3,6-an-}\alpha\text{-Gal6aldp1,2H}_{-2}\text{-}\kappa\text{O}^{1,2})]$. Atoms are numbered as in Fig. 2.93.

	C1	C2	C3	C4	C5	C6	Chelate
$^1\text{C}_4\text{-3,6-an-}\alpha\text{-Gal6aldp1,2H}_{-2}$	105.6	83.5	83.3	83.0	72.2	102.8	$\kappa\text{O}^{1,2}$
DFT	110.3	86.8	86.7	75.8	80.1	102.9	
$\Delta\delta$	4.7	3.3	3.4	-7.2	7.9	0.1	

Table 5.27. Observed and calculated $^3J_{\text{H,H}}$ values in Hz of $[\text{Pd}(\text{tmen})(^1\text{C}_4\text{-3,6-an-}\alpha\text{-Gal6aldp1,2H}_{-2}\text{-}\kappa\text{O}^{1,2})]$.

	$^3J_{\text{H1,H2}}$	$^3J_{\text{H2,H3}}$	$^3J_{\text{H3,H4}}$	$^3J_{\text{H4,H5}}$	$^3J_{\text{H5,H6}}$	Conformation
$^1\text{C}_4\text{-3,6-an-}\alpha\text{-Gal6aldp1,2H}_{-2}$	2.5	5.4	<1	<1	<1	$^1\text{C}_4$
DFT	2.83	5.29	0.44	1.75	0.05	

Table 5.28. Observed and calculated ^{13}C NMR chemical shifts (δ/ppm) and shift differences ($\Delta\delta$) of $[\text{Pd}_2(\text{tmen})_2(\beta\text{-Gal6aldf1,3;5,6H}_{-4}\text{-}\kappa\text{O}^{1,3};\kappa\text{O}^{5,6})]$. Atoms are numbered as in Fig. 2.93.

	C1	C2	C3	C4	C5	C6	Chelate
$\beta\text{-Gal6aldf1,3;5,6H}_{-4}$	107.2	80.0	80.7	88.9	83.0	97.6	$\kappa\text{O}^{1,3};\kappa\text{O}^{5,6}$
DFT	106.5	86.7	78.9	92.2	83.9	99.5	
$\Delta\delta$	-0.7	6.7	-1.8	3.3	0.9	1.9	

5 Experimental Section

Table 5.29. Observed and calculated $^3J_{H,H}$ values in Hz of $[\text{Pd}_2(\text{tmen})_2(\beta\text{-Gal6ald}f1,3;5,6\text{H}_{-4}\text{-}\kappa\text{O}^{1,3};\kappa\text{O}^{5,6})]$.

	$^3J_{H1,H2}$	$^3J_{H2,H3}$	$^3J_{H3,H4}$	$^3J_{H4,H5}$	$^3J_{H5,H6}$	Conformation
$\beta\text{-Gal6ald}f1,3;5,6\text{H}_{-4}$	<1	<1	<1	<1	7.5	E_{C2}
DFT	0.49	1.19	0.41	2.03	5.96	

Table 5.30. Observed and calculated ^{13}C NMR chemical shifts (δ/ppm) and shift differences ($\Delta\delta$) of $[\text{Pd}_2(\text{tmen})_2(\beta\text{-D-Man6ald}f1,2;5,6\text{H}_{-4}\text{-}\kappa\text{O}^{1,2};\kappa\text{O}^{5,6})]$. Atoms are numbered as in Fig. 2.96.

	C1	C2	C3	C4	C5	C6	Chelate
$\beta\text{-D-Man6ald}f1,2;5,6\text{H}_{-4}$	109.9	83.7	80.7	81.6	75.4	105.0	$\kappa\text{O}^{1,2};\kappa\text{O}^{5,6}$
DFT	109.2	86.0	77.1	87.9	74.2	103.5	
$\Delta\delta$	-0.7	2.3	-3.6	6.3	-1.2	-1.5	

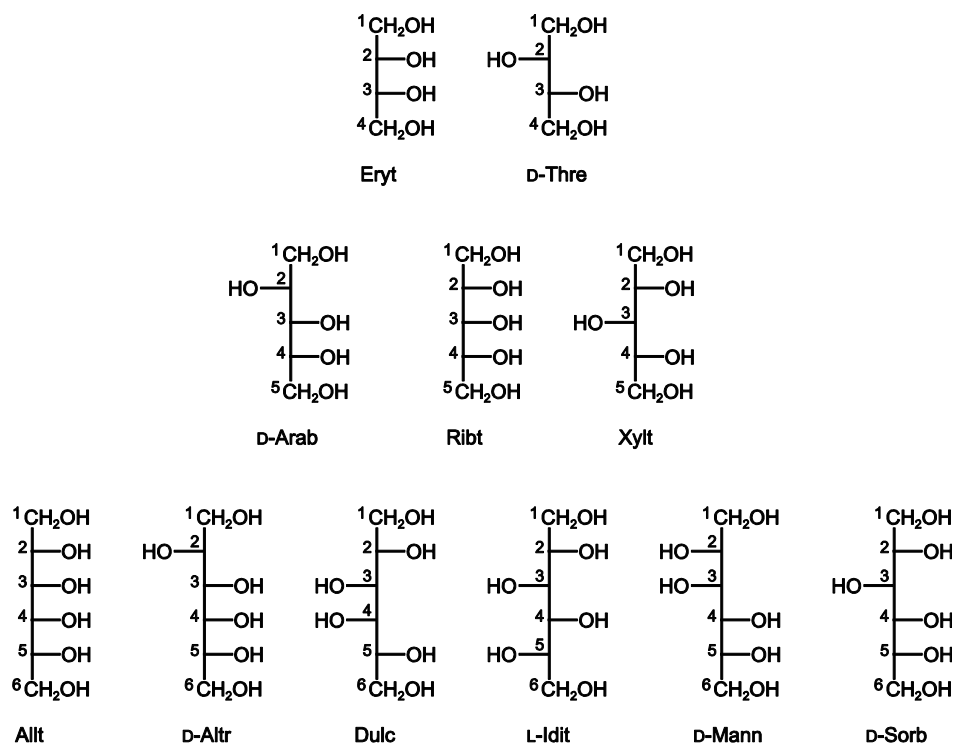
Table 5.31. Observed and calculated ^{13}C NMR chemical shifts (δ/ppm) and shift differences ($\Delta\delta$) of $[\text{Pd}_2(\text{tmen})_2(^1\text{C}_4\text{-}1_{\text{ax}},5_{\text{eq}}\text{-Xyl5ald}p1,2;3,5\text{H}_{-4}\text{-}\kappa\text{O}^{1,2};\kappa\text{O}^{3,5})]$. Atoms are numbered as in Fig. 2.90.

	C1	C2	C3	C4	C5	Chelate
$1_{\text{ax}},5_{\text{eq}}\text{-Xyl5ald}p1,2;3,5\text{H}_{-4}$	98.4	84.0	70.5	73.7	99.2	$\kappa\text{O}^{1,2};\kappa\text{O}^{3,5}$
DFT	99.8	88.0	72.6	80.9	98.8	
$\Delta\delta$	1.4	4.0	2.1	7.2	-0.4	

Table 5.32. Observed and calculated $^3J_{H,H}$ values in Hz of $[\text{Pd}_2(\text{tmen})_2(^1\text{C}_4\text{-}1_{\text{ax}},5_{\text{eq}}\text{-Xyl5ald}p1,2;3,5\text{H}_{-4}\text{-}\kappa\text{O}^{1,2};\kappa\text{O}^{3,5})]$.

	$^3J_{H1,H2}$	$^3J_{H2,H3}$	$^3J_{H3,H4}$	$^3J_{H4,H5_{\text{eq}}}$	Conformation
$1_{\text{ax}},5_{\text{eq}}\text{-Xyl5ald}p1,2;3,5\text{H}_{-4}$	1.8	3.3	3.4	2.0	$^1\text{C}_4$
DFT	2.23	3.22	3.27	2.18	

6 Appendix

6.1 ^{13}C NMR spectra and chemical shifts of uncoordinated carbohydratesC₄, C₅ and C₆ sugar alcohols**Table 6.1.** ^{13}C NMR chemical shifts (δ /ppm) in D₂O, referenced to an internal methanol signal (49.5 ppm).

		C1	C2	C3	C4	C5	C6
Glyc	δ	63.3	72.8				
Eryt	δ	63.3	72.7				
D-Thre	δ	63.3	72.3				
D-Arab	δ	63.7	70.9	71.1	71.6	63.6	
Ribt	δ	63.0	72.7	72.9			
Xylt	δ	63.3	72.6	71.4			
Allt	δ	63.0	72.8	73.0			
D-Altr	δ	63.7	71.1	71.4	72.2	73.3	62.7
Dulc	δ	63.9	70.8	70.0			
L-Idit	δ	63.3	72.3	71.7			
D-Mann	δ	63.8	71.5	69.9			
D-Sorb	δ	63.1	73.5	70.3	71.7	71.6	63.4

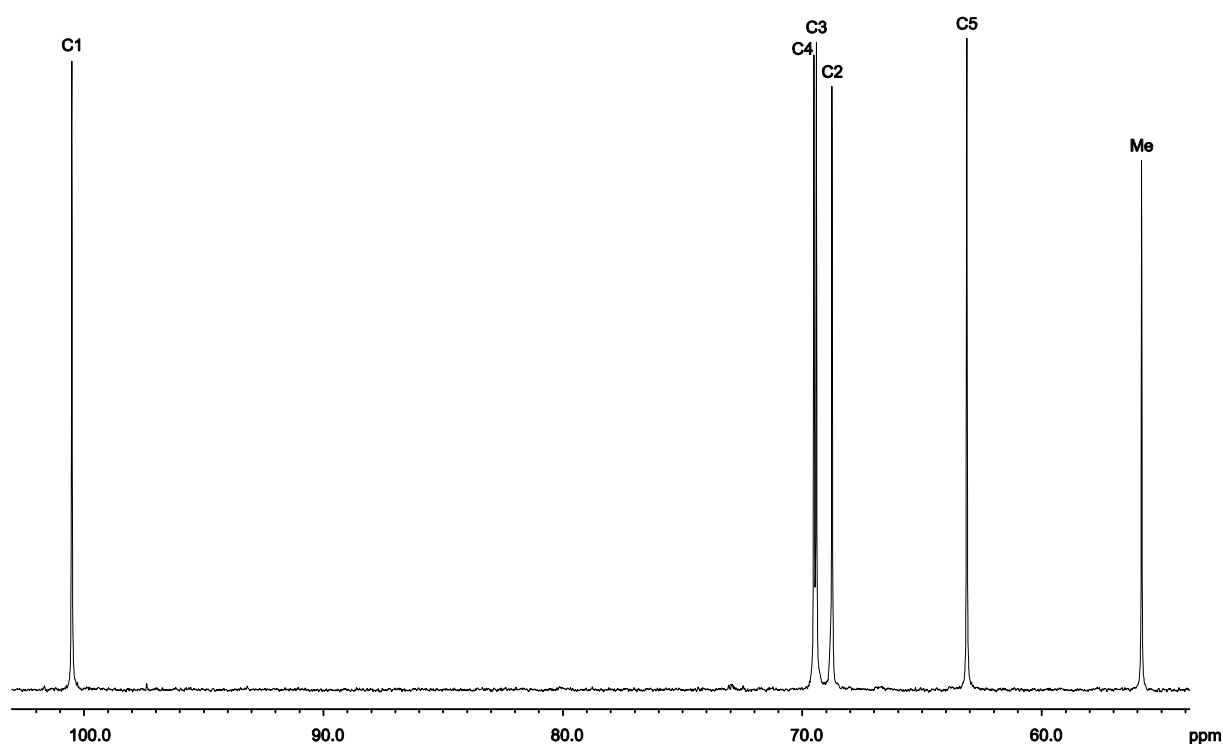
Methyl β -D-arabinopyranoside

Figure 6.1. ^{13}C NMR spectrum in D_2O , referenced to an internal methanol signal (49.5 ppm).

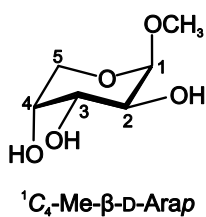


Table 6.2. ^{13}C NMR chemical shifts (δ/ppm) in D_2O , referenced to an internal methanol signal (49.5 ppm).

		C1	C2	C3	C4	C5	CH_3
Me- β -D-Arap	δ	100.5	68.8	69.4	69.5	63.1	55.8

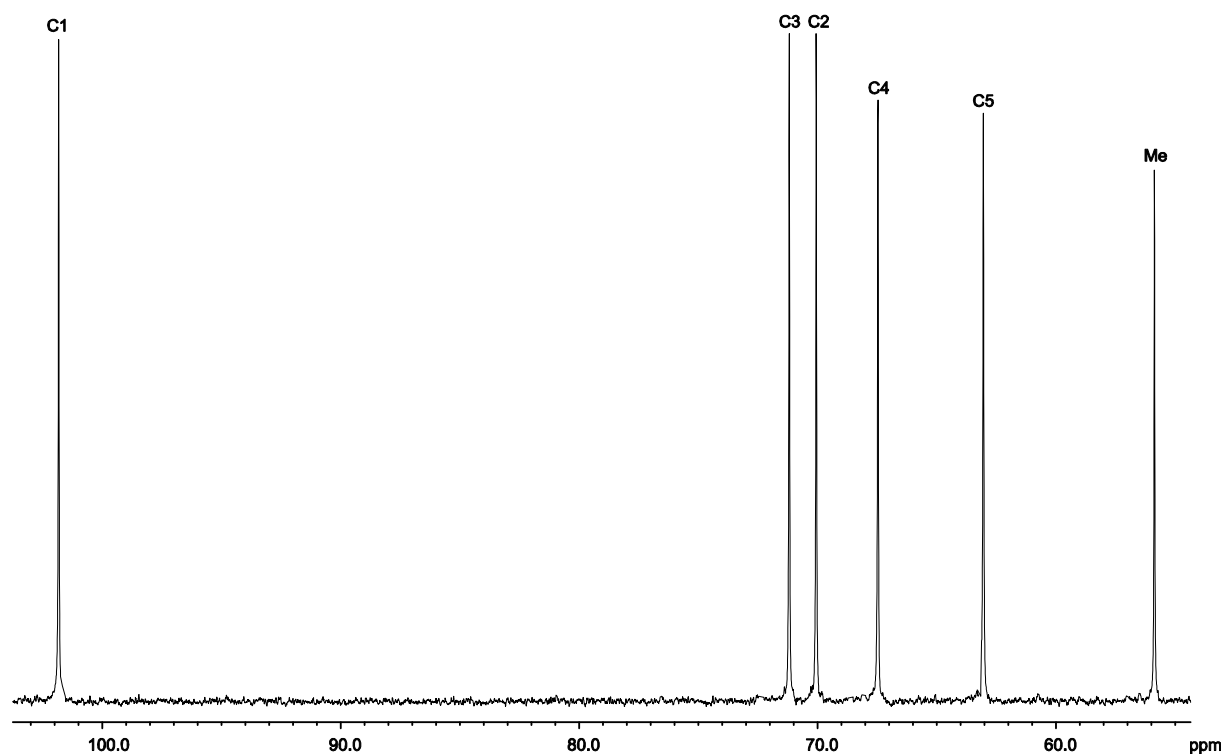
Methyl α -D-lyxopyranoside

Figure 6.2. ^{13}C NMR spectrum in D_2O , referenced to an internal methanol signal (49.5 ppm).



Table 6.3. ^{13}C NMR chemical shifts (δ/ppm) in D_2O , referenced to an internal methanol signal (49.5 ppm).

		C1	C2	C3	C4	C5	CH_3
Me- α -D-Lyxp	δ	101.8	70.1	71.2	67.5	63.1	55.9

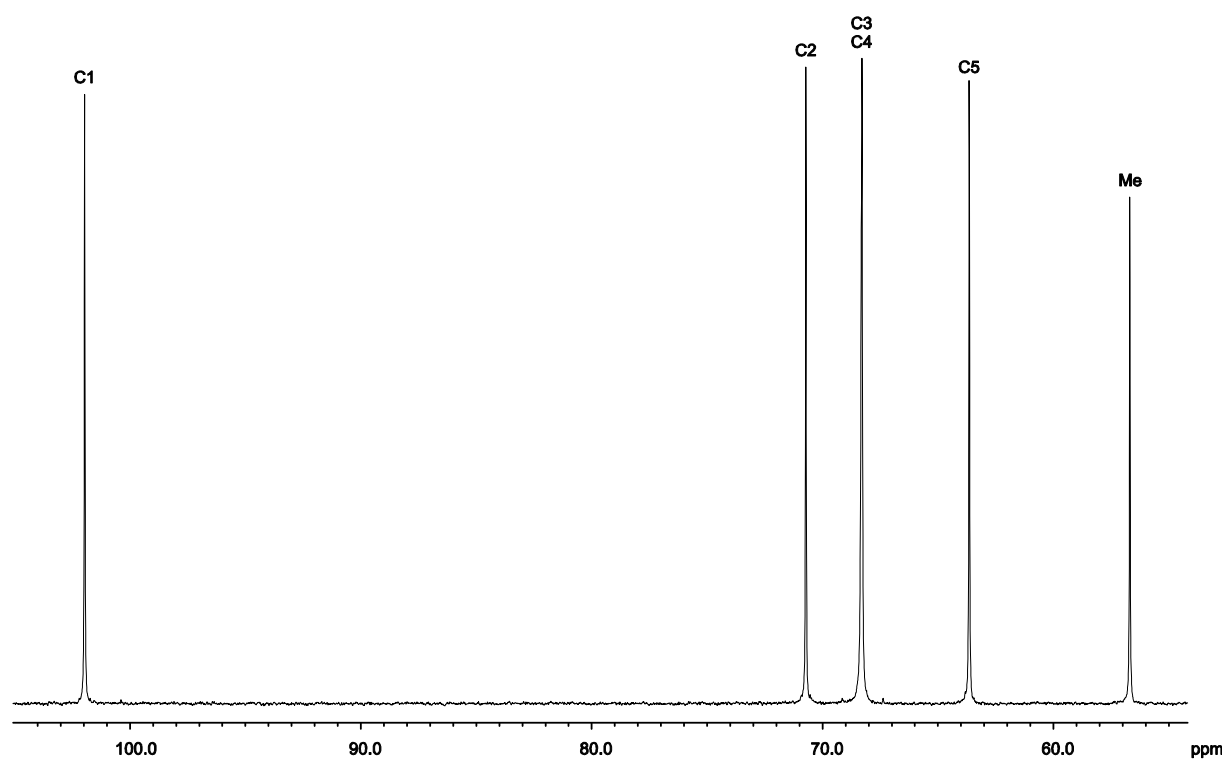
Methyl β -D-ribofuranoside

Figure 6.3. ^{13}C NMR spectrum in D_2O , referenced to an internal methanol signal (49.5 ppm).

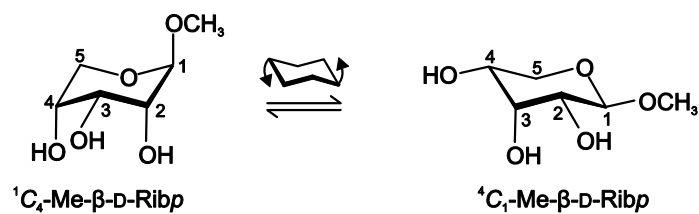


Table 6.4. ^{13}C NMR chemical shifts (δ/ppm) in D_2O , referenced to an internal methanol signal (49.5 ppm).

		C1	C2	C3	C4	C5	CH_3
Me- β -D-Ribp	δ	102.0	70.7	68.3	68.3	63.6	56.7

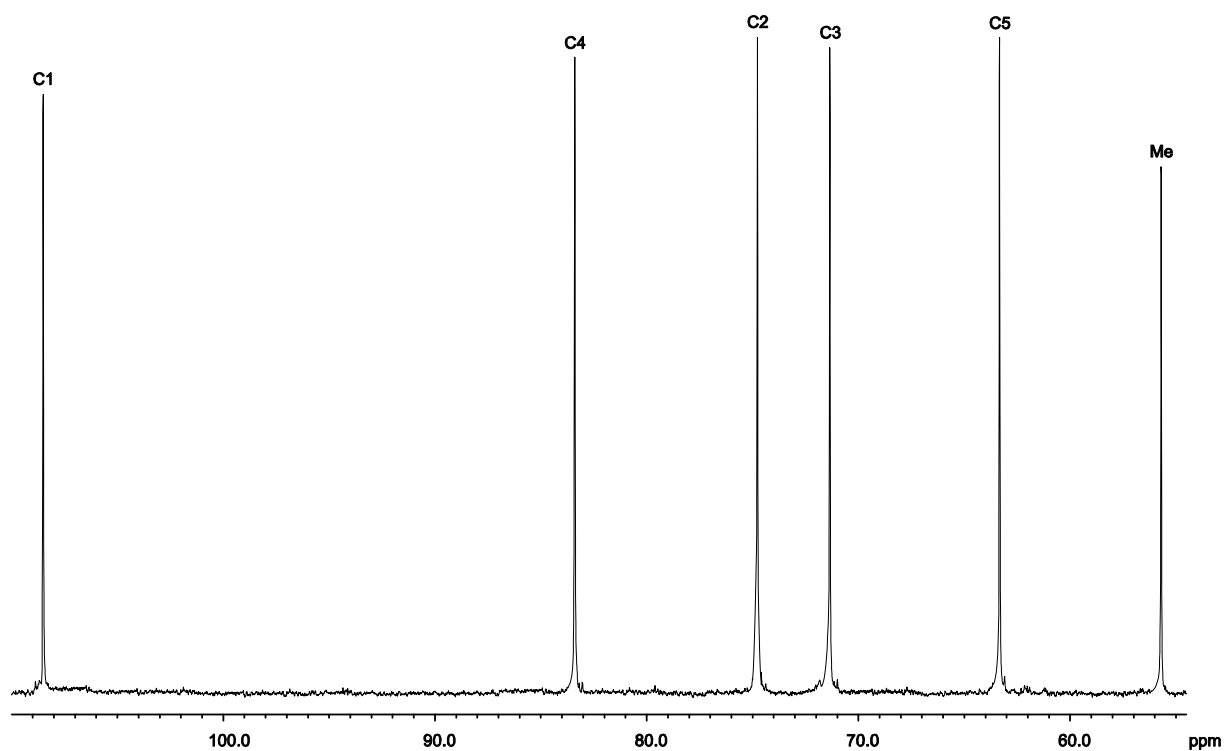
Methyl β -D-ribofuranoside

Figure 6.4. ^{13}C NMR spectrum in D_2O , referenced to an internal methanol signal (49.5 ppm).

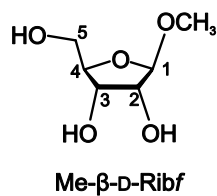


Table 6.5. ^{13}C NMR chemical shifts (δ/ppm) in D_2O , referenced to an internal methanol signal (49.5 ppm).

		C1	C2	C3	C4	C5	CH_3
Me- β -D-Ribf	δ	108.5	74.8	71.4	83.4	63.3	55.7

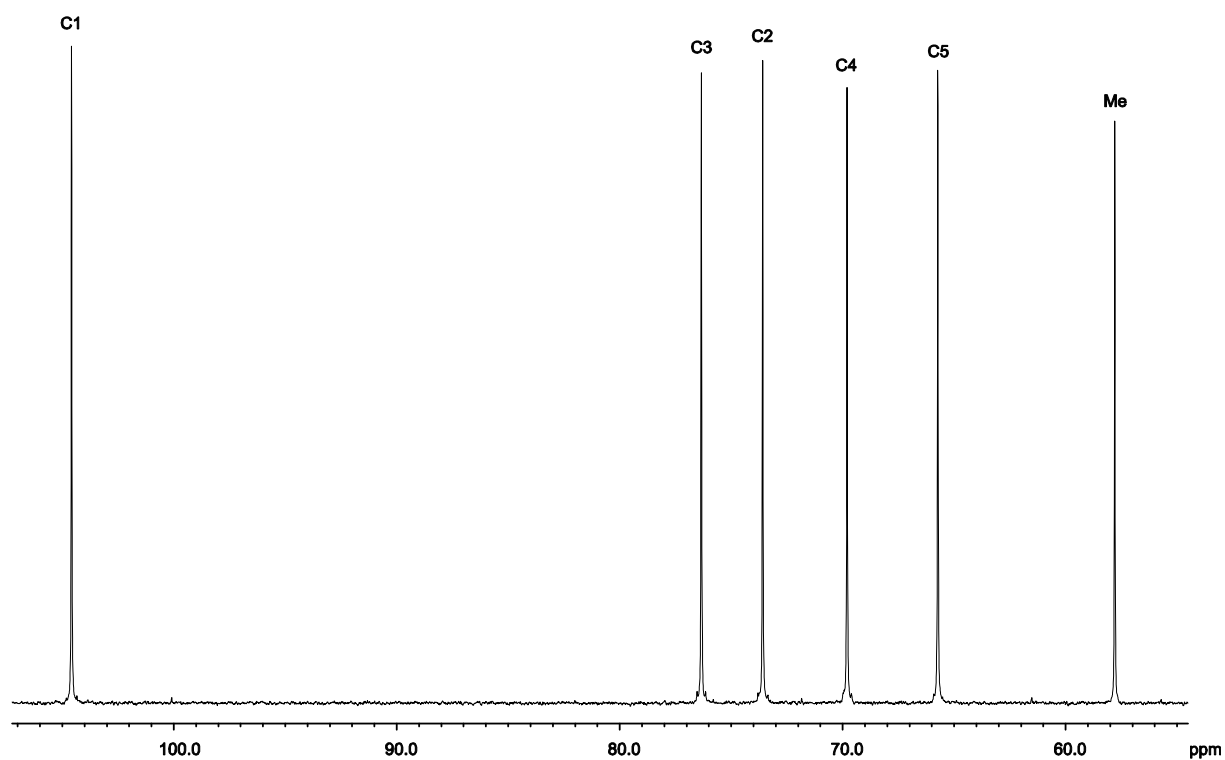
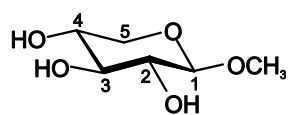
Methyl β -D-xylopyranoside

Figure 6.5. ^{13}C NMR spectrum in D_2O , referenced to an internal methanol signal (49.5 ppm).



$^4\text{C}_1$ -Me- β -D-Xylp

Table 6.6. ^{13}C NMR chemical shifts (δ/ppm) in D_2O , referenced to an internal methanol signal (49.5 ppm).

		C1	C2	C3	C4	C5	CH ₃
Me- β -D-Xylp	δ	104.6	73.6	76.3	69.8	65.7	57.8

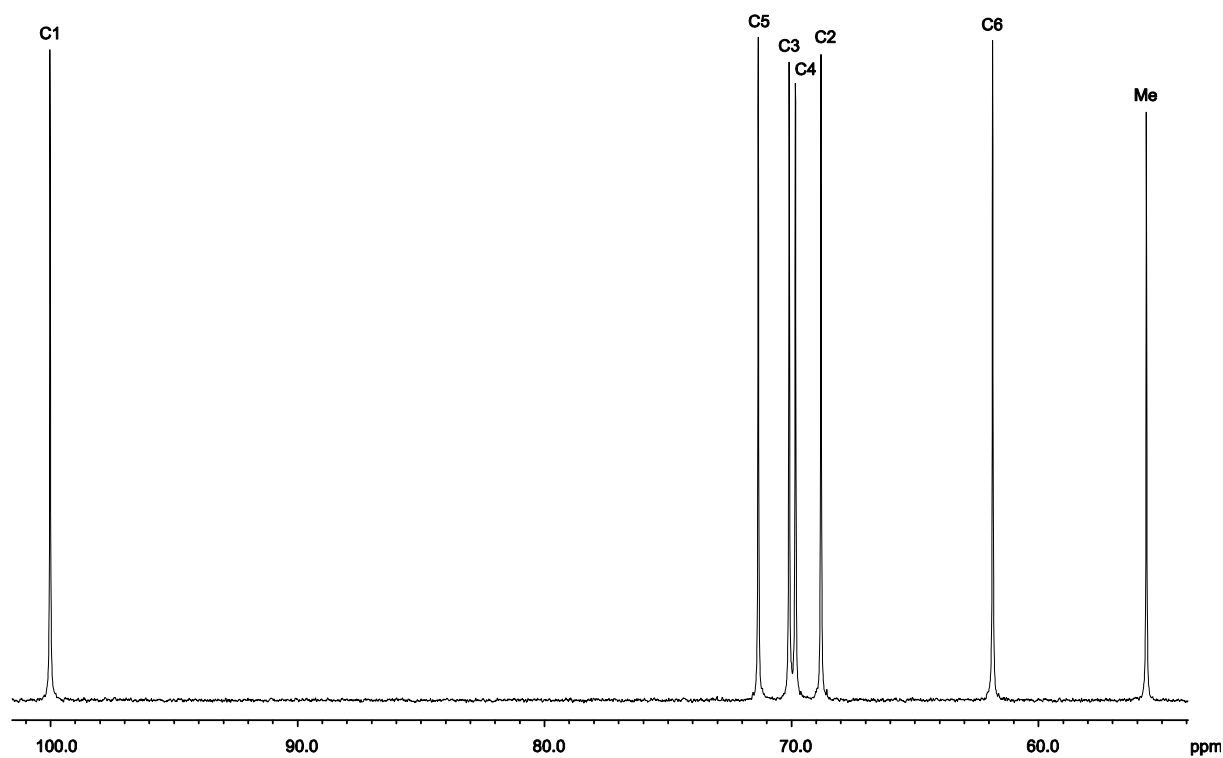
Methyl α -D-galactopyranoside

Figure 6.6. ^{13}C NMR spectrum in D_2O , referenced to an internal methanol signal (49.5 ppm).

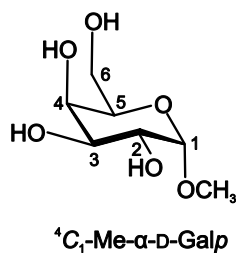


Table 6.7. ^{13}C NMR chemical shifts (δ/ppm) in D_2O , referenced to an internal methanol signal (49.5 ppm).

		C1	C2	C3	C4	C5	C6	CH_3
Me- α -D-Galp	δ	100.0	68.8	70.1	69.8	71.3	61.9	55.6

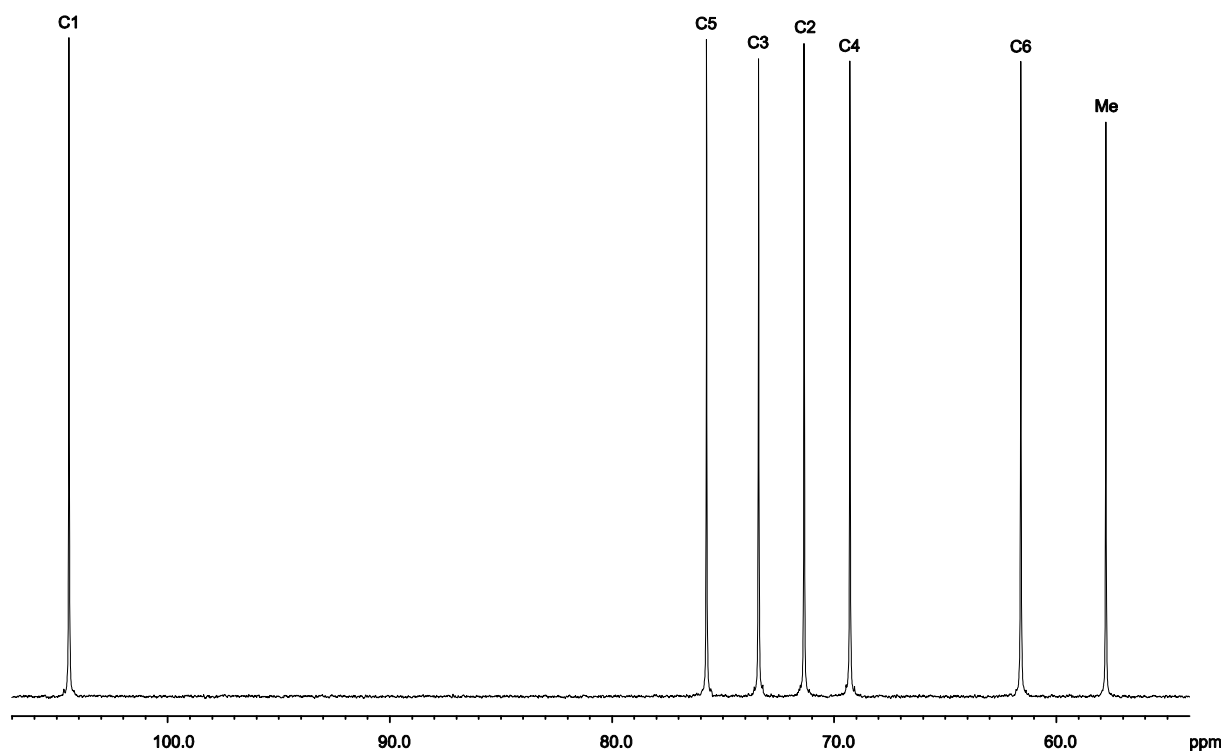
Methyl β -D-galactopyranoside

Figure 6.7. ^{13}C NMR spectrum in D_2O , referenced to an internal methanol signal (49.5 ppm).

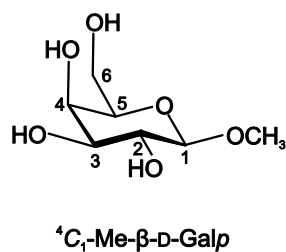


Table 6.8. ^{13}C NMR chemical shifts (δ/ppm) in D_2O , referenced to an internal methanol signal (49.5 ppm).

		C1	C2	C3	C4	C5	C6	CH_3
Me- β -D-Galp	δ	104.4	71.4	73.4	69.3	75.7	61.6	57.8

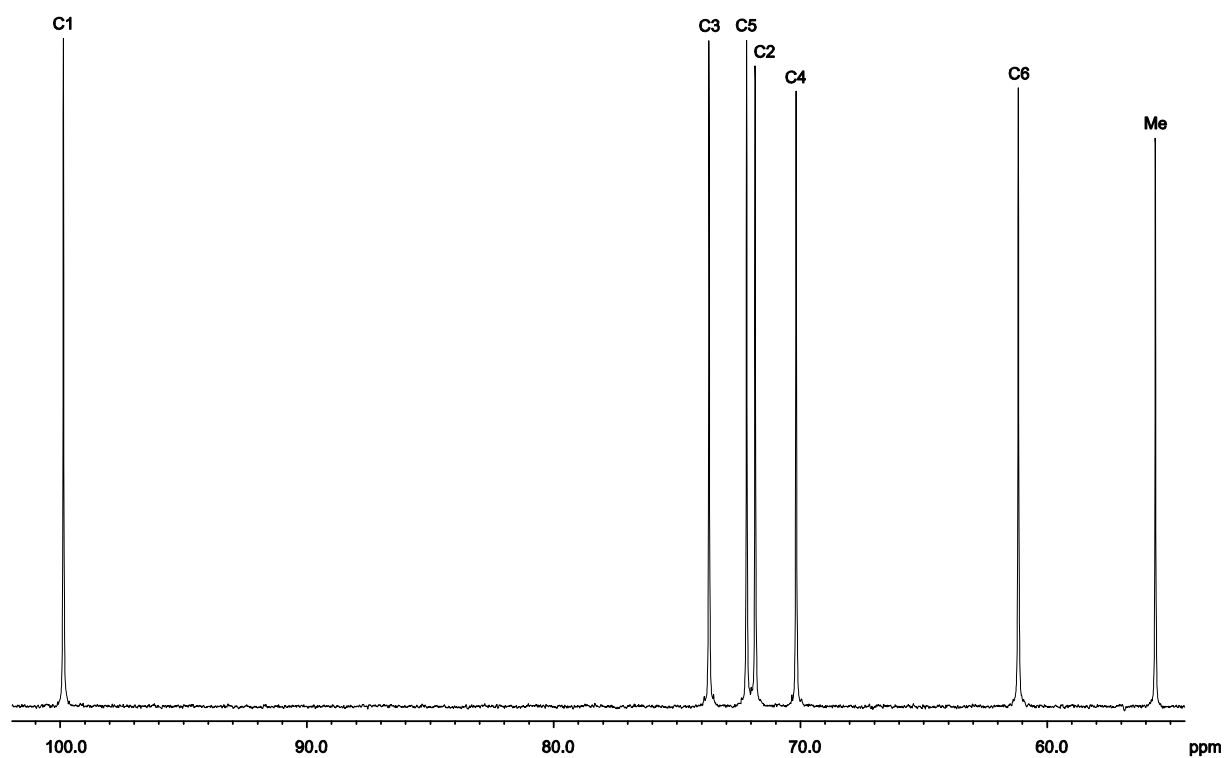
Methyl α -D-glucopyranoside

Figure 6.8. ^{13}C NMR spectrum in D_2O , referenced to an internal methanol signal (49.5 ppm).

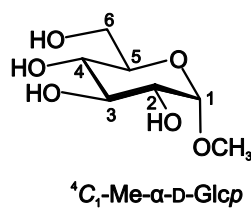


Table 6.9. ^{13}C NMR chemical shifts (δ /ppm) in D_2O , referenced to an internal methanol signal (49.5 ppm).

		C1	C2	C3	C4	C5	C6	CH_3
Me- α -D-Glcp	δ	99.9	71.8	73.7	70.2	72.2	61.2	55.6

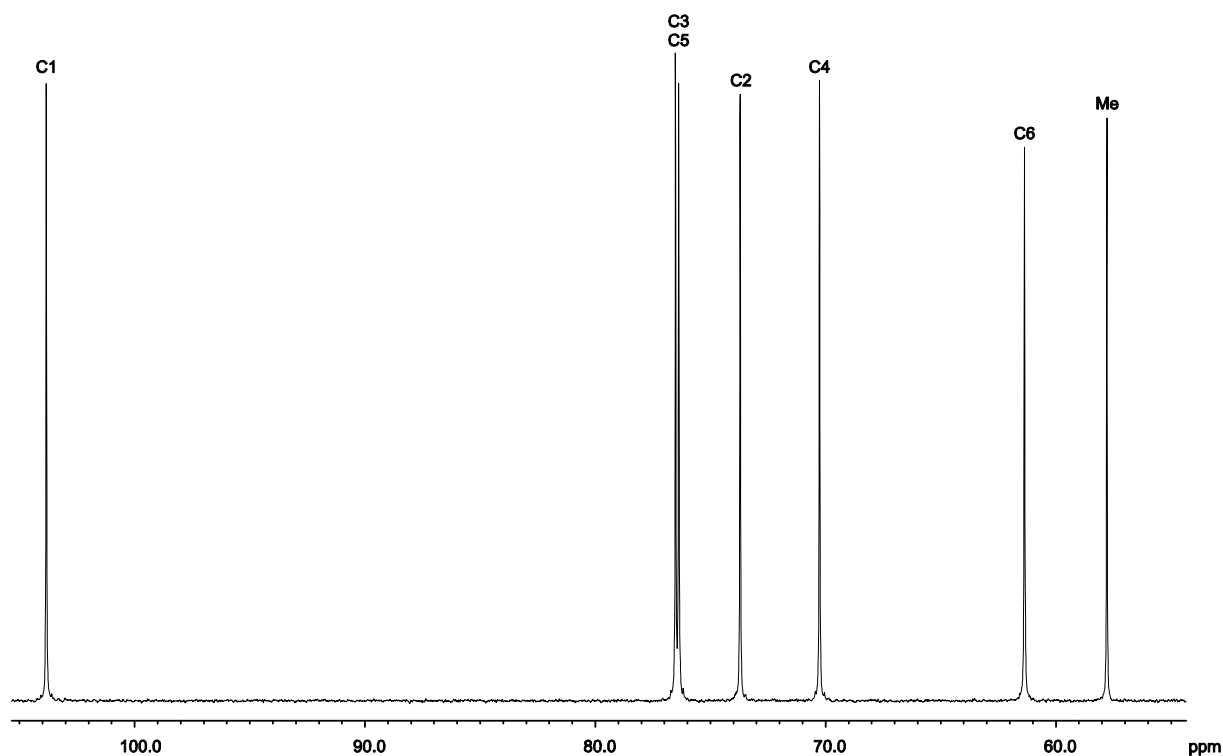
Methyl β -D-glucopyranoside

Figure 6.9. ^{13}C NMR spectrum in D_2O , referenced to an internal methanol signal (49.5 ppm).

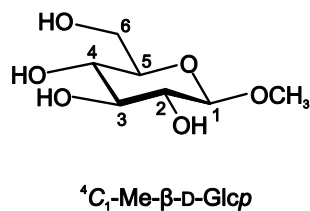


Table 6.10. ^{13}C NMR chemical shifts (δ/ppm) in D_2O , referenced to an internal methanol signal (49.5 ppm).

		C1	C2	C3	C4	C5	C6	CH_3
Me- β -D-Glcp	δ	103.8	73.7	76.4	70.3	76.5	61.4	57.8

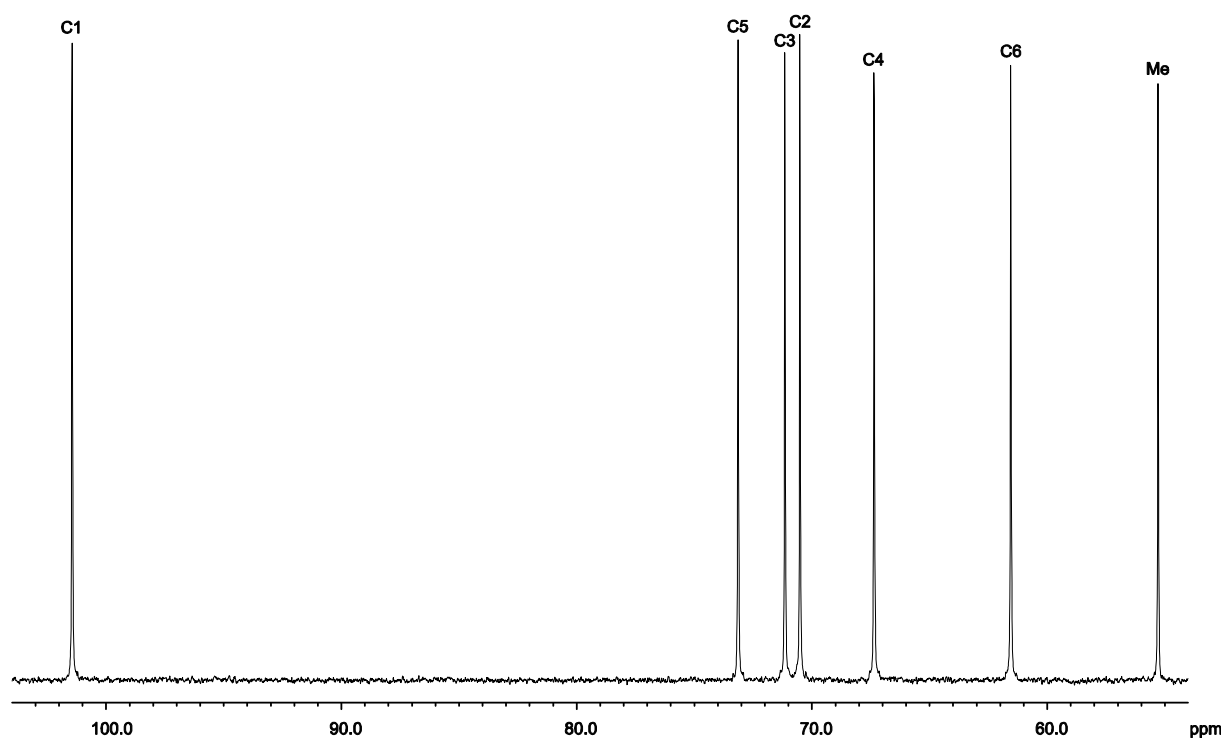
Methyl α -D-mannopyranoside

Figure 6.10. ^{13}C NMR spectrum in D_2O , referenced to an internal methanol signal (49.5 ppm).

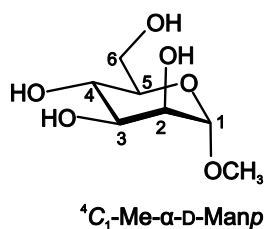


Table 6.11. ^{13}C NMR chemical shifts (δ/ppm) in D_2O , referenced to an internal methanol signal (49.5 ppm).

		C1	C2	C3	C4	C5	C6	CH_3
Me- α -D-Manp	δ	101.4	70.5	71.2	67.4	73.1	61.6	55.3

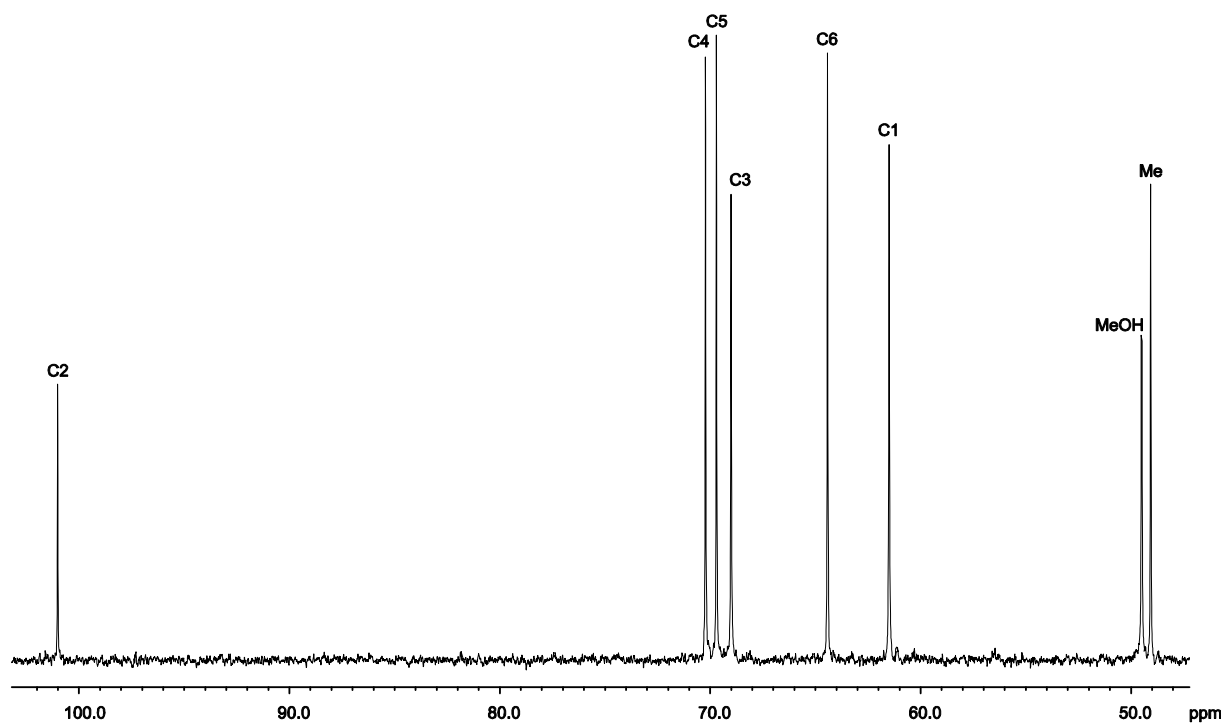
Methyl β -D-fructopyranoside

Figure 6.11. ^{13}C NMR spectrum in D_2O , referenced to an internal methanol signal (49.5 ppm).

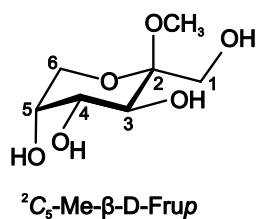


Table 6.12. ^{13}C NMR chemical shifts (δ/ppm) in D_2O , referenced to an internal methanol signal (49.5 ppm).

		C1	C2	C3	C4	C5	C6	CH_3
Me- β -D-Frup	δ	61.5	101.0	69.0	70.2	69.7	64.4	49.1

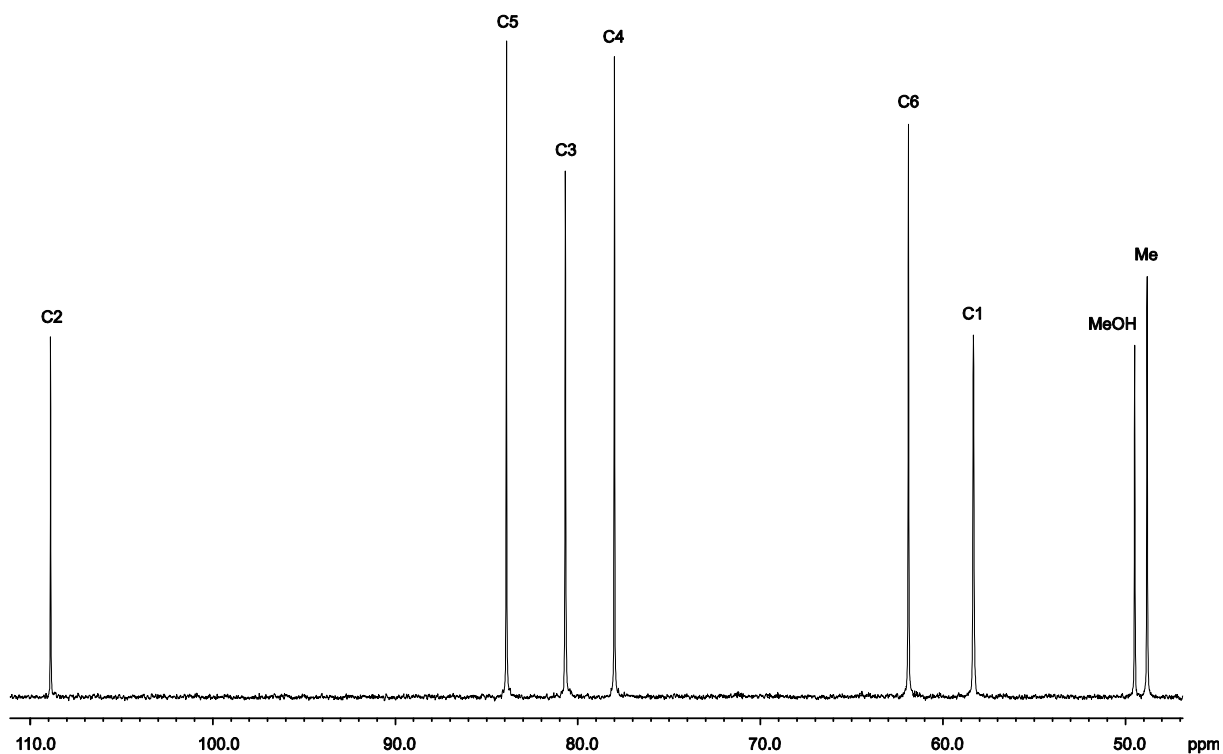
Methyl α -D-fructofuranoside

Figure 6.12. ^{13}C NMR spectrum in D_2O , referenced to an internal methanol signal (49.5 ppm).

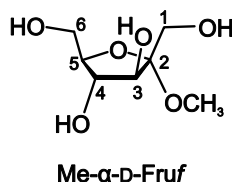


Table 6.13. ^{13}C NMR chemical shifts (δ /ppm) in D_2O , referenced to an internal methanol signal (49.5 ppm).

		C1	C2	C3	C4	C5	C6	CH ₃
Me- α -D-Fruf	δ	58.3	108.9	80.7	78.0	83.9	61.9	48.8

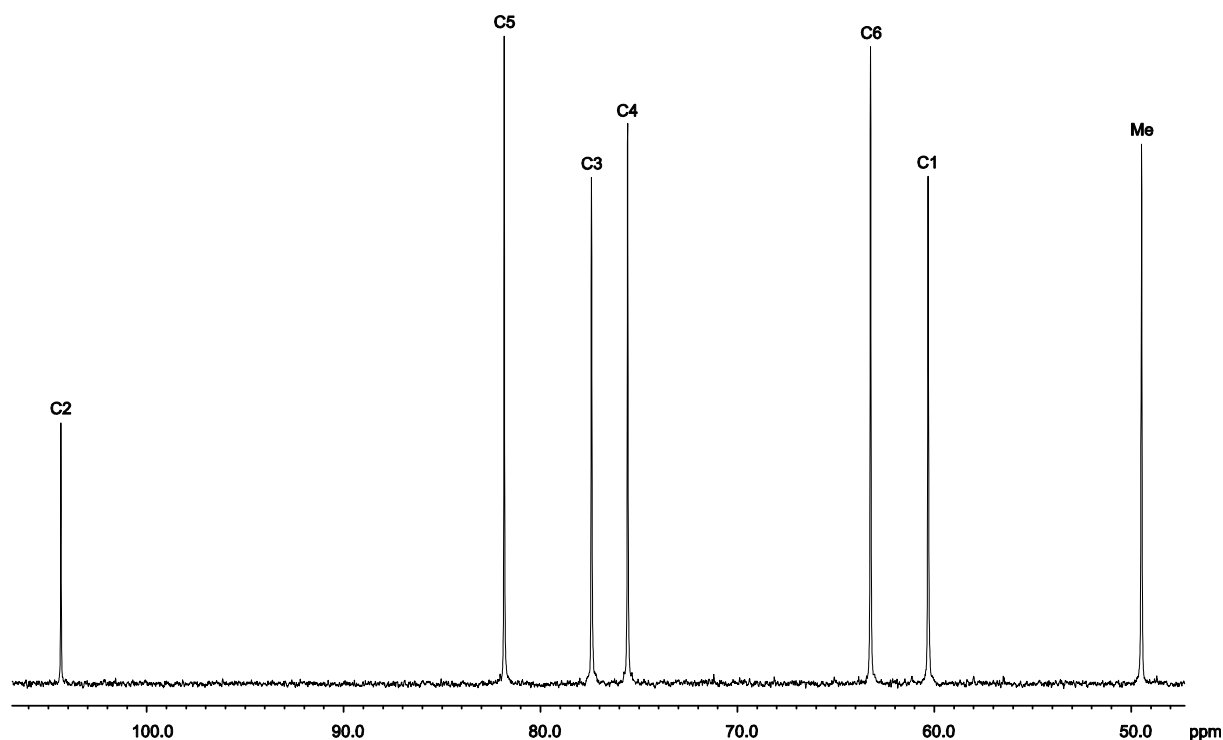
Methyl β -D-fructofuranoside

Figure 6.13. ^{13}C NMR spectrum in D_2O , referenced to an internal methanol signal (49.5 ppm).

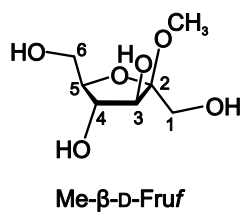


Table 6.14. ^{13}C NMR chemical shifts (δ/ppm) in D_2O , referenced to an internal methanol signal (49.5 ppm).

		C1	C2	C3	C4	C5	C6	CH ₃
Me- β -D-Fruf	δ	60.3	104.4	77.4	75.6	81.8	63.2	49.5

D-Arabinose

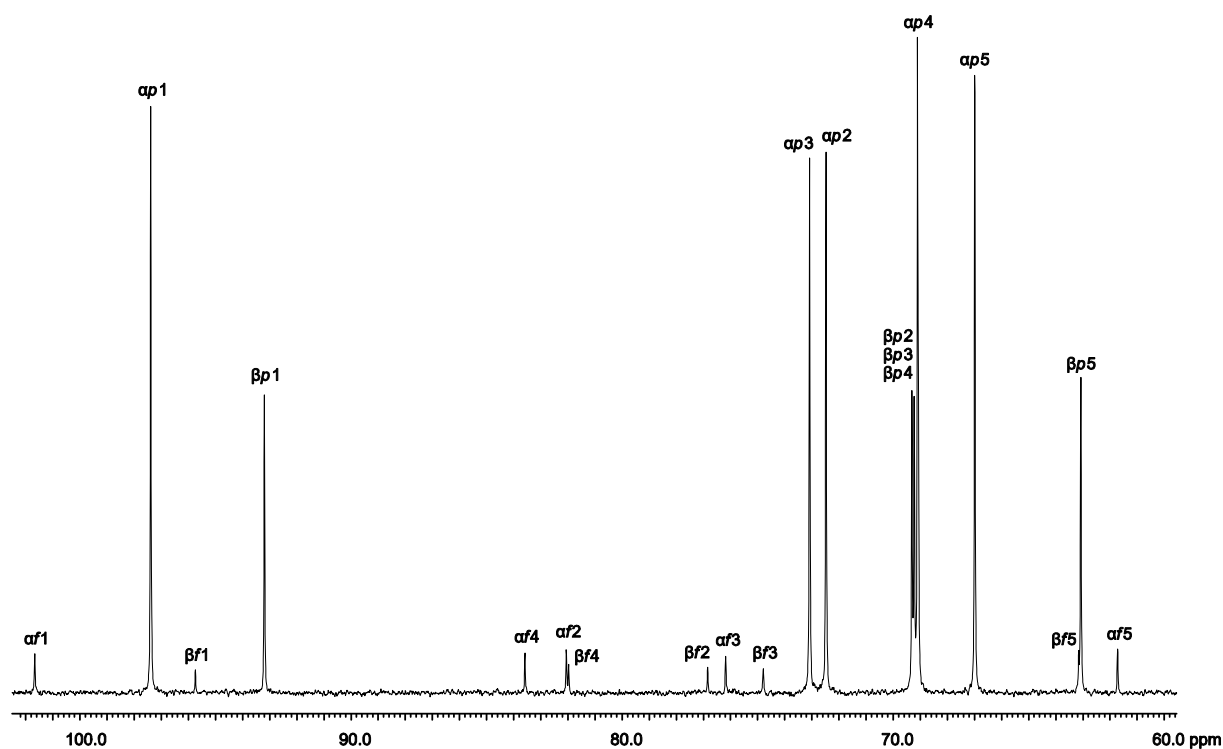


Figure 6.14. ^{13}C NMR spectrum in D_2O , referenced to an internal methanol signal (49.5 ppm).

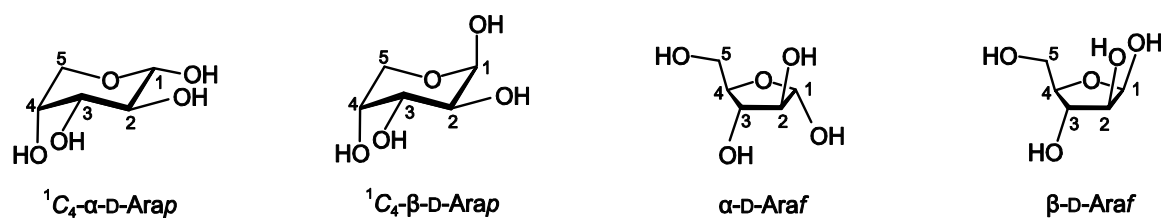


Table 6.15. ^{13}C NMR chemical shifts (δ/ppm) in D_2O , referenced to an internal methanol signal (49.5 ppm).

		C1	C2	C3	C4	C5
$\alpha\text{-D-Arap}$	δ	97.4	72.5	73.1	69.1	67.0
$\beta\text{-D-Arap}$	δ	93.2	69.2	69.2	69.2	63.1
$\alpha\text{-D-Araf}$	δ	101.7	82.1	76.2	83.6	61.7
$\beta\text{-D-Araf}$	δ	95.6	76.8	74.8	82.0	61.7

D-Lyxose

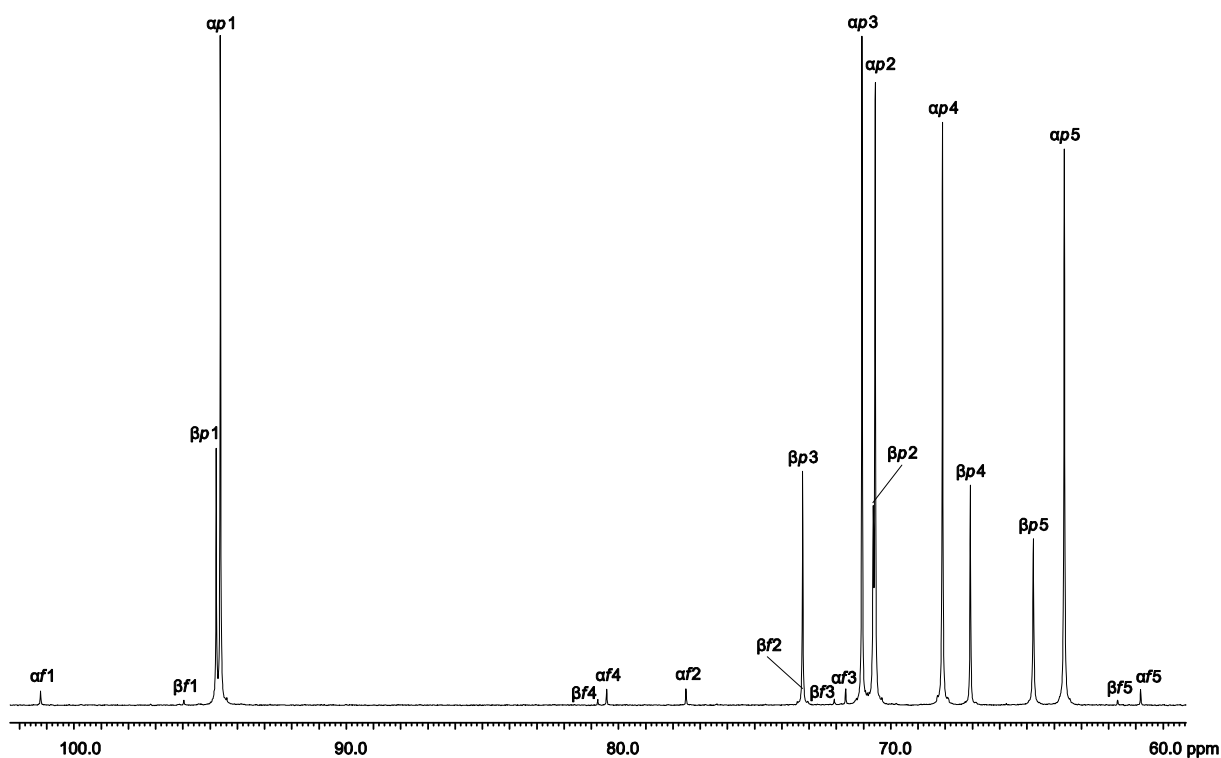


Figure 6.15. ^{13}C NMR spectrum in D_2O , referenced to an internal methanol signal (49.5 ppm).

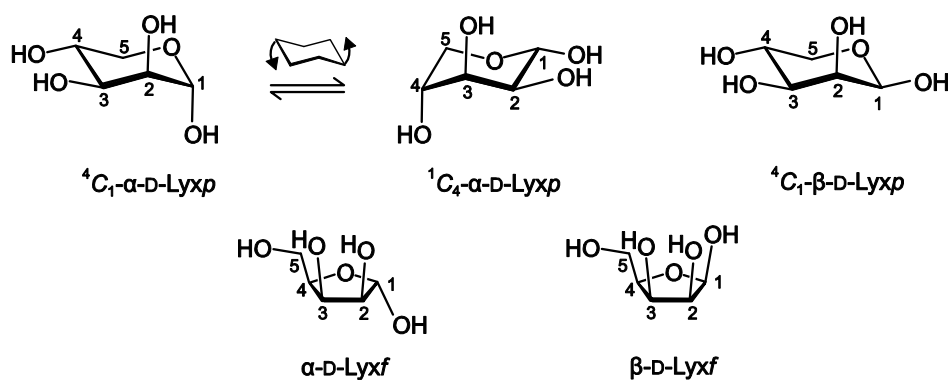


Table 6.16. ^{13}C NMR chemical shifts (δ/ppm) in D_2O , referenced to an internal methanol signal (49.5 ppm).

		C1	C2	C3	C4	C5
$\alpha\text{-D-Lyx}p$	δ	94.7	70.6	71.1	68.2	63.7
$\beta\text{-D-Lyx}p$	δ	94.8	70.7	73.3	67.1	64.8
$\alpha\text{-D-Lyxf}$	δ	101.3	77.6	71.7	80.5	60.9
$\beta\text{-D-Lyxf}$	δ	96.0	73.2	72.1	80.8	61.7

D-Ribose

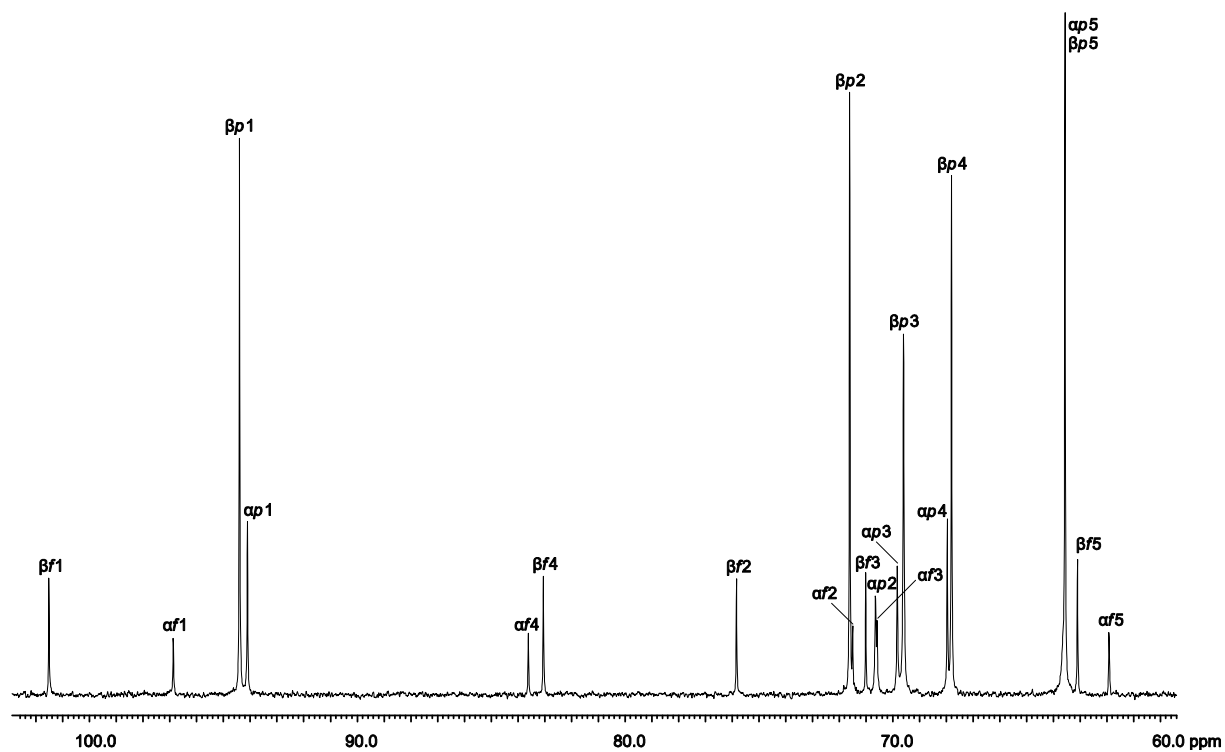


Figure 6.16. ^{13}C NMR spectrum in D_2O , referenced to an internal methanol signal (49.5 ppm).

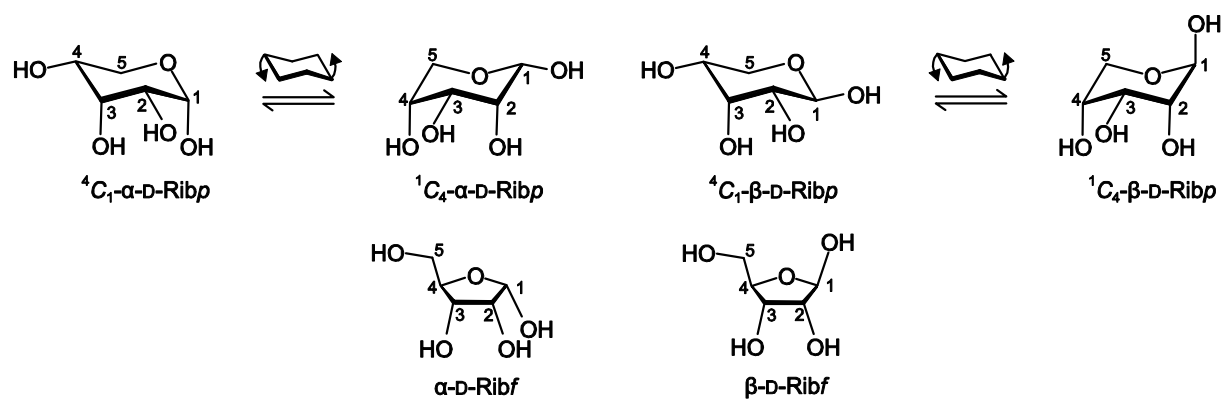


Table 6.17. ^{13}C NMR chemical shifts (δ/ppm) in D_2O , referenced to an internal methanol signal (49.5 ppm).

		C1	C2	C3	C4	C5
$\alpha\text{-D-Ribp}$	δ	94.1	70.6	69.8	68.0	63.6
$\beta\text{-D-Ribp}$	δ	94.4	71.6	69.6	67.8	63.6
$\alpha\text{-D-Ribf}$	δ	96.9	71.5	70.6	83.6	61.9
$\beta\text{-D-Ribf}$	δ	101.5	75.8	71.0	83.1	63.1

6 Appendix

D-Xylose

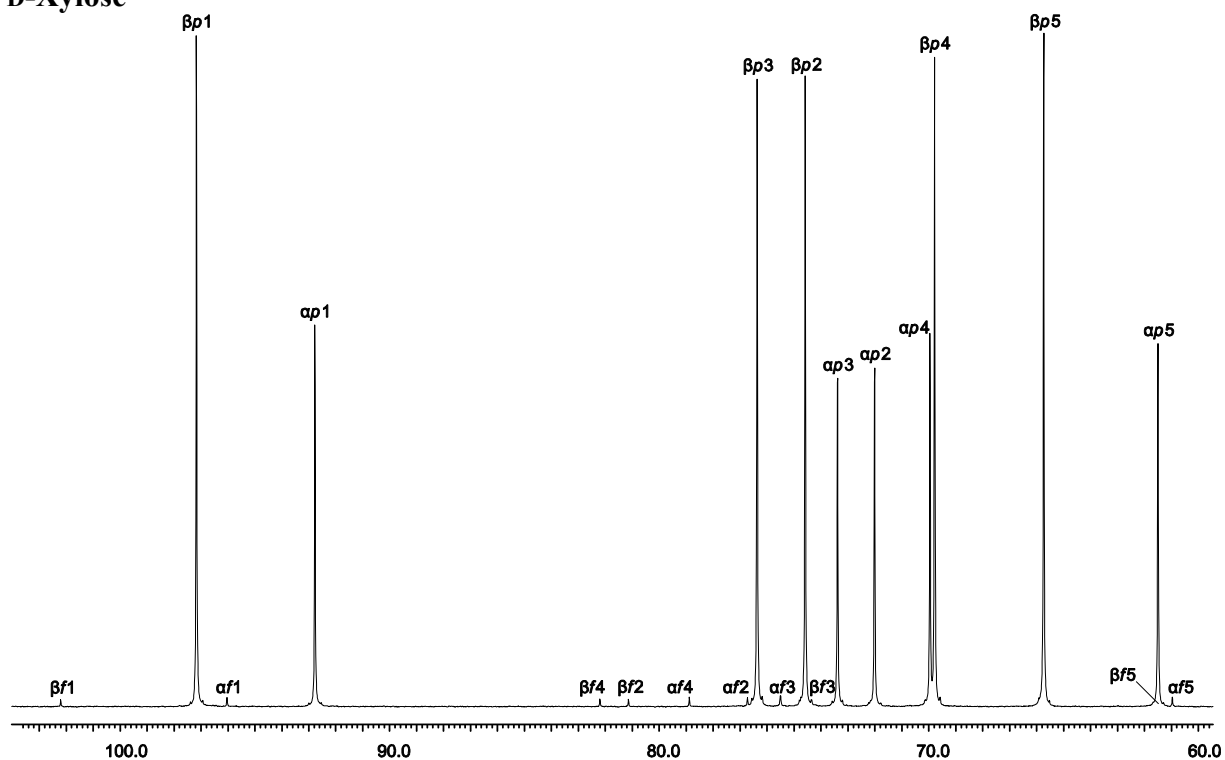


Figure 6.17. ^{13}C NMR spectrum in D_2O , referenced to an internal methanol signal (49.5 ppm).

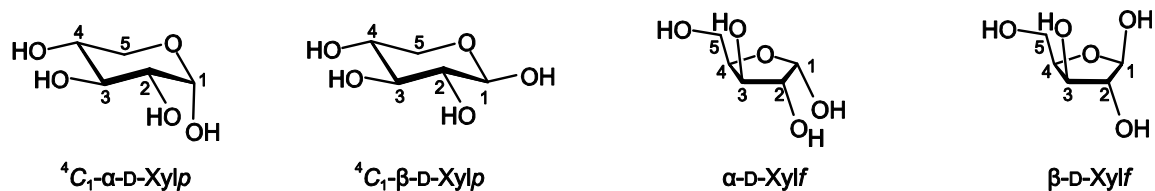


Table 6.18. ^{13}C NMR chemical shifts (δ/ppm) in D_2O , referenced to an internal methanol signal (49.5 ppm).

		C1	C2	C3	C4	C5
$\alpha\text{-D-Xylp}$	δ	92.8	72.1	73.4	70.0	61.6
$\beta\text{-D-Xylp}$	δ	97.2	74.7	76.4	69.8	65.8
$\alpha\text{-D-Xylf}$	δ	96.1	76.7	75.5	78.9	61.0
$\beta\text{-D-Xylf}$	δ	102.2	81.1	74.6	82.2	61.5

D-Galactose

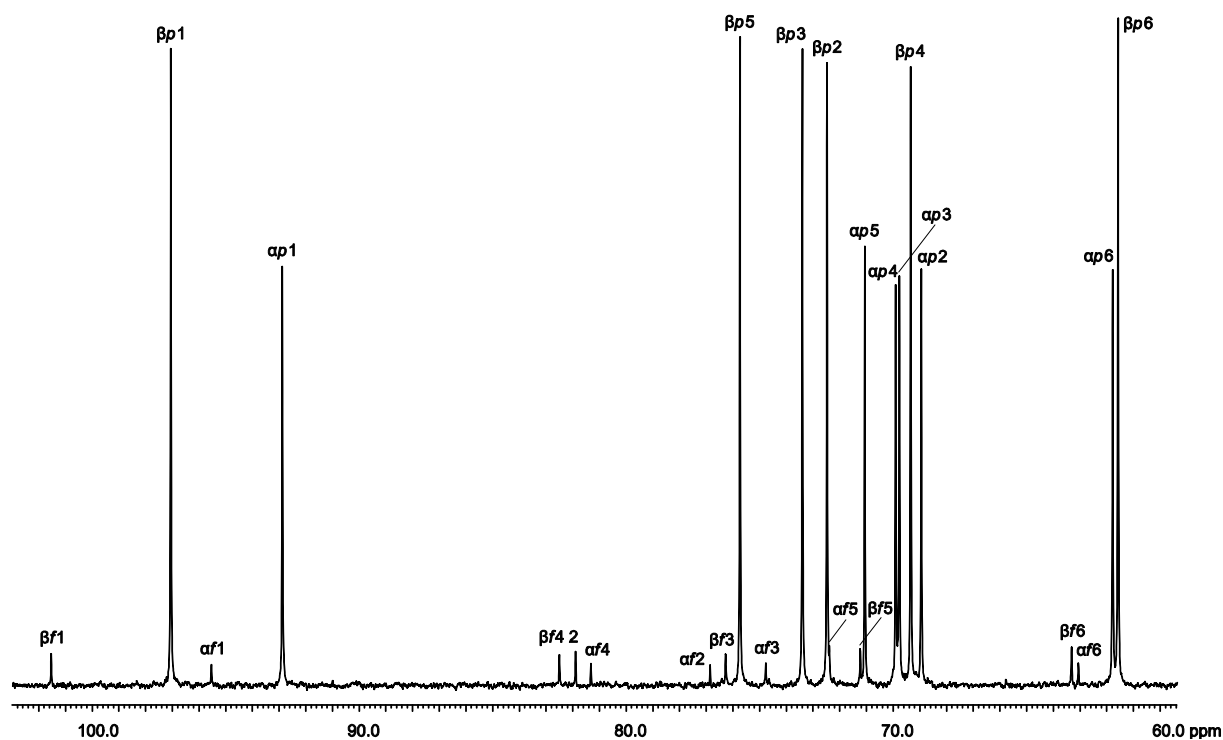


Figure 6.18. ^{13}C NMR spectrum in D_2O , referenced to an internal methanol signal (49.5 ppm).

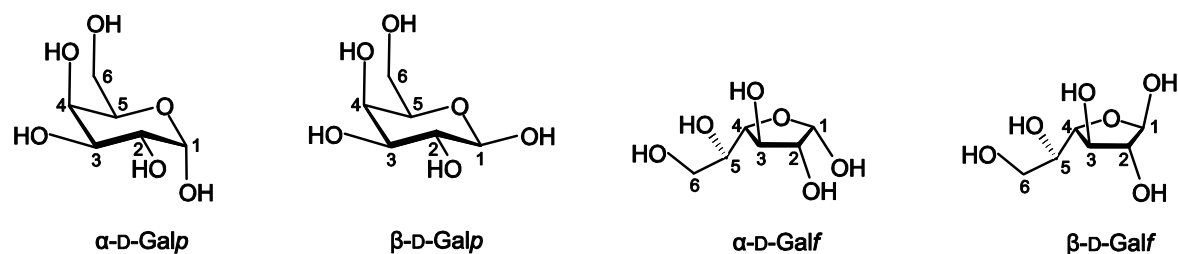


Table 6.19. ^{13}C NMR chemical shifts (δ/ppm) in D_2O , referenced to an internal methanol signal (49.5 ppm).

		C1	C2	C3	C4	C5	C6
$\alpha\text{-D-Galp}$	δ	92.9	69.0	69.8	69.9	71.1	61.8
$\beta\text{-D-Galp}$	δ	97.1	72.5	73.4	69.4	75.8	61.6
$\alpha\text{-D-Galf}$	δ	95.6	76.9	74.8	81.3	72.4	63.1
$\beta\text{-D-Galf}$	δ	101.6	81.9	76.3	82.5	71.3	63.3

D-Glucose

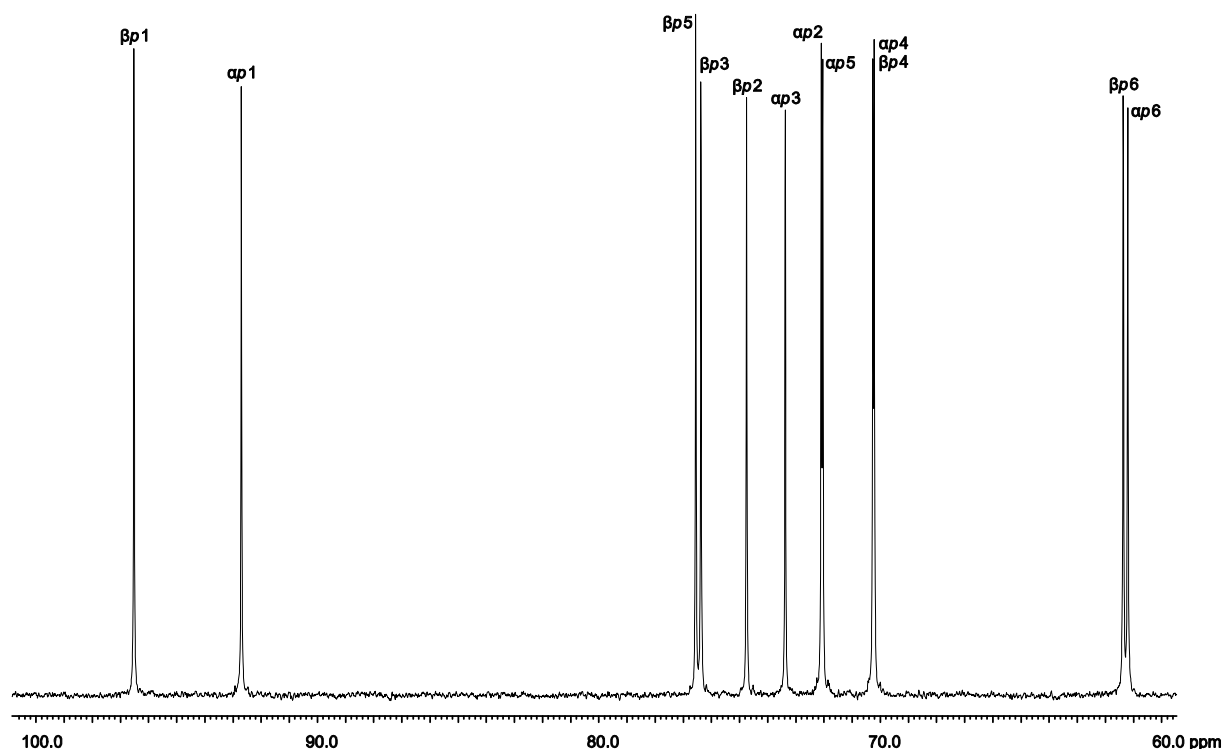


Figure 6.19. ^{13}C NMR spectrum in D_2O , referenced to an internal methanol signal (49.5 ppm).

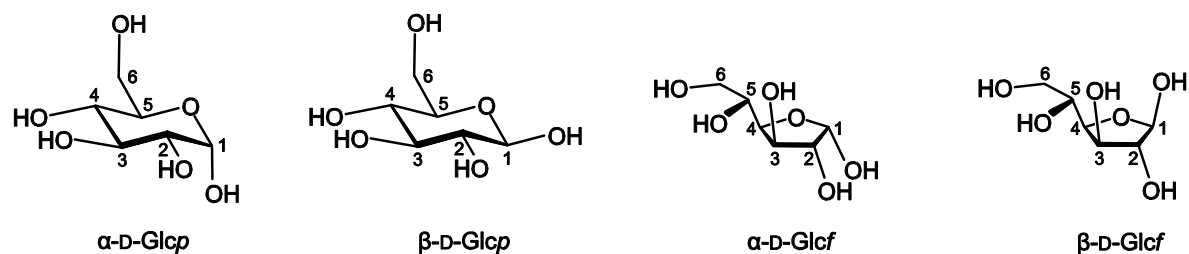


Table 6.20. ^{13}C NMR chemical shifts (δ/ppm) in D_2O , referenced to an internal methanol signal (49.5 ppm).

		C1	C2	C3	C4	C5	C6
$\alpha\text{-D-Glcp}$	δ	92.7	72.1	73.4	70.2	72.0	61.2
$\beta\text{-D-Glcp}$	δ	96.5	74.7	76.4	70.3	76.6	61.4
$\alpha\text{-D-Glcf}^*$	δ	97.4	(78.2)	(77.1)	(79.3)	(71.2)	(64.7)
$\beta\text{-D-Glcf}^*$	δ	103.0	(81.1)	(76.3)	(82.8)	(71.2)	(65.2)

* The furanoses' chemical shifts were adopted from Ref. [14] for C1 and from Ref. [83] for methyl D-glucofuranosides' C2–C6.

D-Mannose

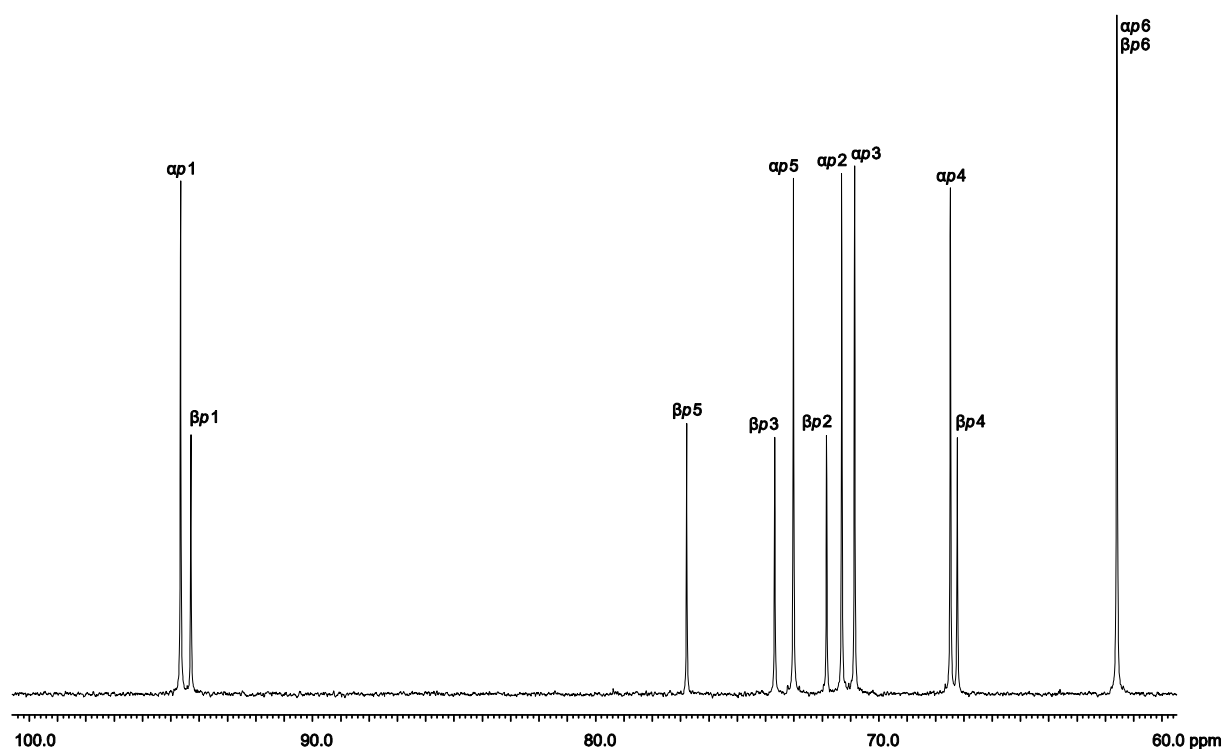


Figure 6.20. ^{13}C NMR spectrum in D_2O , referenced to an internal methanol signal (49.5 ppm).

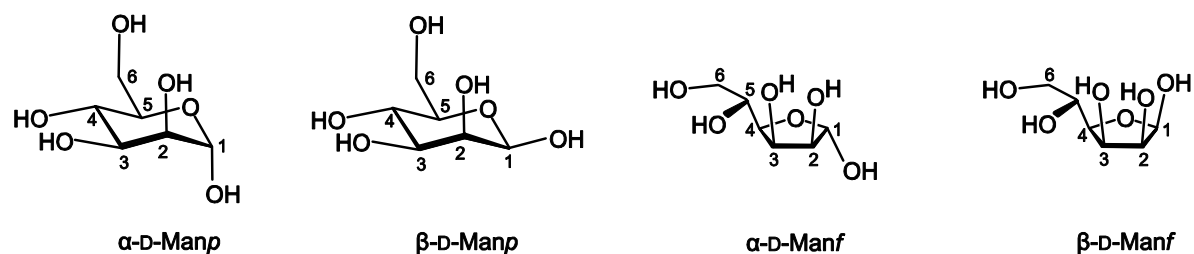


Table 6.21. ^{13}C NMR chemical shifts (δ/ppm) in D_2O , referenced to an internal methanol signal (49.5 ppm).

		C1	C2	C3	C4	C5	C6
$\alpha\text{-D-Manp}$	δ	94.7	71.3	70.8	67.5	73.0	61.6
$\beta\text{-D-Manp}$	δ	94.3	71.8	73.7	67.2	76.8	61.6
$\alpha\text{-D-Manf}^*$	δ	101.6	78.4	73.0	81.0	71.1	65.0
$\beta\text{-D-Manf}^*$	δ	96.2	73.6	71.7	81.2	71.5	64.9

* The furanoses' chemical shifts were adopted from Ref. [14] for C1 and from Ref. [83] for methyl D-glucofuranosides' C2–C6.

D-Fructose

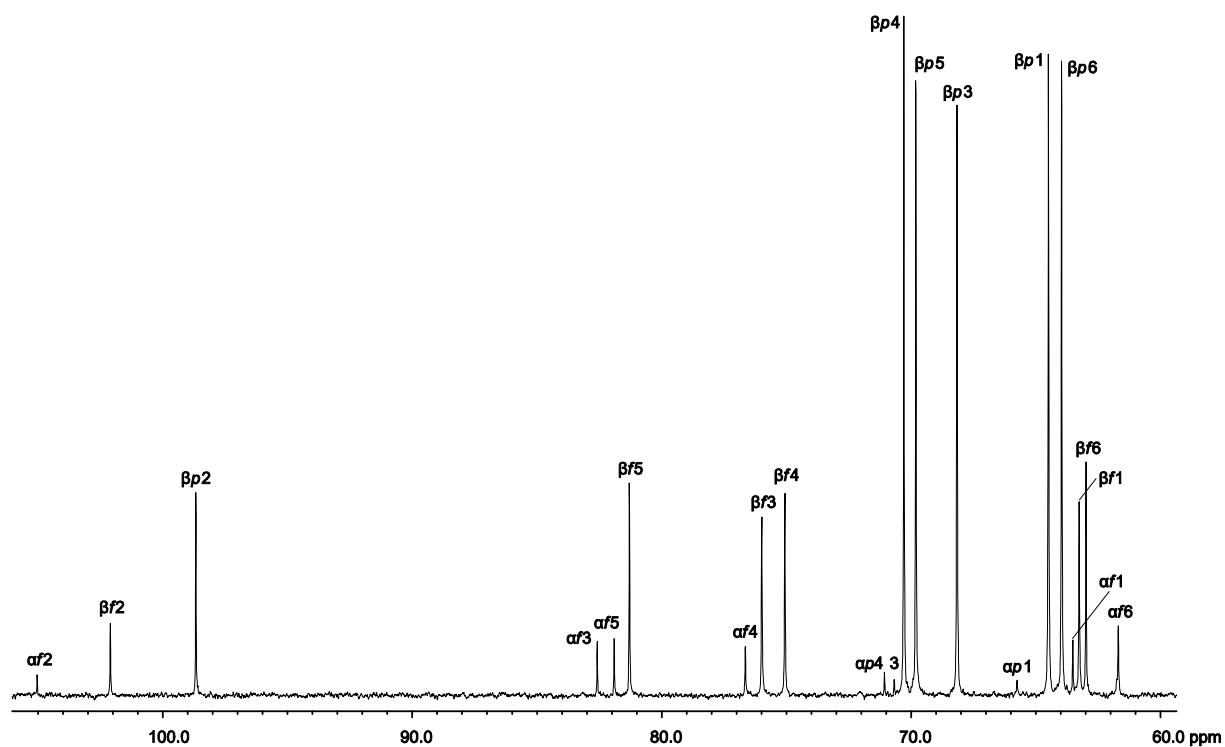


Figure 6.21. ^{13}C NMR spectrum in D_2O , referenced to an internal methanol signal (49.5 ppm).

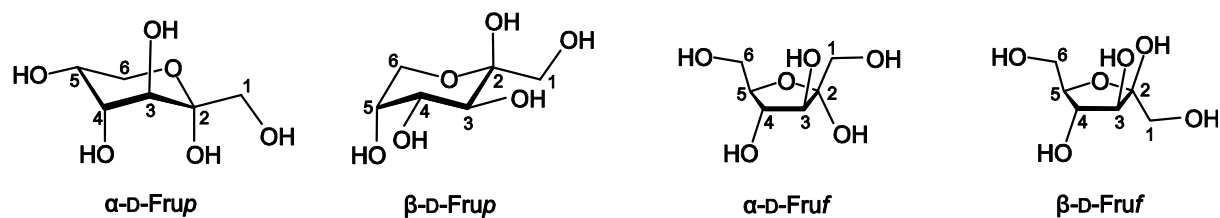


Table 6.22. ^{13}C NMR chemical shifts (δ/ppm) in D_2O , referenced to an internal methanol signal (49.5 ppm).

		C1	C2	C3	C4	C5	C6
α -D-Frup	δ	65.8	98.6	70.7	71.1	61.8	61.7
β -D-Frup	δ	64.5	98.7	68.2	70.3	69.8	64.0
α -D-Fruf	δ	63.5	105.0	82.6	76.6	81.9	61.7
β -D-Fruf	δ	63.3	102.1	76.0	75.1	81.3	63.0

D- Psicose

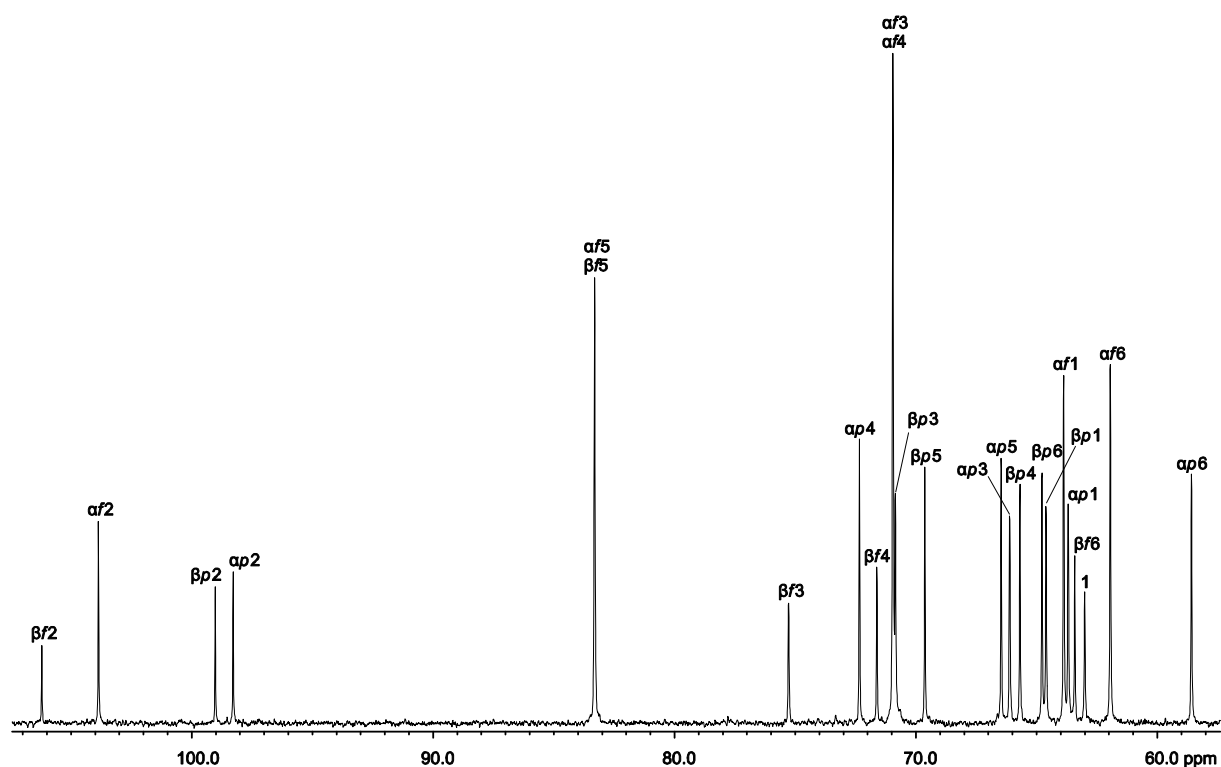


Figure 6.22. ^{13}C NMR spectrum in D_2O , referenced to an internal methanol signal (49.5 ppm).

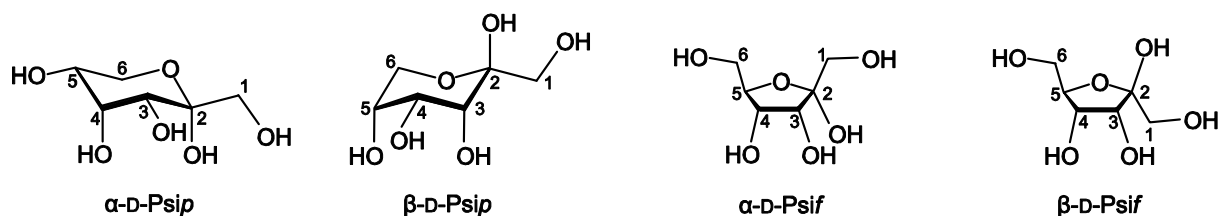


Table 6.23. ^{13}C NMR chemical shifts (δ/ppm) in D_2O , referenced to an internal methanol signal (49.5 ppm).

		C1	C2	C3	C4	C5	C6
$\alpha\text{-D-Psip}$	δ	63.7	98.3	66.1	72.3	66.5	58.6
$\beta\text{-D-Psip}$	δ	64.6	99.0	70.8	65.7	69.6	64.8
$\alpha\text{-D-Psif}$	δ	63.9	103.9	71.0	71.0	83.3	61.9
$\beta\text{-D-Psif}$	δ	63.0	106.2	75.3	71.6	83.3	63.4

L-Sorbose

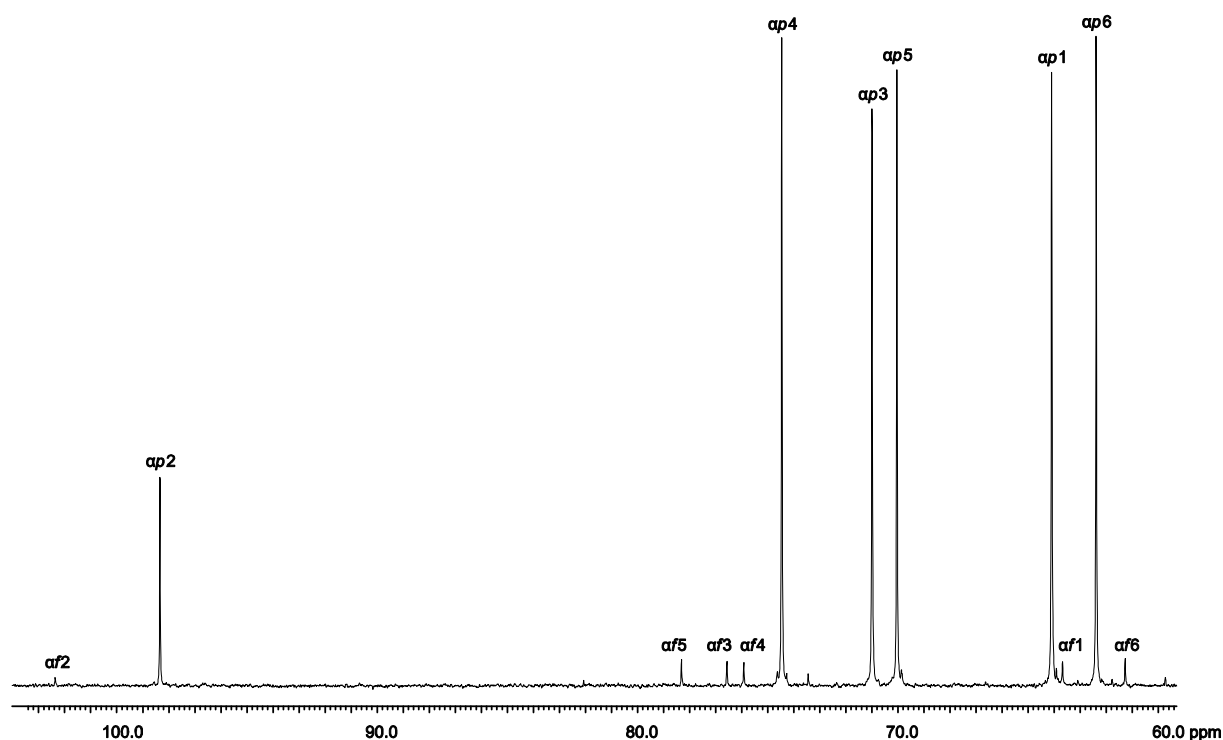


Figure 6.23. ^{13}C NMR spectrum in D_2O , referenced to an internal methanol signal (49.5 ppm).

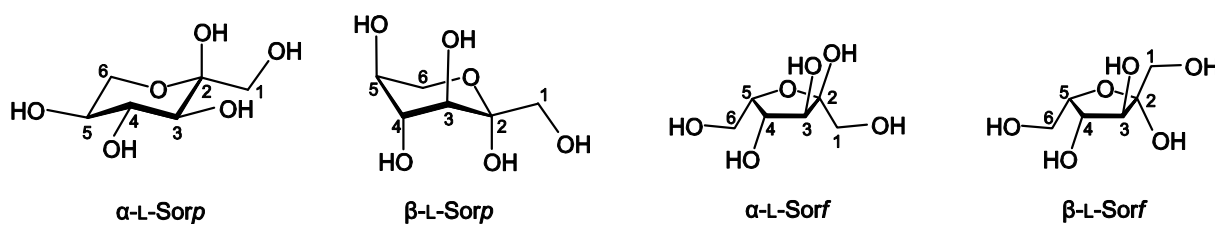


Table 6.24. ^{13}C NMR chemical shifts (δ/ppm) in D_2O , referenced to an internal methanol signal (49.5 ppm).

		C1	C2	C3	C4	C5	C6
$\alpha\text{-L-Sorp}$	δ	64.1	98.3	71.0	74.5	70.0	62.4
$\beta\text{-L-Sorp}$	δ	64.2	99.2	69.8	73.3	70.8	59.5
$\alpha\text{-L-Sorf}$	δ	63.7	102.4	76.6	75.9	78.3	61.3
$\beta\text{-L-Sorf}$	δ	63.2	106.0	81.9	73.9	80.8	61.8

D-Tagatose

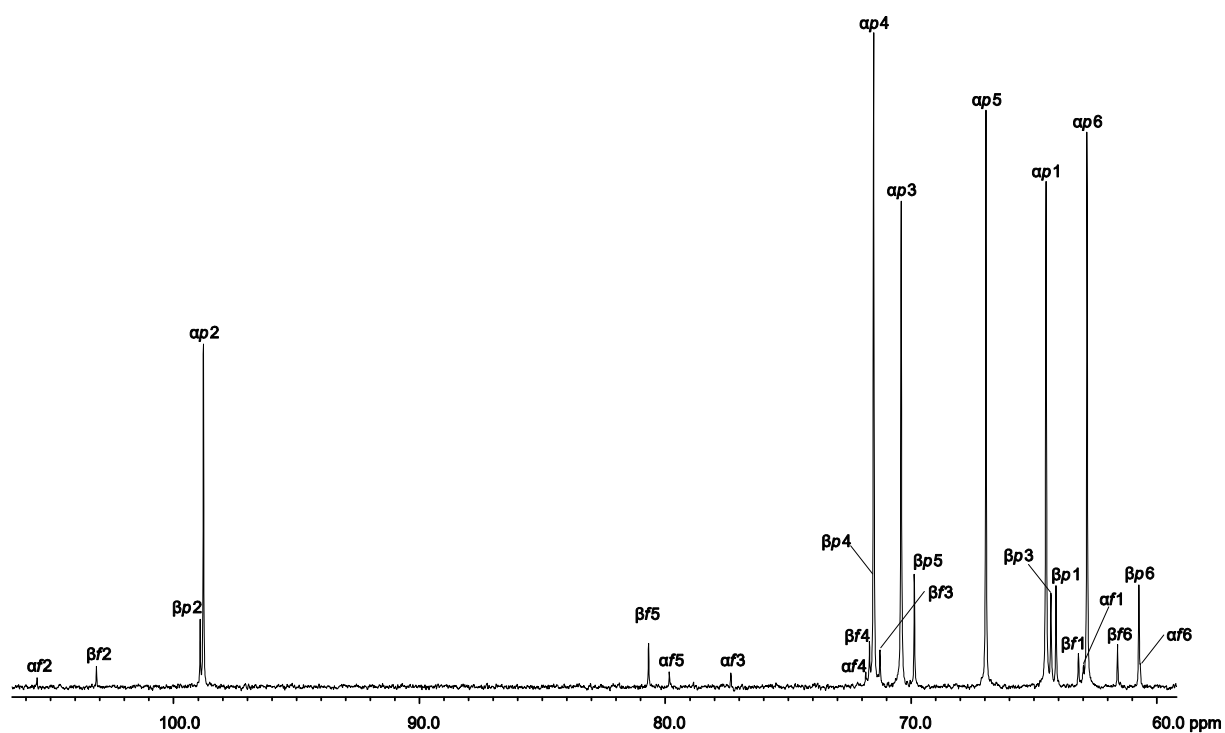


Figure 6.24. ^{13}C NMR spectrum in D_2O , referenced to an internal methanol signal (49.5 ppm).

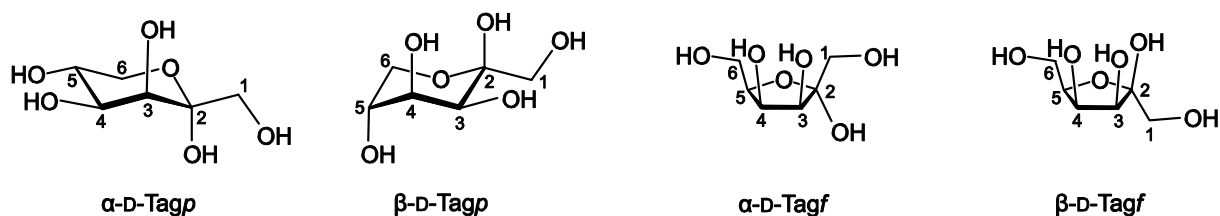


Table 6.25. ^{13}C NMR chemical shifts (δ/ppm) in D_2O , referenced to an internal methanol signal (49.5 ppm).

		C1	C2	C3	C4	C5	C6
$\alpha\text{-D-Tagp}$	δ	64.5	98.8	70.4	71.5	67.0	62.8
$\beta\text{-D-Tagp}$	δ	64.1	98.9	64.3	71.5	69.9	60.7
$\alpha\text{-D-Tagf}$	δ	63.0	105.6	77.3	71.8	79.8	60.7
$\beta\text{-D-Tagf}$	δ	63.2	103.1	71.3	71.7	80.7	61.6

6 Appendix

D-Sucrose

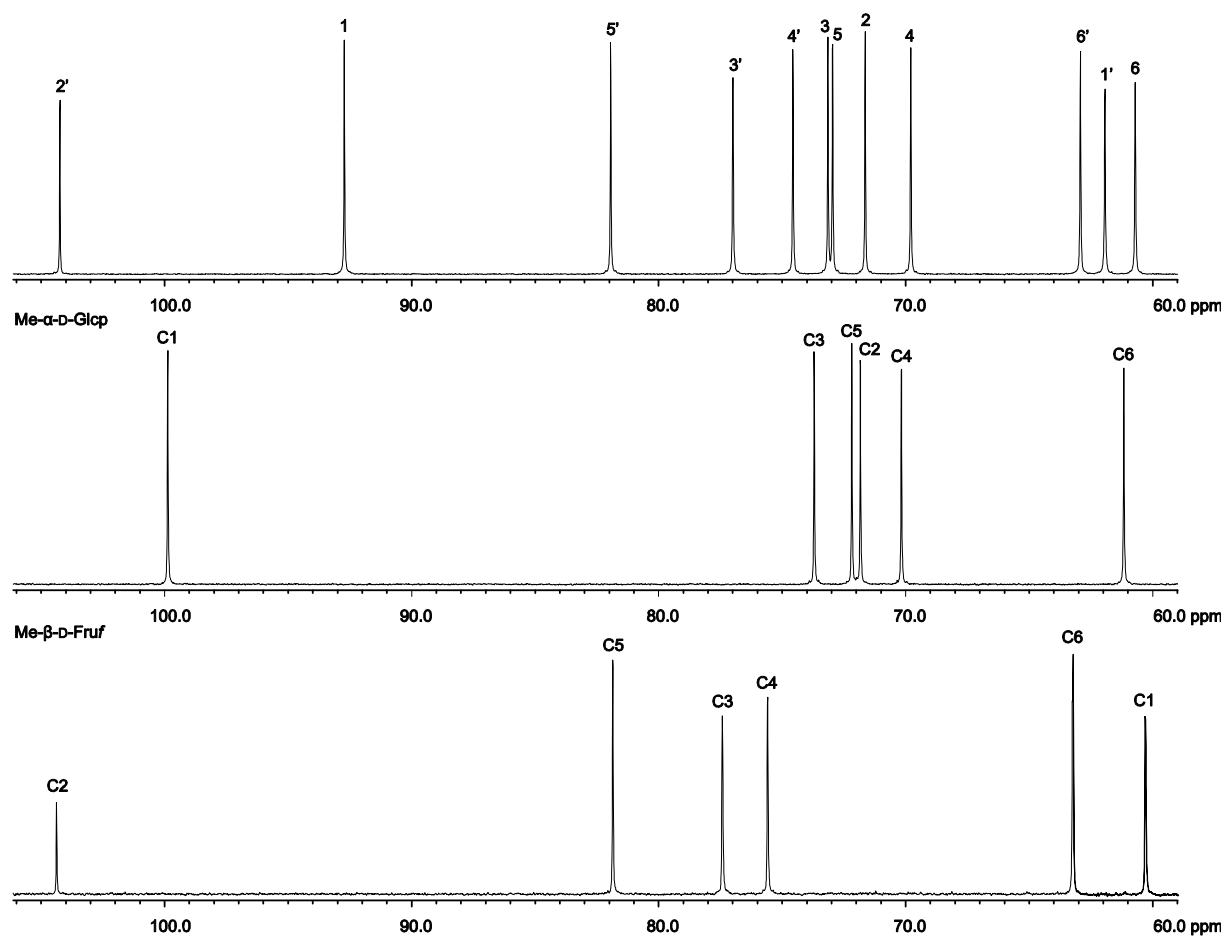


Figure 6.25. ^{13}C NMR spectrum in D_2O , referenced to an internal methanol signal (49.5 ppm).

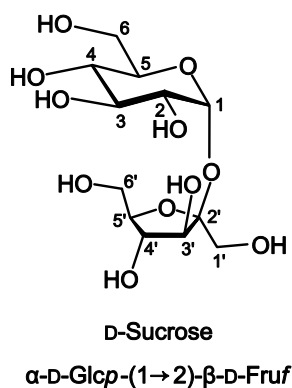


Table 6.26. ^{13}C NMR chemical shifts (δ/ppm) in D_2O , referenced to an internal methanol signal (49.5 ppm).

		C1	C2	C3	C4	C5	C6
$\alpha\text{-D-Glcp}$	δ	92.7	71.6	73.1	69.8	73.0	60.7
$\beta\text{-D-Fruf}(C')$	δ	61.9	104.2	77.0	74.6	81.9	62.9

6 Appendix

D-Turanose

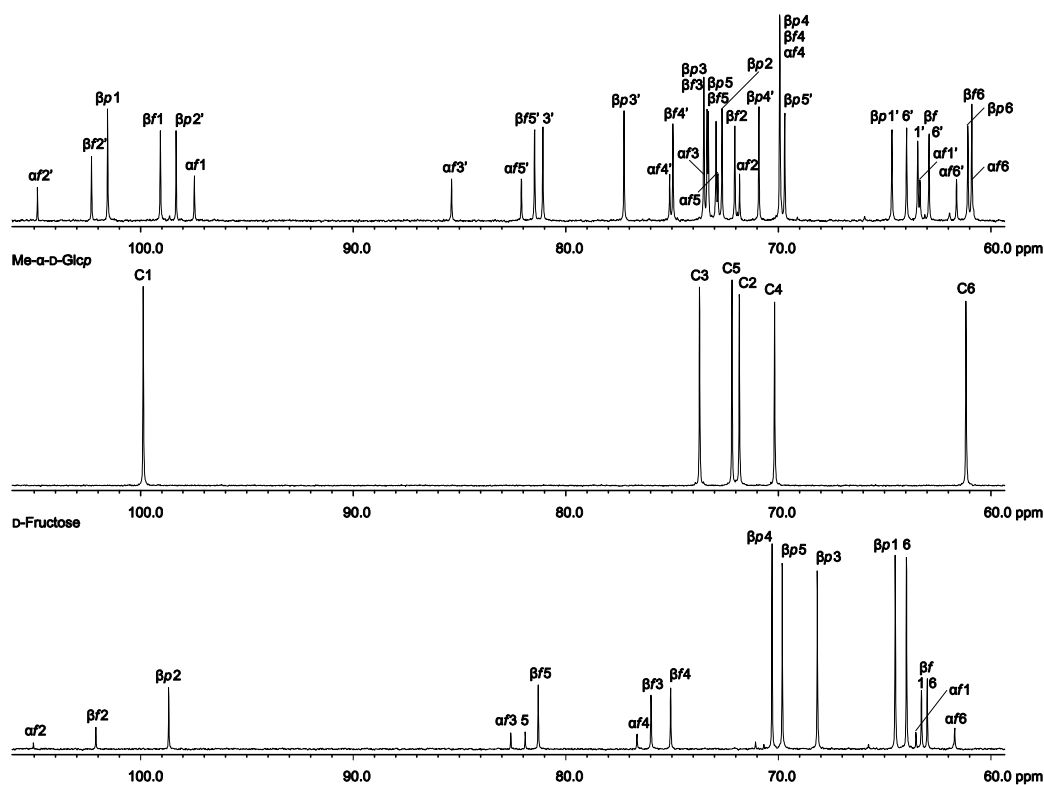


Figure 6.26. ¹³C NMR spectrum in D₂O, referenced to an internal methanol signal (49.5 ppm).

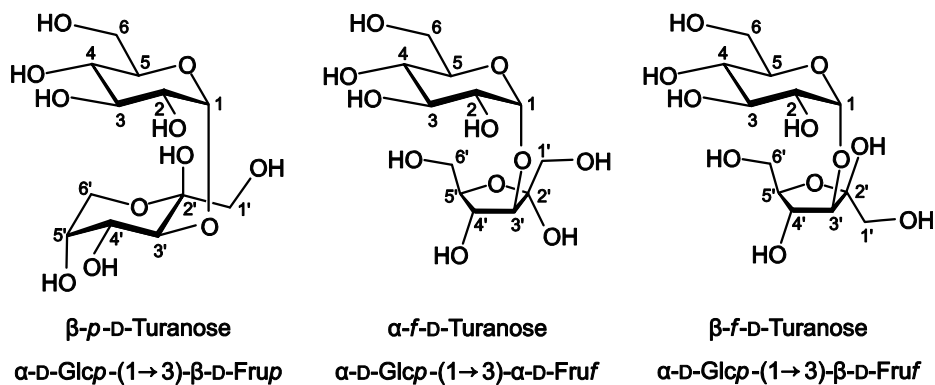


Table 6.27. ¹³C NMR chemical shifts (δ /ppm) in D₂O, referenced to an internal methanol signal (49.5 ppm).

		C1	C2	C3	C4	C5	C6
α -D-Glcp	δ	101.5	72.7	73.4	69.9	73.3	61.1
β -D-Frup (C')	δ	64.7	98.3	77.3	70.9	69.7	64.0
α -D-Glcp	δ	97.5	71.8	73.5	69.9	72.8	60.9
α -D-Fruf (C')	δ	63.3	104.8	85.4	75.1	82.1	61.6
α -D-Glcp	δ	99.1	72.0	73.5	69.9	72.9	60.9
β -D-Fruf (C')	δ	63.4	102.3	81.1	75.0	81.5	62.9

6 Appendix

D-Maltulose

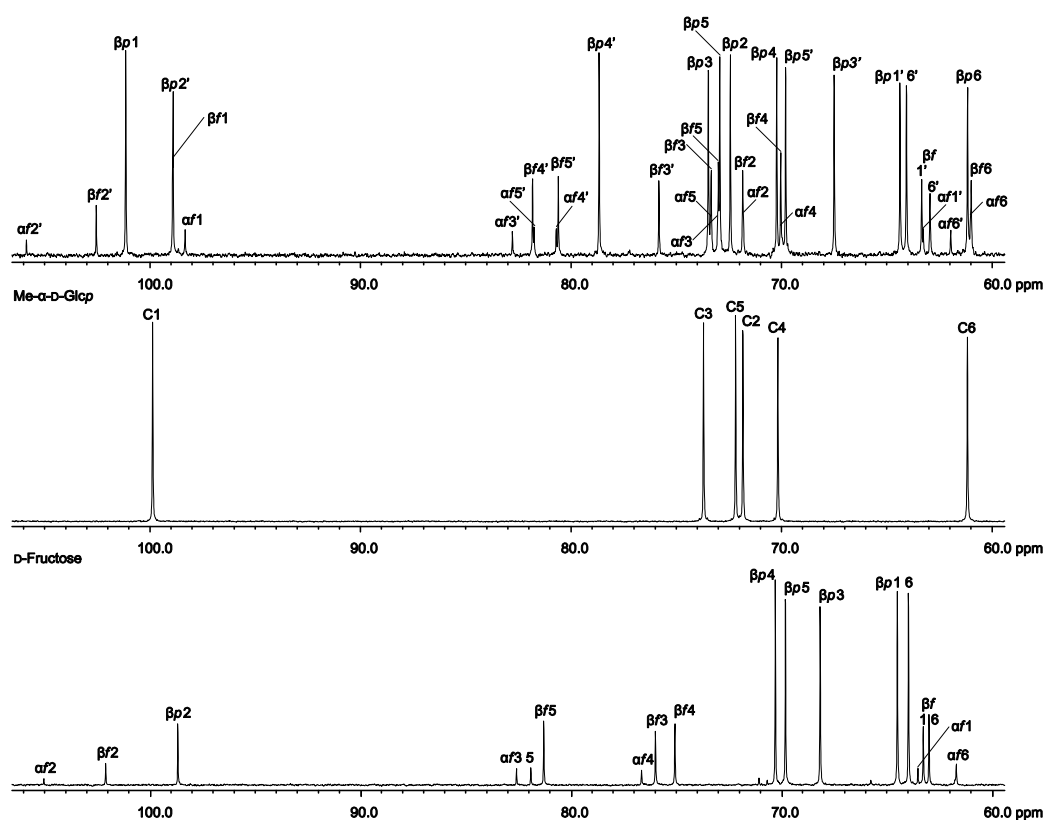


Figure 6.27. ^{13}C NMR spectrum in D_2O , referenced to an internal methanol signal (49.5 ppm).

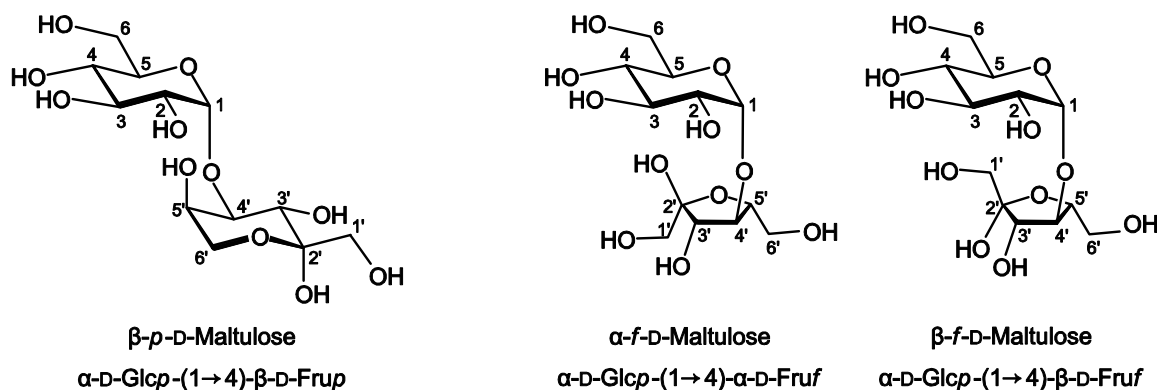


Table 6.28. ^{13}C NMR chemical shifts (δ /ppm) in D_2O , referenced to an internal methanol signal (49.5 ppm).

		C1	C2	C3	C4	C5	C6
α -D-Glcp	δ	101.1	72.4	73.5	70.2	72.9	61.2
β -D-Frup (C')	δ	64.4	98.9	67.5	78.7	69.8	64.0
α -D-Glcp	δ	98.3	71.8	73.3	70.0	73.0	61.0
α -D-Fruf (C')	δ	63.3	105.9	82.8	80.7	81.7	62.0
α -D-Glcp	δ	98.9	71.8	73.3	70.0	73.0	61.0
β -D-Fruf (C')	δ	63.3	102.6	75.8	81.8	80.6	63.0

6 Appendix

D-Lactulose

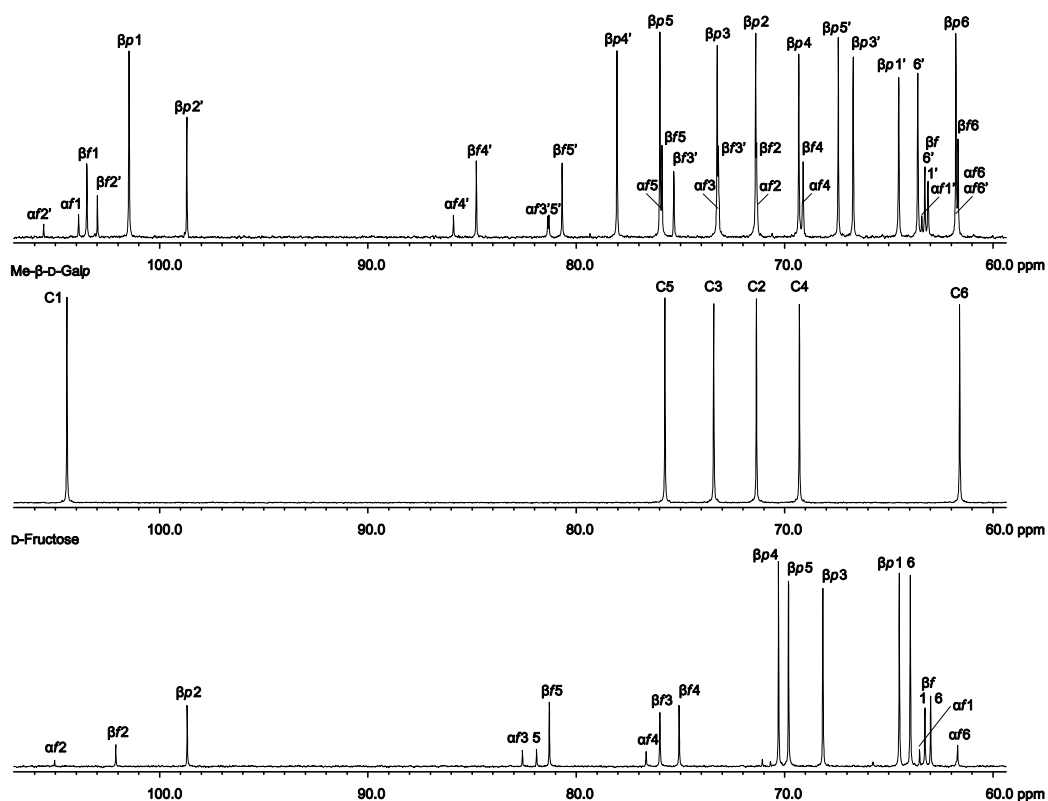


Figure 6.28. ^{13}C NMR spectrum in D_2O , referenced to an internal methanol signal (49.5 ppm).

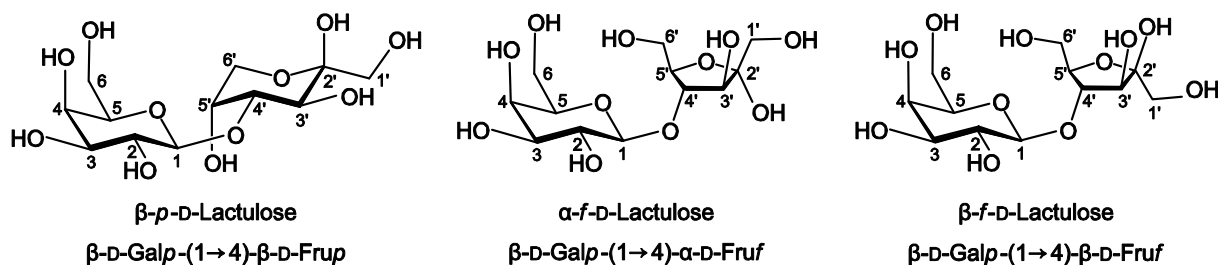


Table 6.29. ^{13}C NMR chemical shifts (δ /ppm) in D_2O , referenced to an internal methanol signal (49.5 ppm).

		C1	C2	C3	C4	C5	C6
β -D-Galp	δ	101.5	71.4	73.2	69.3	76.0	61.8
β -D-Frup (C')	δ	64.5	98.7	66.7	78.0	67.4	63.6
β -D-Galp	δ	103.9	71.3	73.2	69.1	75.9	61.7
α -D-Fruf (C')	δ	63.4	105.6	81.4	85.9	81.3	61.8
β -D-Galp	δ	103.5	71.3	73.2	69.1	75.9	61.7
β -D-Fruf (C')	δ	63.1	103.0	75.3	84.8	80.7	63.3

6 Appendix

D-Leucrose

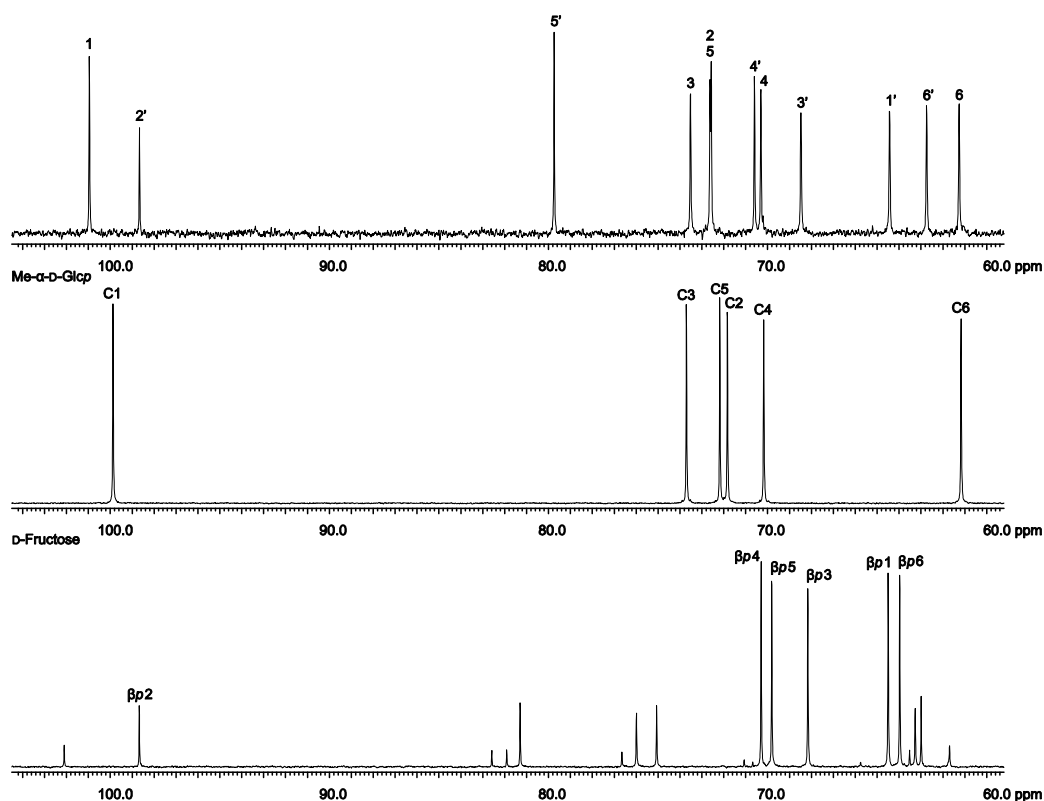


Figure 6.29. ^{13}C NMR spectrum in D_2O , referenced to an internal methanol signal (49.5 ppm).

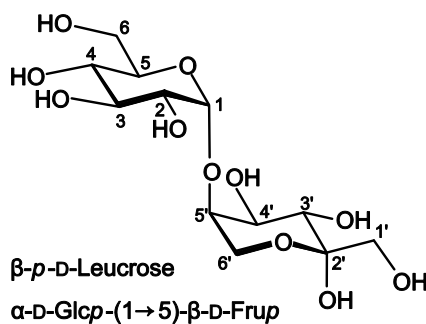


Table 6.30. ^{13}C NMR chemical shifts (δ /ppm) in D_2O , referenced to an internal methanol signal (49.5 ppm).

		C1	C2	C3	C4	C5	C6
α -D-Glcp	δ	101.0	72.6	73.5	70.3	72.6	61.3
β -D-Frup (C')	δ	64.4	98.7	68.5	70.6	79.7	62.7

D-Palatinose

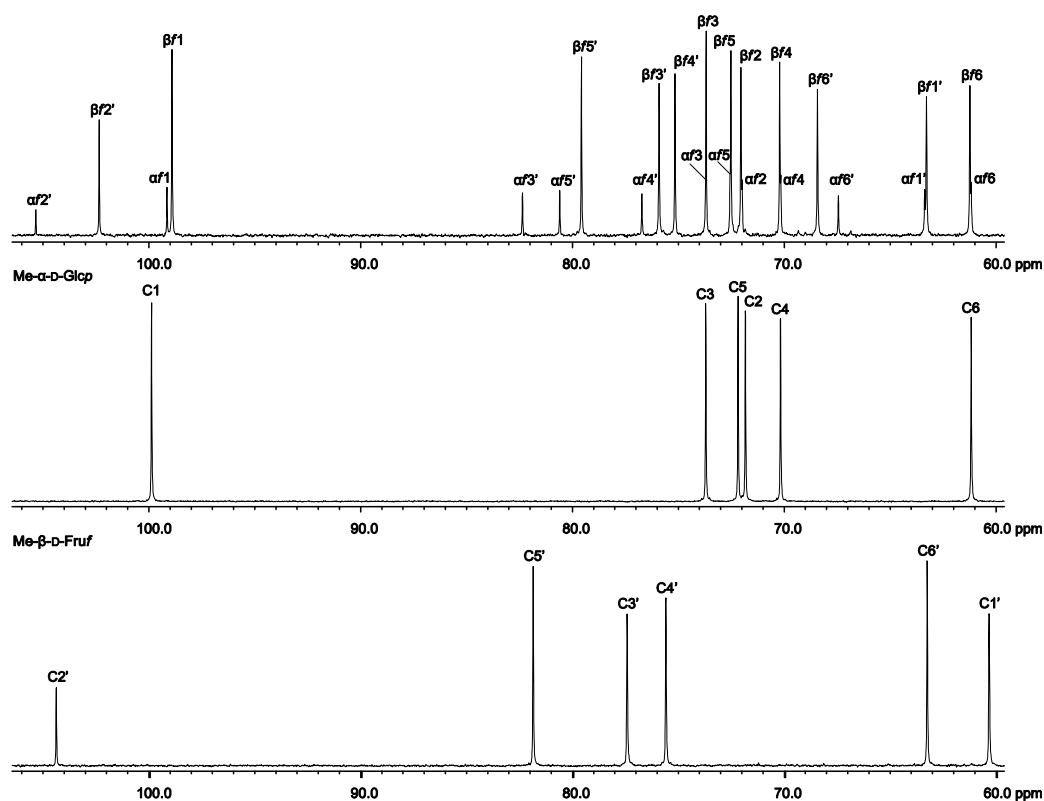


Figure 6.30. ^{13}C NMR spectrum in D_2O , referenced to an internal methanol signal (49.5 ppm).

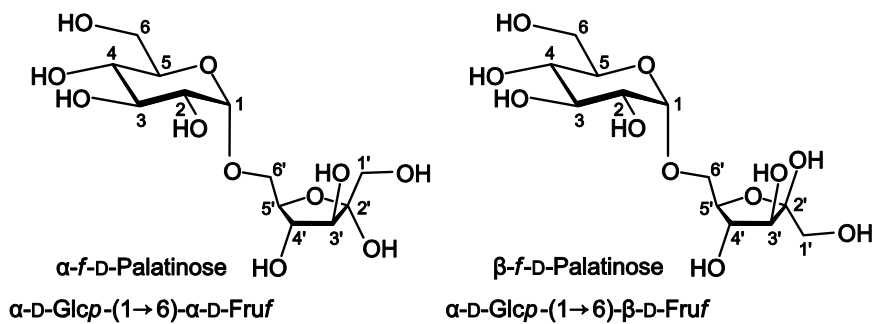


Table 6.31. ^{13}C NMR chemical shifts (δ/ppm) in D_2O , referenced to an internal methanol signal (49.5 ppm).

		C1	C2	C3	C4	C5	C6
$\alpha\text{-D-Glcp}$	δ	99.1	72.0	73.7	70.2	72.5	61.2
$\alpha\text{-D-Fruf}(C')$	δ	63.4	105.3	82.4	76.7	80.6	67.4
$\alpha\text{-D-Glcp}$	δ	98.9	72.0	73.7	70.2	72.5	61.2
$\beta\text{-D-Fruf}(C')$	δ	63.3	102.4	75.9	75.2	79.6	68.4

D-Melicitose

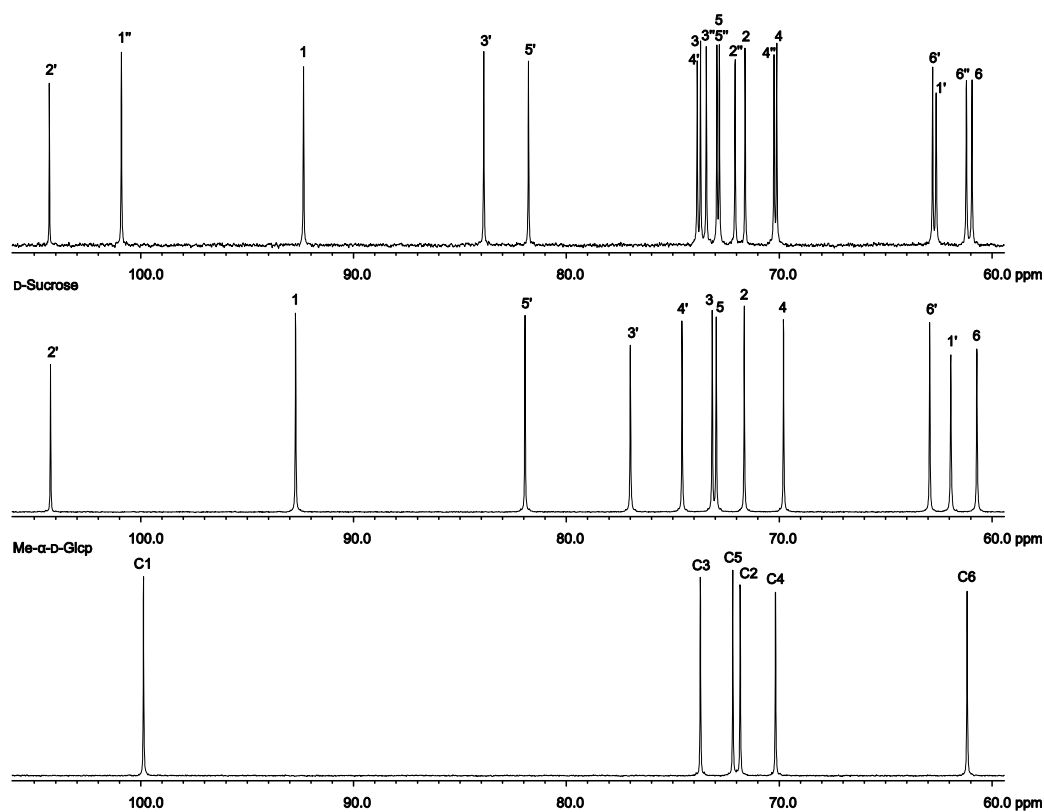


Figure 6.31. ^{13}C NMR spectrum in D_2O , referenced to an internal methanol signal (49.5 ppm).

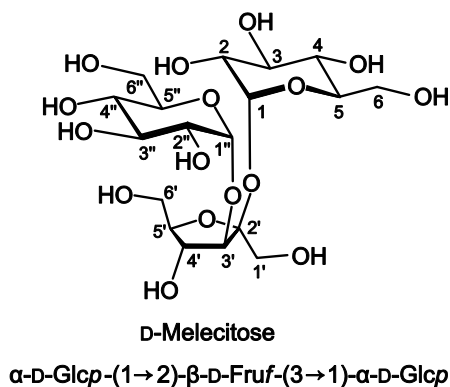


Table 6.32. ^{13}C NMR chemical shifts (δ/ppm) in D_2O , referenced to an internal methanol signal (49.5 ppm).

		C1	C2	C3	C4	C5	C6
$\alpha\text{-D-Glcp}$	δ	92.4	71.6	73.7	70.2	72.9	60.9
$\beta\text{-D-Fruf}$ (C')	δ	62.6	104.3	83.9	73.9	81.8	62.8
$\alpha\text{-D-Glcp}$ (C'')	δ	100.9	72.1	73.4	70.2	72.9	61.2

6 Appendix

D-Raffinose

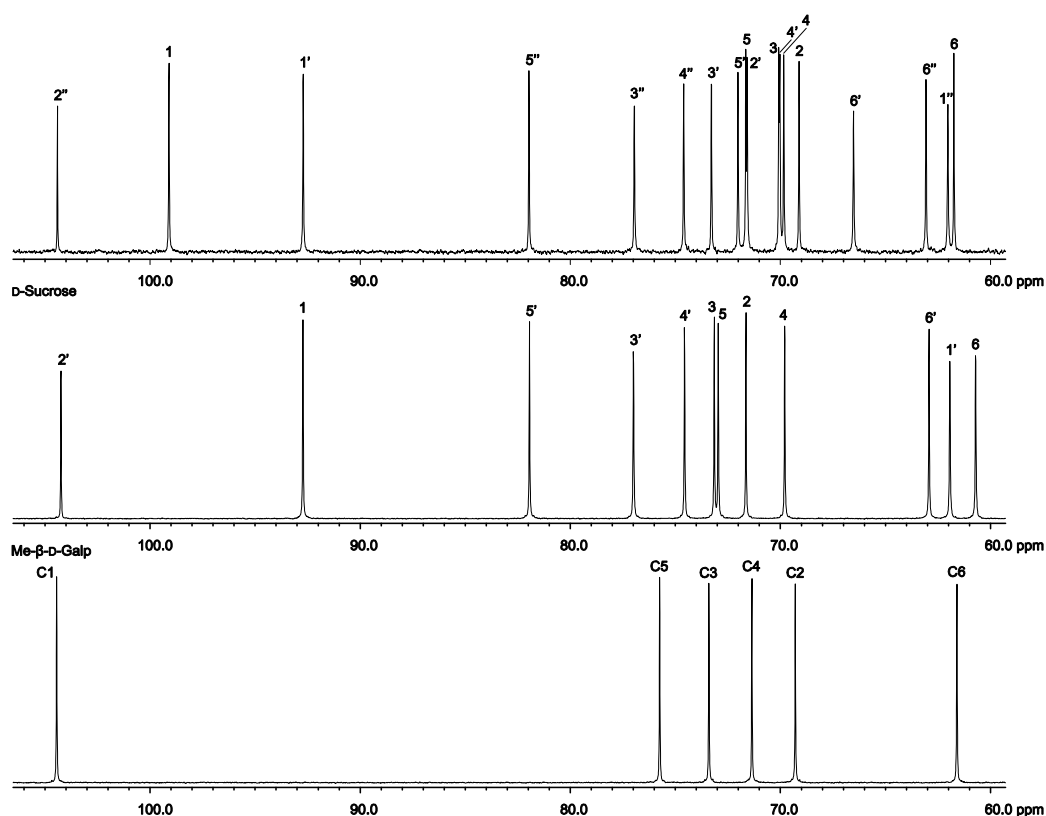


Figure 6.32. ^{13}C NMR spectrum in D_2O , referenced to an internal methanol signal (49.5 ppm).

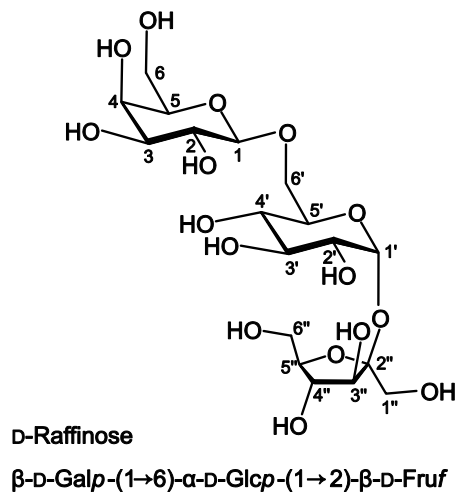


Table 6.33. ^{13}C NMR chemical shifts (δ/ppm) in D_2O , referenced to an internal methanol signal (49.5 ppm).

		C1	C2	C3	C4	C5	C6
$\alpha\text{-D-Galp}$	δ	99.1	69.1	70.1	69.8	71.6	61.7
$\alpha\text{-D-Glcp}$ (C')	δ	92.7	71.6	73.3	70.0	72.0	66.5
$\beta\text{-D-Fruf}$ (C'')	δ	62.0	104.4	77.0	74.6	82.0	63.1

6 Appendix

α,α -D-Trehalose

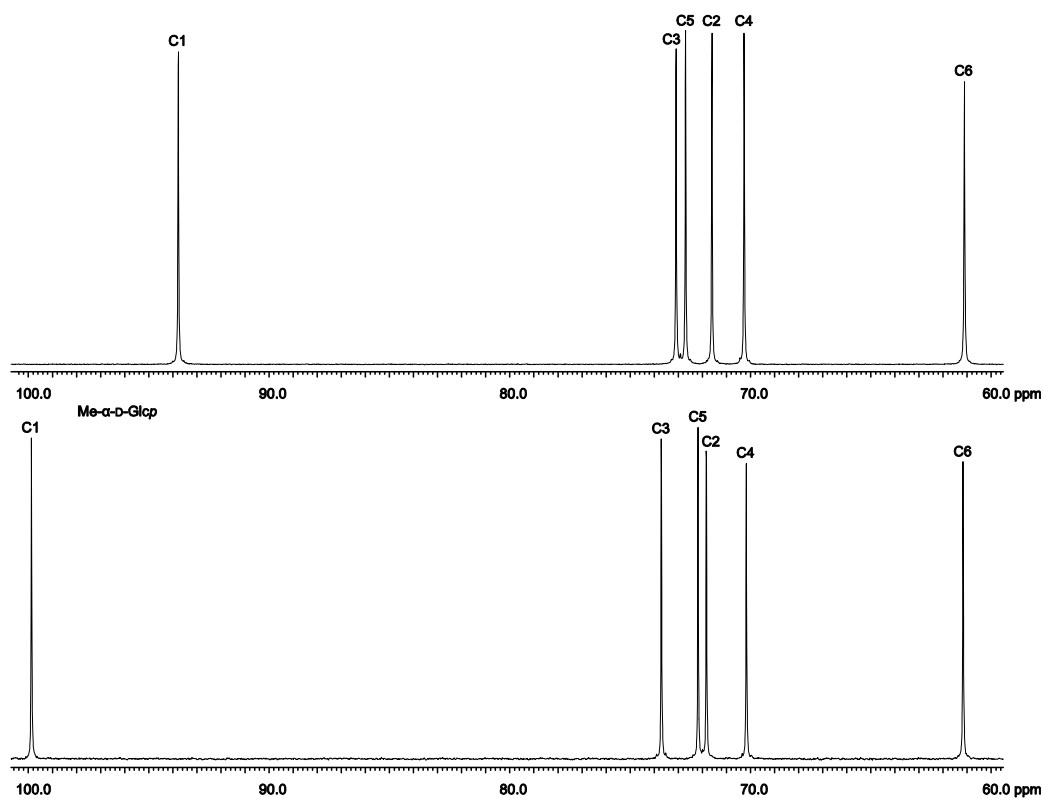


Figure 6.33. ^{13}C NMR spectrum in D_2O , referenced to an internal methanol signal (49.5 ppm).

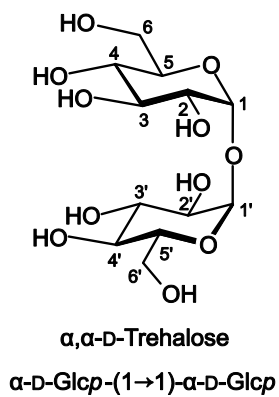


Table 6.34. ^{13}C NMR chemical shifts (δ/ppm) in D_2O , referenced to an internal methanol signal (49.5 ppm).

		C1	C2	C3	C4	C5	C6
$\alpha\text{-D-Glcp}$	δ	93.8	71.6	73.1	70.3	72.7	61.1

D-Melibiose

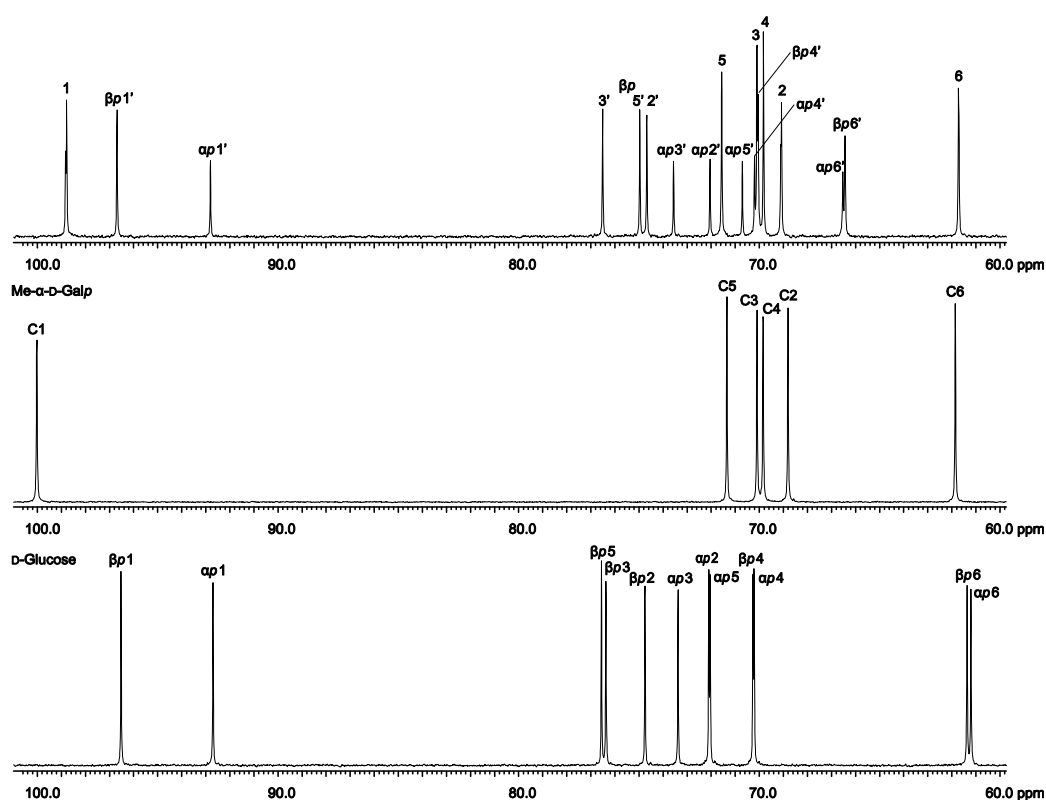


Figure 6.34. ^{13}C NMR spectrum in D_2O , referenced to an internal methanol signal (49.5 ppm).

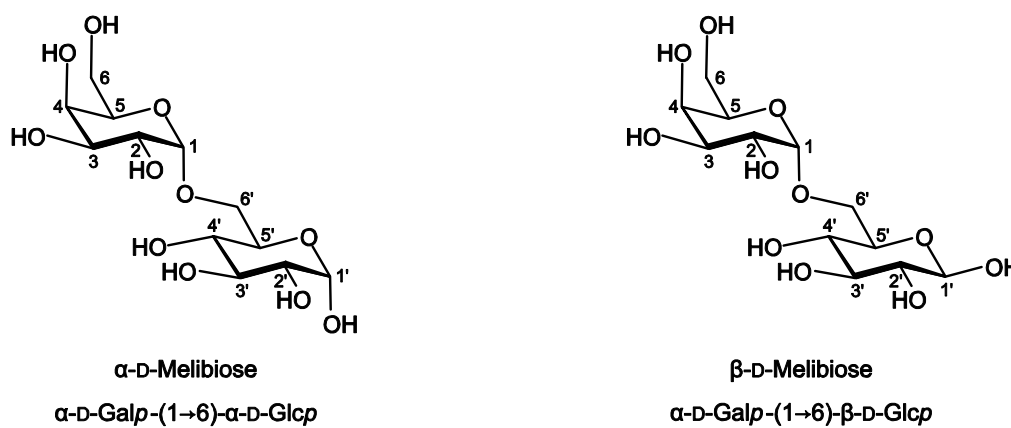


Table 6.35. ^{13}C NMR chemical shifts (δ/ppm) in D_2O , referenced to an internal methanol signal (49.5 ppm).

		C1	C2	C3	C4	C5	C6
α -D-Galp	δ	98.8	69.1	70.1	69.8	71.6	61.7
α -D-Glcp (C')	δ	92.8	72.0	73.6	70.2	70.7	66.5
α -D-Galp	δ	98.8	69.1	70.1	69.8	71.6	61.7
β -D-Glcp (C')	δ	96.7	74.7	76.5	70.0	75.0	66.4

D-Lactose

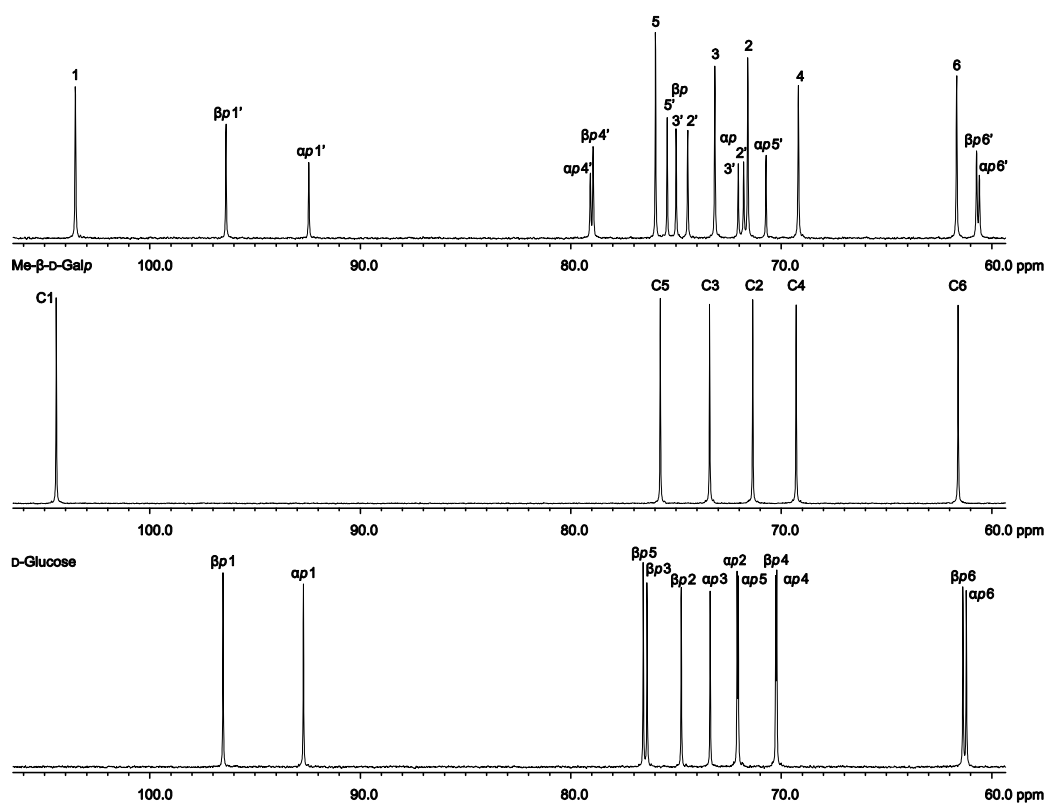


Figure 6.35. ¹³C NMR spectrum in D₂O, referenced to an internal methanol signal (49.5 ppm).

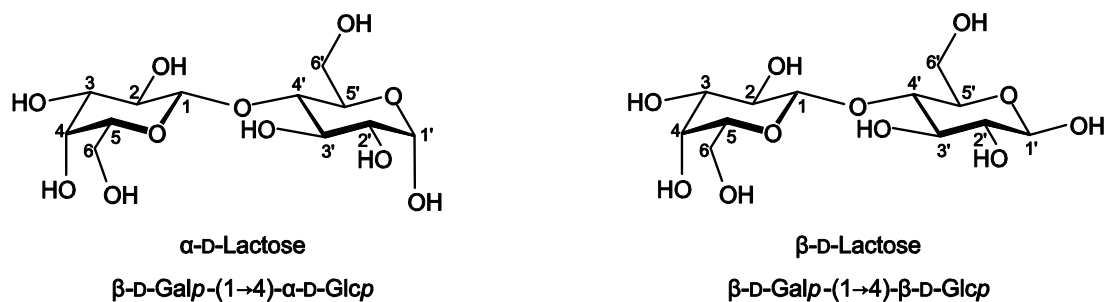


Table 6.36. ¹³C NMR chemical shifts (δ /ppm) in D₂O, referenced to an internal methanol signal (49.5 ppm).

		C1	C2	C3	C4	C5	C6
β-D-Galp	δ	103.5	71.6	73.2	69.2	76.0	61.7
α-D-Glcp (C')	δ	92.4	71.8	72.0	79.1	70.7	60.6
β-D-Galp	δ	103.5	71.6	73.2	69.2	76.0	61.7
β-D-Glcp (C')	δ	96.4	74.4	75.0	78.9	75.4	60.7

D-Cellobiose

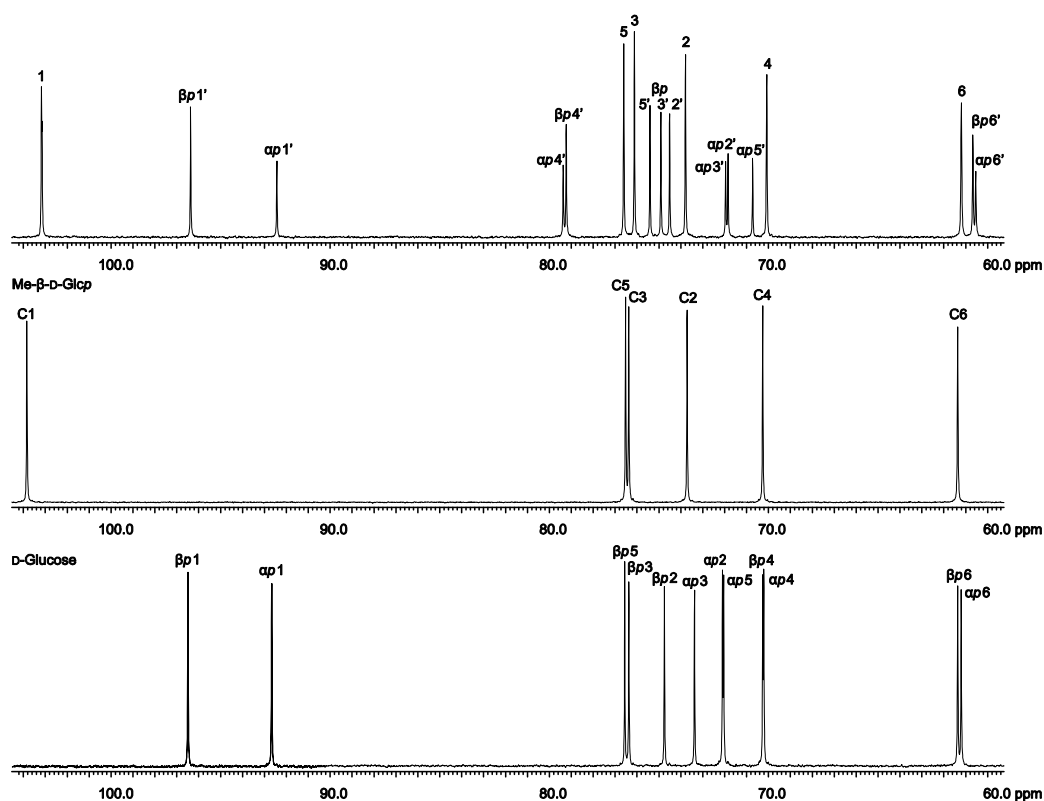


Figure 6.36. ^{13}C NMR spectrum in D_2O , referenced to an internal methanol signal (49.5 ppm).

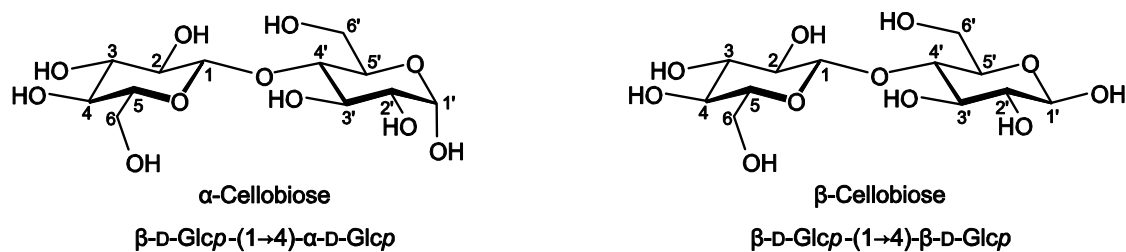


Table 6.37. ^{13}C NMR chemical shifts (δ /ppm) in D_2O , referenced to an internal methanol signal (49.5 ppm).

		C1	C2	C3	C4	C5	C6
β -D-Glcp	δ	103.2	73.8	76.1	70.1	76.6	61.2
α -D-Glcp (C')	δ	92.4	71.8	72.0	79.4	70.7	60.5
β -D-Glcp	δ	103.2	73.8	76.1	70.1	76.6	61.2
β -D-Glcp (C')	δ	96.4	74.5	74.9	79.2	75.4	60.7

D-Maltose

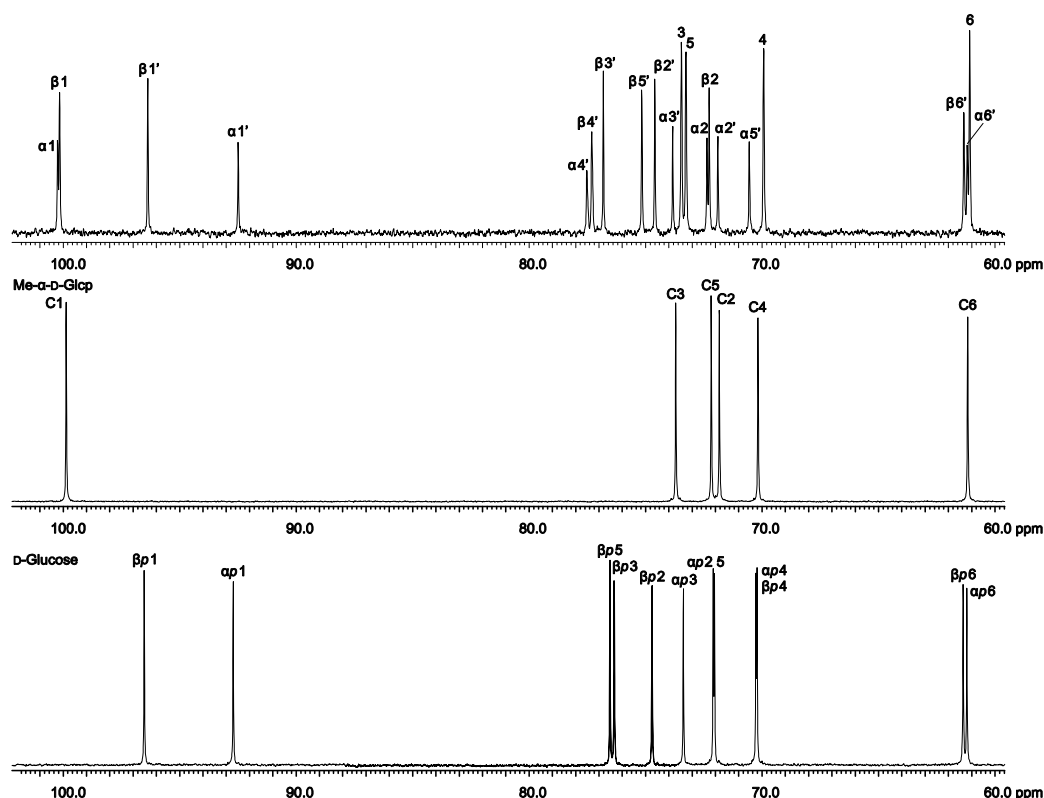


Figure 6.37. ^{13}C NMR spectrum in D_2O , referenced to an internal methanol signal (49.5 ppm).

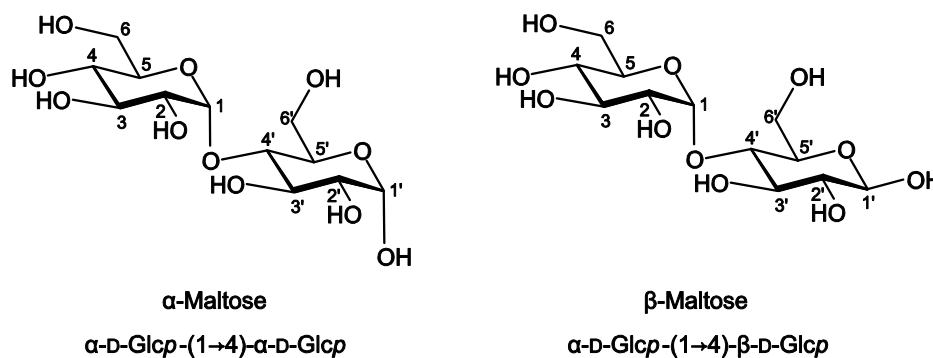


Table 6.38. ^{13}C NMR chemical shifts (δ/ppm) in D_2O , referenced to an internal methanol signal (49.5 ppm).

		C1	C2	C3	C4	C5	C6
α -D-Glcp	δ	100.2	72.4	73.5	69.9	73.3	61.1
α -D-Glcp (C')	δ	92.5	71.9	73.8	77.5	70.6	61.2
α -D-Glcp	δ	100.2	72.3	73.5	69.9	73.3	61.1
β -D-Glcp (C')	δ	96.4	74.6	76.8	77.3	75.2	61.3

D-Maltotriose

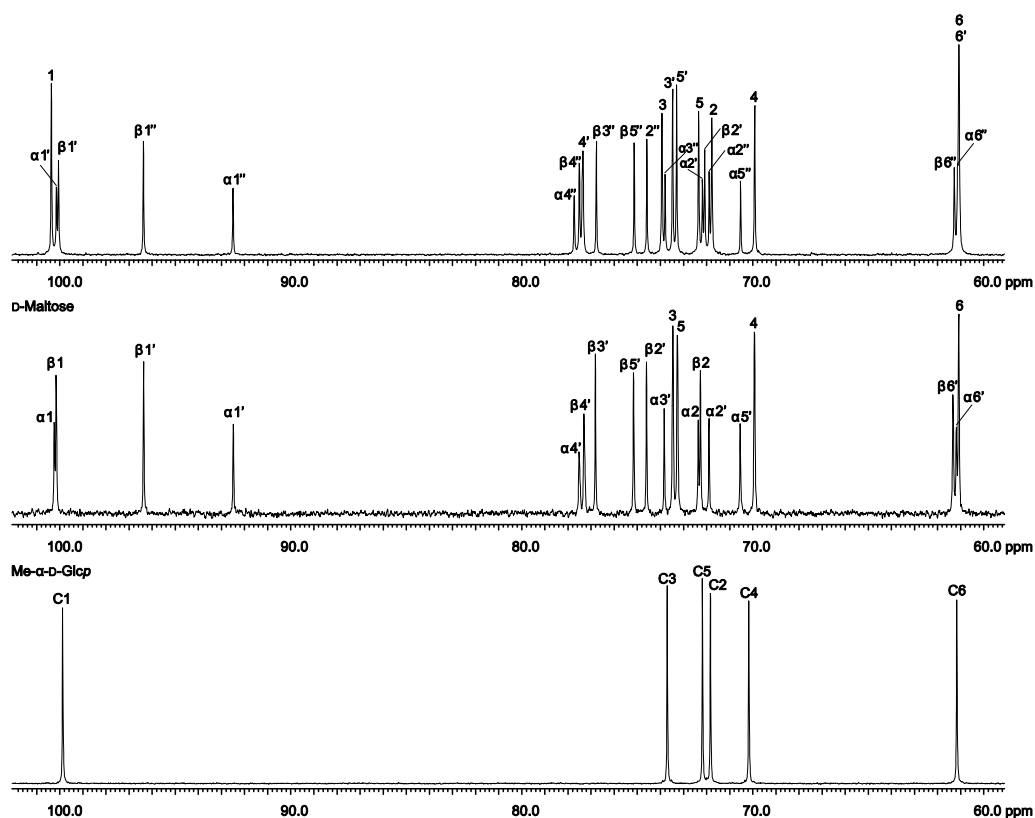


Figure 6.38. ^{13}C NMR spectrum in D_2O , referenced to an internal methanol signal (49.5 ppm).

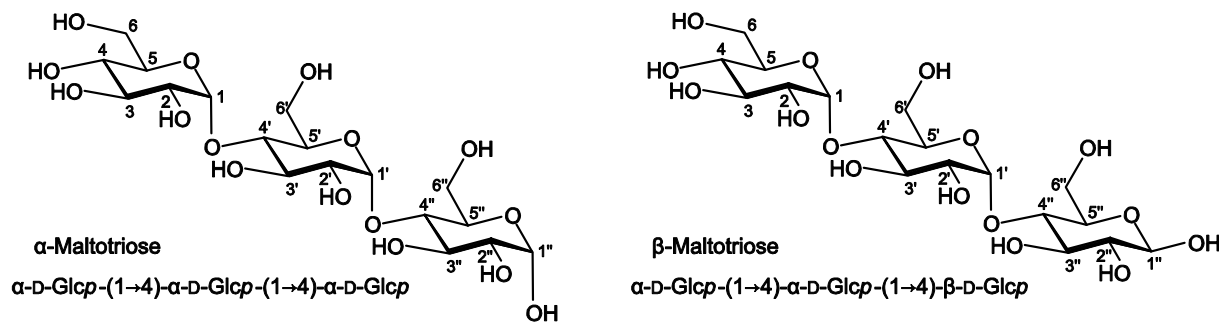


Table 6.39. ^{13}C NMR chemical shifts (δ/ppm) in D_2O , referenced to an internal methanol signal (49.5 ppm).

		C1	C2	C3	C4	C5	C6
$\alpha\text{-D-Glcp}$	δ	100.4	71.8	73.9	69.9	72.3	61.1
$\alpha\text{-D-Glcp (C')}$	δ	100.2	72.2	73.5	77.4	73.3	61.1
$\alpha\text{-D-Glcp (C'')$	δ	92.5	71.9	73.8	77.7	70.5	61.1
$\alpha\text{-D-Glcp}$	δ	100.4	71.8	73.9	69.9	72.3	61.1
$\alpha\text{-D-Glcp (C')}$	δ	100.1	72.1	73.5	77.4	73.3	61.1
$\beta\text{-D-Glcp (C'')$	δ	96.4	74.6	76.8	77.5	75.1	61.3

D-Maltoheptaose

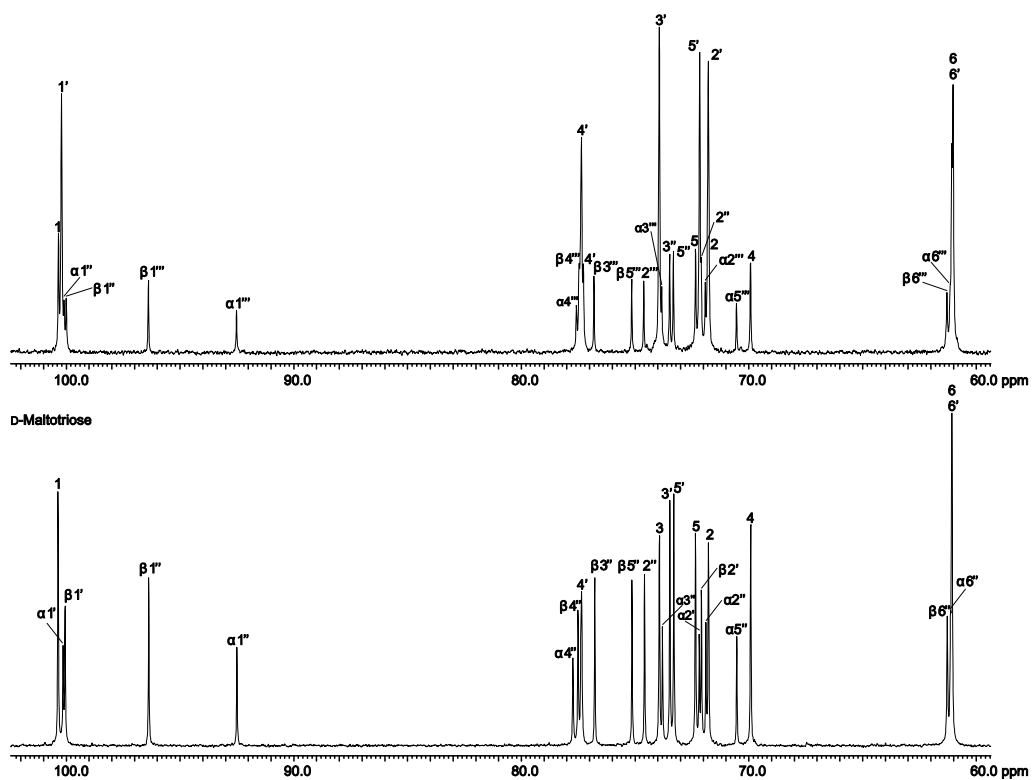
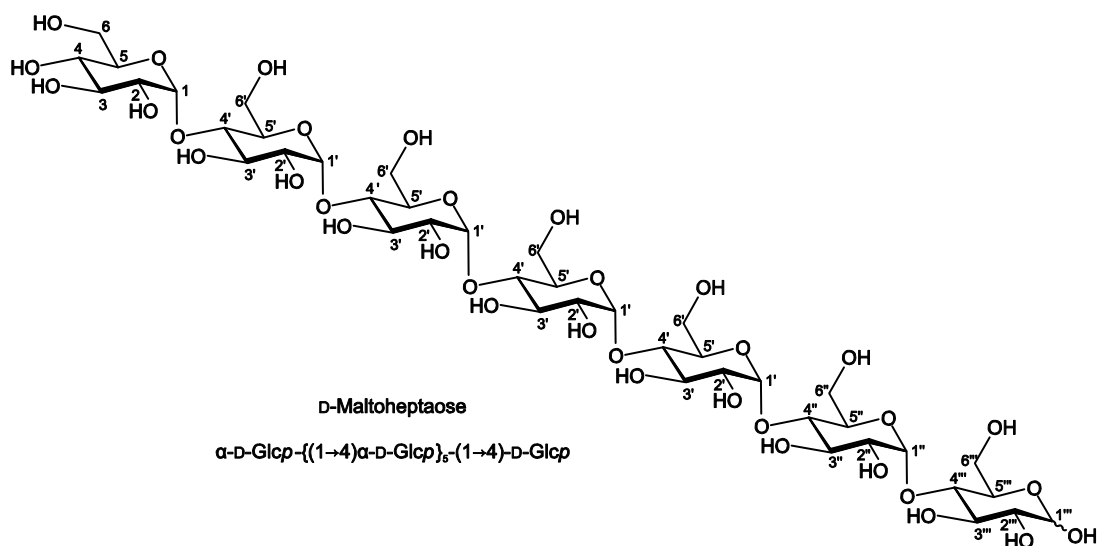


Figure 6.39. ^{13}C NMR spectrum in D_2O , referenced to an internal methanol signal (49.5 ppm).



6 Appendix

Table 6.40. ^{13}C NMR chemical shifts (δ/ppm) in D_2O , referenced to an internal methanol signal (49.5 ppm).

		C1	C2	C3	C4	C5	C6
$\alpha\text{-D-Glcp}$	δ	100.3	71.8	73.9	69.9	72.3	61.1
$\alpha\text{-D-Glcp}$ (5 C')	δ	100.2	71.8	73.9	77.3	72.2	61.0
$\alpha\text{-D-Glcp}$ (C'')	δ	100.1	72.2	73.5	77.3	73.3	61.1
$\alpha\text{-D-Glcp}$ (C''')	δ	92.5	71.9	73.8	77.6	70.5	61.1
$\alpha\text{-D-Glcp}$	δ	100.3	71.8	73.9	69.9	72.3	61.1
$\alpha\text{-D-Glcp}$ (5 C')	δ	100.2	71.8	73.9	77.3	72.2	61.0
$\alpha\text{-D-Glcp}$ (C'')	δ	100.0	72.2	73.5	77.3	73.3	61.1
$\beta\text{-D-Glcp}$ (C''')	δ	96.4	74.6	76.8	77.5	75.1	61.3

6.2 Packing diagrams of the crystal structures

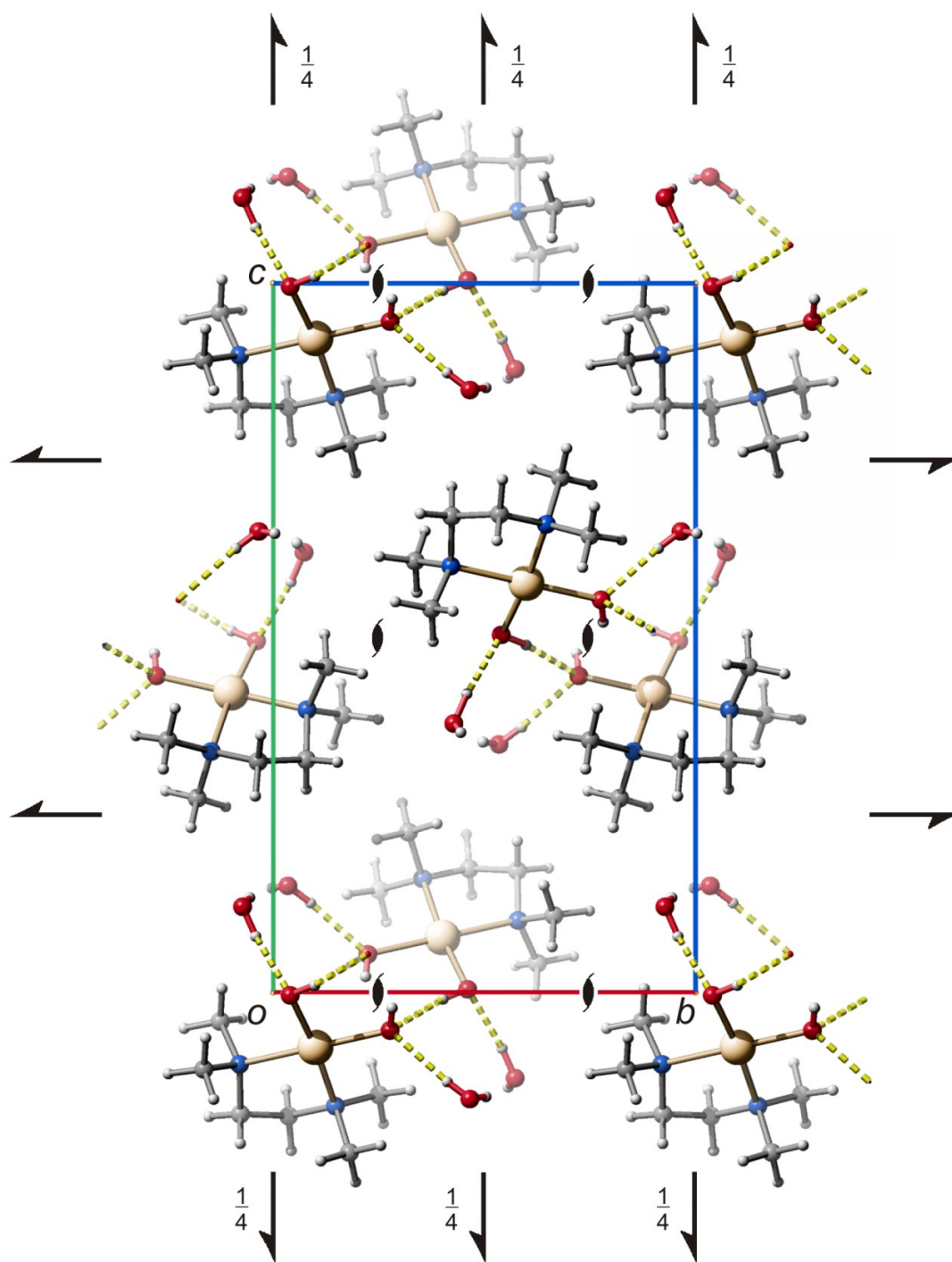


Figure 6.40. SCHAKAL packing diagram of $[\text{Pd}(\text{tmen})(\text{OH})_2]$ in crystals of the dihydrate (**1**) viewed along $[\bar{1}00]$. Hydrogen bonds are indicated by yellow dashed lines. The symmetry elements of the space group $P 2_1 2_1 2_1$ are overlaid. Atoms: carbon (grey), hydrogen (light grey, small), nitrogen (blue), oxygen (red) and palladium (golden).

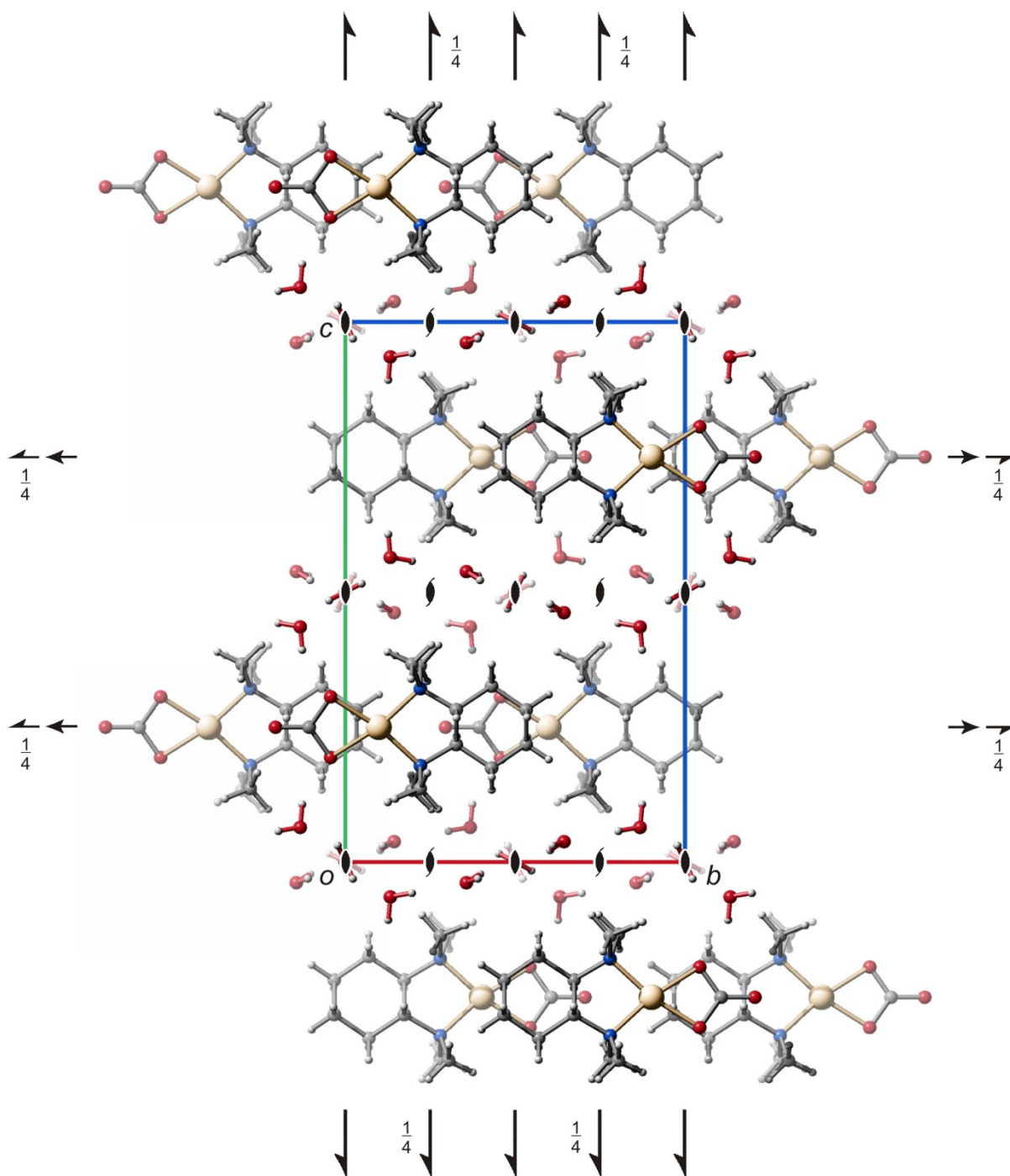


Figure 6.41. SCHAKAL packing diagram of $[\text{Pd}(\text{tmchxn})(\text{CO}_3)]$ in crystals of the 6-hydrate (**2**) viewed along $[\bar{1}00]$. The symmetry elements of the space group $C222_1$ are overlaid. Atoms: carbon (grey), hydrogen (light grey, small), nitrogen (blue), oxygen (red) and palladium (golden).

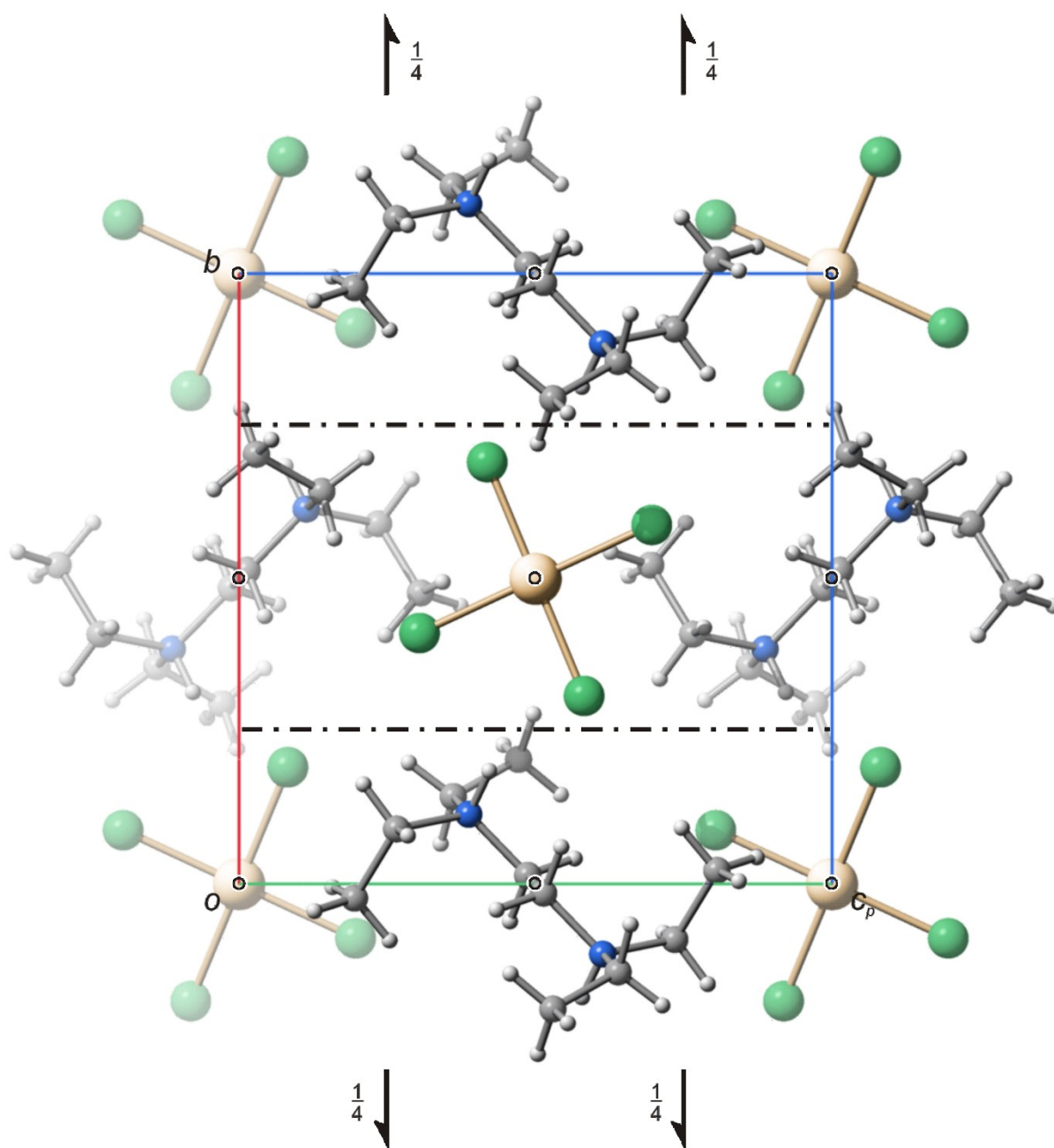


Figure 6.42. SCHAKAL packing diagram of $[(teenH_2)PdCl_4]$ (3) viewed along $[100]$. The symmetry elements of the space group $P2_1/n$ are overlaid. Atoms: carbon (grey), hydrogen (light grey, small), nitrogen (blue), chloride (green) and palladium (golden).

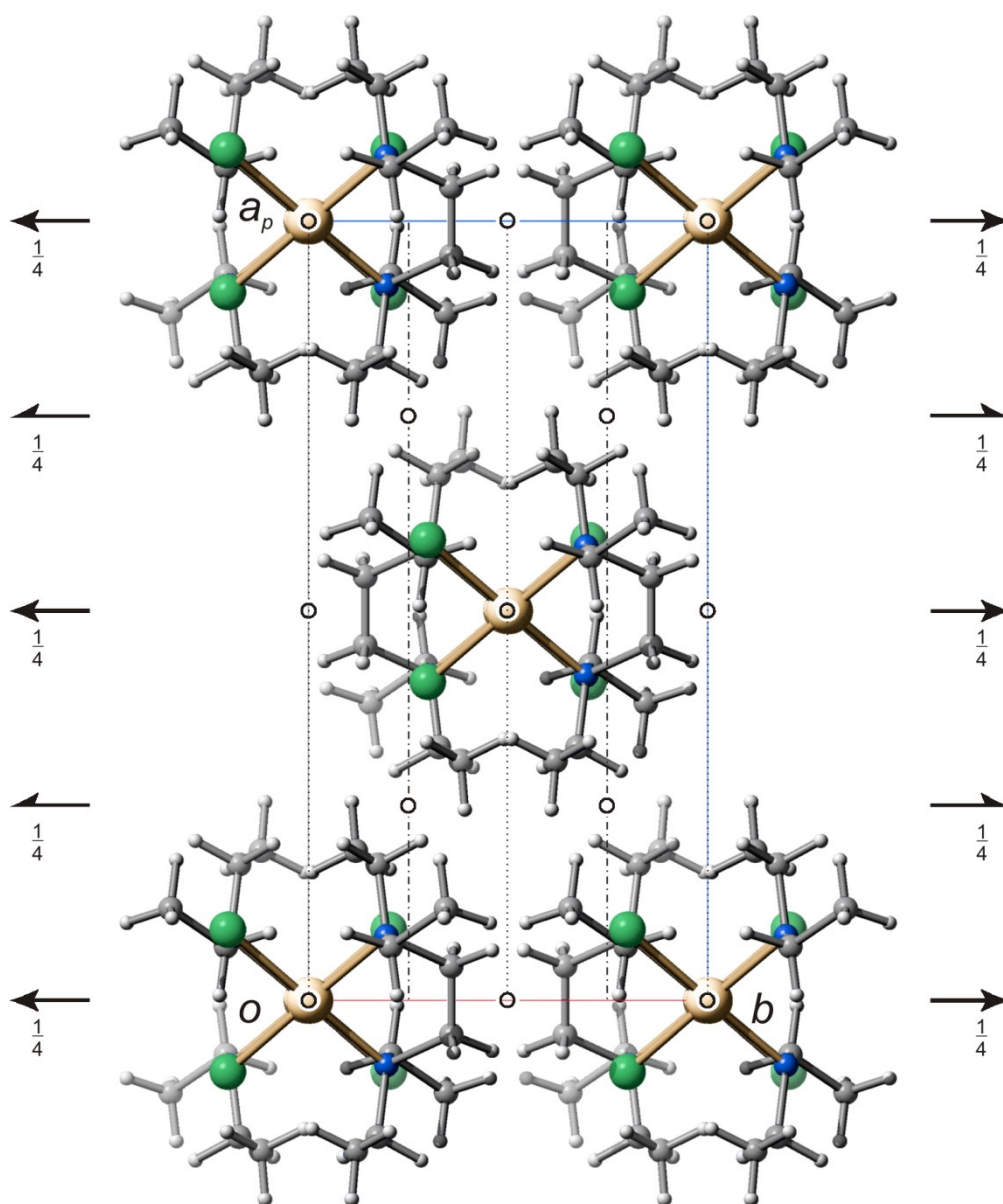


Figure 6.43. SCHAKAL packing diagram of $[\text{Pd}(\text{teen})\text{Cl}_2]$ (**4**) viewed along $[001]$. The symmetry elements of the space group $C2/c$ are overlaid. Atoms: carbon (grey), hydrogen (light grey, small), nitrogen (blue), chloride (green) and palladium (golden).

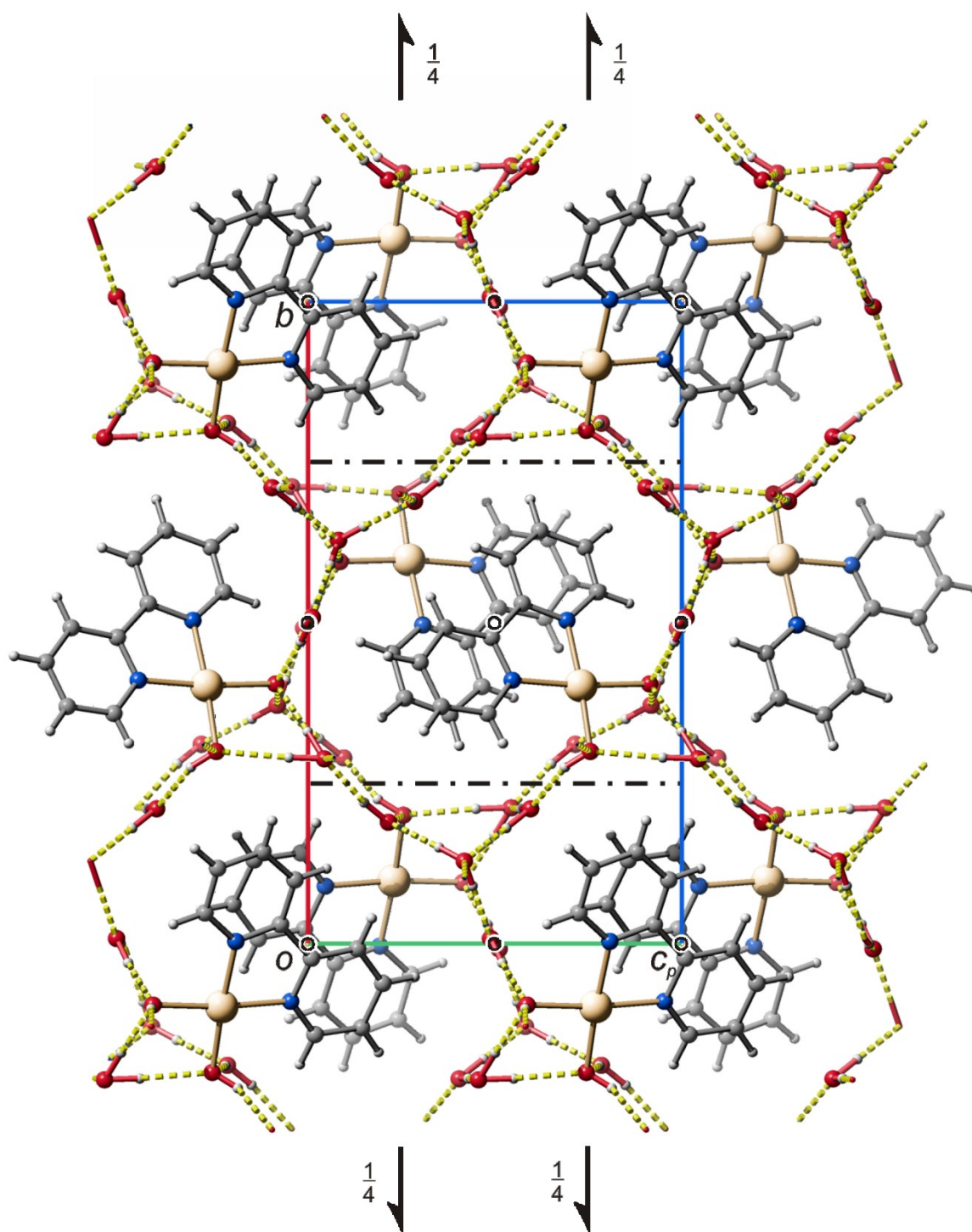


Figure 6.44. SCHAKAL packing diagram of [Pd(bpy)(OH)₂] in crystals of the 5-hydrate (**5**) viewed along [100]. Hydrogen bonds are indicated by yellow dashed lines. The symmetry elements of the space group $P2_1/n$ are overlaid. Atoms: carbon (grey), hydrogen (light grey, small), nitrogen (blue), oxygen (red) and palladium (golden).

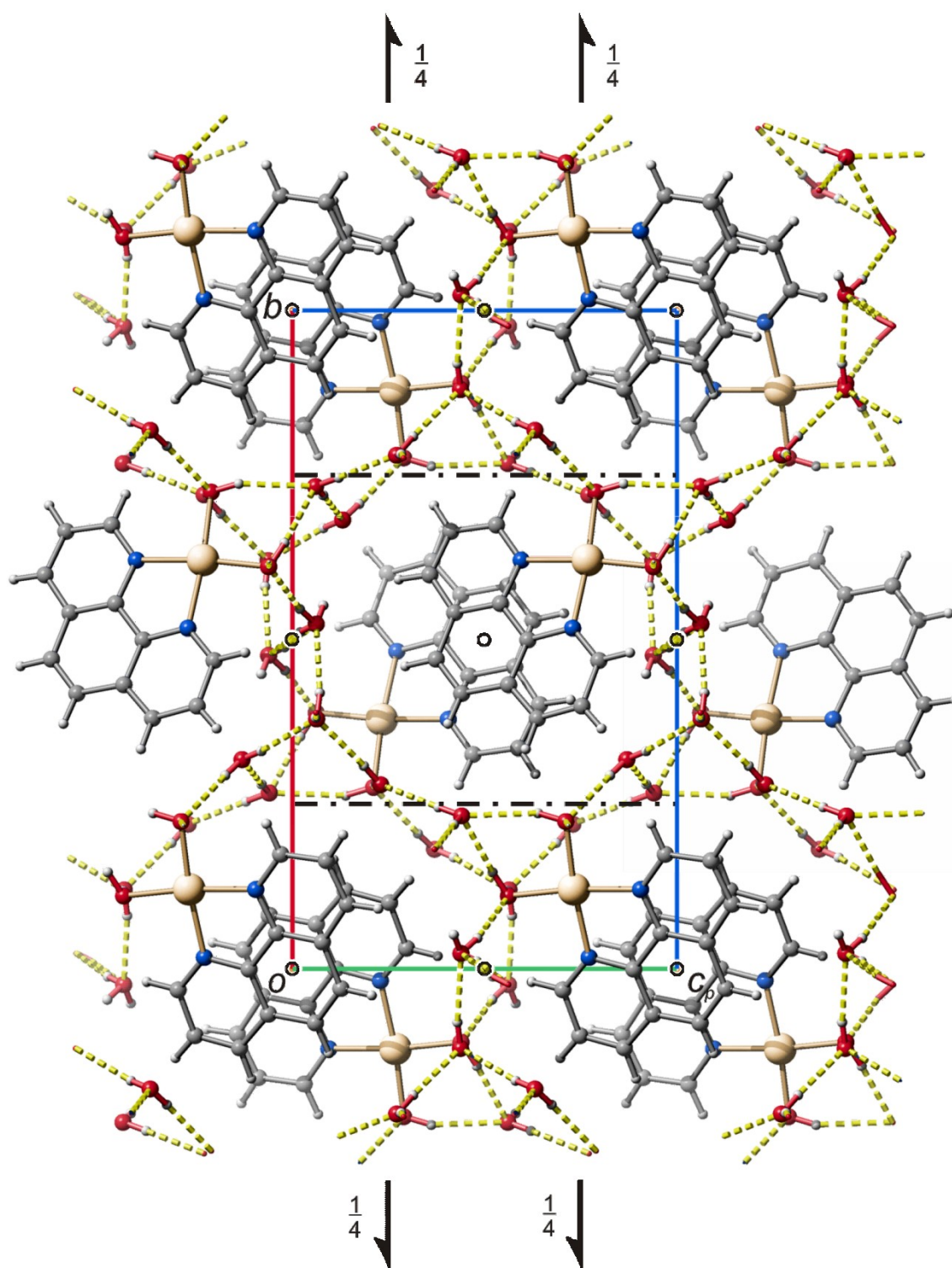


Figure 6.45. SCHAKAL packing diagram of [Pd(phen)(OH)₂] in crystals of the 5-hydrate (**6**) viewed along [100]. Hydrogen bonds are indicated by yellow dashed lines. The symmetry elements of the space group *P*2₁/*n* are overlaid. Atoms: carbon (grey), hydrogen (light grey, small), nitrogen (blue), oxygen (red) and palladium (golden).

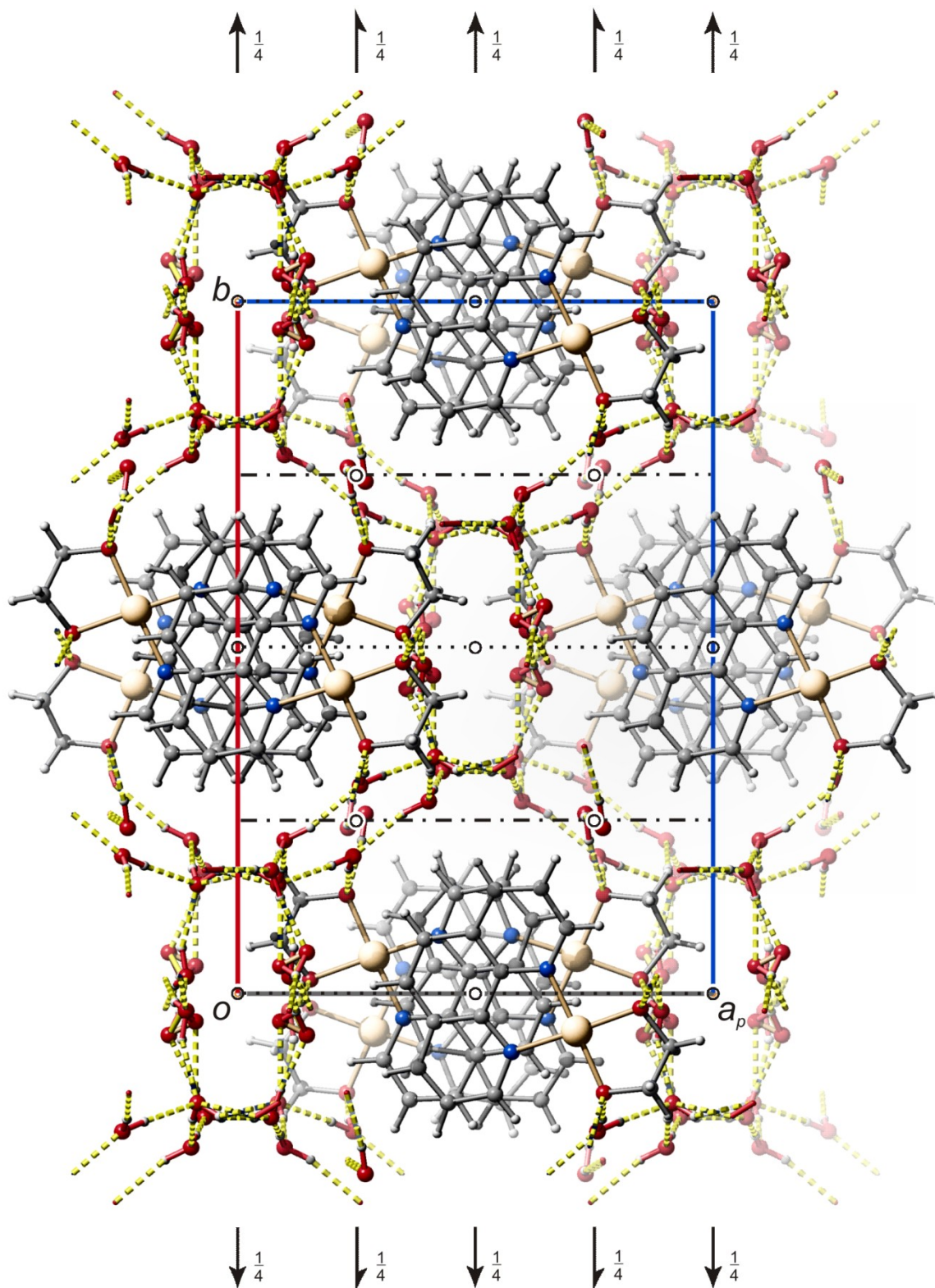


Figure 6.46. SCHAKAL packing diagram of $[\text{Pd}(\text{phen})(\text{EtdH}_2)]$ in crystals of the 7-hydrate (**7**) viewed along $[00\bar{1}]$. Hydrogen bonds are indicated by yellow dashed lines. The symmetry elements of the space group $C2/c$ are overlaid. Atoms: carbon (grey), hydrogen (light grey, small), nitrogen (blue), oxygen (red) and palladium (golden).

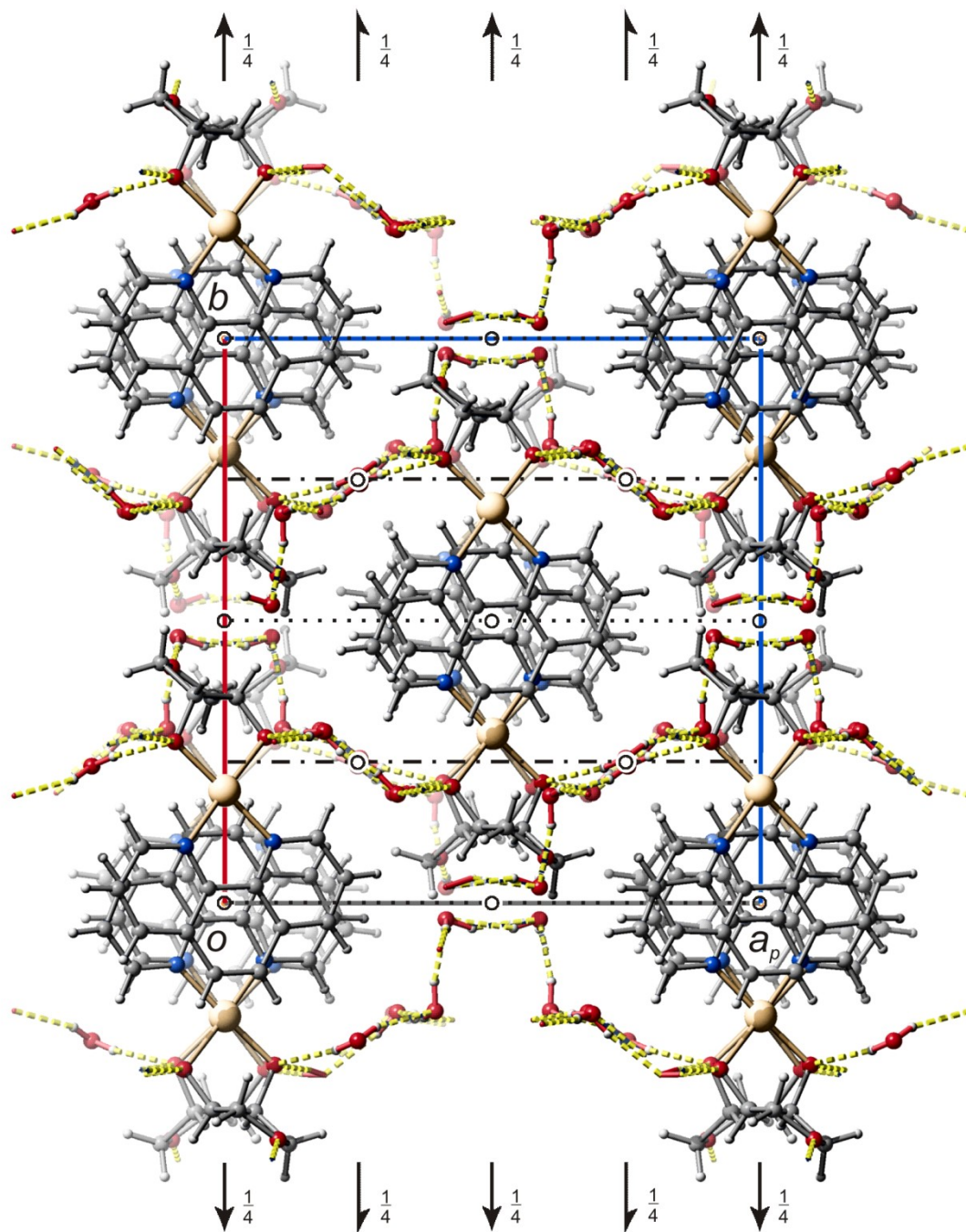


Figure 6.47. SCHAKAL packing diagram of $[\text{Pd}(\text{phen})(\text{AnEryH}_2)]$ in crystals of the 4.5-hydrate (**8**) viewed along $[00\bar{1}]$. Hydrogen bonds are indicated by yellow dashed lines. The symmetry elements of the space group $C2/c$ are overlaid. Atoms: carbon (grey), hydrogen (light grey, small), nitrogen (blue), oxygen (red) and palladium (golden).

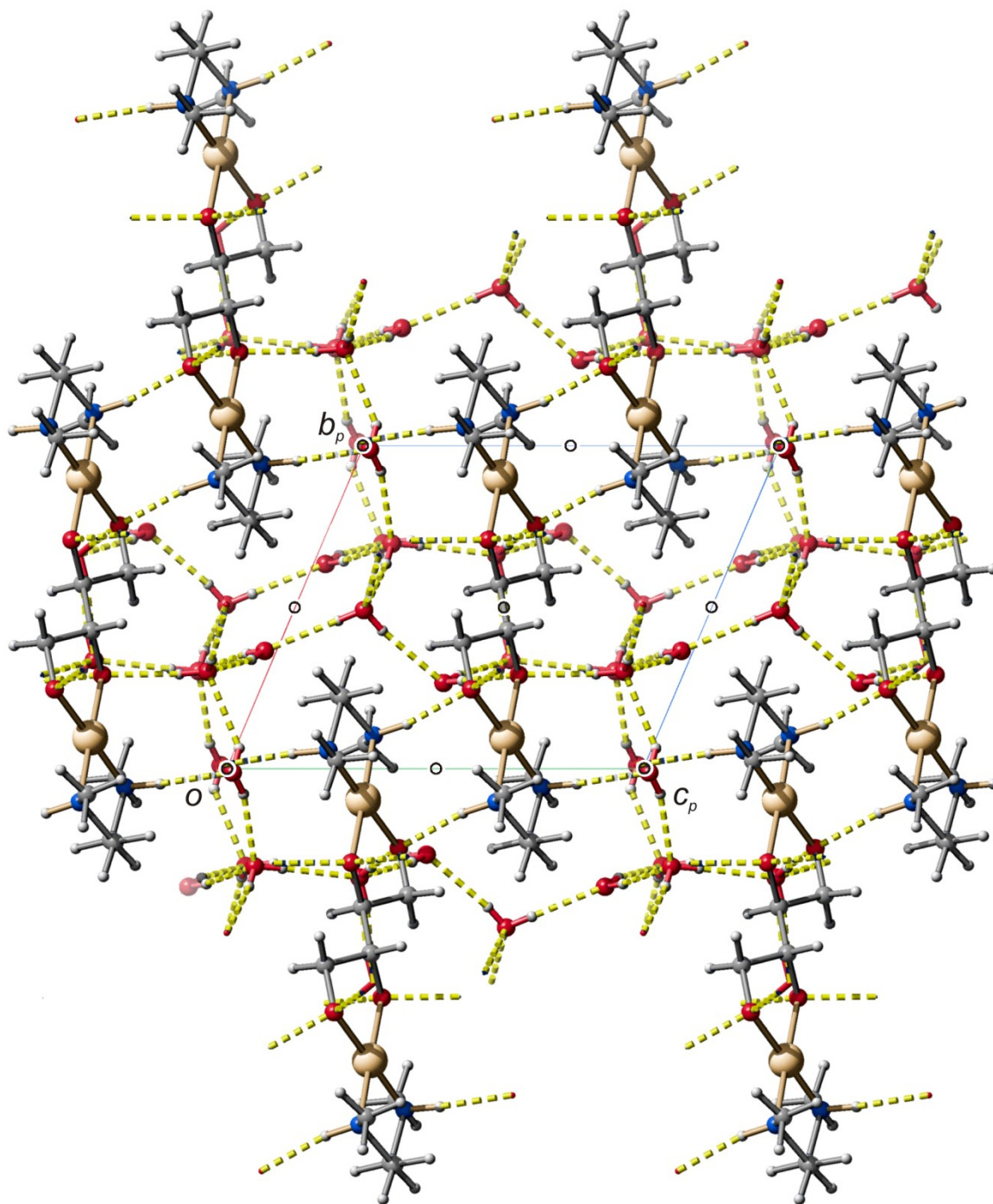


Figure 6.48. SCHAKAL packing diagram of $[\text{Pd}_2(\text{dmen})_2(\text{ErytH}_4\text{-}\kappa\text{O}^{1,2}:\kappa\text{O}^{3,4})]$ in crystals of the 14-hydrate (**9**) viewed along $[100]$. Hydrogen bonds are indicated by yellow dashed lines. The symmetry elements of the space group $P\bar{1}$ are overlaid. Atoms: carbon (grey), hydrogen (light grey, small), nitrogen (blue), oxygen (red) and palladium (golden).

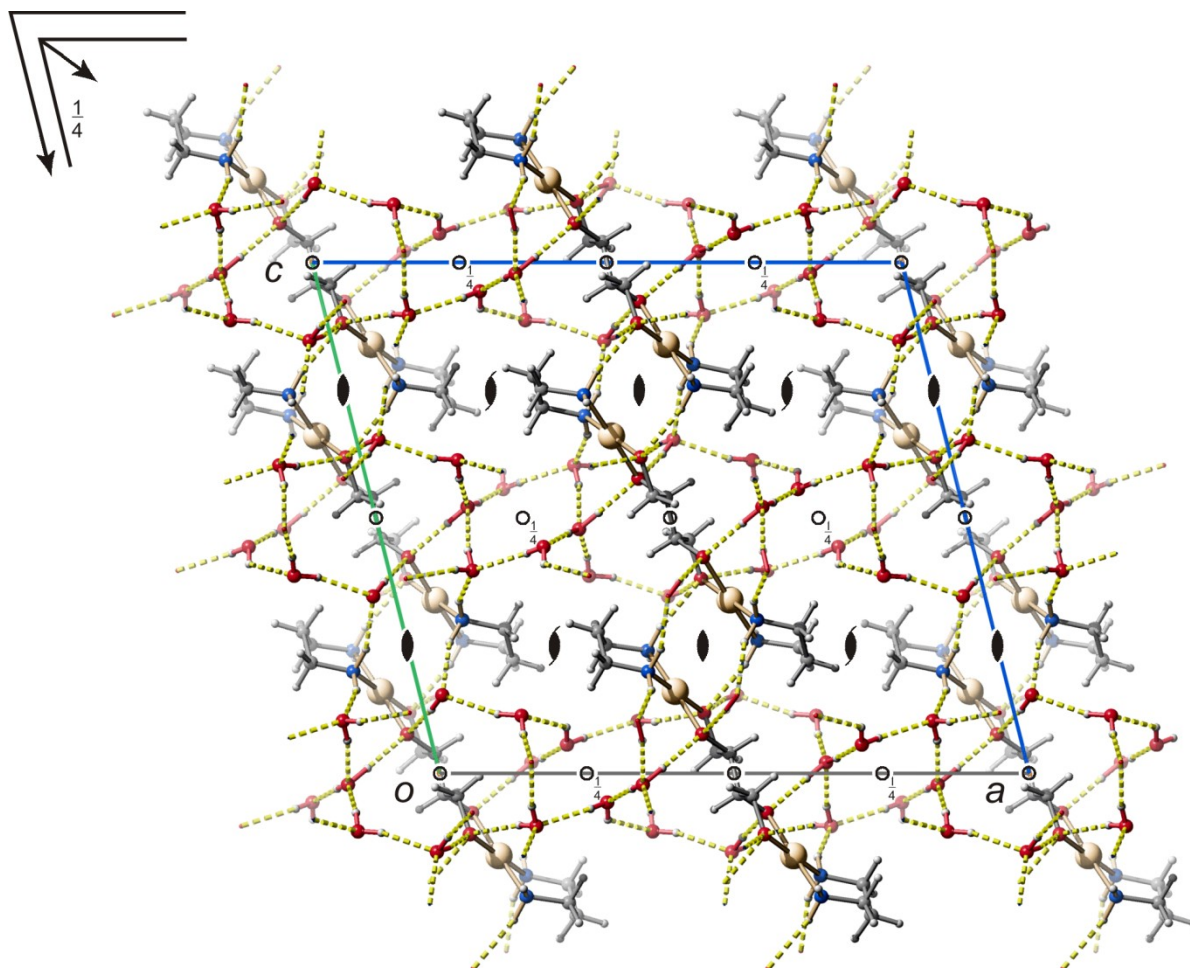


Figure 6.49. SCHAKAL packing diagram of $[\text{Pd}_2(\text{tn})_2(\text{ErytH}_{-4}\text{-}\kappa\text{O}^{1,2}:\kappa\text{O}^{3,4})]$ in crystals of the 10-hydrate (**10**) viewed along $[010]$. Hydrogen bonds are indicated by yellow dashed lines. The symmetry elements of the space group $C2/c$ are overlaid. Atoms: carbon (grey), hydrogen (light grey, small), nitrogen (blue), oxygen (red) and palladium (golden).

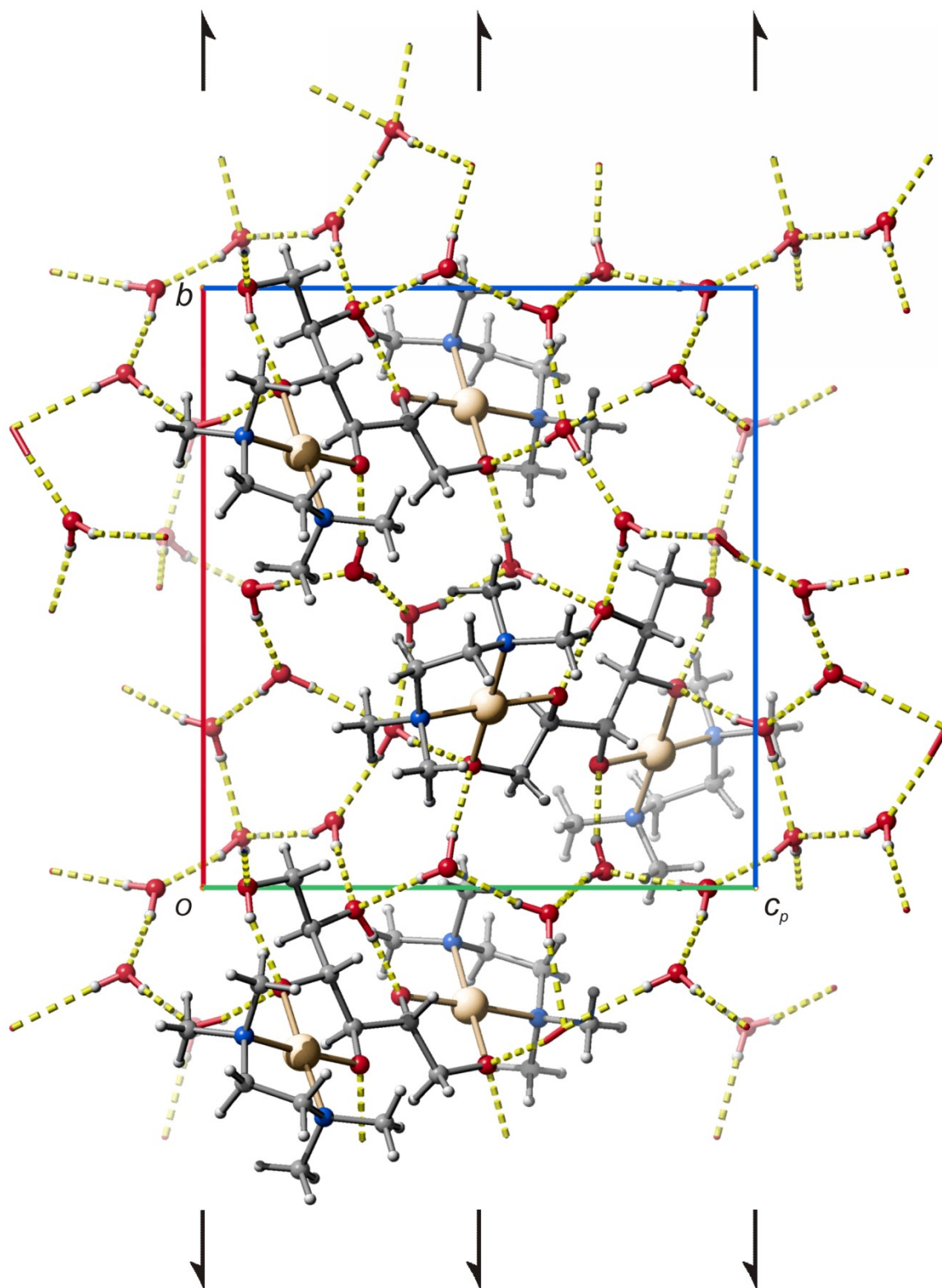


Figure 6.50. SCHAKAL packing diagram of $[\text{Pd}_2(\text{tmen})_2(\text{Mann}1,2;3,4\text{H}-4-\kappa\text{O}^{1,2}:\kappa\text{O}^{3,4})]$ in crystals of the 9-hydrate (**11**) viewed along $[100]$. Hydrogen bonds are indicated by yellow dashed lines. The symmetry elements of the space group $P2_1$ are overlaid. Atoms: carbon (grey), hydrogen (light grey, small), nitrogen (blue), oxygen (red) and palladium (golden).

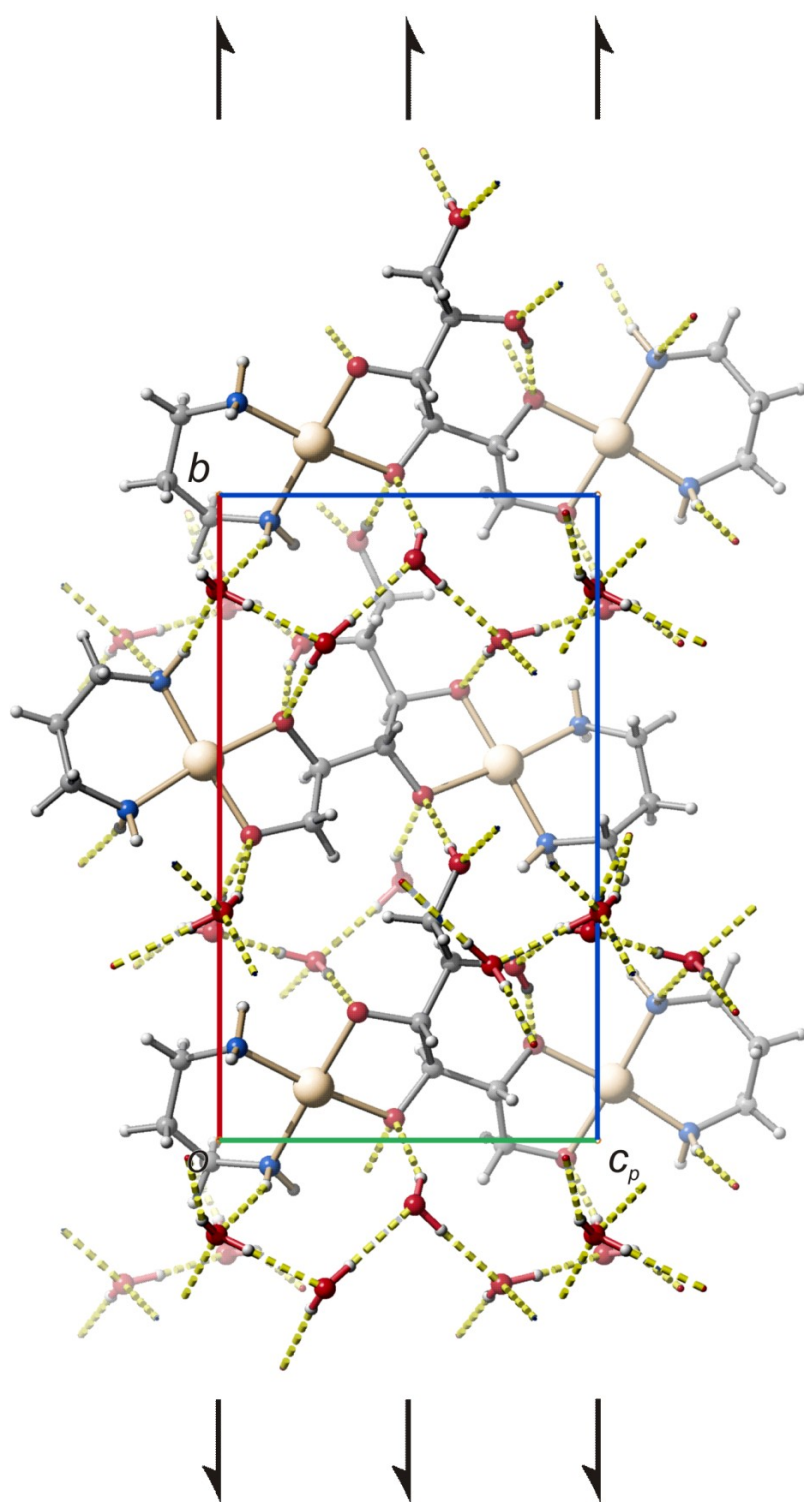


Figure 6.51. SCHAKAL packing diagram of $[\text{Pd}_2(\text{tn})_2(\text{Mann}1,2;3,4\text{H}_{-4}\text{-}\kappa\text{O}^{1,2}:\kappa\text{O}^{3,4})]$ in crystals of the 5-hydrate (**12**) viewed along $[100]$. Hydrogen bonds are indicated by yellow dashed lines. The symmetry elements of the space group $P2_1$ are overlaid. Atoms: carbon (grey), hydrogen (light grey, small), nitrogen (blue), oxygen (red) and palladium (golden).

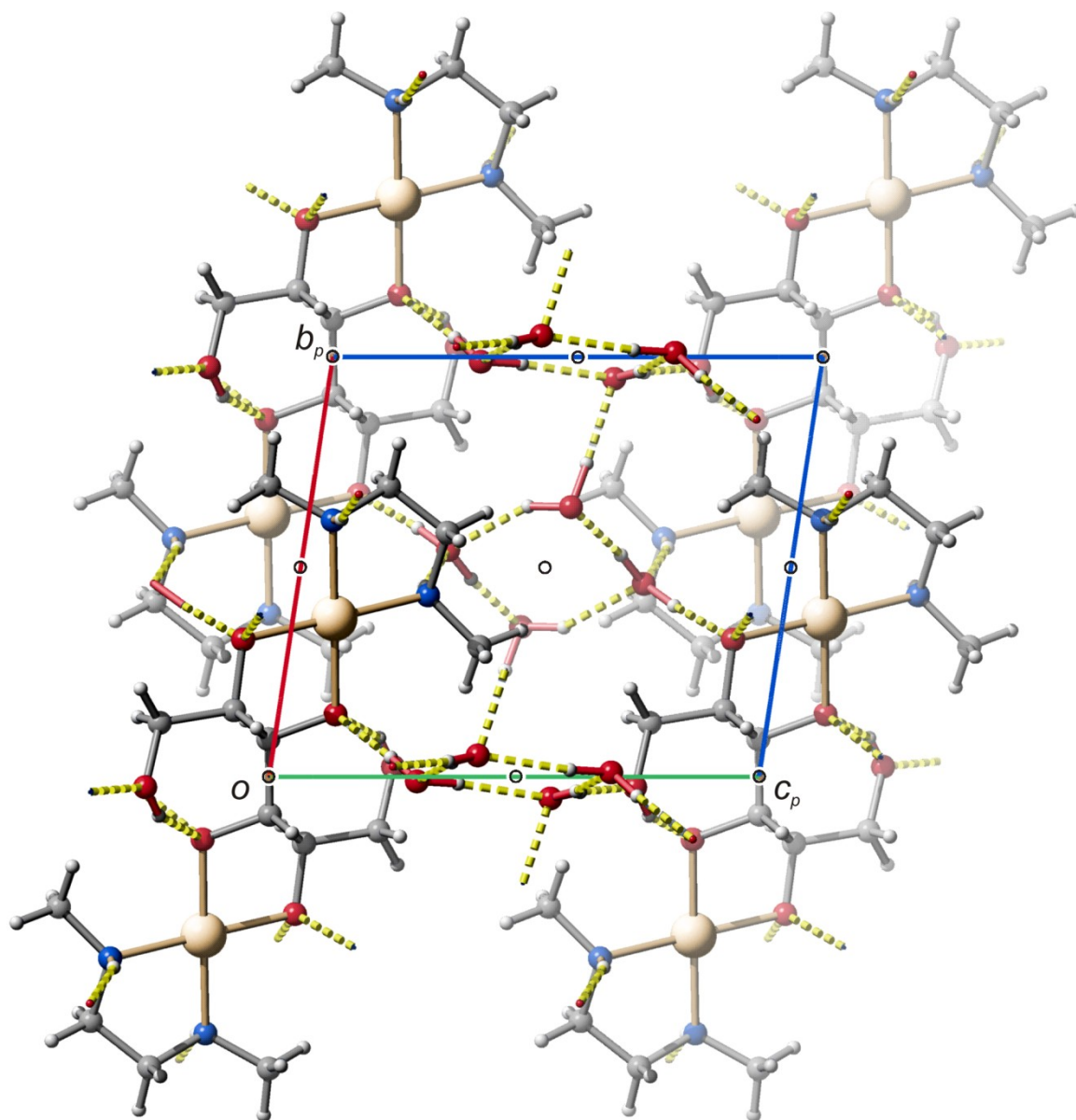


Figure 6.52. SCHAKAL packing diagram of $[\text{Pd}_2(\text{dmen})_2(\text{Dulc}2,3;4,5\text{H}_4\text{-}\kappa\text{O}^{2,3}:\kappa\text{O}^{4,5})]$ in crystals of the 8-hydrate (**13**) viewed along $[100]$. Hydrogen bonds are indicated by yellow dashed lines. The symmetry elements of the space group $P\bar{1}$ are overlaid. Atoms: carbon (grey), hydrogen (light grey, small), nitrogen (blue), oxygen (red) and palladium (golden).

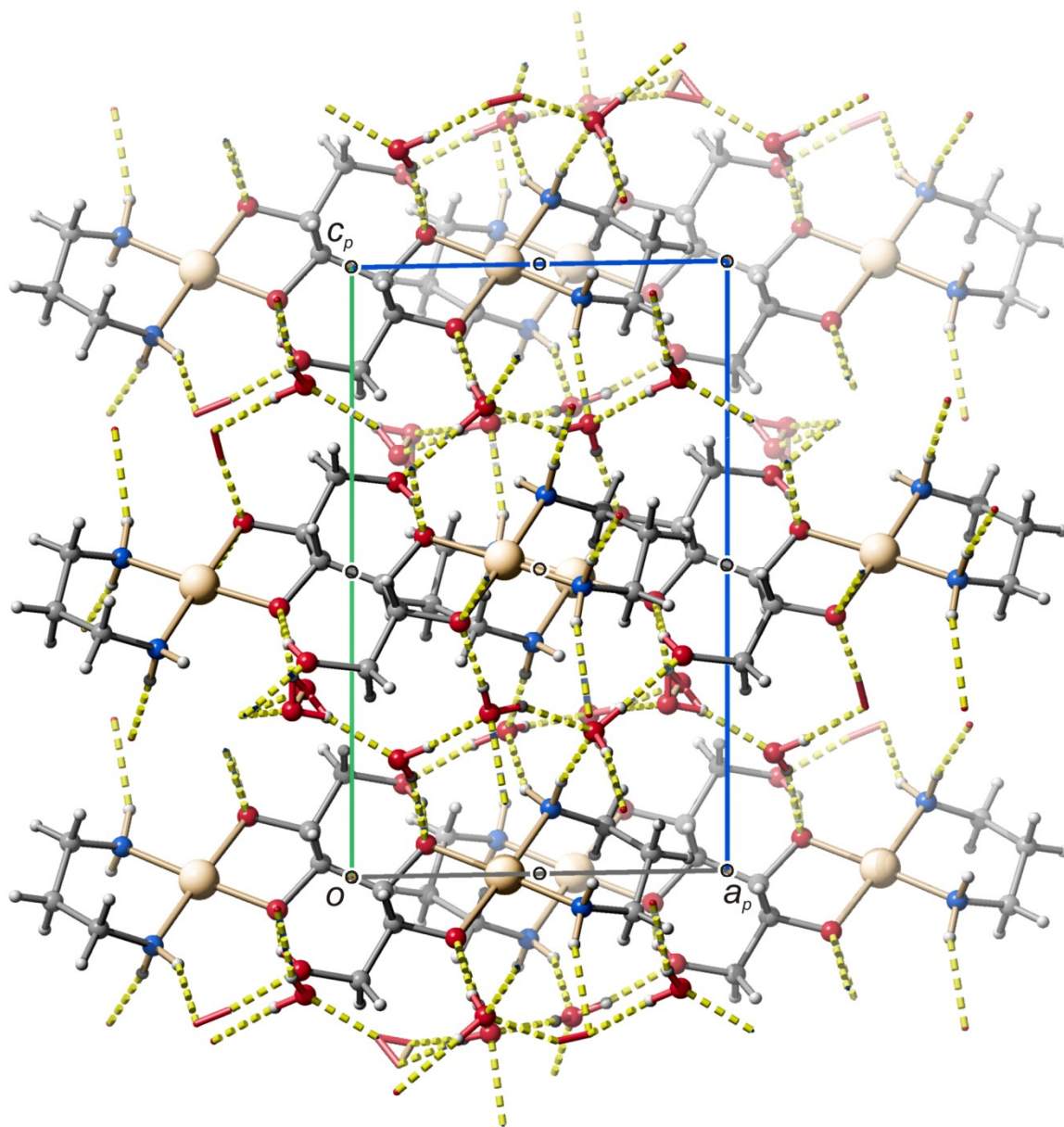


Figure 6.53. SCHAKAL packing diagram of $[\text{Pd}_2(\text{tn})_2(\text{Dulc}_{2,3;4,5}\text{H}_4-\kappa\text{O}^{2,3}:\kappa\text{O}^{4,5})]$ in crystals of the 6-hydrate (**14**) viewed along $[010]$. Hydrogen bonds are indicated by yellow dashed lines. The symmetry elements of the space group $P\bar{1}$ are overlaid. Atoms: carbon (grey), hydrogen (light grey, small), nitrogen (blue), oxygen (red) and palladium (golden).

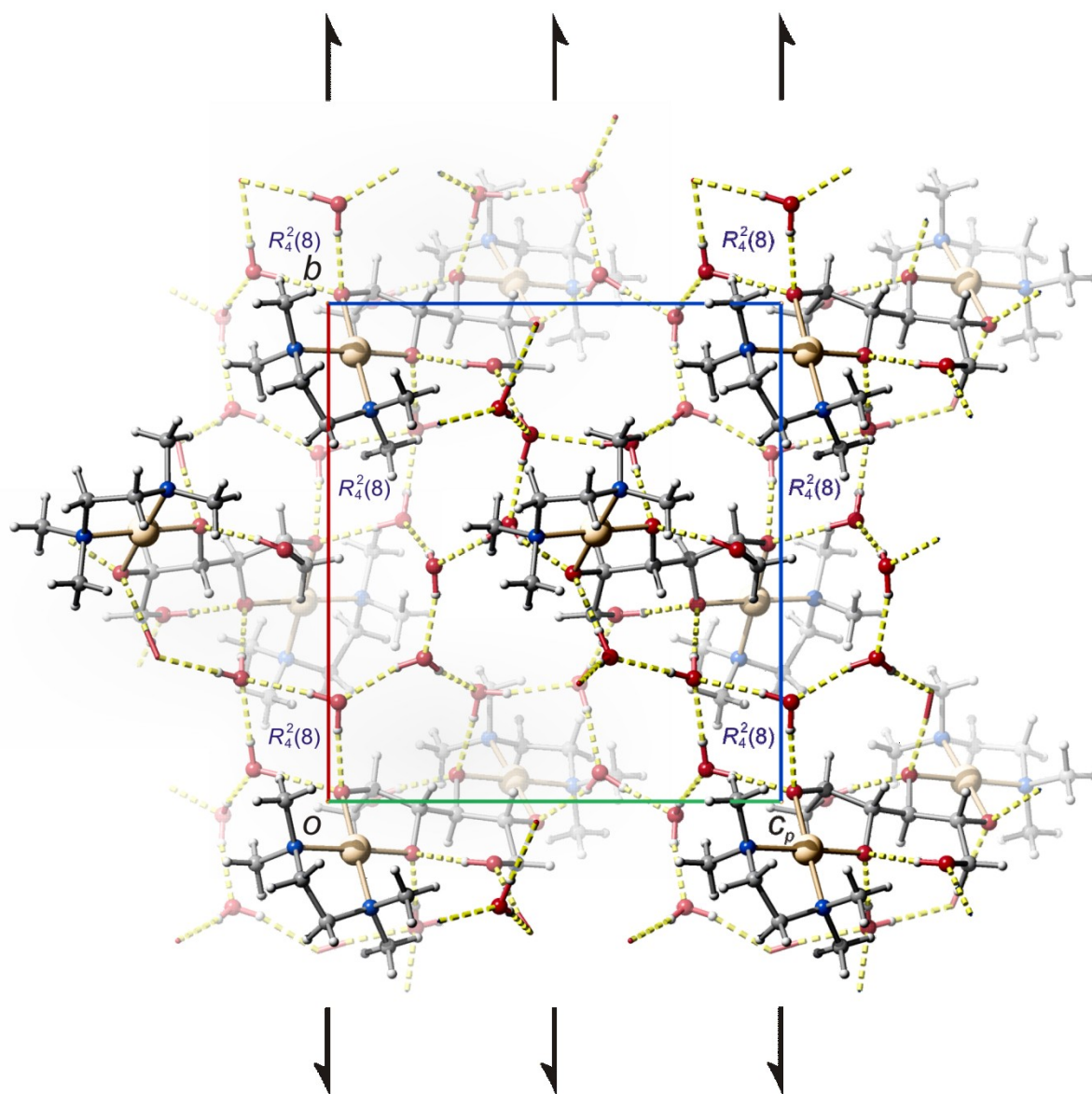


Figure 6.54. SCHAKAL packing diagram of $[\text{Pd}_2(\text{tmen})_2(\text{D-Altr}_{2,3;4,5}\text{H}_4\text{-}\kappa\text{O}^{2,3}:\kappa\text{O}^{4,5})]$ in crystals of the 9-hydrate (**15**) viewed along $[100]$. Hydrogen bonds are indicated by yellow dashed lines. The symmetry elements of the space group $P2_1$ are overlaid. Atoms: carbon (grey), hydrogen (light grey, small), nitrogen (blue), oxygen (red) and palladium (golden).

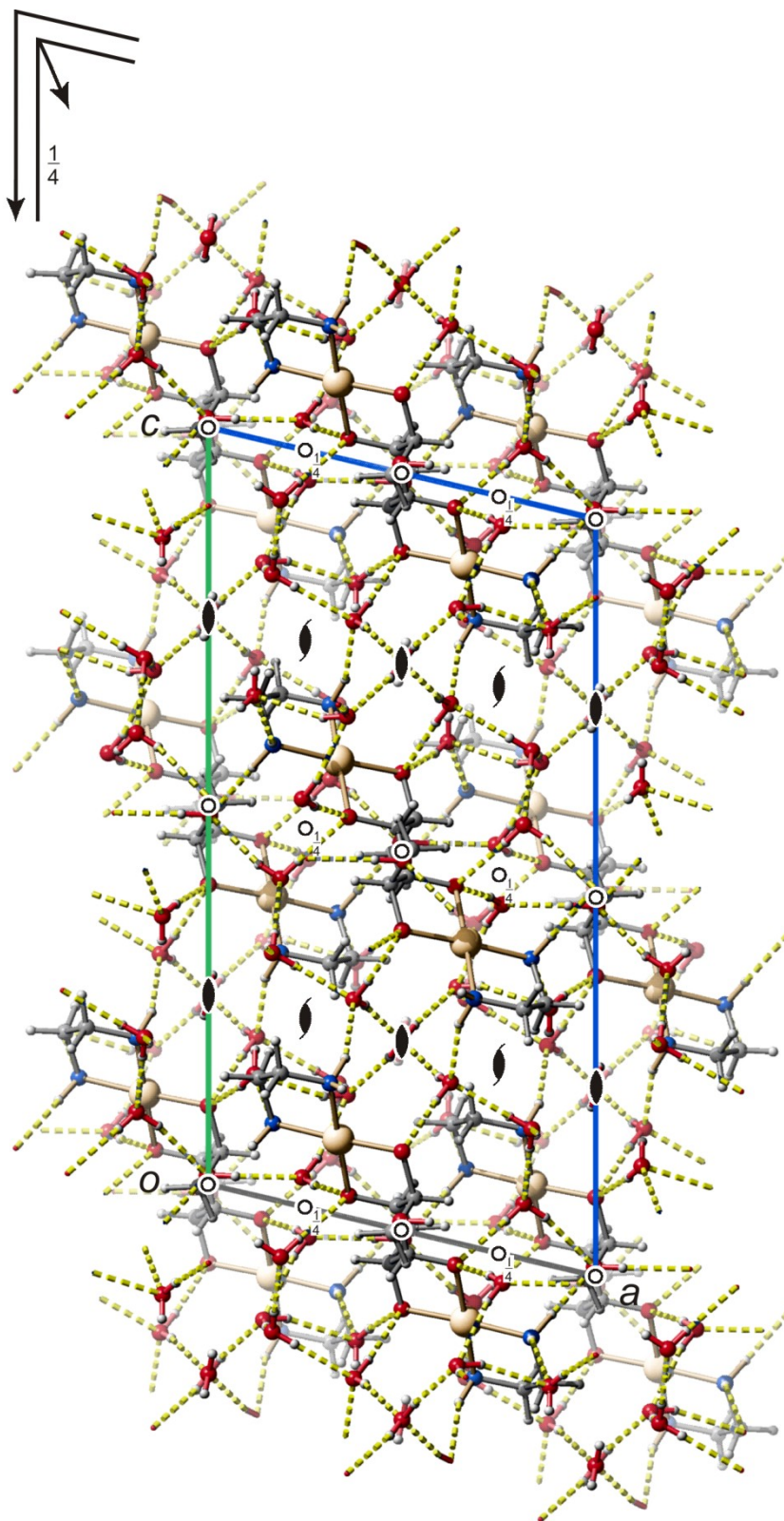


Figure 6.55. SCHAKAL packing diagram of $[\text{Pd}_2(\text{en})_2(\text{Allt}_{2,3;4,5}\text{H}_{-4-\kappa\text{O}^{2,3};\kappa\text{O}^{4,5}})]$ in crystals of the 14-hydrate (**16**) viewed along $[010]$. Hydrogen bonds are indicated by yellow dashed lines. The symmetry elements of the space group $C2/c$ are overlaid. Atoms: carbon (grey), hydrogen (light grey, small), nitrogen (blue), oxygen (red) and palladium (golden).

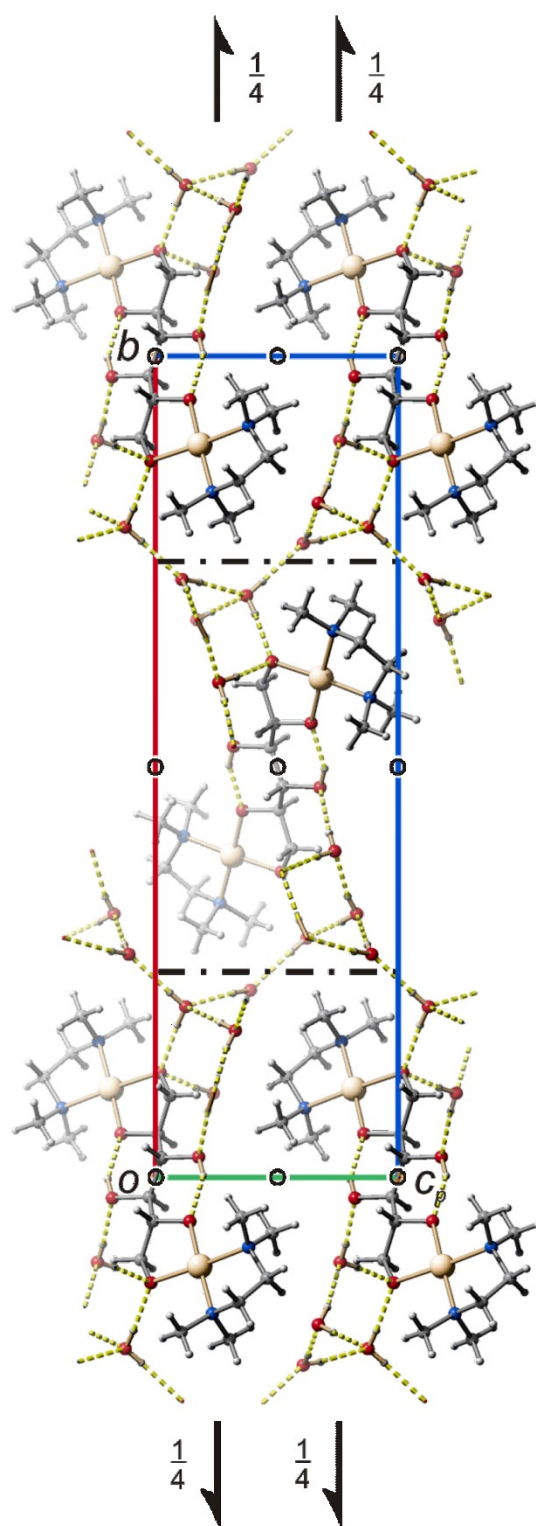


Figure 6.56. SCHAKAL packing diagram of $[\text{Pd}_2(\text{tmen})_2(\text{Allt}_{1,2};5,6\text{H}_{-4}-\kappa\text{O}^{1,2}:\kappa\text{O}^{5,6})]$ in crystals of the 8-hydrate (**17**) viewed along $[100]$. Hydrogen bonds are indicated by yellow dashed lines. The symmetry elements of the space group $P2_1/n$ are overlaid. Atoms: carbon (grey), hydrogen (light grey, small), nitrogen (blue), oxygen (red) and palladium (golden).

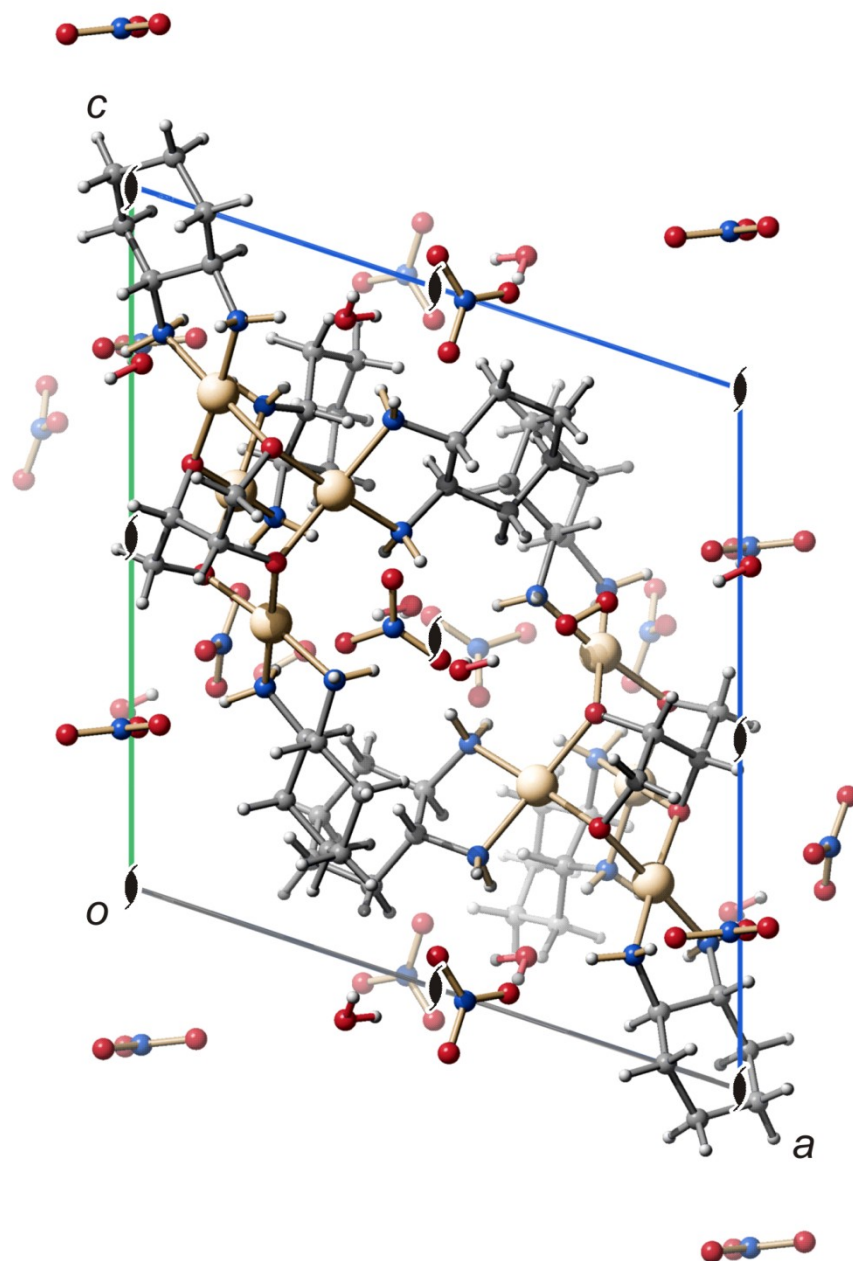


Figure 6.57. SCHAKAL packing diagram of $[\text{Pd}_4(\text{R,R-chxn})_4(\text{L-ThreH-4})](\text{NO}_3)_4$ in crystals of the 4-hydrate (**18**) viewed along $[010]$. The symmetry elements of the space group $P2_1$ are overlaid. Atoms: carbon (grey), hydrogen (light grey, small), nitrogen (blue), oxygen (red) and palladium (golden).

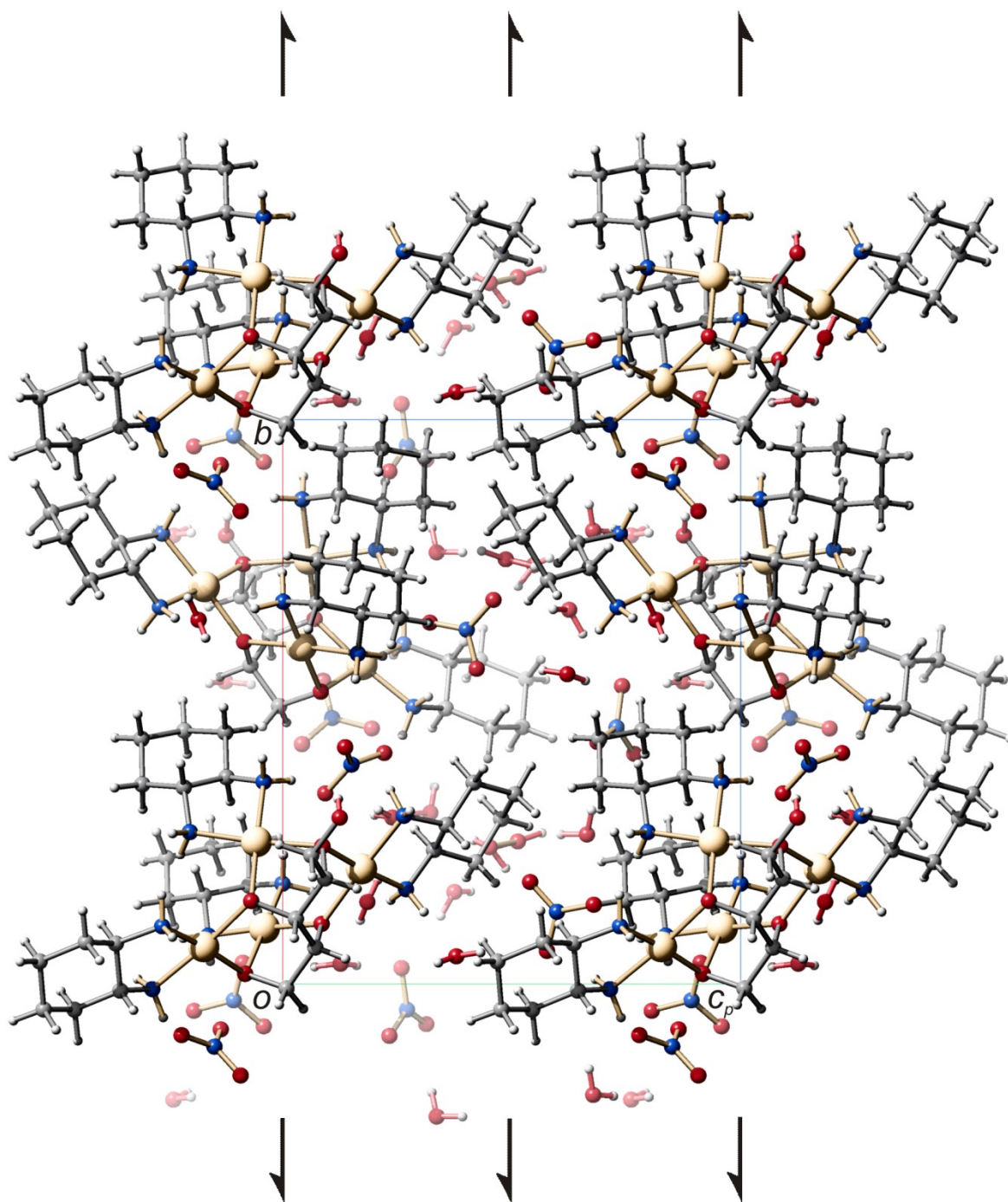


Figure 6.58. SCHAKAL packing diagram of $[\text{Pd}_4(\text{R,R-chxn})_4(\text{Xylt1,2,3,4H-4})](\text{NO}_3)_4$ in crystals of the 4.7-hydrate (**19**) viewed along $[100]$. The symmetry elements of the space group $P2_1$ are overlaid. Atoms: carbon (grey), hydrogen (light grey, small), nitrogen (blue), oxygen (red) and palladium (golden).

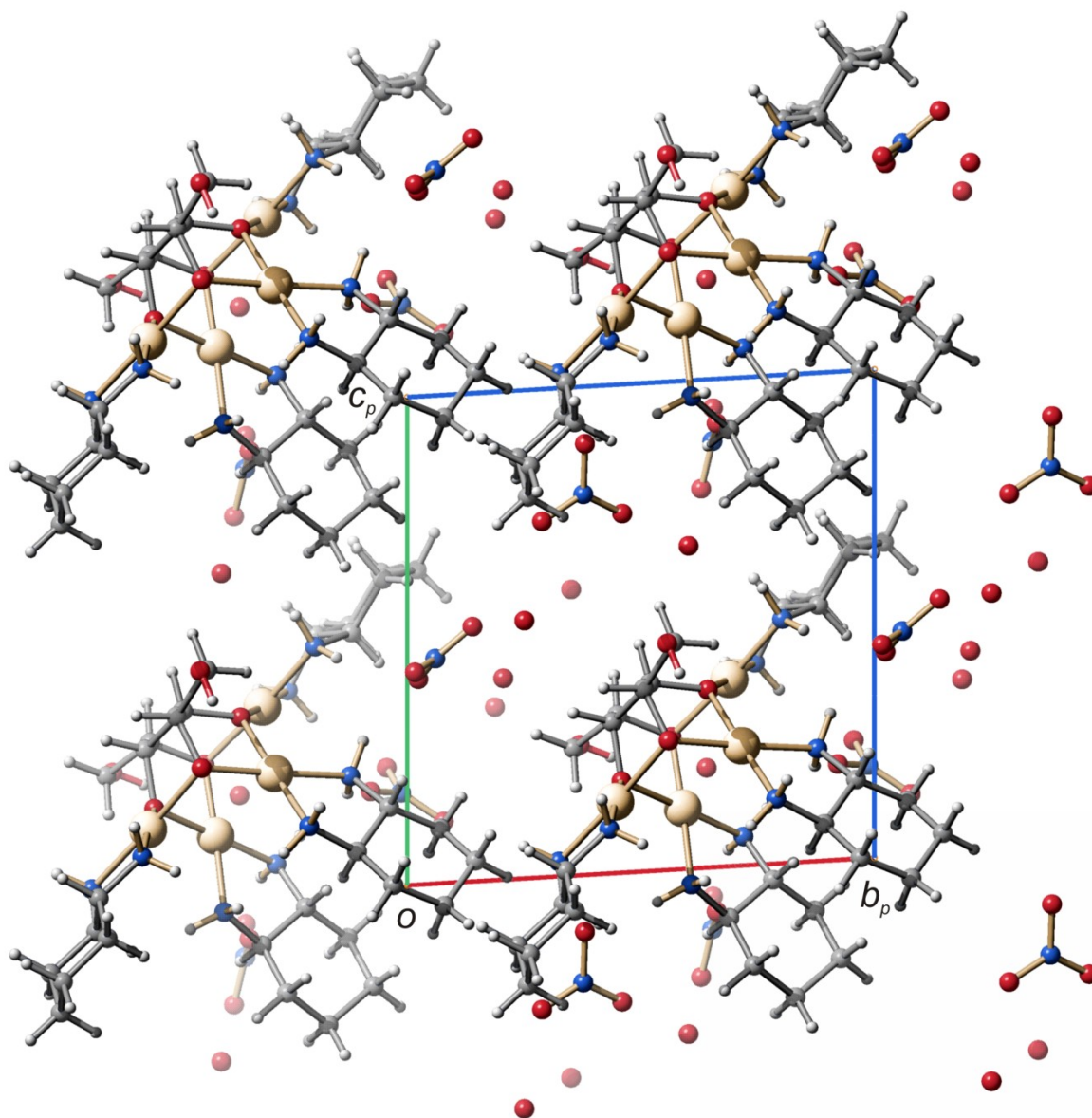


Figure 6.59. SCHAKAL packing diagram of $[\text{Pd}_4(\text{R,R-chxn})_4(\text{L-Idit2,3,4,5H-4})](\text{NO}_3)_4$ in crystals of the 6-hydrate (**20**) viewed along $[\bar{1}00]$. The symmetry elements of the space group $P1$ are overlaid. Atoms: carbon (grey), hydrogen (light grey, small), nitrogen (blue), oxygen (red) and palladium (golden).

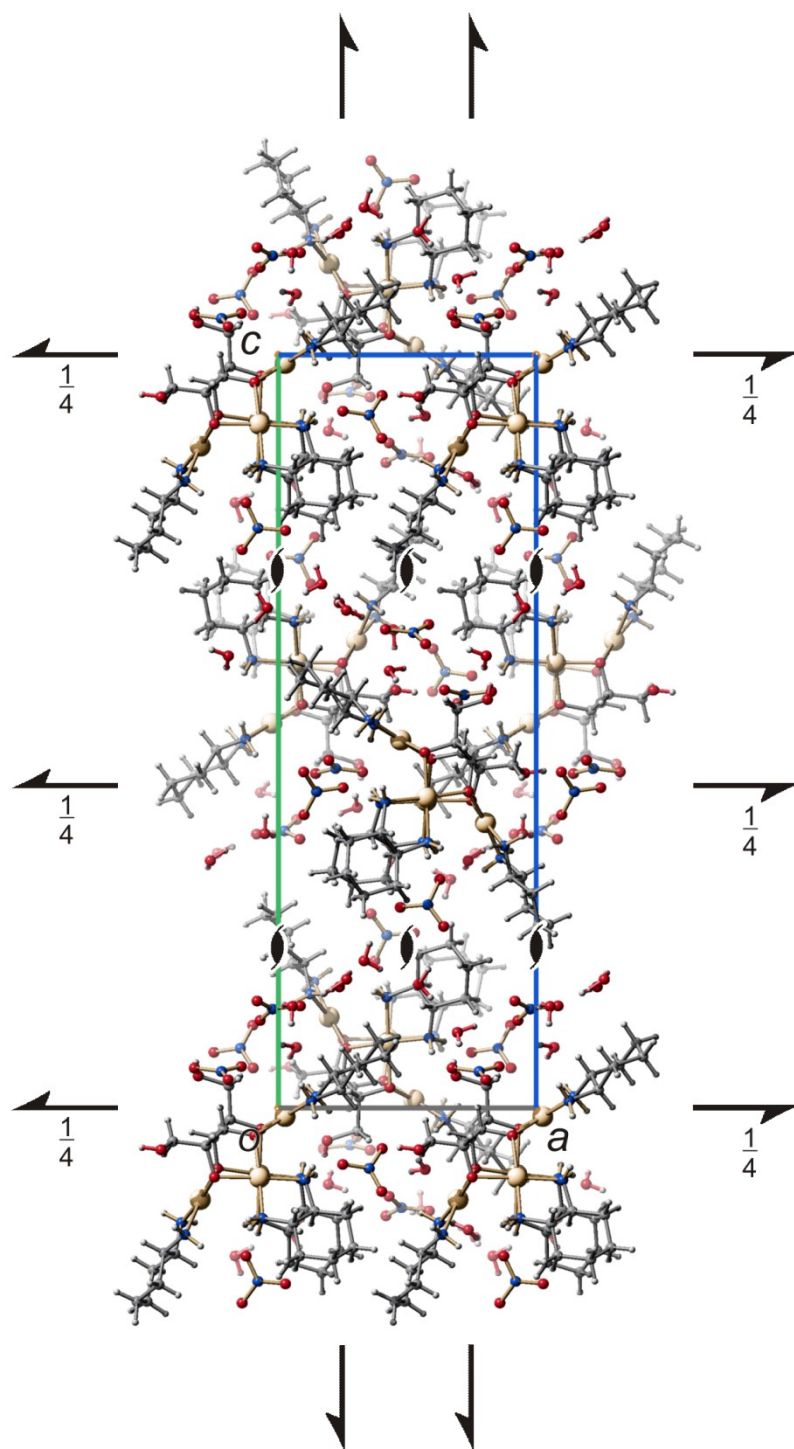


Figure 6.60. SCHAKAL packing diagram of $[\text{Pd}_4(\text{R,R-chxn})_{1.66}(\text{S,S-chxn})_{2.34}(\text{D-Mann}_{2,3,4,5\text{H}-4})](\text{NO}_3)_4$ in crystals of the 7-hydrate (**21**) viewed along [010]. The symmetry elements of the space group *P* 2₁2₁2₁ are overlaid. The atoms of the minor part of disordered chxn are not shown. Atoms: carbon (grey), hydrogen (light grey, small), nitrogen (blue), oxygen (red) and palladium (golden).

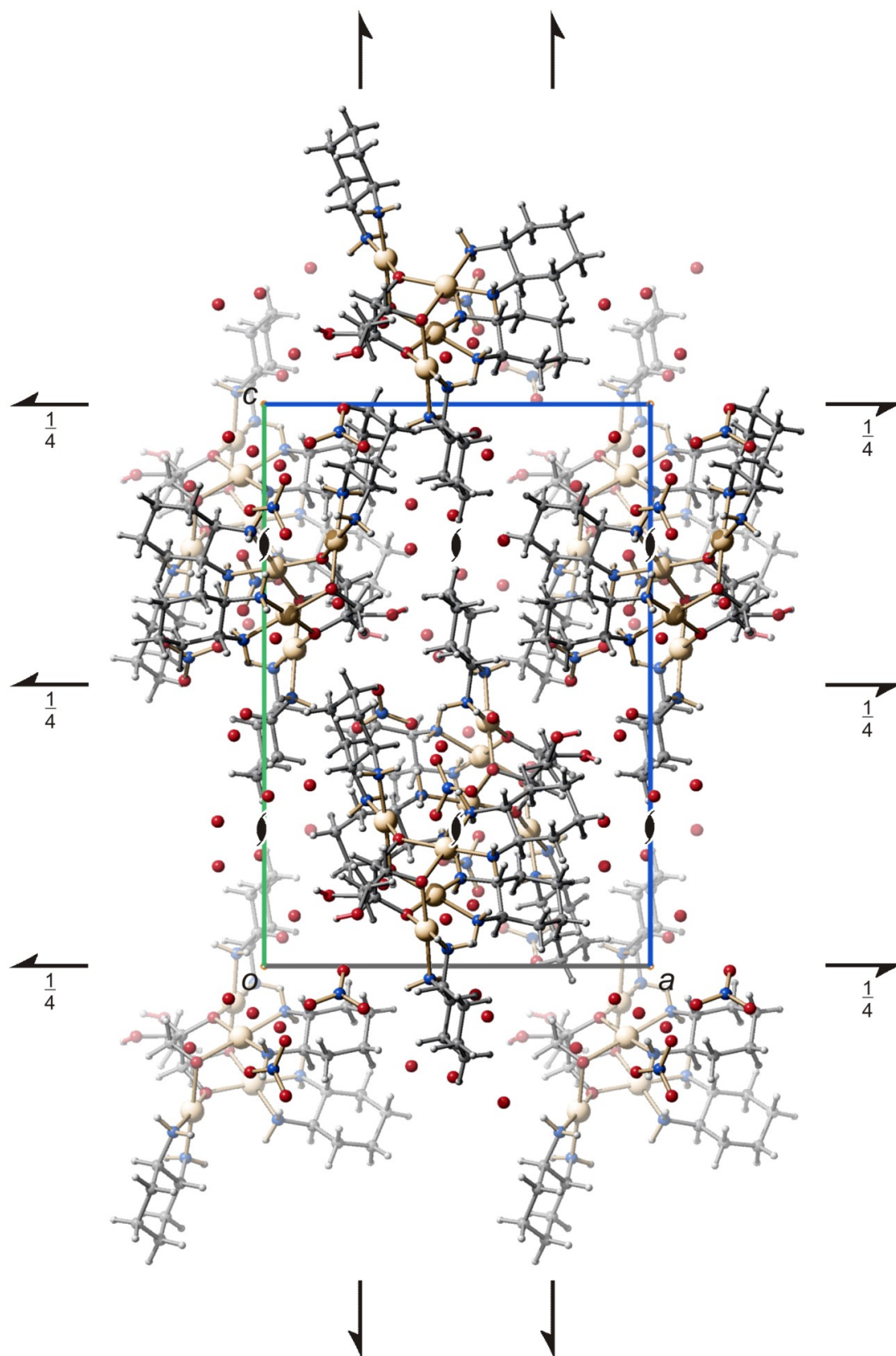


Figure 6.61. SCHAKAL packing diagram of $[\text{Pd}_4(\text{R,R-chxn})_4(\text{D-Altr1,2,3,4H-4})](\text{NO}_3)_{3.57}(\text{OH})_{0.43}$ in crystals of the 12-hydrate (**22**) viewed along $[010]$. The symmetry elements of the space group $P 2_12_12_1$ are overlaid. Atoms: carbon (grey), hydrogen (light grey, small), nitrogen (blue), oxygen (red) and palladium (golden).

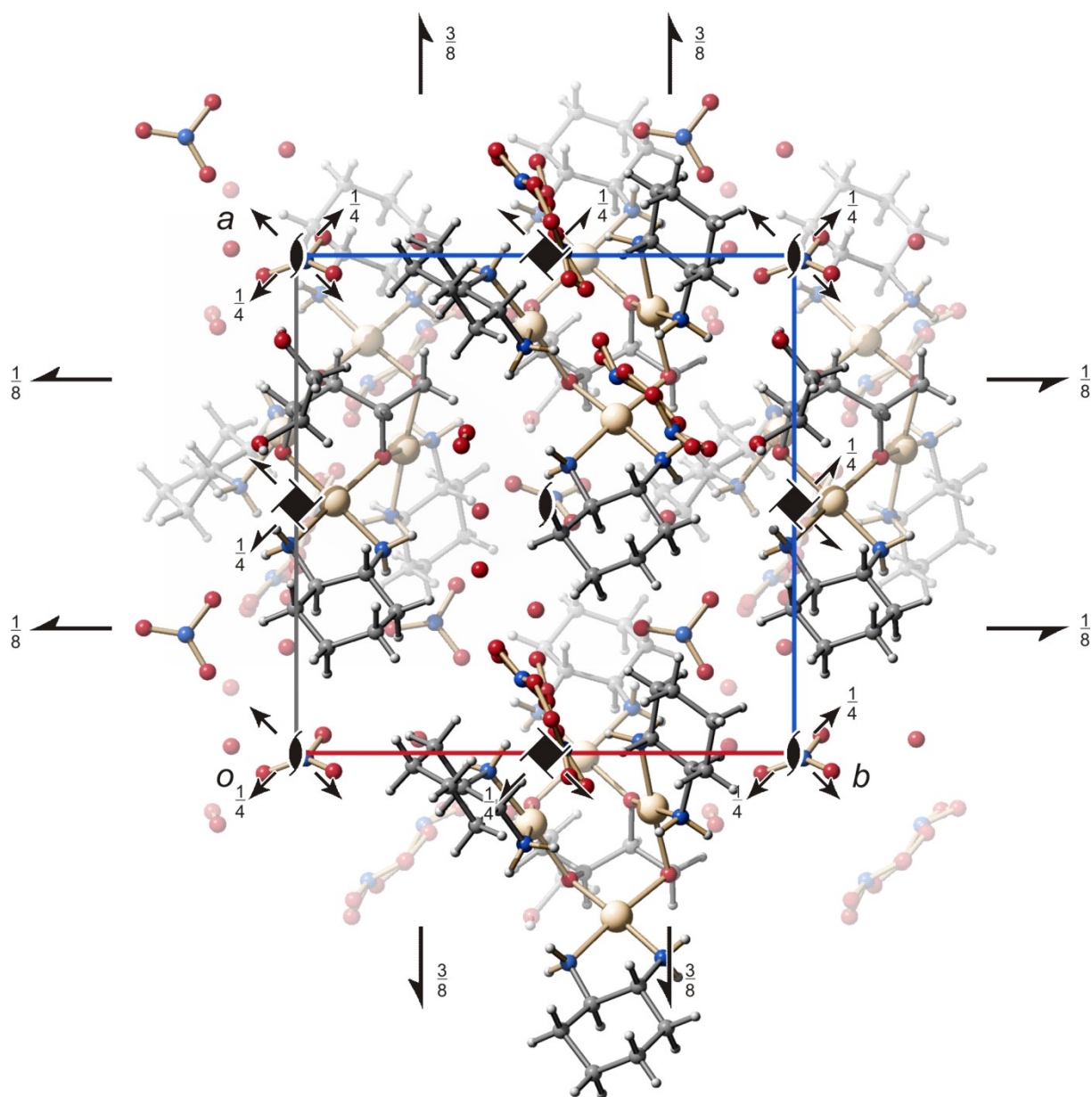


Figure 6.62. SCHAKAL packing diagram of $[\text{Pd}_4(\text{R,R-chxn})_4(\text{Dulc1,2,3,4H-4})](\text{NO}_3)_{3.5}(\text{OH})_{0.5}$ in crystals of the 6.75-hydrate (**23**) viewed along $[001]$. The symmetry elements of the space group $P4_12_12$ are overlaid. Atoms: carbon (grey), hydrogen (light grey, small), nitrogen (blue), oxygen (red) and palladium (golden).

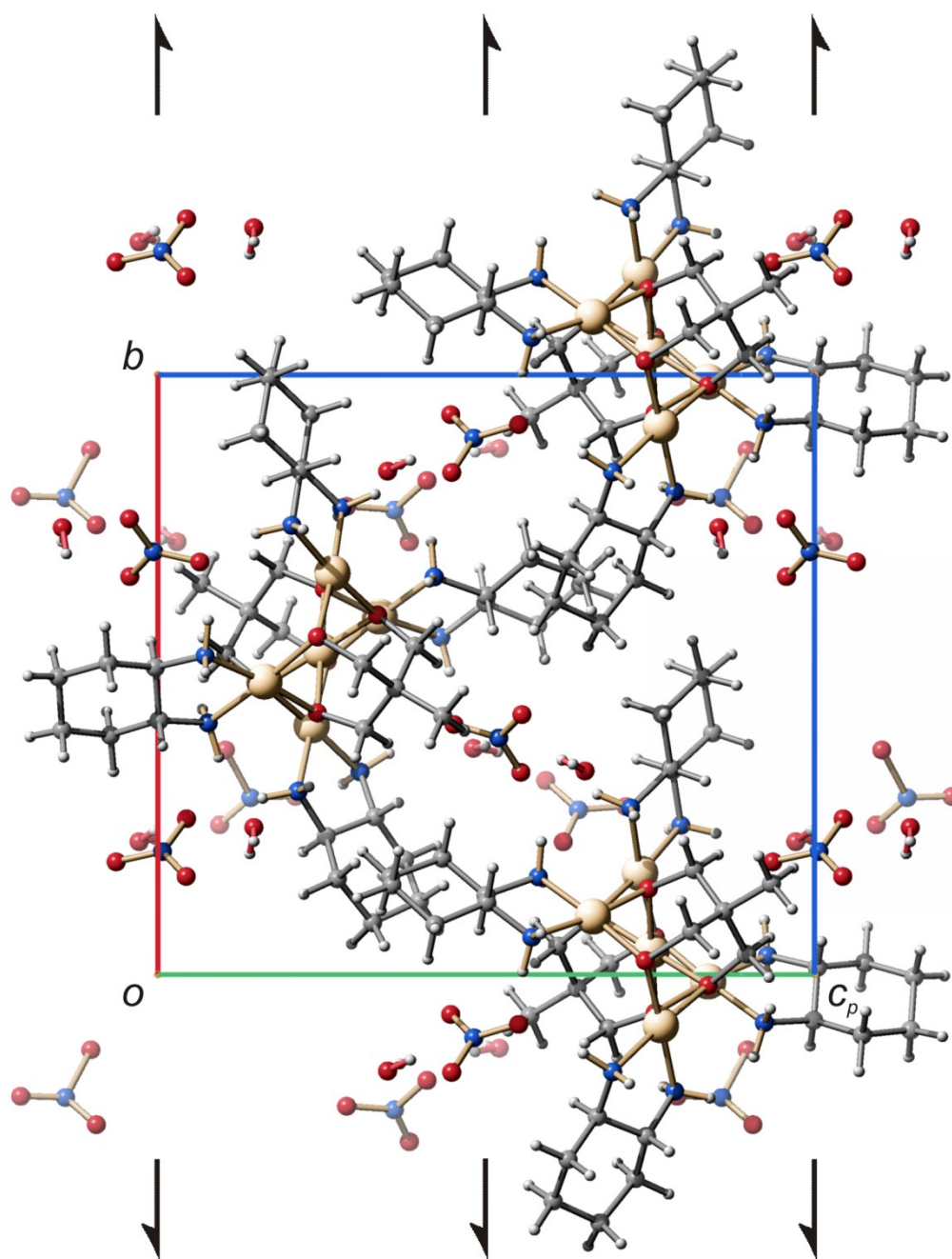


Figure 6.63. SCHAKAL packing diagram of $[\{Pd_2(R,R\text{-chxn})_2(HmmpdH_{-3})\}_2Pd](NO_3)_4$ in crystals of the 4-hydrate (**24**) viewed along $[100]$. The symmetry elements of the space group $P2_1$ are overlaid. Atoms: carbon (grey), hydrogen (light grey, small), nitrogen (blue), oxygen (red) and palladium (golden).

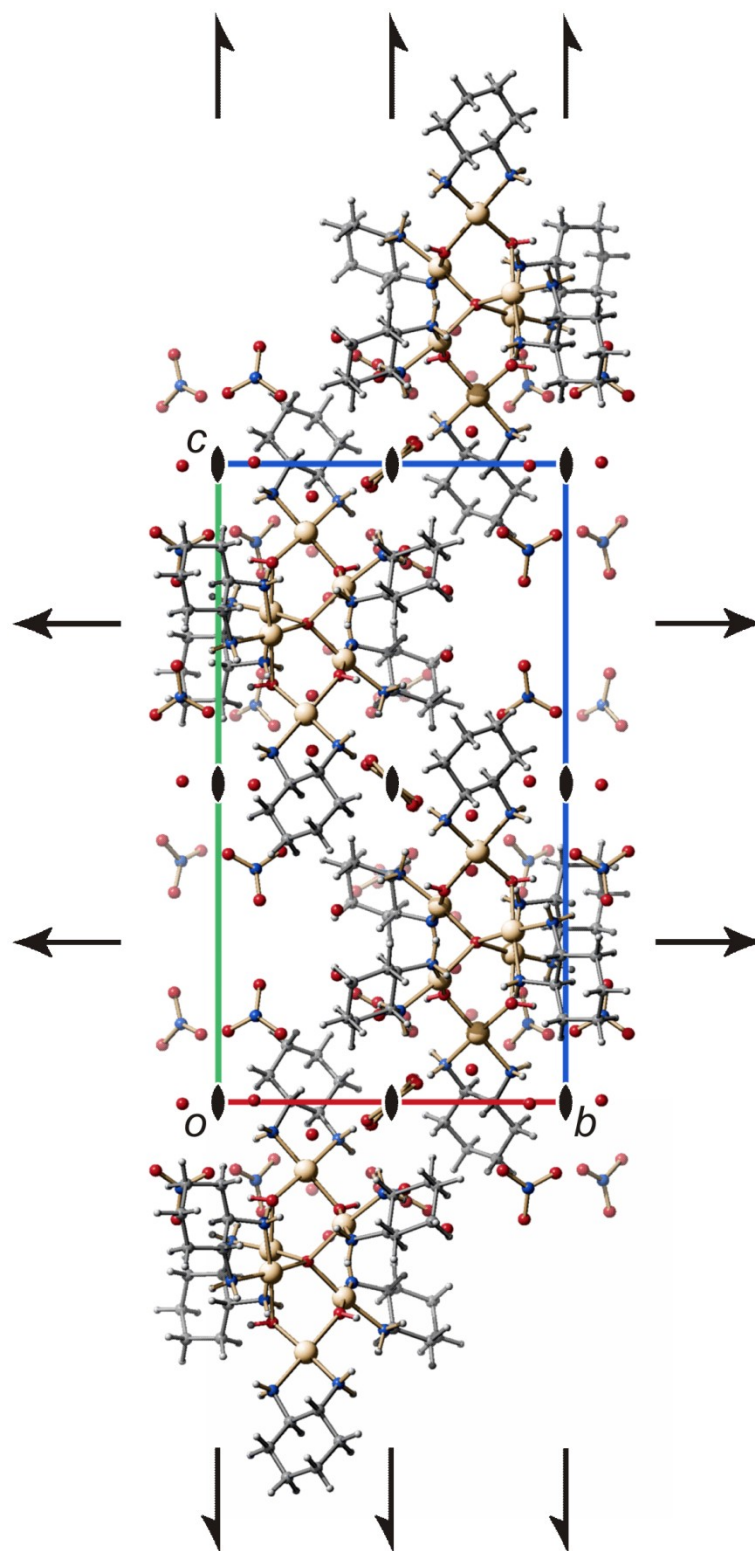


Figure 6.64. SCHAKAL packing diagram of $[\text{Pd}_6(\text{R,R-chxn})_6(\mu_4\text{-O})(\mu\text{-OH})_4](\text{NO}_3)_6$ in crystals of the 12.5-hydrate (25) viewed along $[\bar{1}00]$. The symmetry elements of the space group $P 222_1$ are overlaid. Atoms: carbon (grey), hydrogen (light grey, small), nitrogen (blue), oxygen (red) and palladium (golden).

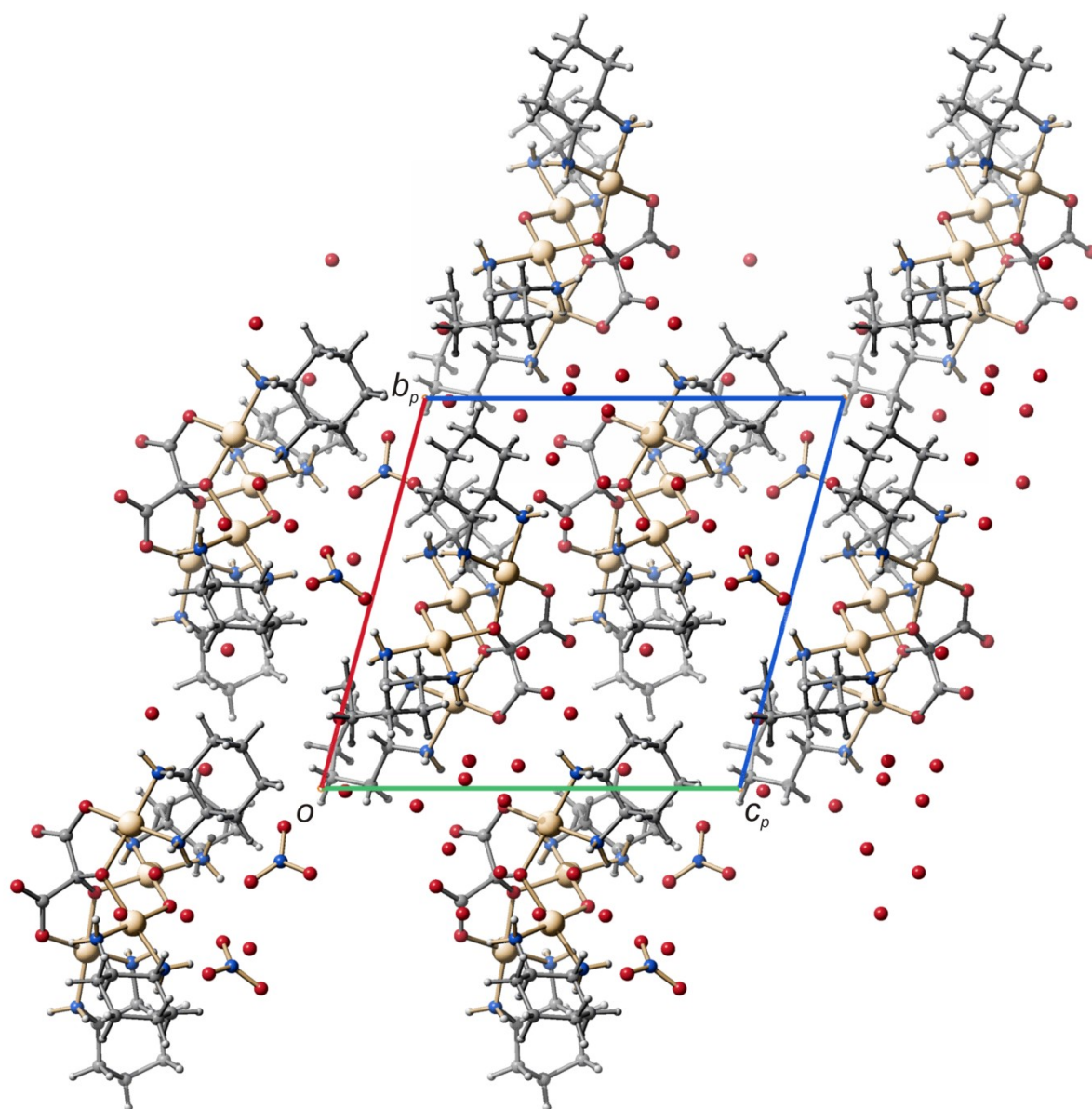


Figure 6.65. SCHAKAL packing diagram of $[\text{Pd}_4(\text{R,R-chxn})_4(\text{C}_3\text{O}_6)(\mu\text{-OH})](\text{NO}_3)_3$ in crystals of the 8-hydrate (**26**) viewed along $[100]$. The symmetry elements of the space group $P 1$ are overlaid. Atoms: carbon (grey), hydrogen (light grey, small), nitrogen (blue), oxygen (red) and palladium (golden).

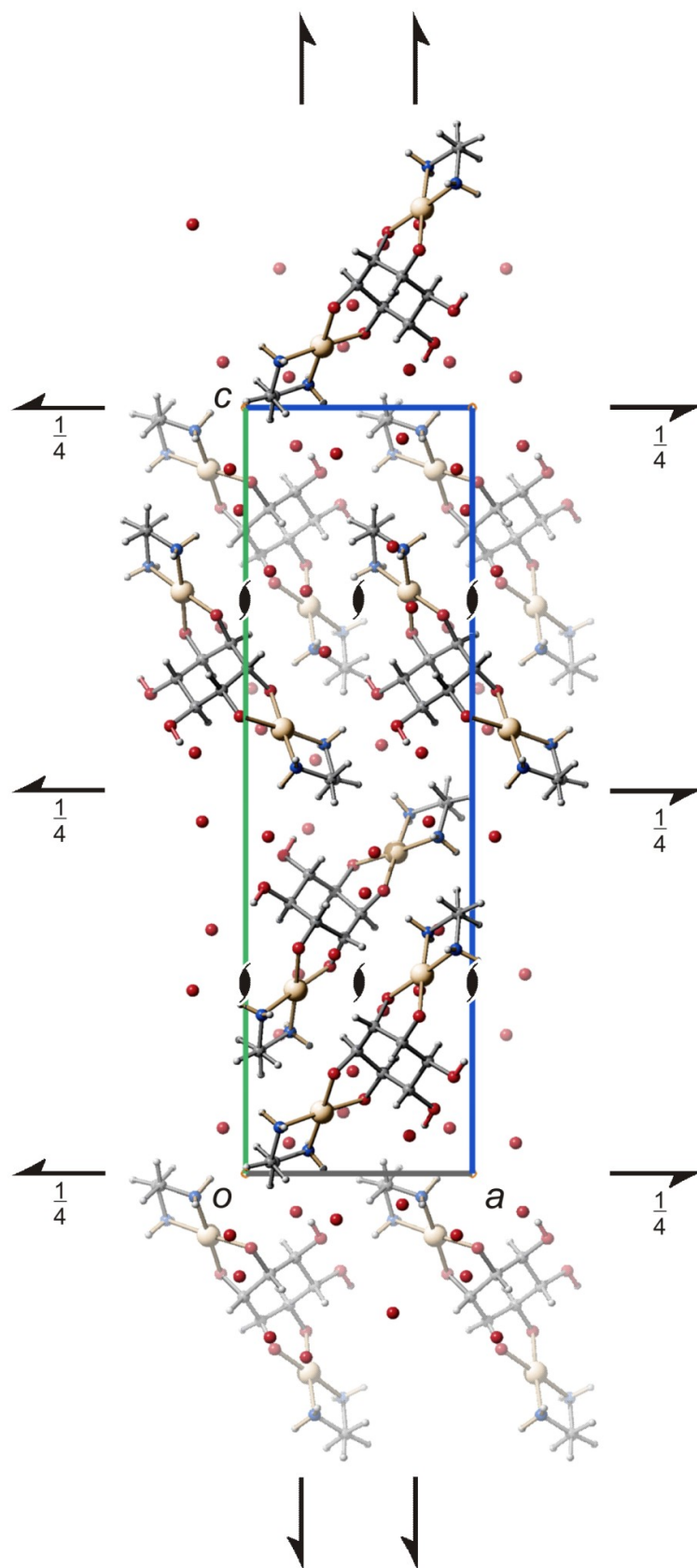


Figure 6.66. SCHAKAL packing diagram of $[\text{Pd}_2(\text{en})_2(\text{D-chiro-Ins}1,2;5,6\text{H-4-}\kappa\text{O}^{1,2};\kappa\text{O}^{5,6})]$ in crystals of the 8-hydrate (**27**) viewed along $[010]$. The symmetry elements of the space group $P 2_12_12_1$ are overlaid. Atoms: carbon (grey), hydrogen (light grey, small), nitrogen (blue), oxygen (red) and palladium (golden).

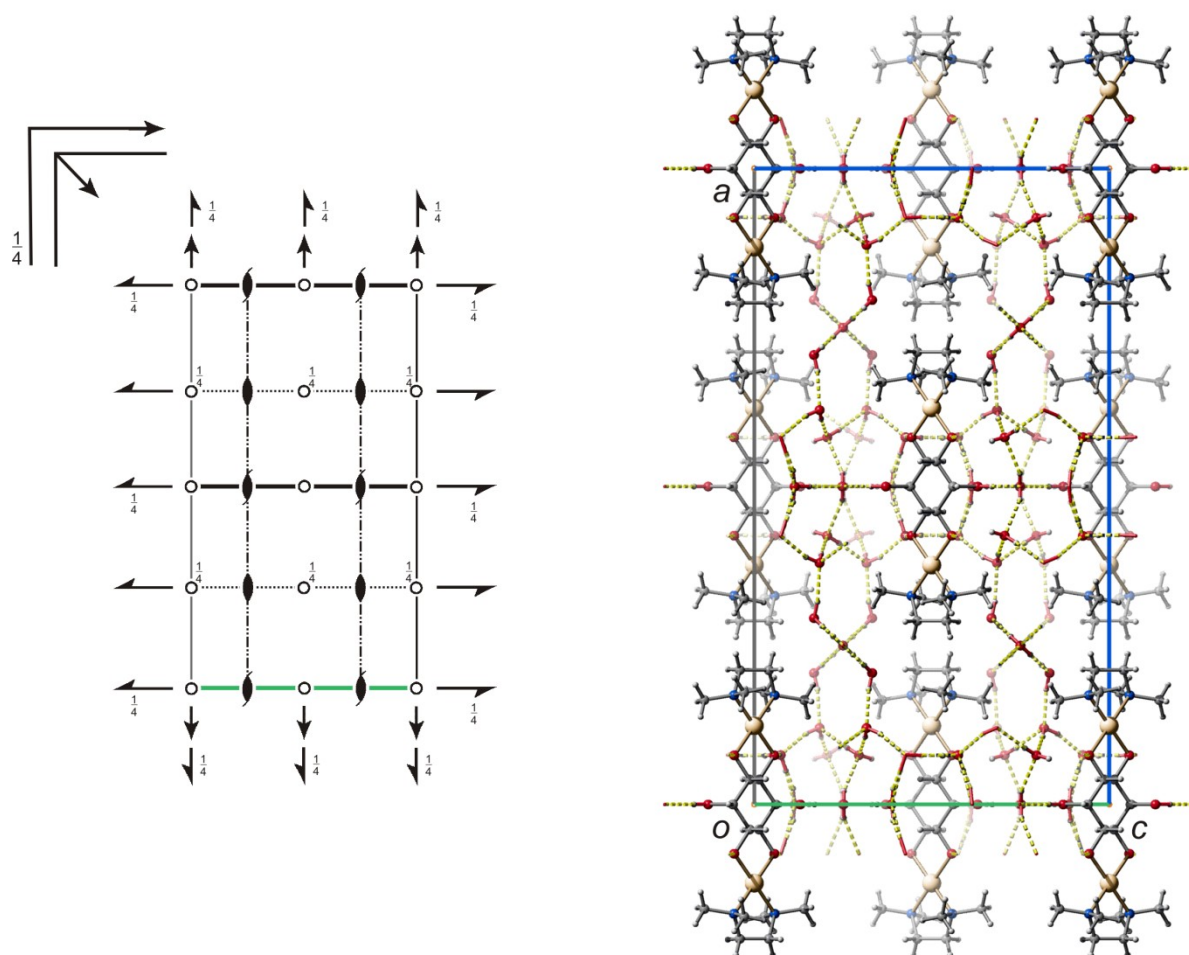


Figure 6.67. SCHAKAL packing diagram of $[\text{Pd}_2(\text{tmen})_2(\text{neo-Ins})_{1,6};3,4\text{H-}_4\text{-}\kappa\text{O}^{1,6};\kappa\text{O}^{3,4}]]$ in crystals of the 22-hydrate (**28**) viewed along $[0\bar{1}0]$. Hydrogen bonds are indicated by yellow dashed lines. The symmetry elements of the space group $Cmce$ are overlaid. Atoms: carbon (grey), hydrogen (light grey, small), nitrogen (blue), oxygen (red) and palladium (golden).

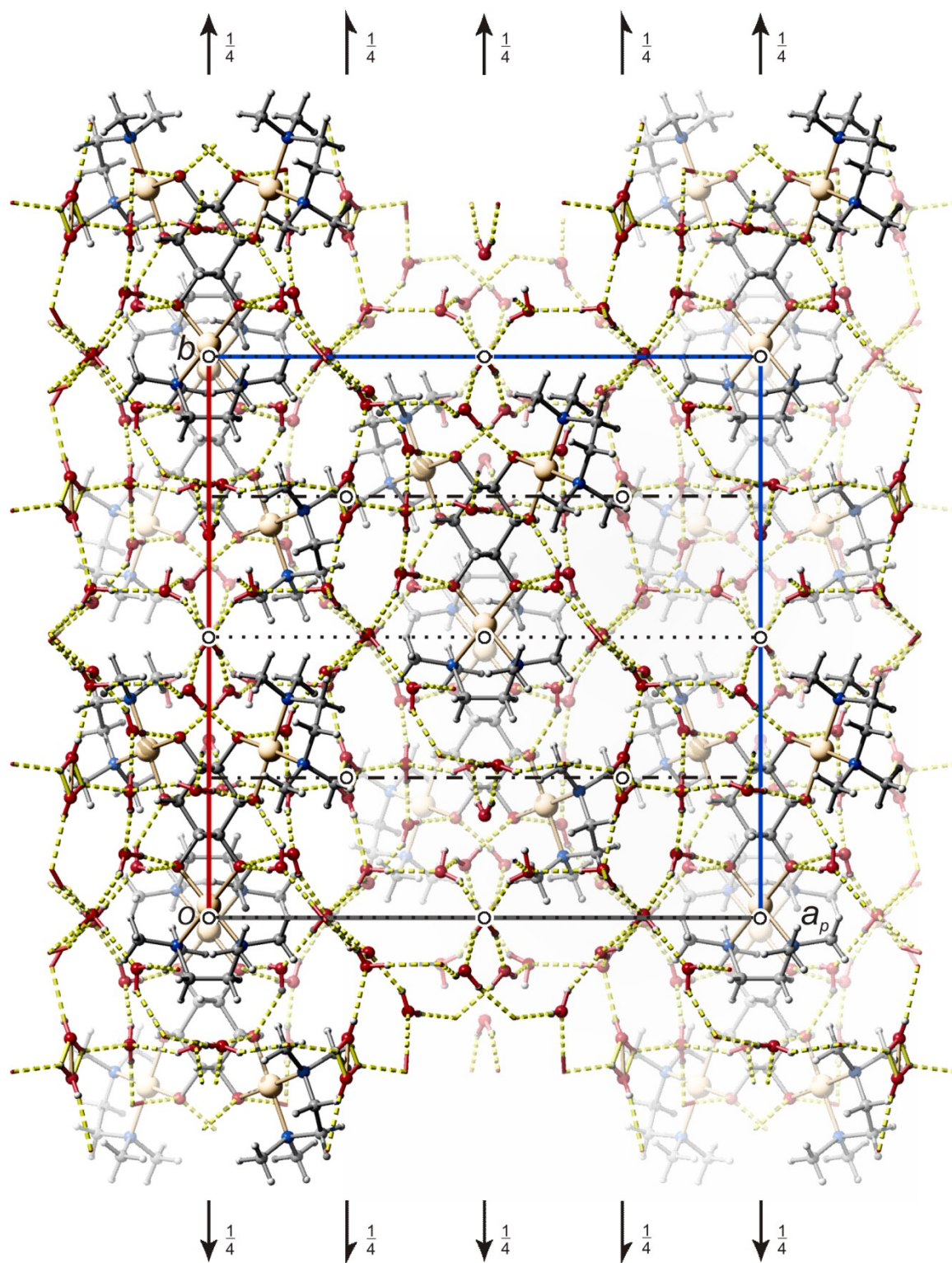


Figure 6.68. SCHAKAL packing diagram of $\text{Pd}_3(\text{tmen})_3(\text{scylo-InsH-6-}\kappa\text{O}^{1,2}:\kappa\text{O}^{3,4}:\kappa\text{O}^{5,6})$ in crystals of the 23-hydrate (**29**) viewed along $[00\bar{1}]$. Hydrogen bonds are indicated by yellow dashed lines. The symmetry elements of the space group $C2/c$ are overlaid. Atoms: carbon (grey), hydrogen (light grey, small), nitrogen (blue), oxygen (red) and palladium (golden).

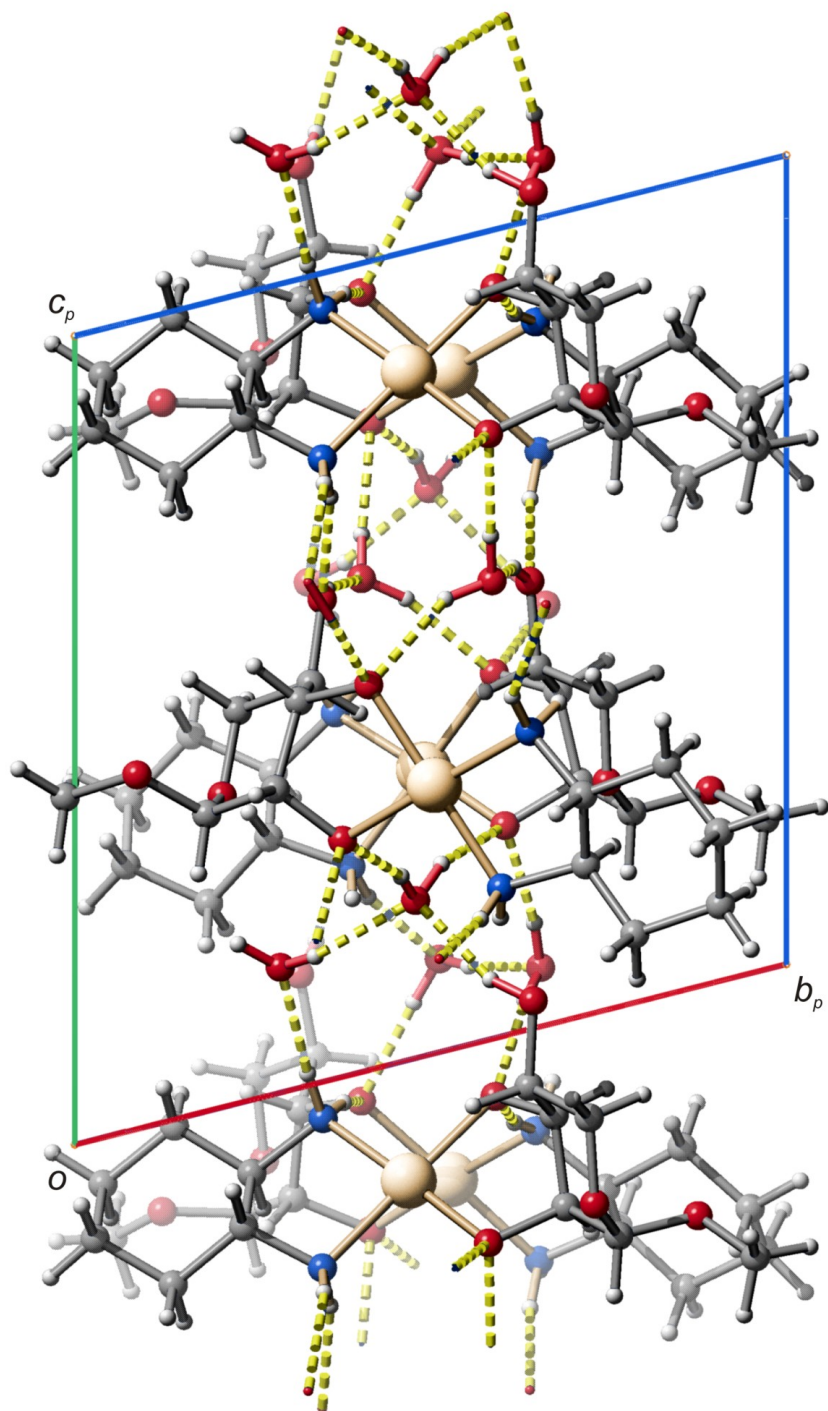


Figure 6.69. SCHAKAL packing diagram of $[\text{Pd}(\text{R},\text{R}\text{-chxn})(\text{Me-}\alpha\text{-D-Lyxp2,3H-2-}\kappa\text{O}^{2,3})]$ in crystals of the 2.25-hydrate (**30**) viewed along $[\bar{1}00]$. Hydrogen bonds are indicated by yellow dashed lines. The symmetry elements of the space group $P 1$ are overlaid. Atoms: carbon (grey), hydrogen (light grey, small), nitrogen (blue), oxygen (red) and palladium (golden).

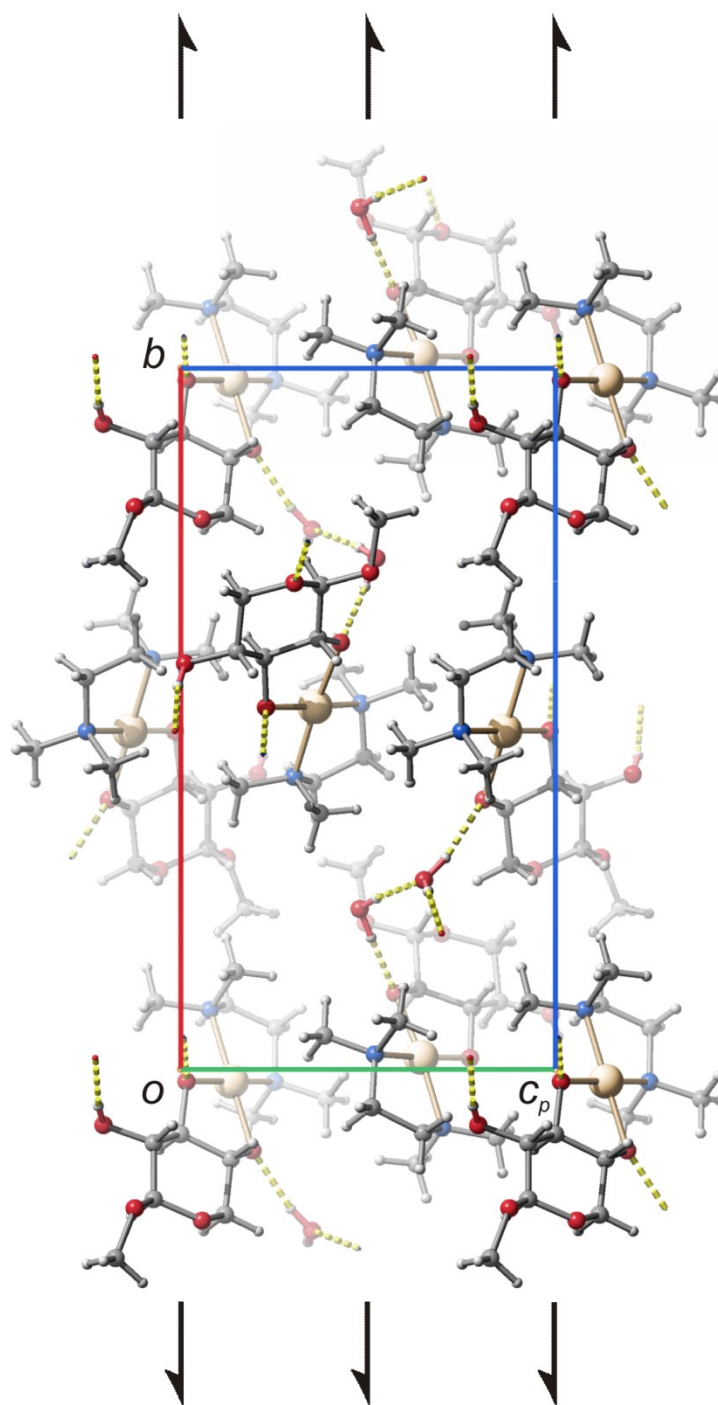


Figure 6.70. SCHAKAL packing diagram of $[\text{Pd}(\text{tmen})(\text{Me-}\beta\text{-D-Xylp2,3H-}\kappa\text{O}^{2,3})][\text{Pd}(\text{tmen})(\text{Me-}\beta\text{-D-Xylp3,4H-}\kappa\text{O}^{3,4})]$ in crystals of the dihydrate (**31**) viewed along $[100]$. Hydrogen bonds are indicated by yellow dashed lines. The symmetry elements of the space group $P2_1$ are overlaid. Atoms: carbon (grey), hydrogen (light grey, small), nitrogen (blue), oxygen (red) and palladium (golden).

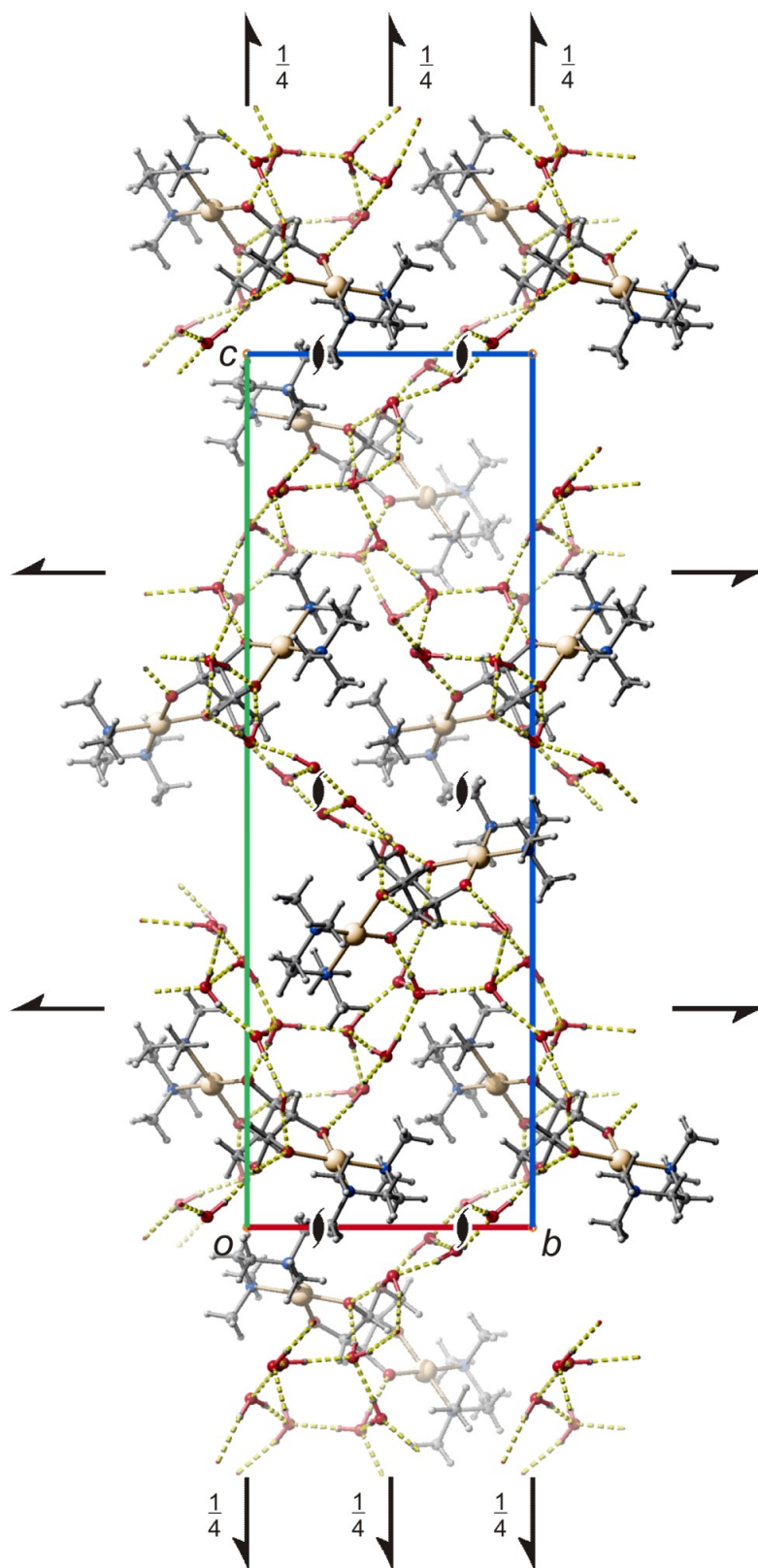


Figure 6.71. SCHAKAL packing diagram of $[\text{Pd}_2(\text{tmen})_2(\beta\text{-D-Arap}1,2;3,4\text{H-4-}\kappa\text{O}^{1,2}:\kappa\text{O}^{3,4})]$ in crystals of the 10-hydrate (**32**) viewed along $[\bar{1}00]$. Hydrogen bonds are indicated by yellow dashed lines. The symmetry elements of the space group $P 2_12_12_1$ are overlaid. Atoms: carbon (grey), hydrogen (light grey, small), nitrogen (blue), oxygen (red) and palladium (golden).

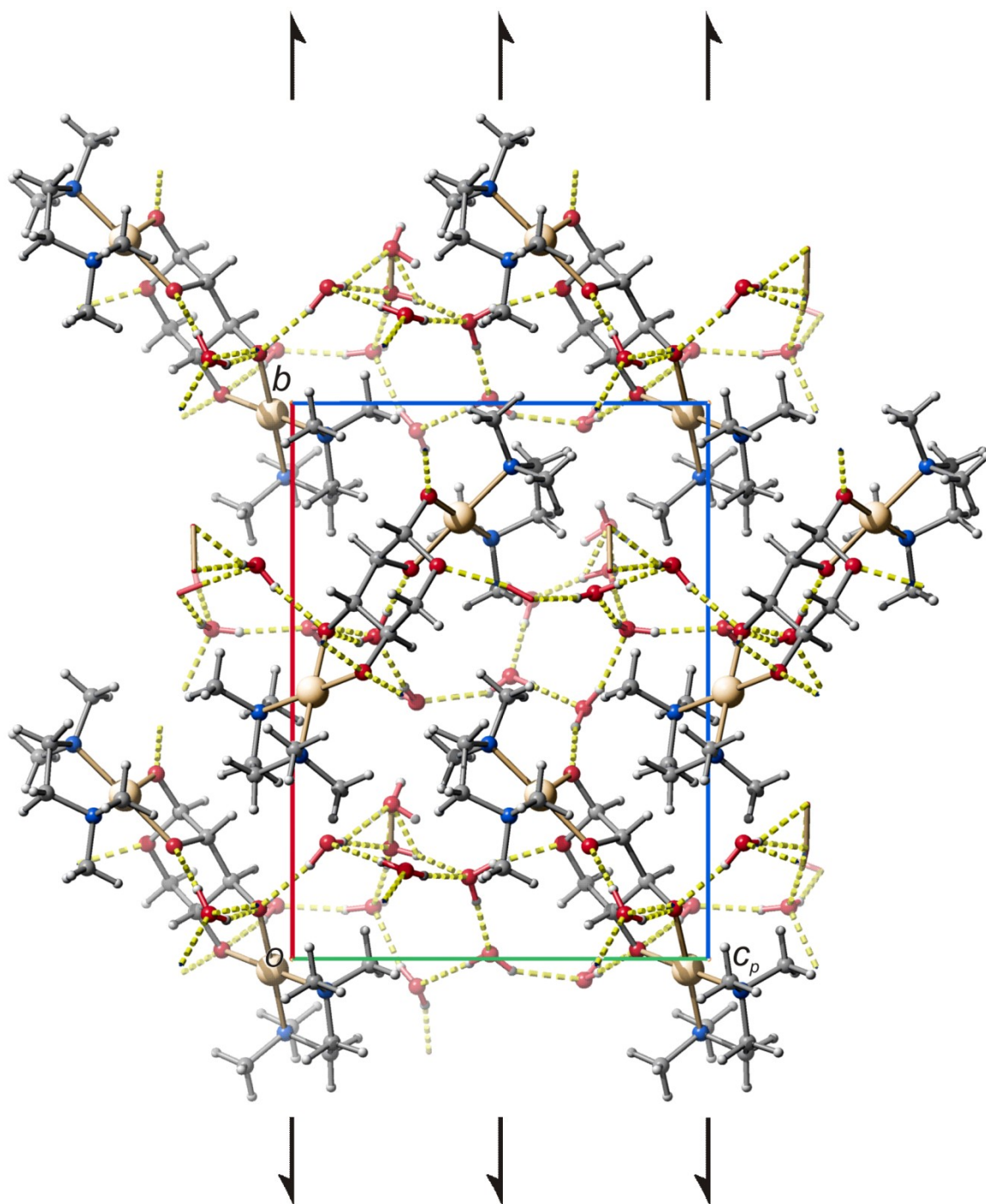


Figure 6.72. SCHAKAL packing diagram of $[\text{Pd}_2(\text{tmen})_2(\beta\text{-D-Lyxp1,2;3,4H}_4\text{-}\kappa\text{O}^{1,2};\kappa\text{O}^{3,4})]$ in crystals of the 10-hydrate (**33**) viewed along $[100]$. Hydrogen bonds are indicated by yellow dashed lines. The symmetry elements of the space group $P2_1$ are overlaid. Atoms: carbon (grey), hydrogen (light grey, small), nitrogen (blue), oxygen (red) and palladium (golden).

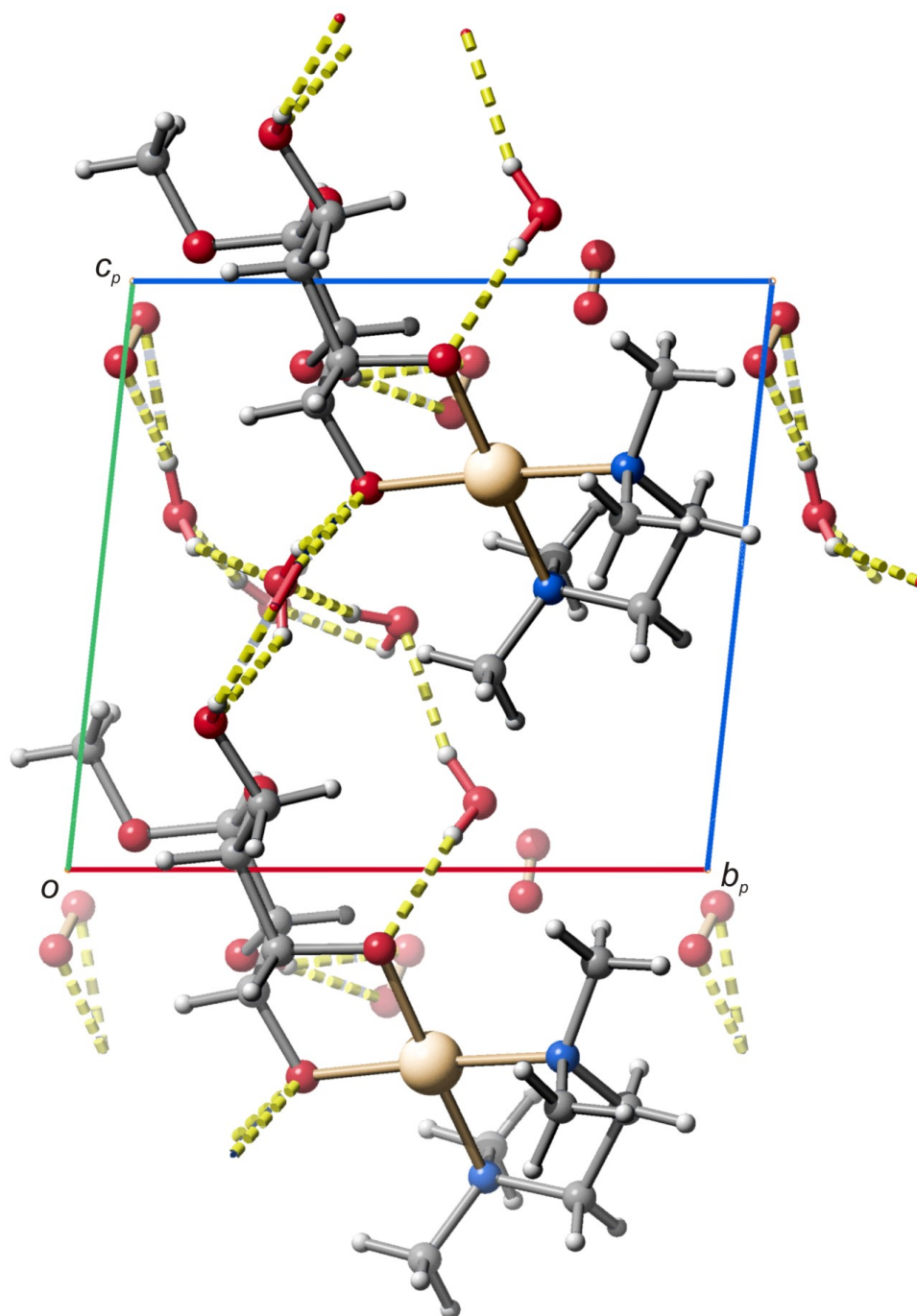


Figure 6.73. SCHAKAL packing diagram of Pd(tmen)(Me- α -D-Galp3,4H₂- κ O^{3,4})] in crystals of the 8-hydrate (**34**) viewed along $[\bar{1}00]$. Hydrogen bonds are indicated by yellow dashed lines. The symmetry elements of the space group $P1$ are overlaid. Atoms: carbon (grey), hydrogen (light grey, small), nitrogen (blue), oxygen (red) and palladium (golden).

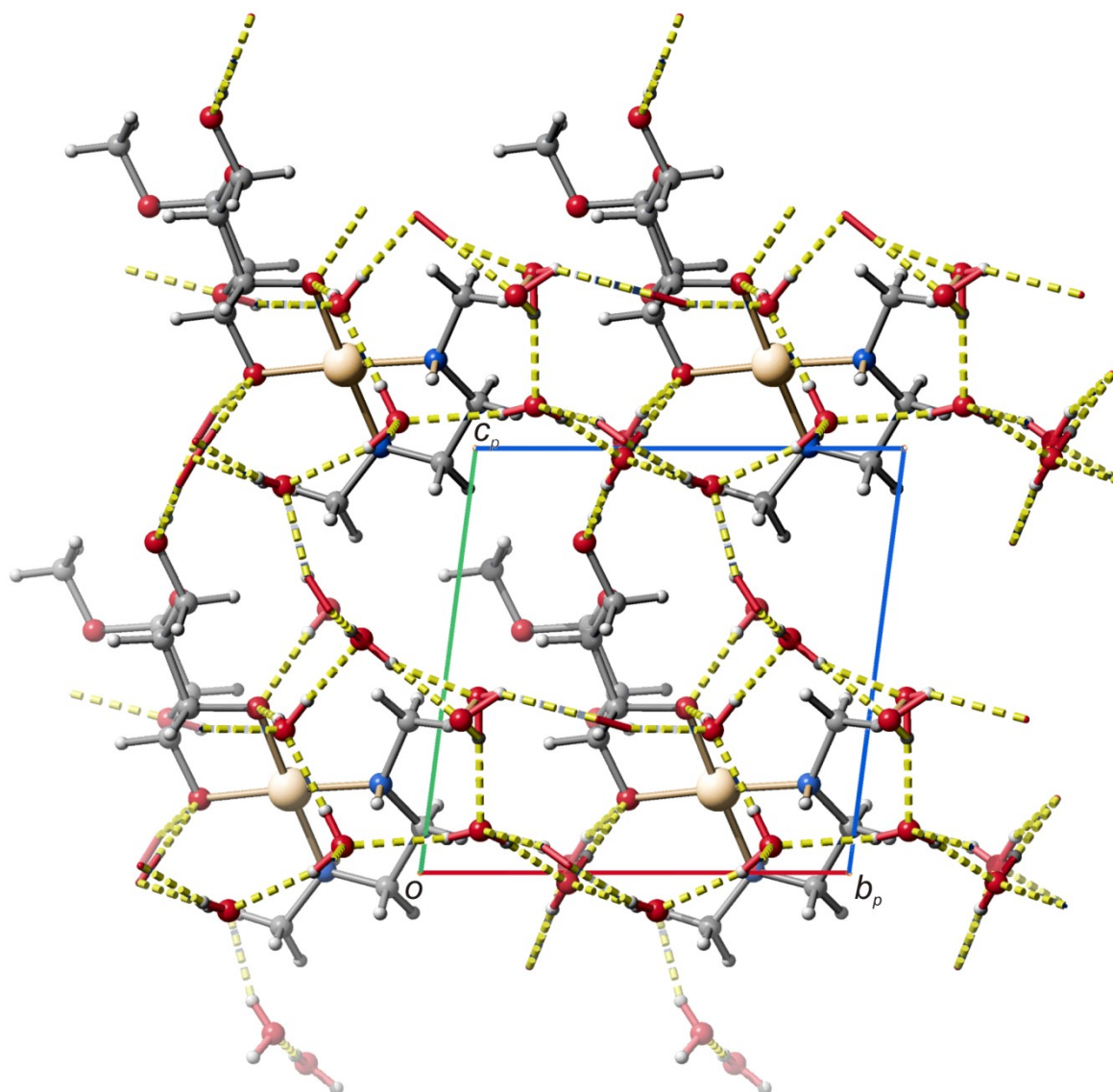


Figure 6.74. SCHAKAL packing diagram of $[\text{Pd}(\text{dmen})(\text{Me-}\alpha\text{-D-Galp3,4H}_2\text{-}\kappa\text{O}^{3,4})]$ in crystals of the 9-hydrate (**35**) viewed along $[\bar{1}00]$. Hydrogen bonds are indicated by yellow dashed lines. The symmetry elements of the space group $P 1$ are overlaid. Atoms: carbon (grey), hydrogen (light grey, small), nitrogen (blue), oxygen (red) and palladium (golden).

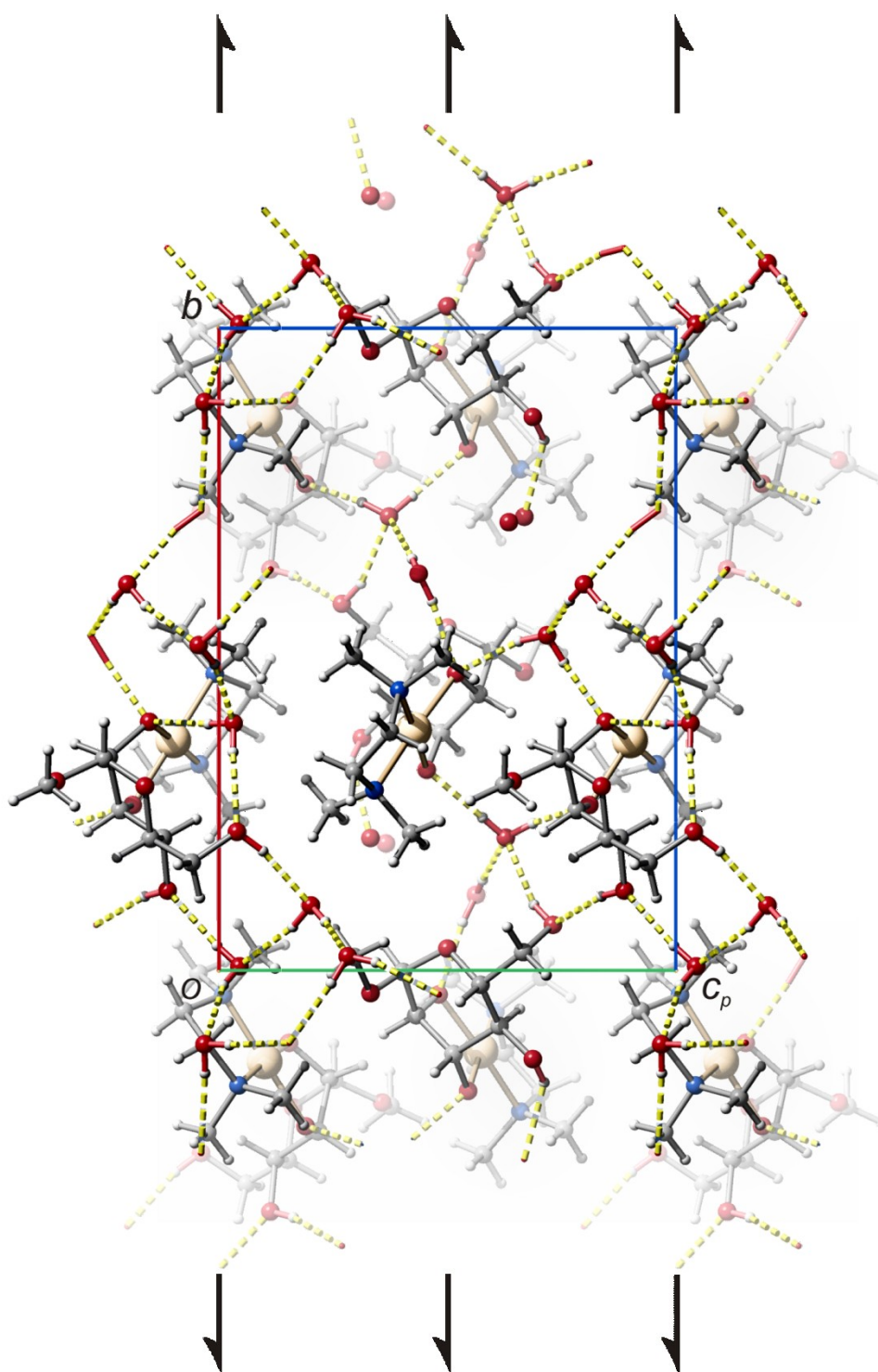


Figure 6.75. SCHAKAL packing diagram of $[\text{Pd}(\text{tmen})(\text{Me-}\alpha\text{-D-Manp}_{2,3}\text{H}_2\text{-}\kappa\text{O}^{2,3})]$ in crystals of the 3.5-hydrate (**36**) viewed along $[100]$. The symmetry elements of the space group $P 2_1$ are overlaid. Atoms: carbon (grey), hydrogen (light grey, small), nitrogen (blue), oxygen (red) and palladium (golden).

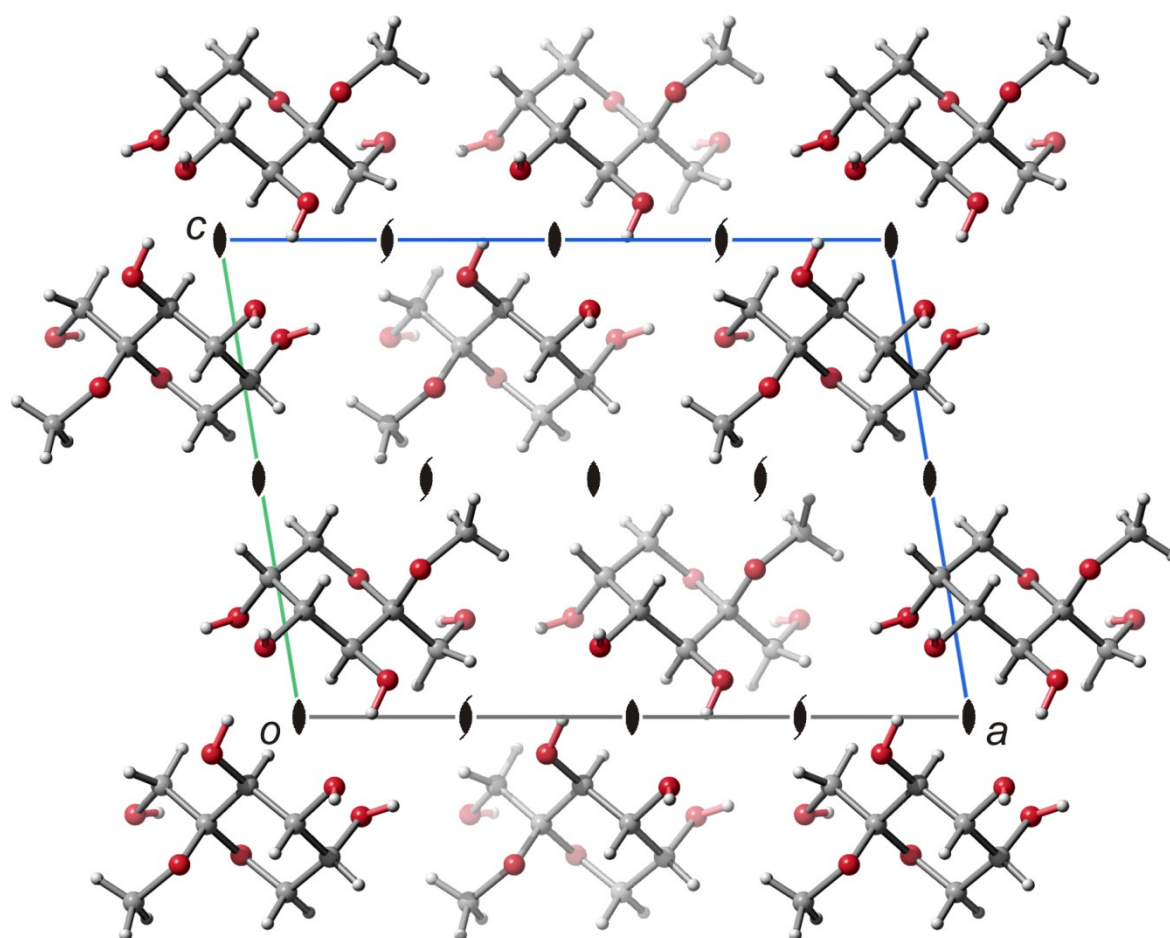


Figure 6.76. SCHAKAL packing diagram of methyl β -D-fructopyranoside (**37**) viewed along [010]. The symmetry elements of the space group $C2$ are overlaid. Atoms: carbon (grey), hydrogen (light grey, small), nitrogen (blue), oxygen (red) and palladium (golden).

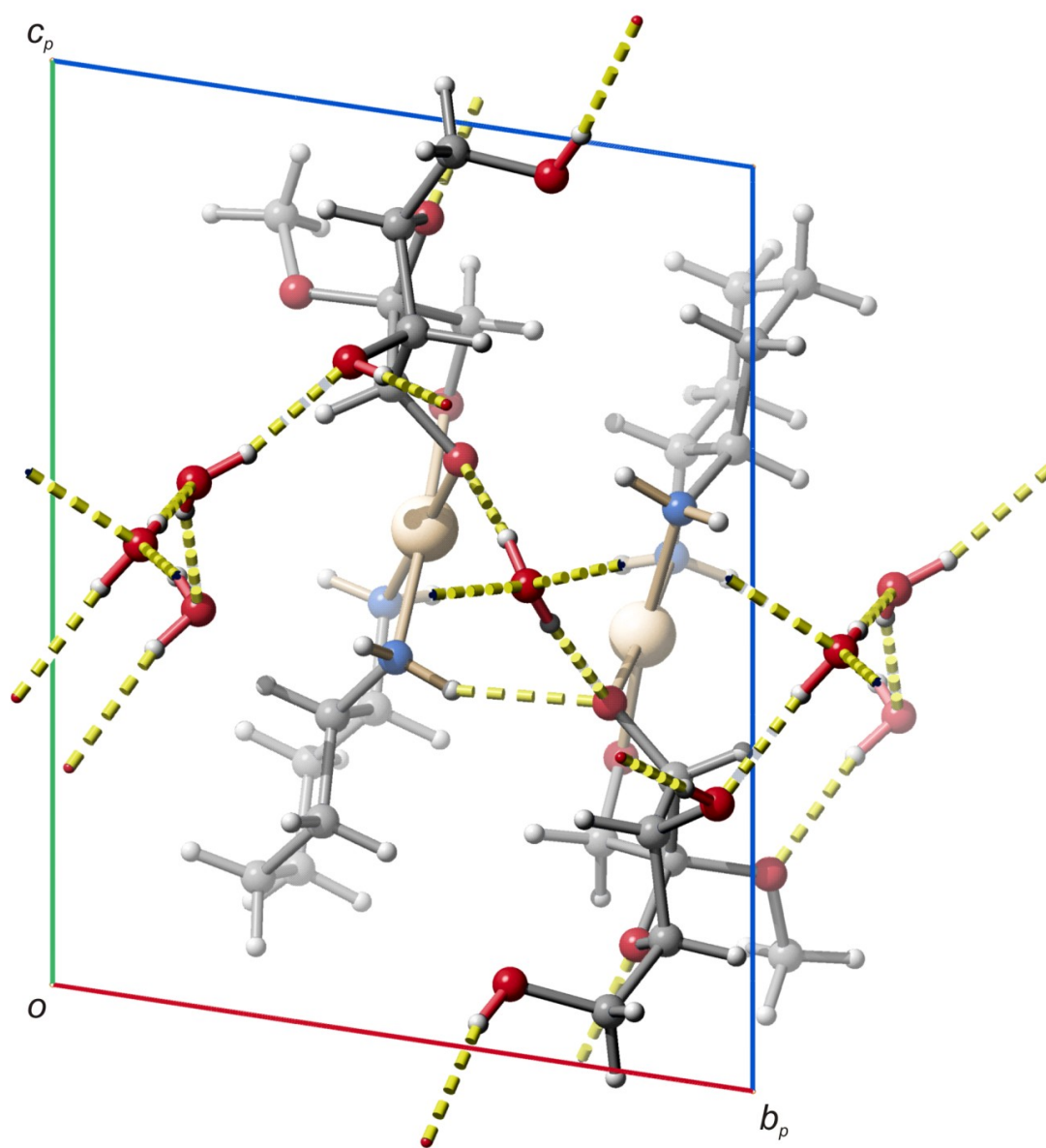


Figure 6.77. SCHAKAL packing diagram of $[\text{Pd}(\text{R,R}\text{-chxn})(\text{Me-}\alpha\text{-D-Fru}/1,3\text{H}_2\text{-}\kappa\text{O}^{1,3})]$ in crystals of the dihydrate (**38**) viewed along $[\bar{1}00]$. Hydrogen bonds are indicated by yellow dashed lines. The symmetry elements of the space group $P 1$ are overlaid. Atoms: carbon (grey), hydrogen (light grey, small), nitrogen (blue), oxygen (red) and palladium (golden).

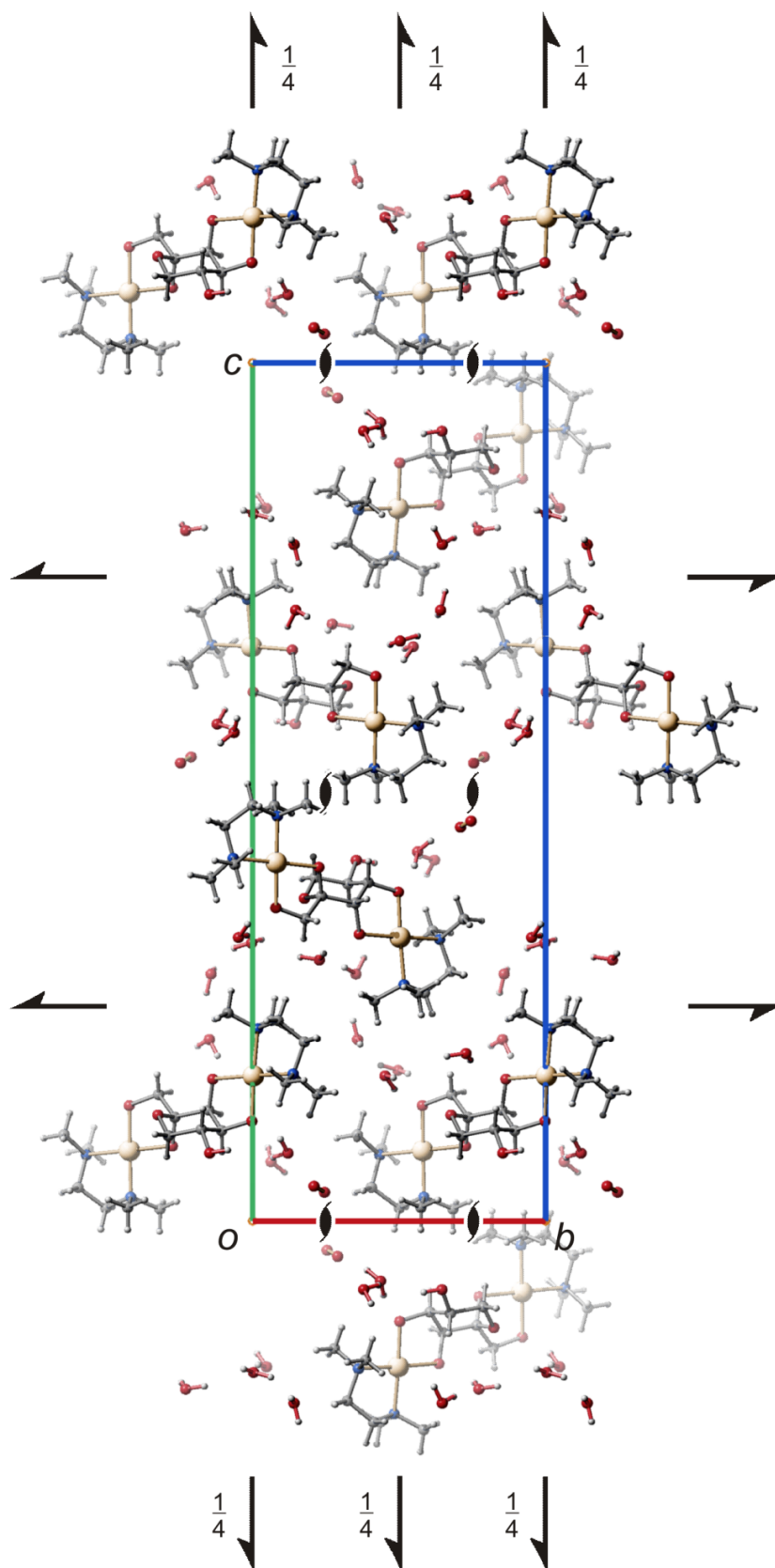


Figure 6.78. SCHAKAL packing diagram of $[\text{Pd}_2(\text{tmen})_2(\alpha\text{-D-Tagp}1,2;3,4\text{H}_4\text{-}\kappa\text{O}^{1,2};\kappa\text{O}^{3,4})]$ in crystals of the 8-hydrate (**39**) viewed along $[\bar{1}00]$. The symmetry elements of the space group $P2_12_12_1$ are overlaid. Atoms: carbon (grey), hydrogen (light grey, small), nitrogen (blue), oxygen (red) and palladium (golden).

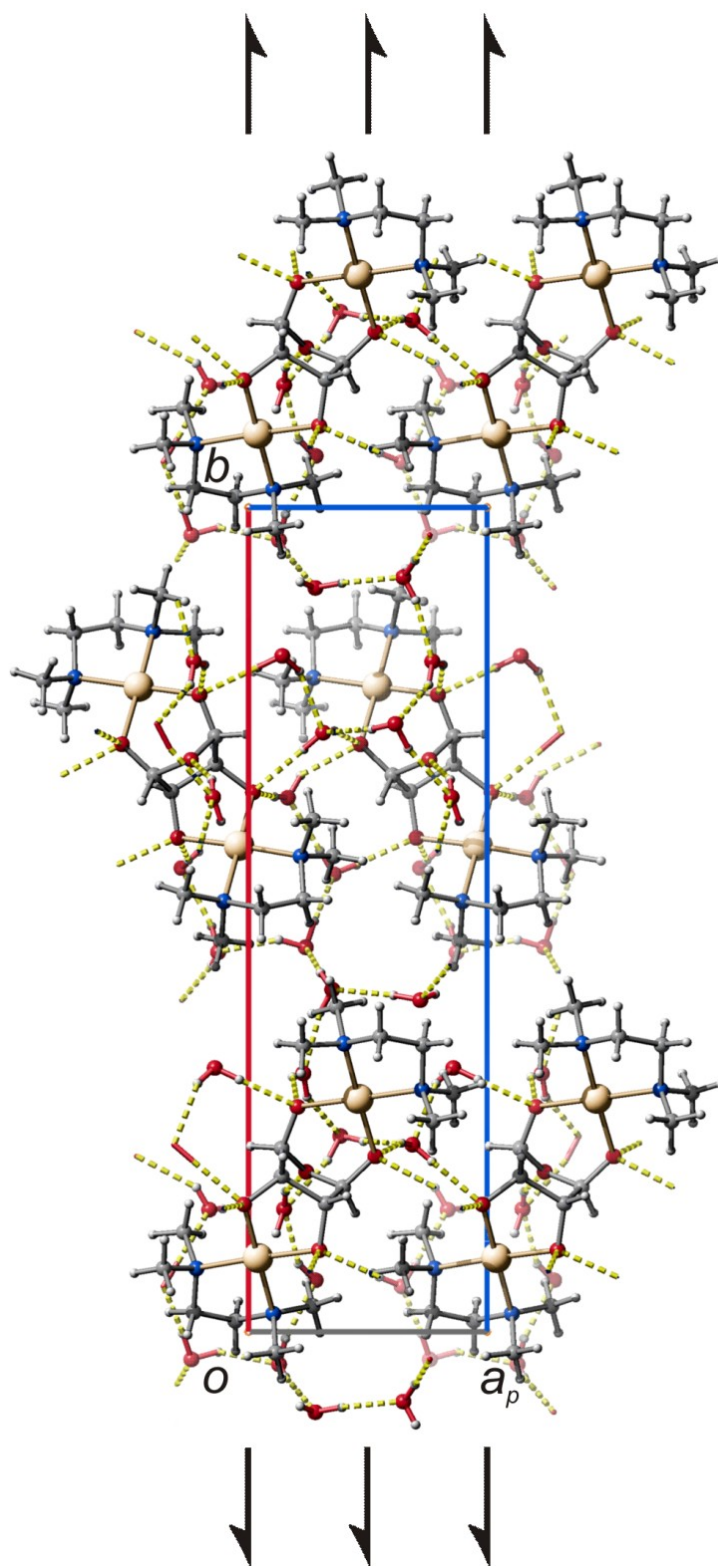


Figure 6.79. SCHAKAL packing diagram of $[\text{Pd}_2(\text{tmen})_2(\text{Ery4ald}/\text{H}_{-4}\text{-}\kappa\text{O}^{1.4}:\kappa\text{O}^{2.3})]$ in crystals of the 12-hydrate (**40**) viewed along $[00\bar{1}]$. Hydrogen bonds are indicated by yellow dashed lines. The symmetry elements of the space group $P2_1$ are overlaid. Atoms: carbon (grey), hydrogen (light grey, small), nitrogen (blue), oxygen (red) and palladium (golden).

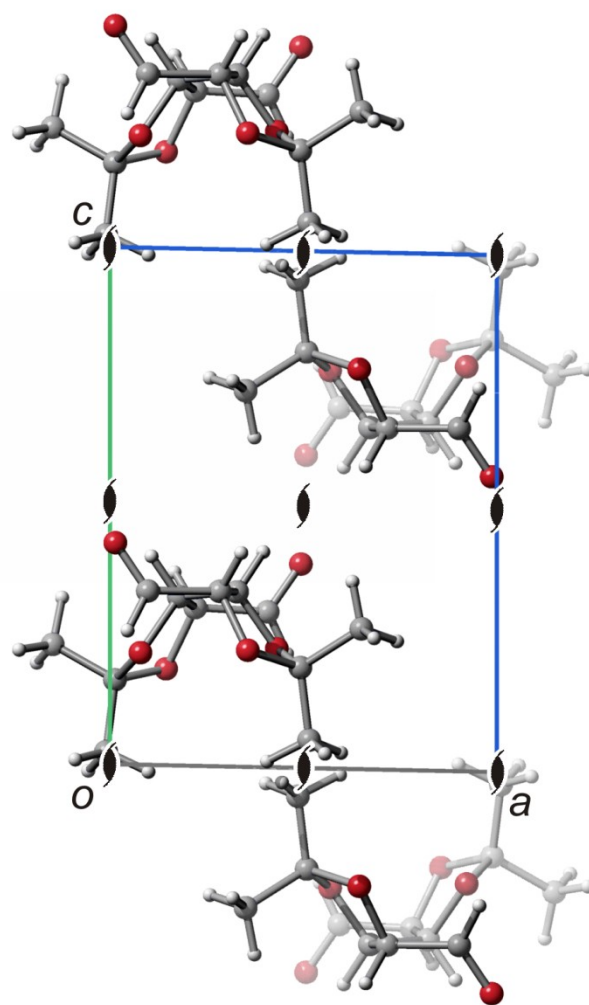


Figure 6.80. SCHAKAL packing diagram of 3,4,5-di-*O*-isopropylidene-*D*-manno-hexodialdose (**41**) viewed along [010]. The symmetry elements of the space group $P 2_1$ are overlaid. Atoms: carbon (grey), hydrogen (light grey, small), nitrogen (blue), oxygen (red) and palladium (golden).

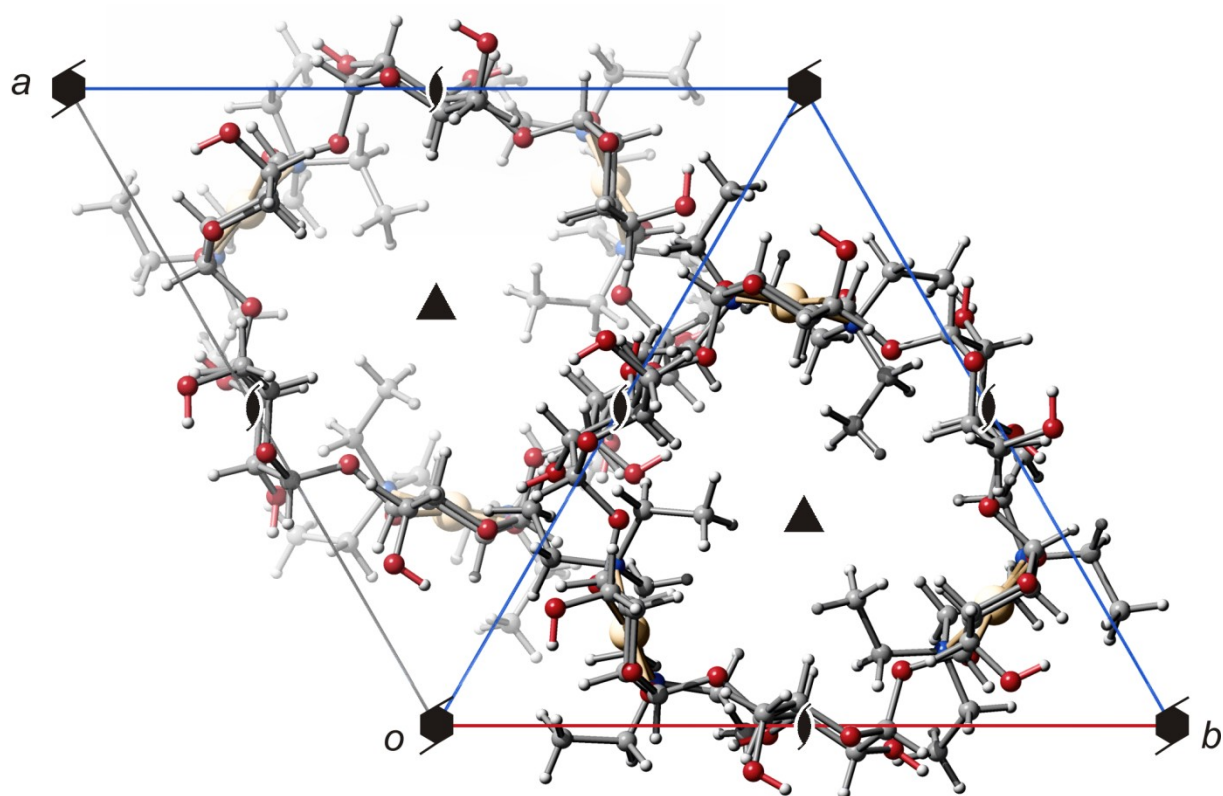


Figure 6.81. SCHAKAL packing diagram of $[\text{Pd}_3(\text{teen})_3(\alpha\text{-CDH}_6)] \cdot 34 \text{H}_2\text{O}$ (**42**) viewed along $[001]$. The symmetry elements of the space group $P6_3$ are overlaid. The atoms of the minor part of disordered fragments and water are not shown. Atoms: carbon (grey), hydrogen (light grey, small), nitrogen (blue), oxygen (red) and palladium (golden).

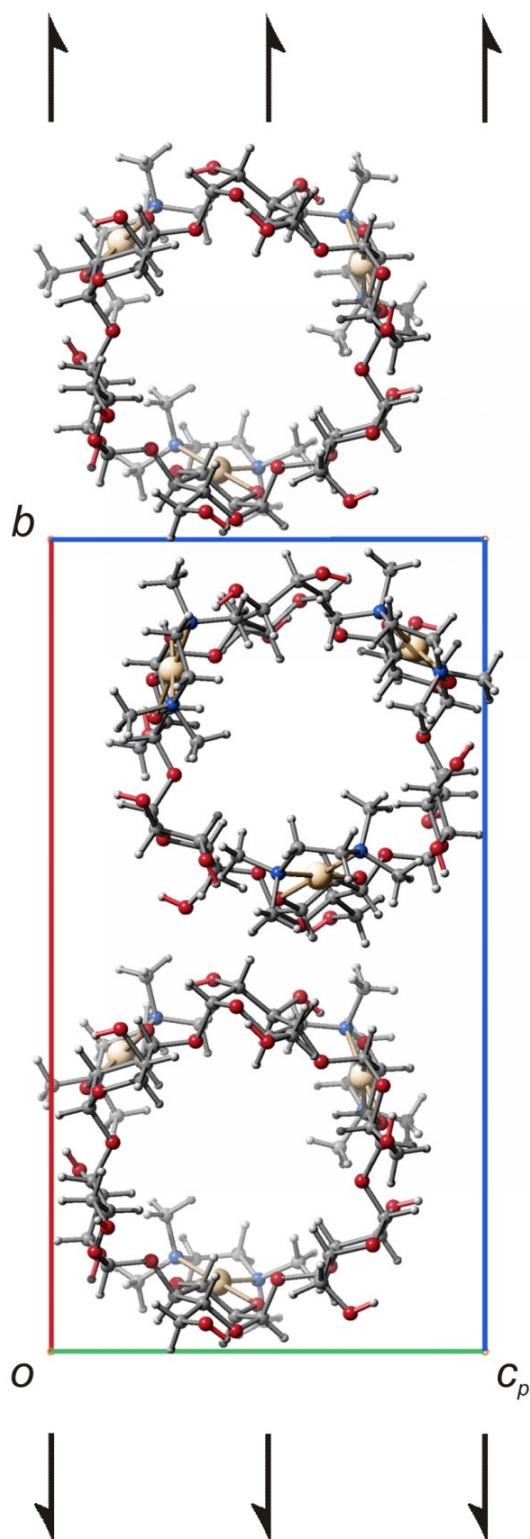


Figure 6.82. SCHAKAL packing diagram of $[\text{Pd}_3(\text{tmen})_3(\alpha\text{-CDH}_6)] \cdot 20.7 \text{H}_2\text{O} \cdot \text{acetone}$ (**43**) viewed along $[100]$. The symmetry elements of the space group $P2_1$ are overlaid. The atoms of the minor part of disordered fragments and water are not shown. Atoms: carbon (grey), hydrogen (light grey, small), nitrogen (blue), oxygen (red) and palladium (golden).

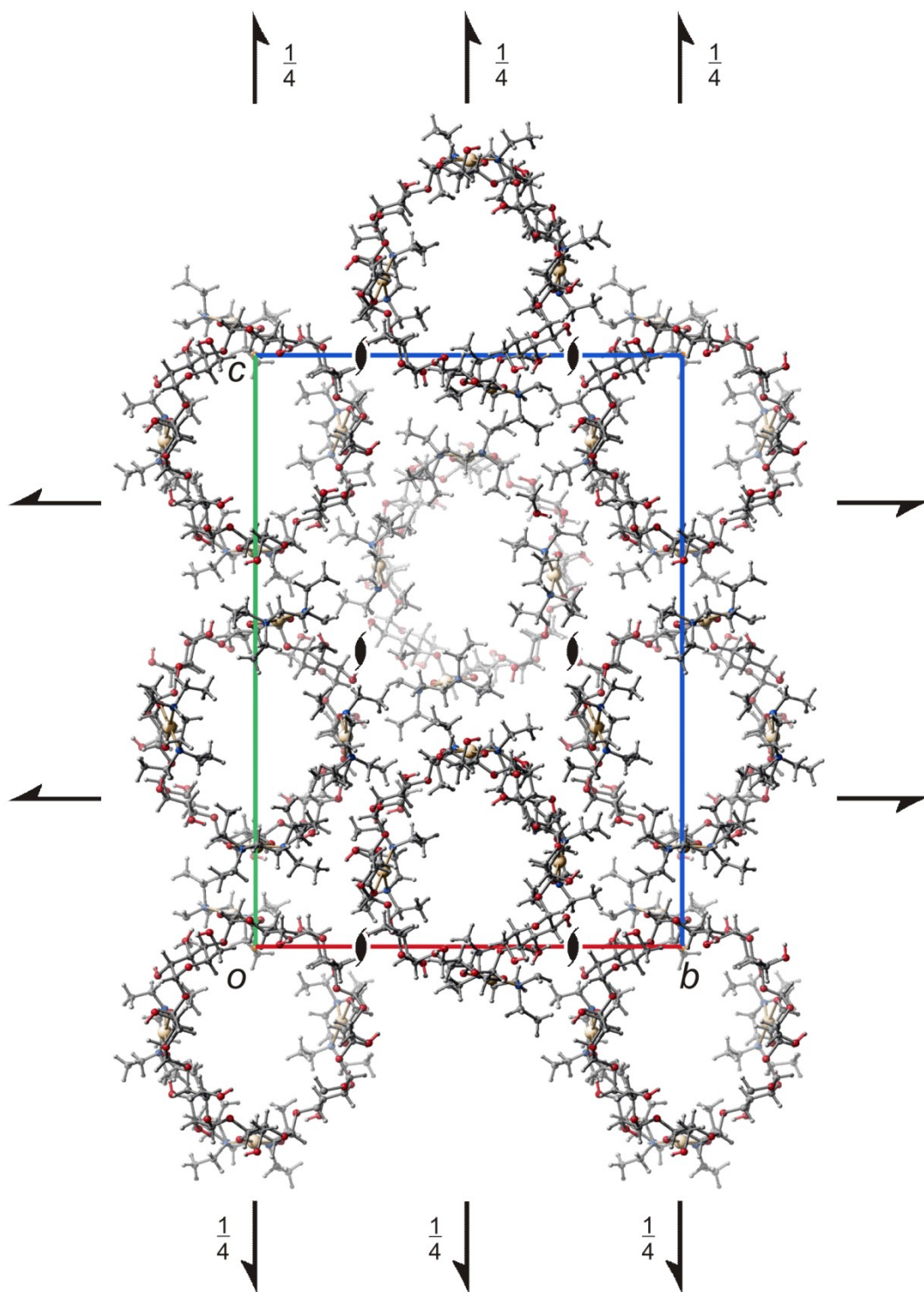


Figure 6.83. SCHAKAL packing diagram of $[\text{Pd}_4(\text{teen})_4(\gamma\text{-CDH-}_8)] \cdot 12 \text{H}_2\text{O}$ (**44**) viewed along $[\bar{1}00]$. The symmetry elements of the space group $P2_12_12_1$ are overlaid. The atoms of the minor part of disordered fragments and water are not shown. Atoms: carbon (grey), hydrogen (light grey, small), nitrogen (blue), oxygen (red) and palladium (golden).

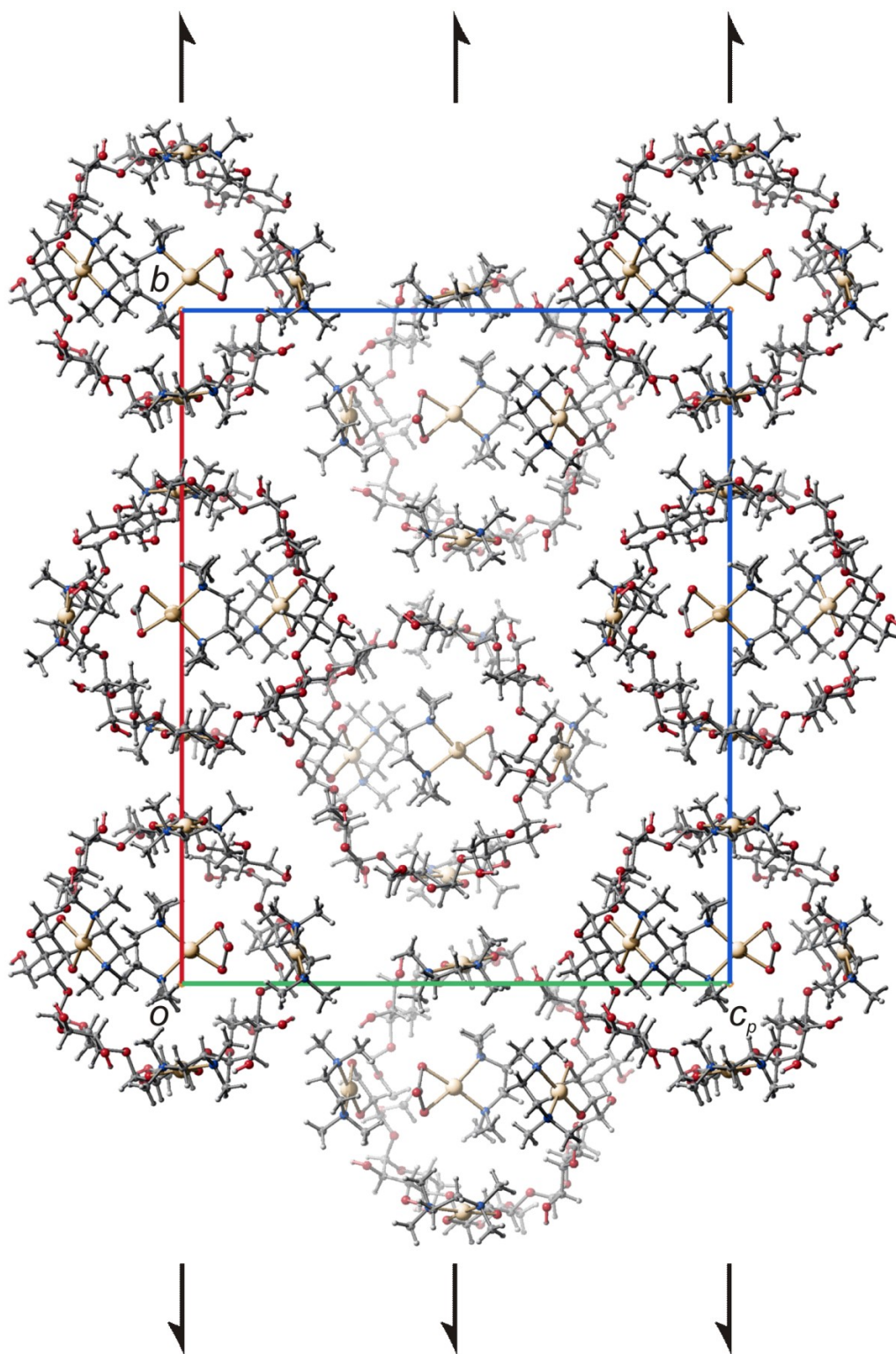


Figure 6.84. SCHAKAL packing diagram of $[\text{Pd}_4(\text{tmen})_4(\gamma\text{-CDH-8})] \cdot 65.79 \text{ H}_2\text{O} \cdot 0.96 [\text{Pd}(\text{tmen})\text{CO}_3]$ (**45**) viewed along $[100]$. The symmetry elements of the space group $P2_1$ are overlaid. The atoms of the minor part of disordered fragments and water are not shown. Atoms: carbon (grey), hydrogen (light grey, small), nitrogen (blue), oxygen (red) and palladium (golden).

6.3 Crystallographic tables

Table 6.41. Crystallographic tables of [Pd(tmen)(OH)₂] · 2 H₂O (**1**), [Pd(tmchxn)(CO₃)] · 6 H₂O (**2**) and (teenH₂)[PdCl₄] (**3**).

Compound	1	2	3
Empirical formula	C ₆ H ₂₂ N ₂ O ₄ Pd	C ₁₁ H ₃₄ N ₂ O ₉ Pd	C ₁₀ H ₂₆ Cl ₄ N ₂ Pd
M_r /g mol ⁻¹	292.67	444.82	422.56
Crystal size /mm	0.17 × 0.10 × 0.08	0.20 × 0.16 × 0.16	0.20 × 0.12 × 0.12
Crystal system	Orthorhombic	Orthorhombic	Monoclinic
Space group	<i>P</i> 2 ₁ 2 ₁ 2 ₁	<i>C</i> 222 ₁	<i>P</i> 2 ₁ / <i>n</i>
<i>a</i> /Å	5.5453(2)	8.0316(3)	7.2647(2)
<i>b</i> /Å	10.9053(5)	12.1857(4)	10.8306(3)
<i>c</i> /Å	18.3138(7)	19.3677(5)	10.7669(4)
α /°	90	90	90
β /°	90	90	102.022(3)
γ /°	90	90	90
<i>V</i> /Å ³	1107.49(8)	1895.53(10)	828.57(4)
<i>Z</i>	4	4	2
ρ_{calcd} /g cm ⁻³	1.75531(13)	1.55871(8)	1.69372(8)
μ /mm ⁻¹	1.666	1.021	1.748
Absorption correction	Multi-scan	None	Numerical
$T_{\text{min}}, T_{\text{max}}$	0.85056, 1.00000	–	0.2545, 0.8683
Refls. measured	8292	6577	4810
R_{int}	0.0444	0.0330	0.1180
Mean $\sigma(I)/I$	0.0569	0.0339	0.0809
θ range	3.82–26.33	3.21–27.47	4.21–30.00
Observed refls.	2005	2002	872
<i>x, y</i> (weighting scheme)	0.0099, 0	0.0291, 2.1805	0.0522, 0
Flack parameter	–0.04(3)	0.00(5)	–
Refls. in refinement	2245	2181	1217
Parameters	140	127	81
Restraints	0	10	0
$R(F_{\text{obs}})$	0.0249	0.0303	0.0456
$R_w F^2$	0.0368	0.0696	0.1001
<i>S</i>	0.904	1.110	0.964
Shift/error _{max}	0.002	0.001	0.001
Max. res. density /e Å ⁻³	0.429	0.994	0.628
Min. res. density /e Å ⁻³	–0.409	–0.994	–1.313

6 Appendix

Table 6.42. Crystallographic tables of [Pd(teen)Cl₂] (**4**), [Pd(bpy)(OH)₂] · 5 H₂O (**5**) and [Pd(phen)(OH)₂] · 5 H₂O (**6**).

Compound	4	5	6
Empirical formula	C ₁₀ H ₂₄ Cl ₂ N ₂ Pd	C ₁₀ H ₂₀ N ₂ O ₇ Pd	C ₁₂ H ₂₀ N ₂ O ₇ Pd
M_r /g mol ⁻¹	349.64	386.70	410.72
Crystal size /mm	0.36 × 0.045 × 0.037	0.29 × 0.07 × 0.06	0.19 × 0.16 × 0.12
Crystal system	Monoclinic	Monoclinic	Monoclinic
Space group	<i>C</i> 2/ <i>c</i>	<i>P</i> 2 ₁ / <i>n</i>	<i>P</i> 2 ₁ / <i>n</i>
<i>a</i> /Å	15.4587(10)	7.8358(5)	7.63440(10)
<i>b</i> /Å	7.9192(5)	17.916(4)	18.68230(40)
<i>c</i> /Å	11.4100(8)	10.4415(15)	10.91670(20)
α /°	90	90	90
β /°	92.629(6)	92.033(8)	91.6894(13)
γ /°	90	90	90
<i>V</i> /Å ³	1395.35(16)	1465.0(4)	1556.352(48)
<i>Z</i>	4	4	4
ρ_{calcd} /g cm ⁻³	1.66437(19)	1.7533(5)	1.75287(5)
μ /mm ⁻¹	1.687	1.298	1.228
Absorption correction	Numerical	Numerical	Multi-scan
$T_{\text{min}}, T_{\text{max}}$	0.7841, 0.9673	0.8030, 0.9456	0.693, 0.863
Refls. measured	1321	11366	25539
R_{int}	0.0622	0.0399	0.0421
Mean $\sigma(I)/I$	0.2277	0.0515	0.0298
θ range	4.53–27.55	3.90–26.04	3.21–27.49
Observed refls.	390	1933	2924
<i>x, y</i> (weighting scheme)	0.0225, 0	0.0615, 1.5586	0.0252, 1.0575
Flack parameter	–	–	–
Refls. in refinement	886	2867	3563
Parameters	69	166	236
Restraints	0	15	17
$R(F_{\text{obs}})$	0.0464	0.0452	0.0279
$R_w F^2$	0.0869	0.1237	0.0626
<i>S</i>	0.805	1.104	1.086
Shift/error _{max}	0.001	0.001	0.001
Max. res. density /e Å ⁻³	1.084	1.601	0.775
Min. res. density /e Å ⁻³	-0.462	-0.864	-0.682

6 Appendix

Table 6.43. Crystallographic tables of [Pd(phen)(EthdH₋₂)] · 7 H₂O (**7**), [Pd(phen)(AnErytH₋₂)] · 4.5 H₂O (**8**) and [Pd₂(dmen)₂(ErytH_{-4-κO^{1,2}:κO^{3,4})] · 14 H₂O (**9**).}

Compound	7	8	9
Empirical formula	C ₁₄ H ₂₆ N ₂ O ₉ Pd	C ₁₆ H ₂₃ N ₂ O _{7.50} Pd	C ₁₂ H ₅₈ N ₄ O ₁₈ Pd ₂
<i>M_r</i> /g mol ⁻¹	472.78	469.78	759.45
Crystal size /mm	0.38 × 0.02 × 0.01	0.63 × 0.06 × 0.05	0.14 × 0.12 × 0.05
Crystal system	Monoclinic	Monoclinic	Triclinic
Space group	<i>C</i> 2/ <i>c</i>	<i>C</i> 2/ <i>c</i>	<i>P</i> $\bar{1}$
<i>a</i> /Å	16.6326(6)	15.5764(3)	8.7675(2)
<i>b</i> /Å	20.2497(8)	16.0200(4)	9.8607(3)
<i>c</i> /Å	13.7653(4)	14.8394(3)	10.8518(3)
α /°	90	90	67.3597(16)
β /°	123.3336(18)	102.7301(14)	86.337(2)
γ /°	90	90	67.5770(17)
<i>V</i> /Å ³	3873.5(2)	3611.91(13)	796.62(4)
<i>Z</i>	8	8	1
ρ_{calcd} /g cm ⁻³	1.62145(8)	1.72785(6)	1.58307(8)
μ /mm ⁻¹	1.006	1.072	1.200
Absorption correction	None	None	Multi-scan
<i>T</i> _{min} , <i>T</i> _{max}	–	–	0.862, 0.942
Refls. measured	15395	15151	17568
<i>R</i> _{int}	0.0401	0.0344	0.0339
Mean $\sigma(I)/I$	0.0340	0.0262	0.0309
θ range	3.16–27.49	3.43–27.49	3.40–27.51
Observed refls.	3456	3549	3290
<i>x</i> , <i>y</i> (weighting scheme)	0.0408, 5.9439	0.0352, 11.1728	0.0333, 0.7853
Flack parameter	–	–	–
Refls. in refinement	4426	4133	3648
Parameters	288	223	209
Restraints	21	15	21
<i>R</i> (<i>F</i> _{obs})	0.0346	0.0352	0.0284
<i>R</i> _w <i>F</i> ²	0.0879	0.0891	0.0679
<i>S</i>	1.055	1.093	1.050
Shift/error _{max}	0.002	0.003	0.001
Max. res. density /e Å ⁻³	0.612	1.241	0.990
Min. res. density /e Å ⁻³	-0.773	-0.753	-0.775

6 Appendix

Table 6.44. Crystallographic tables of $[\text{Pd}_2(\text{tn})_2(\text{ErytH}_{-4}\text{-}\kappa\text{O}^{1,2}:\kappa\text{O}^{3,4})] \cdot 10 \text{ H}_2\text{O}$ (**10**), $[\text{Pd}_2(\text{tmen})_2(\text{Mann1,2;3,4H}_{-4}\text{-}\kappa\text{O}^{1,2}:\kappa\text{O}^{3,4})] \cdot 9 \text{ H}_2\text{O}$ (**11**) and $[\text{Pd}_2(\text{tn})_2(\text{Mann1,2;3,4H}_{-4}\text{-}\kappa\text{O}^{1,2}:\kappa\text{O}^{3,4})] \cdot 5 \text{ H}_2\text{O}$ (**12**).

Compound	10	11	12
Empirical formula	$\text{C}_{10}\text{H}_{46}\text{N}_4\text{O}_{14}\text{Pd}_2$	$\text{C}_{18}\text{H}_{60}\text{N}_4\text{O}_{15}\text{Pd}_2$	$\text{C}_{12}\text{H}_{40}\text{N}_4\text{O}_{11}\text{Pd}_2$
$M_r / \text{g mol}^{-1}$	659.33	785.53	629.31
Crystal size /mm	$0.164 \times 0.033 \times 0.020$	$0.11 \times 0.06 \times 0.02$	$0.218 \times 0.052 \times 0.045$
Crystal system	Monoclinic	Monoclinic	Monoclinic
Space group	$C 2/c$	$P 2_1$	$P 2_1$
$a / \text{\AA}$	20.1147(5)	8.4118(2)	8.997(3)
$b / \text{\AA}$	7.0588(2)	14.5993(5)	14.472(5)
$c / \text{\AA}$	17.9562(5)	13.5747(4)	8.997(3)
$\alpha / ^\circ$	90	90	90
$\beta / ^\circ$	104.0199(16)	98.1214(19)	109.70(3)
$\gamma / ^\circ$	90	90	90
$V / \text{\AA}^3$	2473.58(12)	1650.34(8)	1102.9(6)
Z	4	2	2
$\rho_{\text{calcd}} / \text{g cm}^{-3}$	1.77049(9)	1.58079(8)	1.8950(10)
μ / mm^{-1}	1.520	1.155	1.690
Absorption correction	None	Multi-scan	None
$T_{\text{min}}, T_{\text{max}}$	–	0.873, 0.977	–
Refls. measured	9575	27763	8387
R_{int}	0.0395	0.0932	0.0295
Mean $\sigma(I)/I$	0.0362	0.1077	0.0548
θ range	3.19–27.53	3.18–27.49	3.70–27.50
Observed refls.	2340	5274	4134
x, y (weighting scheme)	0.0427, 11.6587	0.0256, 0	0.0270, 0.7438
Flack parameter	–	0.01(3)	0.00(4)
Refls. in refinement	2823	7212	4918
Parameters	121	418	292
Restraints	15	28	16
$R(F_{\text{obs}})$	0.0350	0.0450	0.0346
$R_w F^2$	0.0913	0.0797	0.0742
S	1.047	1.018	1.066
Shift/error _{max}	0.001	0.001	0.001
Max. res. density /e \AA^{-3}	1.296	1.075	1.009
Min. res. density /e \AA^{-3}	–0.796	–0.712	–0.858

6 Appendix

Table 6.45. Crystallographic tables of [Pd₂(dmen)₂(Dulc2,3;4,5H₋₄-κO^{2,3}:κO^{4,5})] · 8 H₂O (**13**), [Pd₂(tm)₂(Dulc2,3;4,5H₋₄-κO^{2,3}:κO^{4,5})] · 6 H₂O (**14**) and [Pd₂(tmen)₂(D-Altr2,3;4,5H₋₄-κO^{2,3}:κO^{4,5})] · 9 H₂O (**15**).

Compound	13	14	15
Empirical formula	C ₁₄ H ₅₀ N ₄ O ₁₄ Pd ₂	C ₁₂ H ₄₂ N ₄ O ₁₂ Pd ₂	C ₁₈ H ₆₀ N ₄ O ₁₅ Pd ₂
<i>M_r</i> /g mol ⁻¹	711.41	647.32	785.53
Crystal size /mm	0.11 × 0.09 × 0.09	0.279 × 0.072 × 0.061	0.46 × 0.19 × 0.06
Crystal system	Triclinic	Triclinic	Monoclinic
Space group	<i>P</i> $\bar{1}$	<i>P</i> $\bar{1}$	<i>P</i> 2 ₁
<i>a</i> /Å	8.37680(20)	9.5891(2)	8.6504(2)
<i>b</i> /Å	9.08000(20)	9.9439(2)	14.3715(3)
<i>c</i> /Å	10.31420(29)	14.0725(3)	13.4329(2)
α /°	76.3950(16)	77.9963(14)	90
β /°	72.9441(15)	83.5398(14)	103.3687(12)
γ /°	70.0739(16)	62.1802(11)	90
<i>V</i> /Å ³	697.076(31)	1160.63(4)	1624.72(6)
<i>Z</i>	1	2	2
ρ _{calcd} /g cm ⁻³	1.69470(8)	1.85230(6)	1.60571(6)
μ /mm ⁻¹	1.355	1.612	1.173
Absorption correction	Multi-scan	None	Multi-scan
<i>T</i> _{min} , <i>T</i> _{max}	0.742, 0.885	–	0.765, 0.932
Refls. measured	17099	10092	26969
<i>R</i> _{int}	0.0328	0.0194	0.0508
Mean σ(<i>I</i>)/ <i>I</i>	0.0273	0.0306	0.0495
θ range	3.42–27.53	3.44–27.53	3.24–27.61
Observed refls.	2902	4438	6920
<i>x</i> , <i>y</i> (weighting scheme)	0.0290, 0.9502	0.0353, 0.9973	0, 1.1392
Flack parameter	–	–	0.016(19)
Refls. in refinement	3182	5305	7411
Parameters	183	317	434
Restraints	12	20	28
<i>R</i> (<i>F</i> _{obs})	0.0294	0.0270	0.0292
<i>R</i> _w <i>F</i> ²	0.0693	0.0718	0.0588
<i>S</i>	1.074	1.032	1.081
Shift/error _{max}	0.001	0.001	0.001
Max. res. density /e Å ⁻³	0.858	1.431	0.558
Min. res. density /e Å ⁻³	-0.854	-0.881	-0.756

6 Appendix

Table 6.46. Crystallographic tables of [Pd₂(en)₂(Allt2,3;4,5H₄-κO^{2,3}:κO^{4,5})] · 14 H₂O (**16**), [Pd₂(tmen)₂(Allt1,2;5,6H₄-κO^{1,2}:κO^{5,6})] · 8 H₂O (**17**) and [Pd₄(R,R-chxn)₄(L-ThreH₄)](NO₃)₄ · 4 H₂O (**18**).

Compound	16	17	18
Empirical formula	122	C ₁₈ H ₅₈ N ₄ O ₁₄ Pd ₂	C ₂₈ H ₇₀ N ₁₂ O ₂₀ Pd ₄
<i>M_r</i> /g mol ⁻¹	763.39	767.51	1320.60
Crystal size /mm	0.16 × 0.14 × 0.096	0.13 × 0.07 × 0.01	0.16 × 0.10 × 0.05
Crystal system	Monoclinic	Monoclinic	Monoclinic
Space group	<i>C</i> 2/ <i>c</i>	<i>P</i> 2 ₁ / <i>n</i>	<i>P</i> 2 ₁
<i>a</i> /Å	11.5082(13)	5.81720(10)	14.03440(20)
<i>b</i> /Å	12.1545(14)	30.19850(50)	11.58970(20)
<i>c</i> /Å	21.906(3)	9.22700(10)	15.33700(20)
<i>α</i> /°	90	90	90
<i>β</i> /°	103.330(10)	104.2824(9)	108.4452(9)
<i>γ</i> /°	90	90	90
<i>V</i> /Å ³	2981.5(6)	1570.814(41)	2366.474(62)
<i>Z</i>	4	2	2
<i>ρ</i> _{calcd} /g cm ⁻³	1.7007(3)	1.62273(4)	1.85335(5)
<i>μ</i> /mm ⁻¹	1.288	1.209	1.580
Absorption correction	Numerical	None	None
<i>T</i> _{min} , <i>T</i> _{max}	0.8574, 0.9547	–	–
Refls. measured	8581	7045	10583
<i>R</i> _{int}	0.0493	0.0169	0.0410
Mean <i>σ</i> (<i>I</i>)/ <i>I</i>	0.0643	0.0254	0.0296
<i>θ</i> range	3.85–27.50	3.53–27.48	3.25–27.47
Observed refls.	2963	3230	10055
<i>x</i> , <i>y</i> (weighting scheme)	0.0127, 17.3173	0.0113, 1.1406	0.0176, 1.8934
Flack parameter	–	–	–0.034(16)
Refls. in refinement	3418	3600	10583
Parameters	209	203	607
Restraints	22	12	10
<i>R</i> (<i>F</i> _{obs})	0.0659	0.0208	0.0240
<i>R</i> _w <i>F</i> ²	0.0999	0.0455	0.0516
<i>S</i>	1.231	1.063	1.054
Shift/error _{max}	0.001	0.002	0.001
Max. res. density /e Å ⁻³	0.866	0.397	0.469
Min. res. density /e Å ⁻³	–0.473	–0.476	–0.473

6 Appendix

Table 6.47. Crystallographic tables of [Pd₄(*R,R*-chxn)₄(Xylt1,2,3,4H₋₄)](NO₃)₄ · 4.7 H₂O (**19**), [Pd₄(*R,R*-chxn)₄(L-Idit2,3,4,5H₋₄)](NO₃)₄ · 6 H₂O (**20**) and [Pd₄(*R,R*-chxn)_{1.66}(*S,S*-chxn)_{2.34}(D-Mann2,3,4,5H₋₄)](NO₃)₄ · 7 H₂O (**21**).

Compound	19	20	21
Empirical formula	C ₂₉ H ₇₈ N ₁₂ O ₂₄ Pd ₄	C ₃₀ H ₇₈ N ₁₂ O ₂₄ Pd ₄	C ₃₀ H ₈₀ N ₁₂ O ₂₅ Pd ₄
<i>M_r</i> /g mol ⁻¹	1404.68	1416.69	1434.70
Crystal size /mm	0.16 × 0.11 × 0.11	0.06 × 0.04 × 0.03	0.19 × 0.16 × 0.12
Crystal system	Monoclinic	Triclinic	Orthorhombic
Space group	<i>P</i> 2 ₁	<i>P</i> 1	<i>P</i> 2 ₁ 2 ₁ 2 ₁
<i>a</i> /Å	11.54460(10)	9.6520(3)	11.50610(10)
<i>b</i> /Å	16.7369(3)	11.8693(5)	13.58680(20)
<i>c</i> /Å	13.8061(2)	12.2015(6)	33.61050(50)
α /°	90	83.166(2)	90
β /°	100.3147(9)	76.848(3)	90
γ /°	90	73.702(2)	90
<i>V</i> /Å ³	2624.51(6)	1304.20(9)	5254.366(119)
<i>Z</i>	2	1	4
ρ_{calcd} /g cm ⁻³	1.77752(4)	1.80379(12)	1.81366(4)
μ /mm ⁻¹	1.435	1.445	1.437
Absorption correction	None	None	None
<i>T</i> _{min} , <i>T</i> _{max}	—	—	—
Refls. measured	21654	11323	11951
<i>R</i> _{int}	0.0295	0.0000	0.0560
Mean $\sigma(I)/I$	0.0414	0.1115	0.0477
θ range	3.23–27.59	3.22–27.48	3.23–27.52
Observed refls.	10797	9126	10386
<i>x</i> , <i>y</i> (weighting scheme)	0.0216, 1.4224	0.0808, 0	0.0130, 6.9656
Flack parameter	−0.02(2)	−0.01(4)	−0.05(2)
Refls. in refinement	11825	11323	11951
Parameters	567	631	622
Restraints	28	3	21
<i>R</i> (<i>F</i> _{obs})	0.0288	0.0669	0.0343
<i>R</i> _w <i>F</i> ²	0.0630	0.1539	0.0610
<i>S</i>	1.077	1.022	1.032
Shift/error _{max}	0.002	0.001	0.002
Max. res. density /e Å ⁻³	0.717	3.464 ^a	0.548
Min. res. density /e Å ⁻³	−0.496	−1.136	−0.469

^a The max. residue density is found at a distance of 1.035 Å to Pd2.

6 Appendix

Table 6.48. Crystallographic tables of $[\text{Pd}_4(R,R\text{-chxn})_4(\text{D-Altr}1,2,3,4\text{H}_-4)](\text{NO}_3)_{3.57}(\text{OH})_{0.43} \cdot 12 \text{H}_2\text{O}$ (**22**), $[\text{Pd}_4(R,R\text{-chxn})_4(\text{Dulc}1,2,3,4\text{H}_-4)](\text{NO}_3)_{3.5}(\text{OH})_{0.5} \cdot 6.75 \text{H}_2\text{O}$ (**23**) and $[\{\text{Pd}_2(R,R\text{-chxn})_2(\text{HmmpdH}_-3)\}_2\text{Pd}](\text{NO}_3)_4 \cdot 4 \text{H}_2\text{O}$ (**24**).

Compound	22	23	24
Empirical formula	$\text{C}_{30}\text{H}_{90.43}\text{N}_{11.57}\text{O}_{29.14}\text{Pd}_4$	$\text{C}_{30}\text{H}_{80}\text{N}_{11.50}\text{O}_{23.75}\text{Pd}_4$	$\text{C}_{34}\text{H}_{82}\text{N}_{12}\text{O}_{22}\text{Pd}_5$
$M_r / \text{g mol}^{-1}$	1505.43	1407.70	1543.18
Crystal size / mm	$0.26 \times 0.23 \times 0.18$	$0.05 \times 0.05 \times 0.04$	$0.17 \times 0.12 \times 0.07$
Crystal system	Orthorhombic	Tetragonal	Monoclinic
Space group	$P 2_1 2_1 2_1$	$P 4_1 2_1 2$	$P 2_1$
$a / \text{\AA}$	15.11865(18)	14.1520(3)	10.6708(2)
$b / \text{\AA}$	17.6740(4)	14.1520(3)	15.3398(3)
$c / \text{\AA}$	21.9616(4)	53.1914(10)	16.8079(4)
$\alpha / ^\circ$	90	90	90
$\beta / ^\circ$	90	90	92.3206(12)
$\gamma / ^\circ$	90	90	90
$V / \text{\AA}^3$	5868.27(18)	10653.1(4)	2748.99(10)
Z	4	8	2
$\rho_{\text{calcd}} / \text{g cm}^{-3}$	1.70398(5)	1.75541(7)	1.86436(7)
μ / mm^{-1}	1.296	1.414	1.687
Absorption correction	Multi-scan	None	Multi-scan
$T_{\text{min}}, T_{\text{max}}$	0.86850, 1.00000	–	0.777, 0.889
Refls. measured	46583	18221	60056
R_{int}	0.0360	0.0523	0.0719
Mean $\sigma(I)/I$	0.0435	0.0775	0.0665
θ range	4.14–26.32	3.22–25.03	3.15–27.47
Observed refls.	10331	6866	9585
x, y (weighting scheme)	0.0454, 0	0.0765, 18.0469	0.0294, 1.4832
Flack parameter	–0.01(2)	–0.03(5)	0.03(3)
Refls. in refinement	11893	9270	12514
Parameters	664	559	682
Restraints	3	15	13
$R(F_{\text{obs}})$	0.0303	0.0555	0.0376
$R_w F^2$	0.0753	0.1420	0.0785
S	0.995	1.028	1.026
Shift/error _{max}	0.001	0.002	0.001
Max. res. density / $e \text{\AA}^{-3}$	0.712	1.034	0.981
Min. res. density / $e \text{\AA}^{-3}$	–0.479	–0.693	–0.592

6 Appendix

Table 6.49. Crystallographic tables of [Pd₆(*R,R*-chxn)₆(μ₄-O)(μ-OH)₄](NO₃)₆ · 12.5 H₂O (**25**), [Pd₄(*R,R*-chxn)₄(C₃O₆)(μ-OH)](NO₃)₃ · 8 H₂O (**26**) and [Pd₂(en)₂(*D-chiro*-Ins1,2,5,6H₄)] · 8 H₂O (**27**).

Compound	25	26	27
Empirical formula	C ₃₆ H ₁₁₃ N ₁₈ O _{35.50} Pd ₆	C ₂₇ H _{73.61} N ₁₁ O _{24.30} Pd ₄	C ₁₀ H ₄₀ N ₄ O ₁₄ Pd ₂
<i>M_r</i> /g mol ⁻¹	2004.90	1367.02	653.28
Crystal size /mm	0.24 × 0.20 × 0.09	0.15 × 0.11 × 0.08	0.144 × 0.109 × 0.039
Crystal system	Orthorhombic	Triclinic	Orthorhombic
Space group	<i>P</i> 222 ₁	<i>P</i> 1	<i>P</i> 2 ₁ 2 ₁ 2 ₁
<i>a</i> /Å	11.7782(4)	12.8502(3)	8.85720(10)
<i>b</i> /Å	13.5750(4)	14.3042(3)	8.91650(10)
<i>c</i> /Å	24.8998(8)	14.6608(3)	29.9200(5)
α /°	90	74.2946(11)	90
β /°	90	84.3330(11)	90
γ /°	90	79.2674(11)	90
<i>V</i> /Å ³	3981.2(2)	2545.51(9)	2362.94(5)
<i>Z</i>	2	2	4
ρ _{calcd} /g cm ⁻³	1.67249(8)	1.78355(6)	1.83639(4)
μ /mm ⁻¹	1.414	1.477	1.590
Absorption correction	Numerical	Multi-scan	None
<i>T</i> _{min} , <i>T</i> _{max}	0.6705, 0.8343	–	–
Refls. measured	32522	15442	16181
<i>R</i> _{int}	0.0476	0.0000	0.0622
Mean σ(<i>I</i>)/ <i>I</i>	0.0775	0.0295	0.0514
θ range	3.69–26.54	3.16–24.00	3.24–27.51
Observed refls.	5834	14400	4935
<i>x</i> , <i>y</i> (weighting scheme)	0.0592, 0	0.1087, 13.4903	0.0848, 21.5763
Flack parameter	–0.05(4)	0.02(4)	0.06(8)
Refls. in refinement	8274	15442	5396
Parameters	371	939	271
Restraints	17	9	0
<i>R</i> (<i>F</i> _{obs})	0.0406	0.0565	0.0672
<i>R</i> _w <i>F</i> ²	0.1077	0.1689	0.1782
<i>S</i>	1.016	1.049	1.094
Shift/error _{max}	0.002	0.001	0.001
Max. res. density /e Å ⁻³	0.811	1.802	7.035 ^a
Min. res. density /e Å ⁻³	–0.647	–0.685	–1.155

^a The max. residue density is found at a distance of 1.407 Å to O4.

6 Appendix

Table 6.50. Crystallographic tables of [Pd₂(tmen)₂(*neo*-Ins1,6;3,4H₄-κO^{1,6}:κO^{3,4})] · 22 H₂O (**28**), [Pd₃(tmen)₃(*scyllo*-InsH₆)] · 23 H₂O (**29**) and [Pd(*R,R*-chxn)(Me-α-D-Lyxp2,3H₂-κO^{2,3})] · 2.25 H₂O (**30**).

Compound	28	29	30
Empirical formula	C ₁₈ H ₈₄ N ₄ O ₂₈ Pd ₂	C ₂₄ H ₁₀₀ N ₆ O ₂₉ Pd ₃	C ₁₂ H _{28.50} N ₂ O _{7.25} Pd
<i>M_r</i> /g mol ⁻¹	1017.71	1256.33	423.27
Crystal size /mm	0.41 × 0.16 × 0.12	0.33 × 0.31 × 0.16	0.191 × 0.065 × 0.023
Crystal system	Orthorhombic	Monoclinic	Triclinic
Space group	<i>C mce</i>	<i>C 2/c</i>	<i>P 1</i>
<i>a</i> /Å	31.452(5)	21.3176(5)	10.8847(4)
<i>b</i> /Å	7.984(5)	21.1561(5)	12.2073(4)
<i>c</i> /Å	17.578(5)	12.0968(3)	13.9766(4)
α /°	90	90	75.205(2)
β /°	90	102.750(2)	73.759(2)
γ /°	90	90	85.9442(17)
<i>V</i> /Å ³	4414(3)	5321.1(2)	1723.89(10)
<i>Z</i>	4	4	4
ρ _{calcd} /g cm ⁻³	1.5315(10)	1.56826(6)	1.631
μ /mm ⁻¹	0.903	1.088	1.112
Absorption correction	Multi-scan	Multi-scan	Multi-scan
<i>T</i> _{min} , <i>T</i> _{max}	0.74613, 1.00000	0.73718, 1.00000	0.917, 0.975
Refls. measured	16473	17194	11792
<i>R</i> _{int}	0.0342	0.0257	0.0000
Mean σ(<i>I</i>)/ <i>I</i>	0.0369	0.0386	0.0376
θ range	4.28–26.35	3.85–26.32	3.18–25.40
Observed refls.	1427	4048	11256
<i>x</i> , <i>y</i> (weighting scheme)	0.0379, 0	0.0611, 0	0.0313, 1.4978
Flack parameter	–	–	–0.032(17)
Refls. in refinement	2276	5373	11792
Parameters	168	251	864
Restraints	22	37	30
<i>R</i> (<i>F</i> _{obs})	0.0243	0.0332	0.0301
<i>R</i> _w <i>F</i> ²	0.0652	0.0981	0.0725
<i>S</i>	0.964	1.071	1.077
Shift/error _{max}	0.001	0.001	0.001
Max. res. density /e Å ⁻³	1.030	1.491	0.706
Min. res. density /e Å ⁻³	–0.310	–0.710	–0.829

6 Appendix

Table 6.51. Crystallographic tables of [Pd(tmen)(Me-β-D-Xylp2,3H₂-κO^{2,3})]₂[Pd(tmen)(Me-β-D-Xylp3,4H₂-κO^{3,4})] · 2 H₂O (**31**), [Pd₂(tmen)₂(⁴C₁-β-D-Arap1,2;3,4H₄-κO^{1,2}:κO^{3,4})] · 10 H₂O (**32**) and [Pd₂(tmen)₂(⁴C₁-β-D-Lyxp1,2;3,4H₄-κO^{1,2}:κO^{3,4})] · 10 H₂O (**33**).

Compound	31	32	33
Empirical formula	C ₁₂ H ₂₈ N ₂ O ₆ Pd	C ₁₇ H ₅₈ N ₄ O ₁₅ Pd ₂	C ₁₇ H ₅₈ N ₄ O ₁₅ Pd ₂
<i>M_r</i> /g mol ⁻¹	402.78	771.50	771.50
Crystal size /mm	0.27 × 0.16 × 0.14	0.26 × 0.06 × 0.06	0.27 × 0.12 × 0.09
Crystal system	Monoclinic	Orthorhombic	Monoclinic
Space group	<i>P</i> 2 ₁	<i>P</i> 2 ₁ 2 ₁ 2 ₁	<i>P</i> 2 ₁
<i>a</i> /Å	8.8758(3)	8.63210(10)	8.6386(2)
<i>b</i> /Å	18.5971(6)	11.13230(10)	15.7249(4)
<i>c</i> /Å	10.3814(4)	34.1013(4)	11.9237(2)
<i>α</i> /°	90	90	90
<i>β</i> /°	106.680(4)	90	99.1973(12)
<i>γ</i> /°	90	90	90
<i>V</i> /Å ³	1641.50(10)	3276.97(6)	1598.91(6)
<i>Z</i>	4	4	2
<i>ρ</i> _{calcd} /g cm ⁻³	1.62983(10)	1.56379(3)	1.60250(6)
<i>μ</i> /mm ⁻¹	1.157	1.162	1.191
Absorption correction	Numerical	None	None
<i>T</i> _{min} , <i>T</i> _{max}	0.8312, 0.8806	–	–
Refls. measured	16208	39811	25671
<i>R</i> _{int}	0.0308	0.0578	0.0368
Mean <i>σ</i> (<i>I</i>)/ <i>I</i>	0.0614	0.0445	0.0416
<i>θ</i> range	3.73–27.53	3.22–27.54	3.17–27.49
Observed refls.	6039	6665	6473
<i>x</i> , <i>y</i> (weighting scheme)	0.0175, 0	0.0378, 0.6835	0.0320, 0.6978
Flack parameter	–0.034(18)	–0.01(2)	–0.02(2)
Refls. in refinement	7304	7487	6954
Parameters	403	413	429
Restraints	7	30	34
<i>R</i> (<i>F</i> _{obs})	0.0291	0.0315	0.0329
<i>R</i> _w <i>F</i> ²	0.0466	0.0714	0.0737
<i>S</i>	0.897	1.030	1.153
Shift/error _{max}	0.001	0.001	0.001
Max. res. density /e Å ⁻³	0.678	0.858	1.454
Min. res. density /e Å ⁻³	–0.432	–0.481	–0.765

6 Appendix

Table 6.52. Crystallographic tables of [Pd(tmen)(⁴C₁-Me- α -D-Galp3,4H₂- κ O^{3,4})] · 8 H₂O (**34**), [Pd(dmen)(⁴C₁-Me- α -D-Galp3,4H₂- κ O^{3,4})] · 9 H₂O (**35**) and [Pd(tmen)(⁴C₁-Me- α -D-Manp2,3H₂- κ O^{2,3})] · 3.5 H₂O (**36**).

Compound	34	35	36
Empirical formula	C ₁₃ H ₄₄ N ₂ O ₁₄ Pd	C ₁₁ H ₄₂ N ₂ O ₁₅ Pd	C ₁₃ H ₃₅ N ₂ O _{9.50} Pd
<i>M_r</i> /g mol ⁻¹	558.91	548.88	477.84
Crystal size /mm	0.20 × 0.14 × 0.13	0.29 × 0.25 × 0.18	0.24 × 0.17 × 0.12
Crystal system	Triclinic	Triclinic	Monoclinic
Space group	<i>P</i> 1	<i>P</i> 1	<i>P</i> 2 ₁
<i>a</i> /Å	8.0080(3)	7.613(3)	10.4616(2)
<i>b</i> /Å	9.1901(4)	8.9634(16)	16.6146(3)
<i>c</i> /Å	9.1977(3)	9.508(3)	11.8413(2)
α /°	81.453(3)	80.656(18)	90
β /°	66.651(4)	69.15(3)	91.9489(12)
γ /°	82.925(3)	83.10(2)	90
<i>V</i> /Å ³	613.02(4)	596.9(3)	2057.01(6)
<i>Z</i>	1	1	4
ρ_{calcd} /g cm ⁻³	1.51400(10)	1.5270(8)	1.54300(5)
μ /mm ⁻¹	0.821	0.844	0.949
Absorption correction	Numerical	Numerical	Multi-scan
<i>T</i> _{min} , <i>T</i> _{max}	0.7714, 0.9168	0.7986, 0.8981	0.702, 0.892
Refls. measured	11233	6019	32629
<i>R</i> _{int}	0.0320	0.0192	0.0468
Mean $\sigma(I)/I$	0.0559	0.0271	0.0485
θ range	3.69–27.58	4.07–26.32	3.44–27.52
Observed refls.	5317	4054	8858
<i>x</i> , <i>y</i> (weighting scheme)	0.0287, 0	0.0286, 0	0.0352, 1.0101
Flack parameter	-0.049(18)	-0.023(13)	-0.019(19)
Refls. in refinement	5624	4096	9379
Parameters	301	326	496
Restraints	18	30	19
<i>R</i> (<i>F</i> _{obs})	0.0293	0.0186	0.0328
<i>R</i> _w <i>F</i> ²	0.0596	0.0441	0.0753
<i>S</i>	0.976	1.017	1.052
Shift/error _{max}	0.001	0.001	0.002
Max. res. density /e Å ⁻³	0.533	0.523	0.989
Min. res. density /e Å ⁻³	-0.366	-0.303	-0.744

6 Appendix

Table 6.53. Crystallographic tables of methyl β -D-fructopyranoside (**37**), [Pd(*R,R*-chxn)(Me- α -D-Fru) μ 1,3H₂- κ O^{1,3})] · 2 H₂O (**38**) and [Pd₂(tmen)₂(α -D-Tagp1,2;3,4H₄- κ O^{1,2}: κ O^{3,4})] · 8 H₂O (**39**).

Compound	37	38	39
Empirical formula	C ₇ H ₁₄ O ₆	C ₁₃ H ₃₀ N ₂ O ₈ Pd	C ₁₈ H ₅₆ N ₄ O ₁₄ Pd ₂
<i>M_r</i> /g mol ⁻¹	194.182	448.81	765.50
Crystal size /mm	0.51 × 0.49 × 0.15	0.22 × 0.034 × 0.018	0.08 × 0.02 × 0.01
Crystal system	Monoclinic	Triclinic	Orthorhombic
Space group	<i>C</i> 2	<i>P</i> 1	<i>P</i> 2 ₁ 2 ₁ 2 ₁
<i>a</i> /Å	14.9990(8)	7.3885(2)	6.3980(4)
<i>b</i> /Å	5.4114(3)	10.1980(3)	12.9167(8)
<i>c</i> /Å	10.8287(6)	13.1923(4)	37.819(3)
α /°	90	93.4184(16)	90
β /°	99.477(5)	105.5699(18)	90
γ /°	90	107.126(2)	90
<i>V</i> /Å ³	866.92(8)	904.63(4)	3125.4(3)
<i>Z</i>	4	2	4
ρ_{calcd} /g cm ⁻³	1.48781(14)	1.64768(7)	1.62687(16)
μ /mm ⁻¹	0.131	1.067	1.215
Absorption correction	Multi-scan	Multi-scan	None
<i>T</i> _{min} , <i>T</i> _{max}	0.96170, 1.00000	0.957, 0.981	–
Refls. measured	2886	11046	10843
<i>R</i> _{int}	0.0148	0.0340	0.0768
Mean $\sigma(I)/I$	0.0159	0.0535	0.0838
θ range	4.32–26.33	3.20–25.04	3.15–22.47
Observed refls.	914	5559	3115
<i>x</i> , <i>y</i> (weighting scheme)	0.0418, 0.2748	0.0875, 0	0.0255, 23.7372
Flack parameter	– ^a	0.00(3)	–0.03(8)
Refls. in refinement	976	5738	4004
Parameters	123	457	386
Restraints	1	15	21
<i>R</i> (<i>F</i> _{obs})	0.0266	0.0425	0.0639
<i>R</i> _w <i>F</i> ²	0.0694	0.1168	0.1283
<i>S</i>	1.048	1.076	1.118
Shift/error _{max}	0.001	0.001	0.001
Max. res. density /e Å ⁻³	0.187	2.668 ^b	0.857
Min. res. density /e Å ⁻³	–0.153	–0.794	–0.644

^a The absolute structure parameter was meaningless because the compound was a weak anomalous scatterer. Therefore, the Friedel pairs were averaged. ^b The max. residue density is found at a distance of 1.335 Å to Pd2.

6 Appendix

Table 6.54. Crystallographic tables of [Pd₂(tmen)₂(Ery4ald/H₄-κO^{1,4}:κO^{2,3})] · 12 H₂O (**40**), 2,3,4,5-di-*O*-isopropylidene-*D*-manno-hexodialdose (**41**) and [Pd₃(teen)₃(α-CDH₆)] · 34 H₂O (**42**).

Compound	40	41	42
Empirical formula	C ₁₆ H ₆₀ N ₄ O ₁₇ Pd ₂	C ₁₂ H ₁₈ O ₆	C ₆₆ H ₁₉₄ N ₆ O ₆₄ Pd ₃
<i>M_r</i> /g mol ⁻¹	793.50	258.268	2415.51
Crystal size /mm	0.13 × 0.11 × 0.02	0.31 × 0.21 × 0.11	0.33 × 0.20 × 0.18
Crystal system	Monoclinic	Monoclinic	Hexagonal
Space group	<i>P</i> 2 ₁	<i>P</i> 2 ₁	<i>P</i> 6 ₃
<i>a</i> /Å	8.2183(5)	7.9003(13)	16.7917(5)
<i>b</i> /Å	25.2484(18)	7.6953(11)	16.7917(5)
<i>c</i> /Å	8.8236(5)	10.5548(15)	23.9134(7)
α /°	90	90	90
β /°	117.200(3)	91.200(14)	90
γ /°	90	90	120
<i>V</i> /Å ³	1628.43(18)	641.54(17)	5839.3(3)
<i>Z</i>	2	2	2
ρ _{calcd} /g cm ⁻³	1.61832(18)	1.3370(4)	1.37383(7)
μ /mm ⁻¹	1.176	0.107	0.553
Absorption correction	None	Multi-scan	Numerical
<i>T</i> _{min} , <i>T</i> _{max}	–	0.95477, 1.00000	0.8272, 0.9139
Refls. measured	7627	4549	8062
<i>R</i> _{int}	0.0275	0.0337	0.0398
Mean σ(<i>I</i>)/ <i>I</i>	0.0488	0.0423	0.0878
θ range	3.22–25.34	4.20–26.47	3.79–26.31
Observed refls.	4215	1151	2747
<i>x</i> , <i>y</i> (weighting scheme)	0, 5.7724	0.0801, 0	0.0927, 0
Flack parameter	0.44(7) ^a	– ^b	–0.01(5)
Refls. in refinement	5081	1400	4604
Parameters	247	167	418
Restraints	37	1	1
<i>R</i> (<i>F</i> _{obs})	0.0399	0.0466	0.0540
<i>R</i> _w <i>F</i> ²	0.0837	0.1220	0.1526
<i>S</i>	1.140	1.036	0.958
Shift/error _{max}	0.001	0.001	0.001
Max. res. density /e Å ⁻³	0.795	0.315	1.449
Min. res. density /e Å ⁻³	–0.582	–0.208	–1.161

^a The compound was found to be an inversion twin which is indicated by the Flack parameter. ^b The absolute structure parameter was meaningless because the compound was a weak anomalous scatterer. Therefore, the Friedel pairs were averaged.

6 Appendix

Table 6.55. Crystallographic tables of [Pd₃(tmen)₃(α -CDH₋₆)] · 20.7 H₂O · acetone (**43**), [Pd₄(teen)₄(γ -CDH₋₈)] · 12 H₂O (**44**) and [Pd₄(tmen)₄(γ -CDH₋₈)] · 65.79 H₂O · 0.96 [Pd(tmen)CO₃] (**45**).

Compound	43	44	45
Empirical formula	C ₅₇ H _{149.41} N ₆ O _{51.71} Pd ₃	C ₈₈ H ₁₉₂ N ₈ O ₅₂ Pd ₄	C _{150.72} H _{418.94} N _{17.92} O _{148.67} Pd _{8.96}
M_r /g mol ⁻¹	2065.84	2620.17	13766.8
Crystal size /mm	0.38 × 0.25 × 0.17	0.12 × 0.07 × 0.05	0.15 × 0.16 × 0.22
Crystal system	Monoclinic	Orthorhombic	Monoclinic
Space group	$P 2_1$	$P 2_1 2_1 2_1$	$P 2_1$
a /Å	12.6353(3)	12.7934(2)	13.2690(1)
b /Å	26.4900(6)	27.5126(5)	35.6901(4)
c /Å	15.4585(4)	38.1396(7)	29.0741(3)
α /°	90	90	90
β /°	113.631(3)	90	90.9467(5)
γ /°	90	90	90
V /Å ³	4740.2(2)	13424.4(4)	13766.8(2)
Z	2	4	2
ρ_{calcd} /g cm ⁻³	1.44739(6)	1.29643(4)	1.371
μ /mm ⁻¹	0.659	0.608	0.672
Absorption correction	Numerical	None	None
$T_{\text{min}}, T_{\text{max}}$	0.7758, 0.8818	–	–
Refls. measured	35164	55587	67108
R_{int}	0.0309	0.1418	0.0485
Mean $\sigma(I)/I$	0.0557	0.1322	0.0716
θ range	3.86–26.41	3.15–21.96	3.1–23.5
Observed refls.	13713	10103	29826
x, y (weighting scheme)	0.0698, 0	0.1253, 69.0451	0.01046, 58.2289
Flack parameter	–0.057(17)	–0.02(5)	0.01(2)
Refls. in refinement	16966	16336	37973
Parameters	1079	675	1608
Restraints	8	2	1
$R(F_{\text{obs}})$	0.0403	0.0903	0.0758
$R_w F^2$	0.1089	0.2520	0.2046
S	1.024	1.025	1.026
Shift/error _{max}	0.034	0.001	0.001
Max. res. density /e Å ⁻³	0.839	0.893	0.95
Min. res. density /e Å ⁻³	–0.615	–0.587	–0.63

Bibliography

- [1] R. A. Dwek, *Chem. Rev.* **1996**, *96*, 683–720.
- [2] A. Persidis, *Nat. Biotech.* **1997**, *15*, 479–480.
- [3] T. K. Lindhorst, *Chem. Unserer Zeit* **2000**, *34*, 38–52.
- [4] B. Ernst, J. L. Magnani, *Nat. Rev. Drug. Discov.* **2009**, *8*, 661–677.
- [5] V. S. R. Rao, P. K. Qasba, P. V. Balaji, R. Chandrasekaran, *Conformation of Carbohydrates*, Harwood Academic Publishers, **1998**.
- [6] B. Wenig, Fachagentur Nachwachsende Rohstoffe e.V. (FNR), **2007**.
- [7] ECO SYS GmbH, Schopfheim, *Stoffliche Verwertung von Kohlenhydraten in der Bundesrepublik Deutschland, Vol. FKZ 22018709*, Fachagentur Nachwachsende Rohstoffe e.V. (FNR), **2009**.
- [8] R. B. Friedman, in *Glycoscience* (Eds.: B. Fraser-Reid, K. Tatsuta, J. Thiem), Springer-Verlag, Berlin Heidelberg, **2008**, pp. 841–856.
- [9] F. W. Lichtenthaler, in *Methods and Reagents for Green Chemistry: An Introduction* (Eds.: P. Tundo, A. Perosa, F. Zecchini), J. Wiley, Hoboken, NJ, **2007**, pp. 23–63.
- [10] K. Hill, O. Rhode, *Lipid / Fett* **1999**, *101*, 25–33.
- [11] D. Klemm, B. Heublein, H.-P. Fink, A. Bohn, *Angew. Chem.* **2005**, *117*, 3422–3458.
- [12] A. S. Serianni, in *Bioorganic Chemistry: Carbohydrates* (Ed.: S. Hecht), Oxford University Press, **1999**, pp. 244–312.
- [13] S. J. Angyal, *Angew. Chem. Int. Ed.* **1969**, *8*, 157–166.
- [14] Y. Zhu, J. Zajicek, A. S. Serianni, *J. Org. Chem.* **2001**, *66*, 6244–6251.
- [15] O. Hassel, B. Ottar, *Acta Chem. Scand.* **1947**, *20*, 1943–1954.
- [16] R. E. Reeves, *J. Am. Chem. Soc.* **1950**, *72*, 1499–1506.
- [17] R. E. Reeves, *Adv. Carbohydr. Chem.* **1951**, *6*, 107–134.
- [18] M. K. Dowd, W. M. Rockey, A. D. French, P. J. Reilly, *J. Carbohydr. Chem.* **2002**, *21*, 11–25.
- [19] M. K. Dowd, A. D. French, P. J. Reilly, *J. Carbohydr. Chem.* **2000**, *19*, 1091–1114.
- [20] V. Kräutler, M. Müller, P. H. Hünenberger, *Carbohydr. Res.* **2007**, *342*, 2097–2124.
- [21] J. L. Dashnau, K. A. Sharp, J. M. Vanderkooi, *J. Phys. Chem. B* **2005**, *109*, 24152–24159.
- [22] D. Cremer, J. A. Pople, *J. Am. Chem. Soc.* **1975**, *97*, 1354–1358.
- [23] S. T. Rao, E. Westhof, M. Sundaralingam, *Acta Cryst. A* **1981**, *37*, 421–425.
- [24] A. D. French, P. Finch, *Carbohydrates: structures, syntheses and dynamics*, Kluwer Academic Publishers, **1999**.
- [25] M. Karplus, *J. Am. Chem. Soc.* **1963**, *85*, 2870–2871.
- [26] C. Altona, in *Encyclopedia of NMR* (Eds.: D. M. Grant, R. Morris), Wiley, New York, **1996**, pp. 4909–4923.
- [27] M. J. Minch, *Concepts Magn. Reson.* **1994**, *6*, 41–56.
- [28] C. A. G. Haasnoot, F. A. A. M. de Leeuw, C. Altona, *Tetrahedron* **1980**, *36*, 2783–2792.
- [29] H. Booth, *Tetrahedron Lett.* **1965**, *6*, 411–416.
- [30] R. J. Abraham, G. Gatti, *J. Chem. Soc. B* **1969**, 961–968.
- [31] M. L. Huggins, *J. Am. Chem. Soc.* **1953**, *75*, 4126–4133.
- [32] E. Díez, J. San-Fabian, J. Guilleme, C. Altona, L. A. Donders, *Mol. Phys.* **1989**, *68*, 49–63.
- [33] A. Navarro-Vázquez, J. C. Cobas, F. J. Sardina, J. Casanueva, E. Díez, *J. Chem. Inf. Comput. Sci.* **2004**, *44*, 1680–1685.
- [34] G. E. Taylor, J. M. Waters, *Tetrahedron Lett.* **1981**, *22*, 1277–1278.

Bibliography

- [35] T. Allscher, P. Klüfers, *Carbohydr. Res.* **2009**, *344*, 539–540.
- [36] P. Klüfers, T. Kunte, *Angew. Chem. Int. Ed.* **2001**, *40*, 4210–4212.
- [37] Y. Arendt, O. Labisch, P. Klüfers, *Carbohydr. Res.* **2009**, *344*, 1213–1224.
- [38] P. Klüfers, T. Kunte, *Eur. J. Inorg. Chem.* **2002**, *2002*, 1285–1289.
- [39] P. Klüfers, T. Kunte, *Chem. Eur. J.* **2003**, *9*, 2013–2018.
- [40] E. Schweizer, *J. Prakt. Chem.* **1857**, *72*, 109–111.
- [41] R. Ahlrichs, M. Ballauff, K. Eichkorn, O. Hanemann, G. Kettenbach, P. Klüfers, *Chem. Eur. J.* **1998**, *4*, 835–844.
- [42] X. Kästele, P. Klüfers, T. Kunte, *Z. Anorg. Allg. Chem.* **2001**, *627*, 2042–2044.
- [43] M. Steinborn, Bachelor thesis **2007**, Ludwig-Maximilians-Universität München.
- [44] P. Braun, research report **2008**, Ludwig-Maximilians-Universität München.
- [45] S. Amann, research report **2008**, Ludwig-Maximilians-Universität München.
- [46] T. Kunte, Diplomarbeit **1999**, Ludwig-Maximilians-Universität München.
- [47] J. F. Remenar, B. L. Lucht, D. B. Collum, *J. Am. Chem. Soc.* **1997**, *119*, 5567–5572.
- [48] M. Suzuki, Y. Nishida, *Inorg. Chim. Acta* **1979**, *34*, 61–65.
- [49] H. Yasuda, J.-C. Choi, S.-C. Lee, T. Sakakura, *Organometallics* **2002**, *21*, 1216–1220.
- [50] J. Pushkar, O. F. Wendt, *Inorg. Chim. Acta* **2004**, *357*, 1295–1298.
- [51] T. G. Appleton, J. R. Hall, *Inorg. Chem.* **1972**, *11*, 112–117.
- [52] T. G. Appleton, J. R. Hall, *Inorg. Chem.* **1972**, *11*, 117–124.
- [53] J. A. Walmsley, S. Zhu, A. Matilla, T. G. Donowick, J. E. Cramp, J. M. Tercero, T. Dalrymple, *Inorg. Chem.* **2007**, *46*, 9945–9953.
- [54] S. G. Fox, R. D. Gillard, *Polyhedron* **1988**, *7*, 349–352.
- [55] S. Wimmer, P. Castan, F. L. Wimmer, N. P. Johnson, *J. Chem. Soc. Dalton Trans.* **1989**, 403–412.
- [56] M. Odoko, Y. Wang, N. Okabe, *Acta Cryst. E* **2004**, *60*, m1825–m1827.
- [57] M. Achternbosch, P. Klüfers, *Acta Cryst. C* **1994**, *50*, 175–178.
- [58] T. Allscher, X. Kästele, G. Kettenbach, P. Klüfers, T. Kunte, *Chem. Asian J.* **2007**, *2*, 1037–1045.
- [59] X. Kästele, P. Klüfers, T. Kunte, *Z. Anorg. Allg. Chem.* **2001**, *627*, 2042–2044.
- [60] J. Bernstein, R. E. Davis, L. Shimoni, N.-L. Chang, *Angew. Chem. Int. Ed.* **1995**, *34*, 1555–1573.
- [61] T. Allscher, Master thesis **2006**, Ludwig-Maximilians-Universität München.
- [62] P. Gans, A. Sabatini, A. Vacca, *Talanta* **1996**, *43*, 1739–1753.
- [63] L. Cao, M. C. Jennings, R. J. Puddephatt, *Dalton Trans.* **2009**, 5171–5176.
- [64] V. K. Jain, L. Jain, *Coord. Chem. Rev.* **2005**, *249*, 3075–3197.
- [65] V. K. Jain, L. Jain, *Coord. Chem. Rev.* **2010**, *254*, 2848–2903.
- [66] R. Faggiani, B. Lippert, C. J. L. Lock, B. Rosenberg, *J. Am. Chem. Soc.* **1977**, *99*, 777–781.
- [67] R. Faggiani, B. Lippert, C. J. L. Lock, B. Rosenberg, *Inorg. Chem.* **1977**, *16*, 1192–1196.
- [68] J.-P. Macquet, S. Cros, A. L. Beauchamp, *J. Inorg. Biochem.* **1985**, *25*, 197–206.
- [69] F. D. Rochon, A. Morneau, R. Melanson, *Inorg. Chem.* **1988**, *27*, 10–13.
- [70] M. Steinborn, *unpublished*.
- [71] T. Allscher, Y. Arendt, P. Klüfers, *Carbohydr. Res.* **2010**, *345*, 2381–2389.
- [72] T. Allscher, P. Klüfers, O. Labisch, *Carbohydr. Res.* **2007**, *342*, 1419–1426.
- [73] O. Glemser, G. Peuschel, *Z. Anorg. Allg. Chem.* **1955**, *281*, 44–53.
- [74] Y. Zhang, J. Puddephatt, L. Manojlovic-Muir, K. W. Muir, *Chem. Commun.* **1996**, 2599–2600.
- [75] IUPAC, *Eur. J. Biochem.* **1975**, *57*, 1–7.
- [76] M. Freytag, Dissertation **2004**, Ludwig-Maximilians-Universität München.

Bibliography

- [77] K. Bock, H. Thøgersen, in *Annual Reports on NMR Spectroscopy, Vol. 13* (Ed.: G. A. Webb), Academic Press, **1983**, pp. 1–57.
- [78] Y. Arendt, Dissertation **2008**, Ludwig-Maximilians-Universität München.
- [79] K. N. Drew, J. Zajicek, G. Bondo, B. Bose, A. S. Serianni, *Carbohydr. Res.* **1998**, *307*, 199–209.
- [80] F. H. Cano, C. Foces-Foces, J. Jimenez-Barbero, A. Alemany, M. Bernabe, M. Martin-Lomas, *Carbohydr. Res.* **1988**, *175*, 119–131.
- [81] P. Voß, *Starch - Stärke* **1980**, *32*, 24–27.
- [82] T. Allscher, P. Klüfers, *Acta Cryst. C* **2010**, *66*, o321–o323.
- [83] R. G. S. Ritchie, N. Cyr, B. Korsch, H. J. Koch, A. S. Perlin, *Can. J. Chem.* **1975**, *53*, 1424–1433.
- [84] P. C. M. Herve du Penhoat, A. S. Perlin, *Carbohydr. Res.* **1974**, *36*, 111–120.
- [85] G. J. Wolff, E. Breitmaier, *Chem. Ztg.* **1979**, *103*, 232–233.
- [86] S. J. Angyal, G. S. Bethell, *Aust. J. Chem.* **1976**, *29*, 1249–1265.
- [87] F. W. Lichtenthaler, S. Ronninger, *J. Chem. Soc. Perkin Trans. 2* **1990**, 1489–1497.
- [88] D. J. Watkin, A. F. G. Glawar, R. Soengas, U. P. Skytte, M. R. Wormald, R. A. Dwek, G. W. J. Fleet, *Acta Cryst. E* **2005**, *61*, o2891–o2893.
- [89] D. J. Watkin, A. F. G. Glawar, R. Soengas, K. Izumori, M. R. Wormald, R. A. Dwek, G. W. J. Fleet, *Acta Cryst. E* **2005**, *61*, o2949–o2951.
- [90] V. Bonnet, R. Duval, C. Rabiller, *J. Mol. Catal. B: Enzym.* **2003**, *24-25*, 9–16.
- [91] R. Schoevaart, T. Kieboom, *Carbohydr. Res.* **2001**, *334*, 1–6.
- [92] R. Schoevaart, T. Kieboom, *Carbohydr. Res.* **2002**, *337*, 899–904.
- [93] R. Schoevaart, T. Kieboom, *Top. Catal.* **2004**, *27*, 3–9.
- [94] G. Cousins, A. Falshaw, J. O. Hoberg, *Carbohydr. Res.* **2003**, *338*, 995–998.
- [95] H. Paulsen, W. von Deyn, W. Röben, *Liebigs Ann. Chem.* **1984**, 433–449.
- [96] G. F. Painter, A. Falshaw, *J. Chem. Soc., Perkin Trans. 1* **2000**, 1157–1159.
- [97] C. E. Ballou, H. O. L. Fischer, *J. Am. Chem. Soc.* **1953**, *75*, 4695–4698.
- [98] P. E. Pfeffer, K. B. Hicks, *Carbohydr. Res.* **1982**, *102*, 11–22.
- [99] J. C. Hanson, L. C. Sieker, L. H. Jensen, *Acta Cryst. B* **1973**, *29*, 797–808.
- [100] A. Neuman, D. Avenel, H. Gillierpandraud, *Acta Cryst. B* **1978**, *34*, 242–248.
- [101] G. A. Jeffrey, D. B. Huang, P. E. Pfeffer, R. L. Dudley, K. B. Hicks, E. Nitsch, *Carbohydr. Res.* **1992**, *226*, 29–42.
- [102] J. Mayer, J. Conrad, I. Klaiber, S. Lutz-Wahl, U. Beifuss, L. Fischer, *J. Agric. Food Chem.* **2004**, *52*, 6983–6990.
- [103] J. Thiem, M. Kleeberg, K. H. Klaska, *Carbohydr. Res.* **1989**, *189*, 65–77.
- [104] W. Dreissig, P. Luger, *Acta Cryst. B* **1973**, *29*, 503–514.
- [105] D. Avenel, A. Neuman, H. Gillier-Pandraud, *Acta Cryst. B* **1976**, *32*, 2598–2605.
- [106] J. H. Smith, S. E. Dann, M. R. J. Elsegood, S. H. Dale, C. G. Blatchford, *Acta Cryst. E* **2005**, *61*, o2499–o2501.
- [107] E. Kalenius, T. Kekaelaenen, R. Neitola, K. Beyeh, K. Rissanen, P. Vainiotalo, *Chem-Eur J* **2008**, *14*, 5220–5228.
- [108] B. R. Leeftang, J. F. G. Vliegthart, L. M. J. Kroonbatenburg, B. P. Vaneijck, J. Kroon, *Carbohydr. Res.* **1992**, *230*, 41–61.
- [109] F. Takusagawa, R. A. Jacobson, *Acta Cryst. B* **1978**, *34*, 213–218.
- [110] M. E. Gress, G. A. Jeffrey, *Acta Cryst. B* **1977**, *33*, 2490–2495.
- [111] H. Sugiyama, T. Nitta, M. Horii, K. Motohashi, J. Sakai, T. Usui, K. Hisamichi, J.-i. Ishiyama, *Carbohydr. Res.* **2000**, *325*, 177–182.
- [112] J. F. Robyt, in *Glycoscience* (Eds.: B. Fraser-Reid, K. Tatsuta, J. Thiem), Springer-Verlag, Berlin Heidelberg, **2008**, pp. 1437–1472.
- [113] D. Armspach, G. Gattuso, R. Königer, J. F. Stoddart, in *Bioorganic Chemistry: Carbohydrates* (Ed.: S. Hecht), Oxford University Press, **1999**, pp. 458–488.

Bibliography

- [114] W.-Z. Shen, D. Gupta, B. Lippert, *Inorg. Chem.* **2005**, *44*, 8249–8258.
- [115] Y. Mo, *Nat Chem* **2010**, *2*, 666–671.
- [116] G. M. Sheldrick, *Acta Cryst. A* **2008**, *64*, 112–122.
- [117] A. Altomare, M. C. Burla, M. Camalli, G. L. Cascarano, C. Giacovazzo, A. Guagliardi, A. G. G. Moliterni, G. Polidori, R. Spagna, *J. Appl. Crystallogr.* **1999**, *32*, 115–119.
- [118] A. L. Spek, *J. Appl. Crystallogr.* **2003**, *36*, 7–13.
- [119] L. J. Farrugia, *J. Appl. Crystallogr.* **1997**, *30*, 565.
- [120] E. Keller, *J. Appl. Cryst.* **1989**, *22*, 19–22.
- [121] A. G. Evdokimov, F. Frolow, *Acta Cryst. C* **1996**, *52*, 3218–3219.
- [122] J. A. Stapley, J. N. BeMiller, *Carbohydr. Res.* **2007**, *342*, 610–613.
- [123] M. J. Frisch, G. W. Trucks, H. B. Schlegel, G. E. Scuseria, M. A. Robb, J. R. Cheeseman, J. A. Montgomery, T. Vreven, K. N. Kudin, J. C. Burant, J. M. Millam, S. S. Iyengar, J. Tomasi, V. Barone, B. Mennucci, M. Cossi, G. Scalmani, N. Rega, G. A. Petersson, H. Nakatsuji, M. Hada, M. Ehara, K. Toyota, R. Fukuda, J. Hasegawa, M. Ishida, T. Nakajima, Y. Honda, O. Kitao, H. Nakai, M. Klene, X. Li, J. E. Knox, H. P. Hratchian, J. B. Cross, V. Bakken, C. Adamo, J. Jaramillo, R. Gomperts, R. E. Stratmann, O. Yazyev, A. J. Austin, R. Cammi, C. Pomelli, J. W. Ochterski, P. Y. Ayala, K. Morokuma, G. A. Voth, P. Salvador, J. J. Dannenberg, V. G. Zakrzewski, S. Dapprich, A. D. Daniels, M. C. Strain, O. Farkas, D. K. Malick, A. D. Rabuck, K. Raghavachari, J. B. Foresman, J. V. Ortiz, Q. Cui, A. G. Baboul, S. Clifford, J. Cioslowski, B. B. Stefanov, G. Liu, A. Liashenko, P. Piskorz, I. Komaromi, R. L. Martin, D. J. Fox, T. Keith, A. Laham, C. Y. Peng, A. Nanayakkara, M. Challacombe, P. M. W. Gill, B. Johnson, W. Chen, M. W. Wong, C. Gonzalez, J. A. Pople, *Gaussian 03, Revision C.02*, Gaussian, Inc., Wallingford, CT, **2004**.
- [124] W. J. Stevens, M. Krauss, H. Basch, P. G. Jasien, *Can. J. Chem.* **1992**, *70*, 612–630.

List of publications

On the Basics of Carbohydrate-Metal Chemistry: Complexes of Palladium(II) with Hydroxyaldehyde and -ketone Hydrates (Polyol Metal Complexes, Part 56)

T. Allscher, P. Klüfers, O. Labisch, *Carbohydr. Res.* **2007**, *342*, 1419–1426.

Sugar-Alcohol Complexes of Palladium(II): on the Variable Rigidity of Open-Chain Carbohydrate Ligands (Polyol Metal Complexes, Part 57)

T. Allscher, X. Kästele, G. Kettenbach, P. Klüfers, T. Kunte, *Chem. Asian J.* **2007**, *2*, 1037–1045.

Carbohydrate-Metal Complexes: Structural Chemistry of Stable Solution Species

T. Allscher, P. Klüfers, P. Mayer, *Glycoscience*, B. Fraser-Reid, K. Tatsuta, J. Thiem (eds), Springer-Verlag Berlin Heidelberg 2008.

The Complex Packing Pattern of *cis*-1,2-dimethylcyclobutane-1,2-diol

T. Allscher, R. Betz, S. Herdlicka, P. Klüfers, *Acta Cryst. C* **2008**, *C64*, o111–o113.

The Crystal Structure of a Lyxose-bridged Dimolybdate: a Redetermination of the first Monosaccharide-Metal Complex's Structure

T. Allscher, P. Klüfers, *Carbohydr. Res.* **2009**, *344*, 539–540.

4,7-Diaza-1-azoniacyclononane bromide

T. Allscher, P. Klüfers, C. Neumann, *Acta Cryst. E* **2009**, *E65*, o1734.

Methyl β -D-fructopyranoside

T. Allscher, P. Klüfers, *Acta Cryst. C* **2010**, *C66*, o321–o323.

Conformational Fluctuation in Palladium(II)–Methyl Aldopentopyranoside Complexes

T. Allscher, Y. Arendt, P. Klüfers, *Carbohydr. Res.* **2010**, *345*, 2381–2389.

Danksagung

Danksagung

Ich möchte allen danken, die durch ihre Unterstützung zu dieser Arbeit beigetragen haben:

Herrn Prof. Dr. Peter Klüfers möchte ich für die interessante Themenstellung, für die hervorragenden Arbeitsbedingungen, sowie für die wertvollen Anregungen und vor allem für den gewährten wissenschaftlichen Freiraum danken.

Herrn Prof. Dr. Konstantin Karaghiosoff danke ich für die Erstellung des Zweitgutachtens, Herrn Prof. Dr. Manfred Heuschmann, Herrn Prof. Dr. Wolfgang Beck, Herrn Prof. Dr. Jürgen Evers und Herrn PD Hans-Christian Böttcher für die Teilnahme am Promotionskolloquium.

Mein besonderer Dank gilt Christine Neumann für ihre große Unterstützung, Hilfe und für ihre vielen wertvollen Ratschläge. Danke für die gute Zusammenarbeit zu allen Zeiten.

Lida Holowatyj-den Toom möchte ich nicht nur für das Korrekturlesen und ihre Hilfe bei allen organisatorischen Dingen danken, sondern auch für die vielen aufmunternden und interessanten Gespräche.

Xaver Kästele danke ich für die gute Zusammenarbeit bei der Betreuung der Messgeräte und für seine Hilfestellung bei allen Fragen und Problemen. Sandra Albrecht danke vor allem für ihre Unterstützung während des MINT-Projektes.

Ganz besonders möchte ich auch den Mitarbeitern der Analytik, besonders der NMR-Abteilungen der Anorganik und der Pharmazie danken, Herrn Peter Mayer, Herrn Dr. Holger Lerche, Herrn Dr. Lars Allmendinger, Frau Waltraud Bogatsch, Frau Ursula Gross und Frau Claudia Glas, die jede noch so ausgefallene Messung durchgeführt haben und ohne die meine Arbeit nicht in dieser Form möglich gewesen wäre.

Den Aufsetzern Sandra Albrecht, Matthias Hinrichs, Anna Zangl, Phillipp Lorenz, Tobias Kerscher, Helene Giglmeier, Moritz Reichsvilser, Anna Filser, Johanna Schulten und Xaver Wurzenberger danke ich für das oftmals mühevollen Aufsetzen winziger Kristallsplitter.

Danksagung

Martin Steinborn möchte ich besonders für die umfassende Hilfestellung bei den Rechnungen und bei allen Fragen und Problemen rund um Gaussian danken.

Ebenso möchte ich mich bei meinen anderen Bachelor- und Forschungspraktikanten Sebastian Schneider, Sandra Amann und Patricia Braun für ihre Mitarbeit an meinem Forschungsthema bedanken.

Allen ehemaligen und aktuellen Mitarbeitern des Arbeitskreises danke ich für die gute Zusammenarbeit, ganz besonders Yvonne Arendt, auf deren hervorragenden Vorarbeiten ich aufbauen konnte und die mich für dieses Thema begeistert hat.

Mein besonderer Dank gilt Martin Breugst, der mit mir zusammen in den letzten neun Jahren die Höhen und Tiefen des Chemiestudiums und der Promotion durchgestanden hat. Danke für die Unterstützung!

Der allergrößte Dank gebührt meiner Familie. Ohne die bedingungslose Unterstützung in jeglicher Hinsicht hätte ich es nie so weit geschafft. Vielen Dank!

Lebenslauf

Lebenslauf

Persönliche Daten

Name	Thorsten Allscher
Geburtsdatum	02. Februar 1981
Geburtsort	Altötting am Inn
Staatsangehörigkeit	deutsch

Schulbildung

1991–2000	<i>Abitur</i> , Gymnasium Gars, Gars am Inn
-----------	---

Wehrdienst

06/2000–04/2001	Grundwehrdienst Germersheim / Erding
-----------------	--------------------------------------

Hochschulausbildung

09/2001–09/2004	<i>Bachelor of Science</i> , Studium der Chemie und Biochemie an der Ludwig-Maximilians-Universität München
-----------------	---

09/2004–09/2006	<i>Master of Science</i> , Studium der Chemie und Biochemie an der Ludwig-Maximilians-Universität München
-----------------	---

seit 10/2006	Promotion am Lehrstuhl für Bioanorganische Chemie und Koordinationschemie der Ludwig-Maximilians-Universität München
--------------	--

Berufserfahrung

seit 10/2006	<i>Wissenschaftlicher Angestellter</i> , Department Chemie, Ludwig-Maximilians-Universität München
--------------	--

Preise und Auszeichnungen

12/2010	Preis der Dr. Klaus Römer-Stiftung
---------	------------------------------------